Springer Proceedings in Physics 168

Mohamed Belhaq *Editor*

Structural Nonlinear Dynamics and Diagnosis

Selected papers from CSNDD 2012 and CSNDD 2014

Springer

Springer Proceedings in Physics

Volume 168

More information about this series at http://www.springer.com/series/361

Mohamed Belhaq
Editor

Structural Nonlinear Dynamics and Diagnosis

Selected papers from CSNDD 2012 and CSNDD 2014

Springer

Editor
Mohamed Belhaq
Laboratory of Mechanics
Hassan II-Casablanca University
Casablanca
Morocco

ISSN 0930-8989 ISSN 1867-4941 (electronic)
Springer Proceedings in Physics
ISBN 978-3-319-19850-7 ISBN 978-3-319-19851-4 (eBook)
DOI 10.1007/978-3-319-19851-4

Library of Congress Control Number: 2015941355

Springer Cham Heidelberg New York Dordrecht London

Printed on acid-free paper

Springer International Publishing AG Switzerland is part of Springer Science+Business Media (www.springer.com)

Preface

Structural nonlinear dynamics and diagnosis (*SNDD*) are of great concern to engineers, physicists, and mathematicians. They are multidisciplinary and encountered in many applications such as vibro-impact of mechanical structures, aeroelastic flutter, fatigue fracture, microelectromechanical systems, and energy harvesting systems. The aim of the two international conferences *CSNDD'2014* and *CSNDD'2014* held, respectively, in Marrakech (Morocco), April 30–May 2, 2012 and in Agadir (Morocco), May 21–23, 2014, is to provide a forum for the discussion of recent developments in the theory and industrial applications of structural nonlinear dynamics and diagnosis. This *SNDD* biannual conference offers a meeting place where scientists from different branches of applied mathematics, applied mechanics, and advanced physics working in nonlinear dynamics and control can meet to discuss the latest achievements and to exchange ideas in theoretical, numerical, and experimental advances in the field. Focuses are directed toward diverse topics, ranging from the theoretical of dynamical systems to different physical and engineering applications. The link between fundamental and applied nonlinear dynamics is one of the stimulating goals of the *SNDD* conference. A special effort has been to invite active researchers from engineering, science, and applied mathematics communities. These two technical meetings have indeed updated engineers with recent analytical developments of *SNDD* and at the same time allowed engineers and industrial practioners to alert mathematicians with their unresolved issues.

This book presents the contributions of some distinguished participants in the two meetings. Both conferences were organized by the nonlinear dynamic group of the Hassan II University of Casablanca and have attracted representatives from the international scientific community in nonlinear dynamics, from more than 30 nationalities. There were more than 250 communications from scientists working in nonlinear dynamics from all over the world and more than 350 participants attended the meetings. The book addresses the state of the art and presents the most active current lines of research in the field of structural nonlinear dynamics. A wide audience of researchers in this field may have an advantage of the material

presented in this book. The book includes 22 chapters contributed by outstanding colleagues covering various aspects of applications grouped as follows:

- The first group comprises of six chapters related to structural health monitoring, diagnosis, damage detection, and energy harvesting.
- The second group consists of six chapters covering experimental methods, active vibration control, passive control of structures via nonlinear energy sinks, and microelectromechanical systems.
- The third group is comprised of ten chapters dealing with nonlinear dynamics, vibro-impact dynamics, and aeroelastic dynamics.

Researchers and engineers interested in challenges and opportunities posed by nonlinearities in the development of structural health monitoring, diagnosis and damage detection, control strategies, energy harvesting, novel design criteria, modeling, and characterization will find an outstanding introduction and useful resources of their current needs. We hope this book will provide valuable resources to graduate students involved in structural nonlinear dynamics and diagnosis.

The organizers of *CSNDD 2012* and *CSNDD 2014* would like to thank the generous contributions made by a number of individuals and institutions. In particular, the organizers would like to acknowledge the financial contributions of the University Hassan II-Casablanca, the University de Le Havre, University Mohamed I-Oujda, École Centrale de Lyon, ENSEM—Casablanca, the Academy Hassan II of Sciences and Techniques, CNRST, International Union of Mathematics, Polytechnic Institute of Casablanca, MANAGEM group, SOGELAB, and MASTE TEC.

June 2015

Mohamed Belhaq
Laboratory of Mechanics
Hassan II University of Casablanca

Contents

Contributors

Eihab Abdel-Rahman University of Waterloo, Waterloo, ON, Canada

K. Al Hosani The Petroleum Institute, Abu Dhabi, UAE

N. Al Sayari The Petroleum Institute, Abu Dhabi, UAE

M. Al-Numay King Saud University, Riyadh, KSA

Etienne Averlant Faculté des Sciences de l'Université Libre de Bruxelles, Brussels, Belgium; IR-TONA, Vrije Universiteit Brussel, Brussels, Belgium

M.A. Aziz Alaoui Normandie Univ, Caen, France; ULH, LMAH, Le Havre, France; FR CNRS 3335, ISCN, Le Havre, France

José Manoel Balthazar Mechanical Aeronautics Division, ITA—Aeronautics Technological Institute, São José dos Campos, SP, Brazil; Faculty of Mechanical Engineering, UNESP—São Paulo State University, Bauru, SP, Brazil

Mohamed Belhaq University Hassan II-Casablanca, Casablanca, Morocco

Mohamed Bendame University of Waterloo, Waterloo, ON, Canada

Reyolando Manoel Lopes Rebello da Fonseca Brasil CECS—Center of Engineering, Modelling and Applied Social Science, UFABC—Federal University of Santo André, Santo André, SP, Brazil

Michael J. Brennan Universidade Estadual Paulista, Ilha Solteira (SP), Brazil

Atila Madureira Bueno Department of Control and Automation Engineering, UNESP—São Paulo State University, Sorocaba, Brazil

Biagio Carboni Department of Structural and Geotechnical Engineering, Sapienza University of Rome, Rome, Italy

Michel S. Chalhoub Department of Civil and Environmental Engineering, Notre Dame University, Louaize, Lebanon

Olivier Doaré Unité de Mécanique (UME), ENSTA-ParisTech, Palaiseau Cedex, France

Francesco D'Annibale M&MoCS—University of L'Aquila, L'Aquila (AQ), Italy

A. El Aroudi University Rovira i Virgili, Tarragona, Spain

A. El Hami LOFIMS, INSA de Rouen, Rouen, France

Jorge Luis Palacios Felix Technological Center of Alegrete, UNIPAMPA—Federal University of Pampa, Alegrete, RS, Brazil

Gianluca Gatti University of Calabria, Rende (CS), Italy

Svetlana Gurevich Institut Für Theoretische Physik, Münster, Germany

A. Holeyman Université Catholique de Louvain, iMMC, GeoMEM, Louvain-la-Neuve, Belgium

Raouf A. Ibrahim Department of Mechanical Engineering, Wayne State University, Detroit, USA

Itamar Iliuk Department of Telecommunication Engineering and Control, EPUSP—Polytechnic School of the University of São Paulo, São Paulo, Brazil

Elżbieta M. Jarzębowska Warsaw University of Technology, Institute of Aeronautics and Applied Mechanics, Warsaw, Poland

Ilham Kirrou University Hassan II-Casablanca, Casablanca, Morocco

Ivana Kovacic Faculty of Technical Sciences, University of Novi Sad, Novi Sad, Serbia

C.A. Kitio Kwuimy Center for Nonlinear Dynamics and Control, Department of Mechanical Engineering, Villanova University, Villanova, PA, USA

Walter Lacarbonara Department of Structural and Geotechnical Engineering, Sapienza University of Rome, Rome, Italy

Faouzi Lakrad University Hassan II-Casablanca, Casablanca, Morocco

C.-H. Lamarque ENTPE, Université de Lyon, LGCB and LTDS UMR CNRS 5513, Vaulx En Velin, France

Angelo Luongo M&MoCS—University of L'Aquila, L'Aquila (AQ), Italy

Arnaud Malher Unité de Mécanique (UME), ENSTA-ParisTech, Palaiseau Cedex, France

Carlo Mancini Department of Structural and Geotechnical Engineering, Sapienza University of Rome, Rome, Italy

Peter A. Meleshenko Digital Technologies Department, Voronezh State University, Voronezh, Russia; Communication Department, Zhukovsky–Gagarin Air Force Academy, Voronezh, Russia

Lahcen Mokni University Hassan II-Casablanca, Casablanca, Morocco

Francesco Mosti Brembo S.p.A, Stezzano, Italy

C. Nataraj Center for Nonlinear Dynamics and Control, Department of Mechanical Engineering, Villanova University, Villanova, PA, USA

Krassimir Panayotov IR-TONA, Vrije Universiteit Brussel, Brussels, Belgium; Institute of Solid State Physics, Sofia, Bulgaria

Vinícius Piccirillo Department of Mathematics, UTFPR—Federal Technological University of Paraná, Ponta Grossa, Brazil

Alexander Pimenov Weierstrass Institute, Berlin, Germany

Giuseppe Quaranta Department of Structural and Geotechnical Engineering, Sapienza University of Rome, Rome, Italy

B. Radi LIMMII, FST Settat, Settat, Morocco

Rodrigo Tumolin Rocha Faculty of Mechanical Engineering, UNESP—São Paulo State University, Bauru, SP, Brazil

Andrey M. Semenov Materials Science and Nanosystems Technologies Department, Voronezh State University, Voronezh, Russia

Mikhail E. Semenov Meteorology Department, Zhukovsky–Gagarin Air Force Academy, Voronezh, Russia; Digital Technologies Department, Voronezh State University, Voronezh, Russia; Mathematics Department, Voronezh State University of Architecture and Civil Engineering, Voronezh, Russia

Mostafa Soliman Department of Energy Conversion and Power Electronics, Electronics Research Institute, Giza, Egypt

Andrey M. Solovyov Digital Technologies Department, Voronezh State University, Voronezh, Russia

Mustapha Tlidi Faculté des Sciences de l'Université Libre de Bruxelles, Brussels, Belgium

Cyril Touzé Unité de Mécanique (UME), ENSTA-ParisTech, Palaiseau Cedex, France

A. Ture Savadkoohi ENTPE, Université de Lyon, LGCB and LTDS UMR CNRS 5513, Vaulx En Velin, France

Ângelo Marcelo Tusset Department of Mathematics, UTFPR—Federal Technological University of Paraná, Ponta Grossa, Brazil

Andrei Vladimirov Weierstrass Institute, Berlin, Germany

V. Whenham Fugro Geoconsulting Belgium, Brussels, Belgium

Radouane Yafia Polydisciplinary Faculty of Ouarzazate, Ibn Zohr University, Ouarzazate, Morocco

Daniele Zulli M&MoCS—University of L'Aquila, L'Aquila (AQ), Italy

Recent Advances of Structural Life Assessment and Related Problems

Raouf A. Ibrahim

Abstract Structural life assessment (SLA) is a diversified field and is based on the theories of fracture mechanics, fatigue damage process, probability of failure and reliability. SLA is not only governed by the theory of fracture mechanics and fatigue damage process, but by the type of loading. The theory of fracture mechanics may be classified into quasi-static fracture mechanic and dynamic fracture mechanics. The problem of singularity encountered in fracture mechanics has been resolved by the new theory of peridynamics described by integro-differential equation of motion. The basic ingredients of the theory of fracture mechanics will be presented in terms of linear elastic fracture mechanics (LEFM) and elasto-plastic fracture mechanics (EPFM), dynamic fracture mechanics and peridynamics. The amount of energy available for fracture is usually governed by the stress field around the crack, which is measured by the stress intensity factor. SLA depends on the failure modes and the probabilistic description of failure.

1 Introduction

Structural life assessment (SLA) periodically evaluates the state and condition of a structural system and provides recommendations for possible maintenance actions or the end of structural service life. It basically relies on the theory of fracture mechanics and reliability theory. Fracture mechanics deals with the study of the propagation of cracks in a structural element. It seeks to establish the local stress and strain fields around a crack tip in terms of local parameters such as the loading and the geometry of the structure. The theory of fracture mechanics opens the way to analyze engineering structures that experience predetermined amounts of stable and unstable crack growth. On the other hand, the reliability theory describes the probability of a structure to perform its expected function during an interval of time. The opposite of reliability is failure probability per unit time or over time, such as a life cycle.

R.A. Ibrahim (✉)
Department of Mechanical Engineering, Wayne State University, Detroit 48098, USA
e-mail: ibrahim@eng.wayne.edu

M. Belhaq (ed.), *Structural Nonlinear Dynamics and Diagnosis*,
Springer Proceedings in Physics 168, DOI 10.1007/978-3-319-19851-4_1

Reliability-based methods include the analysis of fatigue life of structural details based on the cyclic stress against the logarithmic scale of cycles to failure (known as S-N curve) approach and on the assumption that fatigue damage accumulation is a linear phenomenon. The S-N curve is based on experimental measurements of fatigue life in terms of cycles to failure for different loading levels and specimen geometries. For some materials there is a theoretical value for stress amplitude below which it will not fail for any number of cycles, called *fatigue limit*, *endurance limit*, or *fatigue strength*. Fatigue life is thus specified by the number of stress cycles of a specified character that a specimen sustains before failure of a specified nature occurs.

SLA and structural health monitoring (SHM) are linked and complement each other with the purpose of maintaining structural systems in operation in spite of inevitable aging and degradations resulting from operational environments. The presence of a fatigue crack can lead to loss of effectiveness of a structural element when the crack reaches a critical size. Thus, the net section that resists longitudinal loads is reduced. The two main approaches for assessing fatigue strength are the *S-N* for crack initiation assessment and fracture mechanics for crack propagation assessment. The *S-N* approach predicts the strength based on crack initiation of a critical structural detail as a function of the number of stress cycles. The fracture mechanics approach can be used in risk analysis based on crack propagation assessment.

While SLA relies on periodic evaluations of structure conditions, SHM deals with the detection and identification of the structure damage and its location during operation. SHM also involves the observation of a structure over time using sampled dynamic response measurements from an array of sensors, the extraction of damage-sensitive features from these measurements, and the statistical analysis of these features to determine the current state of the structure health. The damage may be manifested by changes in the material and/or geometric properties of a structural system, including changes to the boundary conditions and system connectivity. These changes adversely affect the structure performance. SLA and SHM are overlapping in the some aspects of structural systems integrity. However, in SHM, the assessment of damage requires a comparison between two system states, namely the state of perfect structure characteristics and the state of defected structure characteristics. SLA and SHM share common issues such as identification and quantification of cracks, fatigue assessment, and impact-induced damage.

An approach for integrating the information obtained from SHM in the life-cycle performance assessment of ship structures under uncertainty was developed by Okasha and Frangopol [69] and Okasha et al. [70]. A strategy was proposed by Lynch et al. [62] for fatigue life estimation of a ship hull using a wireless sensor network installed in the hull for autonomous health monitoring. Experimental tests were conducted on an aluminum hull stiffened element specimen as part of the monitored aluminum hull integrity test program to verify the embedded fatigue life estimation procedures. The Office of Naval Research (ONR) Ship Structural Reliability Program Sielski et al. [83] indicated that SHM can enhance safety and reduce total ownership costs for all ships, particularly high-speed aluminum vessels. The prior experience of high-speed vessels is limited and the operational demands of these vessels require a means to assess the performance of such high-speed ships and

evaluate their structural health conditions in real time. A fully-effective monitoring system would monitor operational loads, detect performance degradation and structural damage in the earliest possible stage, predicting the time to potential structural failure and providing strategies for corrective actions.

This paper is organized as follows. Section 2 provides a brief account of the theory of fracture mechanics starting from the linear elastic fracture mechanics (LEFM) inaugurated by Griffith's criterion and its sequence to the elasto-plastic fracture mechanics (EPFM) described the J-integral. In view of the limitations of quasi-static fracture mechanics, the need for the dynamic fracture characterized for non-Hookean materials (hyperelasticity) is addressed in Sect. 3 including an introduction to the basic foundation of peridynamic as an emerging theory in solid mechanics.

2 Fundamentals of Fracture Mechanics

2.1 Linear and Weakly Nonlinear Criteria

Fracture mechanics was inaugurated by Griffith [43] criterion of linear elastic strains of brittle materials. Fracture mechanics is based on the existence of an initial crack and subsequent crack propagation under cyclic loading. Generally, the theory of fracture mechanics is divided into linear elastic fracture mechanics (LEFM) and elastic-plastic fracture mechanics (EPFM). LEFM is convenient for brittle-elastic materials such as low-carbon steel, stainless steel, certain aluminum alloys and polymers. Plasticity will always precede fracture. The linear theory (LEFM) is governed by a parameter called the stress intensity factor, which determines the entire crack tip stress field and measures the material toughness [80]. On the other hand, if fracture is accompanied by considerable plastic deformation the EPFM is used. The fracture parameters used in EPFM is referred to as the J-integral, which measures the strain energy release rate,[1] and the crack-tip opening displacement (CTOD). The next few subsections provide a brief description of these criteria.

Griffith [43] developed a linear elastic fracture criterion for brittle materials. He recognized that the difference between the energy released if a crack was extended and the energy needed to create new surfaces would result in a force for crack extension. Figure 1 shows a cracked structure with a crack length $2a$ and subjected to uniaxial loading of stress σ. Griffith estimated the strain energy stored per unit thickness to be

$$U_e = -\frac{\pi a^2 \sigma^2}{E} \tag{1}$$

[1] Note that the term "rate" does not refer to derivative with respect to time. In this context it refers to derivative with respect to the size of the crack.

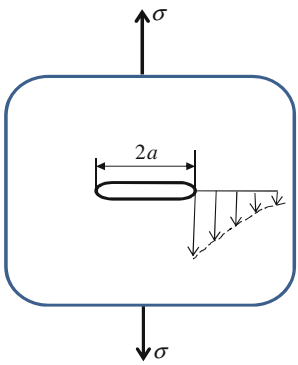

Fig. 1 Cracked structure under uniaxial tension showing the stress concentration at the crack tip

where E is Young's modulus of the material and the minus sign indicates that this energy would be released from the material. The energy associated with the surface area of the crack per unit thickness is

$$U_s = 2(2a)\gamma \tag{2}$$

where γ is the material specific surface energy density. Griffith assumed that the crack will propagate under constant applied stress, σ, if an incremental increase in crack length produces no change in the total energy of the surface. In other words, the derivative of the total energy with respect to a vanishes, i.e.,

$$\frac{d}{da}[U_e + U_s] = 0 \tag{3}$$

This condition results in the critical stress, σ_{cr},

$$\sigma_{cr} = \sqrt{\frac{2E\gamma}{\pi a}} \tag{4}$$

Condition (4) is known as the Griffith criterion, which states that *the change of surface energy must be greater than the change of strain energy in order to maintain the integrity of a structure member*.

In ductile materials, a plastic zone may develop at the tip of the crack as shown in Fig. 2. As the applied load increases, the plastic zone increases in size until the crack grows and the material behind the crack tip unloads. The plastic loading and unloading cycle near the crack tip leads to the dissipation of energy in the form of heat. Hence, a dissipative term has to be added to the energy balance relation devised by Griffith for brittle materials. In physical terms, additional energy is needed for crack growth in ductile materials when compared to brittle materials. Irwin [51, 52] divided the energy into the stored elastic strain energy, which is released as a crack grows, and another portion due to the dissipated energy, which includes plastic dissipation

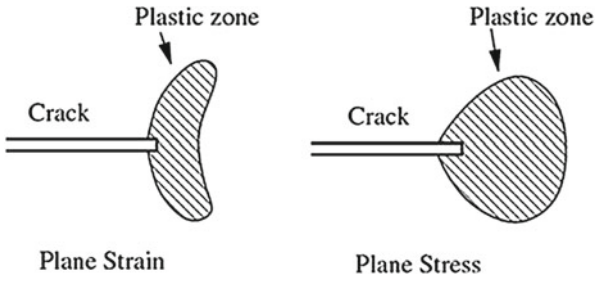

Fig. 2 The plastic zone around a crack tip in a ductile material

and the surface energy. The dissipated energy provides the thermodynamic resistance to fracture and its value per unit area of the crack ($G = -\partial U/\partial a$) is

$$G = 2\gamma + G_p \tag{5}$$

where G_p is the plastic dissipation (and dissipation from other sources) per unit area of crack growth. The modified version of Griffith's energy criterion can then be written as

$$\sigma_f = \sqrt{\frac{EG}{\pi a}} \tag{6}$$

Note that the crack extension occurs when $G = 2\gamma = R$, where R is called the material resistance to crack extension. Depending on how G and R vary with the crack size the crack growth may be stable or unstable. A plot of R versus crack extension is called a resistance or R-curve. The corresponding plot of G versus crack extension is the driving force. Condition for the stable crack growth is $\frac{dG}{dR} \leq \frac{dR}{da}$, while the condition for unstable crack growth is $\frac{dG}{dR} > \frac{dR}{da}$. A material with a rising R-curve, however, cannot be uniquely characterized with a single value of G. According to the condition of unstable crack growth a flawed structure fails when the driving force curve is tangent with R curve, but this point of tangency depends on the shape of the driving force, which depends on configuration of the structure.

The stress intensity factor is usually used to determine the stress state near the tip of a crack. It is applied to homogeneous, linear elastic material and is useful for providing a failure criterion for brittle materials. Irwin determined the amount of energy available for fracture in terms of the asymptotic stress and displacement fields around a crack front in linear elastic solids. This asymptotic expression for the stress field near a crack tip is given in terms of polar coordinates, r, θ by the formula

$$\sigma_{ij} \approx \left(\frac{K}{\sqrt{2\pi r}}\right) f_{ij}(\theta) + \text{higher order terms} \tag{7}$$

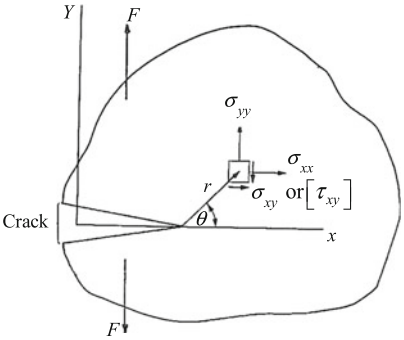

Fig. 3 Stress field with arbitrary crack under mod-I loading

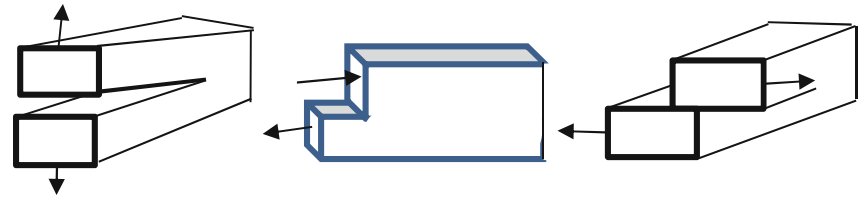

Fig. 4 Modes of crack loading

where σ_{ij} are the Cauchy stresses, r is the distance from the crack tip, θ is the angle with respect to the plane of the crack, and f_{ij} are (nondimensional) functions that are dependent on the geometry and loading conditions (see Fig. 3). Irwin called the quantity K as the *stress intensity factor*. It is seen that (7) involves singularity close to the tip as $r \to 0$. Since the quantity f_{ij} is dimensionless, the stress intensity factor can be expressed in units of stress $\times \sqrt{\text{length}}$.

Three linearly independent cracking modes are used in fracture mechanics usually referred as mode-I, -II, or -III as shown in Fig. 4. Mode-I is an opening (tensile) mode where the crack surfaces move directly apart. Mode-II is a sliding (in-plane shear) mode where the crack surfaces slide over one another in a direction perpendicular to the leading edge of the crack. Mode-III is a tearing (anti-plane shear) where the crack surfaces move relative to one another and parallel to the leading edge of the crack. The energy release rate for crack growth or *strain energy release rate* may then be calculated as the change in elastic strain energy per unit area of crack growth, i.e.,

$$G = -\left(\frac{\partial U}{\partial a}\right)_P = -\left(\frac{\partial U}{\partial a}\right)_u \tag{8}$$

where U is the elastic energy of the system. Subscripts P and u stand for fixed load and fixed displacement, respectively, while evaluating the above expressions.

For isotropic, homogeneous and linear elastic material, Irwin showed that the strain energy release rate, G, for a mode-I crack (opening mode) is related to the stress intensity factor K_I:

$$G = G_I = \begin{cases} \frac{K_I^2}{E} & \text{plane stress} \\ \frac{(1-\nu^2)K_I^2}{E} & \text{plain strain} \end{cases} \tag{9a}$$

where ν is Poisson's ratio, and K_I is the stress intensity factor in mode-I. Irwin also showed that the strain energy release rate of a planar crack in a linear elastic body can be expressed in terms of the three modes' stress intensity factors for the most general loading conditions. For pure mode-II loading relations (9a) are valid by replacing K_I by K_{II}. For mode-III loading, the strain energy release rate is given by the expression

$$G = K_{III}^2 \left(\frac{1}{2\bar{G}} \right) \tag{9b}$$

where $\bar{G}$ is the shear modulus. Under general loading in plane strain, the strain energy release rate takes the following expression

$$G = \left(K_I^2 + K_{II}^2 \right) \frac{(1-\nu^2)}{E} + K_{III}^2 \frac{1}{2\bar{G}} \tag{9c}$$

Irwin made an additional assumption that the size and shape of the energy dissipation zone remain approximately constants during brittle fracture. This assumption suggests that the energy needed to create a unit fracture surface is a constant and depends only on the material. This new material property was given the name *fracture toughness* and designated by G_{Ic}. It is referred to as the critical stress intensity factor, K_c. For mode-I, fracture occurs when $K_I \geq K_{Ic}$.

The material fracture toughness and energy release rate are usually measured by a crack tip opening displacement test. The crack opening displacement (COD) method employs the crack-tip opening displacement (CTOD), see Fig. 5. Crack-tip opening displacement (CTOD or δ) is defined as the displacement transverse to the crack-tip. The apparent advance of the crack tip is known as the crack opening stretch (COS). CTOD is used for materials that can show some plastic deformation before failure occurs causing the tip to stretch open.

The CTOD is estimated from the measurement of the displacement of a clip gage across the crack tips. It is assumed that the CTOD, δ, is the sum of elastic δ_e and plastic, δ_p, components i.e., $\delta = \delta_e + \delta_p$. Approximate expressions for CTOD are given in Broek [16] for LEFM and EPFM as follows:

$$\delta_e \approx \frac{G}{\sigma_y} = \frac{K^2}{E\sigma_y} \qquad \text{(LEFM)} \tag{10a}$$

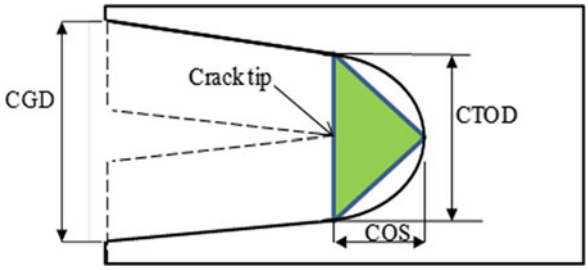

Fig. 5 Definition of crack tip opening displacement (CTOD), crack opening stretch (COS), and clip gage displacement (CGD) or crack opening displacement (COD)

$$\delta \approx \frac{J}{\sigma_y} \qquad \text{(EPFM)} \tag{10b}$$

where G is the energy release rate (dU/da) and σ_y is the yield stress. Fracture occurs at a critical value of G, (or K) or a critical value of the J-integral.

Paris and Erdogan [75] introduced a power law relationship between the crack growth rate during cyclic loading and the range of the stress intensity factor $\Delta K = K_{\max} - K_{\min}$, where $K_{\max}$ and $K_{\min}$ are the maximum and minimum stress intensity factors, respectively, in the form

$$\frac{da}{dN} = c\,(\Delta K)^m \tag{11}$$

where N is the number of load cycles, m is the slope between da/dN and ΔK (in log-log scale) as shown in Fig. 6. c is the material constant and represents the coefficient at the interception of the log-log plot. The term on the left side, known as the *crack growth rate*, denotes the infinitesimal crack length growth per increasing number of load cycles. The three regions shown in Fig. 6 are: region-I exhibits a slow crack growing, region-II represents the power-law region, and region-III is the terminal stage whose end defines the ultimate fracture.

Paris' law can be used to quantify the residual life (in terms of load cycles) of a specimen for a given crack size. Defining the crack intensity factor as

$$K = \sigma Y \sqrt{\pi a} \tag{12}$$

where σ is a uniform tensile stress perpendicular to the crack plane and Y is a dimensionless parameter that depends on the geometry. The range of the stress intensity factor is

$$\Delta K = \Delta\sigma Y \sqrt{\pi a} \tag{13}$$

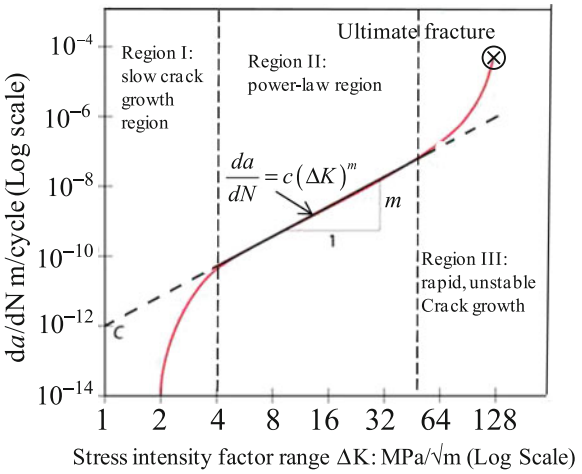

Fig. 6 Typical relationship between the crack growth rate and the range of the stress intensity factor showing three regions of crack development for a given stress ratio

where $\Delta\sigma$ is the range of cyclic stress amplitude. $Y = 1$ is taken for the case of a center crack in an infinite sheet. The remaining cycles can be found by substituting this equation in the Paris law

$$\frac{da}{dN} = C\,(\Delta K)^m = C\left(\Delta\sigma Y\sqrt{\pi a}\right)^m \tag{14}$$

For relatively short cracks, Y can be assumed to be independent of a and the differential equation can be solved using separation of variables to give

$$N_f = \frac{2\left(a_c^{\frac{2-m}{2}} - a_i^{\frac{2-m}{2}}\right)}{C(2-m)\left(\Delta\sigma Y\sqrt{\pi}\right)^m} \tag{15}$$

where N_f is the remaining number of cycles to fracture, a_c is the critical crack length above which instantaneous fracture will occur, and a_i is the initial crack length above which fatigue crack growth starts for the given stress range $\Delta\sigma$. If Y strongly depends on a, numerical methods might be required to find reasonable solutions.

2.2 Nonlinear Criterion and the J-Integral

Most engineering materials show some nonlinear elastic and inelastic behavior under operating conditions involving large loads. In such materials the plastic zone at a crack tip may have a size of the same order of magnitude as the crack size. Furthermore,

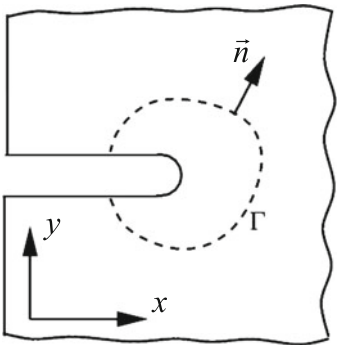

Fig. 7 J-integral around a crack tip in two dimensions

the size and shape of the plastic zone may change as the applied load increases and also as the crack length increases. The J-integral describes the strain energy release rate, $-dU/da$, or energy per unit fracture surface area in a body subjected to monotonic loading. Rice [79] showed that the value of the J-integral represents the energy release rate for planar crack growth. With reference to Fig. 7, the J-integral is a line integral given by the expression

$$J = \int_{\Gamma} \left(W(x, y)dy - \vec{T} \cdot \frac{\partial \vec{u}}{\partial x} ds \right) \tag{16}$$

where $W(x, y) = \int_0^{\varepsilon_{ij}} \sigma_{ij} \cdot d(\varepsilon_{ij})$ is the strain energy density, $\vec{T} = \vec{n} \cdot \vec{\sigma}$ is the surface traction vector acting on a segment ds, $\vec{\sigma}$ is the Cauchy stress tensor, $\vec{n}$ is the normal to the curve Γ, $\vec{u}$ is a displacement vector along arc s. For plane strain, under mode -I loading, this relation takes the form (see (9a)):

$$J_{Ic} = G_{Ic} = K_{Ic}^2 \left(\frac{1 - \nu^2}{E} \right) \tag{17}$$

where G_{Ic} is the critical strain energy release rate, K_{Ic} is the fracture toughness in mode-I loading. For mode-II and mode-III loadings, the relation between the J-integral and the mode fracture toughness takes the same form after replacing the subscript I by II or III, respectively.

2.3 Boundary-Layer Effect

The behavior of a multilayered fiber-reinforced composite laminate near its geometric boundaries received extensive experimental and analytical studies (see, e.g., [53, 71–74, 76–78, 96, 100]). These studies revealed that complex stress states with rapid change of gradients occur along the edges of composite laminates. This phenomenon

is due to interactions of geometric discontinuities of the composite and materials discontinuities through the laminate thickness. It was found to occur only within very local region near the geometric boundaries of a composite laminate. It is frequently referred to as "*boundary-layer effect*" or "*free-edge effect*." This problem is unique to composite laminates and not observed in homogeneous solids in general. It was shown that the boundary-layer effect is three-dimensional in nature and is considered as one of the most fundamental and important problems in the mechanics and mechanical behavior of composite laminates. The high interlaminar stresses are known to be the dominant factor causing delamination. Wang and Choi [97–99] concluded that the boundary-layer or free-edge stress field in a composite laminate is inherently singular in nature due to the geometric and material discontinuities. Furthermore, the order of boundary-layer stress singularity can be determined by solving for the transcendental characteristic equation obtained from the homogeneous solution of the governing partial differential equations. The boundary-layer stress singularity depends only upon material's elastic constants and fiber orientations of adjacent plies in composite laminates.

Pipes et al. [77], Herakovich et al. [49] and Sun and Zhou [95] found that the high stresses developed in the boundary-layer region coupled with the low interlaminar strength are responsible for the initiation and growth of local heterogeneous damage in the forms of interlaminar (delamination) and intralaminar (transverse cracking) fracture in composite laminates under static loading. Christensen [22] and Wilkins et al. [102] found that these stresses have significant effects on the long term strength of composite laminates under cyclic fatigue loading.

The three-dimensional stress field, developed at the free-edge of an externally loaded composite laminated plate, was found to exist in a thin layer close to the free-edge layer. It may cause delamination, well before the expected failure of the matrix or fibers. It is mainly explained by the mismatch of the elastic material properties between two adjacent dissimilar laminate layers. The free-edge effect is characterized by the concentrated three-dimensional and singular stress fields at the free edges in the interfaces between two layers of composite laminates. An assessment of modeling techniques and the effect of stress field for symmetric laminates subjected to different load condition was presented by Soni and Pagano [93], Murthy and Chamis [67], Bar-Yoseph and Ben-David [6, 7] and Mittelstedt and Becker [66]. It was found that the edge effect is more dominant in tension than in bending loading for symmetric and unsymmetric laminates, and more pronounced for symmetric angle-ply than for unsymmetric angle-ply laminates. The main difficulty of analyzing unsymmetrically laminated shells is due to the coupling of different modes of loading and deflection.

Gu and Reddy [46] developed a finite-element model based on the quasi-three-dimensional elasticity theory of Pipes and Pagano [76, 78] to examine the effect of geometric nonlinearity on free-edge stress fields in composite laminates subjected to in-plane loads. It was found that the qualitative nature of the stresses remains the same as those obtained in the linear analysis, but the nonlinear stresses are larger in magnitude by 5–40 %, depending on the laminate. However, in most cases the difference was found to be about 10 %. An analytical, parametric study of the attenuation of bending boundary layers in balanced and unbalanced, symmetrically

and unsymmetrically laminated thin cylindrical shells was presented by Nemeth and Smeltzer [68] for nine contemporary material systems. It was found that the effect of anisotropy in the form of coupling between pure bending and twisting has a negligible effect on the size of the bending boundary-layer attenuation length of symmetrically laminated cylinders. Moreover, the results showed that the coupling of the membrane and flexural anisotropy and the anisotropy caused by unsymmetric lamination is generally unimportant with regards to the primary effect of the individual shell anisotropies on the bending boundary-layer decay length.

Stress singularities in a laminated composite wedge under real three-dimensional corner effects were studied by Dimitrov et al. [26, 27] who developed a numerical approach for the asymptotic analysis of the linear-elastic solution in the neighborhood of some three-dimensional singular points. Their results revealed a strong dependence of the singular exponents on the wedge angle, for wedge angles smaller than π (convex wedges) the singularity is relatively weak, whereas for angles greater than π (concave wedges) the dominant singularity is significantly stronger and reaches quickly its minimum near 0.5. This means, that holes with sharp edges or concave corners are much more dangerous for the composite structures than convex corners or edges.

3 Dynamic Fracture and Peridynamics

3.1 Fracture Dynamics/Instability of Cracks

It is believed that Freund [36] introduced the basic theory of dynamic fracture, which deals with fracture phenomena on a time scale for which *inertial* resistance of the material to motion is significant. The deformable body typically contains a dominant crack or other stress concentrating defect, and the phenomena of primary interest are those associated with conditions for the onset of extension of a crack or its arrest. Material inertia can have a significant effect in a variety of ways. The fundamental theory of dynamic fracture is well documented by Freund [38]. Dynamic fracture in solids has attracted the interest of engineers and physicists due both to its technological interest and to inherent scientific challenge. The relationship between the crack driving force and the crack tip speed was developed in terms of crack tip plastic fields by Freund [37]. The mechanics of crack tip plasticity in dynamic crack growth influences two modes of dynamic fracture, namely cleavage and micro-void nucleation, growth and coalescence. As the fracture energy approaches zero, a crack propagating at its asymptotic velocity is equivalent to a disturbance moving along a free surface. Stroh [94] predicted the crack's limiting velocity to be the Rayleigh wave speed, V_R, which is the highest speed at which a wave can move along a free surface.

Early results revealed some discrepancies. For example, Yoffe [104] predicted that the instability speed of cracks is about 73 % of the Rayleigh-wave speed, V_R, (see

also [15, 38]). On the other hand, experiments measurements showed that the critical instability speed can be much lower than that value for different types of materials. Fineberg et al. [31] and Sharon et al. [82] found experimentally that the instability speed is about one third of the Rayleigh wave speed. Later, Gao [39] showed that Yoffe's model is consistent with a criterion of crack kinking into the direction of maximum energy release rate.

Some experimental observations of fracture mechanics were reported by Fineberg and Marder [34]. In particular, it was indicated that once the flux of energy to a crack tip passes a critical value, the crack becomes unstable, and it propagates in increasingly complicated ways. As a result, the crack cannot travel as quickly as theory had supposed, fracture surfaces become rough, it begins to branch and radiate sound, and the energy cost for crack motion increases considerably. When energy flux to a crack tip passes a certain critical value, efficient steady motion of the tip becomes unstable to the formation of micro-cracks that propagate away from the main crack. The dynamic energy release rate of a rapidly moving crack allows the possibility for the crack to split into multiple branches at a critical speed of about 50 % of the Raleigh speed as indicated by Freund [35]. According to Fineberg and Marder [34] as the crack undergoes a hierarchy of instabilities, the ability of the crack tip to absorb energy is enormously increased.

Abraham et al. [3] proposed that the onset of instability can be understood from the point of view of reduced local lattice vibration frequencies due to softening at the crack tip. Later, Abraham [1] described the onset of the instability in terms of the secant modulus. Close to crack tips, material deformation was found to be extremely large, leading to significant changes of local elasticity, referred to as *hyperelasticity*. Gao [40, 41] indicated that the atomic bonding in real materials tends to soften with increasing strain, leading to the onset of instability when the crack speed becomes faster than the local wave speed. Buehler and Gao [20] emphasized that the hyperelasticity is the key to understanding the existing discrepancies among theory, experiments and simulations on dynamical crack instability. There is a very special set of forces between atoms as reported originally by Slepyan [92]. These forces make it possible to develop analytical solutions for cracks moving in lattices. The behavior of cracks in these models has the following three features proposed by Marder and Gross [64] and Marder and Fineberg [65]:

Birth: There is a range of velocities starting at zero until around 20 % of the sound speed at which steady crack motion is forbidden. Above this range the crack motion becomes possible.

Childhood: Above the above range of velocity a steady stable crack motion is allowed and perfectly stable. At exactly the same externally applied stress, however, a stationary crack could also be stable.

Crisis: Above a critical velocity steady crack motion becomes unstable.

As the crack speeds up, the relativistic contraction discovered by Yoffe [104] becomes more and more important, until eventually horizontal bonds above the crack line begin to snap. The results of numerical simulations are shown in the upper right of Fig. 8. The crack might decide to build tree-like patterns of subsurface cracks once

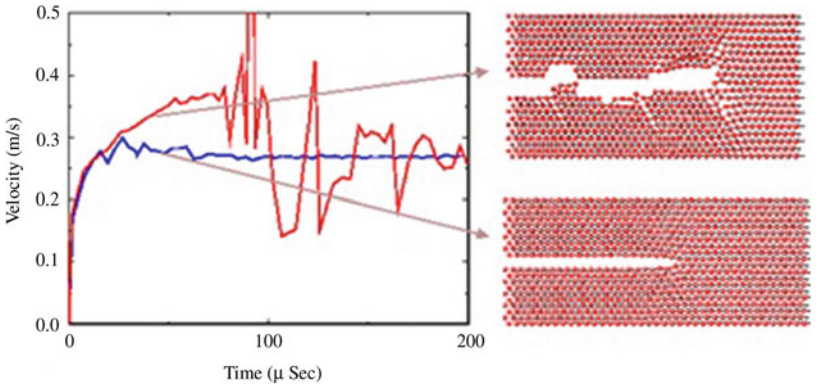

Fig. 8 Computer simulations in a simple model at the atomic scale showing a transition between smoothly moving cracks and a violent branching instability that is similar to experiment. The transition is a function of the energy stored per unit length to the right of the crack [65]

steady motion became impossible. Figure 8 also shows the computer simulations of the evolution of crack velocity in a simple model at the atomic scale showing a transition between smoothly moving cracks and a violent branching instability that is similar to experiment. The transition is a function of the energy stored per unit length to the right of the crack.

Micro-branching is a form of instability of fracture dynamics [33]. Fineberg [30] presented an overview of the dynamics of fast fracture in brittle amorphous materials. The review provided some details on the numerous effects commonly observed in dynamic fracture resulting from an intrinsic (micro-branching) instability of a rapidly moving crack. This micro-branching instability was found to result in large velocity oscillations, the formation of non-trivial fracture surface structure, a large increase in the overall fracture surface area, and a corresponding sharp increase of the fracture energy with the mean crack velocity. It was demonstrated that the loss of translational invariance resulting from crack-front interactions with localized material inhomogeneities causes both localized waves that propagate along the crack front and the acquisition of an effective inertia by the crack. Crack-front inertia coupled with the micro-branching instability provided an explanation of the chain-like form of the micro-branch induced patterns observed both on and beneath the fracture surface.

Large-scale molecular dynamics studies of dynamic fracture in brittle materials involving the limiting speed of cracks, crack tip instabilities and crack dynamics at interfaces were considered by Buehler and Gao [20]. The local elasticity was found to govern the dynamics of fracture, in which case the assumption of linear elastic material behavior becomes insufficient to describe the physics of fracture as indicated by Buehler [17] and Buehler and Gao [18, 19]. The dynamics of fracture that lead to material failure were found to be governed entirely by the material's behavior at the smallest scales as presented by Buehler [17] and Fineberg [29]. Hyperelastic deformation (elasticity of large strain) near a crack tip was found to provide expla-

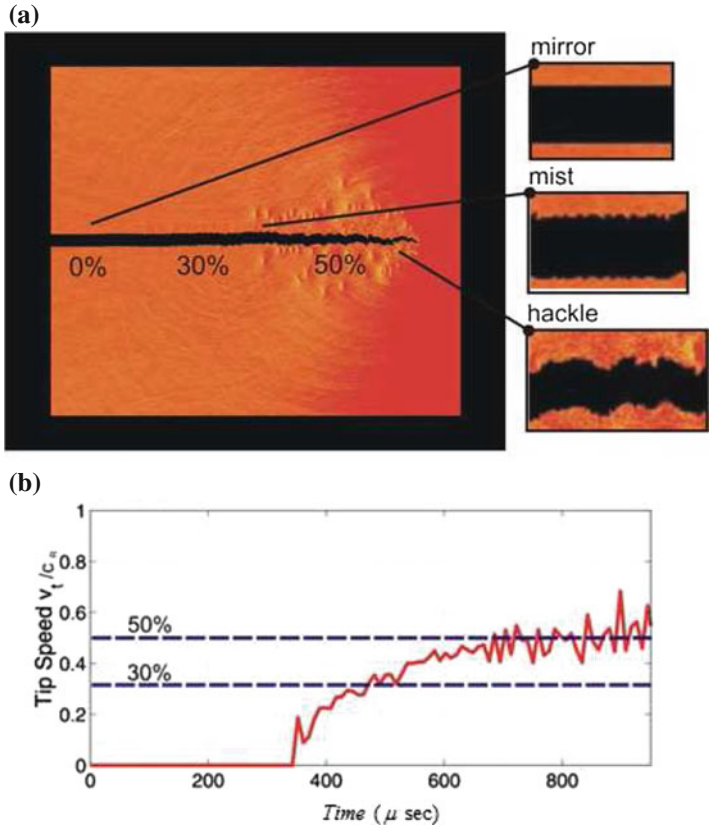

Fig. 9 Crack propagation showing: **a** the dynamical mirror-mist-hackle transition as the crack speed increases, and **b** the crack velocity history (normalized by the Rayleigh-wave speed)

nations for a number of phenomena including the "*mirror-mist-hackle*" instability widely observed in experiments as well as supersonic crack propagation in elastically stiffening materials. The relation of stress and strain in real solids is strongly nonlinear near a moving crack tip. Buehler and Gao [19, 20] showed that hyperelasticity plays an important role in dynamical crack tip instabilities. It was found that the dynamical instability of cracks can be regarded as a competition between different instability mechanisms controlled by local energy flow and local stress field near the crack tip. The result of a large-scale molecular dynamics simulation illustrating the mirror-mist-hackle transition is shown in Fig. 9. Figure 9a shows the transition process of the dynamical *mirror-mist-hackle* as the crack speed increases, while Fig. 9b shows the time evolution of the crack velocity normalized by the Rayleigh-wave speed.

Fracture surfaces in brittle materials usually have the feature of what is known as "*mirror-mist-hackle*". This feature is characterized by the crack face morphology changes as the crack speed increases and is referred to as dynamic instability of

cracks. Up to a critical speed of about one third of the Rayleigh-wave speed, the crack surface is atomically flat (mirror regime). For higher crack speeds the crack starts to roughen (mist regime) and eventually becomes very rough (hackle regime), accompanied by extensive crack branching and perhaps severe plastic deformation near the macroscopic crack tip. The phenomenon of mirror-mist-hackle was found to be a universal behavior that appears in various brittle materials, including ceramics, glasses and polymers. This dynamical crack instability was also observed in computer simulations performed by Abraham et al. [2], Marder and Gross [64], Gumbsch et al. [47], Holland and Marder [50] and Deegan et al. [25].

Crack dynamics in brittle materials was found to be governed by dynamical instabilities of the crack tip (see, e.g., [31]). Gross et al. [45] reported experimental measurements of acoustic emission, crack velocity, and surface structure. The results demonstrated quantitatively similar dynamical fracture behavior in polymethylmethacrylate and soda-lime glass samples. This unexpected agreement suggests that there exist universal features of the fracture energy that result from dissipation of energy in a dynamical instability. Improved measurements with high resolution measurements of the crack's velocity at 1/20 μs intervals for about 10,000 points throughout the duration of an experiment with velocity resolution of ±5 m/s were reported by Gross [44] and Marder and Gross [64] made it possible to follow the long-time dynamics of a crack in more details. In applications to the fracture of Polymethylmethacrylate (PMMA) a spatial resolution between measurements of order 0.2 mm was obtained by Fineberg et al. [32], Sharon et al. [82] and Fineberg and Marder [34]. Figure 10 shows the time evolution of the measured crack velocity propagating in PMMA as reported by Fineberg and Marder [34]. It is seen that the crack first accelerates abruptly, over a time of less than 1 μs, to a velocity on the order of 250 m/s. Above the critical velocity v_c, the crack velocity exhibits rapid oscillations. As the crack's velocity increases, these oscillations increase in amplitude. The crack begins at rest and the tip has ample time to become slightly blunted making it difficult for the crack to begin moving.

High speed interferometric measurements on dynamically propagating interfacial cracks were reported by Lambros and Rosakis [57, 58] for Polymethylmethacrylate (PMMA)/steel bi-material specimen. Impact loadings, using either a drop weight tower device or a high speed gas gun, were used. In gas gun experiments, terminal crack tip speeds of up to $1.5\,C_s^{PMMA}$, where C_s^{PMMA} is the shear wave speed of PMMA, were measured. Very large dynamic effects were observed in all dynamic bi-material tests. It was concluded that the whole process of interfacial crack initiation and growth in these tests is driven by energy "leaking" from the metal side to the PMMA side of the bond. Furthermore, very severe transient effects occurred during the early stages of crack growth. Dynamic complex stress factor histories were obtained by fitting the experimental data to available asymptotic crack-tip fields. A dynamic crack growth criterion for crack growth along bi-material interfaces was proposed. In the subsonic regime of crack growth it was found that the opening and shearing displacements behind the propagating crack tip remain constant and equal to their value at initiation. The dynamic fracture toughness of PMMA compact compression specimen under transient loading was studied by Rittel and Maigre [81].

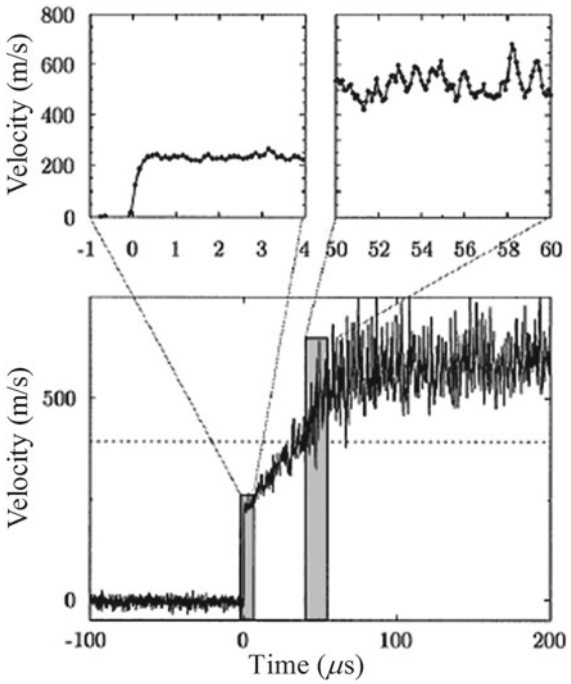

Fig. 10 Measured time evolution of a crack tip velocity in PMMA material. After an initial jump to about 250 m/s the crack accelerates smoothly up to a critical velocity v_c shown by the *dotted horizontal line*. Beyond this velocity, strong oscillations in the instantaneous velocity of the crack develop and the mean acceleration of the crack slows [34]

The evolution of both the mode-I and mode-II stress intensity factors were assessed from the onset of loading until early crack propagation detected by a fracture gage. Dynamic fracture toughness was taken as the value of the mode-I stress intensity factor at fracture time. The fracture toughness was observed to increase markedly with the stress intensity rate. Fractographic examination showed the existence of a characteristic rough zone directly ahead of the notch-tip of dynamically fractured specimen.

Several attempts were made to understand various aspects of the high velocity crack tip instabilities in the framework of linear elastic fracture mechanics by Adda-Bedia [4], Katzav et al. [54], Bouchbinder et al. [8] and Bouchbinder and Procaccia [9]. Direct measurements of the deformation surrounding the tip of dynamic mode-I cracks propagating in brittle elastomers at velocities ranging from 0.2 to 0.8 of the shear wave speed were performed by Bouchbinder et al. [11–14]. The measurements demonstrated how linear elastic fracture mechanics (LEFM) breaks down near the tip of a crack. This breakdown was quantitatively described by extending LEFM to the weakly nonlinear regime, by considering nonlinear elastic constitutive laws up to second-order in the displacement-gradients. It was shown that the scale of the near-tip region is delineated by a dynamic length-scale, ℓ_{nl}, from the crack tip. At this scale the weakly nonlinear theory was found to provide an excellent description of the measured deformation fields. The dynamic length-scale, ℓ_{nl}, is an important scale as

it denotes the scale where LEFM breaks down, second order displacement-gradients become non-negligible compared to the first order ones, and deformation-dependent material behavior is initiated as demonstrated by Gao [40], Buehler et al. [17], Buehler and Gao [19], Bouchbinder et al. [11] and Bouchbinder and Lo [10].

The critical fracture velocity, V_C, was found to be roughly linearly dependent on the lowest crack acceleration rates in PMMA and glass as reported by Livne et al. [59] and Bouchbinder et al. [13]. However, it is seen large apparent scatter in the values of the critical fracture velocity V_C for a given value of the crack acceleration. This uncertainty is believed to be due to the micro-branching instability in gels, which undergoes a sub-critical bifurcation (hysteretic transition) from a single crack to a multiple-crack state. The reverse transition from a crack state with micro-branches to a single-crack state occurs at velocities far less than V_C. Once the system falls within the bistable region of velocities, either a single or multi-crack state can exist.

Bouchbinder et al. [13] indicated that the micro-branching instability can be suppressed by reducing the sample thickness h in the Z-direction. When the thickness h is sufficiently reduced the total number of "noise" (activation) sources was found to be significantly reduced. In addition, any micro-branch chain soon encounters a sample edge and disappears. When this occurs, Livne et al. [60] found that a new and unexpected oscillatory instability is observed at a critical velocity of $0.9\,V_R$. The characteristic scales of this instability such as oscillation wavelengths, λ, or amplitudes, A, are dependent on sample geometry or dimensions. Although such a high velocity oscillatory instability was shown to occur in LEFM, Bouchbinder and Procaccia [9] suggested that the predicted oscillation wavelength must scale with the sample dimensions in the LEFM framework on the account that no other scale exists. It was believed that these observations indicate a new intrinsic/dynamical scale, which is needed to describe these dynamics. The oscillatory instability shown in Fig. 11a contains a sequence of photographs of a propagating crack with an interval of 0.69-ms between each shot. The first top two photo frames indicate that the crack is smooth and then undergoes transition to oscillatory motion in the subsequent frames at approximate speed of $0.9\,V_R$ when micro-branching is suppressed. Figrue 11b shows two frames, the top is the XY profile, while the bottom is the XZ fracture surface of a 0.2-mm thick gel sample where oscillations are developed. Figure 11c is for the case of a 2.0-mm thick gel where the crack preserves its straight line trajectory. The shown fracture surface in Fig. 11c is dominated by micro-branching, while the oscillating crack of Fig. 11b is a mirror surface. Figure 11d, e shows the steady state amplitude and wave-length as functions of the applied stress, respectively for the gel compositions used in Fig. 11a–c. The transition time evolution of the oscillation amplitude and wave-length are shown in the insets of Fig. 11d, e, respectively. The measured and LEFM predictions and measured crack-tip opening displacement (CTOD) were compared by [61] and the results revealed that the discrepancies become significant as the crack velocity increases.

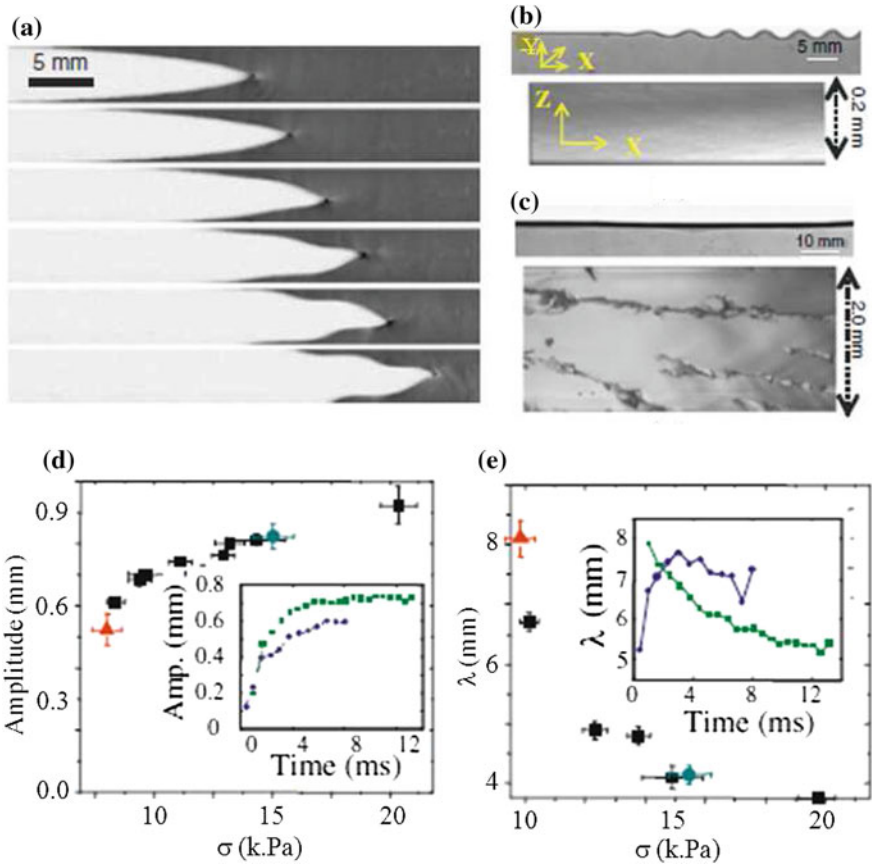

Fig. 11 Oscillatory instability of a crack: **a** a sequence of photographs of a propagating crack, **b** photographs of XY profile (*top*) and (XZ) fracture surface (*bottom*), of a 0.2 mm thick gel sample, **c** the fracture surface is micro-branch dominated, **d** steady state amplitude of oscillations versus the applied stress, **e** wavelengths of the oscillations as a function of the applied stress [9, 13, 60]

3.2 Peridynamics

The classical theory of continuum mechanics is based on partial differential equations whose partial derivatives are continuous. Since partial derivatives do not exist on crack surfaces and other singularities, the classical equations of continuum mechanics cannot be applied directly when such features are present in the structure. Cracks in structural material form discontinuities and their modeling requires special formulation. Such formulation was proposed by Silling [84] who developed the "peridynamic" model of continuum mechanics with discontinuities of fracture. Peridynamics treats internal forces within a continuous solid as a network of pair interactions, similar to springs, which can be nonlinear. The response of the springs depends on their

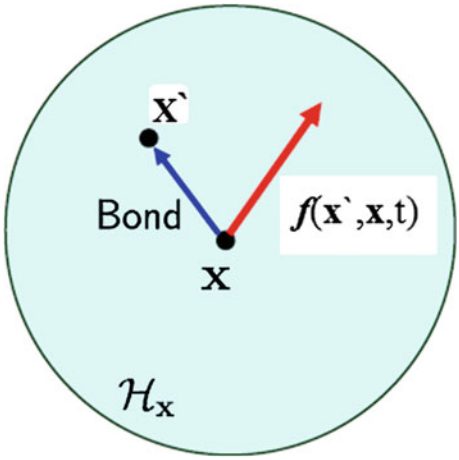

Fig. 12 Spherical region (*horizon*) in a solid showing the bond between two points and the force density vector (pair-wise) applied at both points [86]

direction in the reference configuration, and their length. Pairs of material points can interact through a spring up to a maximum distance, called the horizon.

The peridynamic theory is based on integral equations and thus does not require spatial derivatives to be evaluated within the structure body Silling [84, 85], Silling et al. [87], Silling and Askari [88, 89], Silling and Bobaru [90] and Weckner and Abeyaratne [101]. It was indicated that peridynamics unifies the mechanics of continuous and discontinuous media within a single set of equations. Peridynamics is a recent developed theory in solid mechanics since it replaces the partial differential equations of classical continuum theories with integro-differential equations. The basic equation of peridynamics is usually written in the form:

$$\rho(x)\ddot{u}(x,t) = \int_H f\left(u(x',t) - u(x,t)\right) dV_{x'} + b(x,t) \tag{18}$$

where x is a point in a body horizon H, and u is the displacement vector field. The vector valued function f is the force density that x' exerts on x as shown in Fig. 12. This force density depends on the relative displacement and relative position vectors between x' and x. This force describes how the internal forces depend on the deformation. The term b represents the body force density field. The interaction between any x and x' is called a "bond." The force density f is assumed to vanish if the point x' is outside a neighborhood of x in the undeformed configuration, which is called the *horizon*. Note that bonds can break irreversibly and broken bonds carry no force.

In peridynamics, particles interact nonlocally through a "bond" across the distance between them, much as in molecular dynamics [91]. The term "nonlocal" implies that points separated by a finite distance may exert force upon each other. Values of some quantity at a point are strongly influenced by values of the field in a neighborhood of that point. This is in contrast to the classical partial differential equations models in

which the particles interact locally through direct contact with each other. Chen and Gunzburger [21] applied finite element methods as well as discontinuous Galerkin methods to implement the peridynamic model. They used piecewise constant and discontinuous piecewise linear functions in regions where discontinuities may appear and continuous piecewise linear function in areas where the solutions is smooth. They proposed a methodology to combine the two methods. Peridynamic theory was employed by Henke [48] to describe the mechanical response of the polymer and polymer-nano-tube interfaces. The continuum formulation used in peridynamics allowed the polymer material to be coarse-grained to the scale of the reinforcing nano-fibers. Furthermore failure via nano-tube pull-out and matrix tearing are possible based on energetic considerations alone.

The peridynamic theory depends crucially upon the non-locality of the force interactions and does not explicitly involve the notion of deformation gradients. The linear bond-based non-local peridynamic models with reference to problems associated with nonstandard nonlocal displacement loading conditions were studied by Zhou and Du [106]. Both stationary and time-dependent problems were considered for a one-dimensional scalar equation defined on a finite bar and for a two-dimensional system defined on a square. The study was supported by applications to the numerical analysis of the finite-dimensional approximations to peridynamic models. A review of peridynamic models including the ordinary bond-based, state-based models and non-ordinary triclinic model was presented by Zhou [105]. Later, a functional analytical framework for a linear peridynamic model of a spring network system in any space dimension was developed by Du and Zhou [28]. Different properties of the peridynamic operators were examined for general micro-modulus functions. These properties were utilized to establish the well-posedness of both the stationary peridynamic model and the Cauchy problem of the time dependent peridynamic model.

As an application of peridynamic formulation of elasticity theory, Silling [85] considered the deformation of an infinite bar subjected to a self-equilibrated load distribution. The bar problem was formulated as a linear Fredholm integral equation and solved using Fourier transform methods. The solution was found to exhibit features such as decaying oscillations in the displacement field and progressively weakening discontinuities that propagate outside of the loading region. It was argued that these features, when present, are guaranteed to decay provided that the wave speeds are real. This would lead to a one-dimensional version of St. Venant's principle for peridynamic materials that ensures the increasing smoothness of the displacement field remotely from the loading region. The peridynamic result was found to converge to the classical result in the limit of short-range forces. Silling [85] highlighted some advantages of the peridynamic model. For example it allows for the spontaneous emergence of discontinuities, in contrast to the classical theory, which predicts deformations with infinite smoothness. Furthermore, the model includes long-range forces between material particles, unlike the classical theory, which generally deals only with contact forces between particles.

The peridynamic theory was employed for damage prediction of many problems. For example, Silling [85] considered the Kalthoff–Winkler experiment in which a plate having two parallel notches was subjected to impact by a cylindrical impactor,

and the peridynamic simulations successfully captured the angle of crack growth observed in the experiments. Impact damage was also predicted using peridynamics by Silling and Askari [88, 89] who considered a plate with a center crack to show the convergence of their numerical method. A new constitutive model was introduced for tearing and stretching of rubbery materials by Silling and Askari [89]. The oscillatory crack path was predicted when a blunt tool is forced through a membrane. The peridynamic theory was also applied to damage analysis of plain and reinforced concrete structures by Gerstle and Sau [42]. Askari et al. [5] and Colavito et al. [23, 24] utilized peridynamic to predict damage in laminated composites subjected to low-velocity impact and static indentation. Xu et al. [103] and Kilic [55] considered notched laminated composites under biaxial loads.

In order to take advantage of the computational robustness of finite element method, Macek and Silling [63] implemented the peridynamic model in a conventional finite element analysis code, ABAQUS, by representing the peridynamic interactions with truss elements and using embedded element technique for the overlap region. Macek and Silling [56] adopted the peridynamic theory since it uses displacements rather than displacement derivatives. They developed an approach to combine the peridynamic theory and finite element analysis in one treatment. The regions where failure is expected were modeled using peridynamics while remaining regions were modeled utilizing the finite element method. The coupling introduced an overlap region in which both the peridynamic and finite element equations are used simultaneously.

4 Closing Remarks

Structural life assessment relies on the theory of fracture mechanics, which deals with the study of the propagation of cracks in a structural element under static and dynamic loadings. The basic ingredients of the theory of fracture mechanics in terms of linear elastic fracture mechanics (LEFM) and elasto-plastic fracture mechanics (EPFM) has been briefly outlined. The amount of energy available for fracture is usually governed by the stress field around the crack, which is measured by the stress intensity factor. The value of the stress intensity factor, which depends on the loading mode, has been evaluated by different methods developed by many researchers. Complex stress states with rapid change of gradients occur along the edges of composite laminates. This phenomenon is due to interactions of geometric discontinuities of the composite and materials discontinuities and is found to occur only within very local region known as "*boundary-layer effect*" or "*free-edge effect*." This problem is unique to composite laminates and not observed in homogeneous solids in general. It was shown that the boundary-layer effect is three-dimensional in nature and is considered as one of the most fundamental and important problems in the mechanics and mechanical behavior of composite laminates.

Equally important is the dynamic fracture phenomena when inertial resistance of the material to motion is significant. A rapidly running crack emits stress waves

which can be geometrically reflected or scattered back to the region of the crack. Close to crack tips, material deformation is extremely large, leading to significant changes of local elasticity known as hyperelasticity. Hyperelastic deformation near a crack tip has shown to provide explanations for a number of phenomena including the "*mirror-mist-hackle*" instability widely observed in experiments as well as supersonic crack propagation in elastically stiffening materials. Since partial derivatives do not exist on crack surfaces and other singularities, the classical equations of continuum mechanics cannot be applied directly when such features are present in the structure. Cracks in structural material form discontinuities and their modeling requires special formulation such as the peridynamic model of continuum mechanics with discontinuities of fracture. The development of peridynamics is in its early stage and has not been fully implemented to handle practical engineering problems such as ships and aerospace structures under extreme loadings.

Acknowledgments This work is supported by a grant from ONR under Award No: N00014-08-1-0647. Dr. Kelly B. Cooper is the Program Director.

References

1. Abraham, F.F.: Unstable crack motion is predictable. Adv. Phys. **53**, 1071–1078 (2005)
2. Abraham, F.F., Brodbeck, D., Rafey, R.A., Rudge, W.E.: Instability dynamics of fracture: a computer simulation investigation. Phys. Rev. Lett. **73**(2), 272–275 (1994)
3. Abraham, F.F., Brodbeck, D., Rudge, W.E., Xu, X.P.: A molecular dynamics investigation of rapid fracture mechanics. J. Mech. Phys. Solids **45**(9), 1595–1619 (1997)
4. Adda-Bedia, M.: Brittle fracture dynamics with arbitrary paths III the branching instability under general loading. J. Mech. Phys. Solids **53**, 227–248 (2005)
5. Askari, E., Xu, J., Silling, S.: Peridynamic analysis of damage and failure in composites. In Proceedings 44th AIAA Aerospace Sciences Meeting and Exhibit, Reno, NV, AIAA, Reston, VA, Paper #2006-88
6. Bar-Yoseph, P., Ben-David, D.: On mesh refinement methods of mixed hybrid finite elements for revealing the nature of the singularity in the free edge of a composite laminated plate. Commun. Appl. Numer. Methods **7**, 315–324 (1991)
7. Bar-Yoseph, P., Ben-David, D.: Free-edge effects in unsymmetrically laminated composite plates. Compos. Struct. **30**(1), 13–23 (1995)
8. Bouchbinder, E., Mathiesen, J., Procaccia, I.: Branching instabilities in rapid fracture: dynamics and geometry. Phys. Rev. E **71**, 056118 (2005)
9. Bouchbinder, E., Procaccia, I.: Oscillatory instability in two-dimensional dynamic fracture. Phys. Rev. Lett. **98**, 124302 (2007)
10. Bouchbinder, E., Lo, T.S.: Elastic nonlinearities in a one-dimensional model of fracture. Phys. Rev. E **78**, 056105 (2008)
11. Bouchbinder, E., Livne, A., Fineberg, J.: Weakly nonlinear theory of dynamic fracture. Phys. Rev. Lett. **101**, 264302 (4p.) (2008)
12. Bouchbinder, E., Livne, A., Fineberg, J.: The 1/r singularity in weakly nonlinear fracture mechanics. J. Mech. Phys. Solids **57**, 1568–1577 (2009)
13. Bouchbinder, E., Livne, A., Fineberg, J.: Weakly nonlinear fracture mechanics: experiments and theory. Int. J. Fract. **162**(1–2), 3–20 (2010a)
14. Bouchbinder, E., Fineberg, J., Marder, M.: Dynamics of simple cracks. Annu. Rev. Conden. Matter Phys. **1**, 371–395 (2010b)

15. Broberg, K.B.: Cracks and Fracture. Academic Press, New York (1990)
16. Broek, D.: The Practical Use of Fracture Mechanics. 3rd ed., Kluwer Academic Press, Dordrecht (1994)
17. Buehler, M.J., Abraham, F.F., Gao, H.: Hyperelasticity governs dynamic fracture at a critical length scale. Nature **426**, 141–146 (2003)
18. Buehler, M.J., Gao, H.: Biegen und Brechen im Supercomputer. Physik in unserer Zeit **35**(1), (2004)
19. Buehler, M.J., Gao, H.: Dynamical fracture instabilities due to local hyperelasticity at crack tips. Nature **439**, 307–310 (2006)
20. Buehler, M.J., Gao, H.J.: Modeling dynamic fracture using large-scale atomistic simulations. In: Shukla, A. (ed.) Dynamic Fracture Mechanics. World Scientific, Singapore (2007). Chapter 1
21. Chen, X., Gunzburger, M.: Continuous and discontinuous finite element methods for a peridynamics model of mechanics. Comput. Methods Appl. Mech. Eng. **200**, 1237–1250 (2011)
22. Christensen, R.M.: Mechanics of Composite Materials. Wiley, New York (1979)
23. Colavito, K.W., Kilic, B., Celik, E., Madenci, E., Askari, E., Silling, S.: Effect of void content on stiffness and strength of composites by a peridynamic analysis and static indentation test. In: Proceedings 48th AIAA/ASME/ASCE/AHS/ASC Structures, Structural Dynamics, and Materials Conference, Honolulu, HI, AIAA, Reston, VA, 2007a. Paper #2007-2251
24. Colavito, K.W., Kilic, B., Celik, E., Madenci, E., Askari, E., Silling, S.: Effects of nano-particles on stiffness and impact strength of composites. In: Proceedings 48th AIAA/ASME/ASCE/AHS/ASC Structures, Structural Dynamics, and Materials Conference, Honolulu, HI, AIAA, Reston, VA, 2007b. Paper #2007-2021
25. Deegan, R.D., Chheda, S., Patel, L., Marder, M., Swinney, H.L., Kim, J., de Lozanne, A., et al.: Wavy and rough cracks in silicon. Phys. Rev. E **67**(6), #066209 (2003)
26. Dimitrov, A., Andrä, H., Schnack, E.: Efficient computation of order and mode of corner singularities in 3D-elasticity. Int. J. Numer. Methods Eng. **52**, 805–827 (2001)
27. Dimitrov, A., Andrä, H., Schnack, E.: Singularities near three-dimensional corners in composite laminates. Int. J. Fract. **115**(4), 361–375 (2002)
28. Du, Q., Zhou, K.: Mathematical analysis for the peridynamic nonlocal continuum theory. ESAIM. Math. Model. Numer. Anal. **45**(2), 217–234 (2011)
29. Fineberg, J.: Close-up on cracks. Nature **426**, 131–132 (2003)
30. Fineberg, J.: The dynamics of rapidly moving tensile cracks in brittle amorphous material. In: Dynamic Fracture Mechanics, Chapter 1, pp. 104–146. World Scientific (2006)
31. Fineberg, J., Gross, S.P., Marder, M., Swinney, L.: Instability in dynamic fracture. Phys. Rev. Lett. **67**(4), 457–462 (1991)
32. Fineberg, J., Gross, S.P., Marder, M., Swinney, L.: Instability in the propagation of fast crack. Phys. Rev. B **45**(10), 5146–5156 (1992)
33. Fineberg, J., Gross, S.P., Sharon, E.: Micro-branching as an instability in dynamic fracture. In: Willis, J.R. (ed.) Proceedings IUTAM Conference on Micro-Branching as an Instability in Dynamic Fracture, pp. 177–190. Cambridge, U.K (1996)
34. Fineberg, J., Marder, M.: Instability in dynamic fracture. Phys. Rep. **313**, 1–108 (1999)
35. Freund, L.B.: Crack propagation in an elastic solid subjected to general loading, II: nonuniform rate of extension. J. Mech. Phys. Solids **20**, 141–152 (1972)
36. Freund, L.B.: The mechanics of dynamic fracture. In: Proceedings 10th U.S. National Congress of Applied Mechanics, Austin, TX (1986)
37. Freund, L.P.: Results on the influence of crack tip plasticity during dynamic crack growth. In: Final Report, Brown University, Division of Engineering, Providence, RI. 32p (1987)
38. Freund, L.B.: Dyn. Fract. Mech. Cambridge University Press, Cambridge (1990)
39. Gao, H.: Surface roughening and branching instabilities in dynamic fracture. J. Mech. Phys. Solids **41**(3), 457–486 (1993)
40. Gao, H.: A theory of local limiting speed in dynamic fracture. J. Mech. Phys. Solids **44**(9), 1453–1474 (1996)

41. Gao, H.: Elastic waves in a hyperelastic solid near its plane-strain equi-biaxial cohesive limit. Philos. Mag. Lett. **76**(5), 307–314 (1997)
42. Gerstle, W.H., Sau, N.: Peridynamic modeling of concrete structures. In: Proceedings 5th International Conference on Fracture Mechanics of Concrete and Concrete Structures: Fracture Mechanics of Concrete Structures, vol. 2, pp. 949–956. Ia-FraMCos, Evanston, IL (2004)
43. Griffith, A.A.: The phenomena of rupture and flow in solids. Philos. Trans. Roy. Soc. Lond. A **221**, 163–198 (1921)
44. Gross, S.P.: Dynamics of fast fracture. Ph.D. Dissertation, University of Texas, Austin (1995)
45. Gross, S.P., Fineberg, J., Marder, M., McCormick, W.D., Swinney, H.L.: Acoustic emission from rapidly moving cracks. Phys. Rev. Lett. **71**, 3162–3165 (1993)
46. Gu, Q., Reddy, J.N.: Nonlinear analysis of free-edge effects in composite laminates subjected to axial loads. Int. J. Nonlinear Mech. **27**(1), 27–41 (1992)
47. Gumbsch, P., Zhou, S.J., Holian, B.L.: Molecular dynamics investigation of dynamic crack instability. Phys. Rev. B **55**, 3445 (1997)
48. Henke, S.F.: Peridynamic modeling and simulation of polymer-nanotube composites. Ph.D. Dissertation, Florida State University, College of Arts and Science. Tallahassee, FL (2013)
49. Herakovich, C.T., Nagarkar, A., O'Brien, D.A.: Failure analysis of composite laminates with free edges. In: Vinson, J.R. (ed.) Modern Developments in Composite Materials and Structures, pp. 53–56. ASME (1979)
50. Holland, D., Marder, M.: Ideal brittle fracture of silicon studied with molecular dynamics. Phys. Rev. Lett. **80**(4), 746–749 (1998)
51. Irwin, G.: Analysis of stresses and strains near the end of a crack traversing a plate. J. Appl. Mech. **24**, 361–364 (1957)
52. Irwin, G.: Fracture. In: Flügge, S. (ed.) Handbuch der Physik, vol. 6, Flugge edn, pp. 551–590. Springer, Berlin (1958)
53. Kassapoglou, C.: An efficient method for the calculation of interlaminar stresses in composite materials. J. Appl. Mech. **53**, 744–750 (1986)
54. Katzav, E., Adda-Bedia, M., Arias, R.: Theory of dynamic branching in brittle materials. Int. J. Fract. **143**, 245–271 (2007)
55. Kilic, B.: Peridynamic theory for progressive failure prediction in composite materials. Ph.D. thesis, University of Arizona, Tucson, AZ (2008)
56. Kilic, B., Madenci, E.: Coupling of peridynamic theory and the finite element method. J. Mech. Mater. Struct. **5**(5), 207–233 (2010)
57. Lambros, J., Rosakis, A.J.: Dynamic decohesion of bi-materials: experimental observations and failure criteria. Int. J. Solids Struct. **32**(17/18), 2677–2702 (1995a)
58. Lambros, J., Rosakis, A.J.: Development of a dynamic decohesion criterion for subsonic fracture of the interface between two dissimilar materials. Proc. Roy. Soc. Lond. A **451**, 711–736 (1995b)
59. Livne, A., Cohen, G., Fineberg, J.: Universality and hysteretic dynamics in rapid fracture. Phys. Rev. Lett. **94**, 224301 (2005)
60. Livne, A., Ben-David, O., Fineberg, J.: Oscillations in rapid fracture. Phys. Rev. Lett. **98**, 124301 (2007)
61. Livne, A., Bouchbinder, E., Fineberg, J.: Breakdown of linear elastic fracture mechanics near the tip of a rapid crack. Phys. Rev. Lett. **101**, 264301 (2008)
62. Lynch, J.P., Law, K.H., O'Connor, S.: Probabilistic and Reliability-Based Health Monitoring Strategies for High-Speed Naval Vessels, 31p. Michigan University, Department of Electrical Engineering and Computer Science, Ann Arbor (2012)
63. Macek, R.W., Silling, S.A.: Peridynamics via finite element analysis. Finite Elem. Anal. Des. **43**(15), 1169–1178 (2007)
64. Marder, M., Gross, S.P.: Origin of crack tip instabilities. J. Mech. Phys. Solids **43**, 1–48 (1995)
65. Marder, M., Fineberg, J.: How things break: solids fail through the propagation of cracks, whose speed is controlled by instabilities at the smallest scales, 12p. http://chaos.ph.utexas.edu/~marder/fracture/phystoday/how_things_break/how_things_brea

66. Mittelstedt, C., Becker, W.: Free-edge effects in composite laminates. ASME Appl. Mech. Rev. **60**(5), 217–245 (2007c)
67. Murthy, P.L.N., Chamis, C.C.: Free-edge delamination: laminate width and loading condition effects. J. Compos. Technol. Res. **11**, 15–22 (1989)
68. Nemeth, M.P., Smeltzer, S.S., III.: Bending boundary layers in laminated-composite circular cylindrical shells. In: Proceedings 41st AIAA/ASME/ASCE/AHS/ASC Structures, Structural Dynamics, and Material Conference AIAA Paper No. 2000–1660, Atlanta, Georgia (2000)
69. Okasha, N.M., Frangopol, D.M.: Efficient method based on optimization and simulation for the probabilistic strength computation of the ship hull. J. Ship Res. **54**(4), 1–13 (2010)
70. Okasha, N.M., Frangopol, D.M., Decò, A.: Integration of structural health monitoring in life-cycle performance assessment of ship structures under uncertainty. Mar. Struct. **23**, 303–321 (2010)
71. Pagano, N.J.: On the calculation of interlaminar normal stress in composite laminate. J. Compos. Mater. **8**, 65–82 (1974)
72. Pagano, N.G.: Stress fields in composite laminates. Int. J. Solids Struct. **14**, 385–400 (1978a)
73. Pagano, N.J.: Free-edge stress fields in composite laminates. Int. J. Solids Struct. **14**, 401–406 (1978b)
74. Pagano, N.J., Pipes, R.B.: Influence of stacking sequence on laminate strength. J. Compos. Mater. **5**, 51–57 (1971)
75. Paris, P., Erdogan, F.: A critical analysis of crack propagation laws. ASME J. Basic Eng. **85**(4), 528–534 (1963)
76. Pipes, R.B., Pagano, N.J.: Interlaminar stresses in composite laminates under uniform axial extension. J. Compos. Mater. **4**, 538–548 (1970)
77. Pipes, R.B., Kaminski, B.E., Pagano, N.J.: Influence of the free edge upon the strength of angle-ply laminates. In: Analysis of the Test Methods for High Modulus Fibers and Composites, ASTM STP 52.1, American Society for Testing and Materials, pp 218–228 (1973)
78. Pipes, R.B., Pagano, N.J.: Interlaminar stresses in composite laminates: an approximate elasticity solution. ASME J. Appl. Mech. **41**(3), 668–672 (1974)
79. Rice, J.R.: A path independent integral and the approximate analysis of strain concentration by notches and cracks. J. Appl. Mech. **35**, 379–386 (1968)
80. Rice, J.R.: Some remarks on the elastic crack-tip stress fields. Int. J. Solids Struct. **8**, 751–758 (1972)
81. Rittel, D., Maigre, H.: An investigation of dynamic crack initiation in PMMA. Mech. Mater. **23**(3), 229–239 (1996)
82. Sharon, E., Gross, S.P., Fineberg, J.: Local crack branching as a mechanism for instability in dynamic fracture. Phys. Rev. Lett. **74**, 5146–5154 (1995)
83. Sielski, R.A., Nahshon, K., Salvino, L.W., Anderson, K., Dow, N.: The ONR structural reliability program. In: ASNE Proceedings, 28p (2012)
84. Silling, S.A.: Reformulation of elasticity theory for discontinuities and long-range forces. J. Mech. Phys. Solids **48**, 175–209 (2000)
85. Silling, S.A.: Dynamic fracture modeling with a meshfree peridynamic code. In: Bathe, K.J. (ed.) Comput. Fluid Solid Mech., pp. 641–644. Elsevier, Amsterdam (2003)
86. Silling, S.A.: Introduction to peridynamics, workshop on peridynamics, dissipative particle dynamics, and the Mori-Zwanzig formulation, Brown University (2012)
87. Silling, S.A., Zimmermann, M., Abeyaratne, R.: Deformation of a peridynamic bar. J. Elast. **73**, 173–190 (2003)
88. Silling, S.A., Askari, E.: Peridynamic modeling of impact damage. In: Moody, F.J. (ed.) PVP-489, pp. 197–205. American Society of Mechanical Engineers, New York (2004)
89. Silling, S.A., Askari, E.: A meshfree method based on the peridynamic model of solid mechanics. Comput. Struct. **83**, 1526–1535 (2005)
90. Silling, S.A., Bobaru, F.: Peridynamic modeling of membranes and fibers. Int. J. NonLinear Mech. **40**, 395–409 (2005)
91. Silling, S.A., Lehoucq, R.: Peridynamic Theory of Solid Mechanics, Technical Report, Sandia National Laboraries, April 28, 2010. Albuquerque, New Mexico (2010)

92. Slepyan, L.I.: Dynamics of a crack in a lattice. Soviet Physics Doklady **26**, 538–540 (1981)
93. Soni, S.R., Pagano, N.J.: Analysis of free edge effects in composite laminates. Sadhana **11**(3–4), 341–355 (1987)
94. Stroh, A.N.: A theory of the fracture of metals. Adv. Phys. **6**, 418–465 (1957)
95. Sun, C.T., Zhou, S.G.: Failure analysis of composite laminates with free edge. ASTM Int. **12**(2), 7p (1990)
96. Wang, J., Dickson, J.: Interlaminar stresses in symmetric composite laminates. J. Compos. Mater. **12**, 390–402 (1978)
97. Wang, S.S., Choi, I.: Boundary-layer effects in composite laminates: free-edge stress singularities, NASA CR 165440. In: Final Report—Part VI, NASA Lewis Research Center (1981)
98. Wang, S.S., Choi, I.: Boundary-layer effects in composite laminates. Part I—stress singularities. ASME J. Appl. Mech. **49**(3), 541–548 (1982a)
99. Wang, S.S., Choi, I.: Boundary layer effects in composite laminates. Part II—free-edge stress solutions and basic characteristics. ASME J. Appl. Mech. **49**(3), 549–560 (1982b)
100. Wang, S.S., Yuan, F.G.: A hybrid finite-element approach to laminate elasticity problems with stress singularities. ASME J. Appl. Mech. **50**(4), 835–844 (1983)
101. Weckner, O., Abeyaratne, R.: The effect of long-range forces on the dynamics of a bar. J. Mech. Phys. Solids **53**, 705–728 (2005)
102. Wilkins, D.J., Eisenmann, J.R., Camin, R.A., Margolis, W.S., Benson, R.A.: Characterizing delamination growth in graphite-epoxy. In: Damage in Composite Materials: Basic Mechanisms, Accumulation Tolerance, and Characterization, vol. 775, pp. 168–183. ASTM STP (1982)
103. Xu, J., Askari, A., Weckner, O., Razi, H., Silling, S.: Damage and failure analysis of composite laminates under biaxial loads. In: Proceedings 48th AIAA/ASME/ASCE/AHS/ASC Structures, Structural Dynamics, and Materials Conference Honolulu, HI, AIAA, Reston, VA, 2007. Paper #2007-2315
104. Yoffe, E.H.: The moving Griffith crack. Philos. Mag. **42**, 739–750 (1951)
105. Zhou, K.: The peridynamic theory of solid mechanics. Ph.D. Dissertation, Penn State University, Mathematics Department (2011)
106. Zhou, K., Du, Q.: Mathematical and numerical analysis of linear peridynamic models with nonlocal boundary conditions. SIAM J. Numer. Anal. **48**, 1759–1780 (2010)

Electromagnetic Impact Vibration Energy Harvesters

Mohamed Bendame, Eihab Abdel-Rahman and Mostafa Soliman

Abstract Vibration energy harvesting is the focus of extensive research as an alternative power source for low-power electronic devices. First generation of vibration energy harvesters were based on linear oscillators designed to harvest vibrations in a narrow band in the vicinity of their natural frequency. However, in environments where vibrations are random or distributed over a wide spectrum, those harvesters prove ineffective. In this chapter, we present a new architecter for nonlinear vibration energy harvesters, namely the 'Springless' vibration energy harvesting, that can effectively harvest vibrations over a wide bandwidth and at low levels of vibration. It employs impact oscillators as the harvesting element. We study, characterize, and qualify the performance of those harvesters experimentally, analytically, and numerically.

1 Introduction

Advances in silicon electronics and MEMS technology reduced significantly the power consumption of devices, Table 1, such as wireless sensors, portable, and wearable electronics. A large number of the locations, where those devices are used, are either remote or inaccessible. Most of these low-power devices rely heavily on electrochemical batteries as a source of power. However, batteries have a limited life span and number of recharging cycles. They are also constantly in need for recharging or replacement. For applications such as wireless sensing and remote monitoring, battery replacement or recharging can be expensive, challenging or impossible in some cases. Examples include human implants, sensing devices intended for long

M. Bendame (✉) · E. Abdel-Rahman
University of Waterloo, 200 University Avenue West, N2K 4A2 Waterloo, ON, Canada
e-mail: mbendame@uwaterloo.ca

E. Abdel-Rahman
e-mail: eihab@uwaterloo.ca

M. Soliman
Department of Energy Conversion and Power Electronics,
Electronics Research Institute, Giza, Egypt
e-mail: mostafa.soliman@si-ware.com

M. Belhaq (ed.), *Structural Nonlinear Dynamics and Diagnosis*,
Springer Proceedings in Physics 168, DOI 10.1007/978-3-319-19851-4_2

Table 1 Selected battery-operated systems

Device type	Power consumption
Smartphone	1 W
MP3 player	50 mW
Hearing aid	1 mW
Wireless sensor	100 μW
Cardiac pacemaker	50 μW s
Quartz watch	5 μW

duration, and systems that are physically placed in remote areas [1]. Another serious problem with batteries is the fact that they contain hazardous chemical materials that are harmful to the environment if not recycled. In Canada, for example, over 600 million primary consumer batteries were sold in 2007 and about 95 % of them end up in landfills [2]. With the world's growing reliance on wireless and low-power electronics and the push for a green environment, there is a great need for self-powering and self-sustaining low-power electronic devices.

The low power design trends combined with self-sustainability needs presented an opportunity for researchers to find alternative ways to power such devices and eliminate or reduce dependency on batteries. One promising avenue to achieve this goal is to exploit ambient vibration energy sources. Vibration energy harvesting technology has been making significant strides over the last few years as it aims to provide a continuous and uninterrupted source of power for low-power electronic devices and wireless sensors. While the idea of converting environmental vibration energy into electrical energy has been used before, advances in micro-electronics and low power consumption of silicon-based electronics and wireless sensors have given it an added significance.

In the research literature, the first description of an inertial micro-power-generator was an electromagnetic vibration energy harvester (VEH) presented by Williams and Yates in 1995 [3]. Since then a great deal of research has been conducted in the area of vibration energy harvesting. Earlier works by Beeby, Glynne-Jones, Roundy [4–6] and others focused on the implementation of linear oscillators to maximize the harvested energy at resonance. In this type of harvesters, the seismic mass of the VEH moves under the influence of base excitation supported by a linear spring. The oscillator attains maximum velocity, and thus input kinetic energy, in a frequency band around its natural frequency,

$$\omega = \sqrt{\frac{k}{m}}, \tag{1}$$

where k is the spring stiffness and m is the effective mass of the mechanical oscillator.

While systems in this arrangement are capable of generating electrical energy with output power on the order of few milli-Watts [6, 7], their natural frequency must be tuned to match the frequency of ambient vibrations. In fact these harvesters are

Table 2 Electromagnetic micro-power generators

Generator	f (Hz)	Accel (m/s^2)	m (g)	Power (μW)
Beeby et al. [6]	52	0.589	0.66	45
Glynne-Jones [4]	99	6.85	2.96	4990
Ching et al. [27]	110	95.5	–	830

designed to harvest at a single frequency. A high Q-factor to minimize energy losses means a very limited bandwidths over which energy can be harvested [8]. However, in environments where ambient vibrations are distributed over a wide spectrum of frequencies, with significant predominance of low frequency components, linear harvesters prove to be ineffective because of their high center frequencies and narrow bandwidth [9–11]. It is therefore impractical to use linear VEHs with relatively high center frequency ($\geq$20 Hz) and narrow bandwidth to harvest ambient wideband and low frequency environmental vibrations. Examples of some linear harvesters that have been proposed over the years are listed in Table 2, a more comprehensive lists of electromagnetic energy harvesters can be found in [12]. We note that linear harvesters have high operating frequencies and low power densities. For example, the electromagnetic VIBES harvester (first line in Table 2) has a center frequency of 52 Hz and a maximum power of 45 μW.

Due to these limitations, attention in recent years has focused on the implementation of self-tuning and nonlinear systems in order to increase the vibration energy harvester's frequency bandwidth. A number of approaches have been tried for this purpose including nonlinear stiffness, resonant frequency tuning, mechanical stoppers and exploitation of nonlinear structures that display bandwidth widening behavior. These approaches lead to three main types of nonlinear vibration energy harvesters; Duffing, array, and impact harvesters.

The Duffing type harvester gets its name from the Duffing oscillator since its governing equation reduces to a Duffing equation. In this case, the nonlinearity is added to the harvester either by using nonlinear springs or by introducing magnetic forces to alter the overall system stiffness and make it appear as a nonlinear quantity in the system's model. The Duffing harvester can be classified in three categories: hardening, bistable, and softening [13]. Mann and Sims [10] presented a Duffing type harvester that uses magnetic restoring forces to levitate an oscillating center magnet. The governing equation for the harvester's mass displacement reduces to a Duffing equation, and the introduction of nonlinearities through magnetic levitation resulted in large motion over a wide band of frequencies. Using a similar approach, Mann and Owens [9] presented a nonlinear vibration energy harvester with a bistable well. Theoretical and experimental results reveal that the nonlinear generator with a bistable potential well can be used to broaden the frequency response of the harvester. The output power of the proposed harvester varied from 5 to 200 mW for input accelerations ranging from 5 to 10 m/s^2, and from the presented results the frequency bandwidth was 1, 2, and 3 Hz for input accelerations between 5 and 6.5 m/s^2, and

2 Hz for 10 m/s^2 respectively. Further examples of Duffing-type and other nonlinear vibration energy harvesters can be found in reviews of recently published work [8, 14, 15].

Array harvesters employ a series of mechanical resonators, usually a series of cantilever beams with varying length and center frequencies. The cantilevers are tuned in a way that all resonance frequencies are close to each other. The resonance frequencies are adjusted by tuning the geometry of each energy scavenger or by applying a proof mass. As long as the source vibration has dominant frequency within the band of the array, at least one of the beams operates at its resonance frequency. Hence, as more beams are added to the array, as much bigger is the possible bandwidth [16]. Sari et al. [17] proposed a harvester that used an array of piezoelectric oscillators made of cantilever beams on which planar gold coils were fabricated. The reported generator covers a wide band of external vibration frequencies by implementing a number of serially connected cantilevers of different lengths resulting in an array of cantilevers with varying natural frequencies. The device generates 0.4 W of continuous power in a frequency range covering a band of 800 Hz. Similar approaches were used by Lien and Shu [18] and Rezaeisary et al. [19]. In [20], Yan et al. proposed a multi-frequency energy harvester consisting of three permanent magnets and three sets of two-layer coils supported by a beam. The idea here is that energy is harvested under the first, second, and third resonant modes.

It has been shown that impact harvesters increase the frequency bandwidth and output power of vibration energy harvesters [21–24]. Impact harvesters are realized using mechanical stoppers that limit the motion of the seismic mass. When the seismic mass impacts the stoppers, the overall stiffness of the system is reduced to a piecewise linear or nonlinear function, that results in a nonsmooth system [23]. Soliman et al. [25] proposed a wideband micropower generator that utilized a mechanical stopper placed within the stroke and the cantilever beam. When the cantilever oscillates, it engages the stopper during motion, and therefore changes its stiffness from k_1 to k_2 with ($k_1 \ll k_2$). Le Cuong et al. [26] presented a double-impact electrostatic energy harvester that used a reference device with end-stops and an impact device with movable end-stops functioning as slave transducers. The impact harvester resulted in bandwidth increase by up to a factor of 20 compared to conventional approaches.

In this chapter, we analyze a new architecture of nonlinear VEHs that uses a double-impact oscillator, namely the "Springless" VEH, as its harvesting element. Specifically, we study the response of the horizontally aligned configuration of the VEH experimentally, numerically, and analytically.

2 Springless Vibration Energy Harvester

The schematic of the "Springless" VEH, shown in Fig. 1, consists of an electromagnetic transducer and a double-impact oscillator. The oscillator is composed of an inertial mass comprising four permanent magnets residing inside a steel cage, and

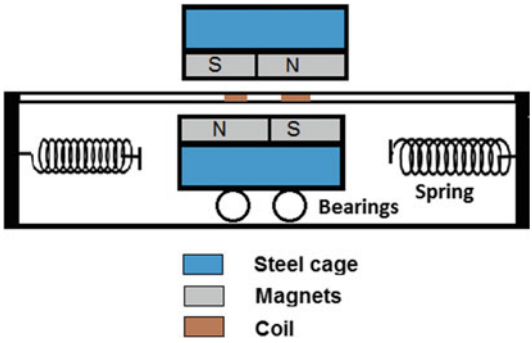

Fig. 1 Schematic of the horizontally-aligned VEH

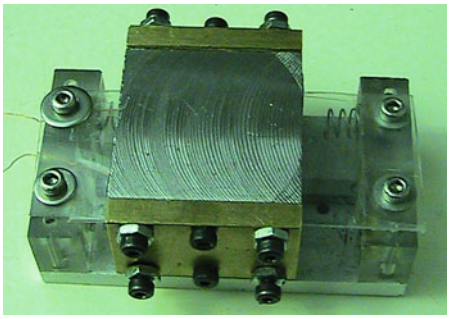

Fig. 2 Prototype of springless vibration energy harvester

two end limiters made of two identical springs attached to two resin walls at each end of the housing unit. The carriage carrying the magnetic seismic mass moves freely along the linear guide with respect to a stationary concentric coil in response to base excitations. A prototype of the VEH is shown in Fig. 2.

The motion of the magnetic carriage induces an electromotive force (emf) across the coil terminals according to Faraday's law of induction;

$$V = \frac{d\phi}{dt} \tag{2}$$

where ϕ is the total magnetic flux given by;

$$\phi = \mathbf{BA} \tag{3}$$

where **A** is the area vector and **B** is the magnetic field vector. For a coil that consists of N loops, the total induced voltage would be N times as large, and (2) becomes;

$$V = N\frac{d}{dt}(BA\cos\theta) \tag{4}$$

Differentiating (4) with respect to time we obtain:

$$V = N\left(\frac{dB}{dt}A\cos\theta + B\frac{dA}{dt}\cos(\theta) + BA\frac{d\theta}{dt}\right) \tag{5}$$

From (5), the harvested power depends on the magnetic field density **B** provided by the permanent magnets, the coil's cross-section area **A** of the coil, and the angle between the magnetic field **B** and the normal to the coil cross section area **A**. It is desired to maximize the output voltage by operating with an angle θ of zero and maximize the constant field density **B**. In this case, the first and last terms of (5) will be suppressed and the equation reduces to:

$$V = NB\frac{dA}{dt} \tag{6}$$

The coil's shape is rectangular with length l and width x, during operation the length l remains constant and the width x varies with respect to the moving mass. This reduces (6) to the following:

$$V = NBl\frac{dx}{dt}, \tag{7}$$

where $\frac{dx}{dt}$ is the velocity of the moving mass.

2.1 Magnetic Field Model

One of the most important elements of the electromagnetic VEH is the magnetic flux density. It is therefore important to accurately design the magnetic circuit with the objective to maximize and stabilize the flux density around the coil. The magnetic circuit of the VEH is shown in Fig. 3, it consists of four magnets arranged as shown in the figure, a steel cage, and an air gap separating the two sets of magnets. The material for the steel cage is mild steel and the magnets are Sintered Neodymium.

The finite element modeling software ANSYS was used to determine the magnetic flux density. The FEM simulations results are compared with measured results for validation purposes. The FEM simulation results of the magnetic field strength obtained from ANSYS are shown in Figs. 4 and 5, while the measured results are shown in Fig. 6.

The measured and simulated results of the magnetic circuit show that the magnetic flux density is constant (0.74T) but has opposite signs on each side of the magnetic circuit. This is due to the fact that the polarities of the two sets of magnets are reversed (S-N and N-S). This setup allows the induced voltage across the coil to add up and hence maximize the harvested power. From Fig. 6, we recognize that the flux density is maximum over a 6–7 mm range, where it is desired that the magnets oscillate with

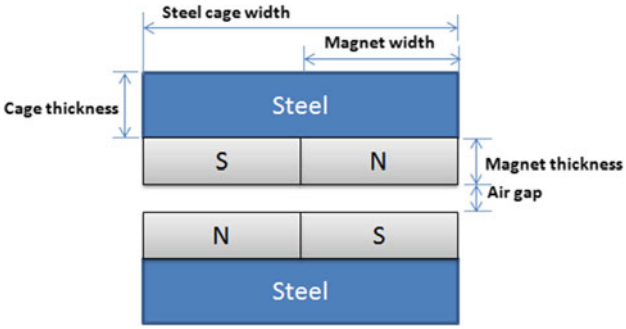

Fig. 3 Magnetic circuit

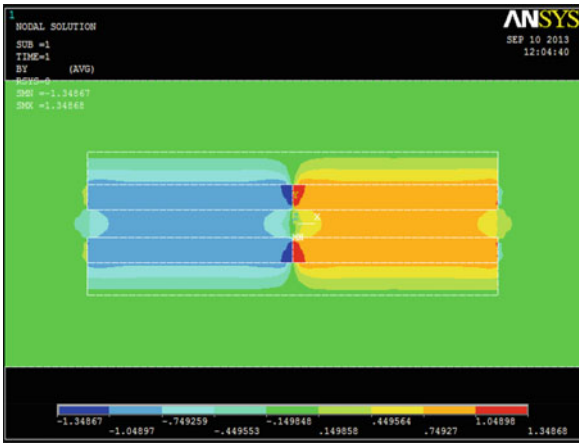

Fig. 4 Calculated magnetic flux density

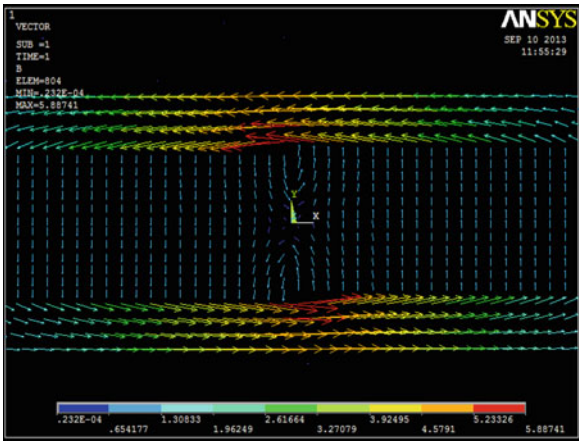

Fig. 5 Calculated magnetic field distribution

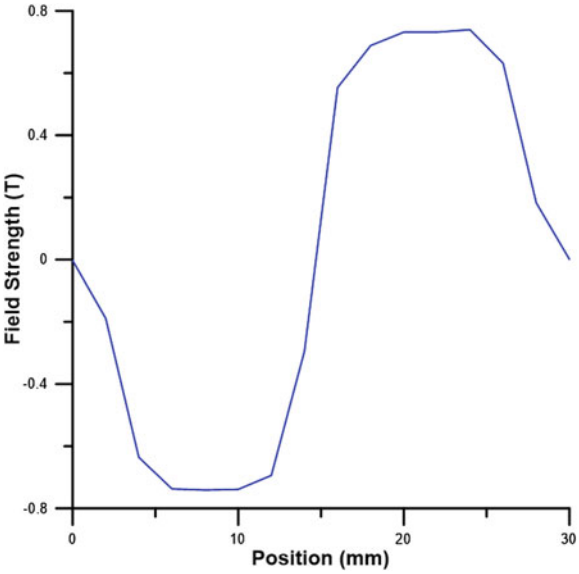

Fig. 6 Measured magnetic flux density

respect to the stationary coil in order to reduce any magnetic softening effects in the harvester.

2.2 Damping

Damping in the vibration energy harvester comes from two sources, mechanical and electrical energy losses. The mechanical damping is usually approximated as viscous linear damping, but in the case of the impact VEH cubic nonlinear damping is added to account for energy losses when the seismic mass impacts the end limiters. The cubic damping is defined as:

$$F_n = b_n \dot{x}\, x^2 \tag{8}$$

where b_n is the nonlinear damping coefficient, and found by fitting experimental data of the frequency-response curve of the model.

2.2.1 Electrical Damping

In electromagnetic vibration energy harvesters, when the current passes through the coil it creates a magnetic field that opposes the field produced by the magnets. The interaction between the two fields produces a force which opposes the motion of the inertial mass. Consequently, the interaction force that acts as electromagnetic

damping produces the harvested power delivered to the load, and it can be expressed as [28]

$$F_{em} = b_e \frac{dx}{dt} \tag{9}$$

The electrical power is extracted from the mechanical oscillator and is given by [6]

$$P_{em} = F_{em} \frac{dx}{dt} \tag{10}$$

A small part of this power is dissipated in the coil resistance R_c, and the rest is delivered to the load resistance R_L. Equating the power dissipated to that generated by the electromagnetic force gives

$$P_{em} = b_e \left(\frac{dx}{dt}\right)^2 = \frac{V^2}{R_L + R_C + j\omega L} \tag{11}$$

where L is the coil inductance. Substituting for the voltage using (2), we can write the electromagnetic damping as

$$b_e = \frac{1}{R_L + R_C + j\,\omega\, L} \left(\frac{d\phi}{dx}\right)^2 \tag{12}$$

Assuming that the coil inductance is negligible and the magnetic field intensity B is constant, the electromagnetic damping coefficient can be expressed as:

$$b_e = \frac{(Bl)^2}{R_L + R_C} \tag{13}$$

where l is the effective length of the coil. The electrical damping can, therefore, be calculated using (13) and the parameter values given in Table 3.

2.2.2 Mechanical Damping

The viscous mechanical damping is estimated from the measured open-load frequency-response curve of the harvester, which determines the quality factor Q of the VEH, while the nonlinear damping coefficient is found by matching the experimental frequency-response curve to the numerical results of the model.

Table 3 Electromagnetic transducer parameters

Parameter	Value
Magnetic field B (T)	0.74
Effective coil length l (m)	1.75
Coil resistance R_C (Ω)	3.4

Table 4 Mechanical damping parameters

Parameter	Value
Mass, m (kg)	0.12
Stiffness, k_1 (N/m)	950
Center frequency, f_0 (Hz)	21
Low cut-off frequency, f_1 (Hz)	20.2
High cut-off frequency, f_2 (Hz)	22.5

The quality factor of the VEH is defined as:

$$Q_m = \frac{f_0}{\Delta f} \tag{14}$$

where f_0 is the center frequency and $\Delta f = f_2 - f_1$, with f_1 and f_2 are the two half-power frequencies. The quality factor relates to the mechanical damping of the harvester as follows;

$$Q_m = \frac{m\,\omega}{b_m} \tag{15}$$

where b_m is the mechanical damping coefficient of the open-load harvester. The mechanical damping is found using (14) and (15) and the values of the VEH's parameters given in Table 4, $b_m = 1.16$ kg/s. The center frequency and half-power bandwidth were found from a frequency-sweep curve of the base acceleration of the VEH at an amplitude of $A_0 = 0.05g$.

2.3 Gravity

The response of the VEH undergoes significant qualitative changes when the orientation of the gravitational field with respect to the linear guide changes. When the linear guide is aligned horizontal with respect to the surface of earth, such that gravity is perpendicular to the track, the harvester motions are symmetric with respect to the track mid-point. As soon as a component of the gravitational field acts along the track, it breaks the symmetry of the harvester motions.

First, in Sect. 3, the response of the symmetric HEV is analyzed when it is aligned horizontally. Then, in Sect. 4, we will model and analyze the response of the limiting case for asymmetric VEHs, a VEH aligned vertically.

3 Horizontal VEH

3.1 Model

The harvester is modeled as a single degree of freedom oscillator with piecewise-linear stiffness, Fig. 7, subject to harmonic base excitations applied directly to the housing unit.

We set the origin of the coordinate system used to describe the motion of seismic mass at the half point between the springs. The seismic mass m is assumed to be a point mass, as shown in Fig. 8. The free distance along the rail (not occupied by the cage) between the upper and lower uncompressed springs is denoted L. The uncompressed length of each spring is denoted x_s and the fully compressed length is denoted x_c. In this configuration, the governing equation of motion of the moving mass is given by:

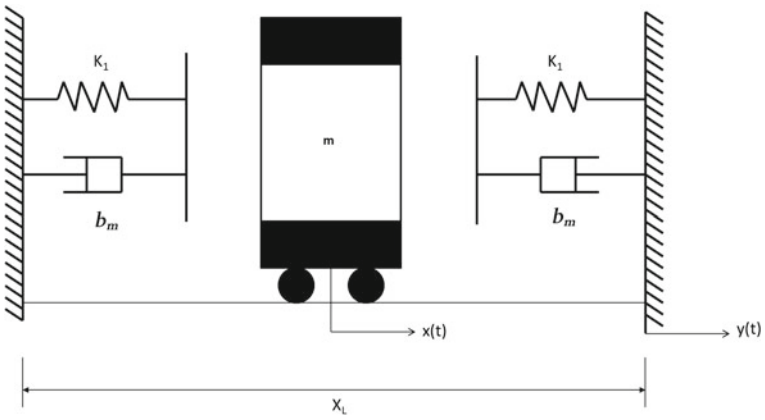

Fig. 7 Horizontal VEH schematic

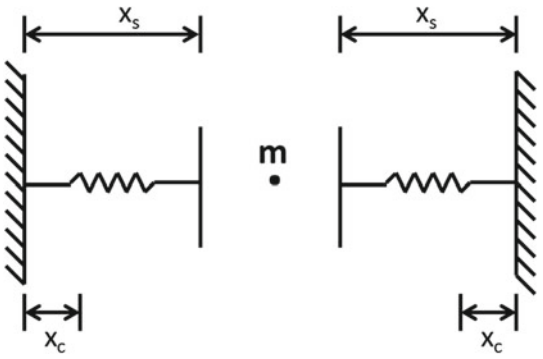

Fig. 8 Horizontal VEH simplified schematic

$$m\ddot{x} + b_m\dot{x} + b_n x^2\dot{x} + F_e + F(x) = -m\ddot{y} \tag{16}$$

where x and y are the displacements of the seismic mass m and the housing unit, respectively, and $F(x)$ is a nonsmooth function representing the system's stiffness given by (19), and F_e is the induced *emf* given by (9),

$$F_e = b_e\dot{x} \tag{17}$$

Substituting (17) in (16) we obtain the equation of motion of the "Springless" VEH;

$$m\ddot{x} + (b_m + b_e)\dot{x} + b_n x^2\dot{x} + F(x) = -m\ddot{y} \tag{18}$$

The restoring force $F(x)$ is defined such that:

- The springs stiffness is set to the linear stiffness of the spring k_1 when it is not fully compressed (no impact)
- The springs stiffness is set to a higher stiffness k_2 when it is fully compressed (impact) with $k_2 \gg k_1$

The force-displacement relationship shown in Fig. 9, $F(x)$ can be written as follows:

$$F(x) = \begin{cases} 0 & -x_s \le x \le x_s \\ k_1(x - x_s) & x_s < x \le x_c \\ k_2(x - x_c) + k_1(x_c - x_s) & x_c < x \le \frac{L}{2} \\ k_1(x + x_s) & -x_c < x < -x_s \\ k_2(x + x_c) + k_1(x_s - x_c) & -\frac{L}{2} \le x \le -x_c \end{cases} \tag{19}$$

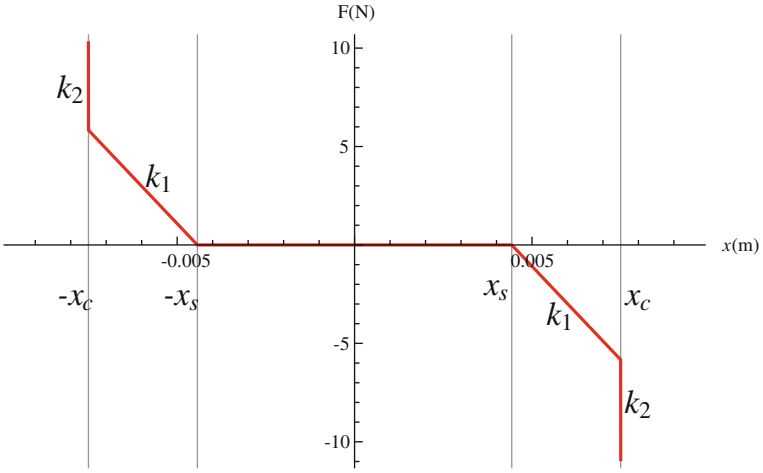

Fig. 9 Force-displacement relationship

The VEH scavenges vibration energy transmitted to it from an environmental vibration source represented by the base acceleration,

$$\ddot{y} = a(t) = A_0 \cos \omega t \tag{20}$$

where A_0 and ω are the amplitude and frequency of the external excitation. The equation of motion (18) is nondimensionalized using the nondimensional variables,

$$\begin{aligned} &\omega_n = \sqrt{\frac{k_1}{m}},\ \omega_h = \sqrt{\frac{k_2}{m}},\ \alpha_1 = \frac{x_s}{L},\ \alpha_2 = \frac{x_c}{L},\ \zeta_2 = \frac{b_n}{2\,m\,\omega_n} \\ &A = \frac{A_0}{L\,m\,\omega_n^2},\ \zeta_1 = \frac{b_e + b_m}{2\,m\,\omega_n},\ \gamma = \left(\frac{\omega_h}{\omega_n}\right)^2,\ \Omega = \frac{\omega}{\omega_n}. \end{aligned} \tag{21}$$

and is written as,

$$\ddot{x} = A\,\cos(\Omega t) - 2\,\dot{x}\,(\zeta_1 + \zeta_2\,x^2) - F(x) \tag{22}$$

where the nondimensional restoring force is given by:

$$F(x) = \begin{cases} 0 & -\alpha_1 \le x \le \alpha_1 \\ x - \alpha_1 & \alpha_1 < x \le \alpha_2 \\ -\alpha_1 + \alpha_2 + \gamma(x - \alpha_2) & \alpha_2 < x \le 1 \\ \alpha_1 + x & -\alpha_2 \le x < -\alpha_1 \\ \alpha_1 - \alpha_2 + \gamma(\alpha_2 + x) & -1 \le x < -\alpha_2. \end{cases} \tag{23}$$

3.2 Experimental Results

The "Springless" VEH was tested using a feedback-controlled vibration shaker that provides base excitations with constant acceleration and different frequencies. The testing setup is shown in Fig. 10. Different experiments were performed to examine the harvesters time response and frequency response. Different time response waveforms of the VEH, shown in Fig. 11, were obtained by applying different input base excitations with constant amplitude at different frequencies, the figures show waveforms for an input amplitude $A_0 = 0.5g$ at frequencies in the region of the natural frequency of the oscillator (f= 15, 17, 18, 20 Hz).

The frequency response curves shown in Fig. 12 represent the up and down frequency sweep for input accelerations $A_0 = 0.3 - 0.6g$ and a 40 turns concentric coil. We note from Fig. 12 a number of characteristics associated with nonlinear systems: (1) The existence of a hysteresis band between the up and down frequency sweep, (2) existence of the jump phenomena, (3) the frequency response curve peak shifts to the right as the amplitude of input excitation is increased, and (4) the frequency bandwidth increases with increase in the base excitation amplitude. We also confirm

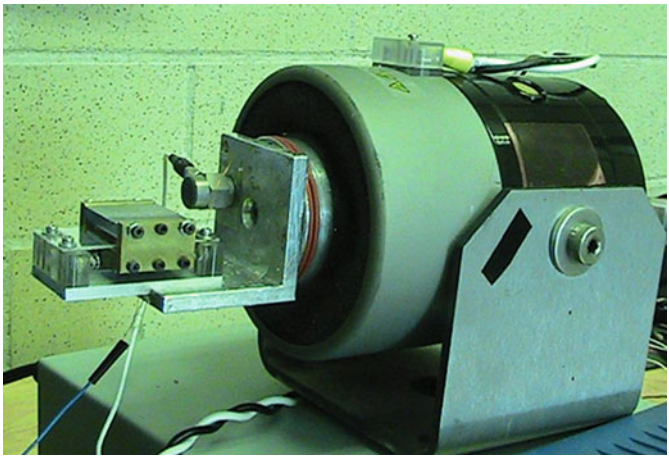

Fig. 10 Experimental setup of the horizontal "Springless" VEH

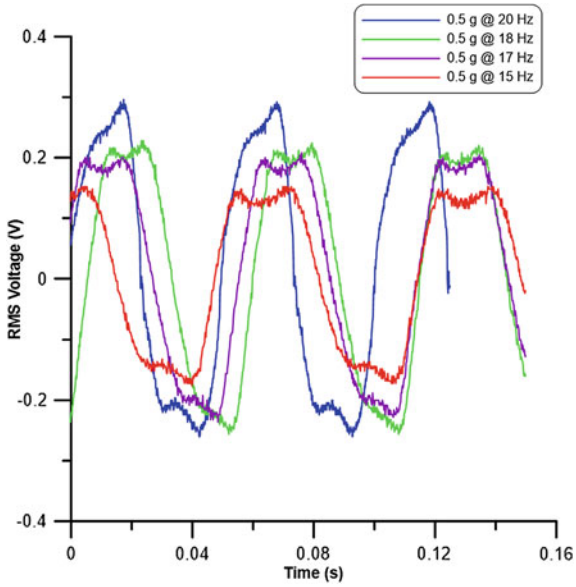

Fig. 11 Experimental time response waveforms of the "Springless" VEH for input $A_0 = 0.5g$ and frequencies $\Omega = 15, 17, 18$ and 20 Hz

from the results shown in Fig. 13 that as the coil's number of turns is increased the output voltage increases as well as the frequency bandwidth. The increase in the frequency bandwidth is due to the increase of the parasitic resistance which in turns reduces the electrical damping of the system.

Tests were carried out on the VEH to determine its optimal power and optimal load. A resistive load was connected across the coil's terminals and the base excitation input frequency was varied over the frequency range $f = 5$–20 Hz. The test was repeated

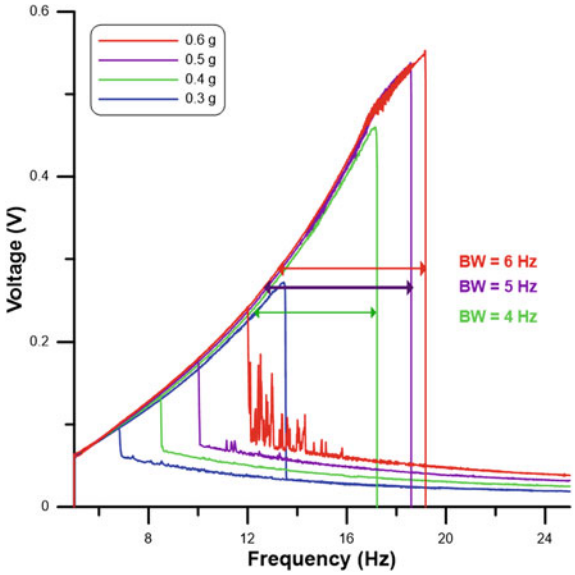

Fig. 12 VEH Experimental frequency response curves for input accelerations $A_0 = 0.3 - 0.6g$

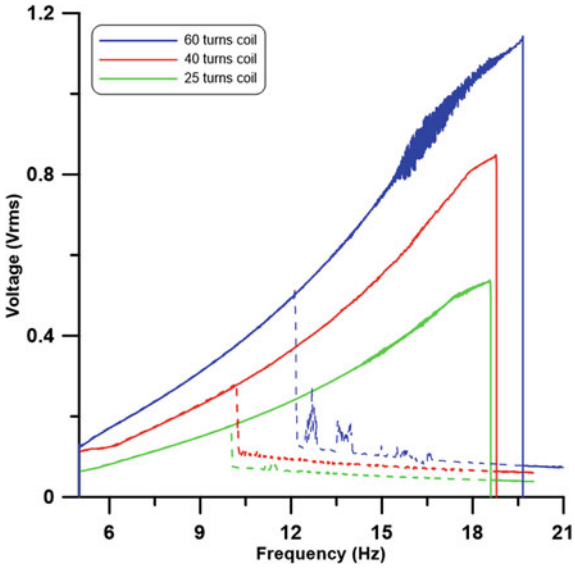

Fig. 13 Experimental frequency response curves for coils with number of turns $N = 25$, 40, and 60

using different values of the resistive load. Results shown in Fig. 14 represent the frequency-response curves of the VEH for different loads. From the figures, we conclude that the optimal power is 8.5 and 12 mW while the optimal voltage is 0.8 and 1.2 mV for a 40 and 60 turns coil respectively.

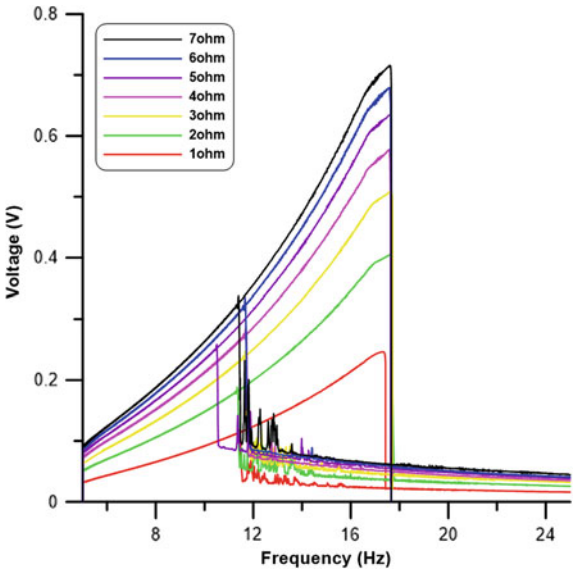

Fig. 14 Harvester's output voltage for input acceleration $A_0 = 0.5g$ and a coil with 60 turns for loads $R = 1{-}7\ \Omega$

3.3 Numerical Results

Nonlinear dynamical systems are usually solved using numerical long-time integration. However, the long-time integration method might not yield periodic solutions easily and provides no information about the system's stability. Therefore, other numerical methods for finding periodic solutions and analyzing their stability must be used. The shooting method is a well known numerical method that uses numerical integration in conjunction with Floquet theory to obtain periodic solution and assesses their stability [29]. For validation purposes, the averaging method is used to find approximate closed-loop form solutions.

3.3.1 Shooting Method

The shooting method described in [29] is applied to the VEH equation of motion given by (18), which is written as a system of first order differential equation:

$$\begin{aligned} \dot{x}_1 &= x_2 \\ \dot{x}_2 &= -\frac{b_e + b_m}{m} x_2 \; - \; \frac{b_n}{m} x_2 \, x_1^2 \; - \; \frac{F_{st}(x_1)}{m} - y \end{aligned} \tag{24}$$

Equation (24) can be written as;

$$\dot{\mathbf{x}} = \mathbf{F}(\mathbf{x}, t), \tag{25}$$

where $\mathbf{x}$ is the state variables vector (x_1, x_2), and $\mathbf{F}$ is a vector function. The shooting method is used to find a periodic solution, $\mathbf{x}(t) = \mathbf{x}(t+T)$, that satisfies (25) by solving the boundary-value problem:

$$\begin{aligned} \dot{\mathbf{x}} &= \mathbf{F}(\mathbf{x}, t) \\ \mathbf{x}(0) = \eta,\ \mathbf{x}(T) &= \eta \end{aligned} \tag{26}$$

where η is a vector of initial guesses and T is the period, both of which are in general unknown a priori. Applying the shooting technique, the two-point boundary-value problem is converted into a initial-value problem, and the resulting system of equations is

$$\begin{aligned} \dot{\mathbf{x}} &= \mathbf{F}(\mathbf{x}) \\ \mathbf{x}(0) = \eta_0,\ \mathbf{x}(T) &= \eta_0 \\ \frac{d}{dt}\left(\frac{\partial \mathbf{x}}{\partial \eta}\right) &= D_{\mathbf{x}} F(\mathbf{x}) \frac{\partial \mathbf{x}}{\partial \eta} \\ \frac{\partial \mathbf{x}}{\partial \eta}(0) &= I \end{aligned} \tag{27}$$

where I is the two dimensional identity matrix. Applying the shooting method to our system we obtain the following system of differential equations;

$$\begin{aligned} &\dot{x}_1(t) = x_2(t) \\ &\dot{x}_2(t) = -x_2(t)\,\frac{b_e + b_m}{m} - x_2(t)\,x_1(t)^2\,\frac{b_n}{m} - \frac{F_{st}}{m} - y(t) \\ &\frac{d}{dt}\left(\frac{\partial x_1}{\partial \eta_1}\right) = \frac{\partial x_2}{\partial \eta_1} \\ &\frac{d}{dt}\left(\frac{\partial x_1}{\partial \eta_2}\right) = \frac{\partial x_2}{\partial \eta_2} \\ &\frac{d}{dt}\left(\frac{\partial x_2}{\partial \eta_1}\right) = -\frac{b_e + b_m}{m}\frac{\partial x_2}{\partial \eta_1} - \frac{b_n}{m}\frac{\partial (x_2\,x_1^2)}{\partial \eta_1} - \frac{1}{m}\frac{\partial F_{st}}{\partial x_1}\frac{\partial x_1}{\partial \eta_1} \\ &\frac{d}{dt}\left(\frac{\partial x_2}{\partial \eta_2}\right) = -\frac{b_e + b_m}{m}\frac{\partial x_2}{\partial \eta_2} - \frac{b_n}{m}\frac{\partial (x_2\,x_1^2)}{\partial \eta_2} - \frac{1}{m}\frac{\partial F_{st}}{\partial x_1}\frac{\partial x_1}{\partial \eta_2} \\ &\mathbf{x}(0) = \eta_0 \\ &\frac{\partial x_1}{\partial \eta_1}(0) = 1,\ \frac{\partial x_1}{\partial \eta_2}(0) = 0,\ \frac{\partial x_2}{\partial \eta_1}(0) = 0,\ \frac{\partial x_2}{\partial \eta_2}(0) = 1 \end{aligned} \tag{28}$$

The shooting algorithm requires an initial guess, this is done by solving (24) by long time integration for a given base acceleration amplitude and frequency, then a point on the obtained orbit is used as an initial guess to solve the system of (27). A periodic solution is found once the change in the initial guess between two iterations falls within a predefined error criteria. The amplitude or frequency

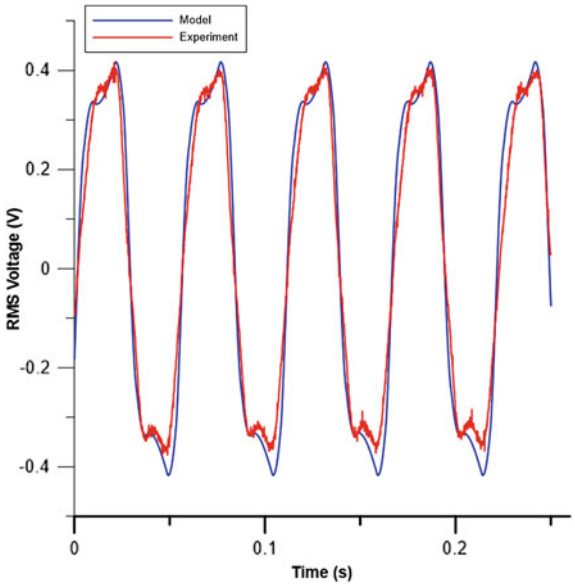

Fig. 15 Harvester's experimental and model output voltage for input acceleration $A_0 = 0.5g$ and frequency $f = 18$ Hz, and a coil with 60 turns

of base acceleration is then updated and the process is repeated to obtain an orbit corresponding to the new forcing parameters. Figure 15 shows the waveforms of the VEH obtained numerically and experimentally. From the figure we note a very close match between numeric and experimental results. Figure 16 shows the numeric and experimental frequency response curves of the VEH. The numerical results match those experimentally indicating the model captures and reproduces the behavior of the VEH.

3.4 Analytical Results

The averaging method is used to obtain an approximate closed-form solution of the harvester's equation of motion given by (18). We assume a solution of the form:

$$x(t) = a \sin(\Omega\, t + \beta) \tag{29}$$

where a and β are slowly varying amplitude and phase. We also assume that:

$$\dot{x}(t) = a\Omega\, \cos(\Omega\, t + \beta) \tag{30}$$

subject to the constraint:

$$\dot{a} \sin\phi + a\dot{\beta} \cos\phi = 0. \tag{31}$$

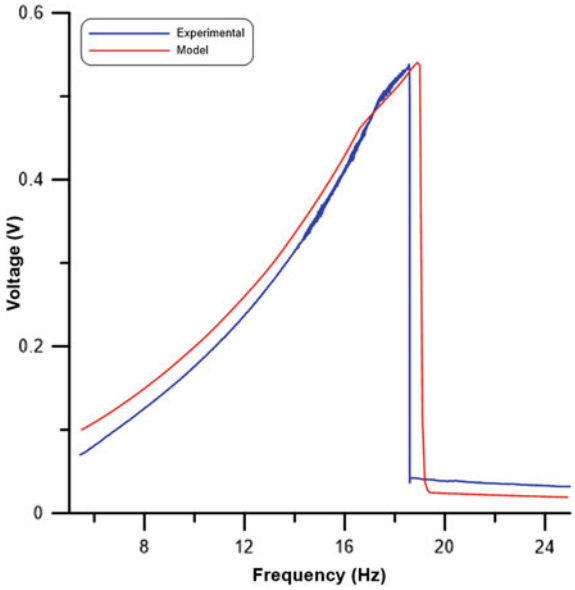

Fig. 16 VEH's experimental and numerical frequency response curves for input acceleration $A_0 = 0.5g$ and a coil with 60 turns

where we set $\phi = \Omega\, t + \beta$. Using (29) and (30) in the normalized equation of motion (18), we obtain the second constraint:

$$\begin{aligned} &\dot{a}\cos\phi + 2\,a\,\zeta\,\cos\phi\,((1+a^2)\,\sin(t+\beta))^2)) \;+ F(x) \\ &= a(\dot{\beta}+1)\sin\phi + A\,\cos(\Omega\, t). \end{aligned} \tag{32}$$

Solving (31) and (32) for $\dot{a}$ and $\dot{\beta}$ yields:

$$\dot{a} = -\left[2\,a\,\zeta\,\cos\phi\,(1+a^2\sin^2\phi) - a\,\sin(\phi) - A\cos(\Omega t) + F(\phi)\right]\cos\phi \tag{33}$$

$$a\,\dot{\beta} = \left[2a\,\zeta\,\cos(\phi)\,(1+a^2\,\sin^2\phi) - a\sin(\phi) - A\,\cos(\Omega\, t) + F(\phi)\right]\sin(\phi) \tag{34}$$

Next, we use (29) to write the restoring force in terms of the phase angle ϕ as

$$F(\phi) = \begin{cases} 0 & 0 \le \phi \le \phi_1 \\ a\sin\phi - \alpha_1 & \phi_1 \le \phi \le \phi_2 \\ a\gamma\,\sin\phi + \alpha_2(1-\gamma) - \alpha_1 & \phi_2 \le \phi \le \pi - \phi_2 \\ 0 & \pi - \phi_1 \le \phi \le \phi_1 + \pi \\ a\sin\phi + \alpha_1 & \phi_1 + \pi \le \phi \le \phi_2 + \pi \\ a\gamma\,\sin\phi + \alpha_2(\gamma-1) + \alpha_1 & \phi_2 + \pi \le \phi \le 2\pi - \phi_2 \\ a\sin\phi + \alpha_1 & 2\pi - \phi_2 \le \phi \le 2\pi - \phi_1 \\ 0 & 2\pi - \phi_1 \le \phi \le 2\pi \end{cases} \tag{35}$$

where

$$\phi_1 = \sin^{-1}\left(\frac{\alpha_1}{a}\right), \quad \phi_2 = \sin^{-1}\left(\frac{\alpha_2}{a}\right)$$

are the phase angles corresponding the seismic mass contacting the linear spring at $x = x_s$ and the fully compressed spring $x = x_c$, respectively.

We define a detuning parameter describing the difference between the forcing frequency Ω and ω_n as

$$\sigma = \Omega - 1$$

and average (33) and (34) over the interval of one period $(0,\ 2\pi)$ to obtain the modulation equations

$$\begin{aligned}
\dot{a} =& -a\frac{1}{2}\zeta\,(4+a^2) + \frac{A}{2}\cos(\sigma\, t - \beta)\\
\dot{\beta} =& \frac{1}{2\pi}\Bigg[-2\alpha_2(\gamma-1)\sqrt{1-\frac{\alpha_2^2}{a^2}} - 2\alpha_1\sqrt{1-\frac{\alpha_1^2}{a^2}}\\
&+ a\left(-2(\gamma-1)\sin^{-1}\left(\frac{\alpha_2}{a}\right) - 2\sin^{-1}\left(\frac{\alpha_1}{a}\right) + \pi\gamma\right)\Bigg] - \frac{1}{2}\\
&- \frac{A}{2a}\sin(\sigma t - \beta)
\end{aligned} \tag{36}$$

Defining the phase angle $\psi = \sigma t - \beta$, we write the modulation equations in autonomous form as

$$\begin{aligned}
\dot{a} =& -a\frac{1}{2}\zeta\,(4+a^2) + \frac{A}{2}\cos\psi\\
\dot{\psi} =& \sigma - \frac{1}{2\pi}\Bigg[2\alpha_2(\gamma-1)\sqrt{1-\frac{\alpha_2^2}{a^2}} + 2\alpha_1\sqrt{1-\frac{\alpha_1^2}{a^2}}\\
&+ a\left(-2(\gamma-1)\sin^{-1}\left(\frac{\alpha_2}{a}\right) - 2\sin^{-1}\left(\frac{\alpha_1}{a}\right) + \pi\gamma\right)\Bigg] - \frac{1}{2}\\
&- \frac{A}{2a}\sin\psi
\end{aligned} \tag{37}$$

The steady-state periodic solutions correspond to the fixed points $(a_0,\ \psi_0)$ of the modulation equations. These equations are solved numerically for the fixed points as a function of the detuning parameter σ. Substituting the fixed point at $\sigma = 0$, which corresponds to the resonance frequency, in the assumed solution form, (29), we obtain the seismic mass response shown in Figs. 17 and 18. Figure 17 shows the time response of the seismic mass displacement when the frequency of base excitation matches the natural frequency of the oscillator. Figure 18 shows the corresponding orbits of the seismic mass obtained numerically and analytically.

4 Vertical Configuration

A vertical implementation of the VEH, is suitable for environments where motions are predominantly in the vertical direction. The linear guide, aligned vertically as shown in Fig. 19, allows the carriage to move freely along the rail. When the assembly vibrates due to a base excitation $y(t)$, the seismic mass m moves with respect to the housing producing a relative displacement $x(t)$. In this section the mathematical model of the vertically aligned VEH is derived and the numerical method used to obtain the periodic orbits of the system. Experimental results are then used to validate the model.

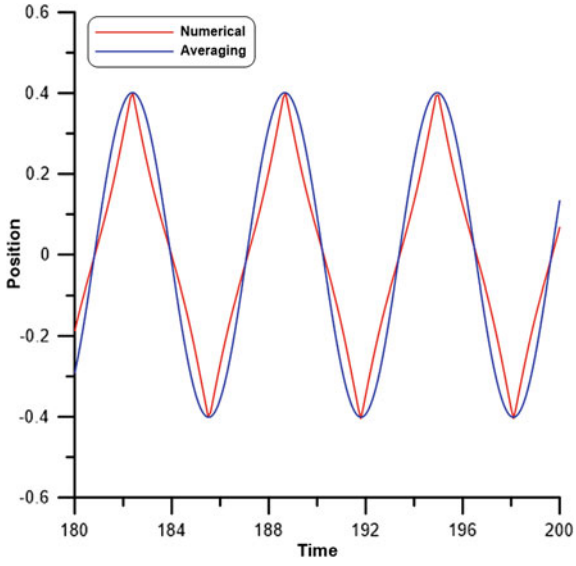

Fig. 17 Displacement of VEH's mass m: numerical (*red*) and analytical (*blue*) for base acceleration amplitude of $A_0 = 0.6g$

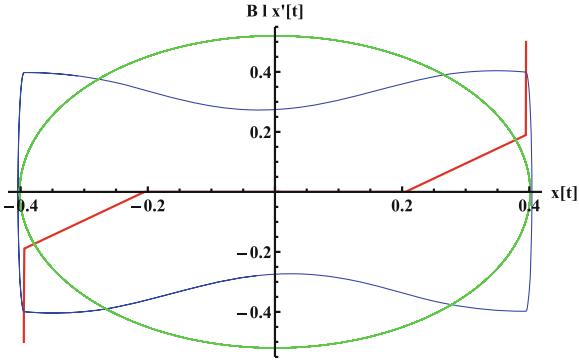

Fig. 18 VEH orbits: numerical (*blue*) and averaging (*green*) for base acceleration amplitude of $A_0 = 0.6g$

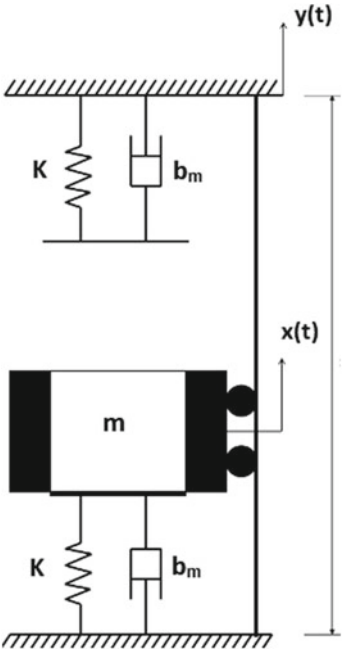

Fig. 19 Schematic of the vertically-aligned springless VEH

4.1 Model

The equation of motion of the vertically-aligned harvester can be written as:

$$m\,\ddot{x} = -\,(b_e + b_m)\,\dot{x} - F_{st}(x) - m\,\ddot{y} - m\,g, \tag{38}$$

where $F_{st}(x)$ is the restoring force. The VEH harvests kinetic energy transmitted to it from the host vibrations represented by the base acceleration

$$\ddot{y} = A_0 \cos(\Omega\, t), \tag{39}$$

where A_0 and Ω are the amplitude and frequency of the external excitation.

The origin of the coordinate system is placed at the point where mass m rests on the lower spring. The seismic mass m is assumed to be a point mass, as shown in Fig. 20. The free distance along the rail, not occupied by the cage, between the upper and lower uncompressed springs is denoted x_t. The uncompressed length of each spring is denoted x_s and the fully compressed length is denoted x_c. The restoring force $F_{st}(x)$ varies with the position of the inertial mass m according to the equation:

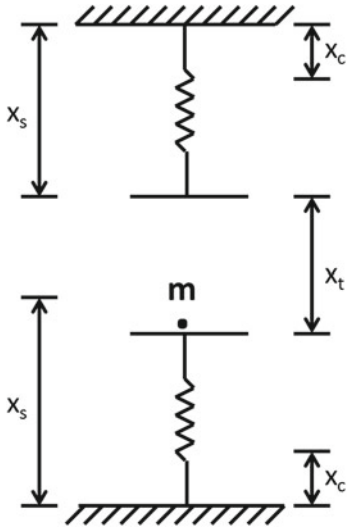

Fig. 20 Simplified schematic of the VEH

$$F_{st}(x) = \begin{cases} 0 & 0 \le x \le x_t \\ k_1 x & x_c - x_s < x \le 0 \\ k_1(x_c - x_s) + & \\ k_2(-x_c + x_s + x) & -x_s \le x \le x_c - x_s \\ k_1(x - x_t) & x_t < x < -x_c + x_s + x_t \\ k_1(x_s - x_c) + & -x_c + x_s + x_t < x < x_s + x_t \\ k_2(x_c - x_s - x_t + x) & \end{cases} \tag{40}$$

where x_s is the position where the mass touches the uncompressed spring, x_c is the position where the spring is fully compressed, k_1 is the linear spring stiffness, and k_2 the linear stiffness of the fully compressed spring. The force-displacement relationship is shown in Fig. 21.

5 Results

A prototype of the VEH is mounted on an electromagnetic shaker as shown in Fig. 22 and a base acceleration is applied as input excitation with amplitude A_0 and frequency Ω. The voltage across the coil terminals is measured using an oscilloscope.

Experimental results show that the vertically-aligned harvester possesses three different regions of operation. For amplitudes ($A_0 \le 0.05g$), the VEH response is linear, since the seismic mass remains attached to the lower spring throughout motion, this region will be known as the linear regime. For acceleration amplitudes in the range ($0.1g < A_0 < 0.5g$), the mass detaches from the lower spring during motion without impacting the upper one. In this region, the response is that of a

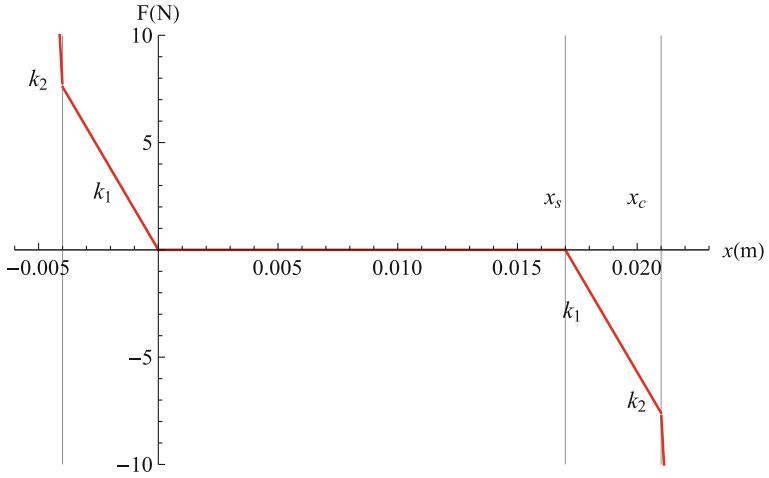

Fig. 21 Restoring force-displacement relationship

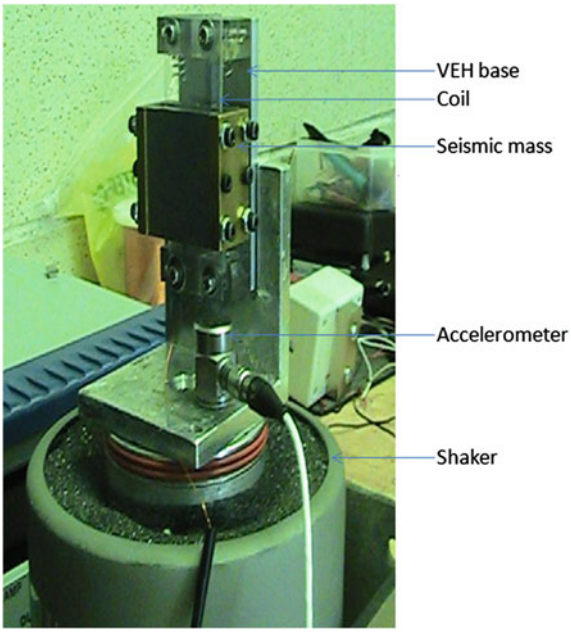

Fig. 22 Experimental setup of the VEH

single-impact oscillator and will be therefore called the single impact regime. For acceleration amplitudes ($A_0 > 0.5g$), the mass impacts both springs and the response is that of a double-impact oscillator, this will be called the double impact regime. The experimental and numerical results for the three different regimes are presented next.

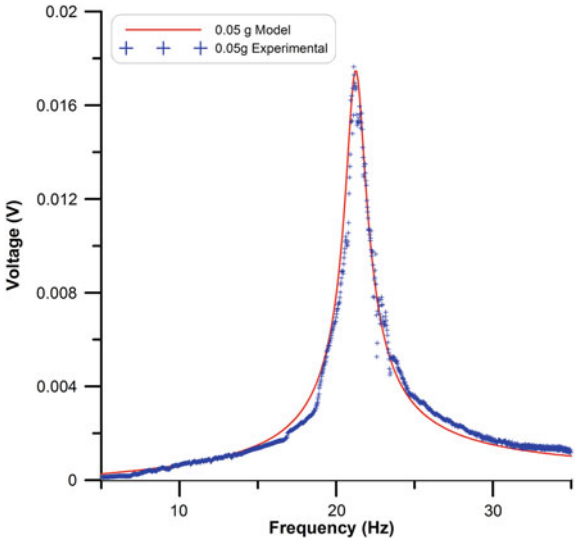

Fig. 23 The numerical (*red line*) and experimental (*blue* +) open circuit voltage (RMS) for an excitation of amplitude $A_0 = 0.03g$ (Color figure Online)

5.1 Linear Regime

In this case, the mass remains in contact with the lower spring. Test results show that the response of the VEH is linear. Figure 23 shows the measured and numerically obtained frequency-response curves of the voltage (RMS) across the open circuit terminals of the coil. Base acceleration amplitude is held constant at $A_0 = 0.03g$, while the frequency is swept up and down in the range 12–30 Hz.

Since the response of the VEH system is linear, the piecewise restoring force reduces to a linear relationship between stiffness and displacement, and the equation of motion is reduced to a simple spring-mass-damper model given by:

$$\ddot{x} = -\frac{b_m}{m}\dot{x} - \frac{k_1}{m}x - \ddot{y} - g, \tag{41}$$

The steady-state response x of linear model under a base acceleration

$$\ddot{y} = \Omega^2 Y_0 \cos \Omega t = A_0 \cos \Omega t \tag{42}$$

is given by:

$$x(t) = a \cos(\Omega t + \Phi) \tag{43}$$

where a and Φ are the amplitude and phase of the system response and their expressions can be found in books that deal with linear one DOF oscillators. The open circuit voltage is given by:

$$V_L = Bl\dot{x} \tag{44}$$

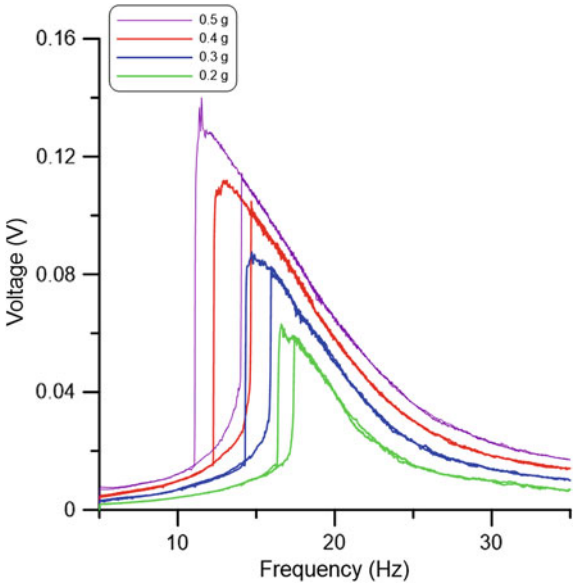

Fig. 24 Frequency-response curves of the VEH under base acceleration amplitudes in the range of $A_0 = 0.2{-}0.5g$

The harvester's response is obtained by substituting the parameter values listed in Table 4 into (41) and numerically integrating. The results, shown in Fig. 23, agree reasonably well with the experimental results. The maximum output voltage is 18 mV obtained at the center frequency $f_c = 21$ Hz and the harvesting bandwidth is 3 Hz.

5.2 Single Impact

The experimental frequency-response curves of the voltage across the open circuit terminals of the coil for base acceleration amplitudes in the range 0.2–0.5 g are shown in Fig. 24. The figure shows the up- and down-sweeps in the frequency range 5–35 Hz. We note the existence of hysteresis between the up and down frequency sweeps and jumps between an upper and a lower branches of response in the frequency-response curves. We note in Fig. 24 that the jump to the lower branch occurs as the frequency is swept down indicating the existence of a softening nonlinearity in the VEH [29]. The hysteresis range increases with base acceleration amplitude from 1 Hz at $A_0 = 0.2g{-}3\,Hz$ at $A_0 = 0.5g$.

The harvester response for a base acceleration amplitude $A_0 = 0.4g$ was obtained numerically and the results compare reasonably well with the experimental results as shown in Fig. 25. The stiffness and damping were reduced for this regime to $k_1 = 880$ N/m and $b_m = 0.6$ N m/s, respectively. This is expected since in this regime the mass looses contact with the spring and spends significant time in air and thus reducing the effective stiffness and damping of the VEH.

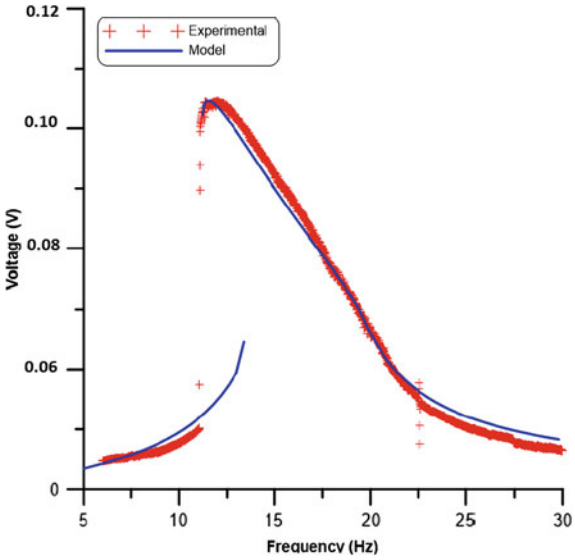

Fig. 25 The open circuit voltage between the coil terminals for a base acceleration amplitude $A_0 = 0.4g$

We note that the reduction in effective stiffness shifts the center frequency from $f_c = 21$ Hz to the range 12–16.5 Hz, which indicates that nonlinearities in the system facilitate low frequency harvesting. Further, as the base acceleration amplitude was increased, the peak frequency dropped, from $f_c = 16.5$ Hz at $A_0 = 0.2g$–$f_c = 14.5$ Hz at $A_0 = 0.3g$ and $f_c = 12$ Hz at $A_0 = 0.4g$, as the carriage spent more time in air away from the lower spring.

Meanwhile, the maximum output voltage continued to increase with base acceleration amplitude as expected. For base acceleration amplitude $A_0 = 0.4g$, the maximum output voltage was 110 mV (RMS) obtained at a frequency of $f_c = 12$ Hz.

5.3 Double Impact

For large excitations, the base acceleration amplitude was set to the range of $A_0 = 0.6 - 1g$. Figure 26 shows the frequency-response curves obtained for the open-circuit output voltage of the VEH. As in the case of moderate excitations, note the up and down jumps between branches of response and hysteresis between up and down-sweeps in the frequency range of 5–35 Hz.

We also observe a new branch of responses in the harvester frequency response. Two additional jumps appear to the right (at higher frequency) of the two original jumps in the frequency-response curves leading up to the new branch during frequency down-sweeps and down from it during up-sweeps. The harvester response is linear along this new branch. For instance, for base acceleration amplitude $A_0 = 0.8g$ the new jumps occur at $f = 13$ and $f_c = 15$ Hz.

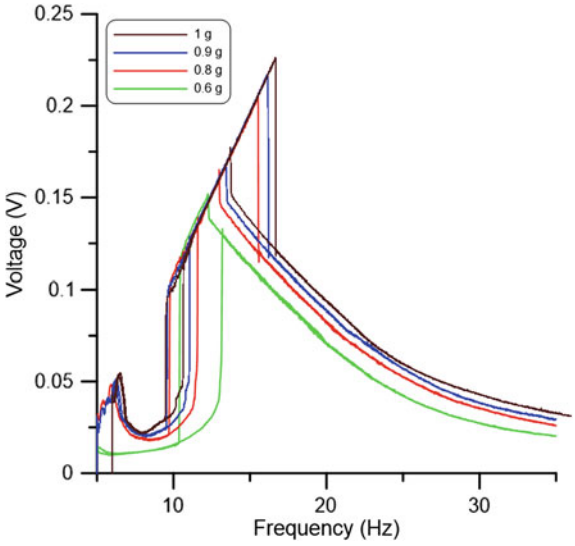

Fig. 26 Frequency-response curves of the VEH for base acceleration amplitude in the range of $A_0 = 0.6{-}1g$

This new phenomenon is attributed to large seismic mass motions covering the entire track between the two springs. Along this branch of response, the mass motions reach the maximum allowable displacement

$$D \approx x_t + x_s - x_c$$

which remains almost constant as the excitation frequency varies since it is limited by the two hard springs k_2. As a result, the velocity along this branch is

$$\dot{x} \approx \omega D \sin(\omega t + \phi)$$

Using (44), we obtain the output voltage (RMS) as

$$V = \frac{B\,l\,D}{\sqrt{2}}\omega \tag{45}$$

We note that the measured output voltage varies linearly with the frequency, Fig. 26, in accordance with (45). Further, since base acceleration amplitude does not appear in (45), the voltage output falls on the same line for all acceleration amplitude values reported here.

6 Conclusion

In this paper we investigated the response of a wideband impact VEH numerically and experimentally when aligned horizontally and vertically. Results show that using a double-impact oscillator and a concentric coil enhanced the harvester's output power and its bandwidth. A maximum output power of 12 mW over a frequency bandwidth $BW = 6$ Hz was achieved using a 60 turns coil with an effective length $l = 1.75$ m and a 3.6Ω, from an input acceleration $A_0 = 0.6g$. We also note that the impact produced a hardening/softening type nonlinearity in the horizontal/vertical configuration of VEH. The VEH's bandwidth increased with increase of the input acceleration and an increase in the number of turns in the concentric coil. Numerical analysis of the VEH show the existence of nonlinear phenomena that are reminiscent of impact oscillator, in particular, the jump phenomena in the frequency response of the VEH and the existence of hysteresis.

References

1. Arnold, D.P.: Review of microscale magnetic power generation. J. IEEE Trans. Matwo Magn. **43**, 3940–3951 (2007)
2. www.ec.gc.ca/gdd-mw/default.asp?lang=En&n=52DF915F-1&offset=1&toc=show
3. Williams, C.B., Yates, R.B.: Analysis of a micro-electric generator for microsystems. Solid State Sens. Actuators **1**, 369–372 (1996)
4. Glynne-Jones, P.: Vibration powered generators for self-powered microsystems, University of Southampton, PhD Thesis (2001)
5. Roundy, S., Leland, E.S., Baker, J.: Improving power output for vibration-based energy scavengers. J. Pervasive Comput. IEEEXplore (2005)
6. Beeby, S.P., O'Donnell, T.: Chapter 5, pp. 130–132, in energy harvesting technology. In: Priya, S., Inman, D.J.(eds.) Springer, New York (2009)
7. Hadas, Z., Kluge, M., Singule, V., Ondrusek, C.: Electromagnetic vibration power generator. IEEE (2007)
8. Zhu, D., Beeby, S.: Energy Harvesting Systems, Springer, ISBN 978-1-4419-7565-2 (2011)
9. Mann, B.P., Owens, B.A.: Investigations of a nonlinear energy harvester with a bistable potential well. J. Sound Vib. **329**, 1215–1226 (2010)
10. Mann, B.P., Sims, N.D.: Energy harvesting from the nonlinear oscillations of magnetic levitation, J. Sound Vib. **319**, 515–530 (2009)
11. Cammarano, A., Burrow, S.G., Barton, D.A.W.: An energy harvester with bistable compliance characteristics, DETC2010-29222. In: 12th International Conference on Advanced Vehicle and Tire Technologies; 4th International Conference on Micro- and Nanosystems, vol. 4, pp. 725–732. publisher Asme (2010)
12. Gilbert, J.M., Balouchi, F.: Comparison of energy harvesting systems for wireless sensor networks. Int. J. Autom. Comput. **5**, 334–347 (2008)
13. Duy, S.N., Einar, H.: Wideband MEMS energy harvester driven by colored noise. J. Microelectromech. Syst. IEEE **22**(4) (2013)
14. Harne, R., Wang, K.: A review of the recent research on vibration energy harvesting via bistable systems. J. Smart Mater. Struct. **22** (2008)
15. Daqaq, M.F., Masana, R., Erturk, A., Dane, Q.: On the role of nonlinearities in vibratory energy harvesting: a critical review and discussion. J. Appl. Mech. Rev. **66** (2014)
16. Twiefel, J., Westermann, H.: J. Intell. Mater. Syst. Struct. 24, 1291–1302 (2013)

17. Sari, I., Balkan, T., Kulah, H.: An electromagnetic micro power generator for wideband environmental vibrations. J. Micromech. Microeng. **146**, 405–413 (2008)
18. Lien, I., Shu, Y.: Array of piezoelectric energy harvesting by equivalent impedance approach, J. Smart Mater. Struct. **21** (2012)
19. Rezaeisary, M., El Gowini, M., Sameoto, D., Raboud, D., Moussa, W.: Wide-bandwidth piezoelectric energy harvester with polymeric structure. J. Micromech. Microeng. **25** (2004)
20. Yang, B., Lee, C., Xiang, W., Xie, J., Han He, J., Kotlanka, R.K., Low, S.P., Feng, H.: Electromagnetic energy harvesting from vibrations of multiple frequencies. J. Micromech. Microeng. **19** (2009)
21. Dhakar, L., Liu, F.E.H., Tay, F.E., Lee, C.: A new energy harvester design for high power output at low frequencies. J. Sens. Actuators **199**, 344–352 (2013)
22. Lihua, T., Yaowen, Y., Soh, C.K.: Broadband Vibration Energy Harvesting Techniques. Springer, New York (2013)
23. Soliman, M.S., Abdel-Rahman, E., El-Saadany, E., Mansour, R.R.: A wideband vibration-based energy harvester. J. Micromech. Microeng. **18**, 1257–1265 (2008)
24. Jacquelin, E., Adhikari, S., Friswell, M.: A piezoelectric device for impact energy harvesting. J. Smart Mater. Struct. **20**, 1–12 (2011)
25. Soliman, M.S., Abdel-Rahman, E., El-Saadany, E., Mansour, R.R.: A design procedure for wideband micropower generators. J. Microelectromech. Syst. **18**, 1288–1299 (2009)
26. Le, C.P., Halvorsen, E.: MEMS electrostatic energy harvesters with end-stop effects. J. Micromech. Microeng. **22**, 074013 (2012)
27. Ching, N.H., Wong, H.Y., Li, H.W.J., Leong, P.H.W., Wen, Z.: A laser-micromachined multimodal resonating power transducer for wireless sensing systems. J. Sens. Actuators **97–98** (2002)
28. Mahmoud, M.A.E., Abdel-Rahman, E.M., Mansour, R.R., El-Saadany, E.F.: Springless vibration energy harvesters. In: ASME IDETC 2010, Montreal, Canada, DETC2010-29046, Aug 2010
29. Nayfeh, A., Mook, D.: Nonlinear Oscillations. Wiley, New York (1997)

Numerical and Experimental Assessment of the Modal Curvature Method for Damage Detection in Plate Structures

Francesco Mosti, Giuseppe Quaranta and Walter Lacarbonara

Abstract Use of modal curvatures obtained from modal displacement data for damage detection in isotropic and composite laminated plates is addressed through numerical examples and experimental tests. Numerical simulations are carried out employing COMSOL Multiphysics as finite element solver of the equations governing the Mindlin-Reissner plate model. Damages are introduced as localized non-smooth variations of the bending stiffness of the baseline (healthy) configuration. Experiments are also performed on steel and aluminum plates using scanning laser vibrometry. The obtained results confirm that use of the central difference method to compute modal curvatures greatly amplifies the measurement errors and its application leads to unreliable predictions for damage detection, even after denoising. Therefore, specialized ad hoc numerical techniques must be suitably implemented to enable structural health monitoring via modal curvature changes. In this study, the Savitzky-Golay filter (also referred to as least-square smoothing filter) is considered for the numerical differentiation of noisy data. Numerical and experimental results show that this filter is effective for the reliable computation of modal curvature changes in plate structures due to defects and/or damages.

F. Mosti
Brembo S.p.A, viale Europa 2, 24040 Stezzano, Italy
e-mail: francesco.mosti.1089@alice.it

G. Quaranta
Department of Structural and Geotechnical Engineering, Sapienza University of Rome, via Eudossiana 18, 00184 Rome, Italy
e-mail: giuseppe.quaranta@uniroma1.it

W. Lacarbonara (✉)
Department of Structural and Geotechnical Engineering, Sapienza University of Rome, via Eudossiana 18, 00184 Rome, Italy
e-mail: walter.lacarbonara@uniroma1.it

M. Belhaq (ed.), *Structural Nonlinear Dynamics and Diagnosis*,
Springer Proceedings in Physics 168, DOI 10.1007/978-3-319-19851-4_3

1 Introduction

Vibration-based damage detection techniques have an advantage associated with their global approach by which faults within a mechanical system can be identified without a priori information about their location and regardless of their accessibility. Moreover, automatic real-time vibration-based structural health monitoring (SHM) systems can be effectively implemented. In this context, approaches based on changes of the modal characteristics of the structure induced by damages are widely used. While the validity of modal damping as damage index is still a controversial topic, variations of natural frequencies and mode shapes have been largely exploited to assess the occurrence of damage. Natural frequencies are particularly attractive for damage identification because they can be estimated from a few measurement points and are usually contaminated by small levels of noise, however, their sensitivity to damage is rather poor. Changes in mode shapes yield local information which turn out to be more suitable for damage localization than variations of the natural frequencies, provided that a sufficient number of measurement points is acquired. Notwithstanding the mentioned desirable features, several studies have shown that modal displacements, as expected, are not very sensitive to faults.

Conversely, changes in the modal curvatures with respect to those of the baseline (healthy) structure lead to a more effective definition and computation of damage indices. In [14] it was observed that the localized occurrence of a spike in the function obtained by subtracting the modal curvature of the undamaged structure from that of the damaged situation is an indicator of the damage location. Therefore, in view of practical applications, the main issue is concerned with the processing of the modal curvatures, a task that can be accomplished by means of direct measurements or via numerical methods. The possibility of directly measuring modal curvatures using optical fibre strain sensors was discussed in [6], but most of the current applications are based on the extraction of modal displacements from dynamic measurements. To this end, the use of accelerometers, electronic speckle pattern interferometry or scanning laser vibrometry is frequent. In this scenario, the whole reliability of the damage detection procedure largely depends on the accuracy of the numerical differentiation procedure. Attention has to be paid on the calculation of modal curvatures because differentiation of noisy data is well known to be an ill-posed problem. The central difference method is certainly the most popular tool for estimating the curvatures from modal displacements, see for instance [1, 2, 7, 12]. However, some studies have shown that errors amplification may become so large as to make the central difference method inappropriate for reliable damage localization [2]. As a consequence, some recent attempts have been made to circumvent the difficulties that can be found when implementing damage detection techniques based on numerically obtained modal curvatures. They include the use of wavelets [4, 8], Gaussian function derivatives [13], Laplace operator [5], smoothing spline and Savitzky-Golay filter [16].

The present contribution is part of a larger effort aimed at assessing the effectiveness of damage detection by modal curvatures as well as at improving their

reliability for practical SHM applications. This chapter is concerned with the use of modal curvatures for damage detection in thin plate structures. Along these lines, damage detection in composite laminated plates based on modal curvatures has been discussed in [15]. Bending modal curvatures were calculated using the central difference method, and dynamic measurements were acquired by using a scanning laser vibrometer (SLV). Curvatures obtained from measured modal displacements were also recently considered to identify defects in composite T-stiffened panels [10].

In the present work, an extensive numerical study is conducted for isotropic and composite laminated plates. Simulations are performed using COMSOL Multiphysics. The Mindlin-Reissner plate model is implemented and defects are introduced as localized non-smooth variations of the bending stiffness of the baseline configuration. Experiments are also performed on steel and aluminum plates using SLV. Although the central difference method is often preferred to calculate the modal curvatures, our study confirms that it greatly amplifies measurement errors. Its final outcomes are ineffective for damage detection, even if measurement errors are as low as possible and denoising is performed. On the contrary, numerical and experimental investigations demonstrate that the Savitzky-Golay filter yields reliable predictions of modal curvatures changes for practical SHM applications.

2 Damage Detection by Modal Curvatures

We assume that noisy modal displacements ϕ_i are available at positions (x_i, y_j), and the measurement points along a given y coordinate are taken to be spaced by the constant sampling distance Δx. The problem is concerned with the determination of the second derivative with respect to x denoted by $\phi''(x_i)$, i.e., a suitable estimate of the exact modal curvature at x_i about direction $y = y_j$ (note that this is the exact linear bending curvature within the Kirchhoff-Love plate theory whereby the transverse shear strains are neglected). Therefore, the 2D numerical differentiation problem is reduced to multiple 1D problems, as it was done in previous works [15]. In the present study, two numerical differentiation techniques are considered, namely, the standard central difference approximation and the Savitzky-Golay filter. The methods described below apply to all targeted mode shapes and plate configurations (undamaged or damaged). Any reference to the mode number and to the structural configuration is, therefore, omitted for sake of conciseness.

The most popular approach for obtaining curvatures via numerical differentiation from (displacement) mode shapes ϕ is based on the central difference approximation. For the ith point, the central difference method yields the following expression:

$$\phi''(x_i) = \frac{\phi_{i-1} - 2\phi_i + \phi_{i+1}}{\Delta x^2}. \tag{1}$$

The original Savitzky-Golay filter [17] (also referred to as least-square smoothing filter) and its variants represent an important class of local methods for numerical

differentiation of noisy data [3]. In their seminal paper, Savitzky and Golay demonstrated that fitting a polynomial to a set of input samples and then evaluating the obtained polynomial at a single point within the approximation interval is equivalent to discrete convolution with a fixed impulse response. The key derivation steps are summarized next for a better appreciation of the proposed application to damage detection. A set of $(2m + 1)$ consecutive samples is considered together with a local coordinate system, i.e., $q \in \{-m, \ldots, 0, \ldots, +m\}$. The lth-order least-square polynomial is represented by

$$f(q) = \sum_{r=0}^{l} b_r q^r. \tag{2}$$

The Savitzky-Golay approach applies (2) at the midpoint only ($q = 0$) whereas the value of the output at the next sample is obtained by shifting the analysis interval to the right by one sample and repeating the procedure at the new midpoint. The sth-order derivative of $f(q)$ in (2) evaluated at $q = 0$ only requires the expression for b_s. The central sth-order derivative of the polynomial form in (2) can also be expressed as

$$\phi^s(0) = \sum_{q=-m}^{m} h_q^s \phi_q \tag{3}$$

in which h_q^s is the convolution weight of the qth filter point. Instead of considering a power series, the approach developed in [9] is based on use of discrete orthogonal polynomials, whereby the Gram polynomials turn out to be particularly suitable to the present case. In doing so, the sth-order derivative at any point ξ is obtained by using the following expression:

$$\phi^s(\xi) = \frac{1}{(\Delta x)^s} \sum_{q=-m}^{m} h_q^{\xi,s} \phi_q \tag{4}$$

where the scale factor is needed when the original coordinate system is considered (i.e., the points are separated by $\Delta x \neq 1$). The convolution weight for ϕ_q with $-m \leq q \leq m$ has the form:

$$h_q^{\xi,s} = \sum_{r=0}^{l} \frac{(2r+1)(2m)^{(r)}}{(2m+r+1)^{(r+1)}} P_r^m(q) P_r^{m,s}(\xi), \tag{5}$$

where

$$P_r^m(\xi) = \sum_{a=0}^{r} \frac{(-1)^{a+r}(a+r)^{(2a)}(m+\xi)^{(a)}}{(a!)^2 (2m)^{(a)}} \tag{6}$$

and

$$P_r^{m,s}(q) = \frac{2(2r-1)}{r(2m-r+1)}\left[qP_{r-1}^{m}(q) + sP_{r-1}^{m,s-1}(q)\right] - \frac{(r-1)(2m+r)}{r(2m-r+1)}P_{r-2}^{m,s}(q) \tag{7}$$

denote the rth-order Gram polynomial and its sth-order derivative, respectively. The calculation of the modal curvature through (4) is best performed by constructing the table $H^s(\xi, q) = \{h_q^{\xi,s} : -m \leq \xi \leq +m, -m \leq q \leq +m, s = 2\}$ using (5). This strategy is computationally efficient because the convolution weights do not change, provided that the measurement points as well as m and l do not vary with the mode shape number in both undamaged and damaged situations. Note that the classical Savitzky-Golay approach [17] does not allow the calculation of the modal curvatures at the first m points and at the last m points. By using the Gram polynomial-based strategy developed in [9], the curvatures at the first m points and at the last m points are calculated by using the coefficients of $H^s(\xi, q)$ for ξ from $-m$ to -1 and for ξ from 1 to m, respectively. As in the classical Savitzky-Golay approach, the rest of the n samples uses the center point weighting, which is obtained by setting $\xi = 0$.

Once the experimental modal displacements have been acquired, the modal curvatures are numerically obtained and the damage can be identified by comparison. To this end, the modal curvature-based damage index $I(x_i|y = y_j)$ proposed in [1] is

$$I(x_i|y = y_j) = \sum_{k=1}^{n_t} \left|{\phi^0}''_{ik} - \phi''_{ik}\right| \tag{8}$$

where n_t is the number of target modes, ${\phi^0}''_{ik}$ is a numerical estimate of the modal curvature of the kth undamaged mode shape at the ith measurement point x_i about the direction $y = y_j$, and ϕ''_{ik} is the corresponding curvature for the damaged structure. Ho and Ewins [11] (see also [2]) presented the mode shape curvature squared method based on the following proposition of the damage index:

$$I(x_i|y = y_j) = \sum_{k=1}^{n_t} \left|{\phi^0}''^{\,2}_{ik} - \phi''^{\,2}_{ik}\right|. \tag{9}$$

On the other hand, the following different formulation of the damage index was proposed in [16]:

$$I(x_i|y = y_j) = \left(\sum_{k=1}^{n_t}\left({\phi^0}''_{ik} - \phi''_{ik}\right)^2\right)^p. \tag{10}$$

Numerical analyses presented in [16] showed that if the numerical estimation of the modal curvatures is sufficiently accurate, then the damage index given by (10)

with $p > 1$ (e.g., $p = 2$) magnifies the distance between peaks due to damage and those that appear in other positions. This turns out to be beneficial in reducing false positives when noisy data are considered.

3 Numerical and Experimental Applications

The Mindlin-Reissner plate model is considered wherein damage or defects are introduced as localized non-smooth variations of the bending stiffness of the undamaged original configuration. The finite element software COMSOL Multiphysics is used to perform FE discretization of the equations of motion provided in PDE form. The considered composite plate has four layers with lay-up 0°/45°/90°/−45°. The elastic constants are: $E_1 = 137.137$ GPa, $E_2 = 9.308$ GPa, $\nu_{12} = 0.304$, $\nu_{21} = 0.017$, $G_{12} = 4.551$ GPa, $G_{23} = 4.206$ GPa, and the mass per unit volume is $\rho = 1568$ kg/m^3. A specific damage is introduced by halving the stiffness of the second layer within a region having an extension equal to 4 % of the plate side length. A white Gaussian noise was added to the modal displacements so that the final error (about 1 %) is able to simulate experimental data after denoising. The damage index is computed according to (10) with $n_t = 5$ and $p = 1$. The damage index function is then normalized by dividing it by its absolute maximum value. Figure 1 shows a sample of the obtained numerical results for the composite laminated plate.

These results show that the central difference method does not lead to the proper damage identification because of countless false positives. On the other hand, use of the Savitzky-Golay filter gives a clear definite spike at the exact damage location

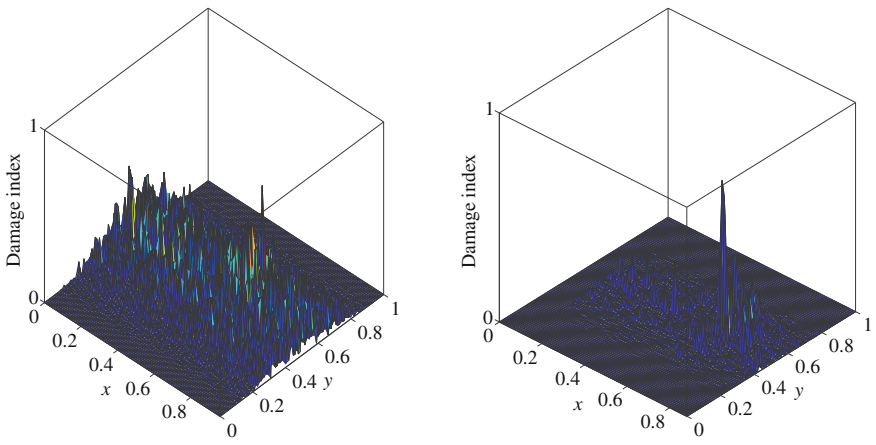

Fig. 1 Damage detection in composite laminated plate based on numerical data (the coordinates of the midpoint of the narrow damaged region are $x = 0.67$ and $y = 0.59$): comparison between central difference method (*left*) and Savitzky-Golay filter (*right*)

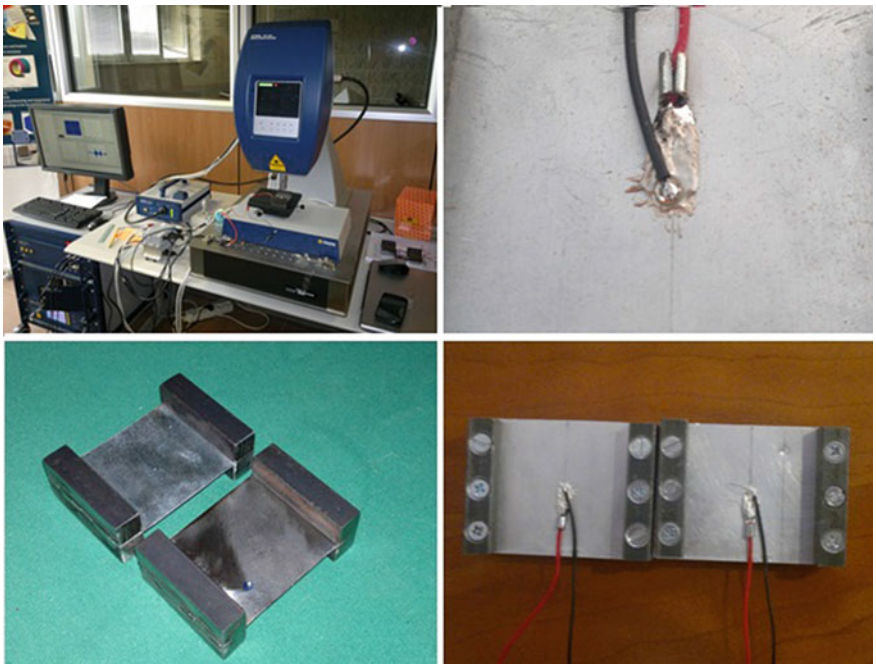

Fig. 2 Experimental layout (clockwise from the *upper left corner*): Polytec scanning laser vibrometer, piezoelectric actuator, undamaged and damaged 50 mm × 50 mm aluminum and steel plates (thickness equal to 0.5 mm). The plates have clamped boundary conditions on two sides and free conditions on the other two sides. Damage is introduced by halving the plate thickness within a circle having 2 mm diameter and the center about 14 mm far from one corner

while reducing the number of peaks due to error amplifications induced by the numerical differentiation procedure.

Experiments were also performed on isotropic plate structures using SLV (see Fig. 2 for an overview of the experimental layout). The results shown in Fig. 3 further confirm that use of the Savitzky-Golay filter for the computation of the modal curvatures provides a satisfactory identification of the damage in thin plate-like structures (the damage index is computed according to (10) with $p = 1$). The purposefully introduced damage is well identified in both cases, i.e., the maximum values of the damage index (red-colored zone) lie within the region of the plate where the defect is introduced whereas very low values can be found elsewhere. The center of the identified damaged region and that of the defect are roughly coincident for the steel plate. For the aluminum plate, the location of the center is slightly off from the exact one.

The effectiveness of the Savitzky-Golay filter with respect to the central difference method was also evaluated for defects having different shapes. The experimental results shown in Fig. 4, for instance, are referred to a stretched narrow damaged region (the damage index is here computed according to (10) with $p = 2$). Results

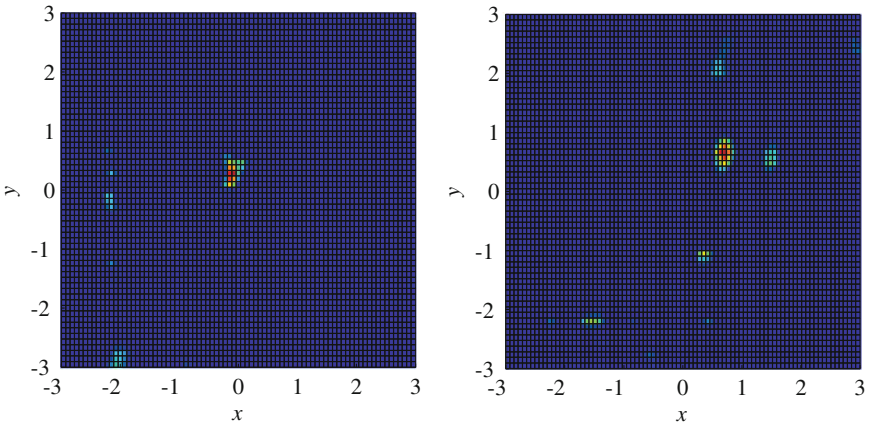

Fig. 3 Damage detection in isotropic plates based on experimental data (the curvatures are computed by the Savitzky-Golay filter over a 50 × 50 grid of points centered at the damaged region): steel plate (*left*) and aluminum plate (*right*)

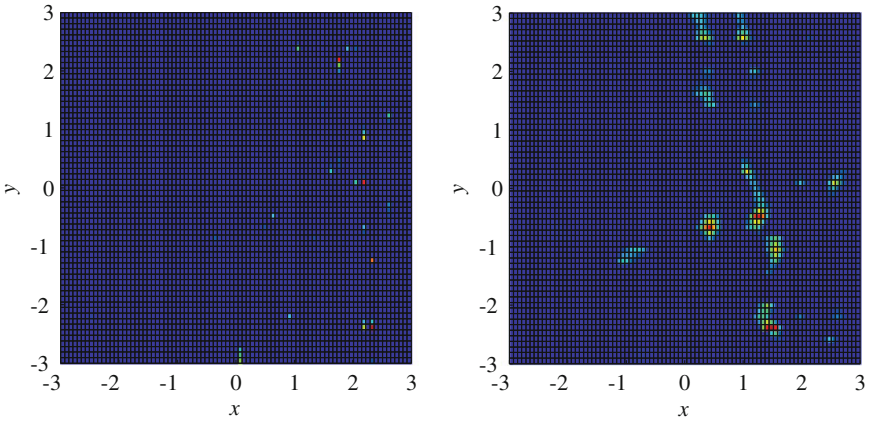

Fig. 4 Detection of a stretched damaged region in an isotropic plate based on experimental data (the vertical axis of the damaged region is $x = 1$ and the curvatures are computed over a 50 × 50 grid): results obtained using the central difference method (*left*) and the Savitzky-Golay filter (*right*)

in Fig. 4 corroborate the fact that the central difference method does not provide a clear evidence about the existence of damage whereas the defect is well identified by means of the Savitzky-Golay filter. Specifically, high values of the damage index calculated through the Savitzky-Golay filter can be easily recognized at the bounds of the stretched damaged region, thus highlighting the location and extension of the defect.

4 Conclusions

This chapter provides an overview of a computational procedure for damage detection in plate structures based on modal curvatures estimated via numerical differentiation of modal displacement data. The ill-posedness of such inverse problem can cause abnormal amplifications in the calculation of the numerical derivatives, especially when considering relatively dense arrays of measurement points. Although the central difference method is extensively employed, this study—in consonance with previous recent works—confirmed that this method is not suitable for damage detection. Keeping measurement errors as low as possible and reducing the noise level may turn out to be beneficial to some extent for damage identification but does not fix the problem. Therefore, different numerical procedures have to be explored and, in this perspective, the present work illustrates the application of the least-square smoothing filter, also known as Savitzky-Golay filter. Despite its simplicity, this technique proved to be a reliable, rapid tool for a satisfactory numerical estimation of the modal curvatures from noisy modal displacements. Numerical and experimental results discussed herein demonstrated that the implementation of the Savitzky-Golay filter leads to a more effective identification of relatively small damages in thin plate structures together with a remarkable reduction of the number of false alarms.

Acknowledgments This work was partially supported by the Italian Ministry of Education, University and Scientific Research (PRIN Grant No. 2010BFXRHS-002). The work of Giuseppe Quaranta is framed within the research project "DPC-ReLUIS 2014, RS 4—Osservatorio sismico delle strutture e monitoraggio".

References

1. Abdel Wahab, M.M., De Roeck, G.: Damage detection in bridges using modal curvatures: application to a real damage scenario. J. Sound Vib. **226**(2), 217–235 (1999)
2. Adewuyi, A.P., Wu, Z., Kammrujaman Serker, N.H.M.: Assessment of vibration-based damage identification methods using displacement and distributed strain measurements. Struct. Health Monit **8**(6), 443–461 (2009)
3. Ahnert, K., Abel, M.: Numerical differentiation of experimental data: local versus global methods. Comput. Phys. Commun. **177**(10), 764–774 (2007)
4. Cao, M., Xu, W., Ostachowicz, W., Su, Z.: Damage identification for beams in noisy conditions based on Teager energy operator-wavelet transform modal curvature. J. Sound Vib. **333**(6), 1543–1553 (2014)
5. Cao, M., Qiao, P.: Novel Laplacian scheme and multiresolution modal curvatures for structural damage identification. Mech. Syst. Signal Pr. **23**(4), 1223–1242 (2009)
6. De Roeck, G., Reynders, E.: Measurement of modal curvatures using optical fiber strain sensors and application to damage identification using vibration monitoring. Proc. SPIE **5855**, 1076–1079 (2005)
7. Dutta, A., Talukdar, S.: Damage detection in bridges using accurate modal parameters. Finite Elem. Anal. Des. **40**(3), 287–304 (2004)
8. Gentile, A., Messina, A.: On the continuous wavelet transforms applied to discrete vibrational data for detecting open cracks in damaged beams. Int. J. Solids Struct. **40**(2), 295–315 (2003)

9. Gorry, P.A.: General least-squares smoothing and differentiation by the convolution (Savitzky-Golay) method. Anal. Chem. **62**(6), 570–573 (1990)
10. Herman, A.P., Orifici, A.C., Mouritz, A.P.: Vibration modal analysis of defects in composite T-stiffened panels. Compos. Struct. **104**, 34–42 (2013)
11. Ho, Y.K., Ewins, D.J.: On the structural damage identification with mode shapes. Proc. European COST F3 Conf. System Ident. Struct. Health Monit. 677–684 (2000)
12. Humar, J., Bagchi, A., Xu, H.: Performance of vibration-based techniques for the identification of structural damage. Struct. Health Monit. **5**(3), 215–241 (2006)
13. Lopes, H.M.R., Araújo dos Santos, J.V., Mota Soares, C.M., Guedes, R.J.M., Pires Vaz, M.A.: A numerical-experimental method for damage location based on rotation fields spatial differentiation. Comput. Struct. **89**(19–20), 1754–1770 (2011)
14. Pandey, A.K., Biswas, M., Samman, M.M.: Damage detection from changes in curvature mode shapes. J. Sound Vib. **145**(2), 321–332 (1991)
15. Qiao, P., Lu, K., Lestari, W., Wang, J.: Curvature mode shape-based damage detection in composite laminated plates. Compos. Struct. **80**(3), 409–428 (2007)
16. Quaranta, G., Carboni, B., Lacarbonara, W.: Damage detection by modal curvatures: numerical issues. J. Vib. Control (in press), doi:10.1177/1077546314545528
17. Savitzky, A., Golay, M.J.E.: Smoothing and differentiation of data by simplified least squares procedures. Anal. Chem. **36**(8), 1627–1639 (1964)

Proposal of a Nonlinear Piezoelectric Coupling Term to Energy Harvesting Interactions

Ângelo Marcelo Tusset, Itamar Iliuk, Rodrigo Tumolin Rocha, Vinícius Piccirillo, José Manoel Balthazar, Jorge Luiz Palacios Felix and Reyolando Manoel Lopes Rebello da Fonseca Brasil

Abstract Nowadays, new technologies have triggered the needs of new energy sources, smaller and more efficient, so the research about energy harvesting has increased substantially. Several researchers have developed the conversion of wasted mechanical energy to electrical energy using piezoelectric materials as a

Â.M. Tusset · V. Piccirillo
Department of Mathematics, UTFPR - Federal Technological
University of Paraná, Ponta Grossa, Brazil
e-mail: tusset@utfpr.edu.br

V. Piccirillo
e-mail: piccirillo@utfpr.edu.br

I. Iliuk
Department of Telecommunication Engineering and Control,
EPUSP - Polytechnic School of the University of São Paulo, São Paulo, Brazil
e-mail: itamar.iliuk@usp.br

R.T. Rocha
Faculty of Mechanical Engineering, UNESP - São Paulo State University,
Bauru, SP, Brazil
e-mail: digao.rocha@feb.unesp.br

J.M. Balthazar (✉)
Mechanical Aeronautics Division, ITA - Aeronautics Technological Institute,
São José dos Campos, SP, Brazil
e-mail: jmbaltha@gmail.com

J.M. Balthazar
Faculty of Mechanical Engineering, UNESP - São Paulo State University,
Bauru, SP, Brazil

J.L.P. Felix
Technological Center of Alegrete, UNIPAMPA - Federal University of Pampa,
Alegrete, RS, Brazil
e-mail: jorge.felix@unipampa.edu.br

R.M.L.R. da Fonseca Brasil
CECS - Center of Engineering, Modelling and Applied Social Science,
UFABC - Federal University of Santo André, Santo André, SP, Brazil
e-mail: reyolando.brasil@ufabc.edu.br

M. Belhaq (ed.), *Structural Nonlinear Dynamics and Diagnosis*,
Springer Proceedings in Physics 168, DOI 10.1007/978-3-319-19851-4_4

transducer. This chapter proposes a mathematical model for the constitutive equation of a piezoelectric transducer. Experimental results involving piezoelectric elements were considered. The proposed mathematical model allows a considerably better description. The results are closer to those obtained in a real system, reducing inaccuracy of predictive behaviour of the piezoelectric energy harvesting system. In this work, the numerical simulations show a significant difference between results obtained with the proposed model and other models available in literature.

1 Introduction

Nowadays, new technologies have triggered the needs of new energy sources, smaller and more efficient. The research on energy harvesting system has increased substantially. Several different devices have been developed. In all these devices, a new way to harvest energy is the use of piezoelectric material as a transducer to harvest energy from ambient mechanical vibrations. Many researchers have recently explored this sort of energy harvesting based on piezoelectric material. As some examples, we mention that the piezoceramics can be used as piezomagnetoelasctic structure and harvest energy from an ambient vibration [1, 2]. A vast and important study of piezoelectric energy harvesting system can be found in [3–5]. These authors explored the reuse of the wasted energy that is very important nowadays to some applications, including renewable energy.

Linear and nonlinear piezoelectric coupling have been considered. The nonlinear coupling incorporates the more realistic effects of the piezo elements, because of the constitutive laws of piezoelectric materials specifically the nonlinear relationship between the strain and the electric field in the piezoceramic material [6–9]. A good approximation to a relation of the nonlinear piezoelectric coupling was firstly developed by Triplett and Quinn [10] that shows good results comparing to the experimental results. Hence, the authors conclude that the role of nonlinearities in the piezoelectric materials has a great impact over the responses of the system. Thus, for better design of an energy harvester, the nonlinear effects of electromechanical coupling must be taken into account [11].

In order to check this, we propose a new approximation of experimental curve of the piezoelectric material response to modelling this behaviour. Using the theoretical model of piezoelectric energy harvesting in [12–14], a comparison was performed among a reference function (RF) proposed by Triplett and Quinn [10] for piezoelectric coupling and the proposed model (PM) by us present in this work.

This chapter is organized into five sections. Section 1 is essentially an introduction to energy harvesting vibrating systems. Section 2 presents the proposed mathematical nonlinear piezoelectric coupling, showing how it can be relevant in the mathematical

modelling of the real problem, taking into account the nonlinear coupling proposed by Triplett and Quinn [10]. Section 3 presents the mathematical modelling of the energy harvesting system considering a proposal nonlinear piezoelectric coupling. Section 4 exhibits the results of numerical simulations, those were carried out, comparing the average power using the reference function to the proposed model. Section 5 presents the main conclusion of the work.

2 The Proposed Nonlinear Coupling Term

The piezoelectric element behaviour was checked experimentally by Crawley and Anderson [7] as we can observe in Fig. 1. Figure 1b shows the function to dimensionless piezoelectric coupling coefficient suggested by [10], where the dimensional piezoelectric coefficient $d(x)$ were approximated to: $d(x) = d_{linear}(1 + d_{nonlinear}|x|)$, having defined as the dimensionless counter-party as: $\hat{d}(x) = \theta(1 + \Theta|x|)$, where the piezoelectric coefficient is constituted by a linear part represented by θ and a nonlinear part represented by Θ. In Fig. 1a, the nonlinear model curve is the approximation stipulated by Triplett and Quinn [10].

As can be seen in Fig. 1a, neither linear model and nonlinear approximation nor the model of Fig. 1b are good approximations of experimental model. We can also observe that the experimental model try to reach a saturation point, behaviour that is not observed in the models. The goal of this research is to determine a model which has a better mathematical representation of the experimental model. For this, we are

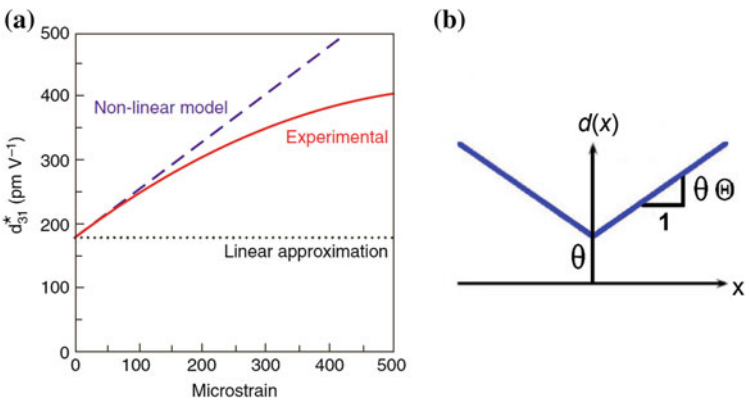

Fig. 1 **a** The experimental *curve* obtained by Crawley and Anderson [7]. **b** Reference approximation of piezoelectric nonlinearity defined by Triplett and Quinn [10]

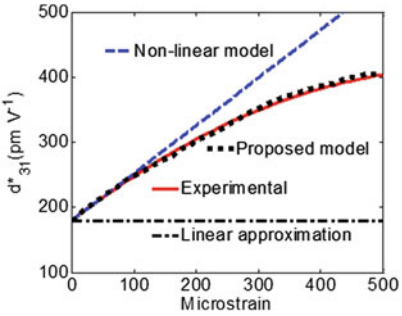

Fig. 2 Proposed model to approximation of piezoelectric nonlinearity

going to consider an approximation normalized function $y = d^*[pmV^{-1}]/408$ and $x = Microstrain/500$ determined by using the least square method [15, 16]. The method could show us the approximation normalized functions as

$$y = \frac{0.0610646e^{5.6668x}}{1.01 + 0.06046e^{5.6668x}} + e^{-2.8x}(0.3654cos2x + 1.2sin2x) \tag{1}$$

In Fig. 2 we can observe a comparison considering the dimensional model proposed in (1).

3 Mathematical Modelling

In this section will be shown the energy harvesting mathematical model using a nonlinear piezoelectric coupling and the governing equations of movement of the system.

The energy harvesting model in Fig. 3 was proposed in [12–14], that are studied using the proposed nonlinear piezoelectric coupling of Triplett and Quinn [10]. This time, the new nonlinear piezoelectric coupling was used to compare its efficient with the other coupling in [10].

The coupled equations of motion were defined in the dimensionless form in [12–14] as:

$$\begin{aligned} &x'' + \varepsilon\alpha x' + \beta x + \varepsilon\beta_1 x^3 + \varepsilon\psi v = \varepsilon\delta_1\phi''cos\phi - \varepsilon\delta_2\phi'^2 sin\phi \\ &\phi'' = \varepsilon\mu_1 - \mu_2\phi' + \varepsilon\gamma x''cos\phi \\ &\rho v' - \Psi x + v = 0 \end{aligned} \tag{2}$$

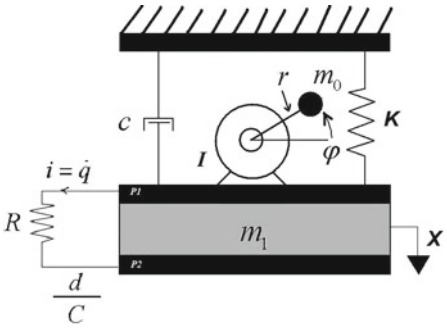

Fig. 3 Mathematical model of the energy harvester proposed in [12–14]

The parameter Ψ in (2) represents the piezoelectric coupling function. The dimensionless electrical power harvested from the system has the form $P = \rho v'^2$. The averaged power harvested is given by

$$P_{average} = \frac{1}{T}\int_0^T P(\tau)d\tau \tag{3}$$

4 Numerical Simulations and Results

In Figs. 4 and 5, we can observe the behaviour of the system (2) for the following parameters [10, 14]: $\alpha = 0.01, \beta = 1.00, \beta_1 = 0.25, \rho = 1.00, \varepsilon = 0.10, \delta_1 = 0.40$, $\delta_2 = 0.40$, $\gamma = 0.60$, $\mu_2 = 1.50$, $\theta = 1.00$, $\Theta = 1.00$, $x_1(0) = 0$, $x_2(0) = 0$, $x_3(0) = 0$, $x_4(0) = 0$, $x_5(0) = 0$. The μ_1 parameter had to be adjusted in order to reach the resonant frequency of the model for each of the tested functions.

Figure 4a, b are depicting the resonance curve of the system using the reference function RF, proposed model PM, and as can be seen the jumping occurs for the value of the parameter $\mu_1 = 1.55$ and $\mu_1 = 1.52$, respectively.

Figure 5 shows the dynamic response of the system comparing the proposed model PM to the reference function RF proposed in [10]. Figure 5a, b show the phase plane and the time history of the displacement of the two functions, respectively. We observe that the PM starts with a higher amplitude and at steady state keeps a little higher amplitude of displacement than in the RF. To see what happens with the power harvested Fig. 5c, d show the time history of the power harvested and the average power, respectively. We can see the power harvested has higher peaks in the PM than in RF, but it doesn't occur to the average power. We see that at steady state the average power of the PM is a little lower than the RF. It was expected by the fact shown in Fig. 2 that the PM approximates is closer to the experimental result than the RF. Hence, the energy harvesting would be a little lower in PM than in RF.

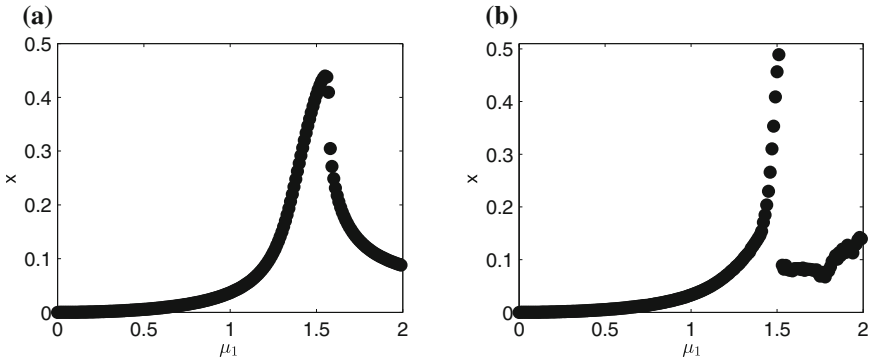

Fig. 4 **a** Sommerfeld effect of the system (2). **a** Reference function. **b** Proposed model

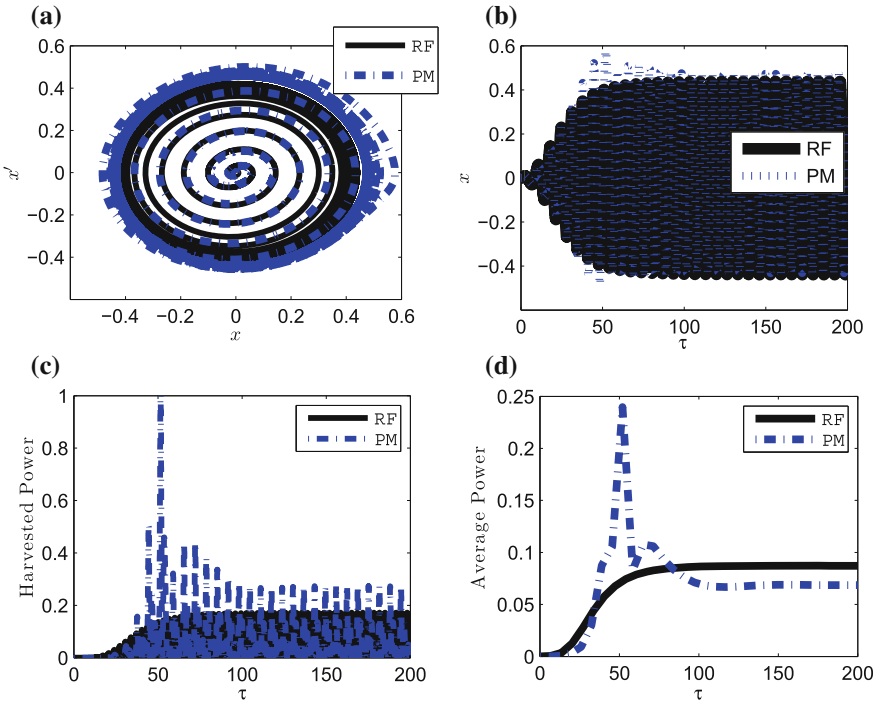

Fig. 5 Dynamic response using the proposed model (*blue line*) and the reference function (*black line*). **a** Phase plane. **b** Time history of the displacement. **c** Time history of the harvested power. **d** Time history of the average power

5 Conclusions

By using the least square method proposed in [15, 16], it was possible to obtain the nonlinear model, Fig. 2, which resulted in an approximation function that considers the operation mode d_{31}, where mechanical strain is applied in the axial direction, but the voltage is obtained from the perpendicular direction. With the application of the proposed model, it was possible to observe the change of the Sommerfield effect ($\mu_1 = 1.55$ (RF) for $\mu_1 = 1.52$ (PM)). This is an important point because it indicates a reduction in the quantity of energy necessary to the system to achieve the resonant frequency corresponding to of maximum displacement that can harvest more energy.

We also observed in Fig. 5c, d that the curve represented by (1) has a little lower energy harvester forecast as regard to the reference function, indicating that we would be overestimating the power generation in numerical simulations, while the reference function continue to be a good approximation. This is because the overestimated power harvested is just a little part of it, considering the piezoelectric material harvests low amount of energy.

It can be concluded that the obtained results shown the efficiency of the proposed model in improving the prediction of the piezoelectric energy harvested in steady state, thereby correcting the values obtained previously by the reference function, due to a correct matching with the profile of the behaviour of the experimental curve in Fig. 1a.

References

1. Erturk, A., Hoffmann, J., Inman, D.J.: A piezomagnetoelastic structure for broadband vibration energy harvesting. Appl. Phys. Lett. **94**(25), 254102 (2009)
2. Litak, G., Friswell, M.I., Kwuimy, C.A.K., Adhikari, S., Borowiec, M.: Energy harvesting by two magnetopiezoelastic oscillators with mistuning. Theor. Appl. Mech. Lett. **2**(4), 043009 (2012)
3. Erturk, A., Inman, D.J.: Piezoelectric Energy Harvesting. Wiley, Chichester (2011)
4. Priya, S., Inman, D.J. (eds.): Energy Harvesting Technologies. Springer, New York (2009)
5. Stephen, N.G.: On energy harvesting from ambient vibration. J. Sound Vib. **293**(1), 409–425 (2006)
6. Jalili, N.: Piezoelectric-based vibration control. From Macro to Micro/Nano Scale Systems. Springer, New York (2010)
7. Crawley, E.F., Anderson, E.H.: Detailed models of piezoceramic actuation of beams. J. Intell. Mater. Syst. Struct. **1**(1), 4–25 (1990)
8. DuToit, N.E., Wardle, B.L.: Experimental verification of models for microfabricated piezoelectric vibration energy harvesters. AIAA J. **45**(5), 1126–1137 (2007)
9. Twiefel, J., Richter, B., Sattel, T., Wallaschek, J.: Power output estimation and experimental validation for piezoelectric energy harvesting systems. J. Electroceram. **20**(3–4), 203–208 (2008)
10. Triplett, A., Quinn, D.D.: The effect of non-linear piezoelectric coupling on vibration-based energy harvesting. J. Intell. Mater. Syst. Struct. **20**(16), 1959–1967 (2009)

11. Iliuk, I., Balthazar, J.M., Tusset, A.M., Felix, J.L.P., de Pontes, B.R.: Nonlinear dynamics and control strategies: on a energy harvester vibrating system with a linear form to non-ideal motor torquet. In: MATEC Web of Conferences, vol. 1, p. 08003. EDP Sciences (2012)
12. Iliuk, I., Balthazar, J.M., Tusset, A.M., Piqueira, J.R., de Pontes, B.R., Felix, J.L., Bueno, Á.M.: Application of passive control to energy harvester efficiency using a nonideal portal frame structural support system. J. Intell. Mater. Syst. Struct. 1045389X13500570 (2013)
13. Iliuk, I., Balthazar, J.M., Tusset, A.M., Piqueira, J.R.C., de Pontes, B.R., Felix, J.L.P., Bueno, Á.M.: A non-ideal portal frame energy harvester controlled using a pendulum. European Phys. J. Spec. Top. **222**(7), 1575–1586 (2013)
14. Iliuk, I., Brasil, R.M.L.R.D.F., Balthazar, J.M., Tusset, A.M., Piccirillo, V., Piqueira, J.R.C.: Potential application in energy harvesting of intermodal energy exchange in a frame: FEM analysis. Int. J. Struct. Stab. Dyn. (2014)
15. Tusset, A.M., Balthazar, J.M., Felix, J.L.P.: On elimination of chaotic behavior in a non-ideal portal frame structural system, using both passive and active controls. J. Vib. Control. **19**, 803–813 (2013) 1077546311435518 (2012)
16. Tusset, A.M., Balthazar, J.M., Chavarette, F.R., Felix, J.L.P.: On energy transfer phenomena, in a nonlinear ideal and nonideal essential vibrating systems, coupled to a (MR) magneto-rheological damper. Nonlinear Dyn. **69**(4), 1859–1880 (2012)

Effect of Reinforced Concrete Deterioration and Damage on the Seismic Performance of Structures

Michel S. Chalhoub

Abstract The response of a system to dynamic excitation depends on the interaction between the forcing function and the system. In practice, change in material properties due to aging, fatigue, or the experience of a hazard are major challenges to the designer. This chapter discusses the effect of material deterioration on the dynamic properties of reinforced concrete structures with consideration to strain compatibility. Aging and loss of steel bond to concrete have significant effects on dynamic response. Aging causes a drop in compressive strength, hence in axial and flexural capacity, altering column interaction diagrams, or beam-column joint strength. The effect of aging in standing structures can be measured through coring and lab tests, but loss of bond is harder to evaluate because its mechanism is interior to structural members. Causes of bond deterioration include poor concrete mix, placement, or protection from chemical agents. However, well-designed mixes and placed materials may lose bond when subjected to an earthquake. Steel bond testing was performed and documented in literature, but there is still a gap in field data. A mathematical model is developed to illustrate the relationship between bond loss and concrete frame stiffness. Field assessment and remedial measures are discussed for structures that are suspected of, or diagnosed with, loss of bond. If the structure is salvageable, such effects call for specialized repairs as a preventive measure against subsequent events. But if loss of bond during an earthquake goes into an irreversible deformation range, the possibility of collapse increases or the structure becomes a candidate for disposal.

1 Introduction

Concrete behavior is complex due to the development of cracks at low stress levels, weathering, creep, and aging effects. Two major reasons for the deterioration of reinforced concrete are attributed to weather changes, including freezing and thawing, and corrosion of reinforcing steel. The structure becomes more susceptible

M.S. Chalhoub (✉)
Department of Civil and Environmental Engineering, Notre Dame University, Louaize, Lebanon
e-mail: mchalhoub@live.com

M. Belhaq (ed.), *Structural Nonlinear Dynamics and Diagnosis*,
Springer Proceedings in Physics 168, DOI 10.1007/978-3-319-19851-4_5

to weathering if protective finishing works are not completed within a reasonable time frame from the completion of the structural system [1]. Common design considerations make an implicit assumption about compressive strength and concrete mechanical properties without much consideration of material life span and building service life. In the 1940s, early construction materials research addressed the porous nature of concrete and its vulnerability through exposure to exterior agents using hydraulic pressure theory. It was found that susceptibility of concrete to changes in weather, especially when it involves frosting and thawing, increases significantly with porosity [2].

The majority of residential and office buildings in countries around the world are built with reinforced concrete due to its ease of placement and construction. The appeal of using concrete, advances in cement manufacturing technology, and the development of higher strength formulas made reinforced concrete a sustainable construction material [3]. In addition, concrete offers desirable features in terms of low sound and thermal transmission, availability of local expertise and materials in most countries. Whether in residential or office buildings, low noise transmission is one of the typical serviceability requirements. With increasing interest and concern for energy efficiency and environmentally friendly buildings, high thermal insulation properties are sought after [4, 5].

Concrete technology is considered to have made large strides over the last sixty years, which places it today at an advantage over other construction materials such as unreinforced or reinforced masonry, and at almost equal footing with industrial steel for a certain range of buildings. In fact, back in the 1950 s and 1960s research was conducted on the vulnerabilities of concrete as building construction material, emphasizing fatigue combined with loss of material strength. Concrete exhibits different behaviors under different stress states. Under simple compressive stress, concrete exhibits a linear-elastic stress-strain curve until it reaches about one third of its compressive strength because the small cracks remain closed [6–8]. Hydraulic pressure and osmotic pressure theories were used for the purpose of early modeling of concrete behavior [9].

Many researchers attribute the attractiveness of concrete to the fact that it lends itself to almost any desired shape, and may be customized to any loading rate or pattern. For example, it was shown in the mid-sixties that concrete resistance to impact increases with the rate of application of the load and is positively correlated with aggregate size [10]. However, cyclic loading in the range of 50 % of f'c causes a decrease in both the elastic modulus of concrete and its compressive strength and exhibits hysteretic behavior. These findings indicate that concrete is vulnerable to load reversals [11]. While considered a weakness, that same micro-crack formation activates the internal friction in concrete, and its hysteretic behavior provides large energy dissipation throughout the structure, attenuates response to dynamic loading, and curbs motion amplification.

As discussed in the following sections, our interest in the present chapter is mainly about changes in reinforced concrete properties especially those caused by deterioration.

2 Background: Reinforced Concrete in Use

Along with its vulnerabilities, concrete offers several advantages related to sustainability and serviceability. It minimizes noise and vibration transfer, and has relatively favorable thermal characteristics and applications in fire protection. Concrete also offers strength suitable for a wide range of building heights as it has been used in low-rise and high-rise building construction [12]. In 1919, the Japanese Urban Building Law limited the height of reinforced concrete buildings to 100 feet in an attempt to minimize risk emanating from the use of such material. Further, lessons learned in 1924 from Japan's earthquake that imparted damage to reinforced concrete buildings were rapidly turned into Code upgrades [13]. Almost a century later, reinforced concrete is used in high-rise construction with supporting Codes that provide the design engineer with simplified procedures to perform the necessary calculations while meeting some basic requirements related to ductility, energy dissipation, and resilience in sustaining tremors [14, 15].

In the United States, the leap into skyscraper construction owes it by and large to advances in industrial steel manufacturing, standard shape production, and accompanying design guidelines [16, 17]. Another challenge faced by the steel construction industry was posed by the scarce execution resources; workers, welders, forepersons, and project managers. However, reinforced concrete remained a viable candidate for high-rise construction with and without its combination with structural steel shapes [18–20].

With the advantages of concrete, there are shortcomings related to environmental impact, especially at its manufacturing stages [21]. Cement manufacturing processes, among other industries, came under scrutiny with the increased public awareness about global warming and the negative effects of industrial activity on the environment [22, 23]. But using concrete entails more than just its manufacturing stages. It involves mixing, placement, maintenance, and down the line disposal or recycling [24, 25]. Crushing of recycled concrete has become a source of aggregates and a means of avoiding volumes of dump material that is neither biodegradable, nor suitable as soil. The approach of recycling concrete has also been applied in bridge construction where reclaimed concrete is used [26, 27]. Testing and studies performed on structural elements and sub-assemblages also showed that recycled concrete was a viable construction material [28]. Concrete mixing processes gradually moved from individual mixers that belong to specific construction sites to ready mix concrete factories. Although these factories provide economies of scale catering from one source to various destinations, they pose problems in terms of increased industrial activity. In many, if not most, countries where concrete is mainstream material for the construction industry, factory emissions control is not yet a priority on the environmental agenda [29, 30].

3 Effect of Aging of Concrete on Strength

A dimension of great interest in construction material science is the durability and performance of concrete [31, 32]. What factors affect its life time? How does it age? How does concrete aging affect its strength and interaction with other materials? Deterioration through exposure to weather conditions, effect of chemicals, and crack formation are related in an intricate cause-and-effect [33, 34].

Concrete aging comprises a broader range of effects than chemical or mechanical deterioration. Such effects which include creep and shrinkage have been researched extensively in the 1950s and the 1960s and were found to have direct impact on strength and serviceability [35, 36]. More recently, shrinkage effects were studied further with the inclusion of recycled aggregates [37]. Aged concrete tends to deteriorate and to exhibit hairline cracks, which may grow and allow weather agents to infiltrate and attack reinforcing steel causing loss of strength [38]. Loss of strength may be dormant until it manifests itself in case of excessive loading beyond safety margins. For this reason it is important to differentiate the effects of aging on static from the effects on dynamic properties [39]. There are distinctive loading types that cause fatigue and cyclic deformation which in turn contribute to the acceleration of concrete aging, hence deterioration and drop in strength [40].

Conversely, overloading causes damage, crack formation, and hence deterioration that accelerates aging of concrete. In both cases, aging is an important aspect of reinforced concrete performance, especially in seismic zones where structural elements are expected to sustain reversal in loading, fatigue, and peak stress levels that may exceed design levels dictated by Codes [41, 42]. Past research on aging of concrete addressed deterioration at a material level, including transformation of the microstructure. However, there is a need to address the cumulative effects on overall structural response taking into consideration changes in material properties such as compressive strength or splitting strength due to aging [43, 44].

American and European Codes have explicit criteria related to the control of cracking and to the repair of damaged concrete [45, 46]. A question precedes a repair proposal in that does the structure, or a structural member, lend itself to repair or should it be disposed of, replaced, or re-cast? When this question is posed at the level of the entire building that has undergone severe irreversible damage from an earthquake, and may pose public hazard, demolition may be the only solution [47]. Therefore, any concrete repair proposal, plan, or operation requires a priori a meticulous assessment of the structural member and a detailed recommendation of a course of action [48]. To reach a reasonable repair recommendation, an assessment needs to reach tangible results such as the extent to which compressive strength f_c' has dropped, or permeability has changed, or porosity has increased by orders of magnitude, among other parametric studies [49, 50]. To answer these questions, it has been common place to take cores out of an existing structure and test the cored samples at the lab. The challenge in this case is threefold. First, coring is an intrusive testing methodology whereby cylinders have to be cut out of members. Second, cores may not fully describe the structural health. Third, even the most

professionally clustered cores do not accurately reveal to what extent the structure has been subjected to loss of bond between the reinforcing steel and the surrounding concrete [51, 52].

Loss of bond is therefore one of the most difficult phenomena to field-test realistically, and therefore it is critical to develop new methodologies that reflect how much a bond has weakened or total detachment has occurred between the reinforcing steel and the surrounding concrete [53]. It is also critical to relate this type of damage to other properties of the building whether physical, or dynamic, such as the natural frequency and equivalent viscous damping.

One of the well-documented consequences of de-bonding between steel and concrete is a significant drop in stiffness. So considering an unchanged mass—of course unless substantial shake-off of concrete occurs—the frequency expressed as $\sqrt{k/m}$ clearly drops. This drop leads to a clear downwards shift in the building response to a given earthquake. Such shift may create a discrepancy between the assumed or anticipated structural performance during its design phase, and its actual real life performance.

4 Basic Assumptions

Due to its anisotropic nature and its non-homogeneous mechanical properties, reinforced concrete requires special assumptions in the development of governing equations in design. In reinforced concrete design literature, the step-wise procedures whether in textbooks or Codes adopt similar simplifying assumptions. Some of the assumptions rely on basic mechanics, and others utilize strain compatibility. For example, in the design of members subjected to bending, assumptions from basic mechanics involve the consideration of plane sections remaining plane in flexure. In the design of members subject to axial loads, mechanics assumptions involve the uniformity of stress distribution on the entire cross section.

Assumptions of strain compatibility are not only a means to simplify calculations and to reach coherent procedures for beam flexure, column axial-flexural interaction equations, and other design formulas, but to also reflect a necessity in maintaining that compatibility in real life applications [54]. This differentiation is very important in design because it dictates the strength and serviceability performance once the structure is put in operation. Depending on several factors which include mix design, placement quality and procedures, or operational loads, strain compatibility may not remain applicable throughout the lifetime of the building. Research literature addressed concrete aging and its effect on overall structural performance [55, 56]. Other studies addressed steel-concrete bond theoretically and experimentally and found that it has a great effect on reinforced concrete member behavior. Early research on bond comprised straight pull out tests that confirmed a significant change in capacity with deterioration of bond [57, 58].

5 Effect of Steel-Concrete Bond

5.1 Localized Versus Member Level Bond Effects

The bond between reinforcing steel and concrete governs the transfer of stress between these two materials. A distinction should be drawn between bond at the localized stress field level, and bond at the reinforced concrete member level. The first category addresses the micro-structure interface whereby the concrete is crushed by the steel lug edge [59, 60]. The second category addresses the cumulative effects of rebar pull-out causing excessive rotation at beam-column joints or crack formation in the tension zone. These effects have a direct effect in the overall stiffness of the structure. They can be modeled directly in the stiffness matrix and found mathematically to impact eigenvalues yielding lower frequencies [61, 62]. Cyclic loading causes alternation between tension and compression at the same member location, and therefore requires the investigation of reversal of member forces computed from static analysis.

5.2 Bond Deterioration at the Local Bar Level

Bond requires development length. If bond resistance deteriorates, reinforcing bars are likely to slip and destroy the steel-concrete composite action. A severe loading such as impulse or earthquake may cause brittle failure. Therefore, bond has multiple functions including overall strength and ductility. It is affected by many factors including concrete cover, rebar spacing, bundling, and position. Depending on the manufacturer, certain bars have ribs at an angle that influences bond and pull-out behavior. It was shown in early research and testing that for the same configuration, bond resistance to straight pull-out is greater under dynamic loading than it is under static loading [63]. This conclusion may not hold under dynamic cyclic loads [64].

Research showed that bond strength decreases as bar diameter increases. This conclusion shed light on the selection of reinforcing steel in practical design, following the determination of a total required steel area [65]. For example a choice of #9 versus #6 bars would not only be affected by placement, but also by increasing the contact surface, or the frictional interface. In this case, smaller bar diameters would be favored, all other design parameters being equal.

Development length of bars was also studied with the effect of confinement. Other factors being constant, ultimate bond stress varies as a function of $f_c^{'}$ because it is related to concrete tensile strength [66]. From traditional tri-axial stress relationships, confinement causes an increase in $f_c^{'}$ and provides larger normal stress between steel and concrete.

Rebar placement, spacing, member width and anchorage also affect bond strength in terms of concrete splitting failure [67]. Studies considering a variety of deformed bar surface properties established a relationship between concrete cracking and

slippage along the embedment length. Results helped formulate resistance to pull-out along embedment length [68]. Related research showed that since confinement increases normal stress around the bar, it has a significant effect on bond [69].

5.3 Bond Slip Effects at the Member Level

The cumulative effects of localized bond slip result in overall drop in performance at the reinforced concrete member level. In particular, beam-column joints would undergo additional rotation beyond the level captured by linear elastic analysis [64]. Once reinforcing steel starts to move relative to concrete, the members connected at the joints go through additional rotation relative to each other. Areas in the vicinity of beam-columns joints in moment-resisting frames subjected to dynamic loading are affected the most [62]. This result is expected because the energy imparted into the superstructure by the earthquake is dissipated through ductile behavior at the joints [70].

6 Model Development

6.1 Mathematical Derivation

We develop a mathematical model that represents the bond slip behavior. Consider the ring of concrete in touch with the bar in between two consecutive lugs. Denote by σ the normal stress exerted by the lug on the concrete. Consider the lug as having an angle θ with the longitudinal axis of the rebar where $45° \leq \theta \leq 90°$. Let d_b denote bar diameter and t_l the height of the lug above the steel surface. The area on the wedge of the steel lug concentric to the bar axis is:

$$A_o = \frac{\pi}{4}\left[\left(\frac{2t_l}{\sin\theta} + d_b\right)^2 - d_b^2\right] \tag{1}$$

For an embedment length l_d, the resultant is:

$$R_o = \sigma \sin\theta \pi t_l (t_l + d_b)\frac{l_d}{s} \tag{2}$$

The projected lug area concentric to the rebar axis is:

$$A_t = \pi[t_l + d_b]\frac{t_l}{\tan\theta} \tag{3}$$

The component of σ exerted on this area contributes to concrete splitting effect. Its resultant is:

$$R_t = \sum_{l_d} \sigma \cos\theta \pi [t_l + d_b] \frac{t_l}{\tan\theta} \tag{4}$$

$$R_t = \sigma \cos\theta \pi [t_l + d_b] \frac{t_l}{\tan\theta} \frac{l_d}{s} \tag{5}$$

The concrete shear area adjacent to the lugis:

$$A_{cv} = \pi [2t_l + d_b] \left[\frac{2t_l}{\tan\theta} + s \right] \tag{6}$$

If f_{cv} is the concrete shear strength, shear resistance is:

$$R_{cv} = \sum_{t_d} f_{cv} \pi [2t_l + d_b] \left[\frac{2t_l}{\tan\theta} + s \right] \tag{7}$$

$$R_{cv} = f_{cv} \pi [2t_l + d_b] \left[\frac{2t_l}{\tan\theta} + s \right] \frac{l_d}{s} \tag{8}$$

The area of an infinitesimal element around the circumference of the steel segment within the clear spacing of two consecutive lugs is:

$$dA_c = \frac{d_b}{2} d\alpha dx \tag{9}$$

where $d\alpha$ is an infinitesimal angle about the rebar centroid, and dx is an infinitesimal distance parallel to the longitudinal rebar axis. Among the range of deformed bar patterns, the simplest pattern has lugs that are parallel to each other, spaced at about $1/2''$ to $1''$ and orthogonal to the bar axis.

To express the frictional resistance mathematically, we consider that the confinement stress, denoted $f_1^{'}$ contributes to frictional resistance to motion, at both the concrete-concrete interface and the steel-concrete interface. Denote μ the friction coefficient, which depends on the pull-out displacement rate, $\dot{x} = dx/dt$ and on the angular location around the rebar periphery, α. The differential force due to friction can be expressed as:

$$dR_s = \mu(\dot{x}, \alpha) f_1^{'} \left(\frac{d_b}{2} \right) .d\alpha.dx \tag{10}$$

The resultant is a double integral over α and x, over the inter-lug segment, summed over the embedment length:

$$R_s = \sum_{l_d} f_1^{'} \frac{d_b}{2} \int_0^{2\pi} \int_0^{s} \mu(\dot{x}, \alpha) d\alpha . dx \tag{11}$$

The inclusion of α in the expression of μ is due to the fact that there may be localized imperfections around the rebar such as air pockets, or a large aggregate instead of bonding mortar, which may cause an uneven frictional resistance around the circumference of the bar. Such local imperfections and their effects can be accounted for separately through a safety reduction factor related to concrete mix and placement quality. As for the relative pull-out displacement rate or velocity range expected at incipient bond slip, we consider that the steel-concrete friction coefficientis constant along the embedment length. Applying these two simplifications to expression (11), performing double integration, and summing over the development length, we have:

$$R_s = \pi \mu f_1^{'} d_b l_d \tag{12}$$

The derivation sheds light on the difference between reversible and irreversible effects of loading. For a steel bar whose strength exceeds the bond slip load level, the effect is considered reversible. However, if bond slip occurs at a load level below the development of the bar strength the effect becomes irreversible.

6.2 Application to Static Equilibrium

The stress resultants in expressions (2), (5), (8) and (12) can be used in equilibrium equations in the longitudinal direction. As discussed earlier, (2), (5) and (12) could be extended into a dynamic equilibrium where the rate of change of the friction coefficient, inertia effects, and other related factors, are accounted for. However, the dynamic equilibrium is treated undera separate scope. Several cases could be identified, which we simplify under two main conditions that are most relevant to our scope. Case 1 pertains to the rebar reaching its full development function, while Case 2 corresponds to a pull-out prior to reaching yield. An optimal equilibrium would be reached under strength and economic conditions simultaneously. Denoting by T_s the tensile force applied to the bar:

$$T_s = A_{st} f_s \tag{13}$$

where A_{st} is a single bar steel section and f_s is the stress applied to that section. If there is no bond slip, we have:

$$T_s = A_{st} f_s \leq R_o + R_s \tag{14}$$

otherwise, the bar would pull-out under the applied section stresses. In this case, we have:

$$T_s = A_{st} f_s \geq R_{cv} \tag{15}$$

Once the concrete shear resistance fails at the envelope layer, both the lug resistance and the frictional resistance along the steel segment between the lugs no longer contribute to bond. Research on steel-concrete friction coefficients shows that their values vary between 0.47 and 0.7 depending on finishing parameters and other factors [71, 72]. For the purpose of the present illustrative examples, we use 0.5. However, the same present derivation and resulting formulas could used over a range for values of the friction coefficient.

The relationship between bar tensile force and bond resistance for a No. 5 bar in 4000 psi compression strength concrete is shown in Fig. 1, where tensile resistance is plotted against development length factor. Yield forces in the bar are T_y (4) = 12.4 k and T_y (6) = 18.6 k for $f_y = 40$ ksi and $f_y = 60$ ksi, respectively. Development length required by ACI is 37 d_b, for $f_y = 40$ ksi, and 57d_b for $f_y = 60$ ksi. For both f_y values, inequality (14) is satisfied and the bar will yield before reaching the pull-out limit. However, shear strengthin the concrete in the vicinity of the bond area is enough to carry the bar to yield for $f_y = 40$ ksi, but bond slip will occur before the bar yields for $f_y = 60$ ksi (Fig. 1). A similar analysis could be performed for various bar diameters, concrete compressive strength, and steel yield stress.

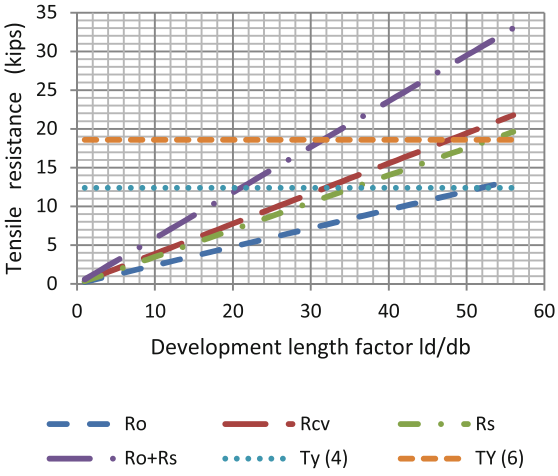

Fig. 1 Bond and frictional tensile resistance versus development length factor for No. 5 deformed bar in 4000 psi concrete

7 Effect on Overall Structural Health

7.1 Effect of Bond Deterioration

Bond deterioration has a significant effect on local critical zones, and it has an influence on the overall structural behavior, especially when subjected to dynamic loading. The additional rotation at the joints due to bond slip exhibits hysteresis behavior represented by a nonlinear curve [64, 70]. The force-deformation curve starts with a straight line over the elastic range then reaches a plateau where the joint rotates at no additional moment. When load reversal occurs, the joint starts rotating in the opposite direction while engaging the bar in friction until it bears against concrete. At that point, the bar on the opposite side of the beam starts its pulling cycle. Theoretically, reversal exhibits equal and opposite values. But if decay is included in the model, cycle $i + 1$ will exhibit deterioration with respect to cycle i, until collapse of the joint, should the cyclic load continue.

7.2 Effect of Aging

Aging of concrete is one of the most determining phenomena in the behavior of structures. Early studies in the 1950s followed by research at the turn of century show continuous interest in long term effects in concrete behavior [32, 35]. There are no standardized direct experimental processes to deliberately age concrete and test it on that basis. For this reason, the most reliable lab for aging would be the outdoors real life situation in cities where reinforced concrete constitutes the vast majority of buildings.

Data collected in various cities in Lebanon was compiled by building age, condition, and ambient environmental effects. A subset of 140 buildings was studied analytically. But coring and compressive strength tests were performed on only 5 buildings that were considered as representative of the others in the sample. The 5 buildings are not statistically significant, but their results were within a coherent range and therefore provided an indication of the state of the concrete in these older buildings. Some of the cylinders gave a compressive strength as low as 790 psi. The detailed field-related experiments were left outside the scope of this paper as a subject of future research [73].

7.3 Effect of Design and Placement Quality

Mix and structural design, and placement quality are very important and have a direct relationship with the two features above; bond deterioration and aging. Concrete that is well proportioned has a superior longevity to concrete that is not. Structural systems that are designed to withstand dynamic loading defined by code, will

Table 1 Basic decision rule that differentiates localized damage from overall distress

Damage categories	Potential causes	Reversibility
Concrete cover spalling	Under-designed cover	Uncover, treat bars, provide new cover
	Mild rebar corrosion	
Chunking around bars	Stress exceeds design stresses	Remove, track damage, rebar implants, re-cast
	Severe corrosion	
Localized steel corrosion stains	Lack of vibration during placement	Uncover, treat bars, provide new cover
	Hairline cracks; air, water, chemicals reach bars	
Fluffy plaster, caulking, or paint	Damage due to humidity or water seepage	Uncover, treat bars, provide new cover
Large structural cracks and visible deflections	Bond deterioration	Fix depends on localized damage
		Inject bond agent, cast shadow member
		Alternative solutions involve exterior wrap
Beam-column joint slack	Bond deterioration	Building may pose hazard in the following event
	Bar pull-out	Consider disposal
	Fatigue, distress	
Structure exhibiting misalignment or out-of-plumb	Bond deterioration	Dispose
	Major loss of strength	

obviously perform better than the ones that are not. Some of the field challenges that we encountered had to do with all three components; mix, design, and placement. In the present paper, we mention some of those challenges as they cannot be fixed retroactively, but we shall rather provide a rational approach for decision-making in terms of types of actions that could be taken.

A challenge in many less developed countries is the lack of code guidelines. Another challenge is the poor or lack of supervision. Even when designed per European or US codes, the execution leaves room for mismanagement of resources and potential mishaps during construction.

7.4 Remediation Choices

Although extensive research on reinforced concrete damage caused by bond deterioration was performed in the 1960s, interest in bond effects for both steel and fiber reinforced concrete resurged in later decades as seismic codes grew more stringent [74, 75].

For existing buildings, parameters needed to perform calculations may not be easily available. To determine $f_c^{'}$ in an older building, coring and testing may be performed. But results from various parts of the same building may exhibit a large spread [73]. A simpler decision rule involves the overall state of the building. Table 1 provides a set of inspection results, with possible solutions. Three categories are defined for strength, serviceability, and aesthetic requirements (Table 1).

8 Effect on Dynamic Behavior

8.1 Effect on Fundamental Period

Studies conducted on beam-column assemblages attempted to cast complex dynamic behavior in formulas. Approaches proposed in literature account for bond slip effect on overall structural dynamic behavior [64, 76].

To get a preliminary result on dynamic performance, considera single bay and three degrees of freedom, one translation u_1 and two rotations at the joints, u_2 and u_3, respectively. We have:

$$\begin{bmatrix} k_{11} & k_{12} & k_{13} \\ k_{21} & k_{22} & k_{23} \\ k_{31} & k_{32} & k_{33} \end{bmatrix} \begin{bmatrix} u_1 \\ u_2 \\ u_3 \end{bmatrix} = \begin{bmatrix} f_e \\ 0 \\ 0 \end{bmatrix} \tag{16}$$

$$k_{11}^{*} u_1 = f_e \tag{17}$$

where k_{11}^{*} condenses the k_{ij} stiffness coefficients ($i = 1, 2, 3$; and $j = 1, 2, 3$; $i \neq 1$, *and* $j \neq 1$) and f_e is the elastic force. The mathematical derivation is under separate scope to focus here on the practical formulas for designers [73]. We define a girder-column stiffness ratio:

$$\varphi = \frac{E_{cg} I_g L_c}{E_{cc} I_c L_g} \tag{18}$$

where E_{cg} and E_{cc} are the moduli of elasticity for the concrete in the girder and in the column respectively, I_g and I_c are the moments of inertia of the girder and column, respectively, and L_g and L_c are the span of the girder and column height respectively. We have:

$$k_{11}^{*} = \frac{E_{cc} I_c}{L_c^3} \left(\frac{a + b.\varphi}{c + d.\varphi} \right) \tag{19}$$

where a, b, c, and d, are constants that depend on column and girder properties [73]. Degradation in girder-column stiffness ratio is denoted by δ_φ. The drop in the condensed stiffness term differs whether the deterioration is occurring in the girder

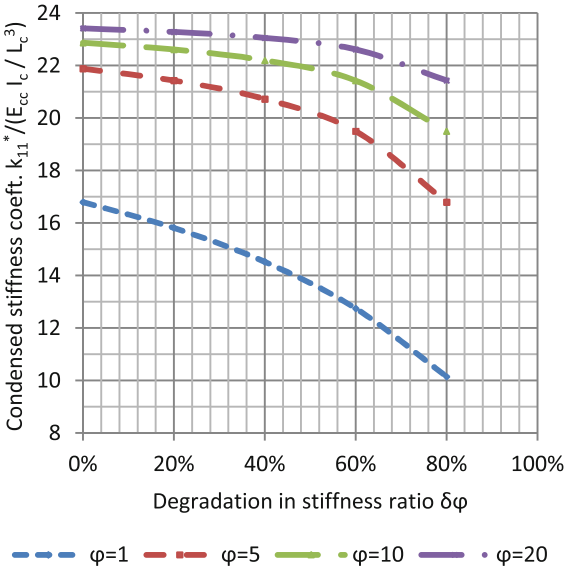

Fig. 2 Drop in condensed stiffness as a function of deterioration in the girder moment of inertia

or the column. In both cases, however, it results in a significant drop in natural frequencies of the structural system. Figure 2 shows the drop in stiffness due to degradation in the girder, while Fig. 3 shows results for degradation in the column.

For a stiffness ratio of 5 that decreases 60 % through deterioration of girder moment of inertia, the condensed stiffness drops from 22 to 19.5. While for the same stiffness ratio, 5, that decreases 60 % through deterioration of column moment of inertia, the condensed stiffness drops from 22 to 9 (Fig. 3). These numerical examples support the strong column weak girder approach in the seismic design of RC structures.

The results can be related to linear elastic structural analysis using basic element stiffness coefficients with various boundary conditions. For example, a free standing cantilever column whose top joint is allowed to rotate and translate without any restraints has a lateral stiffness coefficient equal to $3EI/L^3$, where E, I and L are the modulus of elasticity, moment of inertia, and span, respectively. If the top joint of the column is fixed against rotation, but is allowed to translate horizontally, the lateral stiffness coefficient is $12EI/L^3$. For a portal, the results in the first case yield a coefficient of 6 and in the second case, a coefficient of 24. Therefore, the worst case scenario of girder failure comprises bond deterioration in the girder at the column face, leaving the joint in the column to rotate freely, or with very low deteriorated rotational stiffness. The worst case scenario of column failure through bond deterioration would be a hinge in the column leading to collapse, which is unacceptable form a reinforced concrete design perspective.

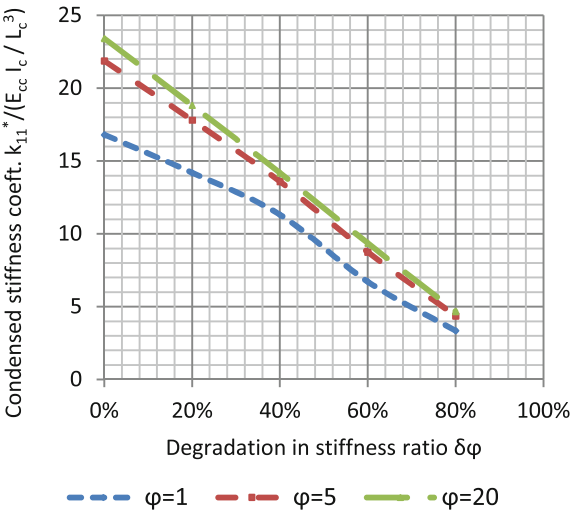

Fig. 3 Drop in condensed stiffness as a function of deterioration in the column moment of inertia

9 Conclusions

Methodologies for predicting earthquake response of a structure based on its known properties and for a given excitation are well established. The challenge resides in the ability to define those properties, especially when the construction material is susceptible to substantial changes through time, or in the wake of a tasking event. For reinforced concrete structures, these two factors are particularly important; aging of concrete is accompanied by shrinkage and creep effects, and events such as earthquakes could drive the members into reversals that change their mechanical properties. What makes the analysis and design of reinforced concrete more demanding is that related formulas are based on strain compatibility assumptions. These assumptions that of steel and concrete deforming in compatible increments as the elements develop nominal strength, do not hold throughout the life of the reinforced concrete member. These assumptions become less applicable to real life behavior when concrete elements age or undergo cyclic loading. Another challenge is related to the possibility of performing tests on various lifetime intervals to ascertain, or adjust, properties in models. The use of field sampling to determine concrete compressive strength may be performed by coring and lab testing. However, field-testing for bond deterioration is much more complex and cannot be determined by sampling an existing structure. Loss of bond between reinforcing steel and surrounding concrete is a complex, internal, often invisible phenomenon that is hard to capture through common sampling techniques. The model developed in the present paper analyzes the structural health of reinforced concrete buildings taking into consideration concrete damage through loss of bond. The analytical model relates steel loading that causes bond distress to design parameters such as development length and bar properties. Potentially, new methodologies for field measurements could be developed to target

bond deterioration through the observation of dynamics properties. This is based on the premise that loss of bond leads to reduced stiffness which results in lower natural frequencies. Those reduced or modified stiffness coefficient could be calculated for mass values kept constant. The analytical model could be checked against the dynamic model and could be complemented by field measurements in future research. The diagnosis method presented in this paper discusses the sustainability of the structure and offers a simplified decision rule whether to perform minor fixes, major rehabilitation, or disposal. The model draws a distinction between joint damage in the girder as opposed to the column, and makes the case for weak-girder strong-column design. Plastic joints formed in the girder may potentially lend themselves to concrete repair, while plastic hinges in the column may cause catastrophic collapse, and thus make the structural health condition irreversible. Empirical results were partially used and discussed to illustrate field challenges that are faced when the structure is subjected to earthquake motion or other severe conditions such as impulse loading.

References

1. Zuber, B., Marchand, J.: Modeling the deterioration of hydrated cement systems exposed to frost action; part 1: description of the mathematical model. Cem. Concr. Res. **30**(12), 1929–1939 (2000)
2. Powers, T.C.: A working hypothesis for further studies on frost resistance of concrete. Research Laboratory of the Portland Cement Association. J. Am. Concr. Inst. **16**(4), 245–272 (1945)
3. Naik, T.R.: Sustainability of concrete construction. ASCE Pract. Period. Struct. Des. Constr. **13**(2), 98–103 (2008)
4. Jacobs, J.B. (ed.): European Concrete Platform: Sustainable Benefits of Concrete Structures. Brussels, Belgium (2008)
5. Park, S.B., Seo, D.S., Lee, J.: Studies on the sound absorption characteristics of porous concrete based on the content of recycled aggregate and target void ratio. Cem. Concr. Res. **35**(9), 1846–1854 (2005)
6. Nordby, G.M.: Fatigue of concrete: a review of research. J. Am. Concr. Inst. **30**(2), 191–219 (1958)
7. Powers, T.C., Copeland, L.E., Hayes, J.C., Mann, H.M.: Permeability of Portland cement paste. J. Am. Concr. Inst. **51**(3), 285–298 (1954)
8. Powers, T.C.: The physical structure and engineering properties of concrete. Bulletin No. 90. Res. Dev. Lab. Portland Cem. Assoc. **1958**, 1–28 (1958)
9. Powers, T.C., Helmuth, R.A.: Theory of volume changes in Hardened Portland cement paste during freezing. Highw. Res. Board Proc. **32**, 285–297 (1953)
10. Green, H.: Impact strength of concrete. Proc. Inst. Civil Eng. London **28**(3), 383–396 (1964)
11. Ople. F.S., Hulsbos, C.L.: Probable fatigue life of plain concrete with stress gradient. Research report. ACI J. **63**(2), 59–81 (1966)
12. Collins, M.P.: In Search of Elegance: The Evolution of the Art of Structural Engineering in the Western World. ACI, Concrete International **23**(7), 55–72 (2001)
13. Sorensen, A.: The Making of Urban Japan: Cities and Planning from Edo to the Twenty First Century. Routledge, New York (2005)
14. El-Numeiri, M., Gupta, P.: Sustainable Structure of Tall and Special Buildings. CTBUH 2^{nd} Annual Special Edition. In: Tall Sustainability, ed. Antony Wind, Wiley, 17(5), (2009)
15. Smith, B.S., Coull, A.: Tall Building Structures: Analysis and Design. Wiley, New York (1991)

16. AISC: American Institute of Steel Construction Design Specifications. AISC Manual 13th edn. New York (2010)
17. Segui, W.T.: Steel Design, 5th edn. Cengage Learning, Stamford (2012)
18. Ali, M.M., Moon, K.S.: Structural developments in tall buildings: current trends and future prospects. Architect. Sci. Rev. **50**(3), 205–223 (2007)
19. Oldfield, P., Trabucco, D., Wood, A.: Five energy generations of tall buildings: a historical analysis of energy consumption in high-rise buildings. Journal of Architecture **14**(5), 591–613 (2009)
20. Oldfield, P., Wood, A.: Tall building in the Global Recession: 2008, 2020, and beyond. Counc. Tall Build. Urban Habitat (CTBUH) J. **1**, 20–26 (2009)
21. Ann, K.Y., Moon, H.Y., Kim, Y.B., Ryou, J.: Durability of recycled aggregate concrete using pozzolanic materials. Waste Manage. **28**(6), 993–999 (2008)
22. Damineli, B.M., Kemeid, F.M., Aguiar, P.S., John, V.M.: Measuring the eco-efficiency of cement use. Cem. Concr. Composit. **32**(8), 555–562 (2010)
23. Mehta, P.K.: Global concrete industry sustainability. Concr. Int. **31**(2), 45–48 (2009)
24. Al-Mutairi, N., Haque, M.N.: Strength and durability of concrete made with crushed concrete as coarse aggregates. In: Proceedings of the International Symposium on Recycling and Reuse of Waste Materials, pp. 499–506. Scotland, UK (2003)
25. Katz, A.: Properties of concrete made with recycled aggregate from partially hydrated old concrete. Cem. Concr. Res. **33**(5), 703–711 (2003)
26. Gomez-Soberon, J.M.V.: Porosity of recycled concrete with substitution of recycled concrete aggregate. Cem. Concr. Res. **32**(8), 1301–1311 (2002)
27. AASHTO MP 16: Standard specification for reclaimed concrete aggregate for use as coarse aggregate in hydraulic cement concrete. In: American Association of State and Highway Transportation Officials, Washington, DC, US (2010)
28. Gonzalez-Fonteboa, B., Martinez-Abella, F.: Concretes with aggregates from demolition waste and silica fume: materials and mechanical properties. Build. Environ. **43**, 429–437 (2008)
29. Kayali, O., Haque, M., Khatib, J.: Sustainability and emerging concrete materials and their relevance to the Middle East. Open Constr. Build. Technol. J. **2**(1), 103–110 (2008)
30. Cole, R.J.: Energy and greenhouse gas emissions associated with the construction of alternative structural systems. Build. Environ. **34**(3), 335–348 (1999)
31. Olorunsogo, F.T., Padayachee, N.: Performance of recycled aggregate concrete monitored by durability indexes. Cem. Concr. Res. **32**(2), 179–185 (2002)
32. Alexander, M.G., Ballim, Y., Maketchnie, J.R.: Guide to the use of durability indexes for achieving durability in concrete structures. Collaborative Research by Universities of Cape Town and Witwatersrand. Res. Monogr. **35**(2), (1999)
33. Hasaba, S., Kawamura, M., Torik, K., Takemoto, K.: Drying shrinkage and durability of concrete made of recycled concrete aggregate. Collaborative Research by Universities of Cape Town and Witwatersrand. Trans. Jpn. Concr. Inst. **3**, 55–60 (1981)
34. Bertolini, L.: Steel corrosion and service life of reinforced concrete structures. J. Struct. Infrastruct. Eng. **4**(2), 123–137 (2008)
35. Troxell, G.E., Raphael, J.M., Davis, R.E.: Long-time creep and shrinkage tests of plain and reinforced concrete. Proc. ASTM **58**, 1–20 (1958)
36. Shank, J.R.: Plastic flow of concrete at high overload. ACI J. **20**(6), 68–76 (1949)
37. Hansen, T.C.: Elasticity and drying shrinkage of recycled aggregate concrete. ACI J. **82**(5), 648–652 (1985)
38. Washa, G., Fluck, D.: Effect of sustained loading on compressive strength and modulus of elasticity of concrete. ACI J. **46**(5), 693–700 (1950)
39. Levtchitch, V., Kvasha, V., Boussalis, H., Chassiakos, A., Kosmatopoulos, E.: Seismic performance capacities of old concrete. In: Proceedings, 13th World Conference on Earthquake Engineering, Vancouver, B. C., Canada, 1–6 Aug 2004, Paper No. 2182 (2004)
40. Levtchitch, V.: Shear fatigue and seismic response of reinforced concrete flexural members. Cyprus J. Sci. Technol. Nicosia **1**(3), 22–32 (1997)

41. Cornelissen, H.A.W., Reinhardt, H.W.: Uniaxial tensile fatigue failure of concrete under constant-amplitude and programme loading. Mag. Concr. Res. **36**(129), 216–226 (1984)
42. Kim, J.K., Han, S.H., Song, Y.C.: Effect of temperature and aging on the mechanical properties of concrete: part I. Experimental results. Cem. Concr. Res. **32**(7), 1087–1094 (2002)
43. Washa, G.W., Wendt, K.F.: Fifty Year properties of concrete. ACI J. Proc. 71–4, 20–28 (1975)
44. Withey, M.O.: Fifty year compression test of concrete. ACI J. Proce. 58(6), 695–712 (1961)
45. American Concrete Institute, ACI 224R–90: Control of Cracking in Concrete Structures. ACI Manual of Concrete Practice, Part 3, American Concrete Institute, Detroit, MI (1992)
46. Base, G.D.: Control of Flexural Cracking in Reinforced Concrete. Civil Engineering Transactions, The Institution of Engineers, Australia, CE **18**(1), 20–23 (1976)
47. Guide to Concrete Repair: Bureau of Reclamation, Technical Service Center, Denver, CO (1996)
48. American Concrete Institute: Concrete Repair Manual, 4th edn, vol. 1, 2 (2013)
49. Popovics, S.: New formulas for the prediction of the effects of porosity on concrete strength. Am. Concr. Inst. J. Proc. **82**(2), 136–146 (1985)
50. Chen, X., Wu, S., Zhou, J.: Influence of porosity on compressive and tensile strength of cement mortar. Construct. Build. Mater. **40**, 869–874 (2013)
51. Bartlett, F.M., MacGregor, J.G.: Assessment of concrete strength in existing structures. Structural Report No. 198, Department of Civil Engineering, University of Alberta, Edmonton, Alberta (1994)
52. American Concrete Institute: Specifications for Structural Concrete—ACI 301–05. Publication SP-15, Field Reference Manual, Farmington Hills (2005)
53. Saether, I.: Bond deterioration of corroded steel bars in concrete. J. Struct. Infrastruct. Eng. **7**(6), 415–429 (2011)
54. American Concrete Institute, ACI Committee 318–11: Building Code Requirements for Structural Concrete and Commentary. ACI 318–11. MI (2011)
55. Gulikers, J.: Pitfalls and practical implications in durability design of reinforced concrete structures. In: Proceedings of the 4th International RILEM PhD Workshop on Advances in Modeling Concrete Service Life, Madrid, Spain (2010)
56. Materials Properties Model of Aging Concrete. Bureau of Reclamation, Technical Service Center, Denver CO (2005)
57. Shi, Z.: Crack Analysis in Structural Concrete: Theory and Applications. Elsevier, New York (2009)
58. Hunaiti, Y.: Aging effect on bond strength in composite sections. ASCE J. Mater. Civil Eng. **6**(4), 469–473 (1994)
59. Goto, Y.: Cracks formed in concrete around deformed tension bars. ACI J. **68**(2), 244–251 (1971)
60. Lutz, L.A.: Analysis of stresses in concrete near a reinforcing bar due to bond and transverse cracking. ACI J. Proc. **67**(10), 778–787 (1970)
61. Scott, R.H., Gill, P.A.T.: Short-term distributions of strain and bond stress along tension reinforcement. Struct. Eng. **65B**(2), 39–48 (1987)
62. Filippou, F.C., Popov, E.P., Bertero, V.V.: Modeling of reinforced concrete joints under cyclic excitations. ASCE J. Struct. Eng. **109**(11), 2666–2684 (1983)
63. Hansen, R.J., Liepins, A.A.: Behavior of bond in dynamic loading. ACI J. **59**, 563–583 (1962)
64. Spacone, E., Filippou, F.C., Taucer, F.F.: Fiber beam-column model for non-linear analysis of R/C frames, part 1: formulation. Earthq. Eng. Struct. Dyn. **25**(7), 711–725 (1996)
65. Mathey, R.G., Watstein, D.: Investigation of bond in beam and pullout specimens with high-yield strength deformed bars. ACI J. T. No. 57–50, 1071–1089 (1961)
66. Ferguson, P.M., Robert, I., Thompson, J.N.: Development length of high strength reinforcing bars in bond. ACI J. T. No. 59–17, 887–922 (1962)
67. Ferguson, P.M., Breen, J.E., Thompson, J.N.: Pull out tests on high strength reinforcing bars. ACI J. T. No 62–55, 933–950 (1966)
68. Abrishami, H., Mitchell, D.: Simulation of uniform bond stress. ACI Mater. J. **89**(2), 161–168 (1992)

69. Malvar, L.J.: Bond of reinforcement under controlled confinement. ACI Mater. J. **89**(6), 593–601 (1992)
70. Bazant, Z.P., Bhat, P.D.: Prediciton of hysteresis of reinforced concrete members. ASCE J. Struct. Div. **103**(ST1), 153–167 (1977)
71. Rabbat, B.G., Russel, H.G.: Friction coefficient of steel on concrete or grout. ASCE J. Struct. Eng. **111**(3), 505–515 (1985)
72. Baltay, R., Gjelsvik, A.: Coefficient of friction for steel on concrete at high normal stress. ASCE J. Mater. Civil Eng. **2**(1), 46–49 (1990)
73. Chalhoub, M.S.: Seismic design and dynamic response of reinforced concrete buildings with the effects of deterioration. Working paper, CEM Rep. No. 02–2014 (2014)
74. Lee, M.G., Chiu, C.T., Wang, Y.C.: The study of bond strength and bond durability of reactive powder concrete. J. ASTM Int. **2**(7), 12960 (2005)
75. Banon, H., Biggs, J.M., Irvine, H.M.: Seismic damage to reinforced concrete frames. ASCE J. Struct. Div. **107**(ST9), 1713–1729 (1981)
76. Emori, K., Schnobrich, W.C.: Inelastic behavior of concrete frame-wall structures. ASCE J. Struct. Div. **107**(ST1), 145–164 (1981)

Recurrence and Joint Recurrence Analysis of Multiple Attractors Energy Harvesting System

C.A. Kitio Kwuimy and C. Nataraj

Abstract The method of recurrence plots and joint recurrence plots are considered as tools for the nonlinear analysis of a dimensionless model of magnetoelastic piezoelectric energy harvester under wind flow excitation with low Reynolds number. The dynamics of the system is investigated by considering the bifurcation of the recurrence rate, the laminarity and the determinism and illustrations of system response are presented though the recurrence plots and phase diagrams. In order to enhance the efficiency of the system, a second degree of freedom is added to the mechanical part. The method of joint recurrence plot is used to analyze the global synchronization of the system. In this spirit, a feedback Master-Slave configuration is adopted to ensure optimal synchronized mechanical excursion and thus maximal electric voltage harvested in the electric load. Throughout the paper, attention is focussed on the effects of feedback coupling and mistuning parameter, as well as the relevance of the method of recurrence plots and joint recurrence plots in the analysis of such system. Specifically, it is shown that the joint recurrence plot synchronization parameter effectively detects domain of maximal output electric power as well as domain of out-of-phase motion leading to minimal output power.

1 Introduction

Energy harvesting systems are designed to transform available ambient energy into electrical energy for small and/or portable devices. These harvesters involve structural vibration, wind flow, physiological and chemical reactions. For the last 10 years several harvesters based on structure excitation and fluid flow have been analyzed [4, 19–22, 31, 42, 43] (and references therein). Although common transduction mechanisms are electromagnetic, piezoelectric and electrostatic, the piezoelectric transducing mechanism is in general preferable because it has highest energy density and no reliance on external magnetic field or initial DC voltage [41]. These

C.A. Kitio Kwuimy (✉) · C. Nataraj
Center for Nonlinear Dynamics and Control, Department of Mechanical Engineering,
Villanova University, Villanova, PA 19085, USA
e-mail: cedrick.kwuimy@villanova.edu

M. Belhaq (ed.), *Structural Nonlinear Dynamics and Diagnosis*,
Springer Proceedings in Physics 168, DOI 10.1007/978-3-319-19851-4_6

systems were found to be only efficient near sole resonance frequency and this limit their applicability in frequency variant, amplitude variant or random excitations. Considerable efforts have been devoted to enhance the performance of these systems by using nonlinear phenomena such as multiple resonance, snap through instability, bifurcation, stochastic resonance [20, 21, 30] and material with fractional order properties [27].

To optimize the harvesting mechanism, multiple degree of freedom systems have been considered. Shahruz [39] analyzed a set of parallel single degree of freedom harvesters tuned at slightly different resonant frequencies, whereas Erturk et al. [10] considered a harvester as a serial set of two beams connected to each other to form an L-shape. Ferrari et al. [12] investigated a piezoelectric multiple frequency energy converter for power harvesting in autonomous microsystems. Ramlan et al. [37] considered a harvester made of two oblique springs and analyzed the potential benefits of the hardening effects of the spring on the output energy. Liu et al. [32] considered an adaptive harvester for wind flow induced vibration involving an additional mechanical arm acting as flow sensor. However, a network of harvesting system is not always optimal since the out of phase motion and mistuning leading to a reduction of the output energy can appear [41]. Litak et al. [31] analyzed the stochastic response of two magnetopiezoelastic energy harvesters with mistuning. Also, for a multiple amplitude response (such as in systems with hysteresis for example), it appears that, some elements of the network can vibrate with lower amplitude [36]. These two problems have lead to the development of the synchronized charge extraction technique [41] (and references therein), the impedance adaptation technique [13] and the synchronized switching harvesting on an inductor technique or voltage source [13, 16, 29]. These techniques have been considered for theoretical and experimental investigations under various assumptions such as resonance, linearity, in-phase motion and weak coupling. Although they give information for the design of network of harvesters, these assumptions are not realistic since mistuning always happen as well as out-of resonance motion [31, 41, 46]. Moreover, for self-excited systems such as wind-induced vibration, out-of phase motion, hysteresis and multiple limit cycle can appear [7].

The idea of extracting useful energy from the surrounding fluid flow has been considered by several authors [2, 5, 6, 20, 21] and they discussed the conditions for efficiency of the harvesters. The motivation of this paper is to investigate the efficiency and the synchronization of multiple attractor wind-induced vibration energy harvester system at low Reynolds number by recurrence. The dynamics under multiple attractors condition were ignored or briefly mentioned in previous contributions [3, 5–7, 19–21, 23]. The originality of this contribution, in addition to its theoretical contribution in energy harvesting, is its relevance to hybrid method for system analysis. Thus, the interest for the method of recurrence is based on the fact that, the recurrence plot (RP) is now a strong numerical tool for time series analysis of complex systems. Very few contributions have considered nonlinear analysis, synchronization or control of complex systems based on RP, see for instance [9, 25, 27]. This could potentially reveals details that can be used in practical applications such as system diagnostics and enhance system design [11, 15, 28, 38]. Recently,

we used the method of RP to investigate the responses of a nonlinear pendulum and detection of dynamics change in the system response [25]. This was extended to the mathematical model describing the behavior of biological oscillator [27].

The rest of the paper is organized as follows: In Sect. 2 we present the physical system and the mathematical model based on the work of Barrero-Gil et al. [7, 8]. Illustration of birhythmicity is highlighted as well as the effects of an additive harmonic excitation. The third Section discusses the possibility of a complete synchronization of the system. The last section recalls and discusses the main results.

2 Brief Review of the Model and System Characterization

2.1 The Mathematical Model

The physical model is made of a cantilevered beam with piezoelectric patches under a transversal wind flow (Fig. 1). It is constituted of an electrical circuit having a load resistance R_ℓ and a flexible beam with distributed piezoelectric patches. The modeling equation of the system is given as

$$\rho_b S \frac{\partial^2 W}{\partial \tau^2} + EI \frac{\partial^4 W}{\partial X^4} + c_a \frac{\partial W}{\partial \tau} = F_a(\tau) + K_0 V(\tau) f(X) \tag{1}$$

$$C_p \frac{dV}{d\tau} + \frac{V}{R} = -K_1 \int_0^L f(X) \frac{\partial^3 W}{\partial X^2 \partial \tau} dX \tag{2}$$

where $W(X, \tau)$ is the transversal beam deflection function of time τ and a coordinate along the beam element X, E is the Young modulus, S is the beam cross section, ρ_b is the beam mass density, L is the beam length, c_a is the viscous damping, $F_a(\tau)$ the aerodynamics force, K_0 and K_1 are the piezoelectric coupling terms acting exclusively on the area of the piezoelectric patches, C_p is the inherent capacitance of the piezoelectric element, R_ℓ is the resistive load, V is the voltage generated by the piezoelectric element. $f(X) = H(X) - H(X - X_1) + H(X - X_2) - H(X - L)$ is a spatial function used to specify that the piezoelectric patches are localized in the region $0 < X < X_1$ and $X_2 < X < L$, where $H(.)$ denotes the Heaviside step function. For the beam in Fig. 1, the displacement and slope at the clamped end ($X = 0$) are zero. Also, at the free end ($X = L$), the bending moment and the share force are zero. The conditions are formulated as [26, 44]

$$W(0, \tau) = \frac{\partial W}{\partial X}(0, \tau) = \frac{\partial^2 W}{\partial X^2}(L, \tau) = \frac{\partial^3 W}{\partial X^3}(L, \tau) = 0 \tag{3}$$

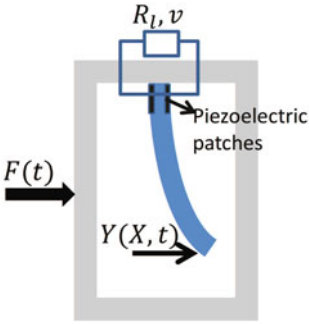

Fig. 1 Schematic representation of the energy harvesting system under wind flow

For system with small Reynolds number ($R_e < 200$), Barrero-Gil et al. [7, 8] showed that the aerodynamics force is given as

$$F_a(\tau) = \frac{1}{2}\rho_a D U^2 \left[a_1 \frac{1}{U}\frac{\partial W}{\partial \tau} - a_3 \left(\frac{1}{U}\frac{\partial W}{\partial \tau}\right)^3 + a_5 \left(\frac{1}{U}\frac{\partial W}{\partial \tau}\right)^5 - a_7 \left(\frac{1}{U}\frac{\partial W}{\partial \tau}\right)^7 \right] \tag{4}$$

where U is the wind velocity, D is characteristic constant of the system, ρ_a is the mass density of the fluid, the coefficients a_i (i = 1, 3, 5, 7) are empirical functions of the Reynolds number and the "+" and "−" are dictated by experimental considerations and the Dan Hartog stability criteria [14].

2.2 Garlekin Approximation: Modal Equations

To facilitate the analysis, we use the dimensionless variables $Y = \frac{W}{h}$, $x = \frac{X}{L}$, $v = \frac{V}{V_0}$, $t = \frac{\tau}{T}$ and $u = \frac{U}{U_0}$ where V_0, T and U_0 are characteristic parameters to be determined. The new form of the equations of the device is thus

$$\frac{\partial^2 Y}{\partial t^2} + \frac{\partial^4 Y}{\partial x^4} - F(t) = \eta_0 v f(x), \tag{5}$$

$$\frac{dv}{dt} + \gamma v = -\eta_1 \int_0^1 f(x) \frac{\partial^3 Y}{\partial t \partial x^2} dx, \tag{6}$$

with

$$F(t) = g_1(u, R_e)\frac{\partial Y}{\partial t}\left[1 - g_2(u, R_e)\left(\frac{\partial Y}{\partial t}\right)^2 + g_4(u, R_e)\left(\frac{\partial Y}{\partial t}\right)^4 - g_6(u, R_e)\left(\frac{\partial Y}{\partial t}\right)^6\right] \tag{7}$$

$$g_1(u, R_e) = -\varepsilon_0 - a_1 u, \quad g_2(u, R_e) = \frac{a_3}{u(a_1 u - \varepsilon_0)}, \tag{8}$$

$$g_4(u, R_e) = \frac{a_5}{u^3(a_1 u - \varepsilon_0)}, \quad g_6(u, R_e) = \frac{a_7}{u^5(a_1 u - \varepsilon_0)} \tag{9}$$

and

$$T = \sqrt{\frac{\rho_b S L^4}{EI}}, \ \varepsilon_0 = \frac{C_a T}{\rho_b A}, \ \eta_0 = \frac{K_0 T^2 V_0}{\rho_b A h_b}, \ \gamma = \frac{T}{RC_p}, \ \eta_1 = \frac{K_1 h}{C_p V_0 L^2}, \ U_0 = h\sqrt{\frac{2\rho_b S h_b}{T^2 \rho_a D}} \tag{10}$$

The boundaries conditions are also transformed into

$$Y(x, t) = 0 \ \text{ and } \ \frac{\partial Y(x, t)}{\partial x} = 0 \tag{11}$$

at the clamped end, and

$$\frac{\partial^2 Y(x, t)}{\partial x^2} = 0 \ \text{ and } \ \frac{\partial Y(x, t)}{\partial t} = 0 \tag{12}$$

at the free end.

The dimensionless model (5) and (6) is a set of linear ordinary differential equation (ODE) coupled to a nonlinear partial differential equation (PDE). For simplicity in the analysis, we decompose the PDE into ODEs by using modal approach. Using the Galerkin decomposition method, the transversal deflection of the beam can be rewritten in single mode decomposed in the following form

$$Y(x, t) = y_m(t)\Phi_m(x), \tag{13}$$

where $y_m(t)$ is the time dependent function of each mode and $\Phi_m(x)$ is the shape function obtained from the undamped natural equation of the beam

$$\frac{\partial^2 Y}{\partial t^2} + \frac{\partial^4 Y}{\partial x^4} = 0, \tag{14}$$

with boundaries conditions given in (11) and (12). Thus, one has

$$\Phi_m(x) = \cos k_m x - \cosh k_m x - \frac{\cos k_m + \cosh k_m}{\sin k_m + \sinh k_m}[\sin k_m x - \sinh k_m x] \tag{15}$$

where k_m is eigenvalue, solution of the transcendatal equation

$$\cos k_m \cosh k_m + 1 = 0 \tag{16}$$

Substituting the resulting mode decomposition in (5) and (6) and projecting back on the mth mode [24, 35] yields the following set of equations

$$\frac{d^2y}{dt^2} - \mu^* F(t) + \Omega_0^2 y = +\eta_{0m} v, \tag{17}$$

$$\frac{dv}{dt} + \gamma v = -\eta_{1m} \frac{dy}{dt}, \tag{18}$$

where $F(t)$ is actually defined as

$$F(t) = \frac{dy}{dt}\left[1 - g_2(u, R_e)\alpha_2 \left(\frac{dy}{dt}\right)^2 + g_4(u, R_e)\alpha_4 \left(\frac{dy}{dt}\right)^4 - g_6(u, R_e)\alpha_6 \left(\frac{dy}{dt}\right)^6\right] \tag{19}$$

and

$$\alpha_i = \int_0^1 (\Phi_m(x))^{i+1} dx,\ \Omega_{0m}^2 = (k_m)^4,\ \mu^* = g_1(u, R_e)\alpha_1,\ \eta_{im} = \eta_i \Phi_m(x_m) \tag{20}$$

In these equations, x_m is the mth solution of transcendental equation (16); based on previous results [24], we consider only one mode of vibration ($n = m = 1$) and the corresponding indices were simply removed for simplicity.

2.3 Existence of Birythmcity

In order to state the conditions for the existence of limit cycle and the number of limit cycle, we set $q = \sqrt{g_2(u, R_e)\alpha_2}\frac{dy}{dt}$ and $v = \frac{dv^*}{dt}$ and follow the application of the Liénard theorem [40, 45]. We rewrite (17) and (18) in the standard form

$$\frac{dq}{dt} = -p - \mu F(q) + \eta_0 v \tag{21}$$

$$\frac{dp}{dt} = q \tag{22}$$

$$\frac{dv^*}{dt} = -\gamma v^* - \eta_1 \frac{dp}{dt} \tag{23}$$

where $F(q)$ is defined as

$$F(q) = -q + \frac{q^3}{3} - \frac{\alpha q^5}{5} + \frac{\beta q^7}{7} \tag{24}$$

and

$$\mu = \frac{\mu^*}{\Gamma},\ \alpha = \frac{g_4(u, R_e)\alpha_4}{\Gamma^4},\ \beta = \frac{g_6(u, R_e)\alpha_6}{\Gamma^6},\ \Gamma = \sqrt{g_2(u, R_e)\alpha_2} \tag{25}$$

In the rest of the paper, we will simply ignore the asterisk.

Since the $3rd$ variable v does not change the dynamics properties of the fix point $q = 0$, the results of [27], obtained for $\eta_0 = \eta_1 = 0$ can be transported here. Hence, we recall the following theorem which proof can be developed as in [27].

Theorem

Setting $H(\alpha, \beta)$ as the discriminant of the algebraic equation $g(\zeta) = -1 + \zeta/3 - \alpha\zeta^2/5 + \beta\zeta^3/7 = 0$, the dynamics system in (21)–(23) has

1. exactly one limit cycle under the condition $H(\alpha, \beta) > 0$
2. at least one stable limit cycle under the condition $H(\alpha, \beta) < 0$

where $H(\alpha, \beta)$ is the discriminant of $g(\zeta) = 0$ and is defined as

$$H(\alpha, \beta) = -\frac{768}{225} + \frac{\alpha^2}{225} + \frac{13188}{19845}\beta - \frac{27}{49}\beta^2 \tag{26}$$

Figure 2a shows the area of existence of one and two limit cycles in the plane (β, α). One notes that the area of parameters leading to birhythmicity is quite small. However, it is interesting to analyze the system in this domain. In fact, for application such as energy harvesting where one takes advantage of large mechanical excursion in producing an important mechanical deformation and thus an important amount of harvested electric power, the limit cycle of large amplitude is advantageous. Thus, it is important to understand how the system behaves in case of birhythmicity in order to efficiently control its dynamics. This states the problem of control and synchronization of the orbit since the behavior of the system in one or another orbit depends on the initial conditions of the system, whose are quite impossible to determine a priori in practise.

As illustration, for $\mu = 3.5$, $\alpha = 0.144$, $\beta = 0.005$, $\eta_0 = 0.1$, $\eta_1 = 0.25$ and $\gamma = 0.2$ with the initial condition of the electrical voltage set at zero (at it is throughout the paper), one obtains the basin of attraction of Fig. 2b. The inner domain (in blue color) corresponds to the domain of attraction of the lower amplitude limit cycle, while the outer domain (in red color) corresponds to the highest amplitude limit cycle. This basin of attraction was obtained by scanning the initial conditions in the space $[-5, 5] \times [-5, 5]$, and solving the differential equations (21)–(23). We found that, as the initial conditions change, the final state of the system converges into two possible limit cycles. Practically, this simply means that, a system initially set in the blue domain will provide less amount of electrical energy than a system set with initial conditions in the red domain. The analytical results of Barrero-Gil et al. [7] show three possible amplitudes: a small one (which corresponds here to

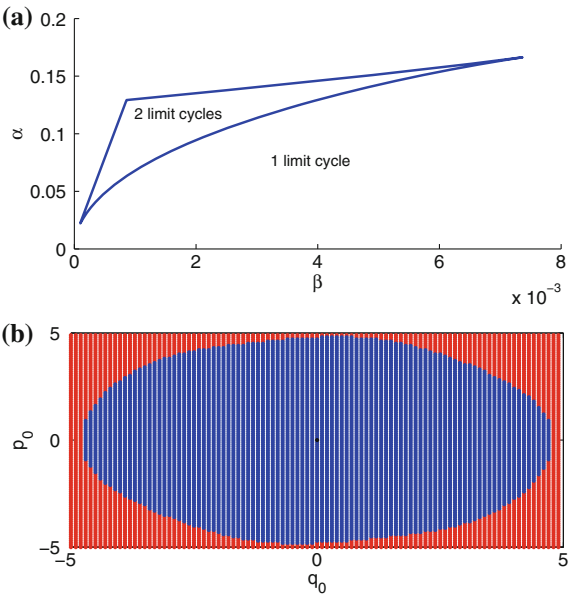

Fig. 2 (Color online) **a** Birithmicity: Boundary of existence of stable limit cycles. The inner domain is the subspace in the (α, β) space leading to 2 limits cycle. The outer domain corresponds to 1 limit cycle. **b** Basins of attraction of two coexisting limit cycles. The parameters are $\alpha = 0.144$, $\beta = 0.005$ and $\mu = 0.1$

the lower amplitude limit cycle) and a large (which corresponds here to the upper amplitude limit cycle), and an intermediate one which is unstable. Moreover, in their study of birhythmicity in biological systems, Kadji et al. [17, 18] obtained the same result using perturbation method and they showed that, the frequency of each limit cycle depends (in a nonlinear fashion) on the amplitude. This can be extended to the phase [35]. The immediate consequence is the possible out of phase motion (case of multi degree of freedom oscillations) leading to minimal harvested energy [41].

3 Recurrence Analysis

3.1 Birhythmicity and Recurrence Analysis

Recurrence analysis for time series are based on the analysis of a matrix **R** whose elements are defined as

$$\mathbf{R}_{ij} = \begin{matrix} 1 : \Phi_i \approx \Phi_j, \\ 0 : \Phi_i \neq \Phi_j, \end{matrix} \quad i, j = 1, ..., N, \tag{27}$$

where $\Phi(q, p, v)$ is the state vector, N is the length of the time series, i and j are related respectively to the line and column of the matrix, $\Phi_i \approx \Phi_j$ means equality

up to an error ε. These indices are also related to the time $t = i\Delta t$ ($\Delta t = 0.01$ being the sampling time). The elements of the matrix $\mathbf{R}$ are obtained by comparing the state of the system at time i and j with a threshold precision ε. Thus, formally one has

$$\mathbf{R}_{ij} = \theta(\varepsilon - ||\Phi_i - \Phi_j||), \tag{28}$$

with $||(.)||$ been the Euclidian norm (L_2-norm) and $\theta(r) = 1$ for $r > 0$, $\theta(r) = 0$ for $r < 0$ is the heaviside function. A RP graph is obtained by plotting the $\mathbf{R}_{ij}$ elements with different colours. The common use consists of using inked colour for $\mathbf{R}_{ij} = 1$ and white colour for $\mathbf{R}_{ij} = 0$. By this definition, a RP graph is always symmetric ($\mathbf{R}_{ij} = \mathbf{R}_{ji}$) and always has colored central diagonal. Note that, for data-based time series analysis it is crucial to reconstruct the phase space of the system (in order to extract dynamic features) by estimating the embedded dimension; that is the dimension of the homeomorphism image of the actual (real) phase space (for which the structure is unknown), in which the dynamics of the system is fully described. In this analysis, it is assumed without lost of generality, that the homeomorphism image is the actual space itself (for which the structure is known). In other words, the embedding dimension is equal to two (dimension of the state vector $\Phi(q, p)$) and the time delay between q and p can be determined using the average mutual information [1].

It is important to recall that the choice of ε is critical. In fact, by definition (see (28)), an ε too small will lead to a no recurrence behavior and an ε too large will lead to an all-to-all recurrence. In this contribution, in order to estimate the best neighbourhood size, we use an optimization procedure proposed by Matassini et al. [34]. The procedure consists of minimizing the quantity

$$\Gamma = \frac{\left|(N_n(\varepsilon) - N_p(\varepsilon)\right|}{N_n(\varepsilon)} \tag{29}$$

where $N_n = \sum_{i,j} \mathbf{R}_{ij}/N$ is the average number of neighbor that points have and N_p is the number of peaks which is estimated from the histogram along the main diagonal direction $h_i = \sum_{k-j=i} \mathbf{R}_{jk}$. See the paper by Matassini et al. [34] for details. In the rest of the paper, the value of ε used was such that the quantity Γ was minimal.

Figures 3 and 4 show the RP of the system as well as the phase diagram of the mechanical system and the time history of the electrical system for different set of the initial conditions and $\mu = 0.05$ (Fig. 3) and $\mu = 3.5$ (Fig. 4). The graphs corresponding to the initial conditions $(q_0, p_0, v_0) = (0.1, 0, 0)$ are plotted in blue, while those for the initial conditions $(q_0, p_0, v_0) = (5, 5, 0)$ are plotted in red.

In Fig. 3, the RP of both initial conditions (Fig. 3a) are indiscernible. However, considering some recurrence quantification analysis parameters (RQA), namely the recurrence rate (*RR*), the laminarity (*LAM*) and the determinism (*DET*) (defined in the Appendix). One observes that, the RP are graphically similar; the distance between

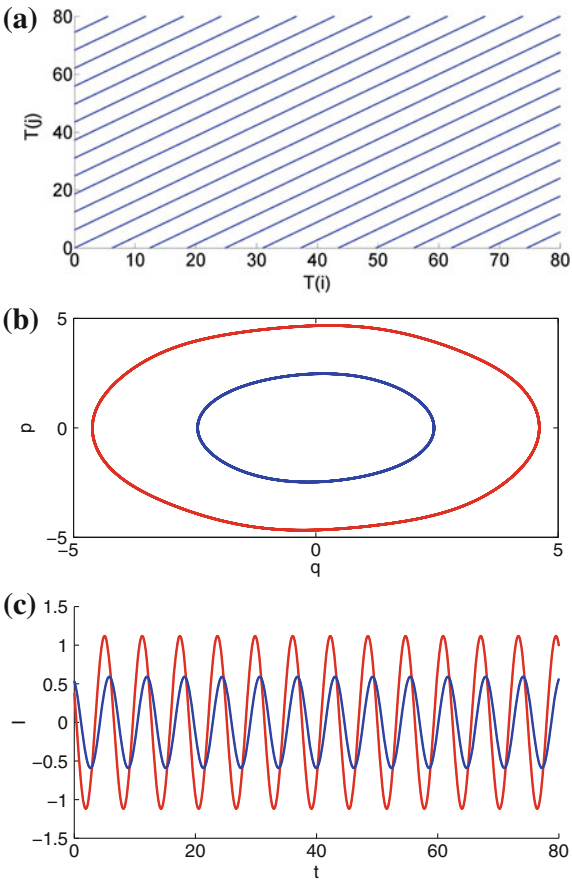

Fig. 3 Response of the system for $\mu = 0.05$, $\alpha = 0.144$, $\beta = 0.005$ and initial conditions vary. **a** The recurrence plot of the system. **b** Phase diagram of the mechanical arm. **c** Time response of the electrical voltage

diagonal along the main diagonal is constant: This implies that both limit cycles have very close (almost equal with the precision used here) period. The RQA vary as shown in Table 1. This is compatible with the phase diagram of the mechanical variable (Fig. 3b) and the time history of the electric variable (Fig. 3c). One notes that the attractor of large amplitude (outer orbit) has a small recurrence rate (large diameter of the attractor) in comparison with the recurrence rate of the inner attractor (small diameter of the attractor). This is simply due to the fact that, since the number of points collected N is maintained constant, and the path in the outer orbit is longer than the one in the inner orbit, less points recur for the outer orbit. Similar observation is made for the determinism, whose reduction is simply due to change in the basin of the initial conditions, rather than increases in the level of complexity in the system (quasi periodic motion, chaos, transient motion,...). However, this observation on the *DET* cannot be generalized. In fact for a large value of $\mu = 3.5$ (Fig. 4), leading to relaxation oscillation, the recurrence rate has still decreased from the inner orbit to the outer orbit. The decreasing in the determinism in this case is due to combine

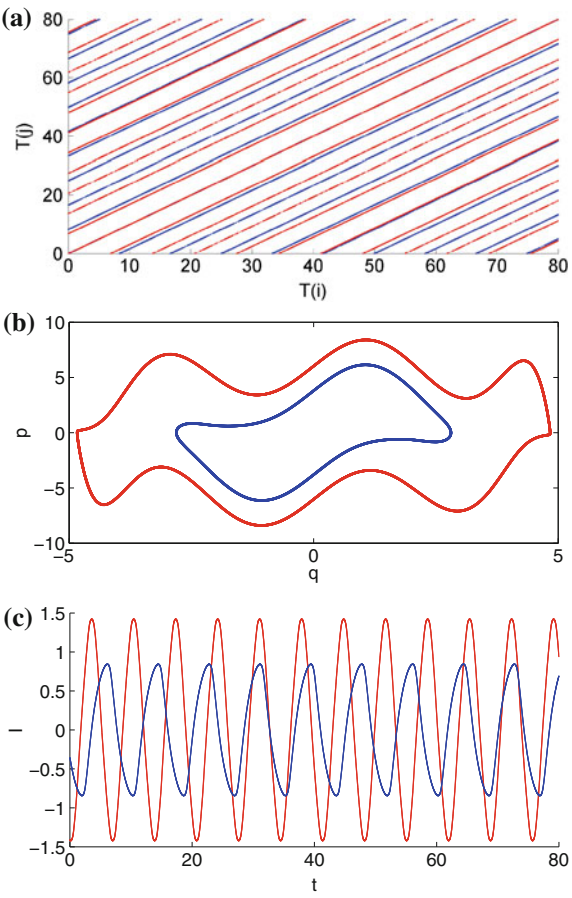

Fig. 4 Response of the system for $\mu = 3.5$, $\alpha = 0.144$, $\beta = 0.005$ and initial conditions vary. **a** The recurrence plot of the system. **b** Phase diagram of the mechanical arm. **c** Time response of the electrical voltage

effects of change in initial conditions (diameter of the attractor) and the presence of more complexity (wiggles and distortion) as shown in the phase diagram of Fig. 5b. Note that, the recurrence plots for both set of initial conditions contains parallel diagonals whose pattern are now discernable. The gap between consecutive red and blue diagonal is different; that is the upper and lower limit cycle have different period. We conducted various numerical simulations corresponding to different value of μ and came to the conclusion that, as general rule, the RP of both orbits are totaly indiscernible for regular oscillation (superposed parallel diagonals) and graphically discernable for relaxation oscillations (combination of strictly parallel diagonals and superposed diagonals). These investigations are corroborated by on the analytical investigation of Kadji et al. [18]. In fact, in their analysis, they showed that the frequency of each limit cycle linearly increases with the square of the damping coefficient (μ^2) and nonlinearly changes with the amplitude of the limit cycle. The graphs of Figs. 4c and 5c obviously show that the inner limit cycle leads to a small

Table 1 Recurrence rate and determinism as function of the initial conditions and the system damping

μ	Initial conditions (q_0, p_0, v_0)	RR	DET
0.07	(1,0,0)	0.0063	0.934
0.07	(5,5,0)	0.0034	0.103
3.5	(1,0,0)	0.0092	0.9523
3.5	(5,5,0)	0.00506	0.8431

amount of electrical energy, while the outer orbit leads to a large amount of electrical energy. For the set of parameter used in this paper, the electric voltage is almost double when changing the initial conditions from the inner to the outer domain.

3.2 Bifurcation and Chaotic Dynamics

The previous sub-section considered the system free of additional excitation. Although this can happen in some environments, it is of interest to consider the effects on the system response of an harmonic perturbation of amplitude e_0 and frequency Ω. Harmonic perturbation can be due to structural excitation, kinematic excitation and perturbation in the fluid flow.

The bifurcation diagrams of the *RR*, *LAM* and *DET* as function of the amplitude of excitation are plotted in Fig. 5. Changing $e_0 \in [0, 14]$, one obtains the *RR*, *DET* and the *LAM* plotted in Fig. 5a–c for $\beta = 0.05$, $\Omega = 3.5$, $\mu = 3.5$ and $(x_0, y_0, v_0) = (5, 5, 0)$. The RQA parameters have higher values for $e_0 = 0$ and as e_0 increases in the first phase of motion, the system progressively becomes more complex marked by a reduction of *RR*. Since the determinism and laminarity are almost constant, one concludes that the system undergoes quasi-periodic motion with superimposed chaotic dynamics [9, 33]. This domain of constant *DET* and *LAM* is followed by an abrupt transition to chaos combined with windows of less complexity (quasi-periodicity, periodicity,...) signed by the presence of distinct maxima peaks at lowest values of the RQA parameters. Beyond the chaotic domain, an abrupt increases in the *RR* is noted, followed by a continuous decrease of the *RR*, *LAM* and *DET*. One can suspect in this domain multi periodic dynamics [33]. A second chaotic domain appears followed by another abrupt increases of the *RR*. Interestingly, beyond the second chaotic domain, the *DET* is smaller than (and decreasing) in the chaotic domain. This is awkward as decreasing in the *DET* (in addition to decreasing in the *RR*) always implies transition from regularity to complexity (non stochastic system). Our explanation is that, the threshold value $\varepsilon = 0.05$ (kept constant) was not appropriate for large value of e_0. In fact, the *RR* is less sensitive to ε than the *DET* and *LAM*. That is, the effects of ε is more visible on the *DET* and *LAM*. Practically, taking ε by using the standard deviation or the phase space diameter would have give

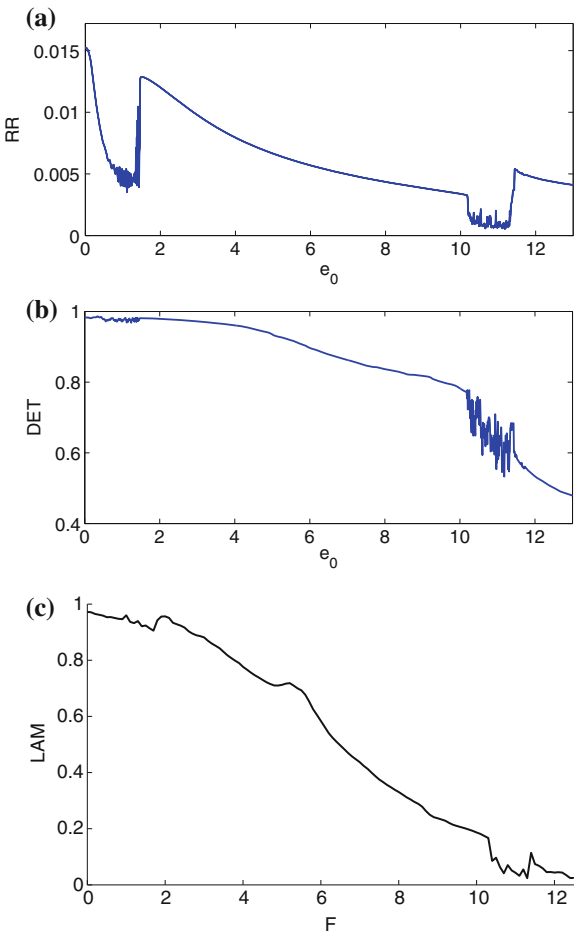

Fig. 5 Bifurcations of the RQA as function of the driven amplitude. **a** Bifurcation of the *RR*. **b** Bifurcation of the *DET*. **c** Bifurcation of the LAM

a variable ε which can be more appropriated. By choosing a fix value of ε for the bifurcation analysis has highlighted to sensitivity and importance of ε. Globally, one can state that as e_0 increases from zero the following transitions occur in the system response: Periodicity-chaos-multi-periodicity-chaos-multi-periodicity.

The bifurcation diagrams of the RQA parameters are not able to detect all details in the system bifurcation (number of period for example). Rather, they give a global picture of the system response. In order to capture details on the system dynamics, we plot the RP (Fig. 6) along with the phase diagram (for consistency—Fig. 7) for the values of Fig. 5.

1. For $e_0 = 1.4$, the RP (Fig. 6a) show a full diagonal and regularly spaced irregularly broken diagonal. This kind of structure is known as signature of quasi-periodic motion [33]. The phase diagram of Fig. 7a corroborates the RP.

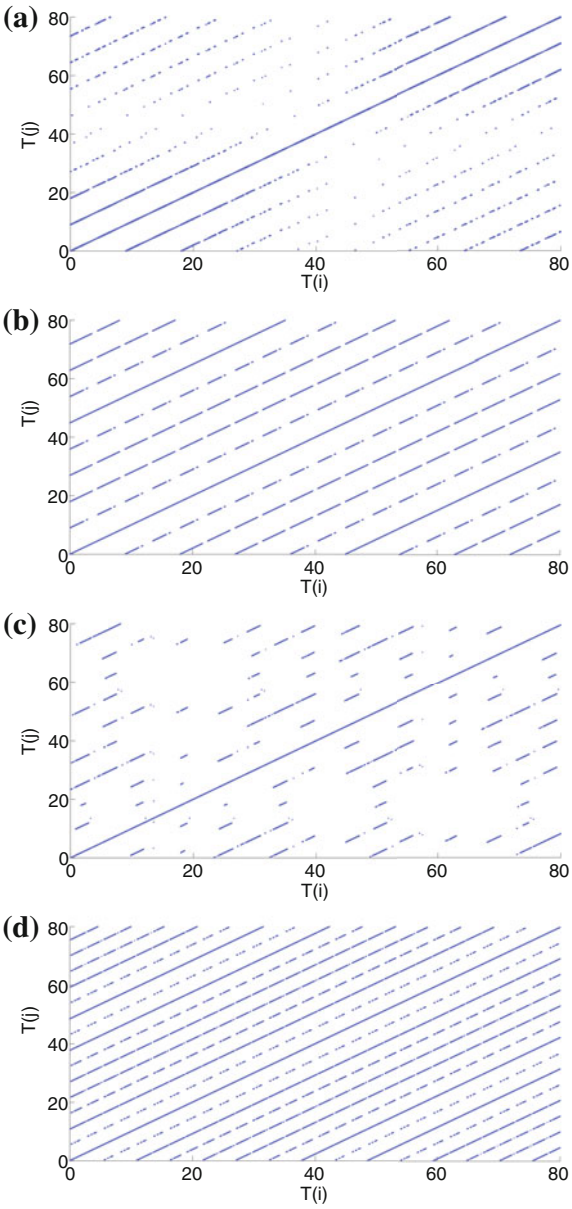

Fig. 6 Recurrence plots of the system under harmonic perturbation. **a** $e_0 = 1.4$, Quasi-periodic motion. **b** $e_0 = 6$, Period 4 motion. **c** $e_0 = 10.4$, Chaotic motion. **d** $e_0 = 12.4$, Period 2 motion

2. The RP of Fig. 6b show regularly spaced full diagonal separated by four regularly broken diagonals that can be classified into two groups according to the scapement between the points along each broken diagonal. This structure corresponds to a 4-period dynamics classified into two groups according to their amplitude and

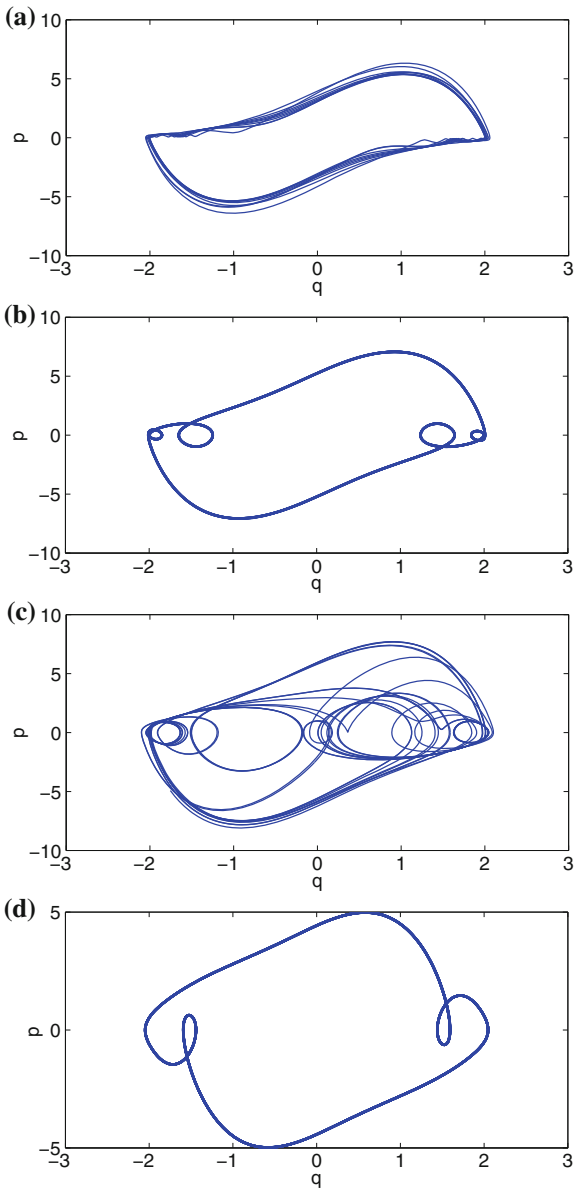

Fig. 7 Phase diagrams of the system under harmonic perturbation. **a** $e_0 = 1.4$, Quasi periodic. **b** $e_0 = 6$, Period 4 motion. **c** $e_0 = 10.4$, Chaotic motion. **d** $e_0 = 12.4$, Period 2 motion

frequency (and thus, rate of recurrence). This is confirmed by the phase diagram of Fig. 7b, which is typical for a 4-period motion.

3. For $e_0 = 10.4$, the RP of Fig. 6c has the structure of chaotic motion: irregularly spaced diagonal with possible a white domain. As well, the phase diagram of Fig. 7c is typically chaotic.

4. For $e_0 = 12.4$, the RP of Fig. 6d show full diagonals as well as regularly broken diagonals. Here, the number of broken diagonal between the two full diagonal is not consistent (as it is for multi periodic motion). In fact, some diagonal seem slightly broken. One can conclude that, for these diagonals, the threshold parameter ε was too small to complete the full diagonal. With larger value of ε, the structure of the RP will be the one of two periodic motion (regularly spaced full diagonal, separated by a regularly broken diagonal). This is consistent with the phase diagram of Fig. 7d and the observations made in the bifurcation diagram of the *DET* for large value of e_0.

The analysis of the harvesting system with a single degree of freedom mechanical oscillator, shows possibility of birhythmicity and complex dynamics in presence of harmonic excitation. These nonlinear phenomena can have drastic consequences in the harvesting process in the case of multi degree of freedom mechanical oscillator. The following section considers a unidirectional coupling between mechanical oscillators to overcome these difficulties.

4 Synchronization Charge Extraction: The Joint Recurrence Plot

4.1 Master-Slave Scheme and Joint Recurrence Plot

Practically, in order to ensure optimal harvested energy, one can consider an unidirectional coupling also called master-slave synchronization. The master is the system with higher diameter of the attractor, while the slave is the system with lower diameter. The schematization of Fig. 8 implies that a fraction of the signal of the master is added to the slave. Practically, this can be ensured through a set of sensors and actuators or set of diodes and condensers [26]. The mathematical model for such enslavement is given as

$$\frac{dq_m}{dt} = -p_m - \mu F(q_m) + \eta_0 v \tag{30}$$

$$\frac{dq_s}{dt} = -p_s - \mu F(q_s) + \eta_0 v \tag{31}$$

$$\frac{dp_m}{dt} = q_m \tag{32}$$

$$\frac{dp_s}{dt} = q_s + \kappa(q_m - q_s) \tag{33}$$

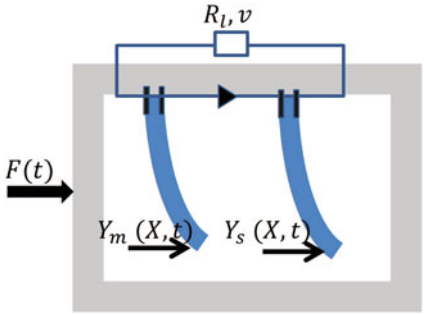

Fig. 8 Schematisation of coupled energy harvesters systems

$$\frac{dv}{dt} = -\gamma v - \eta_1 \left(\frac{dp_m}{dt} + \frac{dp_s}{dt} \right) \tag{34}$$

where, m and s respectively stand for the master and the slave, κ is the coupling strength.

For coupled systems, the joint recurrence (JR) matrix is more suitable to analyze the response of the systems as comparing with recurrence and cross recurrence matrices. In fact the JR gives possibility to analyze the dynamics of two interacting sub-systems by examining their recurrence patterns. Each sub-system has a given dynamics in its phase space and both dynamics can be coupled. This is done by considering the JR matrix defined as

$$\begin{aligned} \mathbf{JR}_{ij}(\varepsilon^m, \varepsilon^s) = \theta \left(\varepsilon^m - \parallel \Phi_i^m - \Phi_j^m \parallel \right) \times \\ \theta \left(\varepsilon^s - \parallel \Phi_i^s - \Phi_j^s \parallel \right) \end{aligned} \tag{35}$$

The JR matrix is in fact obtained as product of the recurrence matrix of the master system

$$\mathbf{R}_{ij} = \theta \left(\varepsilon^m - \parallel \Phi_i^m - \Phi_j^m \parallel \right) \tag{36}$$

and the slave system

$$\mathbf{R}_{ij} = \theta \left(\varepsilon^s - \parallel \Phi_i^s - \Phi_j^s \parallel \right) \tag{37}$$

with $\Phi^m \equiv (x_m, y_m, v)$ and $\Phi^s \equiv (x_s, y_s, v)$. The affectivity of the synchronization is measured by the following dimensionless quantity [33]

$$J = \frac{RR^{ms}}{RR^m} \tag{38}$$

where $J \approx 1$ for global synchronization, and $J \approx 0$ if the master and the slave are independent. In fact the probability of recurrence $RR^{ms} = RR^{m} = RR^{s}$ for global synchronization, and $RR^{ms} = RR^{m}RR^{s}$ for independent systems. Practically, in order to evaluate J, the mathematical model of the master and slave are integrated simultaneously with $\kappa = 0$. After a transient time, the feedback coupling term is set $\kappa \neq 0$ and the following 8000 points are ignored. Then we collected the next $N = 8000$ points for analysis.

4.2 Synchronization of Limit Cycles

The graphs of Fig. 9 are plotted for $e_0 = 0$ and the values of Fig. 4 with initial conditions $(q_0, p_0, v_0) = (5, 5, 0)$ for the master and $(q_0, p_0, v_0) = (0.1, 0, 0)$ for the slave. The probability of recurrence of the master RR^{m}, the salve RR^{s} and the coupled system RR^{ms} are plotted in Fig. 9a; while the synchronization parameter is plotted in Fig. 9b. Clearly, the recurrence rate of the slave (in blue) is the highest (from the previous section) and the recurrence of the joint system is the lowest. One observes a singularity at $\kappa = 0.12$ which can be due to nonlinear interplay between the master and the slave. Note that, in contrary to the classic master-slave coupling [26], the master is not totally independent of the slave. In fact, there is a feedback through the electrical circuit. For $\kappa > \kappa_c = 1.51$, one has a global synchronization: $RR^{m} = RR^{s} = RR^{ms}$.

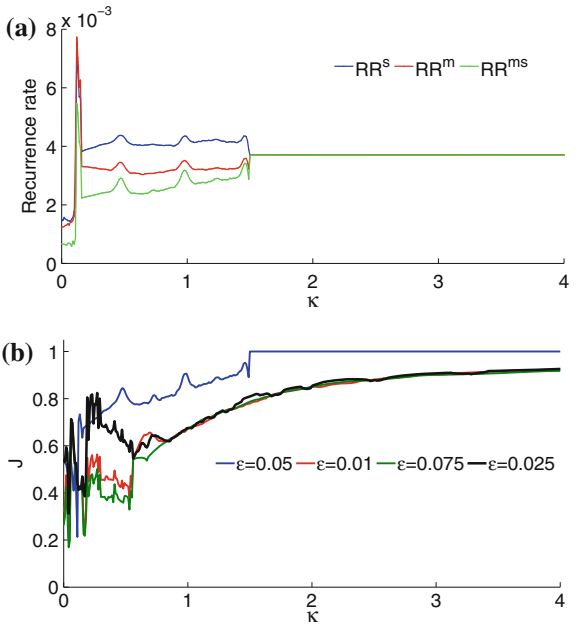

Fig. 9 Recurrence of the system. **a** Comparative analysis between RR, RR_m and RR_s. **b** The synchronization parameter as function of the threshold parameter ε

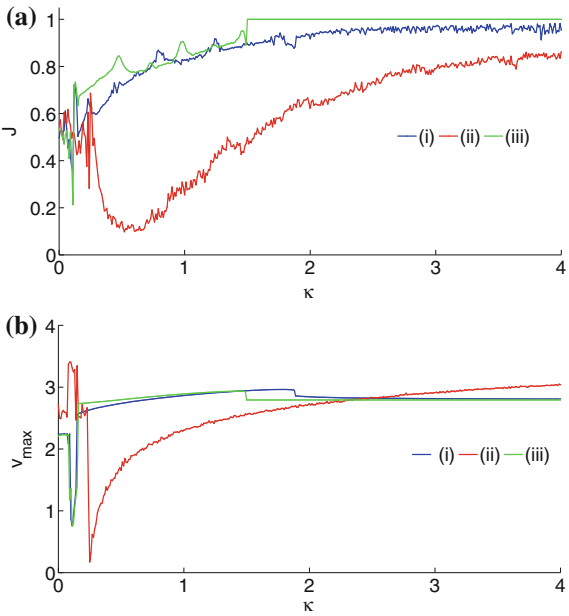

Fig. 10 Effects of mistuning. **a** Mistuning and synchronization parameter. **b** Mistuning and output voltage

Figure 9b illustrates the effects of the threshold parameter ε on the synchronization parameter. In each case, the parameter ε is maintained constant. For small values of κ, the transition regime is very sensitive to ε. Similarly, the threshold for global synchronization is sensitive to ε. However, on observes an increases in the value of J for $\kappa > \kappa_c$ and $\varepsilon \in \{0.01, 0.075, 0.025\}$, while $J \approx 1$ for $\varepsilon = 0.05$.

The effects of mistuning on the synchronization parameter and the output voltage are illustrated in Fig. 10a. Line (i) in blue corresponds to mistuning in the linear system; that is the linear stiffness of the slave reads $(1 - \sigma)$ where σ is a random number between 0 and 1. Line (ii) in red corresponds to the mistuning in coupling: $\eta_0(1 - \sigma)$. Line (iii) corresponds to $\sigma = 0$. Globally, the mistuning plays against the global synchronization and can even lead to desynchronization (minimal value of J). Similar observations are made for the output current in Fig. 10b. Here, it is clearly visible that (as state in the introductive part of this paper), an energy harvester system with multi degree of freedom mechanical arm does not always led to optimal output. Mistuning is an important factor as well as the coupling factor, which need to be appropriately selected in order to overcome the mistuning effects and the "negative" consequence of the nonlinear dynamics interplay.

A visual analysis of the singularity observed for $\kappa = 0.12$ is made in Fig. 11a, b where the phase diagram of the master and the slave are plotted along with the output voltage (Fig. 11b). Here the number (i) and (ii) respectively stand for the slave before and after the onset of coupling. For this value of κ, there is no synchronization, rather, the in-phase motion of the slave has turned to out-of-phase motion (in comparison with the master phase) with similar amplitude and frequency. This corresponds to

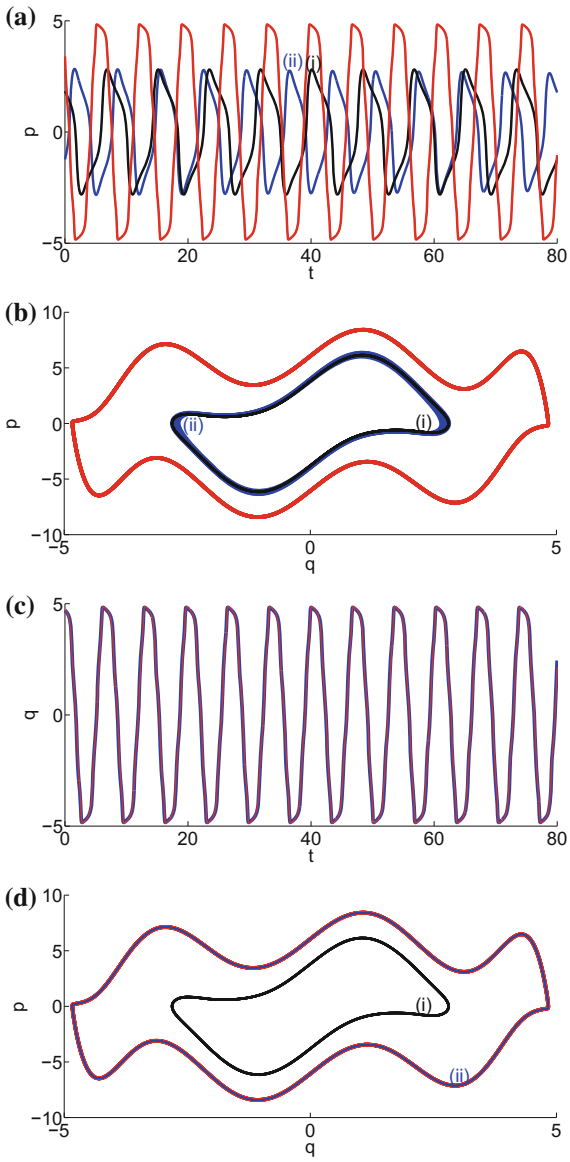

Fig. 11 Synchronization phenomena. **a** and **b** Out of phase motion, $\kappa = 0.12$. **c** and **d** Global synchronization, $\kappa = 1.6$

a lowest value of the synchronization parameter J. Thus, the output of the electric circuit is minimal (see Fig. 10b). For a different value of $\kappa = 1.6$, the phase diagram of the master and slave as well as their time histories are indiscernible (Fig. 11c, d).

4.3 Synchronization of Chaotic States

It is unclear whether the chaotic regime of a single degree of freedom energy harvester system provides more energy than a periodic regime. However, it is certain that for a two or multi degree of freedom system, since chaos is sensitive to initial conditions, difference in dynamics paths and phase angle will appear and thus, an efficient output will be obtained when a global synchronization is achieved. Interestingly, coupling two chaotic devices does not always results in a chaotic system. It is the case for the values of Fig. 7c. In this section, we use the following parameters $\beta = 0.05, e_0 = 12$. The intent is not to repeat the previous analysis but to illustrate some important facts.

Figure 12a–d show the RP of the master (in red crosses) as well as the RP of the slave (in blue squares) for different values of the feedback coupling: $\kappa = 0, \kappa = 0.1$, $\kappa = 1.2, \kappa = 2$, respectively. The crosses and squares were magnified for better visibility. The corresponding electric voltage is plotted in Fig. 13. In all cases, the initial conditions of the master is set at $(q_0, p_0, v_0) = (5, 5, 0)$, and the slave initial conditions are set at $(q_0, p_0, v_0) = (1, 0, 0)$.

1. For $\kappa = 0$, there is no feedback coupling. Thus the master and the slave are quasi-independent. In fact, there is still a undirect coupling between the master and the slave through the electric circuit. This is confirmed by the non-zero value of the synchronization parameter as shown in Table 2. The recurrence rates obey $RR^m > RR^s$; and based on previous analysis, one suspects that the path of the orbit displays by the master is longer than with the slave. The corresponding RP in Fig. 12a is typically chaotic for both sub-system.
2. For $\kappa = 0.1$, the synchronization parameter has increased as well as the recurrence rate of the master while the rate of the slave is remained constant. The pattern of the RP (Fig. 12b) has changed and become more dense.
3. For $\kappa = 1.2$, the synchronization parameter has almost double and the RP (Fig. 12c) is almost red with some presence of blue point. The recurrence rate of the master has increased.
4. For $\kappa = 2$, the synchronization parameter is $J = 1$ and the RP (Fig. 12d) is totally mono color. The recurrence rate of the master and slave are obviously identical.
5. In comparison, Fig. 13 shows the electric voltage for those values of the feedback coupling. One notes that, for $\kappa = 0$ and $\kappa = 0.1$ one obtains to a relative small amount of electric voltage (Line (i) and (ii)). Line (iii) and line (iv) correspond to

Table 2 Probability of recurrence and synchronization parameter as function of feedback coupling

κ	RR^m	RR^s	J
0	0.000737	0.00069	0.4269
0.1	0.000775	0.00069	0.4525
1.2	0.000775	0.001654	0.89106
2	0.000782	0.000782	1

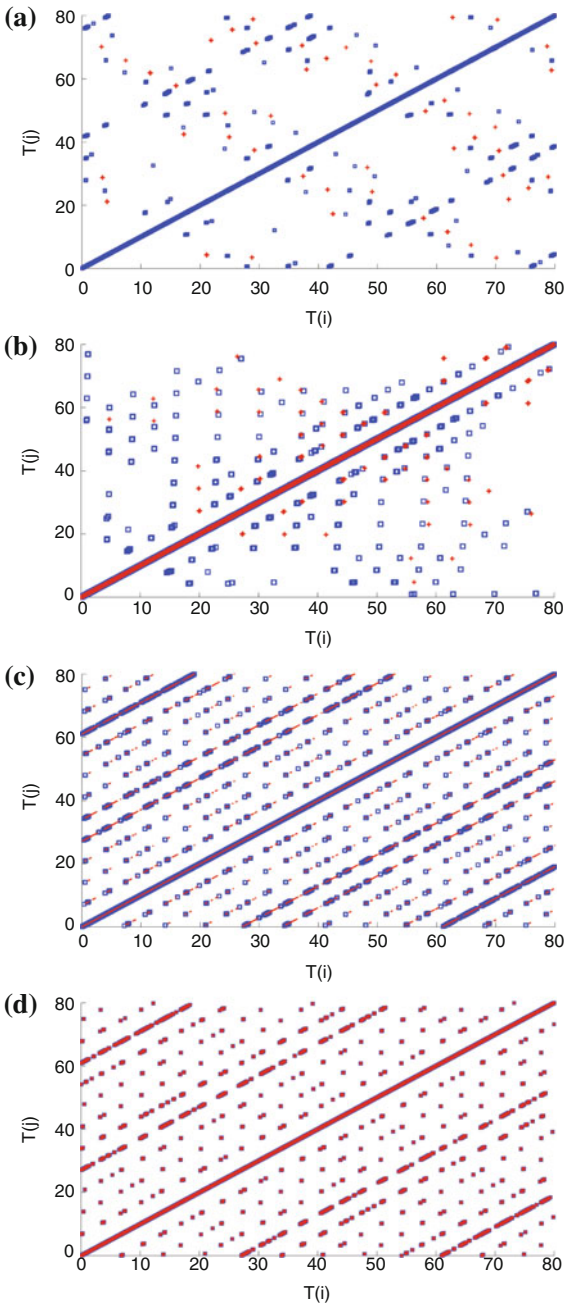

Fig. 12 Synchronization of chaotic dynamics, the master RP in *red* while the slave RP in *blue*. **a** $\kappa = 0$. **b** $\kappa = 0.1$. **c** $\kappa = 1.2$. **d** $\kappa = 2$

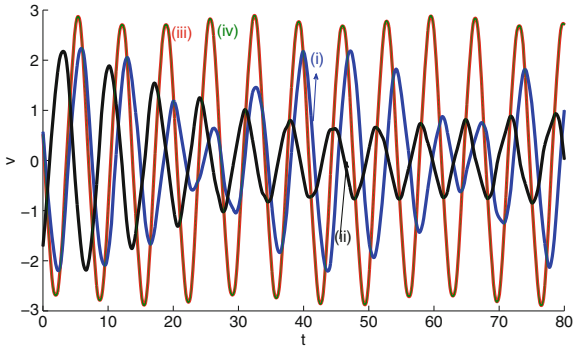

Fig. 13 Harvested electric voltage in chaotic regime. Line (*i*)—$\kappa = 0$. Line (*ii*)—$\kappa = 0.1$. Line (*iii*)—$\kappa = 1.2$. Line (*iv*)—$\kappa = 2$

the same values of the electric voltage (the line are superimposed). Note that, the synchronization has also contributed, in a progressive way, in suppressing chaos as also observed on the RP of Fig. 12d.

5 Summary and Discussion

The interest of this paper was twofold:

- Discuss the harvesting process in a multi limit cycle energy harvesting system and the synchronized charge extraction for both limit cycle and chaotic states under a Master-Slave coupling scheme. This was motivated by the fact that wind-induced vibration for energy harvesting system has strong potential applications. Previous research has mentioned the possibility of multi limit cycles without specifically analyzing its conditions and the system dynamics under such conditions.
- The second interest of the paper was the use of the methods of recurrence (RP) and joint recurrence (JRP) for the analysis and synchronization of physics based mathematical model of a dynamic system. In fact, very few contributions have considered the RP as tool for nonlinear analysis of mathematical based physical systems despite the potential use of such approach in hybrid approach of diagnostic (combination of physics based and data driven models).

The method of recurrence was used to study the dynamics of the limit cycle system as well as the system response under harmonic perturbation. For optimization purpose, a second mechanical degree of freedom is added to the system and the Master-Slave synchronization scheme is used with the method of JRP to ensure synchronized charge extraction in the system. The effects of mistuning and threshold parameters were highlighted. The main results are as follows:

- The existence of birythmicity depends only on two parameters α and β whose practically depend on the fluid flow average velocity and the piezomaterial physical properties.

- Our simulations show that, the domain of birythmicity is quite small as well as the basin of attraction of lower amplitude limit cycle.
- The phase diagram of the lower and upper limit cycle amplitudes limit cycle were discernable. However, the RP were discernable only for large values of the damping which corresponds to relaxation oscillations. The RR of the upper limit cycle was in general smaller than the RR of the lower limit cycle. Similar conclusion was made for the *DET* and the *LAM* without generalization. In fact, complexity such as wiggles and distortion also affects the variation of the *DET* and the *LAM*.
- Obviously, due to the linear nature of the transducing mechanics, the output voltage is higher for the upper limit cycle.
- Considering a harmonic perturbation, the bifurcation of the RR and the DET were plotted in terms of the amplitude e_0 of the perturbation. Region of quasi-periodic, periodic, multiple periodic and chaotic response was identified. Illustrations of these phenomenon were showed using the RP and the phase diagrams.
- For a two degree of freedom mechanical system, the Master-Slave coupling scheme was used to synchronize limit cycle dynamics (toward the upper limit cycle) and perturbed periodic and chaotic dynamics. It was found that, for large value of the synchronization parameter κ the global synchronization is obtained, leading to highest output electric power. However, for small values of κ, complex response of the system is obtained, including out of phase motion leading to minimal output power. The synchronization criterion was defined as the ration between the RR of the master and the slave.
- The effects of mistuning and threshold recurrence parameter ε were discussed. It was shown that mistuning can lead to minimal output power, specifically for a small coupling parameter. Also, the domain of global synchronization is shifted in presence of mistuning.

Globally, beyond the interesting results obtained, the method of RP has demonstrated potential for the feature extraction for application in diagnostics and detection of dynamics change. As for example, the variation of *RR* due to sole changes in initial conditions in the absence of additional excitation is due to existence of multi limit cycle: *RR* can be seen as a feature to detect birhythmicity. In a similar way, the *DET* can be used to measure relaxation in the system. The joint probability of recurrence and the synchronization parameter J are a third feature which can be used to measure the performance of the system: $J = 1$ corresponds to optimal performance and $J < 1$ is an indication to change the coupling parameter. These features can also be used to measure the intensity of mistuning in the system.

Acknowledgments This work has been founded by the US Office of Naval research under the grant ONR N00014-08-1-0435 (Program manager: Mr. Anthony Seman III).

Appendix: Definition of Recurrence Quantification Analysis Parameters

1. *RR* which defines the percentage of recurring points in the whole matrix. The *RR* is higher for periodic dynamics and smaller for chaotic or random dynamics. By definition, one has

$$RR = \frac{1}{N^2} \sum_{i,j=1}^{N} \mathbf{R}_{i,j}(\varepsilon) \cdot \tag{39}$$

2. The percentage of recurrent points that form diagonal lines (of at least length ℓ_{min}) parallel to the main diagonal *DET* gives information on the deterministic nature of the system. A chaotic system tends to have none or very short diagonals in opposite to periodic or quasi-periodic dynamics which tend to form regular diagonals parallel to the central diagonal along with mixture of short and long diagonals. The *DET* is defined as

$$DET = \frac{\sum_{\ell=\ell_{min}}^{N} \ell P(\ell)}{\sum_{\ell=1}^{N} \ell P(\ell)}, \tag{40}$$

where ℓ is the length of the diagonal line and $P(x)$ is the histogram of x for a given threshold ε. If v is the length of the vertical line, one has

$$LAM = \frac{\sum_{v=v_{min}}^{N} vP(v)}{\sum_{v=1}^{N} vP(v)} \tag{41}$$

LAM decreases if the RP consists of more single recurrence points than vertical structures. This is related to the existence of intermittency in the system response [33].

In obtaining the RP of the system, we used the fourth order Runge Kutta algorithm to obtain sets of N = 8000 points for time series. The first 1000 values were ignored (transient time) and the time step was kept constant $\Delta t = 0.01$. The *RR* and *DET* are evaluated using the above definitions in a self made codes. However, various numerical codes are available online.

The bifurcation diagrams were obtained by increasing adiabatically (constant initial conditions) the bifurcation parameter and used the above procedure to generate the *RR*, *LAM* and *DET*.

References

1. Abarbanel, H.D.: Analysis of Observed Chaotic Data. Springer-Verlag, New York (1996)
2. Abdelkefi, A., Hajj, M.R., Nayfeh, A.H.: Power harvesting from transverse galloping of square cylinder. Nonlinear Dyn. **70**, 1355–1363 (2012)
3. Abdelkefi, A., Vasconcellos, R., Marques, F.D., Hajj, M.R.: Bifurcation analysis of an aeroelastic system with concentrated nonlinearities. Nonlinear Dyn. **69**, 57–70 (2012)
4. Abdelkefi, A., Yan, Z., Hajj, M.R.: Modeling and nonlinear analysis of piezoelectric energy harvesting from transverse galloping. Smart Mater. Struct. **22**, 025016 (2013)
5. Barrero-Gil, A., Alonso, G., Sanz-Andres, A.: Energy harvesting from transverse galloping. J. Sound Vib. **329**, 2873–2883 (2010)
6. Barrero-Gil, A., Pindado, S., Avila, S.: Extracting energy from vortex-induced vibrations: a parametric study. Appl. Math. Modell. **36**(7), 3153–3160 (2012)
7. Barrero-Gil, A., Sanz-Andrs, A., Alonso, G.: Hysteresis in transverse galloping: the role of the inflection points. J. Fluids Struct. **25**(6), 1007–1020 (2009)
8. Barrero-Gil, A., Sanz-Andrs, A., Roura, M.: Transverse galloping at low reynolds numbers. J. Fluids Struct. **25**(7), 1236–1242 (2009)
9. Borowiec, M., Litak, G.: Transition to chaos and escape phenomenon in two-degrees-of-freedom oscillator with a kinematic excitation. Nonlinear Dyn. **70**, 1125–1133 (2012)
10. Erturk, A., Hoffmann, J., Inman, D.J.: A piezomagnetoelastic structure for broadband vibration energy harvesting. Appl. Phys. Lett. **94**(25), 254102 (2009)
11. Farrar, C.R., Hemez, F., Park, G., Robertson, A., Sohn, H., Williams, T.O.: A coupled approach to developing damage prognosis solutions. Key Eng. Mater. **245–246**, 289–306 (2003)
12. Ferrari, M., Ferrari, V., Guizzetti, M., Marioli, D., Taroni, A.: Piezoelectric multifrequency energy converter for power harvesting in autonomous microsystems. Sens. Actuators, A **142**(1), 329–335 (2008)
13. Guyomar, D., Lallart, M.: Recent progress in piezoelectric conversion and energy harvesting using nonlinear electronic interfaces and issues in small scale implementation. Micromachines **2**, 274–294 (2011)
14. Hartog, J.D.: Mechanical Vibrations. McGraw-Hill Book Company, New York (1956)
15. Jardine, A.K., Lin, D., Banjevic, D.: A review on machinery diagnostics and prognostics implementing condition-based maintenance. Mech. Syst. Signal Process. **20**(7), 1483–1510 (2006)
16. Ji, H., Qiu, J., Badel, A., Chen, Y., Zhu, K.: Semi-active vibration control of a composite beam by adaptive synchronized switching on voltage sources based on lms algorithm. J. Intell. Mater. Syst. Struct. **20**, 939–947 (2009)
17. Kadji, H.E., Orou, J.C., Woafo, P.: Synchronization dynamics in a ring of four mutually coupled biological systems. Commun. Nonlinear Sci. Numer. Simul. **13**(7), 1361–1372 (2008)
18. Kadji, H.E., Orou, J.C., Yamapi, R., Woafo, P.: Nonlinear dynamics and strange attractors in the biological system. Chaos, Solitons Fractals **32**(2), 862–882 (2007)
19. Kwon, S.D.: A t-shaped piezoelectric cantilever for fluid energy harvesting. Appl. Phys. Lett. **97**(16), 164102 (2010)
20. Kwuimy, C.A.K., Litak, G.: Enhance limit cycle oscillation in a wind flow energy harvester system with fractional order derivatives. Theor. Appl. Mech. Lett. **4**(5), 12 (2014)
21. Kwuimy, C.A.K., Litak, G., Borowiec, M., Nataraj, C.: Performance of a piezoelectric energy harvester driven by air fow. Appl. Phys. Lett. **100**(2), 024103–3 (2012)
22. Kwuimy, C.A.K., Litak, G., Nataraj, C.: Enhancing energy harvesting system using materials with fractional order stiffness. In: Proceedings of the ASME 2013 Dynamic Systems and Control Conference (2013)
23. Kwuimy, C.A.K., Litak, G., Nataraj, C.: Enhancing energy harvesting system using materials with fractional order stiffness. Nonlinear Dynamics In press (2014)
24. Kwuimy, C.A.K., Nbendjo, B.N., Woafo, P.: Optimization of electromechanical control of beam dynamics: analytical method and finite differences simulation. J. Sound Vib. **298**(1–2), 180–193 (2006)

25. Kwuimy, C.A.K., Samadani, M., Nataraj, C.: Bifurcation analysis of a nonlinear pendulum using recurrence and statistical methods: applications to fault diagnostics. Nonlinear Dyn. **76**(4), 1963–1975 (2014)
26. Kwuimy, C.A.K., Woafo, P.: Dynamics, chaos and synchronization of self-sustained electromechanical systems with clamped-free flexible arm. Nonlinear Dyn. **53**(3), 201–213 (2008)
27. Kwuimy, C.A.K., Kadji, H.E.: Recurrence analysis and synchronization of oscillators with coexisting attractors. Phys. Lett. A **3**78(3031), 2142–2150 (2014)
28. Kwuimy, C.K., Samadani, M., Kappaganthu, K., Nataraj, C.: Sequential recurrence analysis of experimental time series of a rotor response with bearing outer race faults. In: Proceedings of the 10th International Conference on Vibration Engineering & Technology of Machinery: VETOMAC X 2014. Springer (2014)
29. Lefeuvre, E., Badel, A., Petit, L., Richard, C., Guyomar, D.: Semi-passive piezoelectric structural damping by synchronized switching on voltage sources. J. Intell. Mater. Syst. Struct. **17**, 653–660 (2006)
30. Litak, G., Friswell, M.I., Adhikari, S.: Magnetopiezoelastic energy harvesting driven by random excitations. Appl. Phys. Lett. **96**(21), 214103 (2010)
31. Litak, G., Friswell, M.I., Kwuimy, C.K., Adhikari, S., Borowiec, M.: Energy harvesting by two magnetopiezoelastic oscillators with mistuning. Theor. Appl. Mech. Lett. **2**, 043009 (2012)
32. Liu, H., Zhang, S., Kathiresan, R., Kobayashi, T., Lee, C.: Development of piezoaeroelastic microcantiliver flow sensor with wind-driven energy harvesting capability. Appl. Phys. Lett. **100**, 223905 (2012)
33. Marwan, N., Romano, M.C., Thiel, M., Kurths, J.: Recurrence plots for the analysis of complex systems. Phys. Rep. **438**(5–6), 237–329 (2007)
34. Matassini, L., Kantz, H., Holyst, J., Hegger, R.: Optimizing of recurrence plots for noise reduction. Phys. Rev. E **65**(2), 021102 (2002)
35. Nayfeh, A.H., Mook, D.: Nonlinear Oscillations. Wiley-Interscience, New York (1979)
36. Ovejas, V.J., Cuadras, A.: Multimodal piezoelectric wind energy harvesters. Smart Mater. Struct. **20**, 1–9 (2011)
37. Ramlan, R., Brennan, M., Mace, B., Kovacic, I.: Potential benefits of a non-linear stiffness in an energy harvesting device. Nonlinear Dyn. **59**, 545–558 (2010)
38. Samadani, M., Kwuimy, C.A.K., Nataraj, C.: Diagnostics of a nonlinear pendulum using computational intelligence. In: Proceedings of the 6th Annual Dynamic Systems and Control Conference, Palo Alto, California, USA (2013)
39. Shahruz, S.M.: Design of mechanical band-pass filters for energy scavenging. J. Sound Vib. **292**(3–5), 987–998 (2006)
40. Strogatz, S.H.: Nonlinear Dynamics and Chaos with Applications to Physics, Biology, Chemistry and Engineering. Perseus Books Publishing, LLC (1994)
41. Tang, L., Yang, Y.: Analysis of synchronized charge extraction for piezoelectric energy harvesting. Smart Mater. Struct. **2**0, 085022 (2011)
42. Tekam, G.T.O., Tchuisseu, E.B.T., Kwuimy, C.A.K., Woafo, P.: Analysis of an electromechanical energy harvester system with geometric and ferroresonant nonlinearities. Nonlinear Dyn. **76**(2), 1561–1568 (2014)
43. Tekam, G.T.O., Kwuimy, C.A.K., Woafo, P.: Nonlinear analysis of tristable energy harvesting having fractional order viscoelastic material. Chaos, In press (2014)
44. Timoshenko, S.: Theory of Elastic Stability. McGraw-Hill, New York (1961)
45. Verhulst, F.: Nonlinear Differential Equations and Dynamical Systems. Springer-Verlag, New York (1990)
46. Wu, H., Tang, L., Yang, Y., Soh, C.K.: A nonvel two-degree-of-freedom piezoelectric energy harvester. J. Intell. Mater. Syst. Struct. **24**(3), 357–368 (2012)

Quasi-Periodic Galloping of a Wind-Excited Tower Under External Forcing and Parametric Damping

Lahcen Mokni, Ilham Kirrou and Mohamed Belhaq

Abstract This paper investigates the influence of combined fast external excitation and internal parametric damping on the amplitude and the onset of the quasi-periodic galloping of a tower submitted to steady and unsteady wind flow. The study is carried out considering a lumped single degree of freedom model and the cases where the turbulent wind activates different excitations are explored. The method of direct partition of motion followed by the multiple scales technique are applied to derive the slow flow dynamic near the primary resonance. The influence of the combined loading consisting in external excitation and parametric damping on the quasi-periodic galloping onset is explored. The performance of the combined loading is compared with the cases where the external excitation and the parametric damping are introduced separately. The results show that the performance of the combined loading on retarding the quasi-periodic galloping onset and quenching the corresponding amplitude is better in all cases of the turbulent wind excitations.

1 Introduction

Considerable efforts have been done to investigate galloping of tall building induced by steady and unsteady wind [1–8]. Such oscillations occur as the wind speed exceeds the onset of galloping resulting in large amplitude oscillations of the structure. To reduce the amplitude of galloping and retard its onset some techniques are used, including, for instance, mass tuned dampers, tuned liquid dampers, friction dampers [6], external excitation [9] and parametric damping [10]. A survey of some control methods in civil infrastructure applications is given in [11].

L. Mokni · I. Kirrou (✉) · M. Belhaq
University Hassan II-Casablanca, Casablanca, Morocco
e-mail: ilhamkirrou@gmail.com

L. Mokni
e-mail: l.mokni@gmail.com

M. Belhaq
e-mail: mbelhaq@yahoo.fr

M. Belhaq (ed.), *Structural Nonlinear Dynamics and Diagnosis*,
Springer Proceedings in Physics 168, DOI 10.1007/978-3-319-19851-4_7

The effect of unsteady wind on the galloping onset of towers has been receiving growing interest. The influence of the unsteady wind on the critical wind speed above which galloping occurs was investigated considering a single degree of freedom (sdof) model [4] and using the multiple scales method (MSM) [12]. It was concluded that the unsteady wind decreases significantly the galloping onset near the primary resonance. The effect of parametric, external and self-induced excitation on galloping onset was examined for a single tower in [7] and for two towers linked by a nonlinear viscous device [8]. The periodic galloping was studied analytically using perturbation method and the quasi-periodic (QP) modulation envelope was approximated numerically. The effects of the unsteady wind on the dynamics of the tower [7] and on the viscous device of the system [8] have been analyzed. Note that the problem of investigating the dynamics of some nonlinear oscillators under the combined effect of parametric, external and self-induced excitation was studied in [13–16]. Frequency response has been examined using the MSM, while the QP modulation envelope was approximated using numerical simulations [15, 16]. Specific phenomena including frequency locking have been presented.

In previous works, attention has been focused on examining the effect of unsteady wind on the periodic galloping onset [3, 4, 7]. The influence of unsteady wind on the QP galloping onset, on the other hand, has been studied recently by Kirrou et al. [17]. Specifically, analytical results supported by numerical simulations shown that QP galloping may occur for relatively small values of the wind velocity demonstrating clearly that the effect of the turbulent wind on the QP galloping onset should not be neglected. Instead, it must be systematically evaluated and considered in the design process of tall buildings in order to enhance their stability performance to QP galloping. Thus, a challenging problem that has arisen is to develop methods able to control such QP galloping. In this context, two techniques have been implemented to tune the QP onset toward higher values of the turbulent wind speed. Firstly, it was shown that introducing a fast harmonic excitation (FHE) retards significantly the QP galloping onset [9]. On the other hand, it was demonstrated that when an internal parametric damping (IPD) is applied, the amplitude of the QP galloping decreases while the QP galloping onset is not influenced [10, 18]. The natural question that arises is how the FHE and IPD influence the QP galloping onset when they are acted simultaneously. Recently, the influence of the combined loading was examined only on the periodic galloping onset [19]. In particular, it was shown that the combined loading of the FHE and IPD not only reduces the amplitude of the periodic galloping, but also retards its galloping onset substantially comparing to the cases where the FHE and the IPD are acted separately [9, 18].

In this paper, we extend the results related to the periodic galloping under the combined loading [19] to the case of the QP galloping. The performance of the combined effect on the QP galloping onset is systematically compared with the cases where the FHE and IPD are introduced separately. In Sect. 2 a brief description of the reduced equation of motion governing the dynamics of the tower exposed to steady and unsteady wind and under the FHE and IPD is provided. The method of direct partition of motion [20, 21] is performed and the MSM is applied to derive the modulation equations of the slow dynamic near the primary resonance. A brief

description of the results on the periodic galloping onset is given [19]. Section 3 explores the effect of FHE and IPD on the QP galloping onset in the cases where the unsteady wind activates different excitations. Section 4 concludes the work.

2 Equation of Motion and Periodic Galloping

The dimensionless sdof equation of motion of a tower subjected to steady and unsteady wind and to the combined effect of FHE and IPD can be written in the form

$$\ddot{x} + x + \left[c_a(1-\bar{U}) - b_1 u(t)\right]\dot{x} + Y\nu^2\cos(\nu t)\dot{x} + b_2\dot{x}^2 + \left[\frac{b_{31}}{\bar{U}} + \frac{b_{32}}{\bar{U}^2}u(t)\right]\dot{x}^3 = \eta_1\bar{U}u(t) + \eta_2\bar{U}^2 + Y\cos(\nu t) \tag{1}$$

where the dot denotes differentiation with respect to the non-dimensional time t. Note that the case where the FHE and IPD are absent has been considered in [4, 7]. Equation (1) contains, in addition to the elastic, viscous and inertial linear terms, quadratic and cubic components in the velocity generated by the aerodynamic forces. The steady component of the wind velocity is represented by $\bar{U}$ and the turbulent wind flow is approximated by a periodic force, $u(t)$, which is assumed to include the two first harmonics, $u(t) = u_1 \sin \Omega t + u_2 \sin 2\Omega t$, where u_1, u_2 and Ω are, respectively, the amplitudes and the fundamental frequency of the response. The coefficients of (1) are given in Appendix 1 and the derivation of the original model ((1) with $Y = 0$) can be found in [7]. Equation (1) also includes the FHE and IPD terms in which Y and ν are, respectively, the dimensionless amplitude and the frequency of the FHE and the IPD. To simplify the calculation, it is convenient to assume that both FHE and IPD have the same amplitude Y and the same frequency ν. However, while the case in which the HFE and IPD have different amplitudes, say Y_1 and Y_2, can be handled without apparent difficulties, the case of different frequencies, say ν_1 and ν_2, would present a serious complexity due to the introduction of an additional frequency in the problem [22].

We shall analyze the case of external excitation, $u(t) = u_1 \sin \Omega t$, parametric one, $u(t) = u_2 \sin 2\Omega t$, and the case where both external and parametric excitations are present simultaneously. Notice that the introduction of a FHE as a control technique was motivated by the experimental work [23] made for vibrating testing purpose of a full size tower. The mechanical vibration exciter system used in such an experiment is placed on the top of the structure and debits a harmonic excitation to the structure. The introduction of the IPD component, on the other hand, can be carried out, for instance, via a damper device in the interfloors damping [24]. Its use as a control strategy was motivated by its simple implementation and beneficial effect in reducing vibration in many applications, including automotive, aerospace, civil and mechanical engineering. To the best of the authors' knowledge, a practical

application of the FHE and IPD devices simultaneously as a control technique has not been reported in the literature.

Equation (1) includes a slow dynamic due to the steady and unsteady wind and a fast dynamic induced by the fast harmonic PD. To separate these dynamics, we perform the method of DPM on (1) by defining a fast time $T_0 = \nu t$ and a slow time $T_1 = t$, and splitting up $x(t)$ into a slow part $z(T_1)$ and a fast part $\phi(T_0, T_1)$ as

$$x(t) = z(T_1) + \mu\phi(T_0, T_1) \tag{2}$$

where z describes the slow main motions at time-scale of oscillations, $\mu\phi$ stands for an overlay of the fast motions and μ indicates that $\mu\phi$ is small compared to z. Since ν is considered as a large parameter, we choose $\mu \equiv \nu^{-1}$ for convenience. The fast part $\mu\phi$ and its derivatives are assumed to be $2\pi-$periodic functions of fast time T_0 with zero mean value with respect to this time, so that $< x(t) >= z(T_1)$ where $<>\equiv \frac{1}{2\pi}\int_0^{2\pi}() dT_0$ defines time-averaging operator over one period of the fast excitation with the slow time T_1 fixed. Averaging procedure gives the following equation governing the slow dynamic of motion

$$\ddot{z} + z + \left[c_a(1-\bar{U}) - b_1 u(t) - H_0 + \left(\frac{b_{31}}{\bar{U}} + \frac{b_{32}}{\bar{U}^2}u(t)\right) H_1\right]\dot{z} + \left[B - B_0\left(\frac{b_{31}}{\bar{U}} + \frac{b_{32}}{\bar{U}^2}u(t)\right)\right]\dot{z}^2 + \left[\frac{b_{31}}{\bar{U}} + \frac{b_{32}}{\bar{U}^2}u(t)\right] H_2\dot{z}^3 = \eta_1\bar{U}u(t) + \eta_2\bar{U}^2 + G \tag{3}$$

where $H_0 = 4b_2Y^2$, $H_1 = 6\left(\frac{Y}{\nu}\right)^2$, $H_2 = 1 + 6Y^2\nu^2$, $B = b_2(1 + 2Y^2\nu^2)$, $B_0 = 12Y^2$ and $G = -2b_2\left(\frac{Y}{\nu}\right)^2$. Note that the case without FHE component in (3) has been studied in [9], the case without IPD term was considered in [10], while the case without FHE and IPD ($Y = 0$) has been examined in [7].

To obtain the modulation equations of the slow dynamic (3) near the primary resonance, the MSM is performed by introducing a bookkeeping parameter ε, scaling as $z = \varepsilon^{\frac{1}{2}}z$, $b_1 = \varepsilon b_1$, $H_0 = \varepsilon H_0$, $H_1 = \varepsilon H_1$, $B = \varepsilon^{\frac{1}{2}}B$, $B_0 = \varepsilon^{\frac{1}{2}}B_0$, $\eta_1 = \varepsilon^{\frac{3}{2}}\eta_1$, $\eta_2 = \varepsilon^{\frac{3}{2}}\eta_2$ and assuming that $\bar{U} = 1 + \varepsilon V$ [7] where V stands for the mean wind velocity. With the resonance condition $\Omega = 1 + \varepsilon\sigma$ where σ is a detuning parameter and scaling $H = \varepsilon H$, a two-scale expansion of the solution is sought in the form

$$z(t) = z_0(t_0, t_1) + \varepsilon z_1(t_0, t_1) + O(\varepsilon^2) \tag{4}$$

where $t_i = \varepsilon^i t$ $(i = 0, 1)$. In terms of the variables t_i, the time derivatives become $\frac{d}{dt} = d_0 + \varepsilon d_1 + O(\varepsilon^2)$ and $\frac{d^2}{dt^2} = d_0^2 + 2\varepsilon d_0 d_1 + O(\varepsilon^2)$, where $d_i^j = \frac{\partial^j}{\partial^j t_i}$. Substituting (4) into (3), equating coefficients of the same power of ε, we obtain the two first orders of approximation

$$d_0^2 z_0 + z_0 = G \tag{5}$$

$$d_0^2 z_1 + z_1 = -2d_0 d_1 z_0 + (c_a V + b_1 u(t_0) + H_0 - H_1(b_{31} + b_{32} u(t_0)))(d_0 z_0)$$
$$-(B - B_0(b_{31} + b_{32} u(t_0)))(d_0 z_0)^2 - H_2(b_{31} + b_{32} u(t_0))(d_0 z_0)^3 + \eta_1 u(t_0) + \eta_2 \quad (6)$$

A solution of (5) is given by

$$z_0 = A(t_1)\exp(i t_0) + \bar{A}(t_1)\exp(-i t_0) + G \quad (7)$$

where i is the imaginary unit and A is an unknown complex amplitude.

Equation (6) can be solved for the complex amplitude A by introducing its polar form as $A = \frac{1}{2} a e^{i\phi}$. Substituting the expression of A into (6) and eliminating the secular terms, the modulation equations of the amplitude a and the phase ϕ can be extracted as

$$\begin{cases} \dot{a} = [S_1 - S_3 \sin(2\phi)]a - S_5 \cos(\phi)a^2 + [-S_2 + 2S_4 \sin(2\phi)]a^3 - \beta \cos(\phi) \\ a\dot{\phi} = [\sigma - S_3 \cos(2\phi)]a + 3S_5 \sin(\phi)a^2 + [S_4 \cos(2\phi)]a^3 + \beta \sin(\phi) \end{cases} \quad (8)$$

where $S_1 = \frac{1}{2}(c_a V + H_0 - H_1 b_{31})$, $S_2 = \frac{3}{8} b_{31} H_2$, $S_3 = \frac{1}{4}(b_1 - H_1 b_{32}) u_2$, $S_4 = \frac{1}{8} b_{32} H_2 u_2$, $S_5 = \frac{1}{8} b_{32} B_0 u_1$ and $\beta = \frac{\eta_1 u_1}{2}$. Before investigating the QP galloping onset, we shall briefly present some results on the influence of both FHE and IPD on the periodic galloping one [19]. The equilibria of (8), corresponding to periodic oscillations of the system, are giving by setting $\dot{a} = \dot{\phi} = 0$. In the absence of unsteady wind ($u_1 = u_2 = 0$), only the first equation of system (8) is used. Besides the trivial solution, $a = 0$, the amplitude of the periodic response is given by

$$a = \sqrt{\frac{4(c_a V + H_0 - H_1 b_{31})}{3 b_{31} H_2}} \quad (9)$$

Figure 1 shows the periodic galloping amplitude a versus the wind velocity V in the absence of the unsteady wind ($u_1 = 0, u_2 = 0$), as given by (9), for $\sigma = 0$ and for two different values of the amplitude Y. It can be seen that increasing the amplitude Y, the galloping onset shifts substantially toward higher values of the wind velocity with a significant decrease of the galloping amplitude. It should be noticed that, for the fixed value of $Y = 0.3$, while the combined effect of the FHE and IPD retards substantially the onset of periodic galloping to $V \approx 2.6$ (Fig. 1), the FHE when applied alone shifts the galloping onset slightly to $V \approx 0.65$ [9] and the IPD when applied alone does not influence it at all [10].

In the case of turbulent wind with external excitation ($u_1 \neq 0, u_2 = 0$), analysis of equilibria of the slow flow (8) yields the following amplitude-response equation

$$\frac{(S_1 a - S_2 a^3)^2}{(\beta + S_5 a^2)^2} + \frac{(-\sigma a)^2}{(\beta + 3S_5 a^2)^2} = 1 \quad (10)$$

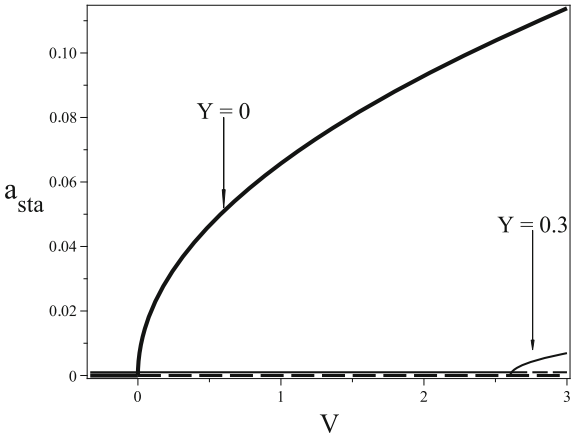

Fig. 1 Effect of Y on the periodic galloping onset versus V for $u_1 = 0, u_2 = 0$, $\nu = 8$. *Solid line* Stable; *Dashed line* Unstable

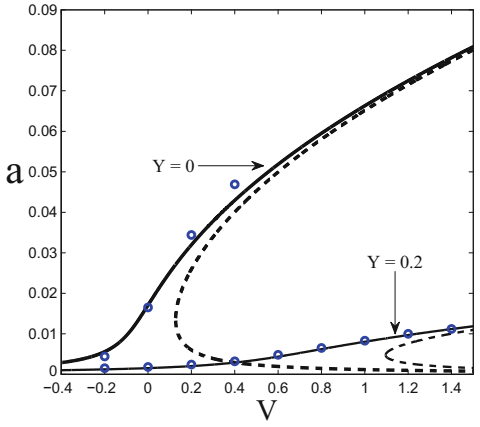

Fig. 2 Effect of Y on the periodic galloping onset versus V for $u_1 = 0.1$, $u_2 = 0, \sigma = 0, \nu = 10$. *Solid line* Stable; *Dashed line* Unstable; *Circle* Numerical simulation

In Fig. 2 we illustrate the variation of the periodic galloping amplitude versus the wind velocity V, as given by (10), for a given value of the external excitation amplitude u_1 and for $Y = 0$ and $Y = 0.2$. The solid line corresponds to the stable branch, the dashed line corresponds to the unstable one and circles are obtained by numerical simulations. One observes that the combined effect of the FHE and IPD decreases significantly the galloping amplitude and shifts substantially its onset toward higher values of the wind speed. It is worthy noticing that, for the fixed value of $Y = 0.2$, while the combined loading decreases the periodic galloping and retards its onset significantly (Fig. 2), the IPD when applied alone produces a similar but moderate effect [10] and the FHE when applied alone only shifts the amplitude curve slightly to the right [9].

In the case of turbulent wind with parametric excitation ($u_1 = 0, u_2 \neq 0$), the amplitude-response equation reads

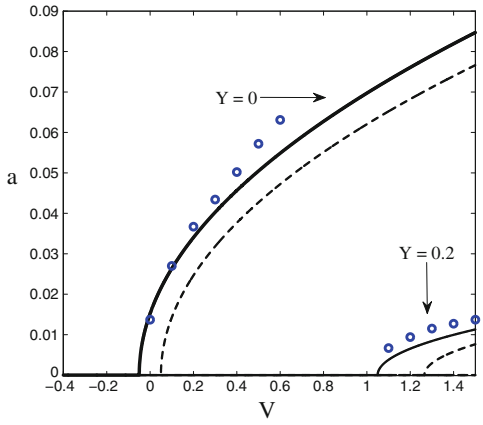

Fig. 3 Effect of Y on the periodic galloping onset versus V for $u_1 = 0$, $u_2 = 0.1$, $\sigma = 0$, $\nu = 8$. *Solid line* Stable; *Dashed line* Unstable; *Circle*: Numerical simulation

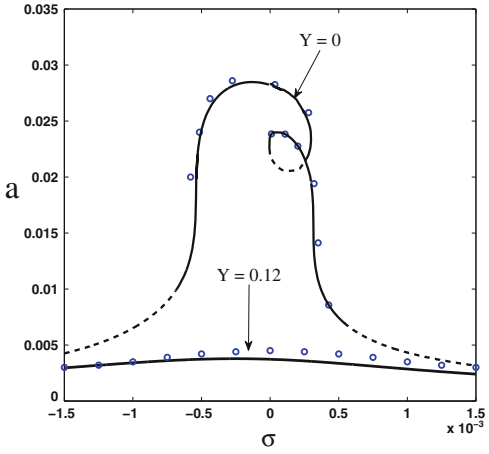

Fig. 4 Effect of Y on the amplitude-frequency response for $V = 0.11$, $u_1 = 0.1$, $u_2 = 0.1$. *Solid line* Stable, *Dashed line* Unstable, *Circle* Numerical simulation

$$\frac{(-S_1 a + S_2 a^3)^2}{(-S_3 a + 2S_4 a^3)^2} + \frac{(-\sigma a)^2}{(-S_3 a + S_4 a^3)^2} = 1 \tag{11}$$

Figure 3 shows, for a given value of the excitation u_2, the effect of the combined loading on the amplitude versus V, as given by (11), indicating also a decrease of the amplitude and a shift of the galloping onset as Y is increased. Note that in this case also, for a fixed value of $Y = 0.2$, the combined loading reduces the amplitude and retards the galloping onset much more comparing to the case where the FHE or the IPD is applied alone [9, 10].

Finally, in the case where the external and parametric excitations are acted simultaneously ($u_1 \neq 0, u_2 \neq 0$), the amplitude-frequency response is shown in Fig. 4. The plots indicate that the amplitude response decreases drastically with a moderate increase of the amplitude Y (for $\sigma = 0$, the approximate amplitude value is

found to be $a \approx 0.003$). Instead, when the FHE acts alone the amplitude decreases moderately (for $\sigma = 0, a \approx 0.02$) [10] and when the IPD is introduced alone the amplitude performs a small decrease (for $\sigma = 0, a \approx 0.012$) [9].

3 Quasi-Periodic Galloping

The influence of both FHE and IPD on the QP galloping and its wind speed onset is explored analytically in this section. To this end, we shall approximate the periodic solutions of the slow flow (8), corresponding to the QP responses of the original system. This can be done by transforming the slow flow (8) from the polar form to the following Cartesian system using the variable change $u = a\cos\phi$ and $v = -a\sin\phi$

$$\begin{cases} \dfrac{du}{dt} = (\sigma + S_3)v - \beta + \eta\{S_1 u - (S_2 u + S_4 v + S_5)(u^2 + v^2) - 2S_5 v^2 - 2S_4 u^2 v\} \\ \dfrac{dv}{dt} = -(\sigma - S_3)u + \eta\{S_1 v + 2S_5 uv - (S_2 v + S_4 u)(u^2 + v^2) - 2S_4 uv^2\} \end{cases} \tag{12}$$

where η is a small bookkeeping parameter introduced in damping and nonlinearity. Using the second step perturbation procedure [25–28], a second MSM is applied on the slow flow (12), to approximate a periodic solution which can be sought in the form

$$\begin{aligned} u(t) &= u_0(T_1, T_2) + \eta u_1(T_1, T_2) + O(\eta^2) \\ v(t) &= v_0(T_1, T_2) + \eta v_1(T_1, T_2) + O(\eta^2) \end{aligned} \tag{13}$$

where $T_1 = t$ and $T_2 = \eta t$. Introducing $D_i = \frac{\partial}{\partial T_i}$ yields $\frac{d}{dt} = D_1 + \eta D_2 + O(\eta^2)$, substituting (13) into (12) and collecting terms, we obtain at different order of η

$$\begin{aligned} D_1^2 u_0 + \lambda^2 u_0 &= 0 \\ \alpha v_0 &= D_1 u_0 + \beta \end{aligned} \tag{14}$$

$$\begin{aligned} D_1^2 u_1 + \lambda^2 u_1 = \alpha \Big[&-D_2 v_0 + S_1 v_0 + 2S_5 u_0 v_0 - (S_2 v_0 + S_4 u_0)\left(u_0^2 + v_0^2\right) - \\ &2S_4 u_0 v_0^2 \Big] - D_1 D_2 u_0 + S_1 D_1 u_0 - D_1 \Big[(S_2 u_0 + S_4 v_0 + S_5)\left(u_0^2 + v_0^2\right) + \\ &2S_4 u_0^2 v_0 \Big] - 4S_5 v_0 D_1 v_0 \\ \alpha v_1 = D_1 u_1 + D_2 u_0 - S_1 u_0 + &(S_2 u_0 + S_4 v_0 + S_5)\left(u_0^2 + v_0^2\right) + \\ &2S_5 v_0^2 + 2S_4 u_0^2 v_0 \end{aligned} \tag{15}$$

where $\alpha = \sigma + S_3$ and $\lambda = \sqrt{\sigma^2 - S_3^2}$ is the frequency of the periodic solution of the slow flow (12) corresponding to the frequency of the QP modulation. This

frequency λ depends, to the leading order, only on the parametric excitation u_2 via the coefficient S_3 given in (8). The solution of the first-order system (14) is given by

$$\begin{aligned} u_0(T_1, T_2) &= R(T_2)\cos(\lambda T_1 + \theta(T_2)) \\ v_0(T_1, T_2) &= -\frac{\lambda}{\alpha} R(T_2)\sin(\lambda T_1 + \theta(T_2)) + \frac{\beta}{\alpha} \end{aligned} \tag{16}$$

Substituting (16) into (15) and removing secular terms gives the following autonomous $slow_{slow}$ flow system on R and θ

$$\begin{cases} \dfrac{dR}{dt} = \left(S_1 - 2\dfrac{\beta^2}{\alpha^2}S_2\right)R - \left(\dfrac{1}{2}S_2 + \dfrac{\lambda^2}{2\alpha^2}S_2\right)R^3 \\ R\dfrac{d\theta}{dt} = \left(\dfrac{3\beta^2}{2\alpha\lambda}S_4 - \dfrac{3\lambda\beta^2}{2\alpha^3}S_4 - \dfrac{\beta S_5}{\lambda}\left(1 + \dfrac{3\lambda^2}{\alpha^2}\right)\right)R - \left(\dfrac{3\lambda^3}{8\alpha^3}S_4 - \dfrac{3\alpha}{8\lambda}S_4\right)R^3 \end{cases} \tag{17}$$

A periodic solution of the slow flow (12) is then approximated by

$$\begin{aligned} u(t) &= R\cos(\phi t) \\ v(t) &= -\frac{\lambda}{\alpha} R\sin(\phi t) + \frac{\beta}{\alpha} \end{aligned} \tag{18}$$

where the amplitude R is obtained by setting $\frac{dR}{dt} = 0$ and given by

$$R = \sqrt{\frac{2\alpha^2 S_1 - 4\beta^2 S_2}{S_2(\alpha^2 + \lambda^2)}} \tag{19}$$

which corresponds to the amplitude of the periodic solution (limit cycle) of the slow flow (12). Using (18), the amplitude modulation of the QP oscillations reads

$$a(t) = \sqrt{\left[\frac{1}{2}R^2 + \frac{\lambda^2}{2\alpha^2}R^2 + \frac{\beta^2}{\alpha^2}\right] - \left[\frac{2\lambda\beta}{\alpha^2}R\sin(\phi t) - \left(\frac{1}{2}R^2 - \frac{\lambda^2}{2\alpha^2}R^2\right)\cos(2\phi t)\right]} \tag{20}$$

and the QP modulation envelope is delimited by a_{min} and a_{max} such that

$$a_{min} = min\left\{\sqrt{\left[\frac{1}{2}R^2 + \frac{\lambda^2}{2\alpha^2}R^2 + \frac{\beta^2}{\alpha^2}\right] \pm \frac{2\lambda\beta}{\alpha^2}R \pm \left(\frac{1}{2}R^2 - \frac{\lambda^2}{2\alpha^2}R^2\right)}\right\} \tag{21}$$

$$a_{max} = max\left\{\sqrt{\left[\frac{1}{2}R^2 + \frac{\lambda^2}{2\alpha^2}R^2 + \frac{\beta^2}{\alpha^2}\right] \pm \frac{2\lambda\beta}{\alpha^2}R \pm \left(\frac{1}{2}R^2 - \frac{\lambda^2}{2\alpha^2}R^2\right)}\right\} \tag{22}$$

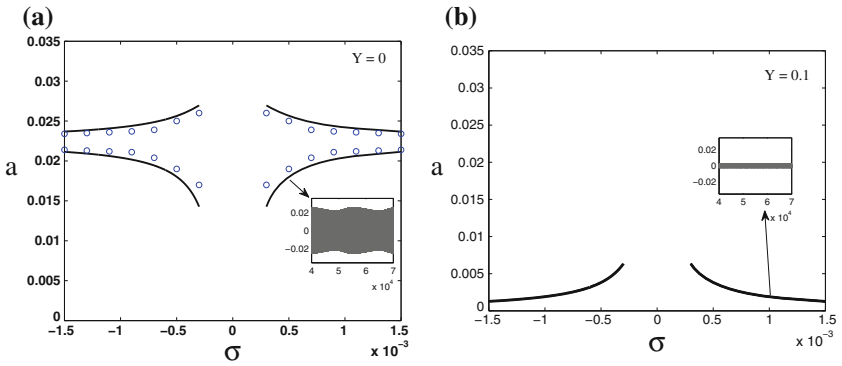

Fig. 5 QP galloping versus σ for $V = 0.117$, $u_1 = 0.033$, $\nu = 10$. *Solid lines* Stable; *Dashed lines* Unstable; *Circle* Numerical simulation

The domain of existence of QP galloping is characterized by stable periodic solution born with zero amplitude. This occurs exactly at critical values where the limit cycle has zero amplitude. Then, setting $R = 0$ in (19), we determine the corresponding critical detuning parameter σ_c given by the condition

$$\sigma_c = S_3 \pm \sqrt{\frac{2\beta^2 S_2}{S_1}} \tag{23}$$

which defines the interval $[-\sigma_c, \sigma_c]$ outside which the galloping is QP, while it is periodic inside the interval.

3.1 Case of External Excitation

In the case of external excitation ($u_1 \neq 0$, $u_2 = 0$), Fig. 5 shows the QP modulation envelope, as given by (21) and (22), for given values of V and u_1 and for different values of Y. The comparison between the analytical predictions (solid lines) and the numerical simulations obtained by using Runge-Kutta method (circles) validates the analytical result. This figure indicates that introducing a small amplitude, $Y = 0.1$, decreases drastically the amplitude of the QP oscillations, while the modulation envelope disappear completely to meet the periodic response, as shown in Fig. 5b. It should be noticed that, for the same value of the amplitude, $Y = 0.1$, the FHE or the IPD when applied separately reduces slightly the QP galloping and the modulation envelope remains relatively large [9, 10].

Figure 6a depicts the variation of the QP galloping as function of the wind speed for a given value of u_1 and $Y = 0$. It can be seen that the QP galloping triggers at a certain critical small value of the velocity wind V. Prior to this value, the tower

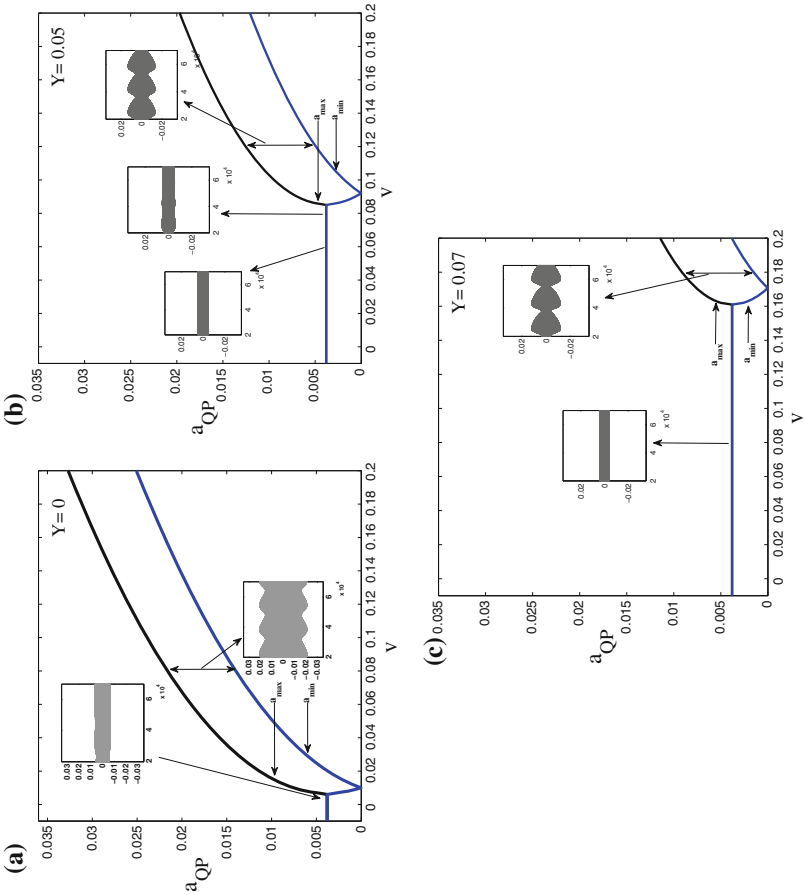

Fig. 6 QP galloping onset versus V for $\sigma = 0.0005$, $u_1 = 0.033$, $\nu = 8$

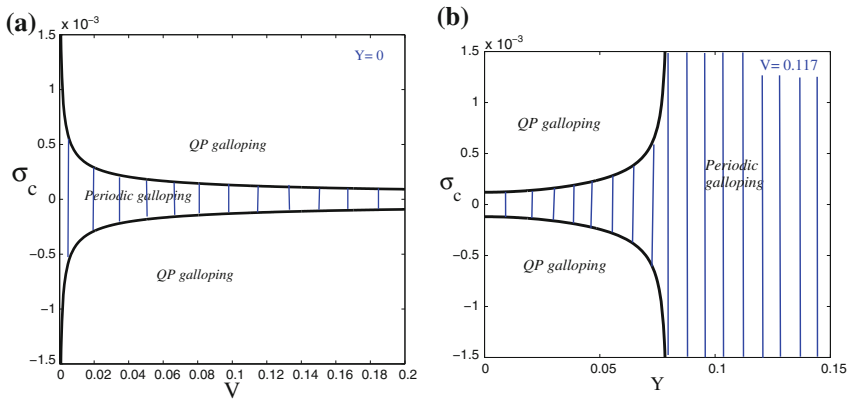

Fig. 7 QP galloping domains, $u_1 = 0.033$ and $\nu = 10$

performs small periodic oscillations due to the external excitation effect, as shown by time histories of the slow dynamic $z(t)$ inset Fig. 6a obtained by numerical simulation of (3). The effect of the combined loading is depicted in Fig. 6b, c, for the values $Y = 0.05$ and $Y = 0.07$, respectively. One observes that the QP galloping onset is substantially retarded as the amplitude Y increases. For instance, for $Y = 0.07$ (Fig. 6c) the value of the wind speed corresponding to the QP galloping onset is found to be $V = 0.161$. By comparison, it is interesting to notice that for the same value of $Y = 0.07$, the QP galloping onset is $V = 0.042$ when the FHE is applied alone, and $V = 0.019$ when the IPD is applied alone. These results clearly demonstrate a better performance of the combined loading over the cases where the loading are acted separately [9, 10]. In Fig. 7 is shown the domains of existence of QP galloping (unhatched region) in the parameter plane σ_c versus V (Fig. 7a) and σ_c versus Y (Fig. 7b), as given by the conditions (23); the periodic galloping occurs in the hatched region. One observes that for $Y = 0$ the domain of QP galloping increases slightly with increasing V (Fig. 7a). More importantly, Fig. 7b shows that there exists a critical value of the amplitude Y at which the QP galloping disappears completely. The approximate critical value is found to be $Y = 0.056$ which is coherent with the plots of Fig. 5b corresponding to $Y = 0.1$ which is chosen beyond the critical value.

Figure 8 depicts the combined effect of the FHE and IPD on the QP galloping domain in the parameter plane (u_1, σ). The plots show that the QP galloping domain decreases substantially by increasing Y. Note that this QP domain decreases slightly in the case where the IPD is acted alone and it is not affected in the case where the FHE is acted alone [9, 10].

3.2 Case of Parametric Excitation

In this case ($u_1 = 0$, $u_2 \neq 0$), Fig. 9 shows the influence of both FHE and IPD on the envelope of the QP oscillations. One observes a decrease of the amplitude and

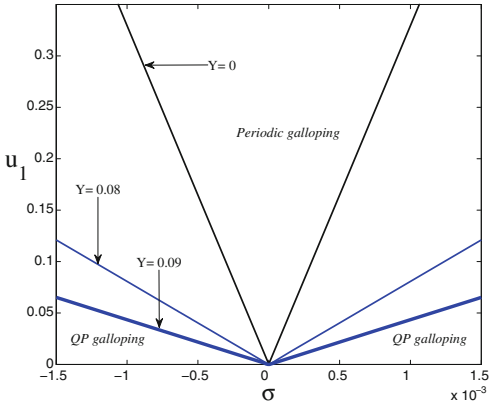

Fig. 8 QP galloping domains in the parameter plane u_1 versus σ_c, $V = 0.167$ and $\nu = 10$

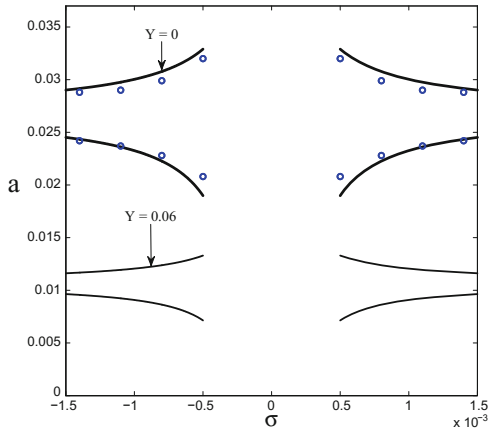

Fig. 9 QP galloping versus σ for $V = 0.167$, $\nu = 8$ and $u_2 = 0.1$

the envelope of the QP galloping with a small increase of Y. The plots show that for $Y = 0.06$, the value of the average amplitude of the QP is found to be approximately $a \approx 0.011$. Instead, in the case of a separate loading, reducing the average amplitude of the QP response to the same amplitude ($a \approx 0.011$) requires an increase of the amplitude to $Y = 0.14$ (which is more than twice that of the combined loading) [9, 10]. Figure 10a shows, in the absence of the loadings ($Y = 0$), the QP galloping amplitude versus the wind velocity V for a given value of the excitation amplitude u_2. It can be seen that as V is increased from zero, the QP galloping onset increases. The boxes inset the figure present time histories of the slow dynamic $z(t)$ for different values of V. The influence of the combined loading on the QP galloping amplitude along with time histories is depicted in Fig. 10b indicating a substantial shift of the QP galloping onset toward higher values of the wind speed and a decrease of the amplitude.

It should be noticed that, while the combined loading retards the QP galloping onset to the value $V = 0.185$ for $Y = 0.08$ (Fig. 10b), the QP galloping onset is

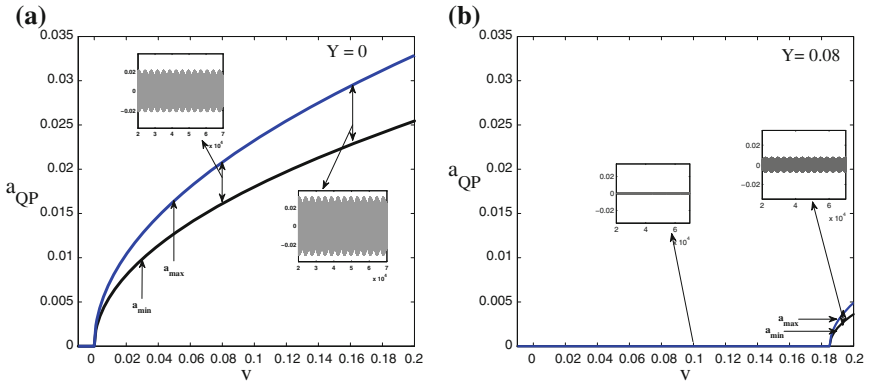

Fig. 10 QP envelope versus V for the parameter values of Fig. 9 with $\sigma = 0.001$

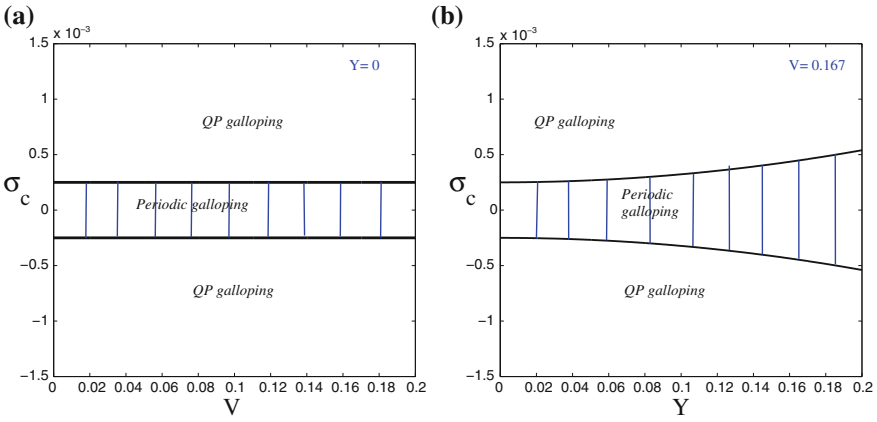

Fig. 11 QP galloping domains, $u_2 = 0.1$

about ($V = 0.046$) when the FHE is applied alone [9] and it is not influenced when the IPD is acted alone [10].

It is worth noticing (as mentioned before) that the modulation frequency λ of the QP galloping caused by the parametric excitation (see inset Fig. 10) is higher than that produced by the external excitation (see inset Fig. 6).

The domains of existence of periodic (hatched) and QP (unhatched) galloping, as given by (23), are shown in Fig. 11 indicating that the domain of QP galloping remains constant with increasing V and decreases slightly with Y.

3.3 Case of External and Parametric Excitations

In the case where the wind activates external and parametric excitations simultaneously ($u_1 \neq 0$, $u_2 \neq 0$), Fig. 12a, b show, respectively, the QP modulation envelope

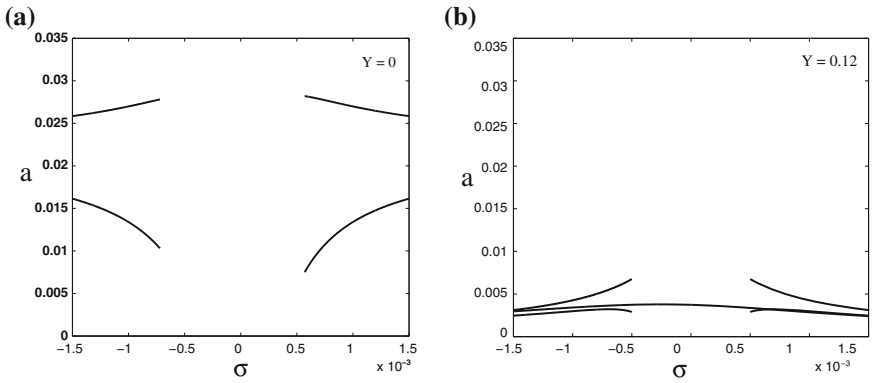

Fig. 12 QP galloping versus σ for $\nu = 8$, $V = 0.11$, $u_1 = 0.1$ and $u_2 = 0.1$

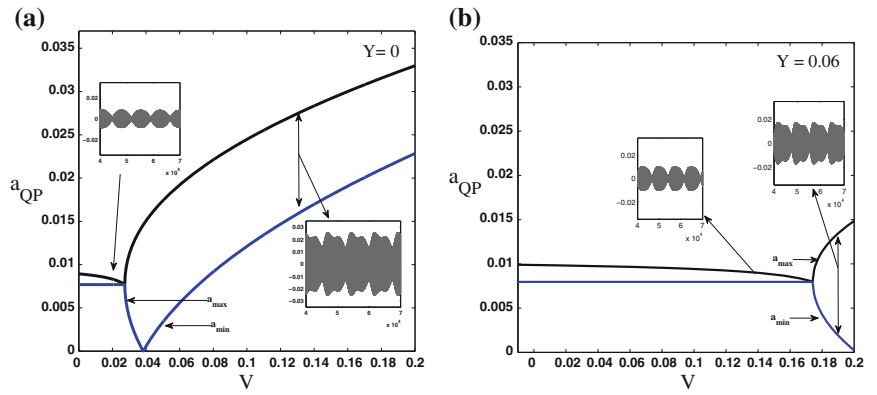

Fig. 13 The original and the new QP envelopes versus V for the parameter values of Fig. 12, $\sigma = 0.001$

in the absence and presence of the FHE and IPD. These figures indicate that increasing the amplitude Y of the FHE and IPD, eliminates the principal QP modulation envelope and gives rise to a new small QP modulation one.

One notices that while in the presence of both FHE and IPD, a decrease of the amplitude of the QP requires a small excitation amplitude (Fig. 12b), the FHE or the IPD when applied separately can not achieve the same performance even for large values of Y [9, 10].

Figure 13a shows, for $Y = 0$, the original and the small QP modulation envelopes versus the wind velocity V for given values of excitation amplitudes u_1, u_2. One notices that as Y is increased, the amplitude of the large QP galloping decreases and its onset is retarded causing the small QP envelope to persists over a large range of the wind velocity, as shown in the boxes inset Fig. 13b. In this situation, the motionof

the wind-excited tower remains QP with small amplitude and relatively large modulation. Finally, a comparison between the different cases of loading indicates that for the small value of the amplitude $Y = 0.06$, the combined effect of the excitation retards the QP galloping onset to $V = 0.167$ (Fig. 13b). Instead, to achieve a comparable performance when the FHE or the IPD is applied separately, one requires the amplitude Y to reach twice the value related to the combined excitation ($Y = 0.06$) [9, 10].

4 Conclusion

The combined effect of the FHE and IPD on the QP galloping onset of a wind-excited tower was studied analytically considering a lumped sdof model and using perturbation methods. The cases where the turbulent wind activates external excitation, parametric one or both have been considered and the analysis was carried out near the primary resonance. Analytical approximation of the QP solutions as well as its modulation envelope were obtained and confirmed by comparison to numerical simulations.

Attention was focused on assessing the performance of the combined influence of the FHE and IPD over that where FHE or IPD is introduced separately, in terms of quenching the QP motion and retarding its galloping onset. The results shown that the combined effect of FHE and IPD greatly improves the decrease of the QP galloping amplitude and the shift of the QP galloping onset compared to the case where FHE or IPD is introduced separately.

The analytical results reported in this work, supported by numerical simulations clearly reveal the importance to analyze the QP galloping onset. In other words, special attention should be given to QP galloping in any stability analysis of long flexible structures under turbulent wind flow. Such a galloping should not be neglected but have to be considered in the design process of buildings in order to enhance their stability performance.

Appendix 1

The expression of the coefficients of (1) are:

$$\omega = \pi \frac{\sqrt{3EI}}{h\ell\sqrt{m}},\quad c_a = \frac{\rho A_1 bh\ell \bar{U}_c}{2\pi\sqrt{3EIm}},\quad b_1 = c_a,\quad b_2 = -\frac{4\rho A_2 b\ell}{3\pi m},\quad b_{31} = -\frac{3\pi\rho A_3 b\ell\sqrt{3EI}}{8h\bar{U}_c\sqrt{m^3}} \tag{24}$$

$$b_{32} = -b_{31},\quad \eta_1 = \frac{4\rho A_0 bh^2\ell\bar{U}_c^2}{3\pi^3 EI},\quad \eta_2 = \frac{\eta_1}{2},\quad U(t) = \bar{U} + u(t), \tag{25}$$

where ℓ is the height of the tower, b the cross-section wide, EI the total stiffness of the single story, m the mass longitudinal density, h the inter story height, and ρ the air mass density. $A_i, i = 0, ...3$ are the aerodynamic coefficients for the squared cross-section. The dimensional critical velocity is given by

$$\bar{U}_c = \frac{4\pi\xi\sqrt{3EIm}}{\rho b A_1 h \ell} \tag{26}$$

where ξ is the modal damping ratio, depending on both the external and internal damping according to

$$\xi = \frac{\zeta h^2}{24EI}\omega + \frac{c_0}{2m\omega} \tag{27}$$

where ζ and c_0 are the external and internal damping coefficients, respectively. Introducing a parametric damper device in the internal damping such as

$$c_0 = c(1 + y_0 \nu^2 \cos \nu t) \tag{28}$$

where y_0 and ν are the amplitude and the frequency of the internal PD, respectively. In this case the equation of motion reads

$$\ddot{x} + x + \left[c_a + Y\nu^2 \cos \nu t\right]\dot{x} - c_a\left[\bar{U} + u(t)\right]\dot{x} + b_2\dot{x}^2 + \left[\frac{b_{31}}{\bar{U}} + \frac{b_{32}}{\bar{U}^2}u(t)\right]\dot{x}^3 = \eta_1\bar{U}u(t) + \eta_2\bar{U}^2 \tag{29}$$

where $Y = \frac{cy_0}{m\omega}$. Re-arranging terms yields the equation of motion (1).

Appendix 2

Introducing $D_i^j \equiv \frac{\partial^j}{\partial^j T_i}$ yields $\frac{d}{dt} = \nu D_0 + D_1$, $\frac{d^2}{dt^2} = \nu^2 D_0^2 + 2\nu D_0 D_1 + D_1^2$ and substituting (2) into (1) gives

$$\begin{aligned}
&\mu^{-1}D_0^2\phi + D_1^2 z + 2D_0D_1\phi + \mu D_1^2\phi + \big(c_a(1-\bar{U}) - b_1u(t)\big)\big(D_1 z + D_0\phi \\
&\quad + \mu D_1\phi\big) + z + \mu\phi + Y\nu^2\cos(\nu t)\big(D_1 z + D_0\phi + \mu D_1\phi\big) + b_2\big((D_1 z)^2 \\
&\quad + 2D_1 z(D_0\phi + \mu D_1\phi) + (D_0\phi)^2 + 2\mu D_0\phi D_1\phi + (\mu D_1\phi)^2\big) \\
&\quad + \left(\frac{b_{31}}{\bar{U}} + \frac{b_{32}}{\bar{U}^2}u(t)\right)\big((D_1 z)^3 + 3(D_1 z)^2(D_0\phi + \mu D_1\phi) \\
&\quad + 3(D_1 z)(D_0\phi + \mu D_1\phi)^2 + (D_0\phi + \mu D_1\phi)^3\big) = \eta_1\bar{U}u(t) + \eta_2\bar{U}^2
\end{aligned} \tag{30}$$

Averaging (30) leads to

$$D_1^2 z + \big(c_a(1-\bar{U}) - b_1 u(t)\big) D_1 z + z + Y v^2 < \cos(T_0)\big(D_0\phi + \mu D_1\phi\big) > + b_2\big((D_1 z)^2 + < (D_0\phi)^2 > + < (2\mu D_0\phi D_1\phi) > + < (\mu D_1\phi)^2 > \big) + \left(\frac{b_{31}}{\bar{U}} + \frac{b_{32}}{\bar{U}^2}u(t)\right)\big((D_1 z)^3 + 3D_1 z(< (D_0\phi)^2 > + < (2\mu D_0\phi D_1\phi) > + < (\mu D_1\phi)^2 >)\big) = \eta_1 \bar{U} u(t) + \eta_2 \bar{U}^2 \tag{31}$$

Subtracting (31) from (30) yields

$$\mu^{-1} D_0^2\phi + 2D_0 D_1\phi + \mu D_1^2\phi + \big(c_a(1-\bar{U}) - b_1 u(t)\big)\big(D_0\phi + \mu D_1\phi\big) + \mu\phi + Y v^2 \cos(T_0)\big(D_0\phi + \mu D_1\phi\big) - Y v^2 < \cos(T_0)\big(D_0\phi + \mu D_1\phi\big) > + b_2\big(2D_1 z(D_0\phi + D_0\phi)^2 - < (D_0\phi)^2 > + 2\mu D_0\phi D_1\phi - (< 2\mu D_0\phi D_1\phi > + (\mu D_1\phi)^2 - < (\mu D_1\phi)^2 > \big) + \left(\frac{b_{31}}{\bar{U}} + \frac{b_{32}}{\bar{U}^2}u(t)\right)\big(3(D_1 z)^2(D_0\phi + \mu D_1\phi) + 3D_1 z(D_0\phi)^2 - 3D_1 z < (D_0\phi)^2 > + 6D_1 z\mu(D_0\phi D_1\phi) - < 6D_1 z\mu(D_0\phi D_1\phi) > + 3D_1 z(\mu D_1\phi)^2 - 3D_1 z < (\mu D_1\phi)^2 > + (D_0\phi)^3 + 3\mu(D_0\phi)^2 D_1\phi + 3D_0\phi(\mu D_1\phi)^2 + (\mu D_1\phi)^3\big) = -Y v^2 \cos(T_0) D_1 z \tag{32}$$

Using the inertial approximation [20], i.e. all terms in the left-hand side of (32), except the first, are ignored, one obtains

$$\phi = Y v \cos(T_0) D_1 z \tag{33}$$

Inserting ϕ from (33) into (31), using that $< cos^2 T_0 > = 1/2$, and keeping only terms of orders three in z, give the equation governing the slow dynamic of the motion (3).

References

1. Parkinson, G.V., Smith, J.D.: The square prism as an aeroelastic non-linear oscillator. Quart. J. Mech. Appl. Math. **17**, 225–239 (1964)
2. Novak, M.: Aeroelastic galloping of prismatic bodies. ASCE. J. Eng. Mech. **96**, 115–142 (1969)
3. Nayfeh, A.H., Abdel-Rohman, M.: Galloping of squared cantilever beams by the method of multiple scales. J. Sound Vib. **143**, 87–93 (1990)
4. Abdel-Rohman, M.: Effect of unsteady wind flow on galloping of tall prismatic structures. Nonlinear Dyn. **26**, 231–252 (2001)
5. Clark, R., Modern, A.: Course in Aeroelasticity, 4th edn. Kluwer Academic Publishers, Dordrecht, The Netherlands (2004)

6. Qu, W.L., Chen, Z.H., Xu, Y.L.: Dynamic analyziz of a wind-excited struss tower with friction dampers. Comput. Struct. **79**, 2817–2831 (2001)
7. Luongo, A., Zulli, D.: Parametric, external and self-excitation of a tower under turbulent wind flow. J. Sound Vib. **330**, 3057–3069 (2011)
8. Zulli, D., Luongo, A.: Bifurcation and stability of a two-tower system under wind-induced parametric, external and self-excitation. J. Sound Vib. **331**, 365–383 (2012)
9. Belhaq, M., Kirrou, I., Mokni, L.: Periodic and quasiperiodic galloping of a wind-excited tower under external excitation. Nonlinear Dyn. **74**, 849–867 (2013)
10. Mokni, L., Kirrou, I., Belhaq, M.: Galloping of a wind-excited tower under internal parametric damping. J. Vib. Acoust. **136**, 024503–024503–7 (2014)
11. Spencer Jr, B.F., Nagarajaiah, S.: State of the art of structural control. J. Struct. Eng. **129**, 845–865 (2003)
12. Nayfeh, A.H., Mook, D.T.: Nonlinear Oscillations. Wiley, New York (1979)
13. Tondl, A.: On the interaction between self-excited and parametric vibrations. National Research Institute for Machine Design, Monographs and Memoranda. No. 25, Prague (1978)
14. Schmidt, G.: Interaction of self-excited forced and parametrically excited vibrations. In: The 9th International Conference on Nonlinear Oscillations. vol. 3, Application of The Theory of Nonlinear Oscillations. Naukowa Dumka, Kiev (1984)
15. Szabelski, K., Warminski, J.: Self excited system vibrations with parametric and external excitations. J. Sound Vib. **187**(4), 595–607 (1995)
16. Szabelski, K., Warminski, J.: Parametric self excited nonlinear system vibrations analysis with inertial excitations. Int. J. Non Linear Mech. **30**(2), 179–189 (1995)
17. Kirrou, I., Mokni, L., Belhaq, M.: On the quasiperiodic galloping of a wind-excited tower. J. Sound Vib. **332**, 4059–4066 (2013)
18. Mokni, L., Kirrou, I., Belhaq, M.: Periodic and quasiperiodic galloping of a wind-excited tower under parametric damping. J. Vib. Control. (2014). doi:10.1177/1077546314526921
19. Mokni, L., Kirrou, I., Belhaq, M.: Galloping of wind-excited tower under external excitation and parametric damping. Int. J. Model. Ident. Control **1**, 1–5 (2013)
20. Blekhman, I.I.: Vibrational Mechanics—Nonlinear Dynamic Effects, General Approach, Applications. World Scientific, Singapore (2000)
21. Thomsen, J.J.: Vibrations and Stability: Advanced Theory, Analysis, and Tools. Springer-Verlag, Berlin-Heidelberg (2003)
22. Abouhazim, N., Belhaq, M., Lakrad, F.: Three-period quasi-periodic solutions in the self-excited quasi-periodic mathieu oscillator. Nonlinear Dyn. **39**(4), 395–409 (2005)
23. Keightley, W.O., Housner, G.W., Hudson, D.E.: Vibration tests of the Encino dam intake tower, California Institute of Technology, Report No. 2163, Pasadena, California (1961)
24. Munteanu, L., Chiroiu, V., Sireteanu, T.: On the response of small buildings to vibrations. Nonlinear Dyn. **73**, 1527–1543 (2013)
25. Belhaq, M., Houssni, M.: Quasi-periodic oscillations, chaos and suppression of chaos in a nonlinear oscillator driven by parametric and external excitations. Nonlinear Dyn. **18**, 1–24 (1999)
26. Rand, R.H., Guennoun, K., Belhaq, M.: 2:2:1 Resonance in the quasi-periodic Mathieu equation. Nonlinear Dyn. **31**, 187–93 (2003)
27. Belhaq, M., Fahsi, A.: Hysteresis suppression for primary and subharmonic 3:1 resonances using fast excitation. Nonlinear Dyn. **57**, 275–286 (2009)
28. Hamdi, M., Belhaq, M.: Quasi-periodic oscillation envelopes and frequency locking in rapidly vibrated nonlinear systems with time delay. Nonlinear Dyn. **73**, 1–15 (2013)

On Optimal Control of a Nonlinear Robotic Mechanism Using the Saturation Phenomenon

Jorge Luis Palacios Felix, José Manoel Balthazar, Ângelo Marcelo Tusset, Vinícius Piccirillo, Atila Madureira Bueno and Reyolando Manoel Lopes Rebello da Fonseca Brasil

Abstract In this paper a robotic arm is modelled by a double pendulum excited in its base by a DC motor of limited power via crank mechanism and elastic connector. In the mathematical model, a chaotic motion was identified for a wide range of parameters. Controlling of the chaotic behaviour of the system were implemented using two control techniques, the nonlinear saturation control (NSC) and the optimal linear feedback control (OLFC). The actuator and sensor of the device are allowed in the pivot and joints of the double pendulum. The NSC is based in the second order differential equations and its action in the pivot/joint of the robotic arm is through of quadratic nonlinearities feedback signals. The OLFC involves the application of two

J.L.P. Felix
Technological Center of Alegrete, UNIPAMPA—Federal University of Pampa, Alegrete, RS, Brazil
e-mail: jorge.felix@unipampa.edu.br

J.M. Balthazar
Mechanical Aeronautics Division, ITA—Aeronautics Technological Institute—São José dos Campos, SP, Brazil

J.M. Balthazar (✉)
Faculty of Mechanical Engineering, UNESP—São Paulo State University, Bauru, SP, Brazil
e-mail: jmbaltha@gmail.com

V. Piccirillo · Â.M. Tusset
Department of Mathematics, UTFPR—Federal Technological University of Paraná, Ponta Grossa, Brazil
e-mail: piccirillo@utfpr.edu.br

Â.M. Tusset
e-mail: tusset@utfpr.edu.br

A.M. Bueno
Department of Control and Automation Engineering, UNESP—São Paulo State University, Sorocaba, Brazil
e-mail: atila@sorocaba.unesp.br

R.M.L.R. da Fonseca Brasil
CECS—Center of Engineering, Modelling and Applied Social Science, UFABC—Federal University of ABC, Santo André, Brazil
e-mail: reyolando.brasil@ufabc.edu.br

M. Belhaq (ed.), *Structural Nonlinear Dynamics and Diagnosis*,
Springer Proceedings in Physics 168, DOI 10.1007/978-3-319-19851-4_8

control signals, a nonlinear feedforward control to maintain the controlled system to a desired periodic orbit, and a feedback control to bring the trajectory of the system to the desired orbit. Simulation results, including of uncertainties show the feasibility of the both methods, for chaos control of the considered system.

1 Introduction

The behavior of dynamical systems with pendulums have been investigated in a variety of approaches such as theoretical and experimental. The non-ideal autoparametric system with pendulum was studied by Sado and Kot [1], and autoparametric system with double pendulum with harmonic excitation was studied by Sado and Gajos [2]. The first detailed study on the non-ideal vibrating systems was done by Kononenko [3]. Following this contribution, the problem of non-ideal vibrating systems has been investigated by a number of authors. A complete review of different theories on non-ideal vibrating systems was discussed and presented in [4]. The dynamic interactions between a parametric pendulum and an electro-dynamical shaker of limited power was investigated in [5]. The authors described a mathematical model of the electromechanical shaker and identified its parameters. The saturation control was proposed in [6–11] using 2:1 internal external resonances in quadratic nonlinearly coupled systems to suppress steady-state vibrations. The effectiveness of the nonlinear saturation control to a non-ideal portal frame was investigated in [12], OFLC was proposed in [13]. In Rafikov and Balthazar [13] the quadratic nonlinear Lyapunov function was proposed to resolve the optimal nonlinear control design problem for a nonlinear system. Being formulated the linear feedback control strategies for nonlinear systems, asymptotic stability of the closed-loop nonlinear system guaranteeing both stability and optimality [14].

We organized this chapter as follows. In Sect. 2 we obtain the mathematical model. In Sects. 3 and 4 we perform the analysis of the dynamic model considering: bifurcation diagrams, time histories, phase portraits, frequency spectrum, wavelet transform and 0–1 test for chaotic behaviour. In Sect. 5 is implemented the NSC and the OLFC. In Sect. 6, through computer simulations, the efficiency and the robustness to parametric errors of each control technique are verified. Finally, some concluding remarks are given.

2 System Description and Governing Equations

We consider a robotic arm modelled by a double pendulum excited at its base (supporting) by a DC motor of limited power via a crank mechanism and a spring, such as the one represented in Fig. 1. The supporting elastic substructure of the robotic arm consists of a rod of mass m and lengths l_1 and l_2 and masses m_1 and m_2, stiffness k and damping c, whose motion is in the vertical direction, and the angular deflection

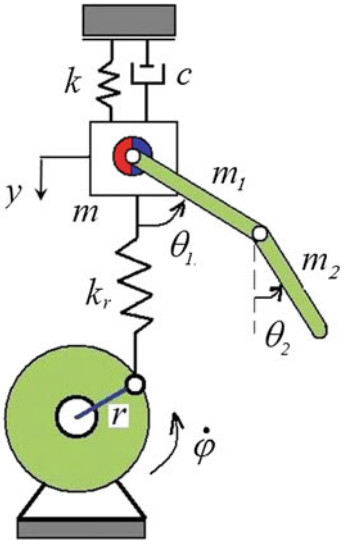

Fig. 1 Robotic arm excited by a non-ideal motor via crank-spring mechanism [15]

of the first pendulum is θ_1 and of the second pendulum is θ_2. We assume that the controlled torque of the unbalanced DC motor as a linear function of its angular velocity, $\Gamma(\dot{\phi}) = V_m - C_m\dot{\phi}$, where V_m is considered as a control parameter and it can be changed according to the voltage of the DC motor, C_m is a constant for each DC motor considered. The coupling between the DC motor and robotic arm will be by a crank mechanism of radius r and elastic connector of stiffness k_r.

From the Lagrange method, the equations of motion for the system can be rearranged as follows:

$$\begin{aligned} l\,(m + m_1 + m_2)\,\ddot{y} + c\dot{y} + ky - l_1(m_1 + m_2)\ddot{\theta}_1 \sin\theta_1 - l_2 m_2 \ddot{\theta}_2 \sin\theta_2 \\ - (m_1 + m_2) l_1 \dot{\theta}_1^2 \cos\theta_1 - m_2 l_2 \dot{\theta}_2^2 \cos\theta_2 = k_r r \sin\phi \end{aligned} \tag{1}$$

$$I\ddot{\phi} = \Gamma(\dot{\phi}) + k_r r(y - r\sin\phi)\cos\dot{\phi} \tag{2}$$

$$\begin{aligned} l(m_1 + m_2) l_1^2 \ddot{\theta}_1 + m_2 l_1 l_2 \ddot{\theta}_2 \cos(\theta_2 - \theta_1) - m_2 l_1 l_2 \dot{\theta}_2^2 \sin(\theta_2 - \theta_1) \\ + (m_1 + m_2) g l_1 \sin\theta_1 + c_1\dot{\theta}_1 - c_2(\dot{\theta}_2 - \dot{\theta}_1) = (m_1 + m_2) l_1 \ddot{y} \sin\theta_1 \end{aligned} \tag{3}$$

$$\begin{aligned} l m_2 l_2^2 \ddot{\theta}_2 + m_2 l_1 l_2 \ddot{\theta}_1 \cos(\theta_2 - \theta_1) + m_2 g l_2 \sin\theta_2 + m_2 l_1 l_2 \dot{\theta}_1^2 \sin(\theta_2 - \theta_1) \\ + c_2(\dot{\theta}_2 - \dot{\theta}_1) = m_2 l_2 \ddot{y} \sin\theta_2 \end{aligned} \tag{4}$$

where dots indicate differentiations with respect to dimensionless time. The following dimensionless quantities are introduced for further analysis:

$$\tau = \omega_0 t, \quad y_0 = \frac{y}{l_1}, \quad \omega_0^2 = \frac{k}{m_t}, \quad m_t = m + m_1 + m_2, \quad \Gamma(\dot{\phi}) = a - b\dot{\phi}, \quad \omega_1^2 = \frac{g}{l_1}, \quad \omega_2^2 = \frac{g}{l_2},$$
$$\alpha_1 = \frac{m_1 + m_2}{m_t}, \quad \alpha_2 = \frac{m_2}{m_t}, \quad R = \frac{l_2}{l_1}, \quad \eta_1 = \frac{k_r r}{k l_1}, \quad \alpha_3 = \frac{m_2}{m_1 + m_2}, \quad \Omega_1 = \frac{\omega_1}{\omega_2}, \quad \Omega_2 = \frac{\omega_2}{\omega_0},$$
$$\mu_1 = \frac{c_1}{(m_1 + m_2)\,\omega_0 l_1^2}, \quad \mu_2 = \frac{c_2}{(m_1 + m_2)\,\omega_0 l_1^2}, \quad \mu_3 = \frac{c_2}{m_2 \omega_0 l_2^2}, \quad \eta_2 = \frac{k_r r l_1}{I\omega_0^2}, \quad \eta_3 = \frac{k_r r^2}{I\omega_0^2}.$$

Thus, the dimensionless form of the mathematical model can be written as follows

$$\begin{cases} x_1' = x_2 \\ x_2' = \alpha_1 x_4' \sin x_3 + R\alpha_2 \sin x_5 + \alpha_1 x_4^2 \cos x_3 + R\alpha_2 x_6^2 \cos x_5 - \mu_0 x_2 - x_1 + \eta_1 \sin x_7 \end{cases} \tag{5}$$

$$\begin{cases} x_3' = x_4 \\ x_4' = \alpha_3 R x_6' \cos(x_5 - x_3) + x_2' \sin x_3 - \Omega_1^2 \sin x_3 + R\alpha_3 x_6^2 \sin(x_5 - x_3) - \mu_1 x_4 + \mu_2 (x_6 - x_4) \end{cases} \tag{6}$$

$$\begin{cases} x_5' = x_6 \\ x_6' = -\frac{1}{R} x_4' \cos(x_5 - x_3) + \frac{1}{R} x_2' \sin x_5 - \Omega_2^2 \sin x_5 \\ -\frac{1}{R} x_4^2 \sin(x_5 - x_3) - \mu_3 (x_6 - x_4) \end{cases} \tag{7}$$

$$\begin{cases} x_7' = x_8 \\ x_8' = a - b x_8 + (\eta_2 x_1 - \eta_3 \sin x_7) \cos x_7 \end{cases} \tag{8}$$

where the prime denotes the derivative with respect to time τ and $x_1 = y_0$, $x_2 = \dot{y}_0$, $x_3 = \theta_1$, $x_4 = \dot{\theta}_1$, $x_5 = \theta_2$, $x_6 = \dot{\theta}_2$, $x_7 = \phi$ and $x_8 = \dot{\phi}$.

For the numerical simulation, the following dimensionless parameters are used: $\alpha_1 = 0.3$, $\alpha_2 = 0.17$, $\alpha_3 = 0.5$, $R = 1$, $\mu_1 = 0.01$, $\mu_2 = 0.01$, $\mu_3 = 0.01$, $a = 1.22$, $b = 1.2$, $\Omega_1 = 0.9$, $\Omega_2 = 0.4$, $\eta_1 = 0.05$, $\eta_2 = 0.2$ and $\eta_2 = 0.3$ [15].

3 Scale Index

The wavelet transform of a one-dimensional (1D) signal consists of the development into a basis constructed via solutions like functions called wavelet, using various internal transformations and shifts [16].

Given $f \in L^2(\mathbb{R})$, the Continuous Wavelet Transform (CWT) of f at time v, scale s and time location t is defined as

$$Wf(v,s) := \left\langle f, \psi_{v,s}^* \right\rangle = \int_{-\infty}^{+\infty} f(t)\, \psi_{v,s}^*(t)\, dt \tag{9}$$

where

$$\psi_{v,s} = \frac{1}{\sqrt{s}} \psi\left(\frac{t-v}{s}\right), v \in \mathbb{R}, s > 0 \tag{10}$$

and $Wf(v,s)$ provides the frequency component of the signal of f at time v and scale s with respect to some analyzing wavelet $\psi_{v,s}$.

The scalogram of f, $\wp$, is defined as follows [17]:

$$\wp(s) := \|Wf(v,s)\| = \left(\int_{-\infty}^{+\infty} |Wf(v,s)|^2\, dv \right)^{1/2} \tag{11}$$

where $\wp(s)$ is the energy of the CWT of f at scale s. The scalogram is a useful tool for studying a signal, since it allows the detection of its most representative scales (or frequencies).

Then, the innerscalogram of f at scale s can be defined by [17]:

$$\wp^{inner}(s) := \|Wf(v,s)\|_{J(s)} = \left(\int_{c(s)}^{d(s)} |Wf(v,s)|^2\, dv \right)^{1/2} \tag{12}$$

where $J(s) = [c(s), d(s)] \subseteq I$ is the maximal subinterval in I for which the supported of $\psi_{u,s}$ is included in I for all $u \in J(s)$ [17]. As regards the length of $J(s)$ it depends on the scale s, so that the values of the inner scalogram at different scales cannot be compared. Therefore, the inner scalogram should be normalized as follows [17]

$$\bar{\wp}^{inner}(s) = \frac{\wp^{inner}(s)}{(d(s) - c(s))^{1/2}} \tag{13}$$

The scale index in the scale interval $[s_0, s_1]$ can be defined by the quotient [18]

$$i_{scale} := \frac{\wp(s_{\min})}{\wp(s_{\max})} \tag{14}$$

where $s_{\max}$ is the smallest scale such that $\wp(s) \leq \wp(s_{\max})$ for all $s \in [s_0, s_1]$, and $s_{\min}$ the smallest scale such that $\wp(s_{\min}) \leq \wp(s)$. Note that for compactly supported signals only the normalized inner scalogram will be considered [17].

From its definition, the scale index i_{scale} is such that $0 \leq i_{scale} \leq 1$ and it can be interpreted as a measure of the degree of non-periodicity of the signal: the scale index will be zero or close to zero for periodic sequences and close to one for highly non-periodic sequences [18].

According to [17], an important corollary about compactly supported wavelet can be announce as

Corollary 1 *Let $f : I = [a, b] \rightarrow \mathrm{C}$ a T-periodic function in $L^2(a, a + b)$. If ψ be a compactly supported wavelet, then (normalized) inner scalogram of f at scale $2T$ is zero. (for more details, see [17]).*

4 Numerical Simulation

This system was simulated using the following initial conditions: $\left[0\ 0\ 0\ 0\ \frac{5\pi}{180}\ 0\ 0\ 0\right]$. Figure 2 shows the bifurcation diagram for the parameter (μ_0). It is possible to see that for a given value of the parameter (μ_0) the system of (5)–(8) have regions with dense bands of points where we cannot identify the period of the attractor, which indicates a chaotic behavior [15].

In order to determine the value of parameter μ_0 in which the system is chaotic, the 0–1 test was applied. The 0–1 test for chaos takes as input a time series of measurements and returns a single scalar value. If this value is closed to 0 (zero) then the system is periodic, on the other hand, when the value is closed to 1 (one) the system is chaotic [20].

According to [19] the correlation coefficient $\bar{K}$ can be obtained from:

$$\bar{K} = \frac{\mathrm{cov}(X, M(c))}{\sqrt{\mathrm{var}(X)\mathrm{var}(M(c))}} \tag{15}$$

where vectors $X = [1, 2, \ldots, \mathrm{n_{max}}]$, $\mathrm{M(c)} = [\mathrm{M(1, c)}, \ldots, \mathrm{M(1, n_{max})}]$, $c \in (0, \pi)$ is a fixed frequency chosen arbitrarily, and:

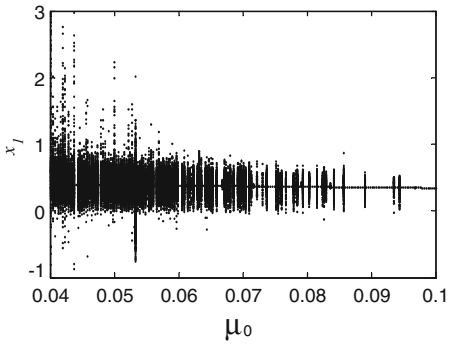

Fig. 2 Bifurcation diagram for μ_0

$$M(n,c) = \lim_{N\to\infty} \frac{1}{N} \sum_{j=1}^{N} \left[(p(j+n) - p(j))^2 + (q(j+n) - q(j))^2 \right] \tag{16}$$

$$p(i) = \sum_{j=0}^{i} \frac{(x_j - \bar{x})}{\sigma_x} \cos(jc); q(i) = \sum_{j=0}^{i} \frac{(x_j - \bar{x})}{\sigma_x} \sin(jc) \tag{17}$$

where $M(n,c)$ is the mean square displacement (MSD) of the variables $p\ q$, $\bar{x}$ is the mean value, σ_x is the square deviation of examined x_i series, and N is the length of the sampled points in the displacement time series.

As a final result, the value of the searched parameter K_c is obtained taking the median of 100 different values of the parameter $\bar{c} \in (0, \pi)$ in (15). A value of $K_c \cong 0$ indicates a non-chaotic data set while a value of $K_c \cong 1$ indicates a chaotic data set. Figure 3 includes the analysis of the system. The parameter range of μ_0 has been verified and a region where chaotic orbits are found.

In Figs. 4, 5 and 6 one can observe the behaviour of the system (5)–(8) for $\mu_0 = 0.076$.

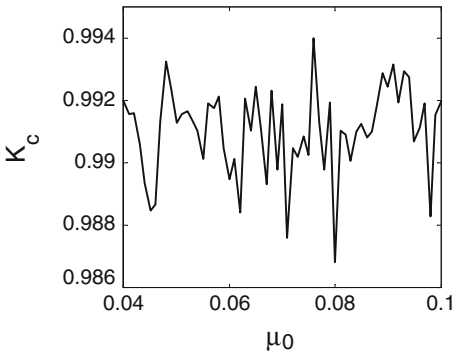

Fig. 3 Asymptotic growth rate (K_c) from 0–1 test as a function of parameter μ_0

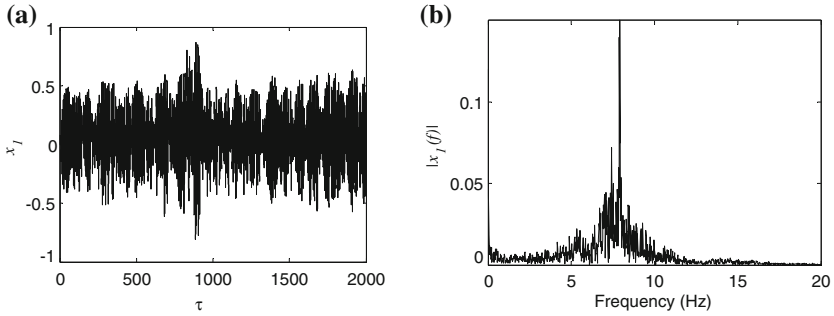

Fig. 4 Behaviour of x_1 for $\mu_0 = 0.076$. **a** Vertical movement. **b** Frequency spectrum

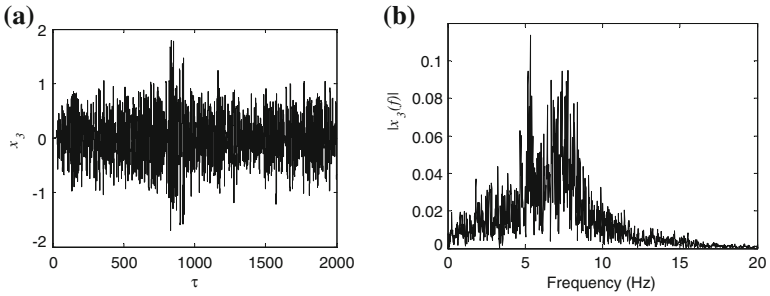

Fig. 5 Behaviour of x_3 for $\mu_0 = 0.076$. **a** Angular movement. **b** Frequency spectrum

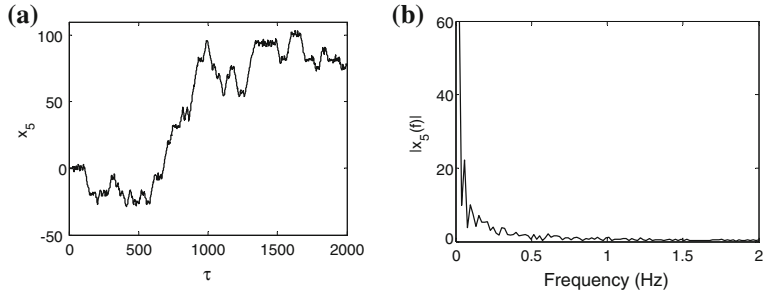

Fig. 6 Behaviour of x_5 for $\mu_0 = 0.076$. **a** Angular movement. **b** Frequency spectrum

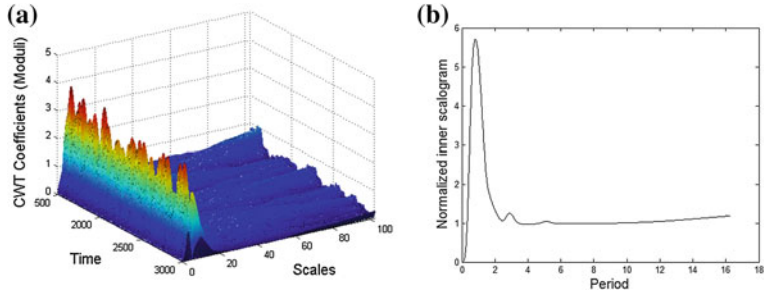

Fig. 7 **a** Modulus of CWT and **b** Normalized inner scalogram for $\mu_0 = 0.076$

As we can see in Figs. 3, 4, 5 and 6 for $\mu_0 = 0.076$, the system (5)–(8) has a chaotic behaviour. Figure 7a shows the modulus of wavelet transform (i. e. $|Wf(u,s)|$) for the time series of $\mu_0 = 0.076$, the wavelet of the 1D analyzed signal is shown as surface in 3D space, in which the z-axis denotes the modulus, the x-axis denotes the time and the y-axis denotes the scales. The relation between frequency parameter α and scale parameter s is $\alpha = \frac{2\pi}{s}$ [20]. It is seen from Fig. 7b that the normalized inner scalogram is not zero, therefore the signal is non-periodic; the same results was observed in 0–1 test. On the other hand, Fig. 8b shows that

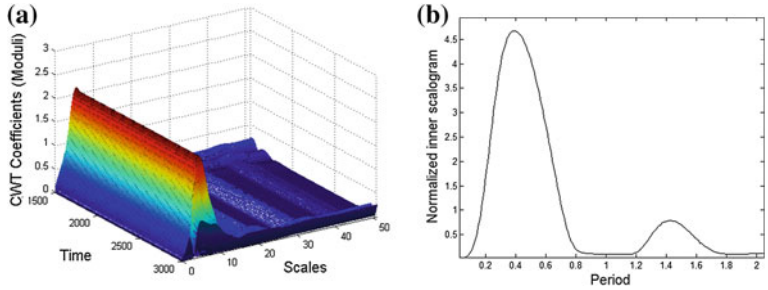

Fig. 8 **a** Modulus of CWT and **b** Normalized inner scalogram for $\mu_0 = 0.0762$

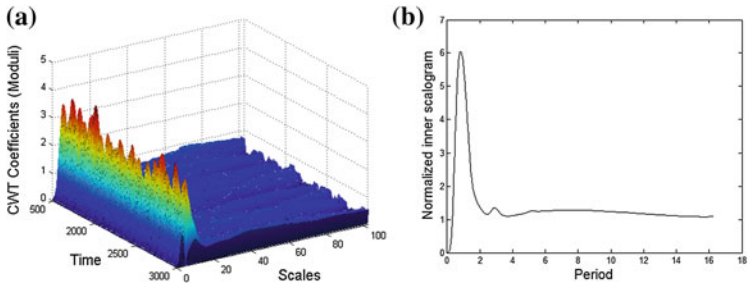

Fig. 9 **a** Modulus of CWT and **b** Normalized inner scalogram for $\mu_0 = 0.0763$

Table 1 Comparative analysis of diagnostic scale index

Parameters	Scale index	Behavior
μ_0	i_{scale}	–
0.076	0.17	Non-periodic
0.0762	0.02	Periodic
0.0763	0.17	Non-periodic

the normalized inner scalogram is equal zero for $\mu_0 = 0.076$ which corresponds to a periodic signal with period $T = 1$. Figure 9 shows one of the main obvious differences is that distribution of scales is randomly vs. time and CWT modulus. It is worth noting that this observation is verified by the normalized inner scalogram which is not zero. In Table 1 are listed the values of the scale index, together with the value of the parameter where highly non-periodic orbits correspond to values close to 1 and where periodic orbits correspond to the values close to 0.

5 Proposed Control

In this section, we propose two control methods with the objective of eliminate the chaotic behaviour of the system (5)–(8). To do so, we consider the introduction of a control signal U applied in the support of the robotic arm to satisfy the saturation phenomenon in linear form and no rotational, into the system (5):

$$\begin{cases} x_1' = x_2 \\ x_2' = \alpha_1 x_4' \sin x_3 + R\alpha_2 \sin x_5 + \alpha_1 x_4^2 \cos x_3 + R\alpha_2 x_6^2 \cos x_5 - \mu_0 x_2 - x_1 \\ + \eta_1 \sin x_7 + U \end{cases} \tag{18}$$

A block diagram representation of the controller proposed in this work is presented Fig. 10.

5.1 Formulation of NSC

In this section, we implement the following nonlinear saturation control:

$$U = \gamma_1 u^2 \tag{19}$$

where u is obtained from the following equation [12]:

$$\ddot{u} + \mu_c \dot{u} + \omega_c^2 u = \gamma_2 x_1 u \tag{20}$$

where ω_c is the controller's natural frequency, γ_1 and γ_2 are positive constants. The internal resonance condition is considered by letting $2\omega_c \approx 1$ and external resonance $\dot{\phi} \approx 1$.

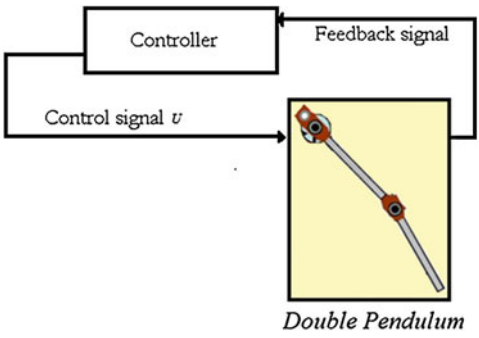

Fig. 10 Control applied in the support of the robotic arm asymptotic growth rate [15]

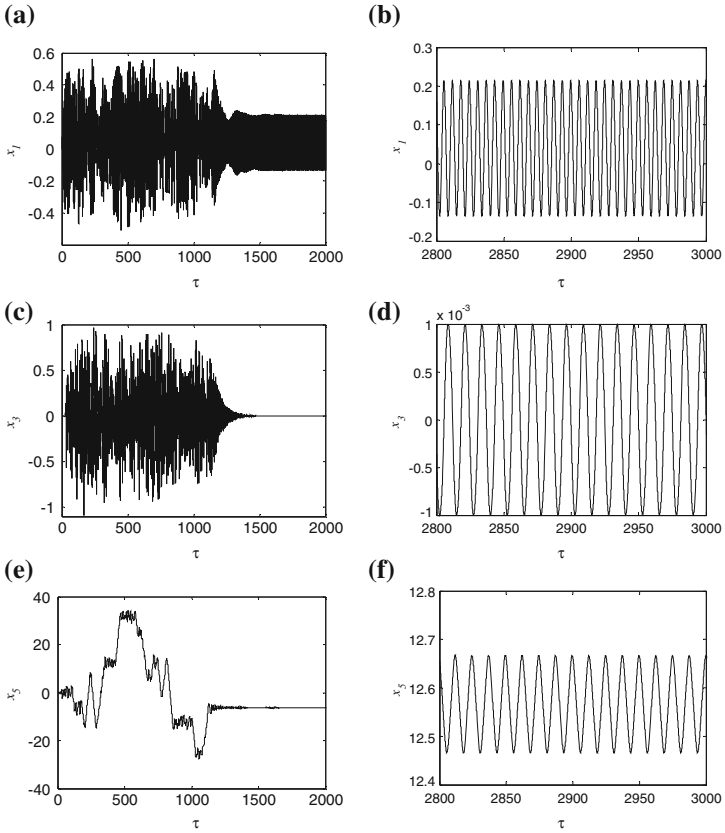

Fig. 11 Behaviours for $\mu_0 = 0.076$. **a** Vertical movement x_1. **b** Vertical movement x_1 excluding the transient behavior. **c** Angular movement x_3. **d** Angular movement x_3 excluding the transient behavior. **e** Angular movement x_5. **f** Angular movement x_5 excluding the transient behavior

In Fig. 11 we can observe the behaviour of the system (5)–(8) with the proposed control (19) considering the following parameters: $\gamma_1 = 0.01$; $\gamma_2 = 0.07$; $\mu_c = 0.01$; $\omega_c = 0.5$ and initial conditions: $u(0) = 0.1$ and $\dot{u}(0) = 0$, excluding the transient behavior. Furthermore, if we compare the results obtained in Figs. 11 and 4, adopting the parameter $\mu_0 = 0.076$, the NSC can effectively suppress the chaotic behavior, and therefore it becomes possible to change the behavior of the system.

We can see in Fig. 11 that the nonlinear saturation control is effective in bringing the system to a periodic behavior with a transient behavior of approximately $\tau \approx 1500$.

5.2 Control Using OLFC

Next, we will present the optimal linear control strategy for nonlinear systems [21]. It is important to observe that this approach is analytical, without dropping any nonlinear term [22]. The vector control U in (18) is consisting of two parts, namely, $U = u_{ff} + u_{fb}$, where u_{ff} is the feedforward control and u_{fb} is the linear feedback control. Defining the period orbit, as being a function of $\left[x_1^*(\tau)\ x_2^*(\tau) \right]^T$, if the function $\left[x_1^*(\tau)\ x_2^*(\tau) \right]^T$ is the solution of (18), without the control U, then $u_{fb} = 0$. In this way, the desired regime is obtained by the following equations:

$$\begin{cases} x_1^{*'} = x_2^* \\ x_2^{*'} = \alpha_1 x_4' \sin x_3 + R\alpha_2 \sin x_5 + \alpha_1 x_4^2 \cos x_3 + R\alpha_2 x_6^2 \cos x_5 - \mu_0 x_2^* - x_1^* \\ +\eta_1 \sin x_7 + u_{ff} \end{cases} \tag{21}$$

Isolating u_{ff} in the second equation (20) we obtain the feedforward control:

$$\begin{aligned} u_{ff} = x_2^{*'} - \alpha_1 x_4' \sin x_3 - R\alpha_2 \sin x_5 - \alpha_1 x_4^2 \cos x_3 - R\alpha_2 x_6^2 \cos x_5 \\ + \mu_0 x_2^* + x_1^* - \eta_1 \sin x_7 \end{aligned} \tag{22}$$

Substituting (22) into (18) and defining the deviation of the desired trajectory as:

$$z = \begin{bmatrix} x_1 - x_1^* \\ x_2 - x_2^* \end{bmatrix} \tag{23}$$

The system can be represented in the matrix form $z' = Az + Bu$ as:

$$\begin{bmatrix} z_1' \\ z_2' \end{bmatrix} = \begin{bmatrix} 0 & 1 \\ -1 & -\mu_0 \end{bmatrix} \begin{bmatrix} z_1 \\ z_2 \end{bmatrix} + \begin{bmatrix} 0 \\ 1 \end{bmatrix} u_{fb} \tag{24}$$

The control u_{fb} can be found to solve the following equation:

$$u_{fb} = -R^{-1} B^T P z \tag{25}$$

where P is a matrix symmetric, and can be find solving the Algebraic Riccati Equation:

$$PA + A^T P - PBR^{-1} B^T P + Q = 0 \tag{26}$$

According to [23], if there exist matrices Q and R, with positive definite symmetric matrix, such that the matrix:

$$\tilde{Q} = Q - G^T(z, u^*) P - PG(z, u^*) \tag{27}$$

is positive definite for the limited matrix $G(z, u^*)$ then the control u_r is optimal and transfers the non-linear systems (18) from any initial state to final state $z(\infty) = 0$, minimizing the functional:

$$J = \int_0^\infty (z^T \tilde{Q} z + u_r^T R u_r) dt \tag{28}$$

In addition, with the feedback control (25), there exists a neighborhood $\Gamma_0 \subset \Gamma$, $\Gamma \subset \Re^n$, of the origin such that if $z_0 \in \Gamma_0$, the solution $z(\tau) = 0, \tau \geq 0$, of the controlled system (18) is locally asymptotically stable, and $J_{\min} = z_0^T P z_0$. Finally, if $\Gamma = \Re^n$ then the solution $z(\tau) = 0, \tau > 0$, of the controlled system (18) is globally asymptotically stable [13, 14].

What can be demonstrated considering the Dynamic Programming rules is that if the minimum of functional (28) exists and if V is a smooth function of the initial conditions, then it satisfies the Hamilton-Jacobi-Bellman equation [13, 14]:

$$\min_u \left(\frac{dV}{dT} + z^T \tilde{Q} z + u_r^T R u_r \right) = 0 \tag{29}$$

Considering a function:

$$V = z^T P z \tag{30}$$

and substituting $\dot{V}$ in the Hamilton-Jacobi-Bellman equation (29) one obtains:

$$z^T \left[A^T P + P A - P B R^{-1} B^T P + G^T(z, u^*) P + P G(z, u^*) + \tilde{Q} \right] z = 0 \tag{31}$$

Then $\tilde{Q} = Q - G^T(z, u^*) P - P G(z, u^*)$. Note that for positive definite matrices $\tilde{Q}$ and R, the derivative of the function (30) is given by $\dot{V} = -z \tilde{Q} z - u_r^T R u_r$ which is negative definite. Then, the function (30) is Lyapunov function, and the controlled system (18) is locally asymptotically stable. Integrating the derivative of the Lyapunov function (31) given by $\dot{V} = -z \tilde{Q} z - u_r^T R u_r$ along the optimal trajectory, we obtain $J_{\min} = z_0^T P z_o$. Finally, if $\Gamma = \Re^n$, global asymptotic stability follows as a direct consequence of the radial unbondedness condition for the Lyapunov function (30) $V(z) \to \infty$ as $\|z\| \to \infty$ [13, 14].

According to [13, 14], and to analyze the cases for which the matrix $\tilde{Q}$ is analytically difficult, it is possible to analyze numerically considering the function:

$$L(\tau) = z^T(\tau) \tilde{Q}(\tau) z(\tau) \tag{32}$$

Define the desired orbits to periodic orbits obtained with the nonlinear saturation control (Fig. 11a) obtained through the use of Fourier series, calculated numerically as [15]:

$$\begin{cases} x_1^* = 0.0393 + 0.1749 \sin\left(\frac{2\pi}{7}\tau\right) \\ x_2^* = \frac{0.3498\pi}{7} \cos\left(\frac{2\pi}{7}\tau\right) \end{cases} \tag{33}$$

The matrixes A, B and G may be represented by:

$$A = \begin{bmatrix} 0 & 1 \\ -1 & -0.076 \end{bmatrix}, \quad B = \begin{bmatrix} 0 \\ 1 \end{bmatrix} \quad \text{and} \quad G = \begin{bmatrix} 0 \\ 0 \end{bmatrix} \tag{34}$$

By defining:

$$Q = \begin{bmatrix} 10^4 & 0 \\ 0 & 10 \end{bmatrix}, \quad R = [10] \tag{35}$$

and solving the Algebraic Riccati equation (26), we get:

$$P = \begin{bmatrix} 1442.2713 & 99.005 \\ 99.005 & 14.3467 \end{bmatrix} \tag{36}$$

Substituting it into (25), we obtain the control:

$$u_{fb} = -99.005 z_1 - 14.3467 z_2 = -99.005(x_1 - x_1^*) - 14.3467(x_2 - x_2^*) \tag{37}$$

Considering (37) and (22) leads to the control U:

$$\begin{aligned} U = {} & -99.005(x_1 - x_1^*) - 14.3467(x_2 - x_2^*) + x_2^{*'} - \alpha_1 x_4' \sin x_3 - R\alpha_2 \sin x_5 \\ & - \alpha_1 x_4^2 \cos x_3 - R\alpha_2 x_6^2 \cos x_5 + \mu_0 x_2^* + x_1^* - \eta_1 \sin x_7 \end{aligned} \tag{38}$$

In Fig. 12 we observe the controlled system (5)–(8) in the orbit (21), with: $\left|x_1 - x_1^*\right| < 10^{-6}$, excluding the transient behavior.

As can be seen, the proposed control (38), took the system to the desired orbit (21), with transient less than 2τ.

It can be observed in Fig. 13 that $L(\tau)$ is positive semidefinite, which ensures that the control (37) is optimal.

5.3 Comparison Between NSC Control and OLFC Control

In Fig. 14 we can observe the behavior of the system (5)–(8) using NSC control and OLFC control.

In Fig. 15 we show the variation of the control signal used to NSC control and OLFC control.

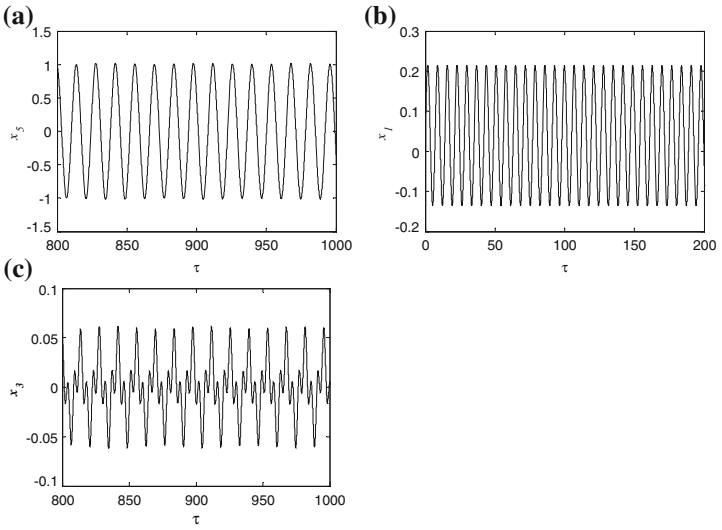

Fig. 12 **a** Vertical movement x_1. **b** Angular movement x_3. **c** Angular movement x_5 for $\mu_0 = 0.076$

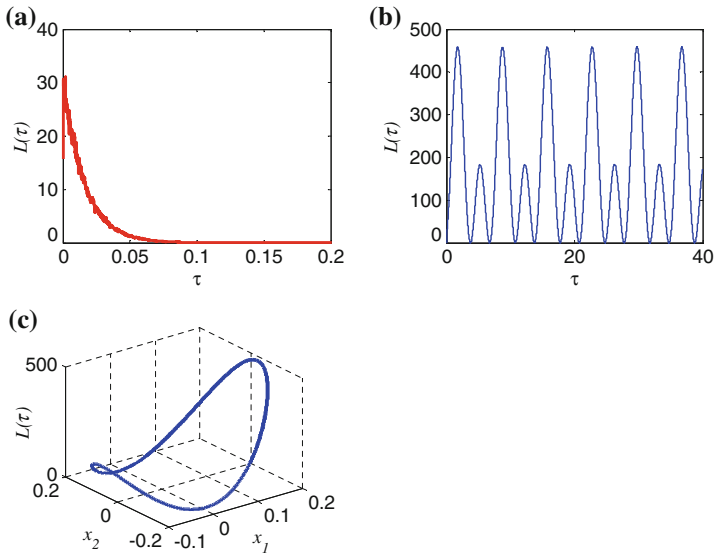

Fig. 13 **a** Variation of the function $L(\tau)$: (a) Variation by z and τ. **b** Variation by x and τ. **c** Variation by x_1 and x_2 for $\mu_0 = 0.076$

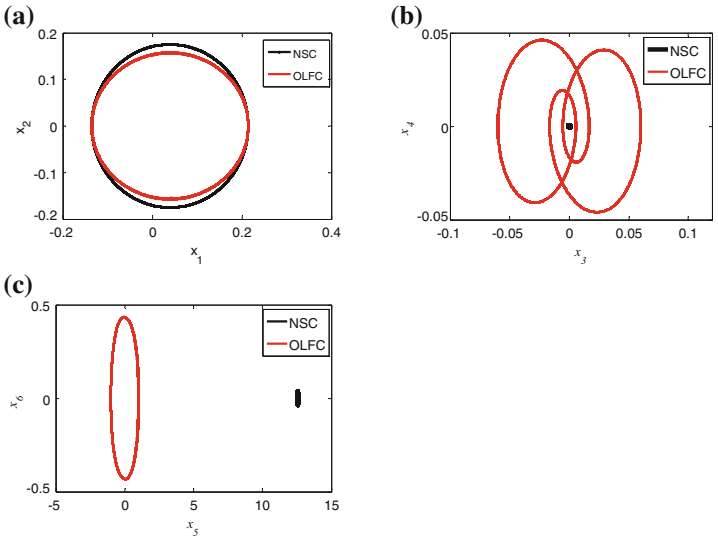

Fig. 14 Phase diagram. **a** Movement x_1. **b** Angular x_3. **c** Angular x_5 for $\mu_0 = 0.076$

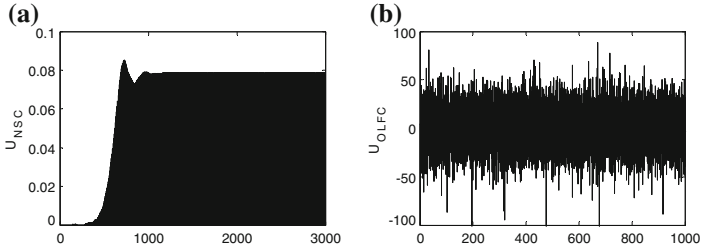

Fig. 15 Control signal U. **a** Signal used in NSC control. **b** Signal used in OLFC for $\mu_0 = 0.076$

To eliminate the transitory period and maintain the system in a defined orbits, the OLFC control uses a higher signal than the NSC control. We can also observed in Fig. 14 that even with x_1 being similar for the two controls, it was not possible to obtain the same behavior for other states.

6 Control in the Presence of Parametric Errors

In order to consider the uncertainty effects on the performance of the controller, the parameters used in the control will be considered as individual variations of $\pm 20\,\%$, and a random error of $\pm 20\,\%$ [24, 25]. A sensitivity analysis will be carried out considering the error: $e_i = x_i - \tilde{x}_i$ for $i = 1 : 6$, where x_i are the states of the system with control, and without parametric error, and $\tilde{x}_i$ are the states with control and parametric errors.

6.1 NSC with Parametric Error

In Fig. 16 we can observe that the NSC control maintains x_1 in periodic orbits, even when parametric errors occur, and in this case we consider: $\gamma_1 = 0.01 \times \psi$, $\gamma_2 = 0.07 \times \psi$, $\mu_c = 0.01 \times \psi$, $\omega_c = 0.5 \times \psi$, where $\psi = 0.8 : 1.2$.

As can be depicted in Fig. 16d the control is sensitive to variations in the parameter ω_c, which should occur because the necessary condition for using this technique is $2\omega_c \approx 1$. In Fig. 17, we can observe the periodic oscillation of the system (5)–(8) with control (13) and $\gamma_1 = 0.008 + 0.004\, r(t)$, $\gamma_2 = 0.056 + 0.028\, r(t)$, $\mu_c = 0.008 + 0.004 r(t)$, $\omega_c = 0.008 + 0.004 r(t)$, and $r(t)$ is normally distributed random function. Furthermore, in this figure we can observe the ability of the control to reproduce the behavior of the system without parametric errors.

It can also be observed in Fig. 17 that the control reproduces satisfactorily the variables x_1 and x_2, but the control is not able to reproduce the behaviour of the other states.

The behavior of the system (5)–(8) with control (38) is illustrated in Fig. 18, considering $\mu_0 = 0.076 \times \psi$,$\alpha_1 = 0.3 \times \psi$, $\alpha_2 R = 0.17 \times \psi$ and $\eta_1 = 0.05 \times \psi$.

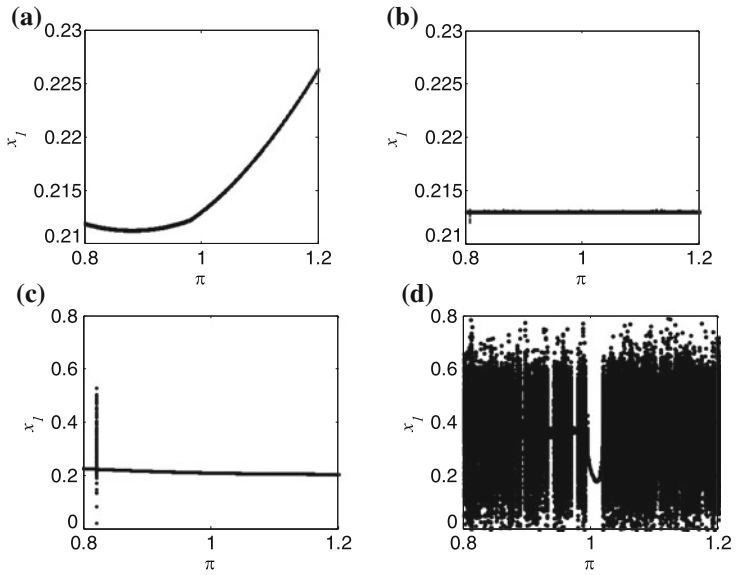

Fig. 16 Sensitivity of NSC control to keep the system on periodic orbits with parametric errors: **a** $\psi \times \mu_c$. **b** $\psi \times \gamma_1$. **c** $\psi \times \gamma_2$. **d** $\psi \times \omega_c$

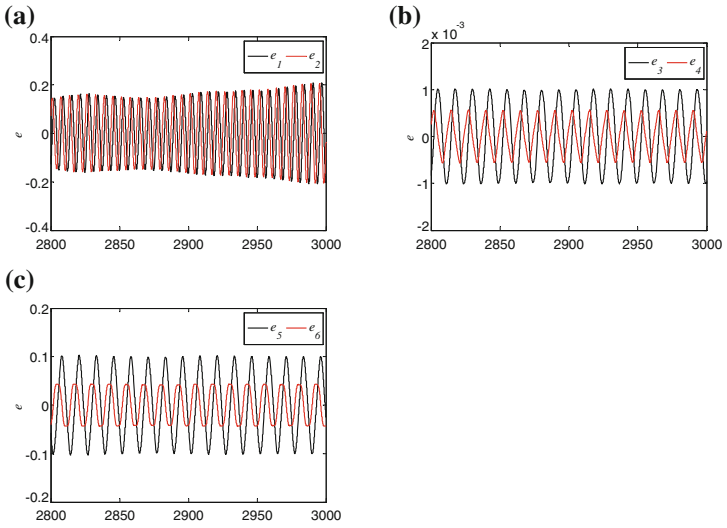

Fig. 17 Sensitivity of NSC control to random parametric errors

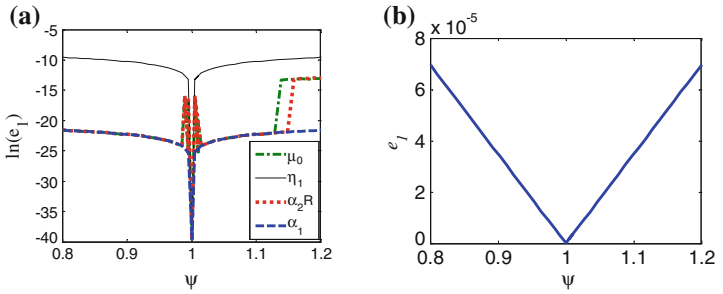

Fig. 18 Sensitivity of OLFC control to parametric errors $e_1 = x_1 - \tilde{x}_1$: **a** $\ln(e_1)$. **b** Error $e_1 = x_1 - \tilde{x}_1$ by parameter μ_0

In Fig. 19, we can observe the periodic oscillations of the system (5)–(8) with control (38), and the following parameters: $\alpha_1 = 0.24 + 0.12\, r(t)$; $\alpha_2 = 0.136 + 0.068\, r(t)$; $R = 0.8 + 0.4 r(t)$; $\mu_0 = 0.0608 + 0.0304\, r(t)$ and $\eta_1 = 0.04 + 0.02\, r(t)$.

As we can see from Figs. 16 and 17, the NSC control is sensitive in maintaining the behavior of the system in a periodic orbit obtained with control without uncertainty in parameters. It is indicated from Figs. 18 and 19 that the OLFC control has proven to be robust to parameter uncertainties.

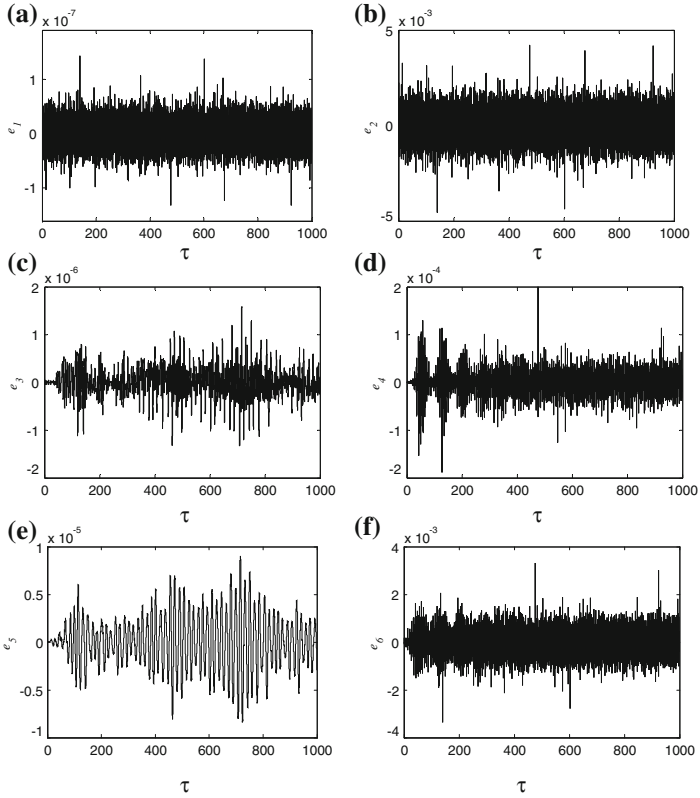

Fig. 19 Sensitivity of OLFC control to random parametric errors

7 Conclusions

We have considered the robotic arm modeled by a double pendulum excited in its base (supporting) by a DC motor of limited power via crank mechanism and spring. The dynamical interactions is investigated by means of phase portraits, bifurcation diagrams, the power spectrum (FFT), wavelet transform and 0–1 test, showing the existence of chaotic behavior for some parameters. The two control strategies have shown to be effective in stabilizing the system in a periodic orbit. With the application of the time delay control for the desired orbit and optimal control to maintain the desired orbit, it was possible to associate the two controls to obtain less time and more robust system a periodic orbit.

NSC technique proved its efficiency to take the system to a periodic orbit, but requiring a relatively large time. We have observed also through the analysis of sensitivity to parametric errors, that this approach is not efficient in maintain the

system in its original orbit, considering the case of the control having variations in their parameters. The results showed that nonlinear saturation control is indicated for cases where there is no need to maintain the system at predetermined orbits, and for the cases where the time stabilization is not a priority and must be a relationship between the internal resonance (ω_c) and the external resonance (ω) is ($2\omega_c \approx \omega$). The OLFC, allow us to obtain a more robust control than the NSC, as demonstrated in sensitivity simulations to parametric errors. The results demonstrate that this control is a good choice for those cases where it is desired to minimize the time stabilization of the system at a predetermined orbit, as well as being able to reproduce the behavior even though the control is subjected to parametric errors. However, for using this control strategy efficiently it is necessary to determine the desired behavior, and it is also necessary to use a much higher control signal used for controlling the NSC.

References

1. Sado, D., Kot, M.: Nonlinear oscillations of a coupled autoparametrical system with ideal and nonideal sources of power. Math. Probl. Eng. **1–20** (2006)
2. Sado, D., Gajos, K.: Note on chaos in three degree of freedom dynamical system with double pendulum. Meccanica **38**, 719–729 (2003)
3. Kononenko, V.O.: Vibrating Systems with Limited Power Supply. Illife Books, London (1969)
4. Balthazar, J.M., Mook, D.T., Weber, H.I., Brasil, R.M.L.R.F., Fenili, A., Belato, D., Felix, J.L.P.: An overview on non-ideal vibrations. Meccanica **38**(6), 613–621 (2003)
5. Xu, X., Pavlosvskaia, E., Wiercigroch, M., Romeo, F., Lenci, S.: Dynamic interactions between parametric pendulum and electro-dynamical shaker. ZAMM **87**(2), 172–186 (2007)
6. Golnaraghi, M.F.: Vibration suppression of flexible structure using internal resonance. Mech. Res. Commun. J. **18**, 135–143 (1991)
7. Oueini, S.S., Nayfeh, A.H., Golnaraghi, M.F.: A theoretical and experimental implementation of a control method based on saturation. Nonlinear Dyn. **13**, 189–202 (1997)
8. Oueini, S.S.: Techniques for controlling structural vibrations, PhD Thesis, Virginia Tech, Blacksburg (1999)
9. Pai, P.F., Schulz, M.J.: A refined nonlinear vibration absorber. Int. J. Mech. Sci. **42**, 537–560 (2000)
10. Pai, P.F., Wen, B., Naser, A.S., Schulz, M.J.: Structural vibration control using PZT patches and non-linear phenomena. J. Sound Vib. **215**(2), 273–296 (1998)
11. Shoeybi, M., Ghorashi, M.: Control of a nonlinear system using the saturation phenomenon. Nonlinear Dyn. **42**, 113–136 (2005)
12. Felix, J.L.P., Balthazar, J.M., Brasil, R.M.L.R.F.: On saturation control of a non-ideal vibrating portal frame foundation type shear-building. J. Vib. Control **11**, 121–136 (2005)
13. Rafikov, M., Balthazar, J.M.: On an optimal control design for Rössler system. Phys. Lett. A **333**, 241–245 (2004)
14. Rafikov, M., Balthazar, J.M., Tusset, A.M.: An optimal linear control design for nonlinear systems. J. Braz. Soc. Mech. Sci. Eng., **XXX**(4), 279–284 (2008)
15. Felix, J.L.P., Silva, E.L., Balthazar, J.M., Tusset, A.M., Bueno, A.M., Brasil, R.M.L.R.F.: On nonlinear dynamics and control of a robotic arm with chaos. MATEC Web of Conferences, **16**, 05002–1:6 (2014)
16. Awrejcewicz, J., krysko, A.V., Soldatov, V.: On the wavelet transform application to a study of chaotic vibrations of the infinite length flexible panels driven longitudinally. Int. J. Bifurcat. Chaos **11**, 3347–3371 (2011)

17. Benítez, R., Bolós, V.J., Ramírez, M.E.: A wavelet-based tool for studying non-periodicity. Comput. Math. Appl. **60**, 634–641 (2010)
18. Akhshani, A., Akhavan, A., Mobaraki, A., Lim, S.-C., Hassan, Z.: Pseudo random number generator based on quantum chaotic map. Commun. Nonlinear Sci. Numer. Simul. **19**, 101–111 (2014)
19. Bernardini, D., Rega, G., Litak, G., Syta, A.: Identification of regular and chaotic isothermal trajectories of a shape memory oscillator using the 0–1 test. Proc. Inst. Mech. Eng. Part K J. Multi-body Dyn. **227**, 14–22 (2013)
20. Wong, L.A., Chen, J.C.: Nonlinear and chaotic behavior of structural system investigated by wavelet transform techniques. Int. J. Non-Linear Mech. **36**, 221–235 (2001)
21. Tusset, A.M., Balthazar, J.M., Chavarette, F.R., Felix, J.L.P.: On energy transfer phenomena, in a nonlinear ideal and nonideal essential vibrating systems, coupled to a (MR) magneto-rheological damper. Nonlinear Dyn. **69**, 1859–1880 (2012)
22. Nozaki, R., Balthazar, J.M., Tusset, A.M., Pontes JR, B.R., Bueno, A.M.: Nonlinear control system applied to atomic force microscope including parametric errors. J. Cont. Auto. Elect. Sys. **24**, 223–231 (2013)
23. Pedroso, M.D., Nascimento, C.B., Tusset, A.M., Kaster M.S.: A hyperbolic tangent adaptive pid+lqr control applied to a step-down converter using poles placement design implemented in fpga, Mathematical problems in engineering, pp. 1–8 (2013)
24. Shirazi, M.J., Vatankhah, R., Boroushaki, M., Salarieh, H., Alasty, A.: Application of particle swarm optimization in chaos synchronization in noisy environment in presence of unknown parameter uncertainty. Commun. Nonlinear Sci. Numer. Simul. **17**(2), 742–753 (2012)
25. Tusset, A.M., Balthazar, J.M., Chavarette, F.R., Felix, J.L.P.: On energy transfer phenomena, in a nonlinear ideal and nonideal essential vibrating systems, coupled to a (MR) magneto-rheological damper. Nonlinear Dyn. **69**, 1859–1880 (2012)

Quasi-Coordinates Based Dynamics Control Design for Constrained Systems

Elżbieta M. Jarzębowska

Abstract The paper presents model-based dynamics control design for constrained systems which exploits dynamics modeling in quasi-coordinates. These non-inertial coordinates are useful in motion description of constrained systems as well as in a controller design, since they offer many advantages in both areas. Specifically, a dynamics model formulation results in a reduced-state form of the motion equations. The selection of quasi-coordinates is arbitrary so they may satisfy the constraint equations and be control inputs directly. The paper presents an approach to control oriented modeling and a controller design based on the generalized Boltzmann-Hamel equations where the generalization refers to constraint kinds which may be put upon systems, i.e. constraints may be material or artificial like control constraints. The control design framework applies to fully actuated and underactuated systems and it is computationally efficient. Examples of controller designs and their comparisons to a traditional Lagrange model-based framework are presented.

1 Introduction

The paper presents model-based control design for constrained systems which applies dynamics modeling in quasi-coordinates. The constrained systems may be subjected to holonomic, nonholonomic or programmed constraints as well as be fully actuated or underactauted. They constitute a large class of systems of a practical interest and they are usually approached by the Lagrange method with generalized coordinates or its modifications to obtain motion equations for them. The Lagrange based dynamics are also used to generate dynamic control models for these systems. This traditional, almost routine, approach to dynamics modeling results in dynamics that lacks some properties significant from the point of view of further control design. Basically, Lagrange based dynamics can be applied to systems with constraints of first order and the number of unknowns that result from Lagrange's equations increases to

E.M. Jarzębowska (✉)
Warsaw University of Technology, Institute of Aeronautics and Applied Mechanics,
Nowowiejska 24 Street, 00-665 Warsaw, Poland
e-mail: elajarz@meil.pw.edu.pl

M. Belhaq (ed.), *Structural Nonlinear Dynamics and Diagnosis*,
Springer Proceedings in Physics 168, DOI 10.1007/978-3-319-19851-4_9

include the multipliers. In order to obtain a dynamic control model, Lagrange's based dynamics require the elimination of the constraint reaction forces (Lagrange multipliers). Finally, solutions obtained from the Lagrange based models require numerical stabilization due to differentiation of constraint equations, that may complicate on-line simulations and control. Only a few works report applying quasi-coordinates to modeling constrained systems, see e.g. [1, 2].

From the perspective of mechanics and derivation of equations of motion, constrained systems may belong to the same class, e.g. be subjected to first order nonholonomic constraints. From the perspective of nonlinear control theory, they may differ and may not be approached by the same control strategies and algorithms. Their control properties depend upon the way they are designed and propelled. Then, from the nonlinear control theory perspective a system design, way of its propulsion, control goals, other motion or work-space constraints may determine the way of the control-oriented modeling.

The dynamics modeling in quasi-coordinates presented herein, which is incorporated in the model-based control design for constrained systems, eliminates many disadvantages related to Lagrange's based dynamics modeling and a subsequent control design.

Motivations for the development of constrained and control dynamics in quasi-coordinates come from the author experience in the area of modeling and control of constrained systems. Firstly, the constraint kinds that have to be dealt with in control setting are different than the ones considered in analytical dynamics modeling. This has led to the definition of the unified constraint formulation and the derivation of the generalized programmed motion equations [3, 4]. Secondly, a dynamics control model that is passed to a control engineer to design and apply to it an appropriate controller, may be made a control oriented, i.e. may facilitate this controller design. The two motivations are not separate from each other. They both can be appropriately treated at the modeling step of a control design project using the latest modeling tools and the modeling process may serve an effective control design.

In the paper we present the theoretical model-based control oriented modeling framework. It yields equations of motion for constrained systems in quasi-coordinates based on the generalized Boltzmann-Hamel equations [3]. This dynamics framework yields equations of motion of a constrained system in a reduced-state form, from which the dynamic control model directly follows. The framework applies to fully actuated and underactuated systems, it is computationally efficient, and may facilitate a subsequent controller design. Based on the framework, a tracking control strategy dedicated to track predefined motions referred to as programmed may be designed. It is referred to as the model reference tracking control strategy for programmed motion and has been developed for dynamics in generalized coordinates [4]. It can be redesigned to constrained dynamics and control dynamics developed in quasi-coordinates.

The paper contribution is then three folds. Firstly, the model-based control oriented framework for the generation of dynamics for constrained systems formulated in quasi-coordinates, where additionally relations between generalized velocities and quasi-velocities may be nonlinear, is presented. Secondly, the dynamics formulation

in quasi-coordinates is unified in the sense that it is suitable for systems constrained by arbitrary order bilateral constraints. Thirdly, based on this formulation a tracking controller for a system motion along a prescribed program may be designed.

Examples that illustrate the theoretical development demonstrate the effectiveness of the generation of dynamics models using the model-based control oriented modeling framework in quasi-coordinates.

2 An Extended Constraint Concept—Material and Non-material Constraints Imposed Upon System Motions

A control design process consists of three main steps, which are a dynamic model building, a control algorithm design, and a controller implementation. Starting from the model building, constraints imposed on a system should be specified first, and inspected if they are holonomic or nonholonomic. We do not address dynamics modeling and control design of holonomic systems, since these are considered solved problems, at least theoretically [5].

Based on the examples of constraints reported in mechanics and control, we start a control-oriented modeling from a constraint concept revisiting. An extended understanding of constraints is suitable for both dynamics modeling and control applications. The constraints can be classified as follows [4]:

1. Material nonholonomic constraints (NC)—they come from an assumption about rolling vehicle wheels without slipping. They are first order and they are typical for wheeled mobile vehicles or multi-finger hands working on surfaces. Their common form reads

$$\varphi_\beta(t, q_1, ..., q_n, \dot{q}_1, ..., \dot{q}_n) = 0 \qquad \beta = 1, ..., b, \quad b < n \tag{1}$$

   Functions φ_β are defined on a $(2n+1)$-dimensional manifold and have continuous derivatives. Often, the kinematic constraints are linear in velocities, i.e.

$$\sum_{\sigma=1}^{n} b_{\beta\sigma}(t, q_1, ..., q_n)\dot{q}_\sigma + b_{\beta o}(t, q_1, ..., q_n) = 0, \tag{2}$$

   Constraints (1) or (2) restrict accelerations but not positions. They are referred to as first order constraints. In classical mechanics setting they are known as material constraints [6, 7].
2. Conservation laws—they come from the angular momentum conservation for free-floating space manipulators, for an astronaut in a space walk or for a sportsman in an exercise flying phase. Their equation form is the same as (1) [8]. Notice, that in mechanics they are not referred to as constraints. They show up in a control setting.

3. Tasks (programmed constraints)—they can be formulated for any physical system, e.g. a robot or a manipulator and they can specify a task, work to do or a limitation in a system motion, e.g. a limitation in velocity or acceleration. Also, they may specify a trajectory to follow but then it is a holonomic constraint. Many task formulations are reported in [9–12]. However, none of the tasks is formulated in algebraic or differential constraint equation forms at a system modeling level. Such equations are formulated later at a level of a controller design and then a specific controller modification for each task is needed the most often. The earliest formulation of programmed constraints (PC) known to the author was given by Appell in [13]. He described them as constraints "that can be realized not through a direct contact". Similar ideas were introduced by Mieszczerski at the beginning of the 20th century. Beghuin [14] developed a concept of servo-constraints. These new "constraint sources" motivated to specify constraints as

$$\varphi_\beta(t, q_1, ..., q_n, \dot{q}_1, ..., \dot{q}_n) = 0, \qquad \beta = 1, ..., k, \quad k < n \tag{3}$$

The history of evolution of the PC (3) confirms both their usefulness in formulations of requirements for dynamical systems performance and leads to a "unified constraint formulation", which is

$$B_\beta(t, q, \dot{q}, ..., q^{(p)}) = 0, \qquad \beta = 1, ..., k, \ k < n \tag{4}$$

where p is a constraint order and B_β is a k-dimensional vector. Equation (4) can be nonlinear in $q^{(p)}$. Differentiation of (4) with respect to time, until the highest derivative of a coordinate is linear, results in constraint equations linear with respect to this highest coordinate derivative. We assume that "p" stands for the highest order derivative of a coordinate which appears linearly in a constraint equation. For simplicity we assume that they are linear in all p-th order derivatives of q's and we rewrite (4) as

$$B(t, q, \dot{q}, ..., q^{(p-1)})q^{(p)} + s(t, q, \dot{q}, ..., q^{(p-1)}) = 0, \tag{5}$$

which is referred to as a unified constraint formulation [4].

4. Design or control constraints—they can be put upon manipulators, robots and other systems with underactuated degrees of freedom [15]. They have the form (5) with $p = 2$.
5. Other design, control or operation constraints on robots, manipulators and other vehicles or robotic systems, which can be presented as (5):

   - in navigation of wheeled mobile robots, to avoid the wheel slippage and mechanical shock during motion, dynamic constraints such as acceleration limits have to be imposed [9, 10],

- in path planning problems, for car-like robots, to secure motion smoothness two additional constraints are added: on a trajectory curvature and its time derivative so additional constraints of the second and third order are imposed [10],
- in manipulator trajectory tracking, jerk must be limited for reducing manipulator wear and improving tracking accuracy [16],
- in vehicle dynamics, constraints are added when different maneuvers are to be performed [17],
- in robotics where lateral acceleration must be bounded, e.g. path tracking experiments depend on the precision of the odometer. If the lateral acceleration of the vehicle is too large, the wheels can lose close contact to the ground and the odometer data is no longer meaningful [18].

The constraint classification in classical mechanics and a variety of requirements on system's motions reported in the literature can be summarized as follows:

1. Many problems are formulated as synthesis problems and motion requirements may be viewed as non-material constraints imposed on a system before it is designed and put into operation.
2. Constraints that specify motion requirements may be of orders higher than one or two.
3. Non-material constraints may arise in modeling and analysis of electro and biomechanical systems.
4. No unified approach to the specification of non-material constraints or any other unified constraint has been formulated in classical mechanics.

These conclusions lead to the idea of an extended constraint concept [4]. It is formulated in two definitions:

Definition 1 A programmed constraint is any requirement put on a physical system motion specified by (5).

Definition 2 A programmed motion is a system motion that satisfies a programmed constraint (5).

A system can be subjected to both material and programmed constraints. Programmed constraints do not have to be satisfied during all motion of a system.

3 Control Oriented Constrained Dynamics Formulation in Quasi-Coordinates

Nonholonomic systems (NS) are a large class of systems. From the perspective of mechanics and derivation of equations of motion, many of them belong to the same class of systems subjected to first order nonholonomic constraints. They may

be approached by Lagrange's equations with multipliers and these equations are used to generate dynamic control models for them most often [7, 19, 20]. From the perspective of nonlinear control theory, NS differ and may not be approached by the same control strategies and algorithms. Some of them may be controlled at the kinematic level and the other at the dynamic level only. Their control properties depend upon the way they are designed and propelled. Usually, they are divided into two control groups, which are treated separately, the group of fully actuated and the group of underactuated NS [6, 7, 15].

The constrained dynamics which we formulate below can be directly used as a control dynamics, and serves both fully actuated and underactuated systems constrained by the constraints (5) [4].

Let us start from recalling the concepts of quasi-coordinates and quasi-velocities. They were introduced to derive the Boltzmann-Hamel equations of motion. Relations between the generalized velocities and quasi-velocities were assumed linear and non-integrable, i.e.

$$\omega_r = \omega_r(t, q_\sigma, \dot{q}_\sigma), \qquad \sigma, r = 1, ..., n, \tag{6}$$

With respect to the extended constraint concept (5), our first step is to let (6) be nonlinear [3]. Inverse transformations for (6) can be computed as

$$\dot{q}_\lambda = \dot{q}_\lambda(t, q_\sigma, \omega_r). \qquad \lambda = 1, ..., n \tag{7}$$

Quasi-coordinates can be introduced as

$$d\pi_r = \sum_{\sigma=1}^{n} \frac{\partial \omega_r}{\partial \dot{q}_\sigma} dq_\sigma, \qquad r = 1, ..., n \tag{8}$$

and (8) are non-integrable. Based on (6)–(8), q's and ω's are related as

$$dq_\lambda = \sum_{\mu=1}^{n} \frac{\partial \dot{q}_\lambda}{\partial \omega_\mu} d\pi_\mu. \qquad \lambda = 1, ..., n \tag{9}$$

The principal form of the dynamics motion equation [4] has the form

$$\frac{d}{dt} \sum_{\sigma=1}^{n} p_\sigma \delta q_\sigma = \delta T + \sum_{\sigma=1}^{n} Q_\sigma \delta q_\sigma + \sum_{\sigma=1}^{n} p_\sigma \left[(\delta q_\sigma)^{\cdot} - \delta \dot{q}_\sigma \right] \delta q_\sigma. \tag{10}$$

Transforming its left and right hand side terms using the relations between $\delta\pi_r$ and δq_λ we obtain

$$\frac{d}{dt} \sum_{\mu=1}^{n} \tilde{p}_\mu \delta \pi_\mu = \delta \tilde{T} + \sum_{\mu=1}^{n} \tilde{Q}_\mu \delta \pi_\mu + \sum_{r=1}^{n} \tilde{p}_r \left[(\delta \pi_r)^{\cdot} - \delta \omega_r \right] - \sum_{r=1}^{n} \tilde{p}_r \sum_{\mu=1}^{n} W_\mu^r \delta \pi_\mu \tag{11}$$

which is the principal form of the equation of motion in quasi-coordinates for nonlinear $\omega_r = \omega_r(t, q_\sigma, \dot{q}_\sigma)$. W_μ^r are generalized Boltzmann symbols. Quantities $\tilde{p}_\mu$, $\tilde{T}$, $\tilde{Q}_\mu$ are all written in quasi-coordinates.

The generalized form of the Boltzmann-Hamel equations can be derived based on (11). It has the form

$$\sum_{\mu=1}^{n}\left[\frac{d}{dt}\left(\frac{\partial\tilde{T}}{\partial\omega_\mu}\right)-\frac{\partial\tilde{T}}{\partial\pi_\mu}+\sum_{r=1}^{n}\frac{\partial\tilde{T}}{\partial\omega_r}W_\mu^r-\tilde{Q}_\mu\right]\delta\pi_\mu=0. \tag{12}$$

For a holonomic system, $\delta\pi_\mu$, $\mu = 1, ..., n$, are independent and equations of motion are

$$\frac{d}{dt}\left(\frac{\partial\tilde{T}}{\partial\omega_\mu}\right)-\frac{\partial\tilde{T}}{\partial\pi_\mu}+\sum_{r=1}^{n}\frac{\partial\tilde{T}}{\partial\omega_r}W_\mu^r=\tilde{Q}_\mu.\quad \mu=1,...,n \tag{13}$$

Equation (13) are the generalized Boltzmann-Hamel equations for a holonomic system with nonlinear relations between quasi and generalized velocities. For linear relations between quasi and generalized velocities (13) become Boltzmann-Hamel equations derived in, e.g. [21]. Also, it can be easily verified that when quasi-coordinates are equivalent to generalized coordinates, i.e. $\pi_r = q_r, r = 1, ..., n$, and quasi-velocities are generalized velocities, i.e. $\omega_r = \dot{q}_r, r = 1, ..., n$, then (13) are Lagrange's equations with $W_\mu^r = \gamma_{\alpha\mu}^r = 0$.

For a system subjected to material or programmed NC of the form

$$\omega_\beta = \omega_\beta(t, q_\sigma, \dot{q}_\sigma) = 0 \qquad \beta = 1, ..., b \tag{14}$$

relations

$$\delta\pi_\beta = \sum_{\sigma=1}^{n}\frac{\partial\omega_\beta}{\partial\dot{q}_\sigma}\delta q_\sigma = 0, \qquad \beta = 1, ..., b \tag{15}$$

hold for all ω_β. A system has $(n-b)$ degrees of freedom and variations $\delta\pi_{b+1}, ..., \delta\pi_n$ are independent. Then, $(n - b)$ equations of motion, based on (12), have the form

$$\frac{d}{dt}\left(\frac{\partial\tilde{T}}{\partial\omega_\mu}\right)-\frac{\partial\tilde{T}}{\partial\pi_\mu}+\sum_{r=1}^{n}\frac{\partial\tilde{T}}{\partial\omega_r}W_\mu^r=\tilde{Q}_\mu \qquad \mu=b+1,...,n \tag{16}$$

to which n kinematic relations

$$\dot{q}_\lambda = \dot{q}_\lambda(t, q_\sigma, \omega_r), \qquad \sigma, \lambda = 1, ..., n, \ r = b + 1, ..., n \tag{17}$$

have to be added.

Equation (16) are the generalized Boltzmann-Hamel equations for a NS. Notice that b of ω's are satisfied based on the constraint equation (17). The rest of quasi-velocities are selected arbitrarily by a designer. Equations (16) and (17) can be presented as

$$M(q)\dot{\omega} + C(q,\omega) + D(q) = \tilde{Q},$$
$$B(q,\omega) = 0. \tag{18}$$

A system dynamics control model follows directly from (18) since they are free from the constraint reaction forces

$$M(q)\dot{\omega} + C(q,\omega) + D(q) = \tilde{Q} + \tilde{\tau},$$
$$B(q,\omega) = 0. \tag{19}$$

Equation (16) have to be extended to be applicable to systems subjected to NC of high order given by (5). To enable this, the following lemma can be formulated [4].

Lemma *For a function* $\tilde{F}$ *of the form*

$$\tilde{F} = \tilde{F}(t, q_\sigma, \omega_r), \qquad \sigma, r = 1, ..., n \tag{20}$$

where q_σ *and* ω_r *are related by* $\omega_r = \omega_r(t, q_\sigma, \dot{q}_\sigma)$*, the following identity holds*

$$\frac{d}{dt}\left(\frac{\partial \tilde{F}}{\partial \omega_\sigma}\right) = \frac{1}{p}\left(\frac{\partial \tilde{F}^{(p)}}{\partial \omega_\sigma^{(p-1)}} - \frac{\partial \tilde{F}}{\partial \pi_\sigma}\right). \qquad p = 1, 2, 3, .. \tag{21}$$

The proof is by mathematical induction [4]. If we replace $\tilde{F}$ by $\tilde{T} = \tilde{T}(t, q_\sigma, \omega_\sigma)$ in (20) and insert it into the generalized Boltzmann-Hamel equation (12), we get

$$\frac{1}{p}\left[\frac{\partial \tilde{T}^{(p)}}{\partial \omega_\mu^{(p-1)}} - (p+1)\frac{\partial \tilde{T}}{\partial \pi_\mu}\right] + \sum_{r=1}^{n} \frac{\partial \tilde{T}}{\partial \omega_r} W_\mu^r = \tilde{Q}_\mu. \qquad \mu = 1, ..., n, \quad p = 1, 2, 3, \tag{22}$$

Equation (22) are the extended form of the Boltzmann-Hamel equations. Now, modify them for systems with NC of high order

$$\tilde{G}_\beta\left(t, q_\sigma, \omega_r, \dot{\omega}_r, ..., \omega_r^{(p-1)}\right) = 0. \quad \beta = 1, ..., b, \qquad \sigma, r = 1, ..., n, \quad b < n \tag{23}$$

Based on the generalized definition of the virtual displacement

$$\delta G_\beta = \sum_{\sigma=1}^{n} \frac{\partial G_\beta}{\partial q_\sigma^{(p)}} \delta q_\sigma = 0, \tag{24}$$

where $G_\beta = G_\beta(t, q_\sigma, \dot{q}_\sigma, ..., q_\sigma^{(p)})$ are constraints of p-*th* order specified in q's, we obtain that

$$\delta \tilde{G}_\beta = \sum_{r=1}^{n} \frac{\partial \tilde{G}_\beta}{\partial \omega_r^{(p-1)}} \delta \pi_r = 0. \tag{25}$$

In the constraint equation (23) we may partition the vector $\omega^{(p-1)}$ as $\omega^{(p-1)} = \left(\omega_\beta^{(p-1)}\ \omega_\mu^{(p-1)}\right)$ with

$$\omega_\beta^{(p-1)} = \Omega_\beta^{(p-1)}\left(t, q_\sigma, \omega_\sigma, \omega_\sigma, ..., \omega_\mu^{(p-1)}\right). \tag{26}$$

By differentiating (26) with respect to time we obtain

$$\omega_\beta^{p} = \Omega_\beta^{p}\left(t, q_\sigma, \omega_\sigma, \omega_\sigma, ..., \omega_\mu^{(p-1)}, \omega_\mu^{p}\right). \tag{27}$$

Now, using the lemma result we rewrite (12) in the form

$$\begin{aligned}&\sum_{\beta=1}^{b}\left\{\frac{1}{p}\left[\frac{\partial \tilde{T}^{(p)}}{\partial \omega_\beta^{(p-1)}} - (p+1)\frac{\partial \tilde{T}}{\partial \pi_\beta}\right] + \sum_{r=1}^{n}\frac{\partial \tilde{T}}{\partial \omega_r}W_\beta^r - \tilde{Q}_\beta\right\}\delta\pi_\beta \\ &+ \sum_{\mu=b+1}^{n}\left\{\frac{1}{p}\left[\frac{\partial \tilde{T}^{(p)}}{\partial \omega_\mu^{(p-1)}} - (p+1)\frac{\partial \tilde{T}}{\partial \pi_\mu}\right] + \sum_{r=1}^{n}\frac{\partial \tilde{T}}{\partial \omega_r}W_\mu^r - \tilde{Q}_\mu\right\}\delta\pi_\mu = 0.\end{aligned} \tag{28}$$

Based on (25) we have that $\delta\pi_\beta = \sum_{\mu=b+1}^{n}\frac{\partial \Omega_\beta^{(p-1)}}{\partial \omega_\mu^{(p-1)}}\delta\pi_\mu$, $\beta = 1, ..., b$, and then (28) takes the form

$$\begin{aligned}&\tfrac{1}{p}\left[\tfrac{\partial \tilde{T}^{(p)}}{\partial \omega_\mu^{(p-1)}} - (p+1)\tfrac{\partial \tilde{T}}{\partial \pi_\mu}\right] + \sum_{r=1}^{n}\frac{\partial \tilde{T}}{\partial \omega_r}W_\mu^r - \tilde{Q}_\mu \\ &+ \sum_{\beta=1}^{b}\left\{\frac{1}{p}\left[\frac{\partial \tilde{T}^{(p)}}{\partial \omega_\beta^{(p-1)}} - (p+1)\frac{\partial \tilde{T}}{\partial \pi_\beta}\right] + \sum_{r=1}^{n}\frac{\partial \tilde{T}}{\partial \omega_r}W_\beta^r - \tilde{Q}_\beta\right\}\frac{\partial \Omega_\beta^{(p-1)}}{\partial \omega_\mu^{(p-1)}} = 0. \qquad \mu = b+1, ..., n\end{aligned} \tag{29}$$

We refer to (29) as the generalized programmed motion equations (GPME) in quasi-coordinates. For p =1, (29) become (16). They may be presented in a form similar to (19)

$$\begin{aligned}M(q)\dot{\omega} + C(q, \omega) + D(q) &= \tilde{Q}, \\ \tilde{G}_\beta\left(t, q_\sigma, \omega_r, \dot{\omega}_r, ..., \omega_r^{(p-1)}\right) &= 0\end{aligned} \tag{30}$$

4 Design of a Control Strategy Based on the GPME in Quasi-Coordinates

We have reported the derivation of the generalized programmed motion equations (GPME) in quasi-coordinates. They enable deriving a constrained system dynamics with $\omega_\beta^{(p-1)} = \Omega_\beta^{(p-1)}\left(t, q_\sigma, \omega_\sigma, \omega_\sigma, ..., \omega_\mu^{(p-1)}\right)$. If the constraints specify a task

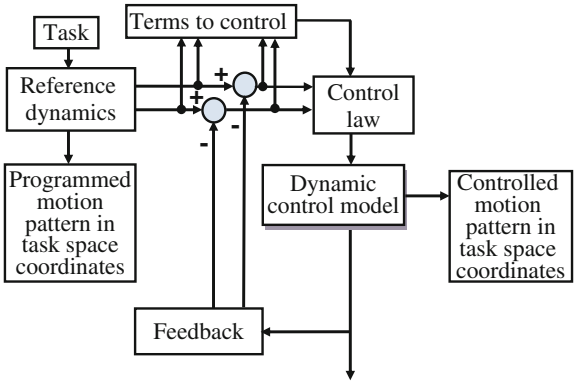

Fig. 1 Architecture of the model reference tracking control strategy for programmed motion

to be done or motion to be followed, a question arises—how to execute this task and how to track the desired motion?

A tracking control strategy dedicated to track predefined programmed motions has been designed. It is referred to as the model reference tracking control strategy for programmed motion. It is based on two dynamic models derived in quasi-coordinates:

1. The reference dynamic model. It governs motion equations of a system subjected to NC, either material, programmed or both. This is the reference dynamics block of the form (30).

2. The dynamic control model. It takes into account only material constraints and conservation laws on the system. This is the control dynamics block (19).

Outputs of the reference dynamics are inputs to the control law and the control dynamics.

Architecture of the tracking strategy, which is presented in Fig. 1, is designed in such a way that it separates the non-material and material constraints. They are merged into separate models. It gives rise to an idea of a derivation of both dynamic models using other set of coordinates.

Definition 3 The unified dynamic model of a constrained system (30) is referred to as a reference dynamic model for programmed motion.

The reference dynamics (30) serves programmed motion planning. It is defined as follows.

Definition 4 Programmed motion planning for a system subjected to the constraints $\tilde{G}_\beta \left(t, q_\sigma, \omega_r, \dot{\omega}_r, ..., \omega_r^{(p-1)}\right) = 0$ consists in finding time histories of positions $q_p(t)$, quasi-velocities $\omega_p(t)$ and their time derivatives in motion consistent with the constraints.

The control goal is as follows: *Given a programmed motion specified by the constraints* (23) *and the system reference dynamics* (30), *design a feedback controller to track the desired programmed motion.*

The strategy for programmed motion tracking is not sensitive to the constraint order and type, and the NS design. This is in contrast to many control designs, in which each constraint type is treated separately and a controller is modified for each of them.

5 Examples

5.1 Example 1—Motion Control of a Car with a Trailer

A car with a trailer model presented in Fig. 2 consists of three pair of wheels, which are replaced by unicycles. According to the figure, the coordinate vector is $q = (x_1, y_1, \theta_1, \Phi_1, \theta_2, \Phi_2)$. The controller design for this vehicle model can be found in literature; however, a controller is designed either at the kinematic level or using classical approach with the Lagrange equations, e.g. [22, 23]. For the first time, we take advantage of the GPME in quasi-coordinates to generate the constrained dynamics and a tracking controller for this model [24].

The wheels do not slip and the three nonholonomic equations have the form

$$\begin{gathered}\dot{x}_1 \, sin\,(\theta_1 + \phi_1) - \dot{y}_1 \, cos\,(\theta_1 + \phi_1) - \dot{\theta}_1 L_0 \, cos\,\phi_1 = 0, \\ \dot{x}_1 \, sin\,\theta_1 - \dot{y}_1 \, cos\,\theta_1 = 0, \\ \dot{x}_1 \, sin\,(\theta_2 + \phi_2) - \dot{y}_1 \, cos\,(\theta_2 + \phi_2) + \dot{\theta}_2 L_1 \, cos\,\phi_2 = 0.\end{gathered}$$

The quasi-velocities are introduced such that they naturally conform to the car driving, i.e.

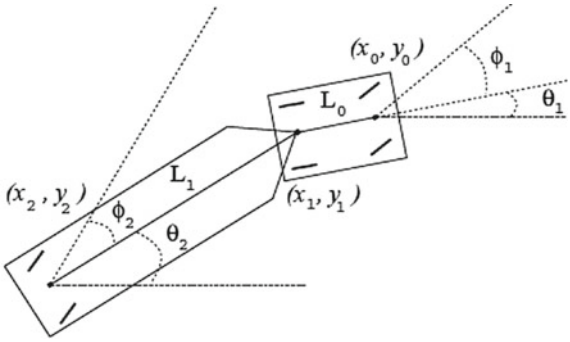

Fig. 2 A car with a trailer model

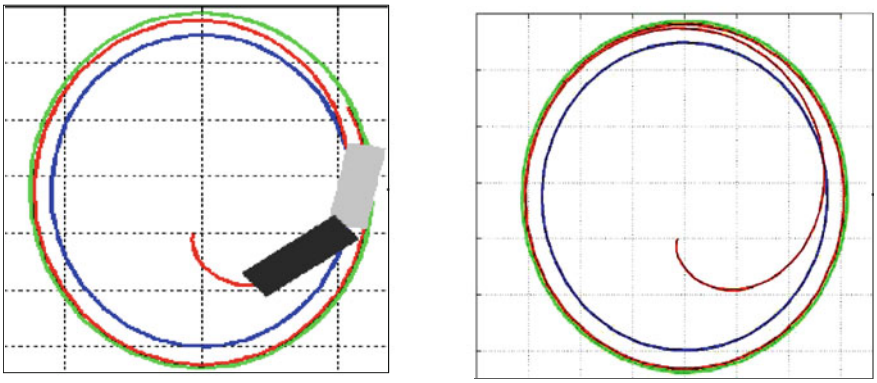

Fig. 3 Driving a prescribed trajectory by a car with a trailer (*blue* car and trailer joint motion, *red* trailer wheel axis motion, *green* car front wheel axis motion)

$$\omega_1 = V = \dot{x}_1 \cos\theta_1 + \dot{y}_1 \sin\theta_1 = 0,$$
$$\omega_2 = \dot{\phi}_1,$$
$$\omega_3 = \dot{\phi}_2,$$

$$\omega_4 = \dot{x}_1 \sin(\theta_1 + \phi_1) - \dot{y}_1 \cos(\theta_1 + \phi_1) - \dot{\theta}_1 L_0 \cos\phi_1 = 0,$$
$$\omega_5 = \dot{x}_1 \sin\theta_1 - \dot{y}_1 \cos\theta_1 = 0,$$
$$\omega_6 = \dot{x}_1 \sin(\theta_2 + \phi_2) - \dot{y}_1 \cos(\theta_2 + \phi_2) + \dot{\theta}_2 L_1 \cos\phi_2 = 0$$

Matlab symbolic toolbox was used to derive the Boltzmann-Hamel equations and its control dynamics form. Due to the complexity of the equations, their final form is (after canceling ω_4, ω_5 and ω_6)

$$M(q)\dot{\omega} + C(q, \omega) = \tau$$

with $M = \begin{bmatrix} M_1 & 0 & 0 \\ 0 & I_{k1} & 0 \\ 0 & 0 & I_{k2} \end{bmatrix}$, $C = \begin{bmatrix} M_2\omega_1\omega_3 + M_3\omega_1^2 + M_4\omega_1\omega_2 \\ 0 \\ 0 \end{bmatrix}$

and $\omega = (\omega_1, \omega_2, \omega_3)$

The control goal is to drive along a circle so the programmed constraint is a desired trajectory for (x_1, y_1). It is presented in Fig. 3.

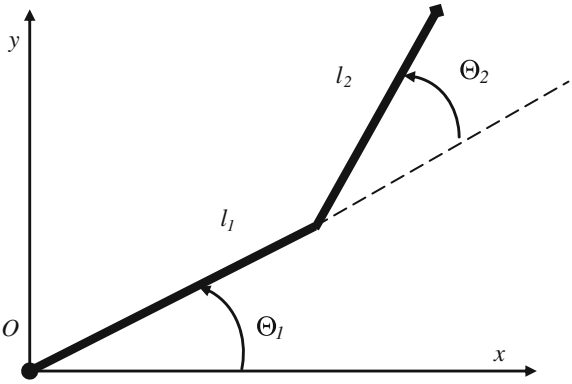

Fig. 4 Two-link planar manipulator model

5.2 *Example 2—Motion Control of an Underactuated 2-Link Planar Manipulator*

A 2-link planar manipulator is a holonomic system. It is presented in Fig. 4. We make it nonholonomic by an imposition of the NC on it and underactuated by removing the second actuator. It moves in the horizontal plane (x, y). Two degrees of freedom are described by Θ_1, Θ_2. Its geometry and inertia properties are: $l_1 = 1, l_2 = 0.6,\ I_{z1} = 0.12, I_{z2} = 0.25, r_1 = l_1/2,\ r_2 = l_2/2$ and $m_1 = 1,\ m_2 = 2$.
We formulate a programmed constraint that the manipulator end-effector is to move along a trajectory for which its curvature changes according to a specified function $\Phi^* = \frac{d\Phi(t)}{dt}$. It has the form

$$\dddot{x} = \frac{-\Phi(\dot{x}^2 + \dot{y}^2)^2\left[\dot{\Phi}(\dot{x}^2 + \dot{y}^2) + 3\Phi(\dot{x}\ddot{x} + \dot{y}\ddot{y})\right]}{\dot{y}(\dot{x}\ddot{y} - \ddot{x}\dot{y})} + \dddot{y}\frac{\dot{x}}{\dot{y}}.$$

Quasi-coordinates may be selected as $\omega_1 = \dot{\Theta}_1 l_1, \quad \omega_2 = (\dot{\Theta}_1 + \dot{\Theta}_2) l_2$.
The programmed constraint specified in quasi-velocities has the form

$$\ddot{\omega}_2 - (1 - F_2)\frac{l_2}{l_1}\ddot{\omega}_1 - F_1 l_2 = 0,$$

where F_1 and F_2 are functions of the manipulator geometric and inertia properties, Φ, ω_1, ω_2 and their first order time derivatives.
The reference dynamics (30) has the form

$$\frac{b_1 - b_2 - F_2(b_2 - \delta)}{l_1}\dot{\omega}_1 + \frac{b_2 - F_2\delta}{l_2}\dot{\omega}_2 + c = 0,$$
$$\ddot{\omega}_2 - \frac{(1 - F_2)l_2}{l_1}\ddot{\omega}_1 - F_1 l_2 = 0.$$

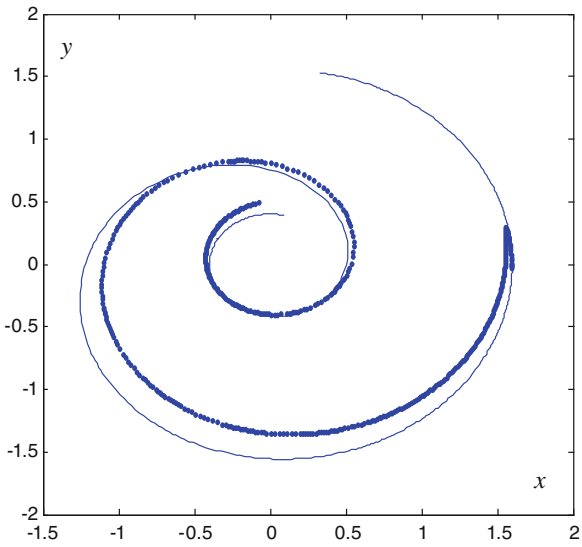

Fig. 5 Tracking by the PD controller

$$\omega_1 = \dot{\Theta}_1 l_1,$$
$$\omega_2 = (\dot{\Theta}_1 + \dot{\Theta}_2) l_2.$$

The control dynamics (19) become

$$\dot{\omega}_1 = u_1,$$
$$\dot{\omega}_2 = \frac{-\beta l_2 \cos \Theta_2}{\delta l_1} \dot{\omega}_1 - \frac{-\beta l_2 \sin \Theta_2}{\delta l_1^2} \omega_1^2,$$

$$\omega_1 = \dot{\Theta}_1 l_1,$$
$$\omega_2 = (\dot{\Theta}_1 + \dot{\Theta}_2) l_2.$$

Tracking the programmed motion using the PD controller is presented in Fig. 5.

Modeling and the controller design for the manipulator model in quasi-coordinates result in the compact forms of the reference and control dynamics. Simulations are faster and numerical stabilization of the constraint equations is not needed.

6 Conclusions

In this chapter we develop the theoretic model-based control oriented modeling framework. It yields equations of motion for a NS in quasi-coordinates. We demonstrate that the framework may offer a fast way to obtain equations of motion for a constrained system either for the dynamic analysis or control. The theoretic model-based control oriented modeling framewor treats the two types of constraints in the same way in modelling and a controller design. Simulation results confirm that

model-based control oriented modeling in quasi-coordinates is efficient and it supports numerical stabilization of the NC equations. Future research is planned in the area of design controllers using quasi-velocities description to fully exploit properties of motion equations in quasi-coordinates and quasi-velocities.

References

1. Cameron, J.M., Book, W.J.: Modeling mechanisms with nonholonomic joints using the Boltzmann-Hamel equations Int. J. Robot. Res. **16**(1), 47–59 (1997)
2. Papastavridis, J.G.: On the Boltzmann-Hamel equations of motion: a vectorial treatment. J. Appl. Mech. **61**, 453–459 (1994)
3. Jarzębowska, E.: Quasi-coordinates based dynamics modeling and control design for nonholonomic systems. Nonlin. Anal. **16**(16), 1741–1754 (2008)
4. Jarzębowska, E.: Model-Based Tracking Control of Nonlinear Systems. CRC Press, Boca Raton (2012)
5. Lewis, F., Dowson, D.M., Abdallah, C.T.: Robot Manipulator Control. Theory and Practice Marcel Dekker Inc., New York (2004)
6. Kwatny, H.G., Blankenship, G.L.: Nonlinear Control and Analytical Mechanics. Birkhauser, A Computational Approach. Boston (2000)
7. Bloch, A.M.: Nonholonomic mechanics and control. Interdisciplinary Applied Mathematics, vol. 24. Springer, New York (2003)
8. Crawford, L.S., Sastry, S.S.: Biological motor control approaches for a planar diver. In: Proceedings of the Conferenc Decision Control, pp. 3881–3886 (1995)
9. Koh, K.C., Cho, H.S.: A smooth path tracking algorithm for wheeled mobile robots with dynamic constraints. J. Intell. Robot. Syst. **24**, 367–385 (1999)
10. Scheuer, A., Laugier, Ch.: Planning sub-optimal and continuous-curvature paths for car-like robots. In: Proceedings of the IEEE/RSJ International Conference on Intelligent Robots and Systems, pp. 25–31 (1998)
11. Vafa.: Space manipulator motion with no satellite attitude disturbances. In: Proceedings of the IEEE International Conference Robotics and Automation, pp. 1770–1775 (1991)
12. Grioli, G.: Particular solutions in stereodynamics. Centro Intern. Matem. Estivo, Roma, 1–65 (1972)
13. Appell, P.: Exemple de mouvement d'un point assujetti a une liaison exprimée par une relation non linéaire entre les composantes de la vitesse. Comptes Rendus de l'Académie des Sciences, Paris **48–50**, (1911)
14. Beghuin, H.: Cours de mécanique. Gauthier-Villars, Paris (1947)
15. Seifried, R.: Dynamics of Underactuated Multibody Systems: Modeling, Control and Optimal Design (Solid mechanics and its applications). Springer, New York (2013)
16. Macfarlane, S., Croft, E.: Manipulator trajectory planning: design for real-time applications. IEEE Trans. Robot. Automat. **19**(1), 42–51 (2003)
17. Chee, W., Tomizuka, M., Patwardhan, S., et al.: Experimental study of lane change maneuver for AHS applications. Proc. Am. Control Conf. **1**, 139–143 (1995)
18. Oriolo, G., De Luca, A., Vendittelli, M.: WMR control via dynamic feedback linearization: Design, implementation, and experimental validation. IEEE Trans. Contr. Systems Techn. **10**(6), 835–852 (2002)
19. Zotov, Y.K: Tomofeyev, A.V.: Controllability and stabilization of programmed motions of reversible mechanical and electromechanical systems. J. Appl. Math. Mech. **5**6(6), 873–880 (1992)
20. Zotov, Y.K.: Controllability and stabilization of programmed motions of an automobile-type transport robot. J. Appl. Maths. Mech. **67**(3), 303–327 (2003)
21. Nejmark, J.I., Fufaev, N.A.: Dynamics of nonholonomic systems. Am. Math. Soc, Rhode Island (1972)

22. Divelbiss, A., Wen, J.T.: Trajectory tracking control of a car-trailer system. IEEE Trans. Cont. Systems Techn. **5**, 269–278 (1997)
23. Tao Sun, T., He, Y., Esmailzadeh, E., Ren, R.: Lateral stability improvement of car-trailer systems using active trailer braking control. J. Mech. Eng. Automat. **2**, 555–562 (2012)
24. Sowińska, M., Jarzębowska, E.: Dynamics and control of a car-trailer vehicle using the Boltzmann-Hamel approach. Techn. Rap. Warsaw Univ, Techn (2013)

Quasi-periodically Actuated Capacitive MEMS

Faouzi Lakrad and Mohamed Belhaq

Abstract This work reports on the effect of a quasi-periodic (QP) voltage on the dynamics of a resonant capacitive micro-electro-mechanical system (MEMS) under DC and AC actuations. We consider that the AC actuation is composed of resonant AC and non resonant AC voltages. The microstructure device is modelled as a lumped mass-spring-damper system. Averaging technique and the method of multiple scales are performed to obtain the modulation equations of the slow dynamic near the primary resonance. The influence of the amplitude and the frequency of a high frequency voltage (HFV) on the occurrence of bistability and jumps in the frequency response is examined and the safe basin of attraction is explored. The results of this work indicate that when the mechanical parameters of the MEMS device are fixed and cannot be tuned, a HFV can be used for controlling the dynamic of the resonant capacitive MEMS.

1 Introduction

Analysis of nonlinear vibrations of MEMS such as resonators, sensors and switches is an active research topic with applications in many engineering fields such as communications, automotive and robotics, to name just a few. One of the most critical issues in the design of MEMS is their reliability, life time, survivability and stability under mechanical, thermal and electrical loads. From dynamical point of view one of the key performances of MEMS is the repeatability and the reproducibility in terms of uniquely determined dynamics. However, this property is affected by nonlinearities, especially hysteresis and pull-in phenomena. Indeed, in capacitive MEMS devices hysteresis and pull-in instability constitutes one of the main way to the device failure [1].

F. Lakrad (✉) · M. Belhaq
University Hassan II Casablanca,
BP. 5366 Maarif, Casablanca, Morocco
e-mail: f.lakrad@fsac.ac.ma

M. Belhaq
e-mail: m.belhaq@fsac.ac.ma

M. Belhaq (ed.), *Structural Nonlinear Dynamics and Diagnosis*,
Springer Proceedings in Physics 168, DOI 10.1007/978-3-319-19851-4_10

Various theoretical and experimental works investigated the dynamic of MEMS actuated by DC and AC resonant voltages. For instance, Mestrom et al. [2] measured the effects of AC voltage on the hysteresis interval. Sahai et al. [3] used a laser beam focused on a MEMS structure to tune its nonlinear behavior from softening to hardening. Nayfeh and co-workers [4, 5] studied the mechanisms leading to the dynamic pull-in of MEMS resonators actuated by a resonant AC voltage. They showed that AC resonant voltage lowers drastically the pull-in threshold caused by the jumps phenomena. Alsaleem et al. [6] studied analytically and experimentally nonlinear resonances and dynamic pull-in of a microbeam. Rhoads et al. [7] studied parametrically excited MEMS oscillators, while Lakrad and Belhaq [8, 9] investigated the effect of a HFV on the pull-in in a microstructure actuated by mechanical shocks and electrostatic forces and the effect of a HF AC tension on the pull-in induced by a DC. Kacem et al. [10] analyzed the nonlinear dynamics of micro- and nanoelectromechanical resonant sensors around the primary resonance. For a comprehensive review on nonlinear static and dynamics of MEMS, the reader can refer to [1].

All the previously cited works deal with periodically driven MEMS. In the present paper, the effect of a QP voltage on a capacitive MEMS is investigated. The QP actuation is composed of a resonant AC voltage and a nonresonant AC one.

The rest of the paper is organized as follows: In Sect. 2, we describe the model, we perform an averaging technique [11] and then we use the method of multiple scales [12] to approximate the QP solutions of the MEMS device. In Sect. 3, analytical results are compared to numerical simulations, QP resonance curves are plotted and the effects of the control parameters are discussed. The dynamic integrity and basin erosion are also computed and commented. Section 4 concludes the work.

2 Equation of Motion and Perturbation Analysis

A single-degree-of-freedom model depicted in Fig. 1 is considered to represent a MEMS device employing DC and AC voltages as actuators. The movable electrode is modelled as a linear mass-spring-damper system. This linearity is valid when the thickness of the movable electrode is greater than the initial gap with the stationary electrode. We suppose that the only nonlinearity exhibited by the MEMS device is caused by the electric actuation. Thus, the equation of motion can be written as

$$m\ddot{x} + c\dot{x} + kx = \frac{\varepsilon S}{2(d-x)^2} V^2(t) \tag{1}$$

where $x(t)$ is the displacement of the movable mass m, c and k are the damping and stiffness of the system, respectively, ε is the dielectric constant of the gap medium, d is the initial capacitor gap width, S is the area of the cross section, and $V(t)$ is the electric load.

The electric tension $V(t)$ is taken as square root of a QP function as follows

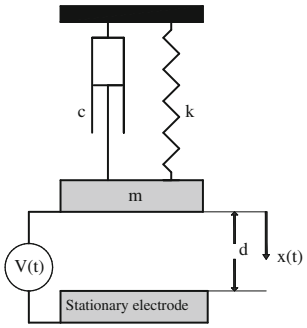

Fig. 1 A single-degree-of-freedom model used to model the capacitive MEMS

$$V(t) = \sqrt{V_0^2 + U_1^2 \cos(\omega^* t) + U_2^2 \cos(\Omega^* t)} \tag{2}$$

where V_0 is the DC voltage, U_1 and ω^* are the amplitude and the frequency of the AC resonant actuation, respectively, while U_2 and Ω^* denote the amplitude and the frequency of the nonresonant voltage, respectively. The specific form of the input voltage (2) is chosen in order to decouple the effects of DC and AC voltages, to avoid the occurrence of other harmonics and to principally prevent coupling with harmonic resonances. Note that a square root of a harmonic voltage was used in [13, 14] to decouple parametric and harmonic excitation.

By setting $X = \frac{x}{d}$, $\tau = \omega_0 t$, $\omega_0 = \sqrt{\frac{k}{m}}$, $\xi = \frac{c}{2m\omega_0}$, $\omega = \frac{\omega^*}{\omega_0}$ and $\Omega = \frac{\Omega^*}{\omega_0}$, where the displacement is normalized with respect to the gap and the frequencies are normalized with respect to the natural frequency ω_0 of the mass-spring system, the nondimensional equation of motion reads

$$X'' + 2\xi X' + X = \frac{\alpha}{(1-X)^2} + \frac{\beta \cos(\omega\tau)}{(1-X)^2} + \frac{\gamma \cos(\Omega\tau)}{(1-X)^2} \tag{3}$$

Here the primes denote the derivatives with respect to the normalized time τ, and the parameters

$$\alpha = \frac{\varepsilon S V_0^2}{2m\omega_0^2 d^3} \tag{4}$$

$$\beta = \frac{\varepsilon S U_1^2}{2m\omega_0^2 d^3} \tag{5}$$

$$\gamma = \frac{\varepsilon S U_2^2}{2m\omega_0^2 d^3} \tag{6}$$

represent the contribution of the DC voltage, the resonant AC and the nonresonant AC voltages, respectively. It should be pointed out that the parameters α, β and γ have to be chosen such that the electric tension $V(t)$ in (2) is real.

Equation (3) is a quasi-periodically driven system both externally and parametrically. In what follows Ω is taken larger than ω and the corresponding voltage is referred to as HFV.

In the absence of the AC voltages, the application of a DC voltage α causes an attractive electrostatic force between the two electrodes that causes a permanent displacement of the mass towards the stationary electrode. The static equilibria X_s are given by solving the following algebraic equation

$$X_s = \frac{\alpha}{(1 - X_s)^2} \tag{7}$$

Note that $X_s = 1$ corresponds to the static pull-in phenomenon which leads to the contact between the two electrodes. This contact is desirable, for instance, for capacitive switches and undesirable for sensors. In this latter, it can cause stiction, plastic deformations of the movable electrode or even its failure.

A static analysis reveals that the pull-in occurs for $\alpha_p = \frac{4}{27} \approx 0.148$ which corresponds to a steady state displacement $X_s = 1/3$. Figure 2 shows the classical variation of the static equilibria X_s with the DC voltage α. The stable (lower) branch and the unstable (upper) branch of equilibrium points collide in a saddle-node bifurcation, resulting in the disappearance of both branches. In order to avoid the static pull-in, the DC voltage α should be taken below 0.148 and the initial conditions should be taken inside the homoclinic loop of the saddle equilibrium. It is worth noting that the pull-in phenomenon could happen for values of α lower α_p, statically determined, due to the transient dynamics and to the modification of the basin of attraction.

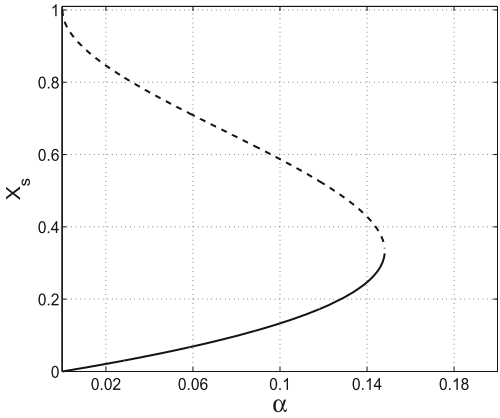

Fig. 2 Static equilibria X_s versus the DC voltage α. *Solid lines* stable, *dashed lines* unstable

2.1 Fast Flow Dynamic

The expression of the electric tension $V(\tau)$ used in (3) contains a slow dynamic which describes the main motion at time-scale of the microstructure natural vibration and a fast dynamic at time scale of the HFV. In what follows the two-step perturbation method is used to approximate QP solutions of (3).

To obtain the main equation governing the slow dynamic of the device, we implement the method of direct partition of motion [11] by introducing two different time-scales: a fast time $T_{-1} = \eta^{-1}\tau$ and a slow time $T_0 = \tau$. Then, the displacement of the mass $X(\tau)$, around a stable static equilibrium X_s, can be split up into a slow part $Z(T_0)$ and a fast part $\phi(T_{-1}, T_0)$ as follows

$$X(\tau) = X_s + Z(T_0) + \phi(T_{-1}, T_0) \equiv X_s + \eta\tilde{Z}(T_0) + \eta^2\tilde{\phi}(T_{-1}, T_0) \tag{8}$$

Here the positive parameter η is introduced to measure the smallness of other parameters ($0 < \eta \ll 1$). The slow part $Z(T_0)$ takes into account the transient motion composed of the natural damped motion of the microstructure and the response to the resonant actuation. In order to give a physical meaning to the perturbation parameter η, the high-frequency is chosen as $\Omega = \eta^{-1}$. The fast motion and its derivatives are assumed to be 2π-periodic functions of the fast time T_0 with zero mean value with respect to it [11]. Thus, $\langle X(\tau)\rangle = Z(T_0)$ where $\langle . \rangle = \frac{1}{2\pi}\int_0^{2\pi}(.)dT_{-1}$ defines the fast time-averaging operator. Introducing $D_m^n = \frac{\partial^n}{\partial T_m^n}$ yields

$$\frac{d}{d\tau} = \eta^{-1}D_{-1} + D_0 + \eta D_1 + \eta^2 D_2 + O(\eta^3) \tag{9}$$

$$\frac{d^2}{d\tau^2} = \eta^{-2}D_{-1}^2 + \eta^{-1}2D_{-1}D_0 + D_0^2 + O(\eta) \tag{10}$$

Setting $\beta = \eta^3\tilde{\beta}$ and $\xi = \eta^2\tilde{\xi}$ where the parameters with tildes are of order $O(1)$ and substituting (9) and (10) into (3), we obtain up to $O(\eta^4)$ order the following equation

$$\begin{aligned}
&(D_{-1}^2\tilde{\phi}) + X_s + \eta[2(D_{-1}D_0\tilde{\phi}) + (D_0^2\tilde{Z}) + \tilde{Z}] + \eta^2[(D_0^2\tilde{\phi}) + 2(D_{-1}D_1\tilde{\phi}) + \tilde{\phi} + 2(D_0D_1\tilde{Z})] \\
&+ \eta^3[2(D_{-1}D_2\tilde{\phi}) + 2(D_0D_1\tilde{\phi}) + 2(D_0D_2\tilde{Z}) + (D_1^2\tilde{Z}) + 2\tilde{\xi}(D_{-1}\tilde{\phi}) + 2\tilde{\xi}(D_0\tilde{Z})] \\
&= \frac{1}{(1-X_s)^2}\left\{\left[\alpha + \gamma\cos(T_{-1})\right] + \eta\left[\frac{2\tilde{Z}}{(1-X_s)}(\alpha + \gamma\cos(T_{-1}))\right]\right. \\
&+ \eta^2\left[(\frac{3\tilde{Z}^2}{(1-X_s)^2} + \frac{2\tilde{\phi}}{(1-X_s)})(\alpha + \gamma\cos(T_{-1}))\right] \\
&+ \left.\eta^3\left[(\frac{4\tilde{Z}^3}{(1-X_s)^3} + \frac{6\tilde{Z}\tilde{\phi}}{(1-X_s)^2})(\alpha + \gamma\cos(T_{-1})) + \tilde{\beta}\cos(\omega T_0)\right]\right\} + O(\eta^4)
\end{aligned} \tag{11}$$

The dominant terms dependent on T_{-1} up to the order $O(\eta)$ in (11) are

$$(D_{-1}^2\tilde{\phi}) = \frac{\gamma}{(1-X_s)^2}\cos(T_{-1}) \tag{12}$$

Thus, up to this leading order, the fast motion is given by

$$\tilde{\phi}(T_{-1}, T_0) = -\frac{\gamma}{(1-X_s)^2}\cos(T_{-1}) + O(\eta) \tag{13}$$

This fast motion ϕ increases by increasing the amplitude γ of the HFV and by considering larger values of static equilibrium X_s which implies having a large DC voltage α.

2.2 Slow Flow Dynamic

To approximate the equation of the slow dynamic, Eq (11) is averaged over a period of the fast time scale T_{-1}. One obtains the following equation up to the order $O(\eta^3)$

$$(D_0^2\tilde{Z}) + \omega_1^2\tilde{Z} = \eta[\alpha_1\tilde{Z}^2 - \gamma_1] + \eta^2[\alpha_2\tilde{Z}^3 - \gamma_2\tilde{Z} - 2\tilde{\xi}(D_0\tilde{Z}) + \tilde{\beta}_1\cos(\omega T_0)] \tag{14}$$

where

$$\alpha_1 = \frac{3\alpha}{(1-X_s)^4}, \alpha_2 = \frac{4\alpha}{(1-X_s)^5}, \tilde{\beta}_1 = \frac{\tilde{\beta}}{(1-X_s)^2}, \gamma_1 = \frac{\gamma^2}{(1-X_s)^5}, \gamma_2 = \frac{3\gamma^2}{(1-X_s)^6}$$

The parameters $\alpha_i (i = 1, 2)$, $\tilde{\beta}_1$ and $\gamma_i (i = 1, 2)$ represent the effects of the DC actuation, the AC resonant actuation and the HFV, respectively. The fast dynamic influences the slow one, in (14), through a biasing term $\eta\gamma_1$ and a linear term $\eta^2\gamma_2\tilde{Z}$.

The normalized natural frequency of the mass actuated by the DC voltage is given by

$$\omega_1^2 = 1 - \frac{2\alpha}{(1-X_s)^3} \tag{15}$$

In Fig. 3 the natural frequency ω_1 given in (15) is plotted versus the DC voltage α. In the same figure are plotted in circles the numerically obtained natural frequencies of (3) in the absence of the AC voltages ($\beta = \gamma = 0$) and damping. In this case the system is Hamiltonian and the physically acceptable solutions are centers that are confined inside a homoclinic loop corresponding precisely to the static pull-in phenomenon. It should be noted that the fundamental frequency of orbits near the centers is computed numerically using a fast Fourier transformation analysis. It can be seen from Fig. 3 that the natural frequency is decreasing with respect to α till reaching zero which corresponds to the pull-in instability.

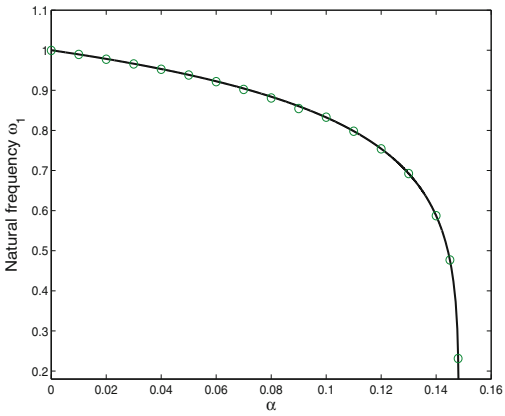

Fig. 3 Natural frequency ω_1 versus α. *Continuous line* (given by (15)) and *circles* (given by numerical simulation of (3))

In order to obtain approximations of periodic solutions of the slow dynamic, we use the multiple scales method [12] up to the second order near the primary resonance i.e., $\omega = \omega_1 + \sigma$ where the small detuning parameter $\sigma = \eta^2\tilde{\sigma}$ is introduced to measure the closeness of the excitation frequency ω to the natural frequency ω_1. New time scales are introduced $T_n = \eta^n\tau$, where n is a positive integer. Then, equating terms of like power of η in (14), we obtain the following hierarchy of problems:

- Order $O(1)$

$$D_0^2\tilde{Z}_0 + \omega_1^2\tilde{Z}_0 = 0 \tag{16}$$

The solution is written as

$$\tilde{Z}_0(T_0, T_1, T_2) = \tilde{A}(T_1, T_2)\exp(i\omega_1 T_0) + c.c \tag{17}$$

where cc denotes the complex conjugate of the preceding terms. The complex amplitude $\tilde{A}(T_1, T_2)$ has to be determined by eliminating the secular terms at the next level of approximations.

- Order $O(\eta)$

$$D_0^2\tilde{Z}_1 + \omega_1^2\tilde{Z}_1 = \alpha_1\tilde{Z}_0^2 - \gamma_1 - 2(D_0D_1\tilde{Z}_0) \tag{18}$$

The secular terms elimination condition is given by

$$D_1\tilde{A} = 0 \tag{19}$$

and the particular solution up to order $O(\eta)$ reads

$$\tilde{Z}_1 = \frac{\alpha_1}{\omega_1^2}\tilde{A}\bar{\tilde{A}} - \frac{\gamma_1}{2\omega_1^2} - \frac{\alpha_1\tilde{A}^2}{3\omega_1^2}\exp(i2\omega_1 T_0) + c.c \tag{20}$$

- Order $O(\eta^2)$

$$\begin{aligned} D_0^2\tilde{Z}_2 + \omega_1^2\tilde{Z}_2 = &-2(D_0D_2\tilde{Z}_0) - (D_1^2\tilde{Z}_0) + 2\alpha_1\tilde{Z}_0\tilde{Z}_1 \\ &+ \alpha_2\tilde{Z}_0^3 - \gamma_2\tilde{Z}_0 - 2\xi(D_0\tilde{Z}_0) + \frac{\tilde{\beta}_1}{2}e^{(i\omega T_0)} \end{aligned} \tag{21}$$

Elimination of secular terms leads to

$$i2\omega_1(D_2\tilde{A}) = -i2\tilde{\xi}\omega_1\tilde{A} + \Gamma_1\tilde{A} + L_2\tilde{A}^2\bar{\tilde{A}} + \frac{\tilde{\beta}_1}{2}e^{i\sigma T_0} \tag{22}$$

where $\Gamma_1 = -\frac{2\alpha_1\gamma_1}{\omega_1^2} - \gamma_2$ and $L_2 = \frac{10\alpha_1^2}{3\omega_1^2} + 3\alpha_2$. The particular solution at this order is given by

$$\tilde{Z}_2 = -\frac{1}{8\omega_1^2}\left(\alpha_2 - \frac{2\alpha_1^2}{3\omega_1^2}\right)\tilde{A}^3 e^{(i3\omega_1 T_0)} + cc \tag{23}$$

Using the polar form $\tilde{A} = (\tilde{a}/2)\exp(i\theta)$, where $\tilde{a}$ and θ are the amplitude and the phase, respectively, separating real and imaginary parts in (22) leads to the following modulation equations of amplitude and phase

$$\frac{d\tilde{a}}{d\tau} = -\xi\tilde{a} + \eta^2\frac{\tilde{\beta}_1}{2\omega_1}\sin(\psi) \tag{24}$$

$$\tilde{a}\frac{d\psi}{d\tau} = \sigma\tilde{a} + \eta^2\left[\Gamma_1\frac{\tilde{a}}{2\omega_1} + L_2\frac{\tilde{a}^3}{8\omega_1} + \frac{\tilde{\beta}_1}{2\omega_1}\cos(\psi)\right] \tag{25}$$

with $\psi = \tilde{\sigma}T_2 - \theta$. One should point out that stationary solutions of (24) and (25) i.e., $\dot{a} = \dot{\psi} = 0$ correspond to periodic solutions of the slow flow (14) and consequently to the QP vibrations of the original system (3). In fact, with $Z = \eta\tilde{Z}$ and $a = \eta\tilde{a}$, the amplitude a of these periodic solutions is obtained by solving the following algebraic equation

$$\xi^2a^2 + \left[\sigma a + \eta^2\Gamma_1\frac{a}{2\omega_1} + L_2\frac{a^3}{8\omega_1}\right]^2 = \left(\frac{\beta_1}{2\omega_1}\right)^2 \tag{26}$$

It can be seen that HFV influences the amplitude a through the parameter Γ_1. The approximated QP solution of (3), up to the leading order, is then given by

$$X(\tau) = X_s - \frac{\gamma}{\Omega^2(1-X_s)^2}\cos(\Omega\tau) + a\cos(\omega\tau+\psi) + \frac{\alpha_1}{2\omega_1^2}\frac{a^2}{\Omega^2} - \frac{\gamma_1}{\Omega^2\omega_1^2} - \frac{\alpha_1}{6\omega_1^2}a^2\cos(2\omega\tau-2\psi) - \frac{1}{32\omega_1^2}(\alpha_2 - \frac{2\alpha_1^2}{3\omega_1^2})a^3\cos(3\omega\tau-3\psi) + O(\eta^4) \quad (27)$$

3 Main Results

In this section, we analyze the effect of different actuations on the dynamic of the micro-system. To validate the analytical prediction, we compare the analytical approximation given by (27) with the results obtained by numerical simulations of (3) using a Fehlberg fourth-fifth order Runge-Kutta method.

Next, attention will be paid on the regions where the behavior of the micro-system is QP precluding the chaotic regions. Indeed, (3) represents a four-dimensional dynamical system in the space $R^2 \times T^2$ and can be written in the form

$$\begin{aligned} X' &= Y \\ Y' &= -2\xi Y - X + \frac{\alpha + \beta\cos(\Phi) + \gamma\cos(\Theta)}{(1-X)^2} \\ \Phi' &= \omega \\ \Theta' &= \Omega \end{aligned} \quad (28)$$

A visual representation of the attractors in the four-dimensional flow (28) can be achieved using Poincaré map by strobing on the fast-evolving phase Θ. The corresponding mapping $(X_n, X'_n, \Phi_n) \to (X_{n+1}, X'_{n+1}, \Phi_{n+1})$ is three dimensional.

In all numerical computations the damping coefficient $\xi = 0.0002$. In Fig. 4 we show the time histories of (3) obtained analytically (27) and numerically for various parameters of control. One can observe from these figures a good match between the analytical and the numerical results.

In Fig. 5 are depicted the power spectra and the Poincaré map of the attractors (shown in Fig. 4a, b) projected on the plane (X_n, Φ_n), with Φ_n is computed modulo $\frac{2\pi}{\omega}$. These plots show that the attractors are QP.

3.1 Case with Resonant Actuation Only

In the absence of the nonresonant voltage ($\gamma = 0$), the system is subject to a DC and an AC resonant voltages. Figure 6 shows, for different values of the static voltage α, the amplitude-frequency response of the mass, as given by (26). The numerical values

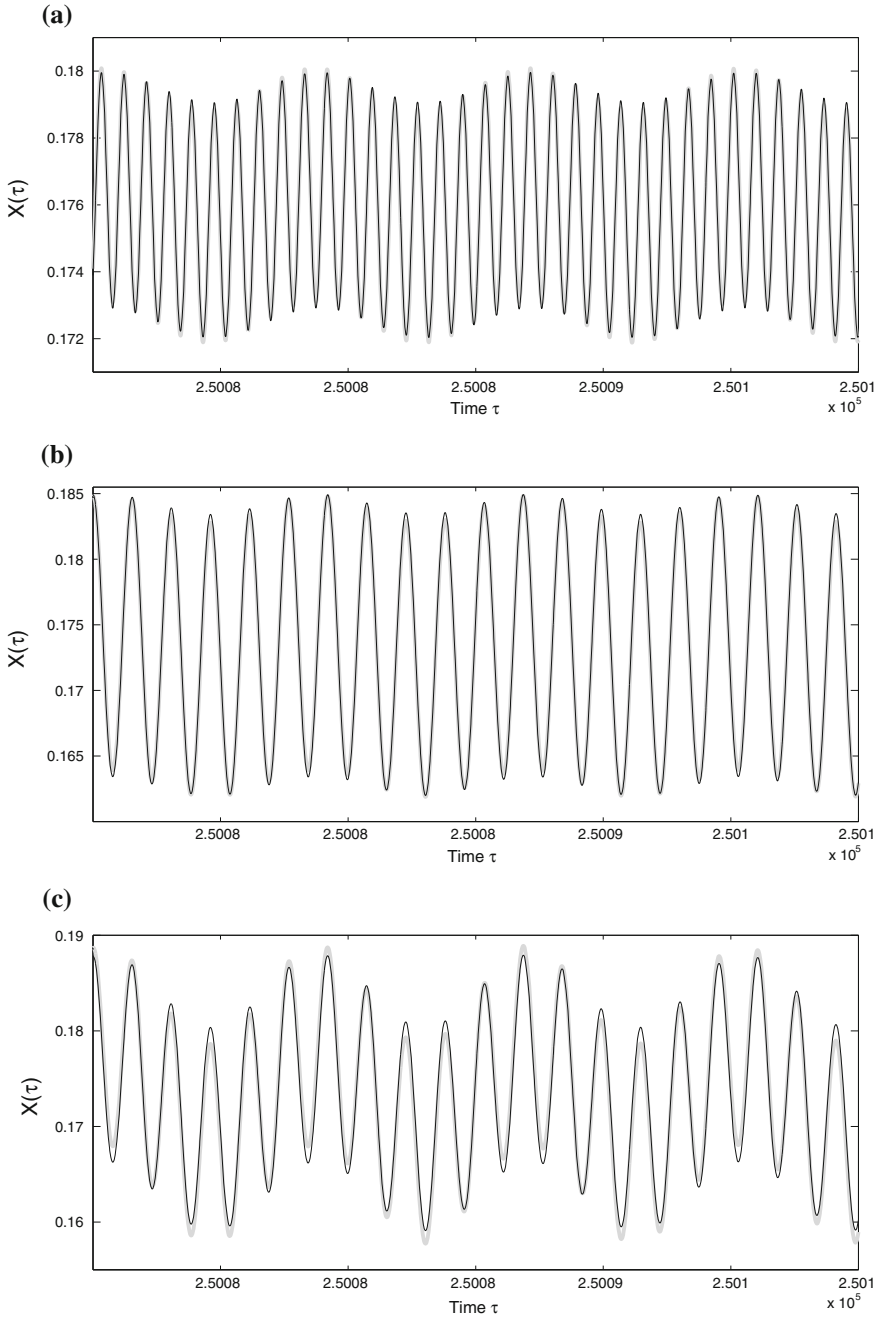

Fig. 4 Time histories for $\alpha = 0.12, \xi = 0.0002, \sigma = 0$ and $\gamma = 0.119$. *Gray line* (analytical solution (27)) and *black line* (numerical solution of (3)). **a** $\beta = 2.10^{-6}$ and $\Omega = 7.1$, **b** $\beta = 10^{-5}$ and $\Omega = 4.1$, **c** $\beta = 5.10^{-5}$ and $\Omega = 4.1$

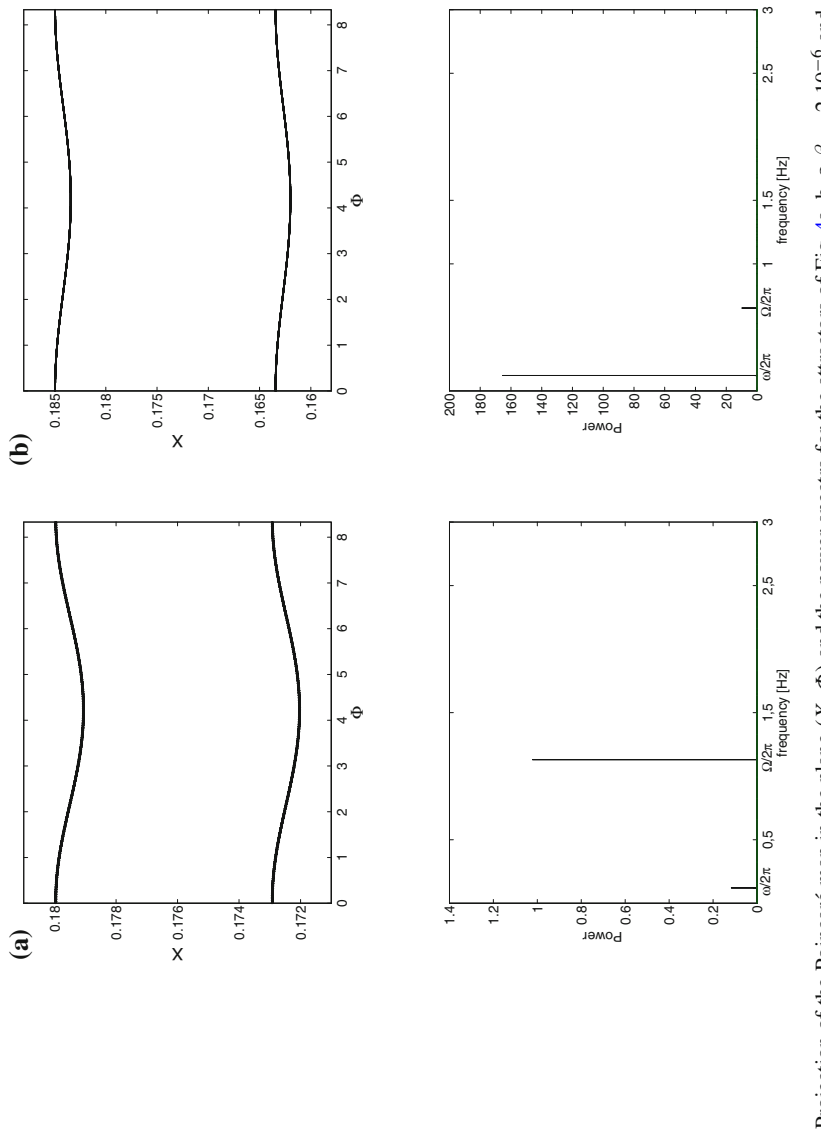

Fig. 5 Projection of the Poincaré map in the plane (X, Φ) and the power spectra for the attractors of Fig. 4a, b. **a** $\beta = 2.10^{-6}$ and $\Omega = 7.1$, *b* $\beta = 10^{-5}$ and $\Omega = 4.1$

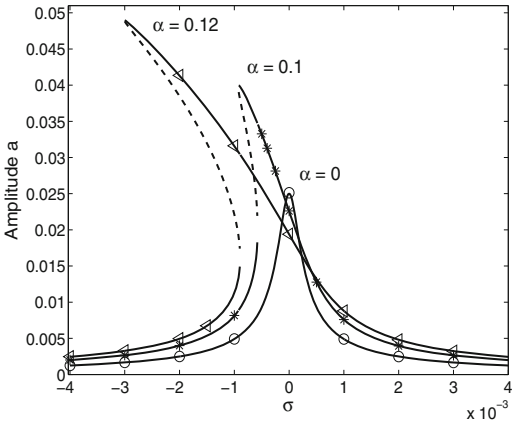

Fig. 6 Resonance curves for various values of α, for $\gamma = 0$, $\xi = 0.0002$ and $\beta = 0.00001$. *Lines* Analytical solutions (24) and (25): *continuous* for stable and *dashed* for unstable. The *stars*, *triangles* and *circles* for numerical solutions of (3)

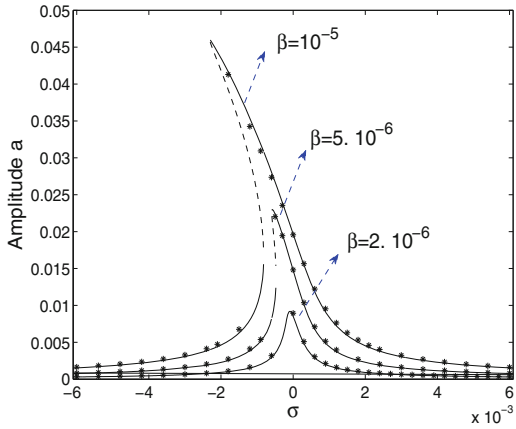

Fig. 7 Resonance curves for various values of β, for $\gamma = 0$, $\xi = 0.0002$ and $\alpha = 0.12$. *Continuous lines* for stable, *dashed lines* to unstable analytic solutions. The *stars* are numerically computed amplitude

of the amplitude a of the periodic solutions are obtained by solving the algebraic equation (26). It can be seen from this figure that increasing the static voltage α increases the softening behavior of the system.

In Fig. 7, we show for fixed DC voltage $\alpha = 0.12$, the frequency response for different values of resonant AC voltage β. One observes that increasing β leads to the softening behavior, hysteresis as well as dynamic pull-in instability [5] for larger values of β.

The bifurcation curves delimiting the existence regions of solutions are shown in Fig. 8 in the plane of the resonant voltage parameters. It is clear that the region of multiplicity of solutions (zone I) increases with increasing β. This results is in agreement with the softening effect of increasing β shown in Fig. 7.

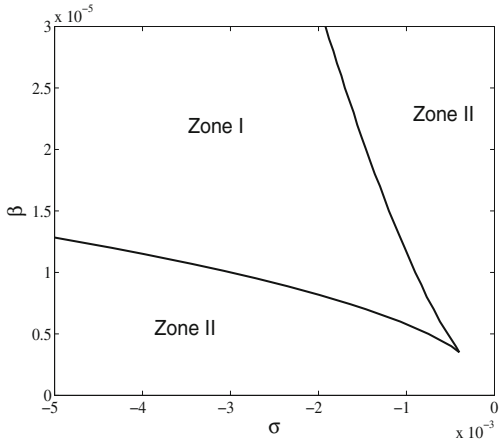

Fig. 8 Number of solutions in the plane (σ, β) for $\gamma = 0$, $\alpha = 0.12$ and $\xi = 0.0002$: *zone I* three solutions and *zone II* one solution

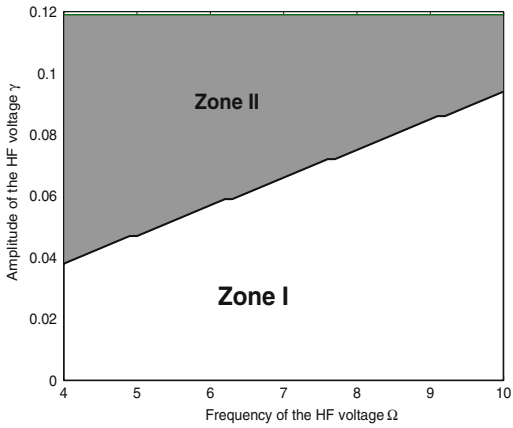

Fig. 9 Number of solutions in the plane (Ω, γ) for $\alpha = 0.12$, $\sigma = -0.002$, *zone I* three solutions, *zone II* one solution

3.2 Effects of the Nonresonant Voltage

In this subsection we investigate the effect of adding the nonresonant AC voltage on the frequency response of the moving mass. In particular, we shall investigate how this voltage can affect the domain of bistability. First, assume that the parameters of the system are chosen in zone I of Fig. 8 ($\sigma = -0.002$, $\beta = 0.00001$) where bistability exists. In Fig. 9 we show in the parameter plane (γ, Ω) of the HFV the region where the bistability can be eliminated (the gray region). Figure 9 indicates that the elimination zone of bistability is optimal for moderate values of the frequency Ω and high values of the amplitude γ of the HFV.

Figure 10 shows, for fixed $\Omega = 7.1$ and $\alpha = 0.12$, the influence of the amplitude γ on the resonance frequency of the slow dynamic obtained analytically in (26). This figure shows that increasing the amplitude γ causes the nonlinear resonance frequency to shift towards higher frequencies. Figure 10 also indicates that by tuning

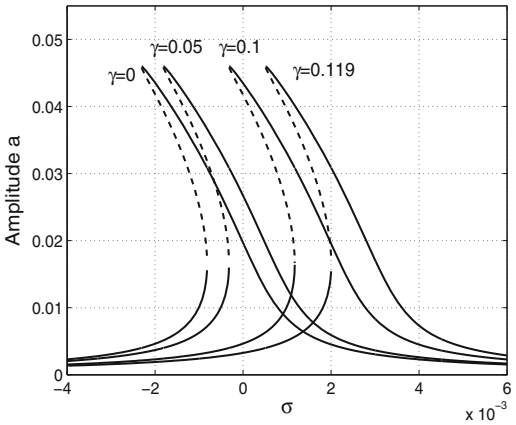

Fig. 10 Analytical resonance curves given by (26) versus the shift of the resonance σ for various values of γ. $\alpha = 0.12$ and $\Omega = 7.1$

the amplitude of the HFV, the amplitude of the resonant mass response might be increased or decreased to a desirable value of operation.

In Fig. 11 are shown the numerically computed resonance curves of the original equation (3) for various values of γ. This figure shows the maximum values of the stationary solution of the QP attractors, after disregarding 6600 resonant period, during 600 times of the resonant period. This figure confirms the analytically obtained results of Fig. 10. The effect of the amplitude γ and frequency Ω of the nonresonant voltage on the resonance shift is presented in Fig. 12. This figure shows that the amplitude γ and the frequency Ω cause opposite effects on the shift of resonance. Indeed, increasing γ increases the shift, while increasing Ω decreases it towards the case $\gamma = 0$.

3.3 Dynamic Integrity and Basin Erosion

It is agreed that the safety of a nonlinear system depends not only on the stability of its solutions but also on the uncorrupted basin surrounding each solution [15]. Indeed, by performing numerical simulations of trajectories from different starting points we are able to detect any significant change in the safe basin of attraction. In this section we analyze and approximate numerically the safe basin of attraction.

The chosen phase space window is $X(\tau) \in [0, 0.5]$ and $X'(\tau) \in [-0.2, 0.15]$ which contains the compact part of the safe basins of attractions. Figures 13 show the basins evolution for increasing value of the AC voltage β in the absence of HFV. The safe basins correspond to the black regions and the corrupted areas correspond to

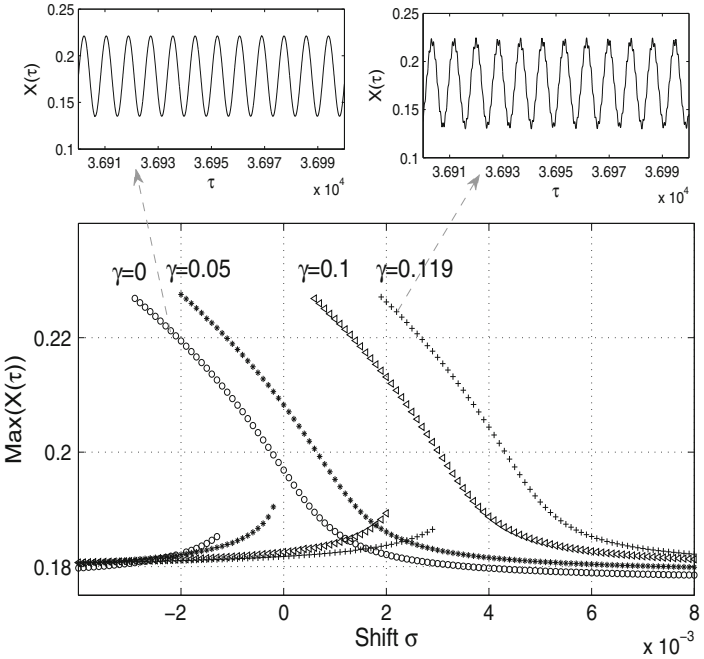

Fig. 11 Numerical resonance curves for different values of γ and $\Omega = 7.1$ of (3). $\beta = 0.00001$, $\xi = 0.0002$, $\alpha = 0.12$

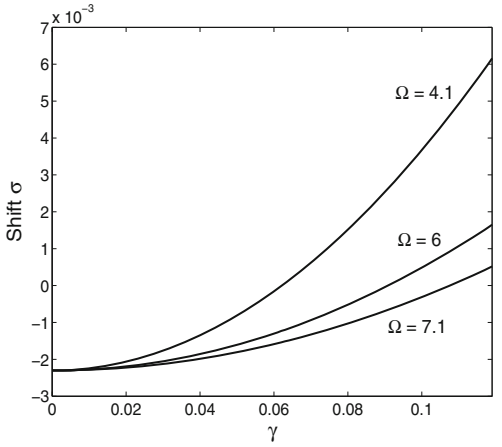

Fig. 12 Shift of the resonance versus the amplitude of the HF voltage γ for various values of Ω

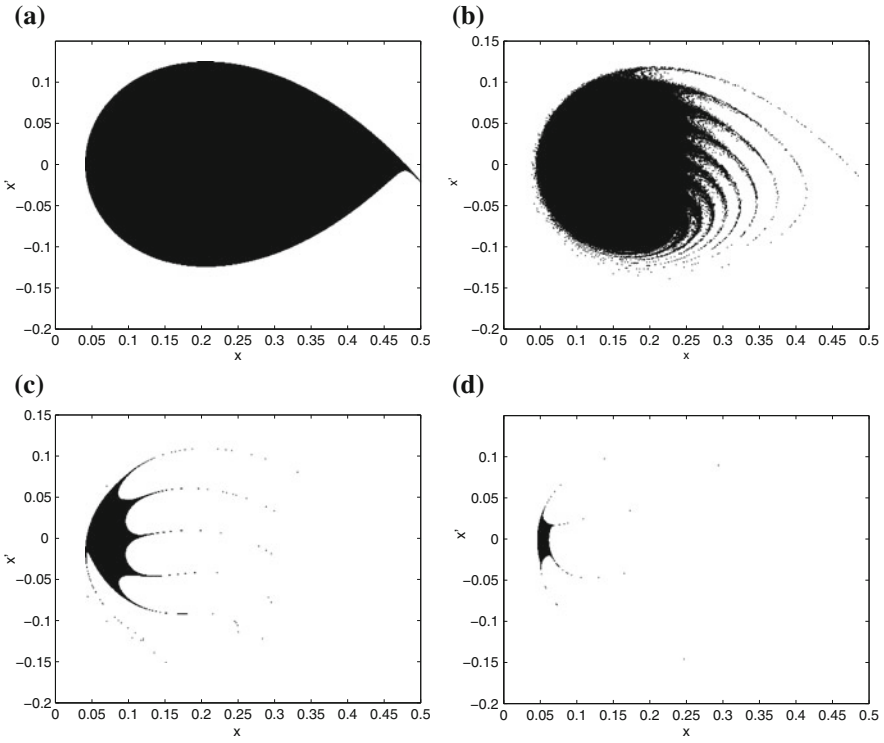

Fig. 13 Basins of attraction for various values of β and for $\alpha = 0.13$, $\sigma = -0.001$ and $\gamma = 0$. **a** $\beta = 0$. **b** $\beta = 0.003$. **c** $\beta = 0.007$. **d** $\beta = 0.01$.

the white regions. These latter regions correspond precisely to the occurrence of the dynamic pull-in phenomenon. The erosion of the safe basins for increasing resonant voltage amplitude β is depicted in Fig. 13.

Figure 14 shows that the safe basin of attraction can be increased by adding a HFV with $\gamma = 0.12$ and $\Omega = 5.1$. The effect of adding the nonresonant voltage on the basins of attractions is given in Fig. 15. It shows the global integrity measure, representing the normalized area of the safe basin [15], versus the amplitude of the resonant voltage amplitude β for various γ. One observes that increasing the amplitude γ may increase the safe basin of attraction for $\beta < 0.005$ while the amplitude of the HFV has no effect on the global integrity measure beyond $\beta = 0.005$. Indeed, increasing the safe basin offers the movable electrode of the capacitive MEMS to gain stability and to operate in larger intervals.

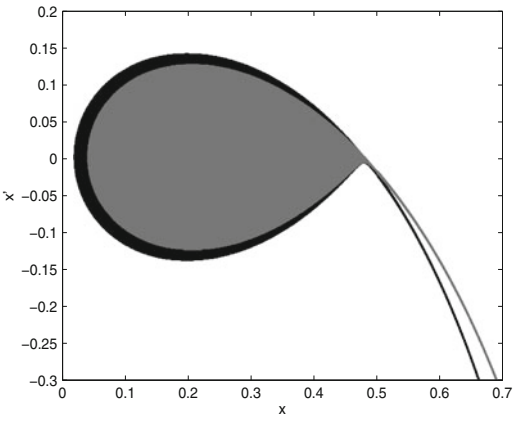

Fig. 14 Basins of attraction for $\alpha = 0.13$, $\beta = 0.00001$, $\xi = 0.0002$, $\sigma = -0.001$ and $\Omega = 5.1$. The *gray zone* corresponds to $\gamma = 0$ and the *black zone* to $\gamma = 0.12$

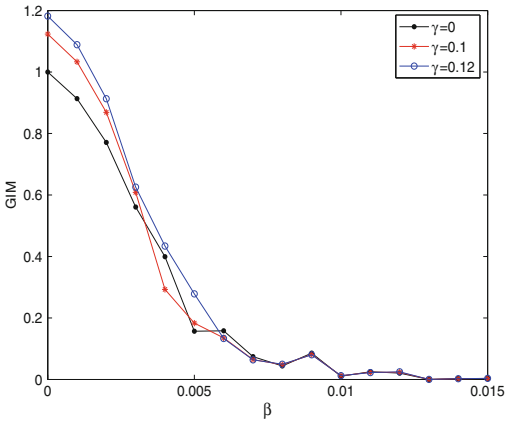

Fig. 15 Global integrity measure versus β for various values of γ and for $\alpha = 0.13$, $\xi = 0.0002$, $\sigma = -0.001$ and $\Omega = 5.1$

4 Conclusion

The dynamics of a quasi-periodically actuated capacitive MEMS is studied analytically and numerically. The MEMS is modelled by a lumped single degree of freedom system actuated by DC and AC electrical voltages. The AC actuation is QP and is composed of a resonant AC voltage and a non resonant fast AC voltage. The QP attractors are approximated by using the two-step perturbation technique. The method of direct partition of motion was performed to approximate the slow dynamic of the device and the multiple scales method was used to obtain the amplitude-frequency response of the slow dynamic near the primary resonance.

The results shown that adding a HFV to the resonant AC actuation shifts the frequency response toward higher frequencies, thereby retarding the occurrence of bistability and jumps in the response amplitude. It was also shown that for appropriate values of the amplitude and the frequency of the HFV, jumps phenomena can be

eliminated. Moreover, by tuning the amplitude of the HFV, the amplitude of the resonant mass might be increased or decreased to a desirable value of operation which can be of interest for sensing specific mechanical parameters. It was also shown that for appropriate amplitude and frequency of the HFV the safe basin of attraction is increased and consequently the dynamic integrity of the device is improved.

The present work reveals that in certain operations where the original mechanical characteristics of the MEMS device are assigned and cannot be tuned, HFV can be considered as a practical alternative for controlling the dynamic of the resonant capacitive MEMS.

Acknowledgments The first author F.L. would like to thank the Alexander von Humboldt Foundation for the financial support.

References

1. Younis, M.I.: MEMS Linear and Nonlinear Statics and Dynamics. Springer, New York (2011)
2. Mestrom, R.M.C., Fey, R.B.H., Van Beek, J.M.T., Phan, K.L., Nijmeijer, N.: Modelling the dynamics of a MEMS resonator: simulations and experiments. Sens. Actuators A **142**, 306–315 (2008)
3. Sahai, T., Bhiladvala, R.B., Zehnder, A.T.: Thermomechanical transitions in doubly-clamped micro-oscillators. Int. J. Non-Linear Mech. **42**, 596–607 (2007)
4. Nayfeh, A.H., Younis, M.I.: Dynamics of MEMS resonators under superharmonic and subharmonic excitations. J. Micromech. Microeng. **15**, 1840–1847 (2005)
5. Nayfeh, A.H., Younis, M.I., Abdel-Rahman, E.M.: Dynamic pull-in phenomenon in MEMS resonators. Nonlinear Dyn. **48**, 153–163 (2007)
6. Alsaleem, F.M., Younis, M.I., Ouakad, H.M.: On the nonlinear resonances and dynamic pull-in of electrostatically actuated resonators. J. Micromech. Microeng. **19**, 045013 (2009)
7. Rhoads, J.F., Shaw, S.W., Turner, K.L., Moehlis, J., DeMartini, B.E., Zhang, W.: Generalized parametric resonance in electrostatically actuated microelectromechanical oscillators. J. Sound Vib. **296**, 797–829 (2006)
8. Lakrad, F., Belhaq, M.: Suppression of pull-in instability in MEMS using a high-frequency actuation. Commun. Nonlinear Sci. Numer. Simulat. **15**, 3640–3646 (2010)
9. Lakrad, F., Belhaq, M.: Suppression of pull-in in a microstructure actuated by mechanical shocks and electrostatic forces. Int. J. Non-Linear Mech. **46**, 407–414 (2011)
10. Kacem, N., Baguet, S., Hentz, S., Dufour, R.: Computational and quasi-analytical models for non-linear vibrations of resonant MEMS and NEMS sensors. Int. J. Non-Linear Mech. **46**, 532–542 (2011)
11. Blekhman, I.I.: Vibrational Mechanics: Nonlinear Dynamic Effects, General Approach, Application. World Scientific, Singapore (2000)
12. Nayfeh, A.H.: Perturbation Methods. Wiley, New York (1973)
13. Turner, K., Miller, S., Hartwell, P., MacDonald, N., Stogatz, S., Adam, S.: Five parametric resonances in a microelectromechanical system. Nature **396**(6707), 149–152 (1998)
14. Rhoads, J.F., Shaw, S.W., Turner, K.L.: Nonlinear dynamics and its applications in micro-and nanoresonators. Proceedings of DSCC (2008)
15. Rega, G., Lenci, S.: Identifying, evaluating, and controlling dynamical integrity measures in non-linear mechanical oscillators. Nonlinear Anal. Theory Methods Appl. **63**, 902–914 (2005)

Localization of Vibratory Energy of Main Linear/Nonlinear Structural Systems by Nonlinear Energy Sink

C.-H. Lamarque and A. Ture Savadkoohi

Abstract Two systems are considered: the system I is composed of a main linear structure which is coupled to a nonsmooth nonlinear energy sink. Here, effects of the gravity forces are not neglected. The system II consists of a main structure with a set of parallel Saint-Venant elements that is attached to a nonlinear energy sink with general odd nonlinear potential function. Time multi-scale energy exchanges between two oscillators is detected; in detail: the invariant manifold of the system at fast time scale is traced while detected equilibrium and singular points at slow time scale give us envision about system behavior(s) at pseudo-steady-state regime(s). All of detected behaviors provide us design tools for tuning necessary parameters of nonlinear energy sink for the localization of vibratory energy of main structural systems.

1 Introduction

It has been proved that pumping the essential part of vibratory energy of main structures is possible by endowing nonlinear properties of coupled oscillators [1, 2]. Later on this phenomenon was used for transferring the energy of main systems to secondary oscillators with very small mass compared to the main one's and with essential cubic geometrical nonlinearity. The phenomenon is named as "energy pumping" and the light and nonlinear oscillator is called as nonlinear energy sink (NES) [3–35]. Efficiency of the NES in localization of vibratory energy and passive control of systems has been proved experimentally as well [36–43]. However in most of above mentioned studies, the nonlinearity of the NES is cubic and the main structural system is supposed to be linear or to present smooth nonlinearity [16, 26, 27]. Some research works have been carried out to consider other types of nonlinearities for

C.-H. Lamarque · A.Ture Savadkoohi (✉)
ENTPE, Université de Lyon, LGCB and LTDS UMR CNRS 5513,
Rue Maurice Audin, 69518 Vaulx En Velin, France
e-mail: lamarque@entpe.fr

A.Ture Savadkoohi
e-mail: alireza.turesavadkoohi@entpe.fr

M. Belhaq (ed.), *Structural Nonlinear Dynamics and Diagnosis*,
Springer Proceedings in Physics 168, DOI 10.1007/978-3-319-19851-4_11

the geometrical potential of the NES and their efficiency in passive control of main systems, e.g. vibro-impact and non-polynomial nonlinearities, non-smooth potential function with constant or time-dependent mass [44–50]. There have been some research works that consider nonlinear main structural system to be controlled by cubic or non-smooth NES; in detail: a main oscillator with piece-wise linear and also Dahl-type behavior and a coupled nonsmooth NES [51, 52]; the main system with hysteresis behavior of Bouc-Wen type and a NES with general nonlinear potential function [53]; the main structure with single or several Saint-Venant elements [54] in parallel and a NES with cubic or general potential function [55, 56]. The current paper is a summary of our two previous research works which deals with the localization of vibratory energy of: (i) vertical main structural systems by a nonsmooth NES [48] and (ii) main structural systems with a set of parallel Saint-Venant elements by a NES with general potential function [56]. Organization of the chapter is as it follows: summary of the general methodology to deal with multiple scale dynamics of a main oscillator and a coupled NES is given in Sect. 2. Energy exchanges between a vertical linear system and a coupled nonsmooth NES is presented in Sects. 3 and 4 deals with studying of the dynamics of a main structural system including a set of parallel Saint-Venant elements and a coupled NES with a general nonlinear potential function. Finally conclusions are collected in Sect. 5.

2 General Methodology to Deal with Two Coupled Oscillators: A Main System + NES

In order to study multiple energy exchanges between a main oscillator and a coupled NES, we implement following steps [53]:

- re-scaling the system.
- transferring the system to the center of mass and relative displacement.
- applying complex variables to the system and using Galerkin technique by keeping first harmonics (and constant terms).
- embedding the time to different scales (fast and slow time scales) and detecting invariant manifold at the fast time scale and equilibrium points and fold singularities of the reduced order form of the system at the slow time scale.

3 Localization of Vibratory Energy of Vertical Main Linear Structural Systems by Coupled Non-smooth NES

Here we would like to analyze time multi-scale energy exchanges between a linear system and a nonsmooth NES. Gravity loads are not neglected. Let us consider the academic model of a system which is subjected to vertical excitations as is depicted

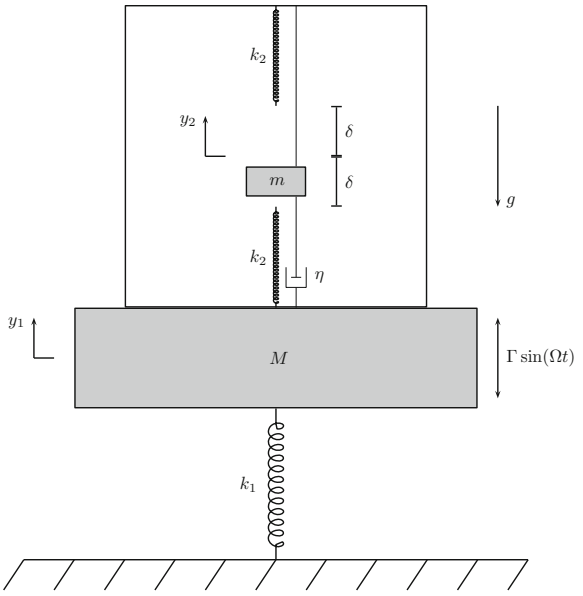

Fig. 1 The academic model of the system under gravity (g) loads and external force $\Gamma \sin(\Omega t)$. $m = \varepsilon M$, $0 < \varepsilon \ll 1$; masses oscillate vertically

in Fig. 1. The system is composed of a linear main structure (M) which is coupled to a non-smooth NES (m) system. Governing system equations can be summarized as:

$$\begin{cases} M\ddot{y}_1 + k_1 y_1 + F(y_1 - y_2) + \eta(\dot{y}_1 - \dot{y}_2) + Mg = \Gamma \sin(\Omega t) \\ m\ddot{y}_2 + F(y_2 - y_1) + \eta(\dot{y}_2 - \dot{y}_1) + mg = 0 \end{cases} \tag{1}$$

where η is the continues linear damping of the NES and F is the non-smooth potential function of the NES which is defined as follows:

$$F(z) = -\frac{\partial V(z)}{\partial z} = -F(-z) = \begin{cases} 0 & \text{if } -\delta \le z \le \delta \\ k_2(z-\delta) & \text{if } z \ge \delta \\ k_2(z+\delta) & \text{if } z \le -\delta \end{cases} \tag{2}$$

If we suppose that $T = t\sqrt{\dfrac{k_1}{M}} = t\vartheta$, then the system (1) in the T domain reads:

$$\begin{cases} \ddot{y}_1 + y_1 + \dfrac{1}{k_1}F(y_1 - y_2) + \dfrac{\eta}{\sqrt{k_1 M}}(\dot{y}_1 - \dot{y}_2) + \dfrac{Mg}{k_1} = \dfrac{\Gamma \sin(\dfrac{\Omega}{\vartheta}T)}{k_1} \\ \varepsilon\ddot{y}_2 + \dfrac{1}{k_1}F(y_2 - y_1) + \dfrac{\eta}{\sqrt{k_1 M}}(\dot{y}_2 - \dot{y}_1) + \dfrac{mg}{k_1} = 0 \end{cases} \tag{3}$$

We introduce the following variables: $\varepsilon = \dfrac{m}{M}$, $\gamma = \dfrac{Mg}{k_1}$, $\varepsilon\lambda = \dfrac{\eta}{\sqrt{k_1 M}}$, $\dfrac{1}{k_1}F(z) = \varepsilon\tilde{F}(z)$, $k = \dfrac{1}{\varepsilon}\dfrac{k_2}{k_1}$, $\omega = \dfrac{\Omega}{\vartheta}$ and $\dfrac{\Gamma}{k_1} = \varepsilon f_0$. So, scaled potential of the NES reads:

$$\tilde{F}(z) = \begin{cases} 0 & if \ -\delta \le z \le \delta \\ k(z-\delta) & if \quad z \ge \delta \\ k(z+\delta) & if \quad z \le -\delta \end{cases} \tag{4}$$

Following system can be derived:

$$\begin{cases} \ddot{y}_1 + y_1 + \varepsilon\tilde{F}(y_1 - y_2) + \varepsilon\lambda(\dot{y}_1 - \dot{y}_2) + \gamma \quad = \varepsilon f_0 \sin(\omega T) \\ \\ \varepsilon\ddot{y}_2 + \varepsilon\tilde{F}(y_2 - y_1) + \varepsilon\lambda(\dot{y}_2 - \dot{y}_1) + \varepsilon\gamma = 0 \end{cases} \tag{5}$$

We are interested to study forced vibration but also the transient behavior occurring before reaching the steady-state regime. The frequency of the main system in (5) is equal to "1" and we would like to analyze system behavior in the vicinity of 1:1 resonance. We will suppose that $\omega = 1 + \sigma\varepsilon$ and since ε is a small, it means that we will pinpoint system behavior around 1:1 resonance. Let us transfer the system to the following coordinates:

$$\begin{cases} v = y_1 + \varepsilon y_2 \\ \\ w = y_1 - y_2 \end{cases} \tag{6}$$

In the second equation of the system (5), the parameter ε has been kept intentionally in order to show coupling terms between two equations of the system (5) and physical orders of respective equations. Especially v is associated to the center of two masses $(1, \varepsilon)$. If we divide the second equation of the system (5) by ε, then we will have a system of two masses at the same order (1, 1), leading to $v = y_1 + y_2$ and $w = y_1 - y_2$ which do not have appropriate physical meanings for the system under consideration. The consequence should be to keep nonlinear terms in both resulting equations for v and w.

By adding and subtraction two equations of the system (5) we will have:

$$\begin{cases} \ddot{v} + \dfrac{1}{1+\varepsilon}(v + \varepsilon w) + \gamma(1+\varepsilon) = \varepsilon f_0 \sin(\omega T) \\ \\ \ddot{w} + \dfrac{1}{1+\varepsilon}(v + \varepsilon w) + (1+\varepsilon)\tilde{F}(w) + (1+\varepsilon)\lambda\dot{w} = \varepsilon f_0 \sin(\omega T) \end{cases} \tag{7}$$

We introduce a modified form of Manevitch's complex variables [57] to the system (7):

$$\begin{cases} B_1 + \varphi_1 e^{i\omega T} = \dot{v} + i\omega v \\ B_2 + \varphi_2 e^{i\omega T} = \dot{w} + i\omega w \end{cases} \tag{8}$$

with $B_1 = ib_1$, $B_2 = ib_2$ and $i^2 = -1$. B_1 and B_2 are constant terms taking into account the fact that the dynamical system (5) (including γ) is not written around the $(y_1, y_2, \dot{y}_1, \dot{y}_2) = (0, 0, 0, 0)$. So, we have to include constant terms to take into account nonlinear terms in averaging. It corresponds to taking into account constant terms of Fourier series together with first harmonic terms. We can present the function $\tilde{F}(w)$ in the form of Fourier series:

$$\tilde{F}(w) = \tilde{F}\Big(\frac{b_2}{\omega} - \frac{i}{2\omega}(\varphi_2 e^{i\omega T} - \varphi_2^* e^{-i\omega T})\Big) = \sum_{j=-\infty}^{+\infty} f_j(b_2, \varphi_2, \varphi_2^*) e^{i\omega j T} \tag{9}$$

where the * represents the complex conjugate of the function under consideration. We implement the Galerkin method using a truncated Fourier series (constant and first harmonic) and then we endow multiple time scales approach to investigate the evolution of the Fourier-coefficients. The constant and first harmonic of the (7) by considering variables of (8) and $j = 0, 1$ in (9) read as:

$$\begin{cases} \dfrac{1}{1+\varepsilon}\left(\dfrac{b_1}{\omega} + \varepsilon\dfrac{b_2}{\omega}\right) + (1+\varepsilon)\gamma = 0 \\ \dfrac{1}{1+\varepsilon}\left(\dfrac{b_1}{\omega} + \varepsilon\dfrac{b_2}{\omega}\right) + (1+\varepsilon) f_z(b_2, \varphi_2, \varphi_2^*) = 0 \end{cases} \tag{10}$$

$$\begin{cases} \dot{\varphi}_1 = -\dfrac{i}{2}\varepsilon f_0 + \dfrac{i}{2\omega(1+\varepsilon)}(\varphi_1 + \varepsilon\varphi_2) - \dfrac{i}{2}\omega\varphi_1 \\ \dot{\varphi}_2 = -\dfrac{i}{2}\varepsilon f_0 + \dfrac{i}{2\omega(1+\varepsilon)}(\varphi_1 + \varepsilon\varphi_2) - \dfrac{\lambda(1+\varepsilon)}{2}\varphi_2 - \dfrac{i}{2}\omega\varphi_2 - (1+\varepsilon) f_f(b_2, \varphi_2, \varphi_2^*) \end{cases} \tag{11}$$

where $f_z(b_2, \varphi_2, \varphi_2^*)$ and $f_f(b_2, \varphi_2, \varphi_2^*)$ are zero and first Fourier coefficients which can be evaluated as:

$$f_z(b_2, \varphi_2, \varphi_2^*) = \frac{\omega}{2\pi}\int_0^{\frac{2\pi}{\omega}} \tilde{F}\Big(\frac{b_2}{\omega} - \frac{i}{2\omega}(\varphi_2 e^{i\omega T} - \varphi_2^* e^{-i\omega T})\Big) dT \tag{12}$$

$$f_f(b_2, \varphi_2, \varphi_2^*) = \frac{\omega}{2\pi}\int_0^{\frac{2\pi}{\omega}} \tilde{F}\Big(\frac{b_2}{\omega} - \frac{i}{2\omega}(\varphi_2 e^{i\omega T} - \varphi_2^* e^{-i\omega T})\Big) e^{-i\omega T} dT \tag{13}$$

It can be proved that [48]:

$$f_f(b_2, \varphi_2, \varphi_2^*) = -\frac{i\varphi_2}{2} G_f\big(|\varphi_2|^2\big) \tag{14}$$

where for any variable $\chi \geq 0$

$$G_f(\chi) = \begin{cases} 0 \quad if \quad \frac{b_2}{\omega} + \frac{\sqrt{\chi}}{\omega} < \delta \\ \frac{k}{2\pi\omega}\Big(\pi + \frac{2b_2}{\chi}\sqrt{\chi - (b_2 - \delta\omega)^2} - \frac{2\delta\omega}{\chi}\sqrt{\chi - (b_2 - \delta\omega)^2} - \\ \frac{2b_2}{\chi}\sqrt{\chi - (b_2 + \delta\omega)^2} - \frac{2\delta\omega}{\chi}\sqrt{\chi - (b_2 + \delta\omega)^2} + \\ 2\arccos\big(\frac{b_2 + \delta\omega}{\sqrt{\chi}}\big) + 2\arcsin\big(\frac{b_2 - \delta\omega}{\sqrt{\chi}}\big)\Big) \quad if \quad \frac{b_2}{\omega} + \frac{\sqrt{\chi}}{\omega} \geq \delta \end{cases} \tag{15}$$

and

$$f_z(\chi) = \begin{cases} 0 \quad if \quad \frac{b_2}{\omega} + \frac{\sqrt{\chi}}{\omega} < \delta \\ \frac{k}{\pi\omega}\Big(b_2\pi + \sqrt{(b_2 + \sqrt{\chi} - \delta\omega)(-b + \sqrt{\chi} + \delta\omega)} - \\ \sqrt{(-b_2 + \sqrt{\chi} - \delta\omega)(b_2 + \sqrt{\chi} + \delta\omega)} + \\ (b_2 - \delta\omega)\arcsin\big(\frac{b_2 - \delta\omega}{\sqrt{\chi}}\big) + (b_2 + \delta\omega)\arcsin\big(\frac{b_2 + \delta\omega}{\sqrt{\chi}}\big)\Big) \\ \quad if \quad \frac{b_2}{\omega} + \frac{\sqrt{\chi}}{\omega} \geq \delta \end{cases} \tag{16}$$

To deal with the systems (10) and (11), an asymptotic approach [58] by introducing slow times $\tau_1, \tau_2, \ldots$with the fast time τ_0 can be implemented as follows:

$$T = \tau_0, \quad \tau_1 = \varepsilon\tau_0, \ldots \quad , \tag{17}$$

so,

$$\frac{d}{dT} = \frac{\partial}{\partial\tau_0} + \varepsilon\frac{\partial}{\partial\tau_1} + \cdots \tag{18}$$

In the next sections we will try to have finer envision into systems (10) and (11) at different orders of ε in order to grasp the system behavior during different scales of time.

3.1 Truncated Fourier Series: Constant Term

The general form of the system (10) show that $\gamma = f_z(N_2^2)$. During the ε^0 order, it leads to:

$$b_1 = -\gamma \tag{19}$$

while during the ε^1 order we have:

$$b_2 = -\gamma(2+\sigma) \tag{20}$$

3.2 Truncated Fourier Series: First Harmonic

3.2.1 ε^0 Order

We assume that the system is around 1:1 resonance ($\omega = 1 + \sigma\varepsilon$). Equation (11) at the ε^0 order yield to:

$$\frac{\partial\varphi_1}{\partial\tau_0} = 0 \Rightarrow \varphi_1 = \varphi_1(\tau_1) \tag{21}$$

$$\frac{\partial\varphi_2}{\partial\tau_0} + \frac{i\left(1 - G_f\left(|\varphi_2|^2\right)\right) + \lambda}{2}\varphi_2 = \frac{i}{2}\varphi_1 \tag{22}$$

so, fixed points of the system ($\Phi(\tau_1)$) can be evaluated by following equation:

$$\frac{i\left(1 - G_f\left(|\Phi|^2\right)\right) + \lambda}{2}\Phi = \frac{i}{2}\varphi_1 \tag{23}$$

Let us assume that $\varphi_1 = N_1 e^{i\delta_1}$ and $\Phi = N_2 e^{i\delta_2}$, so (23) can be re-written as the following form:

$$N_2 - i\lambda N_2 - G_f(N_2^2)N_2 = N_1 e^{i(\delta_1 - \delta_2)} \tag{24}$$

which leads us to follow invariant manifold of the system during τ_0 time scale (τ_0-invariant):

$$N_1 = N_2\sqrt{\lambda^2 + \left(1 - G_f(N_2^2)\right)^2} \tag{25}$$

A typical invariant manifold for given system parameters is illustrated in Fig. 2. It has been proved that stability borders of the τ_0-invariant is defined as it follows [48]:

$$\lambda^2 + \left(1 - G_f(N_2^2)\right)\left(1 - H(N_2^2)N_2 - G_f(N_2^2)\right) > 0 \tag{26}$$

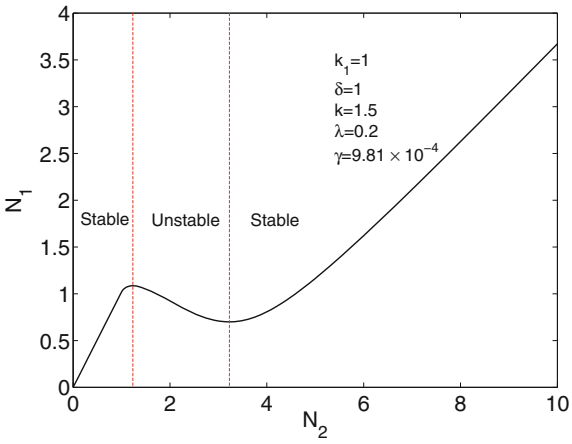

Fig. 2 τ_0-invariant manifold of the system and its stable and unstable zones

Stable and unstable zones of the invariant manifold are depicted in Fig. 2. In fact when the system arrives to the vicinity of the unstable zone, it tries to reach another stable zone via a bifurcation. This will lead to the energy pumping phenomenon.

3.2.2 ε^1 Order

At the order of ε^1 the first equation of the system (11) reads as:

$$\frac{\partial \varphi_1}{\partial \tau_1} = -\frac{i}{2} f_0 + \frac{i}{2}(\Phi - \varphi_1 - \sigma \varphi_1) - \frac{i}{2}\sigma \varphi_1 \tag{27}$$

Let us try to enlighten the behavior of the system at the τ_1 time scale "around" the invariant manifold at the time scale τ_0. By considering (23), following system can be derived:

$$\begin{aligned} &\frac{\partial}{\partial \tau_1}\left(\Phi - i\lambda\Phi - \Phi G_f(|\Phi|^2)\right) \\ &= \frac{i}{2}\Big(- f_0 - 2\sigma\Big(\Phi - i\lambda\Phi - G_f\big(|\Phi|^2\big)\Phi\Big) + i\lambda\Phi + G_f\big(|\Phi|^2\big)\Phi\Big) \end{aligned} \tag{28}$$

and if we suppose that $\Phi = N_2(\tau_1)e^{i\delta_2(\tau_1)}$, following compact for of equations can be obtained:

$$\frac{\partial N_2}{\partial \tau_1} = \frac{f_1(N_2, \delta_2)}{g(N_2)} \tag{29}$$

$$\frac{\partial \delta_2}{\partial \tau_1} = \frac{f_2(N_2, \delta_2)}{g(N_2)} \tag{30}$$

where,

$$f_1(N_2,\delta_2) = f_0\sin(\delta_2)\Big(G_f\big(N_2^2\big)-1\Big) - \lambda N_2 + \lambda f_0\cos(\delta_2) \tag{31}$$

$$f_2(N_2,\delta_2) = -\frac{1-G_f\big(N_2^2\big)-2N_2^2G'_f\big(N_2^2\big)}{N_2}f_0\cos(\delta_2) - \frac{\lambda}{N_2}f_0\sin(\delta_2)$$
$$-\lambda^2(1+2\sigma)+\Big(1-G_f\big(N_2^2\big)-2N_2^2G'_f\big(N_2^2\big)\Big)\Big(-2\sigma+2\sigma G_f\big(N_2^2\big)+G_f\big(N_2^2\big)\Big) \tag{32}$$

$$g(N_2) = 2\Big(1+\lambda^2-2G_f\big(N_2^2\big)-2N_2^2G'_f\big(N_2^2\big)+G_f^2\big(N_2^2\big)+2N_2^2G_f\big(N_2^2\big)G'_f\big(N_2^2\big)\Big) \tag{33}$$

The relation $g(N_2)=0$ provides two values for N_2, namely N_{21} and N_{22}. They are called as fold lines of the system. We will use these equations later on for detailed bifurcation analysis of the system.

For detecting the invariant manifold of the system at the τ_1 time scale (τ_1-invariant), (28) can be re-written as ($\frac{\partial\varphi_1}{\partial\tau_1}=0$):

$$\frac{i}{2}\Big(-f_0-2\sigma\Big(\Phi-i\lambda\Phi-G_f\big(|\Phi|^2\big)\Phi\Big)+i\lambda\Phi+G_f\big(|\Phi|^2\big)\Phi\Big)=0 \tag{34}$$

or

$$f_0 = N_2\sqrt{\lambda^2(1+2\sigma)^2+\Big((1+2\sigma)G_f\big(N_2^2\big)-2\sigma\Big)^2} \tag{35}$$

A typical invariant manifold of the system at the time scale τ_1 is depicted in Fig. 3. Intersections of this invariant manifold (for a given f_0) with the τ_0-invariant are positions of fixed points.

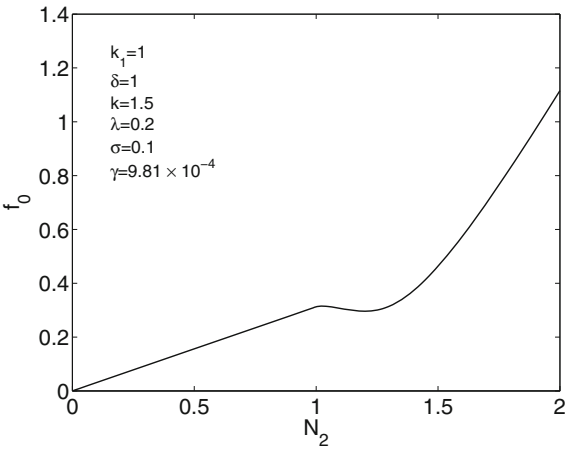

Fig. 3 τ_1-invariant manifold of the system

3.3 Analytical Results Versus Numerical Integrations

Since the overall system is under gravity loading, the initial equilibrium state of each mass (y_{10} and y_{20}) should be evaluated. Let us consider different hypothesis as the equilibrium state for the system (1):

- $-\delta < y_2 - y_1 < +\delta$ so $F(y_2 - y_1) = 0$
  This assumption leads us to following system:

$$\begin{cases} k_1 y_1 + Mg = 0 \\ mg = 0 \end{cases} \tag{36}$$

  which is an impossible equality. So, this assumption is not valid at the equilibrium state of the overall system.
- $y_2 - y_1 < -\delta$ so $F(y_2 - y_1) = k_2(y_2 - y_1) + k_2\delta$
  This leads to following system:

$$\begin{cases} k_1 y_1 - k_2(y_2 - y_1) - k_2\delta + Mg = 0 \\ k_2(y_2 - y_1) + k_2\delta + mg = 0 \end{cases} \tag{37}$$

so,

$$\begin{cases} y_{10} = -\dfrac{Mg}{k_1}(1+\varepsilon) = -\gamma(1+\varepsilon) \\ y_{20} = -\dfrac{Mg}{k_1}(1+\varepsilon) - \delta - \dfrac{mg}{k_2} = -\gamma(1+\varepsilon) - \delta - \varepsilon\dfrac{Mg}{k_2} \end{cases} \tag{38}$$

This equilibrium point should be considered in all numerical results. We can impose equilibrium states to the numerical results as follows:

$$\begin{cases} v_{numerical} = (y_1 - y_{10}) + \varepsilon(y_2 - y_{20}) \\ w_{numerical} = (y_1 - y_{10}) - (y_2 - y_{20}) \end{cases} \tag{39}$$

So, N_1 and N_2 can be defined in terms of original system of equations (N_1^{exact} and N_2^{exact}) as:

$$N_1^{exact} = \sqrt{(v_{numerical})^2 + (\dot{y_1} + \varepsilon\dot{y_2})^2}. \tag{40}$$

$$N_2^{exact} = \sqrt{(w_{numerical})^2 + (\dot{y_1} - \dot{y_2})^2}. \tag{41}$$

Let us consider the following initial conditions for the system:

$$\begin{cases} y_1(0) = 1.5 + y_{10} \ , & \dot{y}_1(0) = 0 \\ y_2(0) = y_{20} \ , & \dot{y}_2(0) = 0 \end{cases} \tag{42}$$

Figure 4 presents τ_0-invariant of the system and corresponding numerical results which are obtained by direct integration of (5) with the external forcing amplitude $f_0 = 0.1$. When the system arrives to the unstable zone, it tries to reach other stable zone by an abrupt jump between its stable branches through a bifurcation. This bifurcation leads the master structure to experience very low amplitude compared to initial stages of the vibration (see Fig. 5).

3.4 Strongly Modulated Response in the Presence of Gravity

The strongly modulated response (SMR) of the system in the vicinity of the 1:1 resonance is characterized by relaxation oscillations between stable branches of the slow invariant manifold, i.e. switches between slow motions at stable critical manifolds of the system and fast jumps between them. Starosvetsky and Gendelman [21] pinpointed this behavior in two coupled oscillators with essential cubic nonlinearity for the NES while Lamarque et al. [46] investigated the same behavior in systems with non-smooth NES. Let us consider (29) and (30). The possible relaxation of the system can occur if the flow in the vicinity of the lower fold line, i.e. N_{21}, experiences some bifurcation, i.e. for some points at the lower fold, N_2' changes its direction, so phase trajectories of the lower stable branch can change their direction and aim at

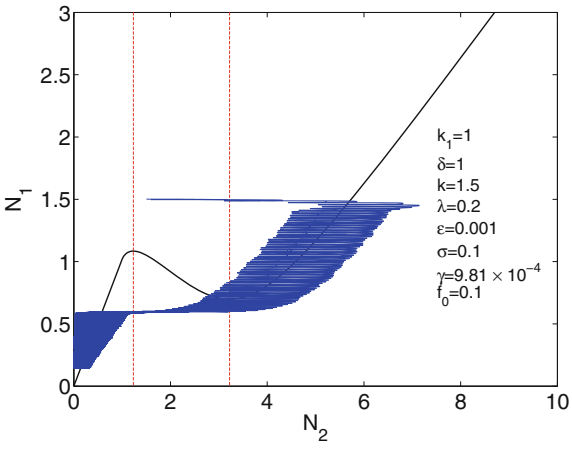

Fig. 4 τ_0-invariant manifold of the system in the presence of the gravity and corresponding numerical result with $f_0 = 0.1$. Numerical results are obtained by direct integration of (5)

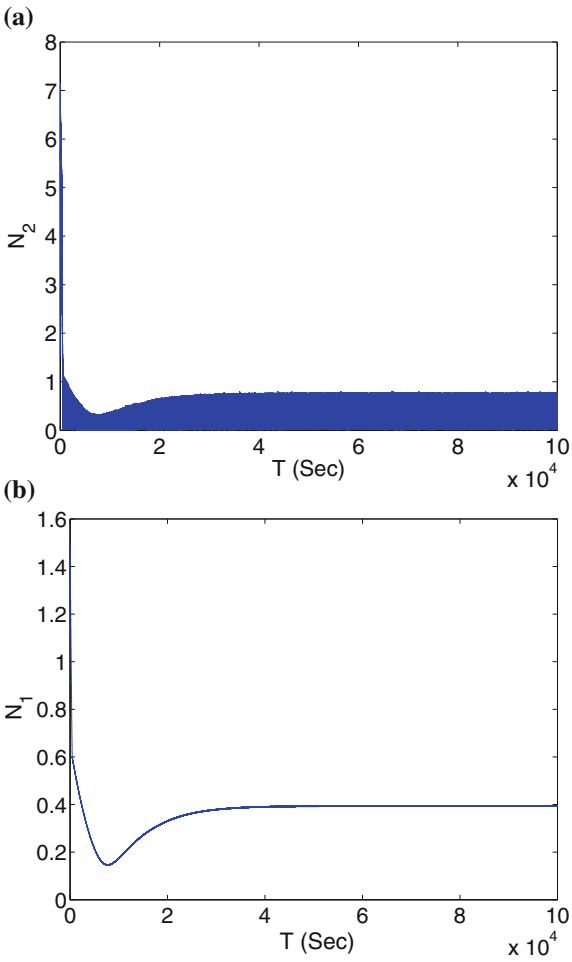

Fig. 5 Variation of system amplitudes with respect to the time ($f_0 = 0.1$): **a** N_2; **b** N_1. Results are obtained by direct integration of (5)

the fold line N_{21} for a jump to upper stable branch. This criterion will be satisfied if in (29) and (30):

$$f_1(N_2, \delta_2) = 0$$
$$f_2(N_2, \delta_2) = 0 \tag{43}$$

which corresponds to ordinary fixed points of the system under consideration. If in addition to this, $g(N_2) = 0$ (the denominator of (29)) then the system will have fold singularities, i.e. singularity and equilibrium points coincide, so $N_2 = N_{21}$ and $N_2 = N_{22}$. It is worthwhile to mention that $g(N_2) = 0$ is exactly equivalent to stability borders which are presented by (26) [48], i.e.

$$\lambda^2 + \left(1 - G_f(N_2^2)\right)\left(1 - H(N_2^2)N_2 - G_f(N_2^2)\right) = 0 \tag{44}$$

Lamarque et al. [46] proved that necessary forcing condition for existence of the first pair of folded singularities, i.e. (N_{21}, δ_{21}), is:

$$f_0 \geq f_{0(1critical)} = \frac{\lambda N_{21}}{\sqrt{\lambda^2 + \left(1 - G_f\left(N_{21}^2\right)\right)^2}} \tag{45}$$

and the second pair of folded singularities on the second fold, i.e. (N_{22}, δ_{21}) and (N_{22}, δ_{22}), exists if:

$$f_0 \geq f_{0(2critical)} = \frac{\lambda N_{22}}{\sqrt{\lambda^2 + \left(1 - G_f\left(N_{22}^2\right)\right)^2}} \tag{46}$$

Let us analyze the system under external forcing term $f_0 = 0.3 > f_{0(1critical)} = 0.254$. The global behavior of the system is depicted in Fig. 6 while histories of system amplitudes are illustrated in Fig. 7. The response of the system is strongly modulated by trapping into hysteresis loops and bifurcations between its stables branches. In order to clarify this, phase portraits of the system is depicted in Fig. 8a while a zoomed area of this figure is illustrated in Fig. 8b. It is seen that some flow lines change their direction toward the fold line N_{21} which gives a hint of the relaxation of the system by facing to folded singularities in the form of saddle and node (see Fig. 8b).

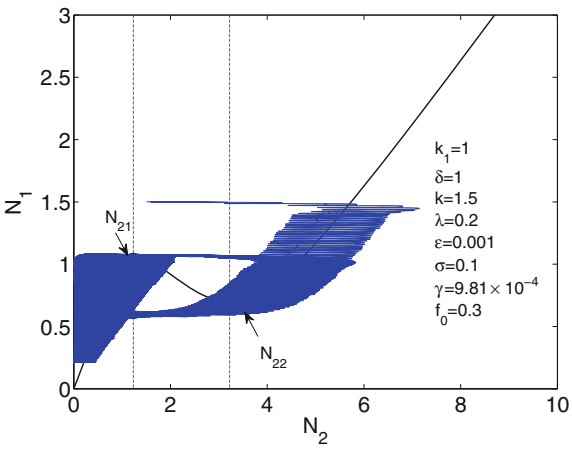

Fig. 6 τ_0-invariant manifold of the system in the presence of the gravity and corresponding numerical result with $f_0 = 0.3$. Numerical results are obtained by direct integration of (5)

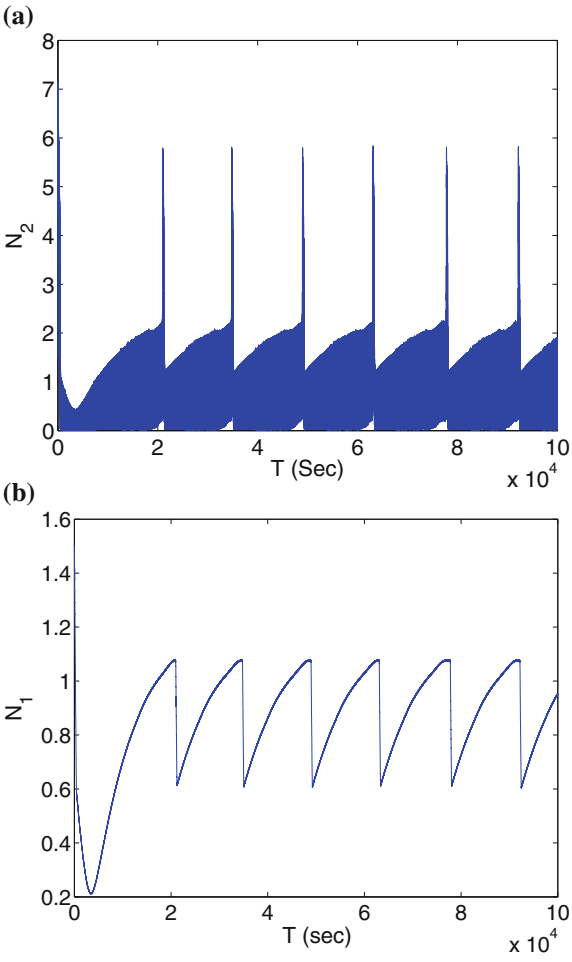

Fig. 7 SMR and Beating response of two oscillators with external forcing term $f_0 = 0.3 > f_{0(1critical)} = 0.254$: a) N_2; b) N_1. Results are obtained by direct integration of (5)

4 Localization of Vibratory Energy of a Main System with a Set of Saint-Venant Elements by a NES with General Nonlinearity

4.1 Representation of the System

We consider the system which is depicted in Fig. 9: It consists of two coupled oscillators. The first one with mass, stiffness and damping as M, k_0 and $\tilde{\lambda}$, which possesses a set of parallel Saint-Venant elements with characteristics as $\tilde{k}_j$ (stiffness) and α_j (threshold of the Saint-Venant element), $j = 1, 2, \ldots, n$. Each Saint-Venant element has an internal variable (displacement u_j). The second oscillator, namely NES has

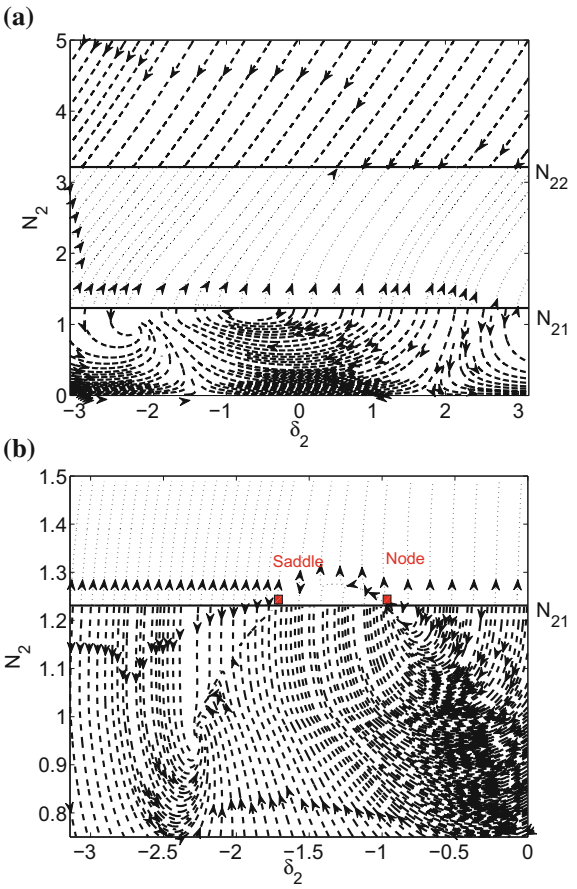

Fig. 8 Phase portrait for the system with $f_0 = 0.3 > f_{0(1critical)} = 0.254$, **a** the overall view; **b** the zoomed area around folded singularities

the mass, stiffness and damping as m ($0 < \varepsilon = \dfrac{m}{M} \ll 1$), $\tilde{c}_1$ and $\tilde{\lambda}_1$. The potential of the NES (F) is supposed to be a general "nonlinear" and "odd" function, i.e. $F(-z) = -F(z)$ (e.g. $F(z) = z^3$) [56]. If x (versus y) be the displacement of the mass M (respectively mass m), governing equations of the system can be summarized as:

$$\begin{cases} M\dfrac{d^2x}{dt^2} + \tilde{\lambda}\dfrac{dx}{dt} + \tilde{\lambda}_1(\dfrac{dx}{dt} - \dfrac{dy}{dt}) + k_0 x + \displaystyle\sum_{j=1}^{n} \tilde{k}_j u_j + \tilde{c}_1 F(x-y) = f_1(t) \\ m\dfrac{d^2y}{dt^2} + \tilde{\lambda}_1(\dfrac{dy}{dt} - \dfrac{dx}{dt}) + \tilde{c}_1 F(y-x) = 0 \\ \left(\dfrac{du_j}{dt} + \beta(\dfrac{u_j}{\eta_j})\right) \ni \dfrac{dx}{dt}, \quad \eta_j = \dfrac{\alpha_j}{\tilde{k}_j}, \quad j = 1, 2, \ldots, n \end{cases} \tag{47}$$

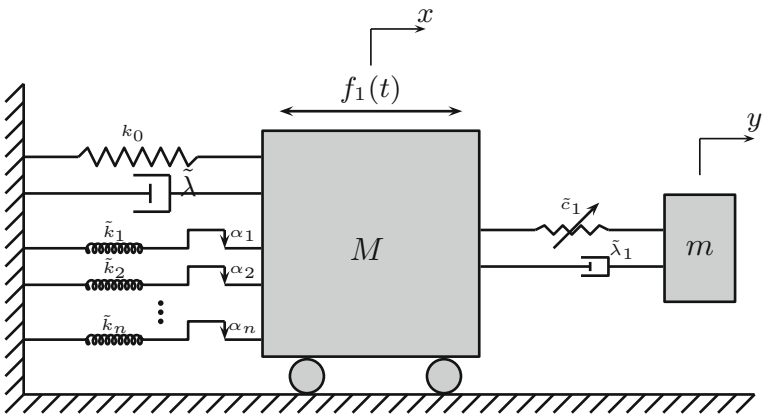

Fig. 9 Two coupled oscillators: the first one with a set of parallel Saint-Venant elements and under external force $f_1(t)$; the second one with general and odd nonlinear potential function ($m = \varepsilon M$, $0 < \varepsilon \ll 1$)

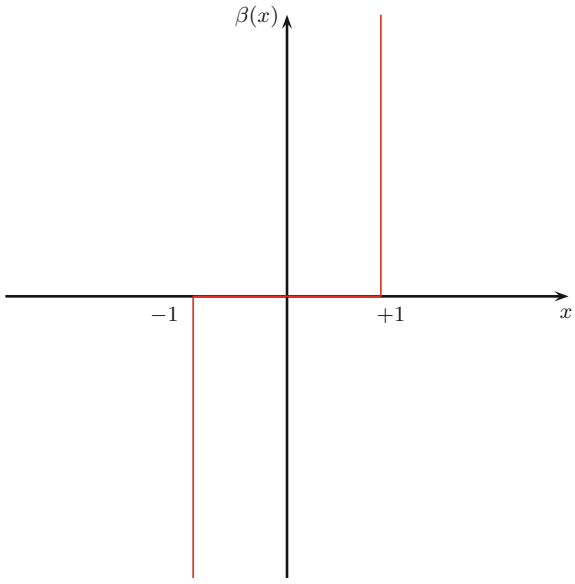

Fig. 10 The β graph in Saint-Venant element

The β graph which is depicted in Fig. 10 can be described as it follows:

$$\beta(x) = \begin{cases} \emptyset & \text{if } x \in \,]-\infty, -1[\cup]1, +\infty[\\ 0 & \text{if } x \in \,]-1, 1[\\ \mathbb{R}_- & \text{if } x = -1 \\ \mathbb{R}_+ & \text{if } x = 1 \end{cases} \tag{48}$$

Let us introduce $\tau = t\sqrt{\frac{k_0}{M}} = \vartheta t$, $\frac{\tilde{\lambda}\vartheta}{M\vartheta^2} = \varepsilon\lambda_0$, $\frac{\tilde{k}_j}{M\vartheta^2} = \varepsilon k_j$, $\frac{\tilde{c}_1}{M\vartheta^2} = \varepsilon c_{10}$, $\frac{\tilde{\lambda}_1\vartheta}{M\vartheta^2} = \varepsilon\lambda_{10}$, $\frac{f_1(\frac{\tau}{\vartheta})}{M\vartheta^2} = \varepsilon f_{10}\sin(\Omega\tau)$.

We mention that the differential inclusions of the model under consideration come from basic constitutive equations of the Saint-Venant elements as:

$$k_j u_j \in \alpha_j \sigma\left(\frac{dx}{dt} - \frac{du_j}{dt}\right), \quad j = 1, 2, \ldots, n \tag{49}$$

where σ is the graph of the sign:

$$\sigma(z) = \begin{cases} -1 & \text{if } z < 0 \\ [-1, 1] & \text{if } z = 0 \\ 1 & \text{if } z > 0 \end{cases} \tag{50}$$

So, one should take into account that $\frac{d.}{dt} = \vartheta\frac{d.}{d\tau}$ and

$$\begin{aligned} &\tilde{k}_j u_j \in \alpha_j \sigma\left(\vartheta\left(\frac{dx}{d\tau} - \frac{du_j}{d\tau}\right)\right) \quad j = 1, 2, \ldots, n \\ \Leftrightarrow\ &\tilde{k}_j u_j \in \alpha_j \sigma\left(\left(\frac{dx}{d\tau} - \frac{du_j}{d\tau}\right)\right) \quad j = 1, 2, \ldots, n \end{aligned} \tag{51}$$

Finally (47) are equivalent to

$$\begin{cases} \dfrac{d^2x}{d\tau^2} + \varepsilon\lambda_0\dfrac{dx}{d\tau} + \varepsilon\lambda_{10}\left(\dfrac{dx}{d\tau} - \dfrac{dy}{d\tau}\right) + x + \varepsilon\displaystyle\sum_{j=1}^{n} k_j u_j + \varepsilon c_{10}F(x-y) \\ = \varepsilon f_{10}\sin(\Omega\tau) \\ \varepsilon\dfrac{d^2y}{d\tau^2} + \varepsilon\lambda_{10}\left(\dfrac{dy}{d\tau} - \dfrac{dx}{d\tau}\right) + \varepsilon c_{10}F(y-x) = 0 \\ \left(\dfrac{du_j}{d\tau} + \beta\left(\dfrac{u_j}{\eta_j}\right)\right) \ni \dfrac{dx}{d\tau}, \quad \eta_j = \dfrac{\alpha_j}{\tilde{k}_j}, \quad j = 1, 2, \ldots, n \end{cases} \tag{52}$$

Let us introduce coordinates of the center of mass and relative displacement via

$$\begin{cases} v = x + \varepsilon y \\ w = x - y \end{cases} \Leftrightarrow \begin{cases} x = \dfrac{v + \varepsilon w}{1+\varepsilon} \\ y = \dfrac{v - w}{1+\varepsilon} \end{cases} \tag{53}$$

System (52) becomes:

$$\begin{cases} \dfrac{d^2v}{d\tau^2} + \dfrac{\varepsilon\lambda_0}{1+\varepsilon}\left(\dfrac{dv}{d\tau} + \varepsilon\dfrac{dw}{d\tau}\right) + \dfrac{v+\varepsilon w}{1+\varepsilon} + +\varepsilon\sum_{j=1}^{n} k_j u_j = \varepsilon f_{10}\sin(\Omega\tau) \\ \dfrac{d^2w}{d\tau^2} + \dfrac{\varepsilon\lambda_0}{1+\varepsilon}\left(\dfrac{dv}{d\tau} + \varepsilon\dfrac{dw}{d\tau}\right) + \dfrac{v+\varepsilon w}{1+\varepsilon} + +\varepsilon\sum_{j=1}^{n} k_j u_j \\ +(1+\varepsilon)\left(\lambda_{10}\dfrac{dw}{d\tau} + c_{10}F(w)\right) = \varepsilon f_{10}\sin(\Omega\tau) \\ \left(\dfrac{du_j}{d\tau} + \beta\left(\dfrac{u_j}{\eta_j}\right)\right) \ni \dfrac{1}{1+\varepsilon}\left(\dfrac{dv}{d\tau} + \varepsilon\dfrac{dw}{d\tau}\right), \quad \eta_j = \dfrac{\alpha_j}{\tilde{k}_j}, \quad j = 1, 2, \ldots, n \end{cases} \tag{54}$$

4.2 Dynamical Behavior Around 1:1 Resonance

Let us set $T = \Omega\tau$ and $\cdot = \dfrac{d}{d\tau}$. We introduce the following complex variables [57] to the system:

$$\begin{array}{ll} \phi_1 e^{iT} = \Omega(\dot{v} + \imath v) & , \phi_1^* e^{-iT} = \Omega(\dot{v} - iv) \\ \phi_2 e^{iT} = \Omega(\dot{w} + iw) & , \phi_2^* e^{-iT} = \Omega(\dot{w} - iw) \\ \phi_{2+j} e^{iT} = \Omega(\dot{u}_j + iu_j) & , \phi_{2+j}^* e^{-iT} = \Omega(\dot{u}_j - iu_j) \ , \ j = 1, 2, \ldots, n \end{array} \tag{55}$$

with $i^2 = -1$. To investigate the 1:1 resonance, we assume $\Omega = 1 + \sigma\varepsilon$.
We consider only equations obtained by Galerkin method and truncated Fourier series: Indeed we take into account only first harmonic e^{iT} for each equation. To calculate the corresponding Fourier coefficients we assume that ϕ_l and ϕ_l^* ($l = 1, 2, \ldots, n + j$) do not depend on T. We will either verify this assumption during the multiple scales analysis, or we will assume that after a transient long enough ϕ_l and ϕ_l^* ($l = 1, 2, \ldots, n + j$) reach to an "asymptotic state" independently of T. Nevertheless we also keep $\dot{\phi}_l$ and $\dot{\phi}_2$ in the equations. Then we obtain following system:

$$\Omega\dot{\phi_1} - \frac{\Omega}{2i}\phi_1 + \frac{\varepsilon\lambda_0(\phi_1+\varepsilon\phi_2)}{2(1+\varepsilon)} + \frac{\phi_1+\varepsilon\phi_2}{2i\Omega(1+\varepsilon)} + \varepsilon\frac{\sum_{j=1}^{n} k_j\phi_{j+2}}{2\Omega i} = \varepsilon\frac{f_{10}}{2i}$$

$$\Omega\dot{\phi_2} - \frac{\Omega}{2i}\phi_2 + \frac{\varepsilon\lambda_0(\phi_1+\varepsilon\phi_2)}{2(1+\varepsilon)} + \frac{\phi_1+\varepsilon\phi_2}{2i\Omega(1+\varepsilon)} + \frac{\sum_{j=1}^{n} k_j\phi_{j+2}}{2\Omega i} + (1+\varepsilon)(c_{10}\mathscr{F} + \frac{\lambda_{10}}{2}\phi_2) = \varepsilon\frac{f_{10}}{2i} \tag{56}$$

$$\phi_{j+2} = \frac{\phi_1+\varepsilon\phi_2}{(1+\varepsilon)\pi}\xi_j\big(\frac{|\phi_1+\varepsilon\phi_2|}{(1+\varepsilon)\Omega}\big), \quad j = 1, 2, \ldots, n$$

where

$$\mathscr{F} = \frac{1}{2\pi}\int_0^{2\pi} e^{-iT} F\big(\frac{\phi_1 e^{iT} - \phi_2^* e^{-iT}}{2i\Omega}\big)\,\mathrm{d}T \tag{57}$$

and $\xi_j(z)(\forall z \in \mathbb{R}_+,\ j = 1, 2, \ldots, n)$ reads:

$$\xi_j(z) = \begin{cases} \pi & \text{if } z \leqslant \eta_j \\ \theta + e^{-i\theta}\sin(\theta) - 4e^{-i\frac{\theta}{2}}\sin(\frac{\theta}{2}) - \dfrac{4\eta_j}{z}e^{-i(\theta+\frac{\pi}{2})} & \text{if } z > \eta_j \end{cases} \tag{58}$$

with

$$\theta = \arccos(1 - \frac{2\eta_j}{z}) \tag{59}$$

As in the Sect. 3 a multiple scale approach [58] with a small (and given) parameter ε is presented by considering fast time $T_0 = T$, and slow times $T_l = \varepsilon^l T, l = 1, 2, \ldots$ so that:

$$\frac{d}{dT} = \frac{d}{dT_0} + \varepsilon\frac{d}{dT_1} + \varepsilon^2\frac{d}{dT_2} + \ldots \tag{60}$$

4.2.1 ε^0-Order of the System

At ε^0 order, following equations can be derived from the system of (56):

$$\frac{\partial\phi_1}{\partial T_0} = 0 \Rightarrow \phi_1 = \phi_1(T_1, T_2, \ldots) \tag{61}$$

$$\frac{\partial\phi_2}{\partial T_0} + \frac{\phi_1-\phi_2}{2i} + c_{10}\mathscr{F} + \frac{\lambda_{10}}{2}\phi_2 = 0 \tag{62}$$

$$\phi_{j+2} = \frac{\phi_1}{\pi}\xi_j(|\phi_1|), \quad j = 1, 2, \ldots, n \tag{63}$$

We can see from equations that ϕ_1 is a constant versus $T_0 = T$, as well as ϕ_{j+2}, $j = 1, 2, \ldots, n$, so the assumption for calculation of Fourier coefficients of $e^{iT} = e^{iT_0}$ is verified a posteriori. For ϕ_2, we can not claim the same property. This is why we process as follows: We assume that when $T_0 \to \infty$, ϕ_2 reaches an asymptotic equilibrium governed by a manifold called T_0-invariant. Then we have:

$$\frac{\phi_1 - \phi_2}{2i} + c_{10}\mathscr{F} + \frac{\lambda_{10}}{2}\phi_2 = 0 \tag{64}$$

so that implicitly ϕ_2 may depend on T_1 now, but no longer on T_0 (after T_0 long enough to approach the asymptotic state of ϕ_2 governed by (64)). We study modulation of the dynamics around periodic solution depending on time T_0 associated to the T_0-invariant. Let us also notice that equations for ϕ_{j+2}, $j = 1, 2, \ldots, n$ are governed by first order differential equations.

4.2.2 ε^1-Order of the System and Modulations Around T_0-Invariant

The ε^1 order of the first equation of system (56) reads:

$$\frac{d\phi_1}{dT_1} + \frac{\lambda_0}{2}\phi_1 + \frac{\phi_2}{2i} - \frac{2\sigma + 1}{2i}\phi_1 + \frac{\sum_{j=1}^{n} k_j\phi_{j+2}}{2i} = \frac{f_{10}}{2i} \tag{65}$$

Let us consider T_0-invariant and also obtained solutions at ε^0 order for ϕ_{j+2}, $j = 1, 2, \ldots, n$. We write (64) in the general form:

$$\phi_1 = H(\phi_2, \phi_2^*) \tag{66}$$

We introduce polar form for ϕ_j, $j = 1, 2, \ldots, n+2$ as it follows:

$$\phi_j = N_j e^{i\delta_j},\ N_j \in \mathbb{R}_+,\ \delta_j \in \mathbb{R} \tag{67}$$

From relation (66) it is clear that we can obtain two explicit analytical solutions providing N_1 and δ_1 as functions of N_2 and δ_2:

$$\begin{aligned} N_1 &= H_1(N_2, \delta_2) \\ \delta_1 &= H_2(N_2, \delta_2) \end{aligned} \tag{68}$$

From the (63) we have:

$$N_{j+2}e^{i\delta_{j+2}} = \frac{N_1}{\pi}e^{i\delta_1}\xi_j(N_1), \quad j = 1, 2, \ldots, n \tag{69}$$

or

$$N_{j+2}e^{i(\delta_{j+2}-\delta_1)} = \frac{N_1}{\pi}\xi_j(N_1), \quad j = 1, 2, \ldots, n \tag{70}$$

so that

$$N_{j+2} = \frac{N_1}{\pi}|\xi_j(N_1)|, \quad j = 1, 2, \ldots, n \tag{71}$$

and δ_{j+2} depends on N_1 and δ_1. Let us write

$$\delta_{j+2} = \rho_j(N_1, \delta_1), \quad j = 1, 2, \ldots, n \tag{72}$$

From (65) we have:

$$\frac{\partial N_1}{\partial T_1} + iN_1\frac{\partial \delta_1}{\partial T_1} + (\frac{\lambda_0}{2} - \frac{2\sigma+1}{2i})N_1 + \frac{N_2}{2i}e^{i(\delta_2-\delta_1)} + \frac{\sum_{j=1}^{n} k_j \frac{N_1}{\pi}\xi_j(N_1)}{2i} = \frac{f_{10}}{2i}e^{-i\delta_1} \tag{73}$$

Introducing real and imaginary parts of ξ

$$\xi_j(N_1) = \xi_{jr}(N_1) + i\xi_{ji}(N_1), \quad j = 1, 2, \ldots, n \tag{74}$$

finally one can obtain:

$$\begin{cases} \dfrac{\partial N_1}{\partial T_1} + \dfrac{\lambda_0}{2}N_1 + \dfrac{N_2}{2}\sin(\delta_2 - \delta_1) + \dfrac{\sum_{j=1}^{n} k_j \frac{N_1}{\pi}\xi_{ji}(N_1)}{2} = -\dfrac{f_{10}}{2}\sin(\delta_1) \\ N_1\dfrac{\partial \delta_1}{\partial T_1} + \dfrac{2\sigma+1}{2}N_1 - \dfrac{N_2}{2}\cos(\delta_2 - \delta_1) - \dfrac{\sum_{j=1}^{n} k_j \frac{N_1}{\pi}\xi_{jr}(N_1)}{2} = -\dfrac{f_{10}}{2}\cos(\delta_1) \end{cases} \tag{75}$$

Then, from (68) we can reach a linear system in $\frac{\partial N_2}{\partial T_1}$ and $\frac{\partial \delta_2}{\partial T_1}$:

$$\begin{cases} \dfrac{\partial H_1}{\partial N_2}\dfrac{\partial N_2}{\partial T_1} + \dfrac{\partial H_1}{\partial \delta_2}\dfrac{\partial \delta_2}{\partial T_1} - m_1 = 0 \\ H_1(\dfrac{\partial H_2}{\partial N_2}\dfrac{\partial N_2}{\partial T_1} + \dfrac{\partial H_2}{\partial \delta_2}\dfrac{\partial \delta_2}{\partial T_1}) - m_2 = 0 \end{cases} \tag{76}$$

where

$$
\begin{aligned}
-m_1 &= \frac{\lambda_0}{2} H_1 + \frac{N_2}{2}\sin(\delta_2 - H_2) + \frac{\sum_{j=1}^{n} k_j \frac{H_1}{\pi}\xi_{ji}(H_1)}{2} + \frac{f_{10}}{2}\sin(\delta_1) \\
-m_2 &= \frac{2\sigma+1}{2} H_1 - \frac{N_2}{2}\cos(\delta_2 - H_2) - \frac{\sum_{j=1}^{n} k_j \frac{H_1}{\pi}\xi_{jr}(H_1)}{2} + \frac{f_{10}}{2}\cos(\delta_1)
\end{aligned}
\tag{77}
$$

Finally, by solving the system (76), the following equations are obtained:

$$
\begin{aligned}
\frac{\partial N_2}{\partial T_1} &= \frac{\tilde{f}_1(N_2,\delta_2)}{\tilde{g}(N_2,\delta_2)} \\
N_2\frac{\partial \delta_2}{\partial T_1} &= \frac{\tilde{f}_2(N_2,\delta_2)}{\tilde{g}(N_2,\delta_2)}
\end{aligned}
\tag{78}
$$

where

$$
\begin{aligned}
\tilde{f}_1(N_2,\delta_2) &= H_1\frac{\partial H_2}{\partial \delta_2}m_1 - \frac{\partial H_1}{\partial \delta_2}m_2 \\
\tilde{f}_2(N_2,\delta_2) &= N_2\left(\frac{\partial H_1}{\partial N_2}m_2 - H_1\frac{\partial H_2}{\partial N_2}m_1\right) \\
\tilde{g}(N_2,\delta_2) &= H_1\left(\frac{\partial H_1}{\partial N_2}\frac{\partial H_2}{\partial \delta_2} - \frac{\partial H_2}{\partial N_2}\frac{\partial H_1}{\partial \delta_2}\right)
\end{aligned}
\tag{79}
$$

4.3 Analysis of the Dynamics: General Method

The analysis of the dynamical behavior corresponding to a modulation at 1:1 resonance around the T_0-invariant is given by:

- geometry of the T_0-invariant in the N_1, N_2 and δ_2 space associated to the relation $N_1 = H_1(N_2, \delta_2)$.
- equilibrium points of the reduced system (78) are given by:

$$
\begin{cases}
f_1(N_2,\delta_2) = 0,\ f_2(N_2,\delta_2) = 0 \\
g_1(N_2,\delta_2) \neq 0,\ g_2(N_2,\delta_2) \neq 0
\end{cases}
\tag{80}
$$

if f_1, f_2, g_1 and g_2 correspond to numerators and denominators of the system (78).

- singular points of the reduced system (78) are given by:

$$\begin{cases} f_1(N_2, \delta_2) = 0,\ f_2(N_2, \delta_2) = 0 \\ \\ g_1(N_2, \delta_2) = 0,\ g_2(N_2, \delta_2) = 0 \end{cases} \tag{81}$$

if f_1, f_2, g_1 and g_2 correspond to numerators and denominators of the system (78). Singular points are potentially associated to bifurcations.

4.4 Analysis of the Dynamics for a Particular Case

Let us choose $n = 2$ and

$$F(z) = z^3 \tag{82}$$

in such a case, we have

$$\mathscr{F} = \frac{1}{2i} G(|\phi_2|^2)\phi_2 \tag{83}$$

with

$$G(\chi) = \frac{3}{4}\chi\ ,\quad \chi \geq 0 \tag{84}$$

Then

$$\begin{aligned} \phi_1 = H(\phi_2, \phi_2^*) &= \phi_2 - 2ic_{10}\mathscr{F} - i\lambda_{10}\phi_2 \\ &= \phi_2 - \frac{3}{4}c_{10}|\phi_2|^2\phi_2 - i\lambda_{10}\phi_2 \end{aligned} \tag{85}$$

and

$$\begin{aligned} H_1(N_2, \delta_2) &= N_2\sqrt{\lambda_{10}^2 + (1 - \frac{3}{4}c_{10}N_2^2)^2} \\ \\ H_2(N_2, \delta_2) &= \delta_2 + \arctan\left(\frac{-\lambda_{10}}{1 - \frac{3}{4}c_{10}N_2^2}\right) \end{aligned} \tag{86}$$

Now, m_1 and m_2 can be obtained from the general expression in (77). Moreover, we have simplified expression for $\tilde{g}$ since H_1 does not depend on δ_2 and H_2 depends linearly on δ_2.

$$\tilde{g}(N_2, \delta_2) = H_1\frac{\partial H_1}{\partial N_2} \tag{87}$$

From the expression of H_1 it is clear that $\tilde{g}$ does not depend on δ_2. We have also:

$$\begin{aligned}\tilde{f_1}(N_2,\delta_2) &= H_1 m_1\\ \tilde{f_2}(N_2,\delta_2) &= \big(\frac{\partial H_1}{\partial N_2}m_2 - H_1\frac{\partial H_2}{\partial N_2}m_1\big)N_2\end{aligned} \tag{88}$$

Finally, let us give expressions of f_1, f_2, g_1 and g_2. The reduced system of equations reads:

$$\begin{aligned}\frac{\tilde{f_1}}{\tilde{g}} &= \frac{m_1}{\frac{\partial H_1}{\partial N_2}}\\ &= \frac{m_1\sqrt{\lambda_{10}^2+(1-\frac{3}{4}c_{10}N_2^2)^2}}{\lambda_{10}^2+(1-\frac{3}{4}c_{10}N_2^2)(1-\frac{9}{4}c_{10}N_2^2)}\\ \frac{\tilde{f_2}}{\tilde{g}} &= \frac{N_2(\frac{\partial H_1}{\partial N_2}m_2 - H_1\frac{\partial H_2}{\partial N_2}m_1)}{H_1\frac{\partial H_1}{\partial N_2}}\\ &= \frac{3\lambda_{10}c_{10}N_2^2m_1+2m_2\big(\lambda_{10}^2+(1-\frac{3}{4}c_{10}N_2^2)(1-\frac{9}{4}c_{10}N_2^2)\big)}{2\big(\lambda_{10}^2+(1-\frac{3}{4}c_{10}N_2^2)(1-\frac{9}{4}c_{10}N_2^2)\big)\sqrt{\lambda_{10}^2+(1-\frac{3}{4}c_{10}N_2^2)(1-\frac{9}{4}c_{10}N_2^2)}}\end{aligned} \tag{89}$$

so that:

$$\begin{aligned}f_1 &= m_1\sqrt{\lambda_{10}^2+(1-\tfrac{3}{4}c_{10}N_2^2)^2}\\ f_2 &= 3\lambda_{10}c_{10}N_2^2m_1+2m_2\big(\lambda_{10}^2+(1-\tfrac{3}{4}c_{10}N_2^2)(1-\tfrac{9}{4}c_{10}N_2^2)\big)\\ g_1 &= \lambda_{10}^2+(1-\frac{3}{4}c_{10}N_2^2)(1-\frac{9}{4}c_{10}N_2^2)\\ g_2 &= 2g_1\sqrt{\lambda_{10}^2+(1-\tfrac{3}{4}c_{10}N_2^2)^2}\end{aligned} \tag{90}$$

Equilibrium points are given by:

$$f_1 = 0\ ,\ f_2 = 0 \text{ and } g_1 \neq 0 \tag{91}$$

and singular points are governed by:

$$f_1 = 0\ ,\ f_2 = 0 \text{ and } g_1 = 0 \tag{92}$$

This is equivalent to:

$$\begin{cases} m_1 = 0\\ g_1 = 0\end{cases} \tag{93}$$

Then $g_1 = 0$ provides analytical values of N_2 (fold lines):

$$N_2 = \frac{2}{3}\sqrt{\frac{1}{c_{10}}\left(2 \mp \sqrt{1 - 3\lambda_{10}^2}\right)} \tag{94}$$

For a given N_2, m_1 depends only on the variable δ_2 and can be solved numerically.

4.5 Analytical Developments Versus Numerical Integrations

Let us set $c_{10} = 1$, $\lambda_{10} = 0.1$, $\lambda_0 = 0.1$, $\eta_1 = 0.1$, $\eta_2 = 0.15$, $k_1 = 1$, $k_2 = 2$, $\varepsilon = 0.001$. We consider that $f_{10} = 0.7$. Euler's scheme [54, 59] with time steps as $\Delta\tau = 10^{-4}$ is endowed for solving system of (52). Assumed initial conditions are $x(0) = 0.5$ and $y(0) = \dot{x}(0) = \dot{y}(0) = u_1(0) = u_2(0) = 0$.

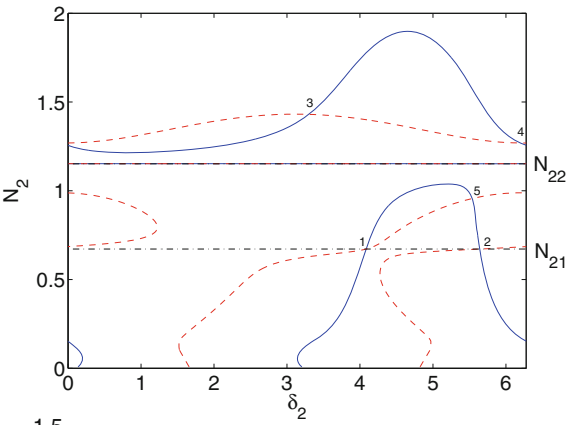

Fig. 11 Positions of equilibrium points and fold singularities of the system with external forcing term $f_{10} = 0.7$ (see (78) and (90)): $f_1 = 0$ (—), $f_2 = 0$ (– – –), $g_1 = 0$ (–·–·–, i.e. fold lines N_{21} and N_{22}). The system possesses two fold singularities (no. 1 and 2) and three equilibrium points (no. 3, 4 and 5)

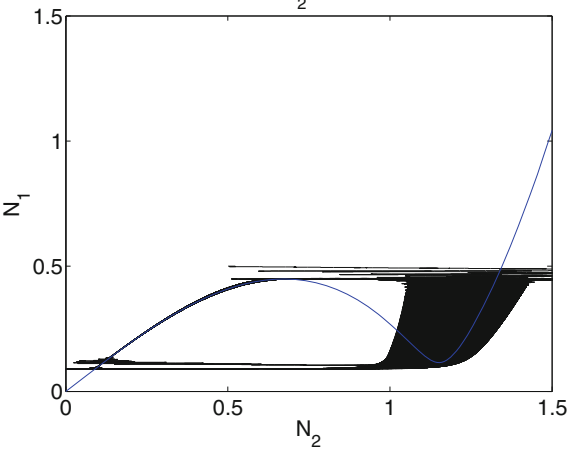

Fig. 12 T_0-invariant of the system (*solid blue line*) and corresponding numerical results (*black line*) that are obtained by integration of (52) with external forcing term $f_{10} = 0.7$

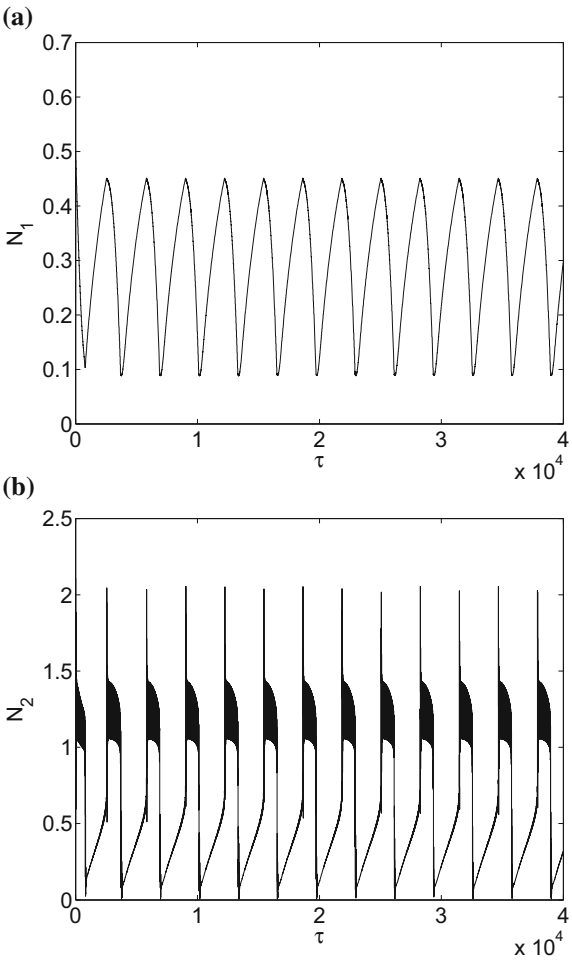

Fig. 13 Histories of system amplitudes that are obtained by integration of (52) with external forcing term $f_{10} = 0.7$: **a** N_1; **b** N_2

Predictions of all possible dynamics of the system until reaching the infinity of the T_1 time scale are shown in Fig. 11. It is seen that the system has two fold singularities on the first fold line N_{21}, namely points 1 and 2, two equilibrium points (no. 3 and no. 4) and another equilibrium point between two fold lines of the system (unstable area) namely point no. 5. T_0-Invariant of the system and corresponding numerical results are presented in Fig. 12. The system presents SMR by persisting direct and reverse bifurcations between its stability borders. This is due to the existence of fold singularities on fold line(s) of the system [21, 46]. This behavior will be more visible

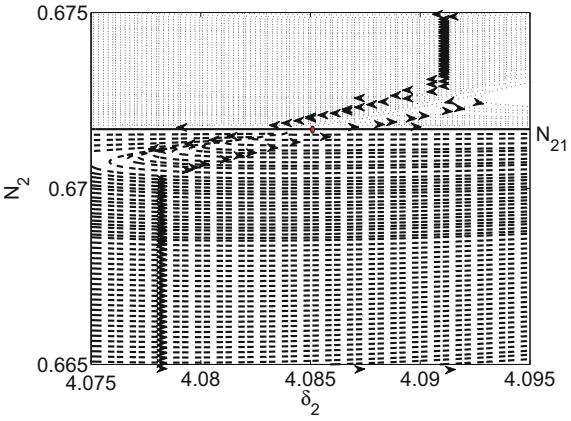

Fig. 14 Phase portraits of the reduced system with external forcing term $f_{10} = 0.7$ (see (78), (89) and (90)) around the singular point no. 1 (saddle)

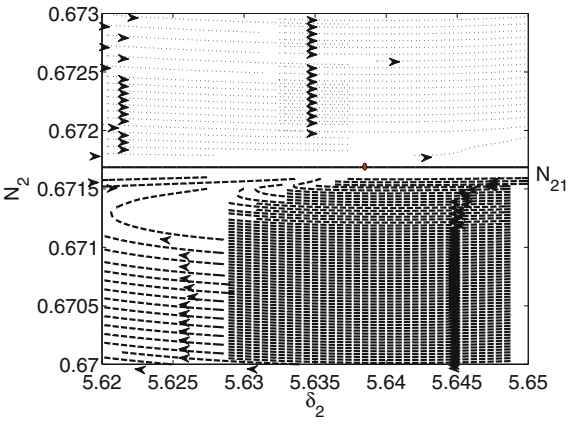

Fig. 15 Phase portraits of the reduced system with external forcing term $f_{10} = 0.7$ (see (78), (89) and (90)) around the singular point no. 2 (node)

by looking at the histories of system amplitudes which are obtained by numerical integration and are illustrated in Fig. 13. Phase portraits of the reduced system (78) around singular points no. 1 and 2 are presented in Figs. 14 and 15 show that these singular points are in the form of saddle and nodes on the fold line of the system (N_{21}). During SMR both oscillators and all of their components present beating responses: displacement histories of two oscillators which are depicted in Fig. 16 and also histories of internal variables of Saint-Venant elements that are presented in Fig. 17 show not only beating responses of all components of two oscillators during SMR but also activations of Saint-Venant elements during energy exchanges. The SMR of an optimized designed system is a very desirable behavior from passive control and also energy harvesting view points since both oscillators continue to exchange the energy with large intervals of energy changes for the NES and small

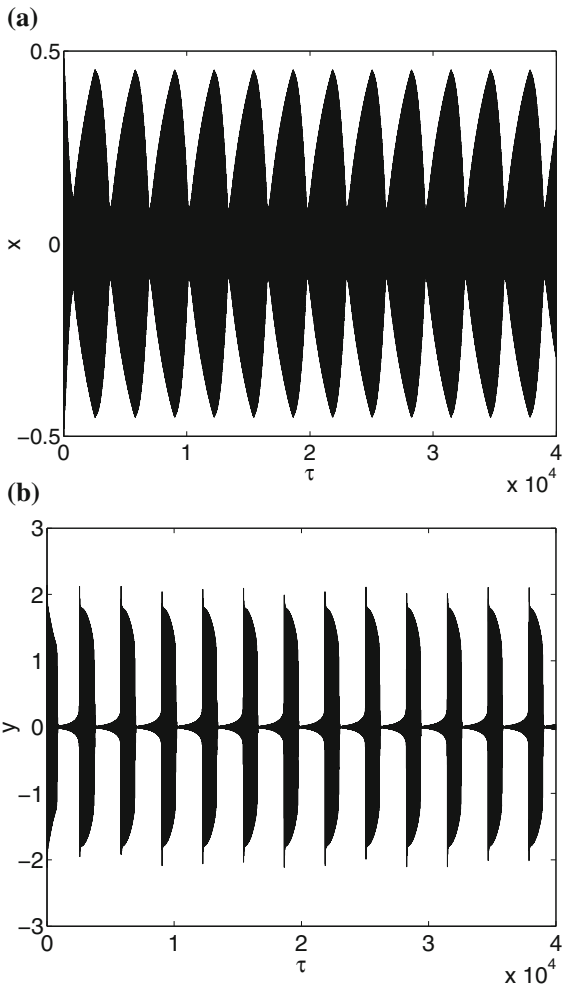

Fig. 16 Displacements histories that are obtained by integration of (52) with external forcing term $f_{10} = 0.7$: **a** x; **b** y

energy intervals for the main system. The system possesses two equilibrium points namely points no. 3 and 4 (see Fig. 11). It can be attracted by one of these points after a very long time at T_1 time scale or during higher time scales (T_2, T_3, …). Due to costly simulation time we did not run it for very long time scales.

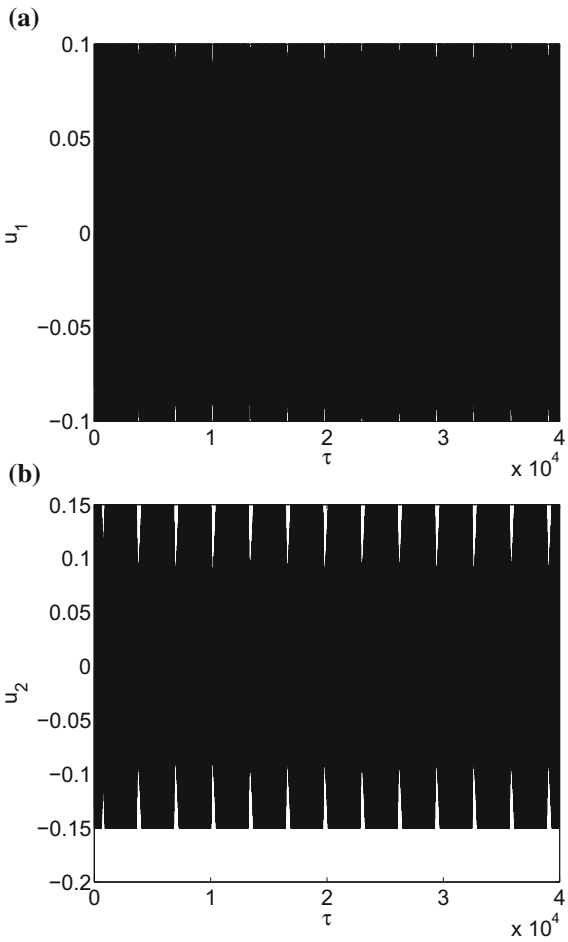

Fig. 17 Histories of internal variables of the Saint-Venant elements that are obtained by integration of (52) with external forcing term $f_{10} = 0.7$: **a** u_1; **b** u_2

5 Conclusions

Multiple scale energy exchanges of two different coupled systems are considered: (I) a vertical system (i.e. consideration of effects of the gravity) which consists of a linear main structural system and a coupled nonsmooth nonlinear energy sink; (II) a main oscillator with a set of Saint-Venant elements that is coupled to a nonlinear energy sink with a general odd nonlinear potential function. Invariants of both systems and their geometries at fast time scale let us understand the process of energy exchanges between two oscillators with explanation of possible bifurcations between two coupled oscillators. Reduced form of equations of systems at slow time scale give us some tools to predict all possible regimes of systems during energy exchanges: systems can face periodic regimes due to existence of equilibrium points while they

can present strongly modulated responses when fold singularities are present. These studies provide analytical design tools for tuning parameters of nonlinear energy sink according to the design goal which can be passive control of linear/nonlinear main structural systems by means of nonlinear energy sink. Experimentally realizations of both systems can be carried out by considering a moving light mass in a (frictionless) guide which is encased between two elastic walls at each end for representing a nonsmooth NES of the system I. Identification of parameters of Magnetorheological dampers which present hysteresis behaviors can lead to models represented by system II (with potentially added smooth nonlinear terms to the main structure) [54, 60].

Acknowledgments The authors would like to thank the following organizations for supporting this research work: (i) LABEX CELYA (ANR-10-LABX-0060) of the "Université de Lyon" within the program "Investissement d'Avenir" (ANR-11-IDEX-0007) operated by the French National Research Agency (ANR); (ii) Peugeot Citroën Automobiles OpenLab, Vibro-Acoustic-Tribology@Lyon (VAT@Lyon).

References

1. Gendelman, O.V., Vakakis, A.F.: Transitions from localization to nonlocalization in strongly nonlinear damped oscillators. Chaos Soliton Frac. **11**, 1535–1542 (2000)
2. Gendelman, O.V., Manevitch, L.I.: Reflection of short rectangular pulses in the ideal string attached to strongly nonlinear oscillator. Chaos Soliton Frac. **11**, 2473–2477 (2000)
3. Gendelman, O.V.: Transition of energy to a nonlinear localized mode in a highly asymmetric system of two oscillators. Nonlinear Dyn. **25**, 237–253 (2001)
4. Gendelman, O.V., Manevitch, L.I., Vakakis, A.F., M'Closkey, R.: Energy pumping in nonlinear mechanical oscillators: part I-dynamics of the underlying Hamiltonian systems. J. Appl. Mech. **68**(1), 34–41 (2001)
5. Vakakis, A.F., Gendelman, O.V.: Energy pumping in nonlinear mechanical oscillators: part II-resonance capture. J. Appl. Mech. **68**(1), 42–48 (2001)
6. Vakakis, A.F.: Shock isolation through the use of nonlinear energy sinks. J. Vib. Control. **9**, 79–93 (2003)
7. Vakakis, A.F., Manevitch, L.I., Gendelman, O.V., Bergman, L.: Dynamics of linear discrete systems connected to local, essentially non-linear attachments. J. Sound Vib. **264**, 559–577 (2003)
8. Gendelman, O.V.: Bifurcations of nonlinear normal modes of linear oscillator with strongly nonlinear damped attachment. Nonlinear Dyn. **37**, 115–128 (2004)
9. Gendelman, O.V., Lamarque, C.-H.: Dynamics of linear oscillator coupled to strongly nonlinear attachment with multiple states of equilibrium. Chaos Soliton Frac. **24**, 501–509 (2005)
10. Kerschen, G., Vakakis, A.F., Lee, Y.S., McFarland, D.M., Kowtko, J.J., Bergman, L.A.: Energy transfers in a system of two coupled oscillators with essential nonlinearity: 1:1 resonance manifold and transient bridging orbits. Nonlinear Dyn. **42**, 283–303 (2005)
11. Gourdon, E., Lamarque, C.-H.: Energy pumping for a larger span of energy. J. Sound Vib. **285**, 711–720 (2005)
12. Gendelman, O.V., Gourdon, E., Lamarque, C.-H.: Quasiperiodic energy pumping in coupled oscillators under periodic forcing. J. Sound Vib. **294**, 651–662 (2006)
13. Kerschen, G., Lee, Y.S., Vakakis, A.F., McFarland, D.M., Bergman, L.A.: Irreversible passive energy transfer in coupled oscillators with essential nonlinearity. SIAM J. Appl. Math. **66**, 648–679 (2006)

14. Manevitch, L.I., Gourdon, E., Lamarque, C.-H.: Parameters optimization for energy pumping in strongly nonhomogeneous 2 dof system. Chaos Soliton Frac. **31**, 900–911 (2007)
15. Manevitch, L.I., Musienko, A.I., Lamarque, C.-H.: New analytical approach to energy pumping problem in strongly nonhomogeneous 2dof systems. Meccanica **42**, 77–83 (2007)
16. Lee, Y.S., Vakakis, A.F., Bergman, L.A., McFarland, D.M., Kerschen, G.: Suppression of aeroelastic instabilities by means of targeted energy transfers: part I, theory. AIAA J. **45**, 693–711 (2007)
17. Panagopoulos, P.N., Gendelman, O.V., Vakakis, A.F.: Robustness of targeted energy transfer in coupled oscillators to changes of initial conditions. Nonlinear Dyn. **47**, 377–387 (2007)
18. Lee, Y.S., Vakakis, A.F., Bergman, L.A., McFarland, D.M., Kerschen, G., Nucera, F., Tsakirtzis, S., Panagopoulos, P.N.: Passive nonlinear targeted energy transfer and its applications to vibration absorption: a review. Proc. Inst. Mech. Eng. K J. Multi-body Dyn. **222**, 77–134 (2008)
19. Vakakis, A.F., Gendelman, O.V., Bergman, L.A., McFarland, D.M., Kerschen, G., Lee, Y.S.: Nonlinear Trageted Energy Transfer in Mechanical and Structural Systems I. Springer, Berlin (2008)
20. Vakakis, A.F., Gendelman, O.V., Bergman, L.A., McFarland, D.M., Kerschen, G., Lee, Y.S.: Nonlinear Trageted Energy Transfer in Mechanical and Structural Systems II. Springer, Berlin (2008)
21. Starosvetsky, Y., Gendelman, O.V.: Strongly modulated response in forced 2DOF oscillatory system with essential mass and potential asymmetry. Physica D. **237**, 1719–1733 (2008)
22. Viguie, R., Peeters, M., Kerschen, G., Golinval, J.C.: Energy transfer and dissipation in a Duffing oscillator coupled to a nonlinear attachment. J. Comput. Nonlinear Dyn. **4**, 041012 (2009)
23. Starosvetsky, Y., Gendelman, O.V.: Vibration absorption in systems with a nonlinear energy sink: nonlinear damping. J. Sound Vib. **324**, 916–939 (2009)
24. Sapsis, T.P., Vakakis, A.F., Gendelman, O.V., Bergman, L.A., Kerschen, G., Quinn, D.D.: Efficiency of targeted energy transfers in coupled nonlinear oscillators associated with 1:1 resonance captures: part II, analytical study. J. Sound Vib. **325**, 297–320 (2009)
25. Pham, T.T., Pernot, S., Lamarque, C.-H.: Competitive energy transfer between a two degree-of-freedom dynamic system and an absorber with essential nonlinearity. Nonlinear Dyn. **62**, 573–592 (2010)
26. Gendelman, O.V., Vakakis, A.F., Bergman, L.A., McFarland, D.M.: Asymptotic analysis of passive nonlinear suppression of aeroelastic instabilities of a rigid wing in subsonic flow. SIAM J. Appl. Math. **70**, 1655–1677 (2010)
27. Vaurigaud, B., Ture Savadkoohi, A., Lamarque, C.-H.: Targeted energy transfer with parallel nonlinear energy sinks part I: design theory and numerical results. Nonlinear Dyn. **66**(4), 763–780 (2011)
28. Vaurigaud, B., Manevitch, L.I., Lamarque, C.-H.: Passive control of aeroelastic instability in a long span bridge model prone to coupled flutter using targeted energy transfer. J. Sound Vib. **330**(11), 2580–2595 (2011)
29. Ture Savadkoohi, A., Manevitch, L.I., Lamarque, C.-H.: Analysis of the transient behavior in a two dof nonlinear system. Chaos Soliton Frac. 44(6), 450–463 (2011)
30. Starosvetsky, Y., Gendelman, O.V.: Response regimes in forced system with non-linear energy sink: quasi-periodic and random forcing. Nonlinear Dyn. **64**, 77–195 (2011)
31. Gendelman, O.V., Sigalov, G., Manevitch, L.I., Mane, M., Vakakis, A.F., Bergman, L.A.: Dynamics of an eccentric rotational nonlinear energy sink. J. Appl. Mech. T. ASME J. **79**, 011012 (2012)
32. Pham, T.T., Lamarque, C.-H., Ture Savadkoohi, A.: Multi-resonance capturing in a two-degree-of-freedom system under two different harmonic excitations. J. Vib. Control. **18**(3), 451–466 (2012)
33. Luongo, A., Zulli, D.: Dynamic analysis of externally excited NES-controlled systems via a mixed multiple scale/harmonic balance algorithm. Nonlinear Dyn. **70**, 2049–2061 (2012)
34. Luongo, A., Zulli, D.: Aeroelastic instability analysis of NES-controlled systems via a mixed multiple scale/harmonic balance method. J. Vib. Control. **20**, 1985–1998 (2014)

35. Wierschem, N.E., Quinn, D.D., Hubbard, S.A., Al-Shudeifatd, M.A., McFarlandc, D.M., Luo, J., Fahnestock, L.A., Spencer Jr, B.F., Vakakis, A.F., Bergman, L.A.: Passive damping enhancement of a two-degree-of-freedom system through a strongly nonlinear two-degree-of-freedom attachment. J. Sound Vib. **331**, 5393–5407 (2012)
36. McFarland, D.M., Kerschen, G., Kowtko, J.J., Lee, Y.S., Bergman, L.A., Vakakis, A.F.: Experimental investigation of targeted energy transfers in strongly and nonlinearly coupled oscillators. J. Acoust. Soc. Am. **118**, 791–799 (2005)
37. Kerschen, G., Kowtko, J.J., McFarland, D.M., Bergman, L.A., Vakakis, A.F.: Theoretical and experimental study of multimodal targeted energy transfer in a system of coupled oscillators. Nonlinear Dyn. **47**, 285–309 (2007)
38. Kerschen, G., Kowtko, J.J., McFarland, D.M., Lee, Y.S., Bergman, L.A., Vakakis, A.F.: Experimental demonstration of transient resonance capture in a system of two coupled oscillators with essential stiffness nonlinearity. J. Sound Vib. **299**, 822–838 (2007)
39. Gourdon, E., Alexander, N.A., Taylor, C.A., Lamarque, C.-H., Pernot, S.: Nonlinear energy pumping under transient forcing with strongly nonlinear coupling: theoretical and experimental results. J. Sound Vib. **300**, 522–551 (2007)
40. Lee, Y.S., Kerschen, G., McFarland, D.M., Hill, W.J., Nichkawde, C., Strganac, T.W., Bergman, L.A., Vakakis, A.F.: Suppressing aeroelastic instability using broadband passive targeted energy transfers, part 2: experiments. AIAA J. **45**, 2391–2400 (2007)
41. Vaurigaud, B., Ture Savadkoohi, A., Lamarque, C.-H.: Efficient targeted energy transfer with parallel nonlinear energy sinks: theory and experiments. J. Comput. Nonlinear Dyn. **6**(4), 041005 (2011)
42. True Savadkoohi, A., Vaurigaud, B., Lamarque, C.-H., Pernot, S.: Targeted energy transfer with parallel nonlinear energy sinks, part II: theory and experiments. Nonlinear Dyn. **67**, 37–46 (2012)
43. Wierschem, N., Luo, J., AL-Shudeifat, M., Hubbard, S., Ott, R., Fahnestock, L., Quinn, D., McFarland, D., Spencer Jr, B., Vakakis, A., Bergman, L.: Experimental testing and numerical simulation of a six-story structure incorporating two-degree-of-freedom nonlinear energy sink. J. Struct. Eng. **140**(6), 04014027 (2014)
44. Gendelman, O.V.: Analytic treatment of a system with a vibro-impact nonlinear energy sink. J. Sound Vib. **331**, 4599–4608 (2012)
45. Gendelman, O.V.: Targeted energy transfer in systems with non-polynomial nonlinearity. J. Sound Vib. **315**, 732–745 (2008)
46. Lamarque, C.-H., Gendelman, O.V., Ture Savadkoohi, A., Etcheverria, E.: Targeted energy transfer in mechanical systems by means of non-smooth nonlinear energy sink. Acta Mech. **221**, 175–200 (2011)
47. Nucera, F., Vakakis, A.F., McFarland, D.M., Bergman, L.A., Kerschen, G.: Targeted energy transfers in vibro-impact oscillators for seismic mitigation. Nonlinear Dyn. **50**, 651–677 (2007)
48. True Savadkoohi, A., Lamarque, C.-H., Dimitrijevic, Z.: Vibratory energy exchange between a linear and a non-smooth system in the presence of the gravity. Nonlinear Dyn. **70**, 1473–1483 (2012)
49. Ture Savadkoohi, A., Lamarque, C.-H.: Vibratory energy localization by non-smooth energy sink with time-varying mass. Appl. Non-Linear Dyn. Syst. Springer Proc. Math. Stat. **93**, 429–442 (2014)
50. Lamarque, C.-H., Ture Savadkoohi, A., Dimitrijevic, Z.: Dynamics of a linear system with time-dependant mass and a coupled light mass with non-smooth potential. Meccanica **49**, 135–145 (2014)
51. Lamarque, C.-H., Ture Savadkoohi, A., Etcheverria, E., Dimitrijevic, Z.: Multi-scales dynamics of two coupled non-smooth systems. Int. J. Bifurcat. Chaos. **22**(1250295), 1–18 (2012)
52. True Savadkoohi, A., Lamarque, C.-H.: Dynamics of coupled Dahl type and non-smooth systems at different scales of time. Int. J. Bifurcat. Chaos **23**(1350114), 1–14 (2013)
53. Lamarque, C.-H., Ture Savadkoohi, A.: Dynamical behavior of a Bouc-Wen type oscillator coupled to a nonlinear energy sink. Meccanica **49**, 1917–1928 (2014)

54. Bastien, J., Bernardin, F., Lamarque, C.-H.: Non Smooth Deterministic or Stochastic Discrete Dynamical Systems: Applications to Models with Friction or Impact, p. 515. Wiley, USA (2013)
55. Weiss, M., Ture Savadkoohi, A., Gendelman, O.V., Lamarque, C.-H.: Dynamical behavior of a mechanical system including Saint-Venant component coupled to a nonlinear energy sink. Int. J. Non-Linear Mech. **63**, 10–18 (2014)
56. Lamarque, C.-H.: Ture Savadkoohi, A.: Targeted energy transfer between a system with a set of Saint-Venant elements and a nonlinear energy sink. Continuum Mech. Thermodyn. (2014). doi:10.1007/s00161-014-0354-9
57. Manevitch, L.I.: The description of localized normal modes in a chain of nonlinear coupled oscillators using complex variables. Nonlinear Dyn. **25**, 95–109 (2001)
58. Nayfeh, A.H., Mook, D.T.: Nonlinear Oscillations. Wiley, New York (1979)
59. Schmidt, F., Lamarque, C.-H.: Energy pumping for mechanical systems involving non-smooth Saint-Venant terms. Int. J. Nonlinear Mech. **45**, 866–875 (2010)
60. Wang, D.H., Liao, W.H.: Magnetorheological fluid dampers: a review of parametric modelling. Smart Mater. Struct. **20**, 023001 (34pp) (2011)

On the Use of the Multiple Scale Harmonic Balance Method for Nonlinear Energy Sinks Controlled Systems

Angelo Luongo and Daniele Zulli

Abstract The Multiple Scale Harmonic Balance Method (MSHBM) is discussed here for several paradigmatic systems (primary structures) equipped with a Nonlinear Energy Sink (NES). This is a small-mass oscillator with essentially nonlinear stiffness, used for passive control purpose. The method permits to overcome the difficulties inherent to standard perturbation methods, which occur as a consequence of the nonlinearizable nature of the NES equation. It combines the Multiple Scale Method and the Harmonic Balance Method to furnish Amplitude Modulation Equations ruling the slow asymptotic dynamics of the augmented system. The MSHBM is illustrated here for a general, internally non-resonant, multi d.o.f. structure equipped with a NES and under multiple concurrent actions, namely steady wind inducing Hopf bifurcation, and 1:1 and 1:3 resonant harmonic forces. The relevant Amplitude Modulation Equations are specialized for simpler cases, where the single contributions of each external action is considered separately. The effect of the NES on the dynamics of the system is discussed for each case and numerical results are displayed.

1 Introduction

Nonlinear Energy Sinks (NES) are strongly nonlinear oscillators, typically equipped with a small mass, a linear damper and an essentially nonlinear spring, attached to a primary structure to be controlled. Their main goal is to induce irreversible transfer of vibrational energy from the primary structure to themselves, and to dissipate it as a passive control device. A comprehensive report on the characteristics and uses on NES is found in [1, 2].

The one-way energy convey from the primary structure to the NES, referred as Target Energy Transfer (TET), and investigated in the literature in analytical, numerical and experimental sense [3–7], as well as the capacity (in theory) of the NES of oscillating at any frequencies, giving rise of large band tuning with the

A. Luongo · D. Zulli (✉)
M&MoCS—University of L'Aquila, Via Giovanni Gronchi, 67100 L'Aquila (AQ), Italy
e-mail: daniele.zulli@univaq.it

A. Luongo
e-mail: angelo.luongo@univaq.it

M. Belhaq (ed.), *Structural Nonlinear Dynamics and Diagnosis*,
Springer Proceedings in Physics 168, DOI 10.1007/978-3-319-19851-4_12

structure to be controlled, are consequences of the essentially nonlinear nature of the NES and its lacking of linear stiffness. Moreover, the presence of small mass is responsible of (almost) singularity in the equations, inducing relaxation oscillations, typically referred as Weakly Modulated Response (WMR) and Strongly Modulated Response (SMR) [8, 9].

Recently, these kind of devices have received great attention in the literature, being used in many applications. In [10, 11], a NES was applied to a main linear oscillator harmonically excited by a 1:1 resonant force. In [12, 13], multiple parallel NESs were considered to dissipate first-mode oscillations of a linear structure under impulse as well as harmonic forcing. In [14] non-smooth NES was considered to control a two-d.o.f. system. In [15], NES was used to suppress aeroelastic instabilities on a rigid wing, modeled as a two-d.o.f. section-model, under steady wind. In [16] a single NES is used to control oscillations of a long-span bridge prone to coupled flutter.

To analytically study the slow-flow dynamics of systems with NES, the researchers generally make use of two steps: (a) the complexification-averaging procedure by Manevitch [17], referred as CX-A, recently extended also to non-polynomial nonlinearity [18] and piece-wise systems [14], and, subsequently, (b) the Multiple Scale Method (MSM, [19]). In fact, due to the non-linearizable nature of the equations of NES, it was stated in [20], where a grounded NES was studied, that "for this type of problem the standard analytical techniques from nonlinear dynamics (such as the method of multiple-scales, and the standard method of averaging), are not directly applicable, and an alternative approach must be followed"; accordingly, the complexification method was employed. Dealing with the same problem, three different methods were used in [21], namely, the method of harmonic balance, a combination of a shooting method and Floquet theory, and direct time integration, but not the MSM. In the same paper, the authors used an adapted version of the method of averaging, and defined their theoretical analysis as "limited".

For all these reasons, the authors of this paper, in a series of work [22–24] investigated the possibility of implementing a nonstandard version of the MSM, for general systems equipped with NES, under specific external actions. In particular, in [22], they used the Multiple Scale Harmonic Balance Method (MSHBM), to get Amplitude Modulation Equations (AME) for a multi d.o.f. system under 1:1 resonant external force. The main advantage of the algorithm is that the initial complexification procedure is avoided, dealing directly with variables having clear physical meanings. In [23], the same algorithm was specialized for a system undergoing a Hopf bifurcation due to steady wind. In [24] the MSHBM was extended to infinite dimensional systems, in direct approach, to deal with an internally nonresonant string under a harmonic force considered resonant to a certain mode.

In this paper, the MSHBM is illustrated for a general discrete system under simultaneous external actions. The scope of the paper is multifold: (a) to collect old results by the authors in a more systematic and exhaustive manner; (b) to present new results concerning subharmonic excitations, not analyzed in the past; (c) to open the way to further investigations relevant to the interaction among simultaneous excitations, here accounted for in formulation, but not addressed in the numerical results, yet. To this ends, a general, nonlinear, multi-d.o.f. system under effect of steady wind,

which induces a Hopf bifurcation, concurrently acting with external 1:1 and 1:3 resonant harmonic excitation, is considered. A NES is attached to it, in order to control amplitude of vibrations, and the MSHBM is applied to the equations of motion, to get the AME ruling the dominant dynamics of the system. Then, numerical results are extracted for simpler cases, when one single component of excitation is applied in turn, with the aim of analyze the effect on the dynamics of the principal structure and to check the reliability of the algorithm. However, a complete unfolding of the dynamics of the proposed examples, as well as a deep analysis of the possible beneficial effect of the NES, are not fulfilled herein, since they are out of the aim of this paper.

The paper is organized as follows: in Sect. 2, the algorithm is applied to a general system; in Section 3, some examples are discussed: in Sect. 3.1 a one d.o.f. system under 1:1 resonant force is studied; in Sect. 3.2 the effect of a NES on the dynamics of a one d.o.f. system under 1:3 subharmonic resonance is discussed; in Sect. 3.3 results on a two-d.o.f. system under steady wind are analyzed; in Sect. 3.4 a N-d.o.f. internally nonresonant string with NES and under harmonic excitation is considered; in Sect. 4 some conclusions are drawn.

2 The Multiple Scale Harmonic Balance Method

A nonlinear multi-d.o.f. mechanical systems, which is close to a Hopf bifurcation caused by aerodynamic forces, and under both 1:1 and 1:3 resonant harmonic excitations, is considered herein. The aerodynamic forces, due to the steady wind of (non-dimensional) speed μ which blows orthogonally to the plane of the structure, are assumed to be described by the quasi-steady theory. The main system is equipped with an essentially nonlinear oscillator with small mass and linear damper, behaving as a Nonlinear Energy Sink (NES), attached at a selected point (see Fig. 1). The relevant nondimensional equations of motion for the whole system read:

$$\begin{aligned} &\mathbf{M}\ddot{\mathbf{x}} + \mathbf{C}(\mu)\dot{\mathbf{x}} + \mathbf{K}(\sigma,\mu)\mathbf{x} + \xi(\mathbf{r}^T\dot{\mathbf{x}} - \dot{y})\mathbf{r} + \kappa(\mathbf{r}^T\mathbf{x} - y)^3\mathbf{r} \\ &\quad + \mathbf{n}(\mathbf{x},\mathbf{x},\mathbf{x}) = \eta_1\mathbf{f}_1\cos(\omega t) + \eta_3\mathbf{f}_3\cos(3\omega t) \qquad (1) \\ &m\ddot{y} - \xi(\mathbf{r}^T\dot{\mathbf{x}} - \dot{y}) - \kappa(\mathbf{r}^T\mathbf{x} - y)^3 = 0 \qquad (2) \end{aligned}$$

where: $\mathbf{x} = \mathbf{x}(t)$ is the time-depending N-dimensional column matrix of the displacements of the main structure; $\mathbf{M}$ is the mass matrix; $\mathbf{C}(\mu)$ is the (non-proportional) damping matrix and $\mathbf{K}(\sigma,\mu)$ is the stiffness matrix; $\mathbf{C}$ depends on μ while $\mathbf{K}$ depends on μ and (linearly) by a structural parameter σ; both μ and σ act as bifurcation parameters; $\mathbf{n}$ is the column of the (cubic) geometric nonlinearities, $\mathbf{f}_1$ is a unitary vector ($||\mathbf{f}_1|| = 1$) providing the shape of the component of the external force, of amplitude η_1, which is modulated by the frequency ω; in analogy, $\mathbf{f}_3$ is the unitary vector ($||\mathbf{f}_3|| = 1$) describing the component of the external force modulated by frequency 3ω and with amplitude η_3; $y = y(t)$ is the time-depending displacement of the added oscillator, m its mass, ξ its damping-ratio and κ the coefficient of its essentially

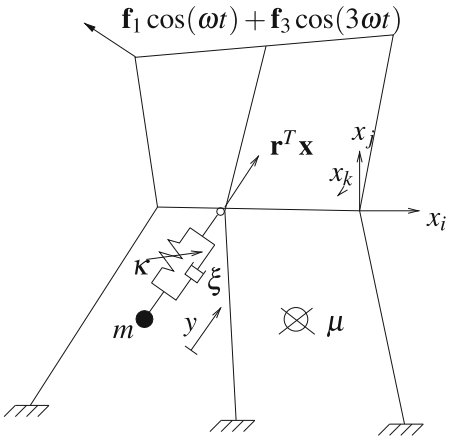

Fig. 1 Sketch of a multi-d.o.f. system equipped with a NES

nonlinear (cubic) spring; $\mathbf{r}$ is the influence coefficient column; finally, the dot represents time-differentiation. It is assumed that, when μ is equal to a critical value, the wind triggers a Hopf bifurcation and the dynamics of the (homogeneous) system with NES disengaged evolves on a critical mode; moreover, when $\sigma = 0$, the external excitation $\mathbf{f}_1$ is 1:1 resonant with the same critical mode of the main structure, and $\mathbf{f}_3$ is 1:3 resonant with the same mode as well, whereas no other resonance combinations are possible; σ acts as a detuning parameter.

It is convenient to introduce the relative displacement between main structure and NES, $z := \mathbf{r}^T\mathbf{x} - y$, so that the (1) and (2) become:

$$\begin{aligned}\mathbf{M}\ddot{\mathbf{x}} + \mathbf{C}(\mu)\dot{\mathbf{x}} + \mathbf{K}(\sigma,\mu)\mathbf{x} + \xi\dot{z}\mathbf{r} + \kappa z^3\mathbf{r} \\ + \mathbf{n}(\mathbf{x},\mathbf{x},\mathbf{x}) = \eta_1\mathbf{f}_1\cos(\omega t) + \eta_3\mathbf{f}_3\cos(3\omega t) \qquad (3)\\ m(\mathbf{r}^T\ddot{\mathbf{x}} - \ddot{z}) - \xi\dot{z} - \kappa z^3 = 0 \qquad (4)\end{aligned}$$

The dependent variables are rescaled through a nondimensional small parameter $\varepsilon > 0$, as $(\mathbf{x}, z) := \varepsilon^{1/2}(\tilde{\mathbf{x}}, \tilde{z})$, consistently with the presence of cubic nonlinearity; the bifurcation parameter μ is expressed as $\mu = \mu_0 + \varepsilon\mu_1$, where μ_0 is its critical value, to be still evaluated, and $\varepsilon\mu_1$ is the small deviation from it. The structural parameter σ is rescaled as $\sigma = \varepsilon\tilde{\sigma}$. The 1:1 external force is rescaled as $\eta_1 = \varepsilon^{3/2}\tilde{\eta}_1$, while the 1:3 force component is rescaled as $\eta_3 = \varepsilon^{1/2}\tilde{\eta}_1$. The parameters of the NES are also rescaled, since both its mass and damping are assumed small: $(m, \xi) := \varepsilon(\tilde{m}, \tilde{\xi})$. The rescaling and series expansion of $\mathbf{C}(\mu)$ and $\mathbf{K}(\sigma, \mu)$ lead to the following equations, after omission of tilde and division by $\varepsilon^{1/2}$:

$$\begin{aligned}\mathbf{M}\ddot{\mathbf{x}} + (\mathbf{C}_0 + \varepsilon\mu_1\mathbf{C}_1)\dot{\mathbf{x}} + (\mathbf{K}_0 + \varepsilon\mu_1\mathbf{K}_\mu + \varepsilon\sigma\mathbf{K}_\sigma)\mathbf{x} \\ + \varepsilon\xi\dot{z}\mathbf{r} + \varepsilon\kappa z^3\mathbf{r} + \varepsilon\mathbf{n}(\mathbf{x},\mathbf{x},\mathbf{x}) \\ = \varepsilon\eta_1\mathbf{f}_1\cos(\omega t) + \eta_3\mathbf{f}_3\cos(3\omega t) \qquad (5)\\ \varepsilon m(\mathbf{r}^T\ddot{\mathbf{x}} - \ddot{z}) - \varepsilon\xi\dot{z} - \varepsilon\kappa z^3 = 0 \qquad (6)\end{aligned}$$

where $\mathbf{C}_0 := \mathbf{C}(\mu_0)$, $\mathbf{K}_0 := \mathbf{K}(0, \mu_0)$, $\mathbf{C}_1 := \partial\mathbf{C}(\mu_0)/\partial\mu$, $\mathbf{K}_\mu := \partial\mathbf{K}(0, \mu_0)/\partial\mu$, and $\mathbf{K}_\sigma := \partial\mathbf{K}(0, \mu_0)/\partial\sigma$.

According to the Multiple Scale Method, independent time scales $t_0 := t, t_1 := \varepsilon t$, $t_2 = \varepsilon^2 t, \ldots$ are introduced and, consistently, the derivatives expressed as $\frac{d}{dt} = d_0 + \varepsilon d_1 + \varepsilon^2 d_2 + \ldots$ and $\frac{d^2}{dt^2} = d_0^2 + 2\varepsilon d_0 d_1 + \varepsilon^2(d_1^2 + 2d_0 d_1) + \ldots$. Moreover, the dependent variables are expanded in series as:

$$\begin{Bmatrix} \mathbf{x} \\ z \end{Bmatrix} = \begin{Bmatrix} \mathbf{x}_0 \\ z_0 \end{Bmatrix} + \varepsilon \begin{Bmatrix} \mathbf{x}_1 \\ z_1 \end{Bmatrix} + \varepsilon^2 \begin{Bmatrix} \mathbf{x}_2 \\ z_2 \end{Bmatrix} + \ldots \tag{7}$$

Substituting in (5) and (6) and collecting terms of the same order in ε, lead to the following perturbation equations:

order ε^0 :

$$\mathbf{M}d_0^2\mathbf{x}_0 + \mathbf{C}_0 d_0\mathbf{x}_0 + \mathbf{K}_0\mathbf{x}_0 = \eta_3\mathbf{f}_3\cos(3\omega t_0) \tag{8}$$

order ε^1 :

$$\begin{aligned}\mathbf{M}d_0^2\mathbf{x}_1 + \mathbf{C}_0 d_0\mathbf{x}_1 + \mathbf{K}_0\mathbf{x}_1 = &-2\mathbf{M}d_0 d_1\mathbf{x}_0 - \mathbf{C}_0 d_1\mathbf{x}_0 \\ &- \mu_1\mathbf{C}_1 d_0\mathbf{x}_0 - \mu_1\mathbf{K}_\mu\mathbf{x}_0 - \sigma\mathbf{K}_\sigma\mathbf{x}_0 - \xi d_0 z_0\mathbf{r} \\ &- \kappa z_0^3\mathbf{r} - \mathbf{n}(\mathbf{x}_0, \mathbf{x}_0, \mathbf{x}_0) + \eta_1\mathbf{f}_1\cos(\omega t_0)\end{aligned} \tag{9}$$

$$m(\mathbf{r}^T d_0^2\mathbf{x}_0 - d_0^2 z_0) - \xi d_0 z_0 - \kappa z_0^3 = 0 \tag{10}$$

order ε^2 :

$$\begin{aligned}\mathbf{M}d_0^2\mathbf{x}_2 + \mathbf{C}_0 d_0\mathbf{x}_2 + \mathbf{K}_0\mathbf{x}_2 = &-\mathbf{M}(d_1^2\mathbf{x}_0 \\ &+ 2d_0 d_2\mathbf{x}_0 + 2d_0 d_1\mathbf{x}_1) - \mathbf{C}_0(d_2\mathbf{x}_0 + d_1\mathbf{x}_1) \\ &- \mu_1\mathbf{C}_1(d_0\mathbf{x}_1 + d_1\mathbf{x}_0) - \sigma\mathbf{K}_\sigma\mathbf{x}_1 - \mu_1\mathbf{K}_\mu\mathbf{x}_1 \\ &- \xi(d_0 z_1 + d_1 z_0)\mathbf{r} - 3\kappa z_0^2 z_1\mathbf{r} - 3\mathbf{n}(\mathbf{x}_1, \mathbf{x}_0, \mathbf{x}_0)\end{aligned} \tag{11}$$

$$\begin{aligned}&m(\mathbf{r}^T d_0^2\mathbf{x}_1 - d_0^2 z_1) - \xi d_0 z_1 - 3\kappa z_0^2 z_1 = \\ &\quad 2m(d_0 d_1 z_0 - \mathbf{r}^T d_0 d_1\mathbf{x}_0) + \xi d_1 z_0\end{aligned} \tag{12}$$

It should be noted that, because of the vanishingly small values of the mass and damping, as well as of the lack of linear stiffness, no equation of motion relevant to NES appears in the generator problem (order ε^0), which therefore describes the linear dynamics of the main structure alone (as if NES were disengaged).

First, the homogeneous version of (8) is considered, in order to evaluate the critical condition due to the wind and the complementary function. It is assumed that, at the specific critical value μ_0, the system experiences a Hopf bifurcation, this entailing that the relevant eigenvalue problems

$$\begin{aligned}(\lambda^2\mathbf{M} + \lambda\mathbf{C}_0 + \mathbf{K}_0)\mathbf{u} &= \mathbf{0} \\ (\bar{\lambda}^2\mathbf{M}^T + \bar{\lambda}\mathbf{C}_0^T + \mathbf{K}_0^T)\mathbf{v} &= \mathbf{0}\end{aligned} \tag{13}$$

have a solution $\lambda_{1,2} = \pm i\omega$, with the associated right ($\mathbf{u}$ and $\bar{\mathbf{u}}$) and left ($\mathbf{v}$ and $\bar{\mathbf{v}}$) eigenvectors (the overbar denoting the complex conjugate and i the imaginary unit), whereas all the other eigenvalues have negative real parts and are far from the imaginary axis.

Then, a particular solution of (8) is sought: the external forces are assumed to be 1:1 and 1:3 resonant with the same critical mode $\mathbf{u}$ of the main system (13_1), and this entails that the remaining non-resonant modes bring a higher-order contribution to the overall response. Therefore, only the contribution related to the resonant mode is retained in the solution of (8), i.e.:

$$\mathbf{x}_0(t_0, t_1, \ldots) = A(t_1, \ldots)\mathbf{u}e^{i\omega t_0} + \eta_3 \mathbf{w}_0 e^{3i\omega t_0} + cc \tag{14}$$

where: $A(t_1, \ldots)$ is a complex modal amplitude, whose modulation on the slower time-scales must be evaluated; cc stands for complex conjugate and $\mathbf{w}_0 := \frac{1}{2}[\mathbf{K}_0 + 3i\omega\mathbf{C}_0 - 9\omega^2\mathbf{M}]^{-1}\mathbf{f}_3$.

The ε-order perturbation equations (9) and (10) are now addressed, and the NES (10) considered first. Since its (steady) solution cannot be expressed by elementary (nor Jacobi) functions, the Harmonic Balance Method is used, letting:

$$z_0(t_0, t_1, t_2) = \sum_k B_{0k}(t_1, t_2)e^{ik\omega t_0} + cc \tag{15}$$

where B_{0k} are complex amplitudes. In this paper, just the terms relevant to the values $k = 1, 3$ are retained in (15), coherently with the idea of obtaining an approximated solution, which contains at least the same frequency components of the generating solution (14). Consequently, balancing the frequencies ω and 3ω in (10), the following nonlinear, complex, algebraic equations are obtained:

$$\begin{aligned} &m\omega^2(-B_{01} + uA) + i\xi\omega B_{01} + 3\kappa(B_{01}^2\bar{B}_{01} + B_{03}\bar{B}_{01}^2 \\ &\quad + 2B_{01}B_{03}\bar{B}_{03}) = 0 \end{aligned} \tag{16}$$

$$\begin{aligned} &m\omega^2(-9B_{03} + 9\eta_3 w_0) + 3i\xi\omega B_{03} + \kappa(B_{01}^3 + 3B_{03}^2\bar{B}_{03} \\ &\quad + 6B_{03}B_{01}\bar{B}_{01}) = 0 \end{aligned} \tag{17}$$

where $u := \mathbf{r}^T\mathbf{u}$ and $w_0 := \mathbf{r}^T\mathbf{w}_0$.

Equations (16) and (17) provide, at the first order of perturbation, an algebraic constrain between the (active) resonant amplitude A of oscillation of the main structure and the (passive) amplitudes of the NES elongation, B_{01} and B_{03}; it, therefore, describes a manifold in the state-space, on which the asymptotic dynamics takes place (at the first perturbation order).

Equation (9) is then considered, in which z_0 is assumed as in (15). By requiring that the resonant forcing term is orthogonal to the null space of the adjoint operator (solvability condition), the following equation must hold

$$\begin{aligned}\mathbf{v}^H[&(2i\omega\mathbf{M}+\mathbf{C}_0\mathbf{u})d_1A+(i\omega\mathbf{C}_1\mathbf{u}+\mathbf{K}_\mu\mathbf{u})\mu_1A\\&+\sigma\mathbf{K}_\sigma\mathbf{u}A+i\omega\xi\mathbf{r}B_{01}\\&+3\kappa\mathbf{r}(B_{01}^2\bar{B}_{01}+B_{03}\bar{B}_{01}^2+2B_{01}B_{03}\bar{B}_{03})\\&+3A^2\bar{A}\mathbf{n}(\bar{\mathbf{u}},\mathbf{u},\mathbf{u})\\&+3\eta_3\bar{A}^2\mathbf{n}(\mathbf{w}_0,\bar{\mathbf{u}},\bar{\mathbf{u}})+6\eta_3^2A\mathbf{n}(\mathbf{w}_0,\bar{\mathbf{w}}_0,\mathbf{u})]=0\end{aligned}\tag{18}$$

producing the following differential equation:

$$\begin{aligned}c_1d_1A=&(\mu_1c_2+\sigma c_3+\eta_3^2c_8)A+\xi c_4B_{01}\\&+\kappa c_5(B_{01}^2\bar{B}_{01}+B_{03}\bar{B}_{01}^2+2B_{01}B_{03}\bar{B}_{03})\\&+c_6A^2\bar{A}+\eta_3c_7\bar{A}^2+\eta_1c_9\end{aligned}\tag{19}$$

where the expression of the complex coefficients c_i is given in Appendix A. It is worth noticing that, when $B_{01}=B_{03}=\eta_3=0$ is put into (19), this reduces to the normal form equation for the Hopf bifurcation of the principal system. This entails that the NES modifies both the bifurcation point and the limit cycle, thus bringing potential benefits to the mechanical behavior of the original system.

If one decided to stop the perturbation analysis at this step, (19) and (16), (17) should be considered together. In this case, since the NES provides an algebraic constraint, its (complex) amplitudes B_{01} and B_{03} would be passive variables, whereas the dynamic evolution of the (active) amplitude A of the main system would be completely restrained onto the manifold (16), (17). To overcome this tight limitation, a further perturbation step must be accomplished.

The non-diverging solution of (9) can now be evaluated, after tacking into account (19): it contains terms of frequency ω, 3ω, 5ω, 7ω and 9ω. However, still driven by the idea of obtaining and approximated solution, just the terms of frequency ω and 3ω are retained in it, which turns out to be:

$$\begin{aligned}\mathbf{x}_1(t_0,t_1,t_2)=&[(\mu_1\mathbf{w}_1+\sigma\mathbf{w}_2+\eta_3^2\mathbf{w}_3)A+\xi\mathbf{w}_4B_{01}\\&+\kappa\mathbf{w}_5(B_{01}^2\bar{B}_{01}+B_{03}\bar{B}_{01}^2+2B_{01}B_{03}\bar{B}_{03})\\&+\mathbf{w}_6A^2\bar{A}+\eta_3\mathbf{w}_7\bar{A}^2+\eta_1\mathbf{w}_8]e^{i\omega t_0}\\&+[\eta_3\mu_1\mathbf{w}_9+\eta_3\sigma\mathbf{w}_{10}+\xi\mathbf{w}_{11}B_{03}\\&+\kappa\mathbf{w}_{12}(B_{01}^3+3B_{03}^2\bar{B}_{03}+6B_{03}B_{01}\bar{B}_{01})\\&+\mathbf{w}_{13}A^3+\eta_3\mathbf{w}_{14}A\bar{A}+\eta_3^3\mathbf{w}_{15}]e^{3i\omega t_0}+cc\end{aligned}\tag{20}$$

where $\mathbf{w}_j$, $(j=1,\ldots,15)$ are defined in Appendix A.

Equation (12) is finally considered: a new harmonic balance is carried out, assuming the following expression for z_1:

$$z_1(t_0,t_1,t_2)=\sum_k B_{1k}(t_1,t_2)e^{ik\omega t_0}+cc\tag{21}$$

Substituting (14), (15), (20) and (21) in (12) and balancing the ω- and 3ω-frequency terms, the following equations are obtained:

$$\begin{aligned}
&-\omega^2 m[(\mu_1 w_1 + \sigma w_2 + \eta_3^3 w_3)A + \xi w_4 B_{01} + \kappa w_5(B_{01}^2 \bar{B}_{01} \\
&\quad + B_{03}\bar{B}_{01}^2 + 2B_{01}B_{03}\bar{B}_{03}) + w_6 A^2\bar{A} + \eta_3 w_3 \bar{A}^2 \\
&\quad + \eta_1 w_8 - B_{11}] - i\omega\xi B_{11} - 3\kappa(B_{01}^2\bar{B}_{11} + 2B_{01}\bar{B}_{03}B_{13} \\
&\quad + 2B_{01}B_{03}\bar{B}_{13} + B_{13}\bar{B}_{01}^2 + 2B_{01}\bar{B}_{01}B_{11} + 2B_{11}\bar{B}_{03}B_{03} \\
&\quad + 2B_{03}\bar{B}_{01}\bar{B}_{11}) - 2im\omega(d_1 B_{01} - u d_1 A) \\
&\quad - i\omega\xi d_1 B_{01} = 0
\end{aligned} \tag{22}$$

$$\begin{aligned}
&-9\omega^2 m[\eta_3\mu_1 w_9 + \eta_3\sigma w_1 0 + \xi B_{03} w_{11} + \kappa w_{12}(B_{01}^3 \\
&\quad + 3B_{03}^2\bar{B}_{03} + 6B_{03}B_{01}\bar{B}_{01}) + w_{13}A^3 + \eta_3 w_{14} A\bar{A} \\
&\quad + \eta_3^3 w_{15} - B_{13}] - 3i\omega\xi B_{13} - 3\kappa(B_{01}^2 B_{11} + B_{03}^2\bar{B}_{13} \\
&\quad + 2B_{01}B_{03}\bar{B}_{11} + 2B_{01}B_{13}\bar{B}_{01} + 2B_{03}B_{13}\bar{B}_{03} \\
&\quad + 2B_{03}B_{11}\bar{B}_{01}) - 6i\omega m d_1 B_{03} - 3i\omega\xi d_1 B_{03} = 0
\end{aligned} \tag{23}$$

where $w_j := \mathbf{r}^T \mathbf{w}_j$, $j = 1, \ldots, 15$. Equations (16) and (22), and (17) and (23), can be reconstituted, respectively, using the definitions $B_1 := B_{01} + \varepsilon B_{11}$ and $B_3 := B_{03} + \varepsilon B_{13}$; coming back to the true time, they become:

$$\begin{aligned}
&-\omega^2 m[(u + \mu_1 w_1 + \sigma w_2 + \eta_3^3 w_3)A + \kappa w_5(B_1^2\bar{B}_1 \\
&\quad + B_3\bar{B}_1^2 + 2B_1 B_3\bar{B}_3) + w_6 A^2\bar{A} + \eta_3 w_3\bar{A}^2 \\
&\quad + \eta_1 w_8 - (1 - \xi w_4)B_1] - i\omega\xi B_1 - 3\kappa(B_1^2\bar{B}_1 \\
&\quad + 2B_1\bar{B}_3 B_3 + B_3\bar{B}_1^2) - 2im\omega(\dot{B}_1 - u\dot{A}) \\
&\quad - i\omega\xi\dot{B}_1 = 0
\end{aligned} \tag{24}$$

$$\begin{aligned}
&-9\omega^2 m[\eta_3(w_0 + \mu_1 w_9 + \sigma w_{10}) + \kappa w_{12}(B_1^3 \\
&\quad + 3B_3^2\bar{B}_3 + 6B_3 B_1\bar{B}_1) + w_{13}A^3 + \eta_3 w_{14} A\bar{A} \\
&\quad + \eta_3^3 w_{15} - (1 - \xi w_{11})B_3] - 3i\omega\xi B_3 \\
&\quad - \kappa(B_1^3 + 3B_3^2\bar{B}_3 + 6B_3 B_1\bar{B}_1) \\
&\quad - 3i\xi\omega B_3 - 6i\omega m\dot{B}_3 - 3i\omega\xi\dot{B}_3 = 0
\end{aligned} \tag{25}$$

It appears that (24) and (25) describe the dynamics of the amplitudes B_1 and B_3, differently from (16) and (17). The key-terms containing $\dot{B}_1$ and $\dot{B}_3$ come out only at the second-order, since they are affected by small coefficients ξ and m, thus revealing the nature of singular perturbation. In contrast, the term proportional to $\dot{A}$, which also appears at this order, does not add any qualitative new contributions, being ruled by (19).

If the perturbation procedure is truncated at order ε for the main system equation, the solvability condition (19) can be written in terms of the true time:

$$\begin{aligned} c_1\dot{A} = &(\mu_1 c_2 + \sigma c_3 + \eta_3^2 c_8)A + \xi c_4 B_1 \\ &+ \kappa c_5(B_1^2\bar{B}_1 + B_3\bar{B}_1^2 + 2B_1B_3\bar{B}_3) \\ &+ c_6 A^2\bar{A} + \eta_3 c_7 \bar{A}^2 + \eta_1 c_9 \end{aligned} \tag{26}$$

Therefore, the prevalent dynamics of the primary system coupled with NES is described by (26), (24), (25), in terms of the complex variables A, B_1 and B_3. To get the real form of the system, either the polar or the Cartesian transformations can be applied to the equations: the first one is $A(t) := \frac{1}{2}a(t)e^{i\alpha(t)}$ and $B_k(t) := \frac{1}{2}b_k(t)e^{i\beta_k(t)}$, for $k = 1, 3$; the second one is $A(t) := \frac{1}{2}(p_1(t) + iq_1(t))$, $B_1(t) := \frac{1}{2}(p_2(t) + iq_2(t))$ and $B_3(t) := \frac{1}{2}(p_3(t) + iq_3(t))$. The substitution of one of the two kinds of transformations in the equations and the separation of real and imaginary parts provides the six real ordinary differential equations in the six real variables $(a(t), \alpha(t), b_1(t), \beta_1(t), b_3(t), \beta_3(t)$ in the polar case, $p_1(t), q_1(t), p_2(t), q_2(t), p_3(t), q_3(t)$ in the Cartesian case). Equilibrium points of the system represent periodic oscillations in the displacements $\mathbf{x}$, z.

3 Sample Systems and Numerical Results

Sample systems are analyzed here, (a) to investigate the mechanical effects of the attached NES on the dynamics of the main system; (b) to check the reliability of the MSHBM via comparison with direct numerical integrations of the equations of motion.

3.1 One d.o.f. Main System Under 1:1 External Force

A sample system, already studied in [2, 11, 22], is considered here. The main system consists of a one d.o.f. linear undamped system, with attached NES, a sketch of which is shown in Fig. 2. The nondimensional equations of motion are:

$$\ddot{x} + (\omega^2 + \sigma)x - \xi(\dot{y} - \dot{x}) - \kappa(y - x)^3 = \eta_1 \cos\omega t \tag{27}$$

$$m\ddot{y} + \xi(\dot{y} - \dot{x}) + \kappa(y - x)^3 = 0 \tag{28}$$

that, for $z := x - y$, become:

$$\ddot{x} + (\omega^2 + \sigma)x - \xi\dot{z} - \kappa z^3 = \eta_1 \cos\omega t \tag{29}$$

$$m(\ddot{z} - \ddot{x}) + \xi\dot{z} + \kappa z^3 = 0 \tag{30}$$

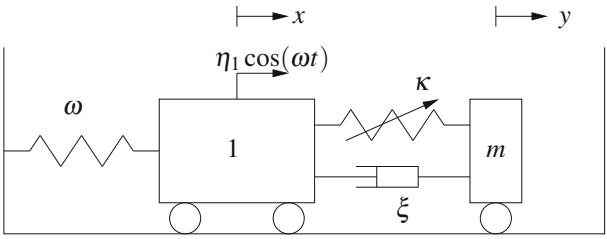

Fig. 2 Principal linear undamped oscillator under 1:1 resonant harmonic force with NES

Therefore, comparing (29) and (30) with (3) and (4), it results $N = 1$ and:

$$\begin{aligned} &\mathbf{x} = x, \quad \mathbf{M} = 1, \quad \mathbf{C} = 0, \quad \mathbf{K}_0 = \omega^2, \quad \mathbf{K}_\mu = 0, \\ &\mathbf{K}_\sigma = 1, \quad \mathbf{n}(\mathbf{x}, \mathbf{x}, \mathbf{x}) = 0, \quad \mathbf{f}_1 = 1, \quad \mathbf{f}_3 = 0 \end{aligned} \tag{31}$$

Since the external excitation has just the component of frequency ω, the generating solution does not contain the component of frequency 3ω, and so is it for the terms z_0 and z_1 ($B_{03} = B_{13} = 0$), leading just to the balance of the frequency ω. The nonlinear manifold, (16), becomes:

$$m\omega^2(-B_{01} + A) + i\xi\omega B_{01} + 3\kappa B_{01}^2 \bar{B}_{01} = 0 \tag{32}$$

which can be easily written in real form in terms of the (real) amplitudes a and b_1:

$$\left(\frac{3\kappa b_1^2}{8m\omega} + \frac{\omega b_1}{2}\right)^2 + \left(\frac{\xi b_1}{2m}\right)^2 - \frac{\omega^2 a^2}{4} = 0 \tag{33}$$

The set of numerical values considered in [2, 11] is used for this example: $m = 0.05$, $\xi = 0.01$, $\kappa = 0.067$, $\omega = 1$.

The Amplitude Modulation Equations (26), (24) read:

$$\dot{A} = \frac{i\sigma}{2\omega}A - \frac{\xi}{2}B_1 - \frac{3i\kappa}{2\omega}B_1^2\bar{B} - \frac{i\eta_1}{4\omega} \tag{34}$$

$$\begin{aligned} 2im\omega\dot{A} - (2im\omega + \xi)\dot{B}_1 = m\omega^2 A \\ + (i\xi\omega - m\omega^2)B_1 + 3\kappa B_1^2\bar{B}_1 \end{aligned} \tag{35}$$

In polar form, they become:

$$\dot{a} = \frac{3kb_1^3 \sin(\alpha - \beta_1)}{8\omega} - \frac{1}{2}\xi b_1 \cos(\alpha - \beta_1) - \frac{\eta_1 \sin\alpha}{2\omega} \tag{36}$$

$$\begin{aligned} a\dot{\alpha} = \frac{a\sigma}{2\omega} + \frac{3b_1^3 k \cos(\alpha - \beta_1)}{8\omega} + \frac{1}{2}b_1\xi \sin(\alpha - \beta_1) \\ - \frac{\eta_1 \cos\alpha}{2\omega} \end{aligned} \tag{37}$$

$$m\dot{a}\sin(\alpha-\beta_1)+ma\dot{\alpha}\cos(\alpha-\beta_1)+\frac{\xi}{2\omega}\dot{b}_1-mb\dot{\beta}_1=$$
$$-\frac{m\omega}{2}a\cos(\alpha-\beta_1)-\frac{3b_1^3k}{8\omega}+\frac{m\omega}{2}b_1 \tag{38}$$
$$m\dot{a}\cos(\alpha-\beta_1)-ma\dot{\alpha}\sin(\alpha-\beta_1)-m\dot{b}_1$$
$$-\frac{\xi}{2\omega}b_1\dot{\beta}_1=\frac{\xi}{2}b_1+\frac{m\omega}{2}a\sin(\alpha-\beta_1) \tag{39}$$

When the NES is disengaged, since the main system is linear, the amplitudes of the periodic solutions in x become

$$a_e=\frac{\eta_1}{\sigma} \tag{40}$$
$$\tan\alpha_e=\frac{a_e\sigma}{2\omega} \tag{41}$$

which are always stable. They are the equilibrium points of (36), (37),when $b=0$. Due to the lack of damping in the main system, the amplitude tends to infinite when σ goes to zero.

When the NES is considered engaged, the branches of equilibrium points of the dynamical system (36)–(39), which represent periodic oscillations in the original variables x and z, are shown in Fig. 3, for $\eta_1=0.075$. The figure is obtained via the software AUTO [25]. It can be observed that multiple solutions exist in some intervals of σ. In particular, the three equilibrium points relevant for $\sigma=-0.3$ are marked by colored points, and only the green one is stable, while the yellow and red ones are unstable; black boxes represent secondary Hopf bifurcation points.

The same three equilibrium points are also shown in Fig. 4, superimposed to the nonlinear manifold. Strongly modulated responses (SMR) are detected by numerical integration of the system (36)–(39). They represent quasi-periodic relaxation oscillations in the variables a and b, typically describing cycles around the two folds of the

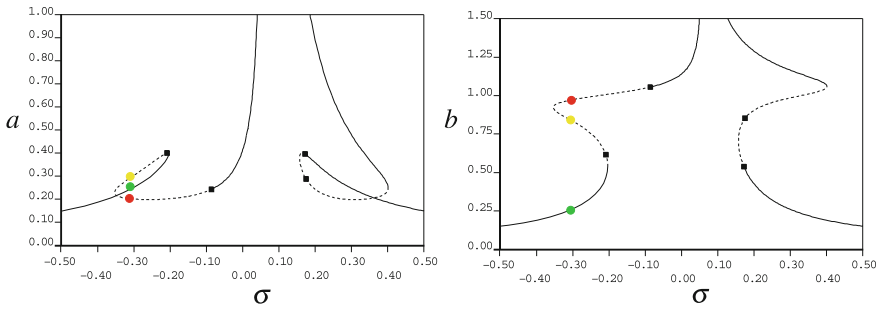

Fig. 3 Amplitudes a and b when NES is engaged, when $m=0.05$, $\xi=0.01$, $\kappa=0.067$, $\omega=1$ and $\eta_1=0.075$. The *filled squares* indicate Hopf bifurcation points. The colored points are equilibria referred to following figures. *Continuous line* stable; *dashed line* unstable

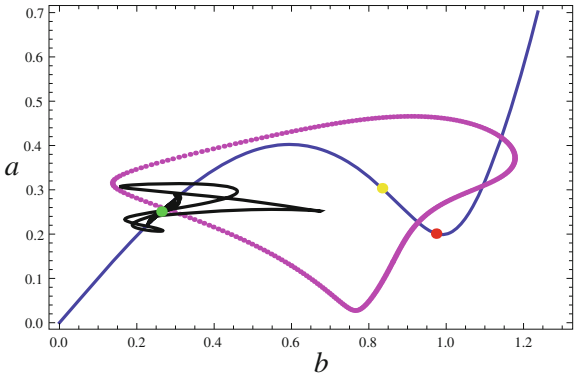

Fig. 4 Nonlinear manifold (*blue line*), three equilibrium points (*red*, *green* and *yellow points*), Poincaré map of the SMR response (*magenta points*), and transitional motion (*black line*) falling to the equilibrium point, when $\sigma = -0.3, f = 0.075, m = 0.05, \xi = 0.01, \kappa = 0.067, \omega = 1$

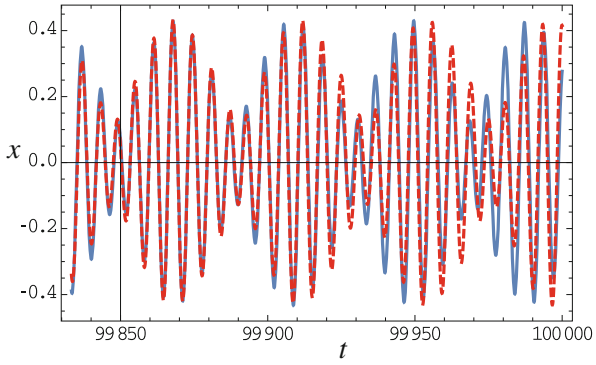

Fig. 5 SMR for example 1, when $\sigma = -0.3$, $\eta_1 = 0.075$, $m = 0.05$, $\xi = 0.01$, $\kappa = 0.067$, $\omega = 1$; $x(t)$ as numerical integration of the original (27), (28) (*red dashed line*) and as reconstituted response from (36)–(39) (*blue continuous line*)

nonlinear manifold shown in Fig. 4. They are triggered in dependence of the position of the equilibrium points. In particular, a Poincaré section is shown (magenta points). For initial conditions close to the stable equilibrium point, a trajectory asymptotically falling on it is also found (black line). The corresponding time evolutions of the (reconstituted) displacement $x(t)$ is shown in Fig. 5, in good agreement with the solutions obtained by numerical integration of the original (27), (28).

A discussion on the use of the higher harmonics $(3\omega, \ldots)$ for this example and the evaluation of their negligible contribution is given in [22].

3.2 One d.o.f. Main System Under 1:3 External Force

A second example is considered here concerning an external force in 1:3 subharmonic resonance. The relevant results are believed to be new, and deserve further investigation.

The principal system is of a one d.o.f. nonlinear damped system, with attached NES, as shown in Fig. 6. The nondimensional equations of motion are:

$$\begin{aligned} &\ddot{x} + 2\zeta\omega\dot{x} + \omega^2(1-\sigma)x + \kappa_c x^3 \\ &\quad + \kappa(x-y)^3 + \xi(\dot{x}-\dot{y}) = \eta_3\cos(3\omega t) \\ &m\ddot{y} - \kappa(x-y)^3 - \xi(\dot{x}-\dot{y}) = 0 \end{aligned} \tag{42}$$

that, for $z := x - y$, become:

$$\begin{aligned} &\ddot{x} + 2\zeta\omega\dot{x} + \omega^2(1-\sigma)x + \kappa_c x^3 \\ &\quad + \kappa z^3 + \xi\dot{z} = \eta_3\cos(3\omega t) \\ &m(\ddot{z} - \ddot{x}) + \kappa z^3 + \xi\dot{z} = 0 \end{aligned} \tag{43}$$

Therefore, comparing (43) with (3) and (4), it results $N = 1$ and:

$$\begin{aligned} &\mathbf{x} = x, \quad \mathbf{M} = 1, \quad \mathbf{C} = 2\zeta\omega, \quad \mathbf{K}_0 = \omega^2, \quad \mathbf{K}_\mu = 0, \\ &\mathbf{K}_\sigma = -1, \quad \mathbf{n}(\mathbf{x},\mathbf{x},\mathbf{x}) = \kappa_c x^3, \quad \mathbf{f}_1 = 0, \quad \mathbf{f}_3 = 1 \end{aligned} \tag{44}$$

Here the generating solution of the principal structure contains both the components of frequency ω and 3ω, therefore the balance of both those frequencies in the NES equation is carried out in this case. The polar form of the three Amplitude Modulation Equations (26), (24), (25) reads:

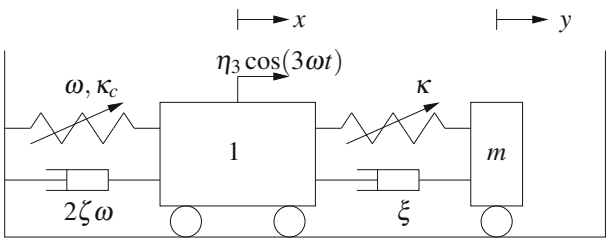

Fig. 6 Principal nonlinear oscillator under 1:3 resonant harmonic force with NES

$$\dot{a} = \mathscr{F}_1(a, b_1, b_3, \alpha, \beta_1, \beta_3) \tag{45}$$

$$a\dot{\alpha} = \mathscr{F}_2(a, b_1, b_3, \alpha, \beta_1, \beta_3) \tag{46}$$

$$m\omega\dot{a}\sin(\alpha-\beta_1) + m\omega\dot{\alpha}\cos(\alpha-\beta_1) + \frac{\xi}{2}\dot{b}_1 - m\omega b_1\dot{\beta}_1 = \mathscr{F}_3(a, b_1, b_3, \alpha, \beta_1, \beta_3) \tag{47}$$

$$m\omega\dot{a}\cos(\alpha-\beta_1) - m\omega\dot{\alpha}\sin(\alpha-\beta_1) - \frac{\xi}{2}b\dot{\beta}_1 - m\omega\dot{b}_1 = \mathscr{F}_4(a, b_1, b_3, \alpha, \beta_1, \beta_3) \tag{48}$$

$$\frac{\xi}{2}\dot{b}_3 - 3m\omega b_3\dot{\beta}_3 = \mathscr{F}_5(a, b_1, b_3, \alpha, \beta_1, \beta_3) \tag{49}$$

$$\frac{\xi}{2}b\dot{\beta}_3 + 3m\omega\dot{b}_3 = \mathscr{F}_6(a, b_1, b_3, \alpha, \beta_1, \beta_3) \tag{50}$$

where $\mathscr{F}_j, j = 1, \ldots, 6$, are reported in Appendix A.

If the NES were disengaged, just (45) and (46) would be retained, being $b_k \equiv \beta_k \equiv 0$, and the steady state response of the system, describing periodic oscillations for $x(t)$, is described by the solution of the system $\mathscr{F}_1 = \mathscr{F}_2 = 0$ (see [19]). In particular the steady state response is governed by the equation

$$(\zeta\omega)^2 + \left(\left(-\frac{\sigma\omega}{2} + \frac{3\kappa_c\eta_3^2}{64\omega^5}\right) + \frac{3\kappa_c}{8\omega}a^2\right)^2 = \left(\frac{3\kappa_c\eta_3 a}{32\omega^3}\right)^2 \tag{51}$$

which, besides $a = 0$ existing everywhere, defines the non-trivial response for the subharmonic resonance condition, which exists in the range

$$\sigma \geq \frac{21\eta_3^3\kappa_c}{256\omega^6} + \frac{256\zeta^2\omega^6}{3\eta_3^2\kappa_c} \tag{52}$$

The frequency-response plot of the subharmonic response is shown in Fig. 7 in black line, for $\eta_3 = 0.3, \zeta = 0.01, \omega = 1, \kappa_c = -5$. It is superimposed to the corresponding one, which is obtained when NES is engaged (red line) for $m = 0.05, \xi = 0.01, \kappa = 1$. In particular, the NES reduces the amplitude of the subharmonic response and its domain of existence; furthermore, in comparison with the case with NES disengaged, it is found that the basin of attraction of the subharmonic response in presence of NES is noticeably reduced in favor of the trivial solution. Moreover, relaxation oscillations are found by means of numerical integrations of (45)–(50). Their phase plot is shown in Fig. 8 (red line) as superimposed to the nonlinear manifold (gray points), which is a surface in the (b_1, b_3, a) space. The relaxation oscillations here described have maximum amplitudes smaller than the corresponding (periodic) oscillations which occur when the NES is disengaged (see Fig. 9).

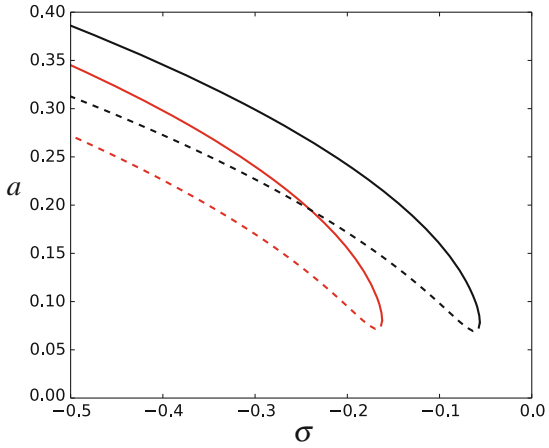

Fig. 7 Frequency-response curve in correspondence of the 1:3 resonance for the system with NES disengaged (*black line*) and with NES engaged (*red line*), for $\eta_3 = 0.3$. *Continuous line* stable; *dashed line* unstable

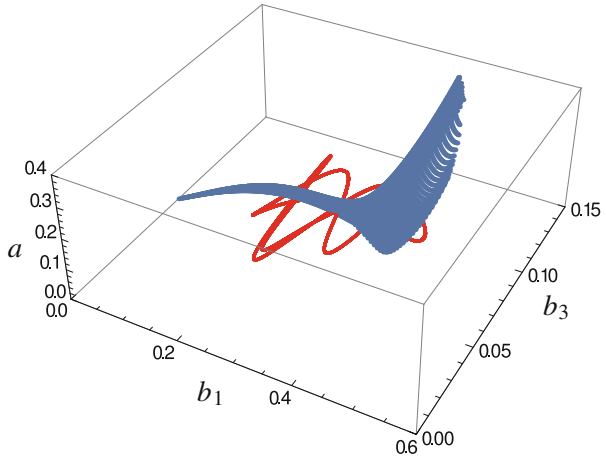

Fig. 8 Nonlinear manifold (*gray points*) and relaxation oscillations (*red line*) for $\sigma = -0.5$, $\eta_3 = 0.3$

3.3 A Two d.o.f. Airfoil

A sample system, already considered in [15, 23], is used to investigate the mechanics of a primary structure subjected to steady wind. It is constituted by a two d.o.f. rigid airfoil engaged to a NES and subjected to the (non-dimensional) steady wind μ, and is sketched in Fig. 10. The (non-dimensional) Lagrangian parameters are x and φ, representing the plunge and the pitch, respectively. The two nonlinear springs, extensional and rotational respectively, have both linear and cubic coefficients. The

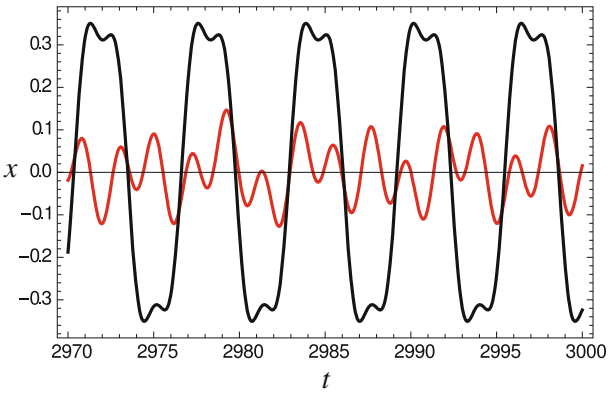

Fig. 9 Time-evolution of the primary system with NES disengaged in subharmonic resonance (*black line*) and with NES engaged (*red line*), for $\eta_3 = 0.3$ and $\sigma = -0.5$

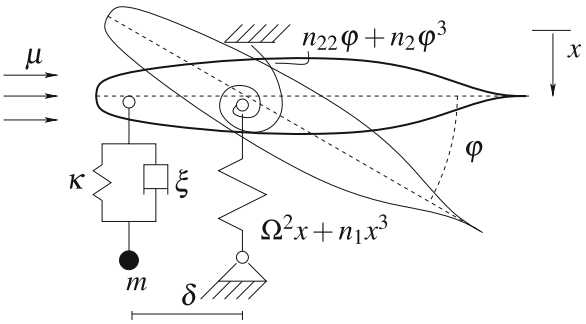

Fig. 10 Rigid airfoil with NES under steady wind

position of the NES with respect to the center of mass of the airfoil is described by the (non-dimensional) parameter δ: if it is positive, then the NES is windward, otherwise, if δ is negative, the NES is leeward. The non-dimensional equations of motion are

$$\begin{aligned}
&\ddot{x} + n_{12}\ddot{\varphi} + \mu g_{11}\dot{x} + \Omega^2 x + \mu^2 g_{11}\varphi - \xi(\dot{y} - \dot{x} + \dot{\alpha}\delta) \\
&\quad - \kappa(y - x + \alpha\delta)^3 + n_1 x^3 = 0 \\
&n_{12}\ddot{x} + n_{22}\ddot{\varphi} + \mu g_{21}\dot{\varphi} + k_{21}x + (n_{22} - \mu^2 g_{21})\varphi \\
&\quad + \xi(\dot{y} - \dot{x} + \dot{\alpha}\delta)\delta + \kappa(y - x + \alpha\delta)^3\delta + n_2\varphi^3 = 0 \\
&m\ddot{y} + \xi(\dot{y} - \dot{x} + \dot{\alpha}\delta) + \kappa(y - x + \alpha\delta)^3 = 0
\end{aligned} \tag{53}$$

The comparison between (53) and (1) allows one to identify $N = 2$ and the relevant matrices and columns as

$$\mathbf{x} = \begin{Bmatrix} x \\ \varphi \end{Bmatrix}, \ \mathbf{M} = \begin{bmatrix} 1 & n_{12} \\ n_{12} & n_{22} \end{bmatrix}, \ \mathbf{C}(\mu) = \mu \begin{bmatrix} g_{11} & 0 \\ g_{21} & 0 \end{bmatrix},$$
$$\mathbf{K}(\mu) = \begin{bmatrix} \Omega^2 & \mu^2 g_{11} \\ k_{21} & n_{22} - \mu^2 g_{21} \end{bmatrix}, \ \mathbf{r} = \begin{Bmatrix} 1 \\ -\delta \end{Bmatrix}, \ \mathbf{n} = \begin{Bmatrix} n_1 x^3 \\ n_2 \varphi^3 \end{Bmatrix} \tag{54}$$

The following numerical values are chosen, corresponding to those used in [15]: $n_{12} = n_{21} = 0.2$, $n_{22} = 0.25$, $g_{11} = 0.2$, $g_{21} = -0.08$, $\Omega = 0.5$, $k_{21} = 0$, $n_1 = n_2 = 1$, $m = 0.02$, $\xi = 0.008$. For the specified values, the critical wind turns out to be $\mu_0 = 0.8704$, the corresponding critical frequency $\omega = 0.8704$ (imaginary part of the eigenvalue) and the right and left eigenvectors $\mathbf{u} = \{0,\ 1\}^T$ and $\mathbf{v} = \{-0.6521 - 0.5635i,\ 0.5217 + 2.7486i\}^T$, respectively. The relevant Amplitude Modulation Equations are not reported in their explicit form for the sake of brevity.

In Fig. 11 the equilibrium branches of the AME, corresponding to periodic motions in the variables x, φ, z, are shown for (a) windward NES ($\delta = 0.75$) and (b) leeward NES ($\delta = -0.75$). The red line describes the branch when the NES is disengaged, and the dots represent results of the numerical integration of the original equations (53), which are in good agreement. It can be seen that, when the NES is disengaged, a super-critical Hopf bifurcation occurs at $\mu_1 = 0$ and stable periodic motions are triggered for increasing values of μ_1, whose amplitudes are represented by the red line. The NES shifts forward the position of the bifurcation points, but it also makes the bifurcation sub-critical. Indeed two turning points occur, as well as two secondary Hopf bifurcation points which trigger stable periodic motions in a, corresponding to quasi-periodic motions in x, φ and z (the amplitude of the limit cycles are shown in the pictures). In case of windward NES (Fig. 11a), next to the second turning point, the amplitude of the branch is larger than that without NES. It means that, in this case, the NES gives a harmful contribution to the dynamics of the system. On the other hand, in case of leeward NES (Fig. 11b), the branch of the amplitude is always underneath the one corresponding to the case without NES. Therefore, for leeward NES, the

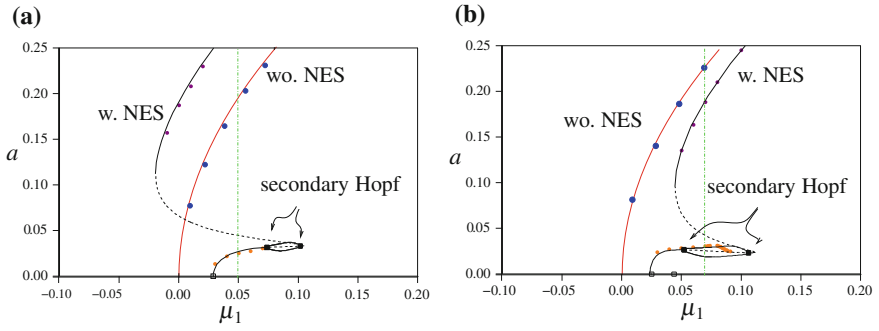

Fig. 11 Equilibrium branches of the slow flow on the plane (μ_1, a): **a** $\kappa = 10$, $\delta = 0.75$; **b** $\kappa = 10$, $\delta = -0.75$. *Red line* without NES; *black line* with NES; *dots* numerical integrations of the originating equations; *continuous line* stable; *dashed line* unstable; *black square* secondary Hopf point

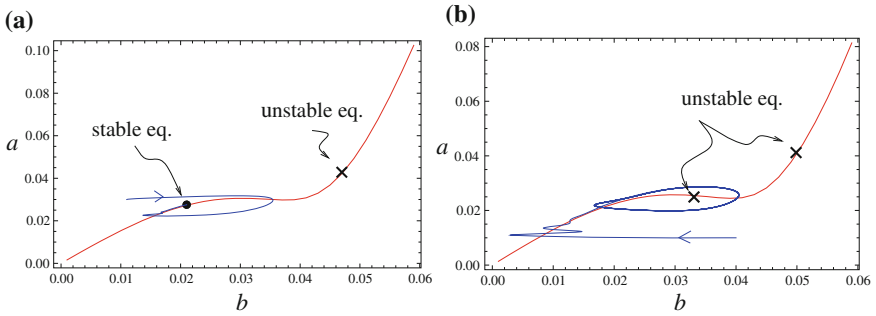

Fig. 12 Phase portrait on the plane (b, a): **a** $\kappa = 10$, $\mu_1 = 0.05$, $\delta = 0.75$; **b** $\kappa = 10$, $\mu_1 = 0.07$, $\delta = -0.75$. *Red line* manifold; *blue line* trajectory; *black circle* stable equilibrium point; *black cross* unstable equilibrium point

effective reduction of the amplitude of oscillations is accomplished. These results are in agreement with [2]. The two vertical dashed-dotted green lines in Fig. 11 represent the values of μ_1 for which the phase portraits of Fig. 12 are produced ($\mu_1 = 0.05$ and $\mu_1 = 0.07$, respectively). In particular, from Fig. 12a it is evident how the stable equilibrium point (black circle), which lies on the manifold, asymptotically attracts the dynamic evolution of the system; as a correspondence, periodic oscillations in the variables (x, φ, z) are produced. On the other hand, in Fig. 12b, realized for a value of μ_1 between the two secondary Hopf bifurcations, the equilibrium points are unstable, and a limit cycle in (b, a) is obtained. It corresponds to quasi-periodic oscillations in (x, φ, z), which are in good agreement with the relevant results of the numerical integrations of the originating equations (53).

3.4 Nonlinear Elastic String

A nonlinear extensible elastic string PQ is considered (see Fig. 13 and [24] for details on this case study). The string is restrained at P, while a concentrated mass m_Q and a vertical elastic spring of linear stiffness k_Q are applied at Q. The string is supposed of initial length ℓ and prestress tensile force $\bar{N}$. An external, distributed, harmonically time-dependent, force $p(x)\cos(\Omega t)$ is supposed to be applied to the string (x being the abscissa measured in the prestressed configuration and t the time). The mass per unit length of the string is ρ and its longitudinal stiffness EA. A NES characterized by a mass m, cubic stiffness coefficient k and linear damping coefficient c, is linked to the string at point C, corresponding to the abscissa x_C. Denoting by $v(x, t)$ the in-plane transverse displacement of a generic point of the string and by $y(t)$ the displacement of the NES, the nonlinear equations of motion, up to the cubic order, read (see [19, 26] for the equations of motion of the string, obtained after the classic condensation procedure of the longitudinal displacement and valid under the hypothesis

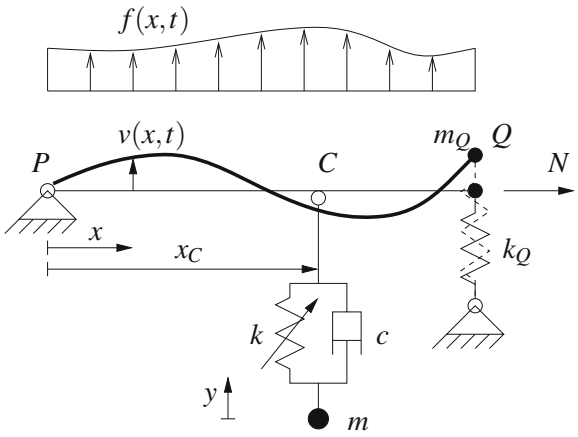

Fig. 13 Internally nonresonant elastic string equipped with a NES

of large ratio between the celerity of longitudinal vs. transverse waves)

$$\begin{aligned}
&\bar{N}v''(x,t) + \frac{EA}{\ell}v''(x,t)\left[\int_0^\ell \frac{v'^2(x,t)}{2}dx\right] - \rho\ddot{v}(x,t) \\
&\quad + p(x)\cos(\Omega t) - \Big[k(v(x,t) - y(t))^3 \\
&\quad + c(\dot{v}(x,t) - \dot{y}(t))\Big]\delta(x - x_C) = 0 \\
&m\ddot{y}(t) - \Big[k(v(x_C,t) - y(t))^3 \\
&\quad + c\,(\dot{v}(x_C,t) - \dot{y}(t))\Big] = 0
\end{aligned} \tag{55}$$

where $\delta(x)$ is the Dirac delta, the dot indicates time-derivative and the prime space-derivative.

The geometric boundary condition at P states that $v(0,t) = 0$, while the mechanical boundary condition, to be applied at Q, reads

$$\begin{aligned}
&\bar{N}v'(\ell,t) + \frac{EA}{\ell}v'(\ell,t)\left[\int_0^\ell \frac{v'^2(x,t)}{2}dx\right] \\
&\quad = -k_Q v(\ell,t) - m_Q\ddot{v}(\ell,t)
\end{aligned} \tag{56}$$

In nondimensional form, the partial differential problem becomes:

$$\begin{aligned}
&\ddot{v} + \zeta\dot{v} - v'' - \eta v''\left[\int_0^1 \frac{v'^2}{2}dx\right] \\
&\quad + \Big[\kappa z^3 + \xi\dot{z}\Big]\delta(x - x_C) = p\cos(\Omega t) \\
&m(\ddot{z} - \ddot{v}_C) + \kappa z^3 + \xi\dot{z} = 0
\end{aligned} \tag{57}$$

and the relevant boundary conditions are:

$$\begin{aligned} v(0,t) &= 0 \\ v'(1,t) + \eta v'(1,t) \left[\int_0^1 \frac{v'^2}{2} dx \right] & \\ = -k_Q v(1,t) - m_Q \ddot{v}(1,t) & \end{aligned} \tag{58}$$

where $v_C(t) := v(x_C, t)$, $\eta = EA/\bar{N}$ and $z(t) := v(x_C, t) - y(t)$, and an external linear damping is introduced through the coefficient ζ.

The application of a Galerkin projection of (57)–(58), using as trial functions the first N eigenfunctions $\varphi_j(x) = \sin(\omega_j x)$ ($j = 1, \ldots, N$) of the homogeneous linearized problem when NES is disengaged (ω_j are the natural frequencies of the string), allows one to obtain a discrete, approximate, version of the equations of motion, which read as (3) and (4). In particular, indicating with $x_j(t)$ the unknown modal amplitudes ($v(x,t) = \sum_{j=1}^{N} x_j(t)\varphi_j(x)$), the relevant matrices and columns read:

$$\begin{aligned} &\mathbf{x} = \{x_h\},\ \mathbf{M} = \{m_{hk}\},\ \mathbf{C} = \{c_{hk}\}, \\ &\mathbf{K} = \{k_{hk}\},\ \mathbf{r} = \{r_h\},\ \mathbf{n} = \{n_h\} \end{aligned} \tag{59}$$

where

$$m_{hk} = \begin{cases} 1 \\ 0 \end{cases}, \ c_{hk} = \begin{cases} 2\xi_h \omega_h \\ 0 \end{cases}, \ k_{hk} = \begin{cases} \omega_h^2 & h = k \\ 0 & h \neq k \end{cases} \tag{60}$$

and

$$\begin{aligned} &\mathbf{r} = \{\varphi_h(x_C)\}, \quad \mathbf{n} = \left\{ n_h x_h \sum_{j=1}^{N} j^2 x_j^2 \right\}, \\ &\mathbf{f}_1 = \{p_h\}, \quad \mathbf{f}_3 = \{0\} \end{aligned} \tag{61}$$

with n_h elastic coefficients, ξ_h modal damping factors and p_h modal forces, $h, k = 1, \ldots, N$.

Actually, the MSHBM was extended in [24] for infinite dimensional systems, i.e. directly working on partial differential equations as (57) with b.c. (58). Being the results in very good agreement with those obtained for a Galerkin projection with large N, here pictures relevant to the direct case of [24] are shown, obtained when $\eta = 2.825$, $m_Q = 0.3167$ and $k_Q = 3.9 \times 10^{-3}$, the external force is assumed as uniform ($p(x) \equiv p$) with frequency $\Omega = \omega_2(1 + \sigma)$ close to the 1:1 resonance with the second mode of the string (here the detuning is directly applied to the forcing frequency and not considered as a modification of the stiffness) and the external damping coefficient of the string is $\zeta = 1.557\%$. The (nondimensional) parameters of the NES are $m = 0.05$, $\kappa = 400$, $\xi = 0.01$. Moreover, the first four

(nondimensional) natural frequencies of the string are $\omega_1 = 1.208$, $\omega_2 = 3.831$, $\omega_3 = 6.722$, $\omega_4 = 9.738$. The NES is supposed to be applied at about the antinode of the resonant mode, i.e. $x_C = 0.4$. In the generating solution, the contribution of the resonant mode is retained only, so that it contains just the term of frequency $\omega = \omega_2$; the harmonic balance is then applied exclusively in correspondence of the frequency ω. The relevant Amplitude Modulation Equations are not shown here for the sake of brevity.

Amplitude of periodic motions of both the string and NES, for force amplitude value $\eta_1 = 0.007$, are shown in Fig. 14 in terms of frequency detuning σ. In particular, in Fig. 14a, the frequency-response curve obtained for disengaged NES (black curve) is superimposed to the corresponding curve obtained when NES is engaged (red line). In Fig. 14b, the amplitude of oscillation b of the NES is shown. Blue points represent Hopf bifurcations. It is evident the beneficial effect of the NES, whose presence reduces the peak of the string amplitude of oscillations a.

In Fig. 15a, b, the WMR (for $\sigma = 0.064$) and SMR (for $\sigma = 0.070$) are superimposed to the invariant manifold, respectively. The first one develops itself close to the fold of the invariant manifold, while the second one describes relaxation oscillations around it.

In Fig. 16, the periodic time-evolutions of the vertical displacement of the midspan of the string ($v_m := v(1/2, t)$)is shown for $\sigma = 0.02$. They are superimposed to the corresponding evolutions (dotted line) obtained by time-integration of the approximated system of ODE, which is drawn after the Galerkin projection of (57), (58) on a basis constituted by the 8 first natural modes of the string. They show a very good agreement.

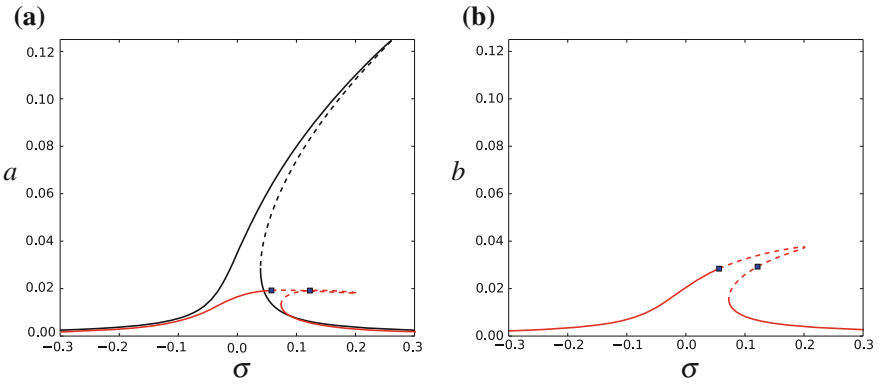

Fig. 14 Frequency-response curves of the string (**a**) and NES (**b**), for $\eta_1 = 0.007$. *Red line* response with NES at the antinode; *black line* response with NES disengaged. *Blue points* indicate Hopf bifurcations. *Continuous line* stable; *dashed line* unstable

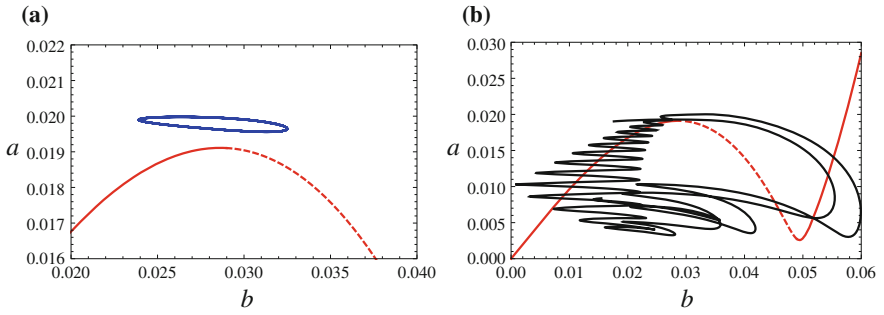

Fig. 15 Weakly modulated response ($\sigma = 0.064$, *blue line* (**a**)) and strongly modulated response ($\sigma = 0.070$, *black line* (**b**)) with NES at the antinode, for $\eta_1 = 0.007$; *red line* invariant manifold. *Continuous line* stable; *dashed line* unstable

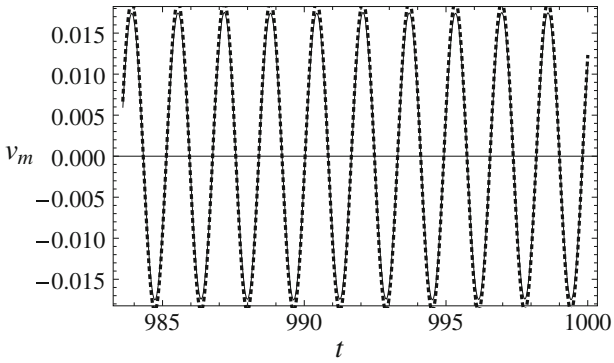

Fig. 16 Periodic time-evolution of the string mid-span, for $p = 0.007$ and $\sigma = 0.02$. *Continuous line* reconstituted functions from MSHBM; *dotted line* reconstituted functions from a discrete Galerkin model

4 Conclusions

In this paper, a general, nonlinear, multi-d.o.f. system, equipped with an essentially nonlinear oscillator with small mass, NES, is considered. Aim of the NES is to passively control the amplitude of vibrations of the primary system, which here is excited by concurrent effect of steady wind, inducing a Hopf bifurcation, and both 1:1 and 1:3 resonant harmonic forces; no internal resonances are allowed. The MSHBM is applied in order to obtain the Amplitude Modulation Equations, which turn out to be singular perturbed equations. Numerical results are shown for different case studies, in order to detect the single effect of the excitations and how the NES modifies the predominant dynamics of the principal system. The outcomes guarantee good agreement with the response as obtained by numerical integrations of the equations

of motion; moreover they assure good reliability of the MSHBM (a) to detect the predominant dynamics of the system and (b) to be used as valid tool for optimization purposes in the choice of the parameters and position of the NES.

Acknowledgments This work was granted by the Italian Ministry of University and Research (MIUR), under the PRIN10-12 program, project No. 2010MBJK5B.

Appendix A: Coefficients of the Equations

The index H indicates the Hermitian (transpose and complex conjugate). The expression of the coefficients of (19) are:

$$
\begin{aligned}
&c_1 = 2i\omega \mathbf{v}^H \mathbf{M}\mathbf{u} + \mathbf{v}^H \mathbf{C}\mathbf{u}, \quad c_2 = -i\omega \mathbf{v}^H \mathbf{C}_1 \mathbf{u} - \mathbf{v}^H \mathbf{K}_\mu \mathbf{u}, \\
&c_3 = -\mathbf{v}^H \mathbf{K}_\sigma \mathbf{u}, \quad c_4 = -i\omega \mathbf{v}^H \mathbf{r}, \quad c_5 = -3\mathbf{v}^H \mathbf{r}, \\
&c_6 = -3\mathbf{v}^H \mathbf{n}(\mathbf{u}, \mathbf{u}, \bar{\mathbf{u}}), \quad c_7 = -3\mathbf{v}^H \mathbf{n}(\mathbf{w}_0, \bar{\mathbf{u}}, \bar{\mathbf{u}}), \\
&c_8 = -6\mathbf{v}^H \mathbf{n}(\mathbf{u}, \mathbf{w}_0, \bar{\mathbf{w}}_0), \quad c_9 = \frac{1}{2}\mathbf{v}^H \mathbf{f}_1
\end{aligned} \tag{62}
$$

In (20) the column matrices $\mathbf{w}_j$ $(j = 1, \ldots, 8)$ are the solutions of the following singular algebraic problems:

$$
\begin{aligned}
\mathbf{w}_1: \quad & (\mathbf{K}_0 + i\omega \mathbf{C}_0 - \omega^2 \mathbf{M})\mathbf{w}_1 = -i\omega \Big(\mathbf{C}_1 \mathbf{u} \\
& - \frac{1}{c_1}(\mathbf{v}^H \mathbf{C}_1 \mathbf{u})(2i\omega \mathbf{M}\mathbf{u} + \mathbf{C}_0 \mathbf{u}) \Big) \\
& - \Big(\mathbf{K}_\mu \mathbf{u} - \frac{1}{c_1}(\mathbf{v}^H \mathbf{K}_\mu \mathbf{u})(2i\omega \mathbf{M}\mathbf{u} + \mathbf{C}_0 \mathbf{u}) \Big)
\end{aligned} \tag{63}
$$

$$
\begin{aligned}
\mathbf{w}_2: \quad & (\mathbf{K}_0 + i\omega \mathbf{C}_0 - \omega^2 \mathbf{M})\mathbf{w}_2 = -\Big(\mathbf{K}_\sigma \mathbf{u} \\
& - \frac{1}{c_1}(\mathbf{v}^H \mathbf{K}_\sigma \mathbf{u})(2i\omega \mathbf{M}\mathbf{u} + \mathbf{C}_0 \mathbf{u}) \Big)
\end{aligned} \tag{64}
$$

$$
\begin{aligned}
\mathbf{w}_3: \quad & (\mathbf{K}_0 + i\omega \mathbf{C}_0 - \omega^2 \mathbf{M})\mathbf{w}_3 = -6\Big(\mathbf{n}(\mathbf{u}, \mathbf{w}_0, \bar{\mathbf{w}}_0) \\
& - \frac{1}{c_1}\mathbf{v}^H \mathbf{n}(\mathbf{u}, \mathbf{w}_0, \bar{\mathbf{w}}_0)(2i\omega \mathbf{M}\mathbf{u} + \mathbf{C}_0 \mathbf{u}) \Big)
\end{aligned} \tag{65}
$$

$$
\begin{aligned}
\mathbf{w}_4: \quad & (\mathbf{K}_0 + i\omega \mathbf{C}_0 - \omega^2 \mathbf{M})\mathbf{w}_4 = -i\omega \Big(\mathbf{r} \\
& - \frac{1}{c_1}\mathbf{v}^H \mathbf{r}(2i\omega \mathbf{M}\mathbf{u} + \mathbf{C}_0 \mathbf{u}) \Big)
\end{aligned} \tag{66}
$$

$$
\begin{aligned}
\mathbf{w}_5: \quad & (\mathbf{K}_0 + i\omega \mathbf{C}_0 - \omega^2 \mathbf{M})\mathbf{w}_5 = -3\Big(\mathbf{r} \\
& - \frac{1}{c_1}\mathbf{v}^H \mathbf{r}(2i\omega \mathbf{M}\mathbf{u} + \mathbf{C}_0 \mathbf{u}) \Big)
\end{aligned} \tag{67}
$$

$$\mathbf{w}_6: \quad (\mathbf{K}_0 + i\omega\mathbf{C}_0 - \omega^2\mathbf{M})\mathbf{w}_6 = -6\Big(\mathbf{n}(\mathbf{u},\mathbf{u},\bar{\mathbf{u}}) - \frac{1}{c_1}\mathbf{v}^H\mathbf{n}(\mathbf{u},\mathbf{u},\bar{\mathbf{u}})(2i\omega\mathbf{M}\mathbf{u} + \mathbf{C}_0\mathbf{u})\Big) \tag{68}$$

$$\mathbf{w}_7: \quad (\mathbf{K}_0 + i\omega\mathbf{C}_0 - \omega^2\mathbf{M})\mathbf{w}_7 = -6\Big(\mathbf{n}(\mathbf{w}_0,\bar{\mathbf{u}},\bar{\mathbf{u}}) - \frac{1}{c_1}\mathbf{v}^H\mathbf{n}(\mathbf{w}_0,\bar{\mathbf{u}},\bar{\mathbf{u}})(2i\omega\mathbf{M}\mathbf{u} + \mathbf{C}_0\mathbf{u})\Big) \tag{69}$$

$$\mathbf{w}_8: \quad (\mathbf{K}_0 + i\omega\mathbf{C}_0 - \omega^2\mathbf{M})\mathbf{w}_8 = -\frac{1}{2}\Big(\mathbf{f}_1 - \frac{1}{c_1}\mathbf{v}^H\mathbf{f}_1(2i\omega\mathbf{M}\mathbf{u} + \mathbf{C}_0\mathbf{u})\Big) \tag{70}$$

The solution is made unique by the normalization condition $\mathbf{w}_j^T\mathbf{u} = 0$.

Moreover $\mathbf{w}_j$ ($j = 9,\ldots,15$) are the solutions of the following non-singular algebraic problems, in which, however, compatibility is satisfied.

$$\mathbf{w}_9: \quad (\mathbf{K}_0 + 3i\omega\mathbf{C}_0 - 9\omega^2\mathbf{M})\mathbf{w}_9 = -3i\mathbf{C}_1\mathbf{w}_0 - \mathbf{K}_\mu\mathbf{w}_0 \tag{71}$$

$$\mathbf{w}_{10}: \quad (\mathbf{K}_0 + 3i\omega\mathbf{C}_0 - 9\omega^2\mathbf{M})\mathbf{w}_{10} = -\mathbf{K}_\sigma\mathbf{w}_0 \tag{72}$$

$$\mathbf{w}_{11}: \quad (\mathbf{K}_0 + 3i\omega\mathbf{C}_0 - 9\omega^2\mathbf{M})\mathbf{w}_{11} = -3i\omega\mathbf{r} \tag{73}$$

$$\mathbf{w}_{12}: \quad (\mathbf{K}_0 + 3i\omega\mathbf{C}_0 - 9\omega^2\mathbf{M})\mathbf{w}_{12} = -\mathbf{r} \tag{74}$$

$$\mathbf{w}_{13}: \quad (\mathbf{K}_0 + 3i\omega\mathbf{C}_0 - 9\omega^2\mathbf{M})\mathbf{w}_{13} = -\mathbf{n}(\mathbf{u},\mathbf{u},\mathbf{u}) \tag{75}$$

$$\mathbf{w}_{14}: \quad (\mathbf{K}_0 + 3i\omega\mathbf{C}_0 - 9\omega^2\mathbf{M})\mathbf{w}_{14} = -6\mathbf{n}(\mathbf{w}_0,\mathbf{u},\bar{\mathbf{u}}) \tag{76}$$

$$\mathbf{w}_{15}: \quad (\mathbf{K}_0 + 3i\omega\mathbf{C}_0 - 9\omega^2\mathbf{M})\mathbf{w}_{15} = -3\mathbf{n}(\mathbf{w}_0,\mathbf{w}_0,\bar{\mathbf{w}}_0) \tag{77}$$

In (45)–(50), the expressions of the right hand side terms are:

$$\begin{aligned}\mathscr{F}_1 &= -\zeta\omega a - \frac{3}{32\omega^3}\eta_3\kappa_c a^2\sin(3\alpha) - \frac{1}{2}\xi b_1\cos(\alpha-\beta_1)\\ &+ \frac{3}{8\omega}\kappa b_1^3\sin(\alpha-\beta_1) + \frac{3}{8\omega}\kappa b_1^2 b_3\sin(\alpha+2\beta_1-\beta_3)\\ &+ \frac{3}{4\omega}\kappa b_1 b_3^2\sin(\alpha-\beta_1)\end{aligned} \tag{78}$$

$$\begin{aligned}\mathscr{F}_2 &= \frac{3}{64\omega^5}\eta_3^2\kappa_c a - \frac{\sigma\omega}{2}a - \frac{3}{32\omega^3}\eta_3\kappa_c a^2\cos(3\alpha) + \frac{3}{8\omega}\kappa_c a^3\\ &+ \frac{1}{2}\xi b_1\sin(\alpha-\beta_1) + \frac{3}{8\omega}\kappa b_1^3\cos(\alpha-\beta_1)\\ &+ \frac{3}{8\omega}\kappa b_1^2 b_3\cos(\alpha+2\beta_1-\beta_3) + \frac{3}{4\omega}\kappa b_1 b_3^2\cos(\alpha-\beta_1)\end{aligned} \tag{79}$$

$$\mathscr{F}_3 = -\frac{1}{2}m\omega^2 a\cos(\alpha-\beta_1) + \frac{1}{2}m\omega^2 b_1$$

$$- \frac{3}{8}\kappa b_1^2 b_3 \cos(3\beta_1 - \beta_3) - \frac{3}{4}\kappa b_1 b_3^2 \tag{80}$$

$$\mathscr{F}_4 = \frac{1}{2}m\omega^2 a \sin(\alpha - \beta_1) + \frac{1}{2}\xi\omega b_1 - \frac{3}{8}\kappa b_1^2 b_3 \sin(3\beta_1 - \beta_3) \tag{81}$$

$$\begin{aligned}\mathscr{F}_5 = {} & \frac{9}{8}\eta_3 m \cos(\beta_3) - \frac{9}{64}\eta_3 m\sigma \cos(\beta_3) + \frac{27}{32}\eta_3 m\zeta \sin(\beta_3) \\ & + \frac{27}{4096\omega^6}\eta_3^3 m\kappa_c \cos(\beta_3) + \frac{27}{128\omega^2}\eta_3 m\kappa_c a^2 \cos(\beta_3) \\ & - \frac{9}{64}\kappa_c m a^3 \cos(3\alpha - \beta_3) - \frac{1}{8}\kappa b_1^3 \cos(3\beta_1 - \beta_3) \\ & - \frac{9}{64}\kappa m b_1^3 \cos(3\beta_1 - \beta_3) + \frac{9}{2}m\omega^2 b_3 \\ & - \frac{3}{4}\Big(1 + \frac{9}{8}\mu_1\Big)\kappa b_1^2 b_3 - \frac{3}{8}\Big(1 + \frac{9}{8}\mu_1\Big)\kappa b_3^3\end{aligned} \tag{82}$$

$$\begin{aligned}\mathscr{F}_6 = {} & \frac{27}{32}\eta_3 m\zeta \cos(\beta_3) - \frac{9}{8}\Big(1 - \frac{1}{8}\sigma\Big)\eta_3 m \sin(\beta_3) \\ & - \frac{27}{4096\omega^6}\eta_3^3 \kappa_c m \sin(\beta_3) - \frac{27}{128\omega^2}\eta_3 \kappa_c m a^2 \sin(\beta_3) \\ & - \frac{9}{64}\kappa_c m a^3 \sin(3\alpha - \beta_3) - \frac{1}{8}\Big(1 + \frac{9}{8}m\Big)\kappa b_1^3 \sin(3\beta_1 - \beta_3) \\ & - \frac{3}{2}\Big(1 + \frac{9}{8}m\Big)\xi\omega b_3\end{aligned} \tag{83}$$

References

1. Vakakis, A.F., Gendelman, O.V., Bergman, L.A., McFarland, D.M., Kerschen, G., Lee, Y.S.: Nonlinear Targeted Energy Transfer in Mechanical and Structural Systems I. Springer, New York (2008)
2. Vakakis, A.F., Gendelman, O.V., Bergman, L.A., McFarland, D.M., Kerschen, G., Lee, Y.S.: Nonlinear Targeted Energy Transfer in Mechanical and Structural Systems II. Springer, New York (2008)
3. Maniadis, P., Kopidakis, G., Aubry, S.: Classical and quantum targeted energy transfer between nonlinear oscillators. Physica D **188**, 153–177 (2004)
4. Kerschen, G., Kowtko, J.J., McFarland, D.M., Bergman, L.A., Vakakis, A.F.: Theoretical and experimental study of multimodal targeted energy transfer in a system of coupled oscillators. Nonlinear Dyn. **47**, 285–309 (2007)
5. Panagopoulos, P.N., Gendelman, O., Vakakis, A.F.: Robustness of nonlinear targeted energy transfer in coupled oscillators to changes of initial conditions. Nonlinear Dyn. **47**, 377–387 (2007)
6. Aubry, S., Kopidakis, G., Morgante, A.M., Tsironis, G.P.: Analytic conditions for targeted energy transfer between nonlinear oscillators or discrete breathers. Physica B: Phys. Conden. Matter **296**, 222–236 (2001)

7. Tsakirtzis, S., Panagopoulos, P.N., Kerschen, G., Gendelman, O., Vakakis, A.F., Bergman, L.A.: Complex dynamics and targeted energy transfer in linear oscillatorscoupled to multi-degree-of-freedom essentially nonlinear attachments. Nonlinear Dyn. **48**, 285–318 (2007)
8. Guckenheimer, J., Wechselberger, M., Young, L.-S.: Chaotic attractors of relaxation oscillators. Nonlinearity **19**, 701–720 (2006)
9. Guckenheimer, J., Hoffman, K., Weckesser, W.: Bifurcations of relaxation oscillations near folded saddles. Int. J. Bifurcat. Chaos **15**, 3411–3421 (2005)
10. Gendelman, O.V., Starosvetsky, Y., Feldman, M.: Attractors of harmonically forced linear oscillator with attached nonlinear energy sink. Part I: description of response regimes. Nonlinear Dyn. **51**, 31–46 (2008)
11. Starosvetsky, Y., Gendelman, O.V.: Response regimes of linear oscillator coupled to nonlinear energy sink with harmonic forcing and frequency detuning. J. Sound Vib. **315**, 746–765 (2008)
12. Vaurigaud, B., Savadkoohi, A.T., Lamarque, C.-H.: Targeted energy transfer with parallel nonlinear energy sinks. Part I: design theory and numerical results. Nonlinear Dyn. **66**(4), 763–780 (2011)
13. Savadkoohi, A.T., Vaurigaud, B., Lamarque, C.-H., Pernot, S.: Targeted energy transfer with parallel nonlinear energy sinks. Part II: theory and experiments. Nonlinear Dyn. **67**(1), 37–46 (2012)
14. Lamarque, C.-H., Gendelman, O.V., Savadkoohi, A.T., Etcheverria, E.: Targeted energy transfer in mechanical systems by means of non-smooth nonlinear energy sink. Acta Mechanica **221**, 175–200 (2011)
15. Gendelman, O.V., Vakakis, A.F., Bergman, L.A., McFarland, D.M.: Asymptotic analysis of passive nonlinear suppression of aeroelastic instabilities of a rigid wing in subsonic flow. SIAM J. Appl. Math. **70**(5), 1655–1677 (2010)
16. Vaurigaud, B., Manevitch, L.I., Lamarque, C.-H.: Passive control of aeroelastic instability in a long span bridge model prone to coupled flutter using targeted energy transfer. J. Sound Vib. **330**, 2580–2595 (2011)
17. Manevitch, L.: The description of localized normal modes in a chain of nonlinear coupled oscillators using complex variables. Nonlinear Dyn. **25**, 95–109 (2001)
18. Gendelman, O.V.: Targeted energy transfer in systems with non-polynomial nonlinearity. J. Sound Vib. **315**, 732–745 (2008)
19. Nayfeh, A.H., Mook, D.T.: Nonlinear Oscillations. Wiley, New York (1979)
20. Jiang, X., McFarland, D.M., Bergman, L.A., Vakakis, A.F.: Steady state passive nonlinear energy pumping in coupled oscillators: theoretical and experimental results. Nonlinear Dyn. **33**, 87–102 (2003)
21. Malatkar, P., Nayfeh, A.H.: Steady-state dynamics of a linear structure weakly coupled to an essentially nonlinear oscillator. Nonlinear Dyn. **47**, 167–179 (2007)
22. Luongo, A., Zulli, D.: Dynamic analysis of externally excited NES-controlled systems via a mixed Multiple Scale/Harmonic Balance algorithm. Nonlinear Dyn. **70**(3), 2049–2061 (2012)
23. Luongo, A., Zulli, D.: Aeroelastic instability analysis of NES-controlled systems via a mixed Multiple Scale/Harmonic Balance Method. J. Vib. Control **20**(13), (2014)
24. Zulli, D., Luongo, A.: Nonlinear energy sink to control vibrations of an internally nonresonant elastic string. Meccanica (2014). doi:10.1007/s11012-014-0057-0
25. Doedel, E.J., Oldeman, B.E.: AUTO-07P: Continuation and Bifurcation Software for Ordinary Differential Equation (2012). http://cmvl.cs.concordia.ca/auto/
26. Nayfeh, S.A., Nayfeh, A.H., Mook, D.T.: Nonlinear response of a taut string to longitudinal and transverse end excitation. J. Vib. Control **1**(3), 307–334 (1995)

Hysteretic Beam Model for Steel Wire Ropes Hysteresis Identification

Biagio Carboni, Carlo Mancini and Walter Lacarbonara

Abstract A nonlinear hysteretic beam model based on a geometrically exact planar beam theory combined with a continuum extension of the Bouc-Wen model of hysteresis is proposed to describe the memory-dependent dissipative response of short wire ropes which have the unique feature of exhibiting hysteretic energy dissipation due to the interwire friction. With the proposed model, hysteresis is introduced in the constitutive equation between the bending moment and the curvature within the special Cosserat theory of shearable beams. The model is indeed capable of describing the hysteretic behavior exhibited by short steel wire ropes subject to flexural cycles. The model parameters which best fit a series of experimental measurements for selected wire ropes are identified employing the Particle Swarm Optimization method. The identified parameters are used to reproduce other experimental tests on the same wire ropes obtaining a good accuracy.

1 Introduction

Wire ropes are structural elements usually employed to resist large axial loads while providing high strength, durability and reliability. In these applications the ropes length is much larger than the diameter usually resulting in a negligible bending stiffness along the cable length except in regions near the boundaries or point loads where boundary layers are produced. On the contrary, when the wire ropes are relatively short (i.e., the ratio between length and diameter is comparable to that characteristic for beams) and subject to cyclic loadings, the bending stiffness cannot be neglected and the force-displacement response shows hysteresis loops due to the

B. Carboni · C. Mancini · W. Lacarbonara (✉)
Department of Structural and Geotechnical Engineering, Sapienza University of Rome,
Via Eudossiana 18, 00184 Rome, Italy
e-mail: walter.lacarbonara@uniroma1.it

B. Carboni
e-mail: biagio.carboni@uniroma1.it

C. Mancini
e-mail: mancinicarlo@libero.it

M. Belhaq (ed.), *Structural Nonlinear Dynamics and Diagnosis*,
Springer Proceedings in Physics 168, DOI 10.1007/978-3-319-19851-4_13

relative sliding between the wires. The idea of exploiting the bending behavior of short wire ropes to absorb and dissipate energy was proposed for the first time by Stockbridge in the last century [36]. More recently, several applications based on the interwire friction exhibited by short wire ropes have been explored [6, 11, 17, 18, 37, 43]. Within this context, Carboni et al. proposed a new rheological device capable of providing several types of hysteretic responses employing assemblies of wire ropes made of steel and shape memory alloy materials [5].

Challenging issues are inherent in the mathematical modeling and prediction of the complicated mechanical behavior of wire ropes. Costello [9] proposed a theory in which the individual wires are modeled using Loves equations for bending and twisting of thin helical rods [26]. However, this model does not describe the frictional effects. A direct approach based on the finite element method (FEM) consists in constructing solid models which, upon reflecting the actual helical wire rope geometry, are treated as a deformable continuum with frictional contacts [27, 30, 44]. The high computational burden due to the complexity associated with handling the evolving contact regions between the wires does not allow to use three-dimensional FEM models for predicting the wire rope hysteretic behavior. Analytical [20, 21] or semi-analytical methods based on one-dimensional polar continuum formulations supplemented by rheological models for the constitutive laws are more suitable for describing the hysteresis exhibited by wire ropes. Sauter and Hagedorn [32] extended the Masing model for a continuous system to model the short cables of a Stockbridge damper. Rafik and Gerges [16] developed a model based on a curved beam to describe wire rope springs deforming in tension-compression cycles.

A phenomenological model often used to describe the mechanical behavior of hysteretic systems is the Bouc-Wen (BW) model [3, 45]. It has been used in a wide variety of studies for modeling discrete hysteretic restoring forces or stresses. Several extended versions of the BW model have been proposed to take into account stiffness and strength degradation or pinching behavior [1, 2, 5]. Recently, the BW model has been generalized to continuous systems for describing materially nonlinear problems such as elastoplastic structures. Sivaselvan and Reinhorn [35], starting from the original model proposed by Bouc [3], developed a smooth hysteretic method based on the viscoplasticity theory in the context of the flexibility approach to simulate inelastic frame structures according to a state space formulation [34]. A three-dimensional BW-type model obtained by smoothening a three-dimensional yield surface was proposed by Casciati [7]. Triantafyllou and Koumousis [39] introduced an elastoplastic hysteretic constitutive relationship derived by the BW model in the classical Euler-Bernoulli beam formulation to conduct small and large displacement dynamic analysis of frame structures. The same authors [38, 40] extended the plastic formulation based on the BW model to plane stress elements.

Another important task in the design of applications that rely on hysteretic behaviors is represented by the identification of the model parameters on the basis of experimental measurements. Identification strategies can be classified according to several

criteria. A useful distinction is between parametric and non parametric methods. An example of a non parametric method is the restoring force method initially developed by Masri and Caughey [28] and by Donnell and Crawley [10]. This method deals with the identification of nonlinear dynamical systems for which accelerations, velocities and displacements are directly measured or obtained via integration/differentiation. Extensive studies were carried out to devise suitable techniques for data processing [46] and suitable excitation signals selection [47].

More recently there has been an extensive use of heuristic methods belonging to the family of genetic algorithms for global optimization problems. The Particle Swarm Optimization (PSO) is a gradient-free method proposed by Kennedy and Eberhart [22]. The main advantages are (i) the applicability to a single type of data without requiring differentiation or integration, (ii) the robustness against instrumental noise, and (iii) the property of converging to the global minimum of an objective function without restrictions. On the other hand, the main disadvantage consists in the lack of well-posed proofs of convergence. The PSO algorithm has been used for a wide number of applications such as topology and shape optimization [14, 15], truss and frame structures optimization [12, 19, 33], aircraft wings optimization [41]. Several variants of the original PSO algorithm have been proposed mainly targeted to the identification or optimization of nonlinear hysteretic and chaotic systems [23, 25, 48]. Charalampakis and Dimou [8] employed two variants of the PSO algorithm to calibrate the BW model parameters which best fitted the hysteretic force-displacement curves of a steel welded-bolted joint. Quaranta et al. [31] compared different PSO versions for identifying the parameters of the van der Pol-Duffing oscillators.

In this paper, a continuum hysteretic beam formulation based on the BW model of hysteresis is proposed to describe the hysteretic behavior of steel wire ropes subject to flexural cycles (see Fig. 1). The considered theory is the Special Cosserat theory of shear deformable planar beams undergoing finite displacements and rotations. A BW-type hysteretic relationship is established between the bending moment and the associated curvature. Experimental quasistatic tests are performed on assemblies of steel wire ropes, clamped at both ends, fixing one end and prescribing to the other end a cyclic displacement in the direction orthogonal to the ropes length. The restoring forces developed by the wire ropes are measured for several displacement amplitudes. The wire ropes undergo a deflection with opposite curvatures having the nodal point at the midspan. The parameters which best fit the experimentally obtained force-displacement curves are identified by means of the PSO algorithm. The proposed model represents a step forward from phenomenological towards mechanical modeling. The equivalent beam model presents the actual geometric features (length and circular cross section) and boundary conditions of the wire rope while the BW-type moment-curvature constitutive law is adopted for modeling the memory effects due to the interwire friction. Hysteresis is introduced in the bending moment according

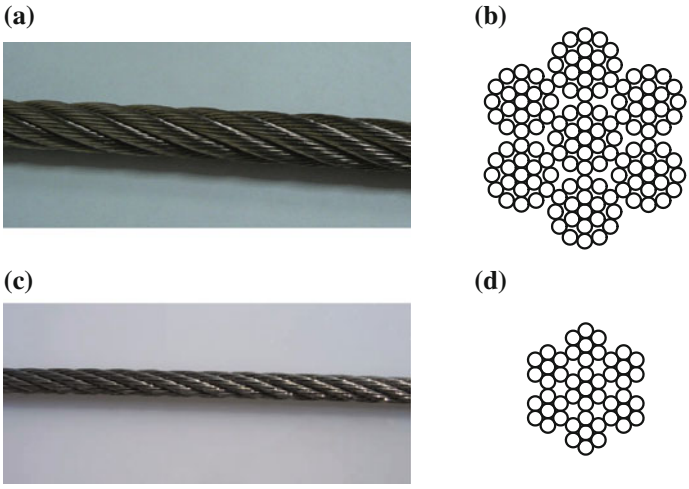

Fig. 1 The investigated wire ropes: **a** 7 × 19 and **c** 7 × 7 and their cross sections (**b**) and (**d**), respectively

to the assumption that this loading state causes most of the relative sliding of the wires. For more general loading states, hysteresis can be also associated to the axial force by defining a suitable interaction law with the hysteretic bending moment.

2 The Bouc-Wen Model of Hysteresis

The restoring force f of the BW model enhanced with a cubic term is the summation of the elastic force $k_e x + k_3 x^3$ and hysteretic force z, respectively, in which x denotes the displacement, k_e indicates the elastic stiffness and k_3 is the coefficient of the cubic restoring term. The hysteretic force evolution is described by the first-order differential equation

$$\dot{z} = [k_d - (\gamma + \beta \operatorname{sgn}(z\dot{x}))\,|z|^n]\dot{x} \tag{1}$$

where k_d, γ, β and n together with k_e and k_3 are the constitutive parameters of the model and the overdot indicates differentiation with respect to time t. The tangent stiffness of the hysteretic force denoted by z_x is obtained by multiplying the left- and right-hand sides of (1) by dt, and dividing the resulting equation by dx thus giving

$$z_x = k_d - (\gamma + \beta \operatorname{sgn}(z\dot{x}))\,|z|^n\,. \tag{2}$$

The hysteretic tangent stiffness at the origin is k_d, while the tangent stiffness of the overall restoring force f is $k_e + k_d$. Along the loading and unloading branches, the

hysteretic force z reaches upper and lower bounds equal to $\pm[k_d/(\gamma+\beta)]^{\frac{1}{n}}$ when the displacement is such that $z_x = 0$. Thus, if the cubic restoring term is set to zero, the tangent stiffness of the restoring force becomes k_e which thus represents the post-elastic stiffness. These considerations are valid only when $\gamma + \beta > 0$ for which the model exhibits a softening behavior. Moreover, these model properties can guide the initial choice of the parameters design space.

The nondimensional form of the restoring force and the evolution equation of the hysteretic component read

$$\tilde{f} = \delta\tilde{x} + (1-\delta)\tilde{z} + \tilde{k}_3\tilde{x}^3, \tag{3}$$

$$\dot{\tilde{z}} = [1 - (\tilde{\gamma} + \tilde{\beta}\,\mathrm{sgn}(\tilde{z}\dot{\tilde{x}}))\,|\tilde{z}|^n]\dot{\tilde{x}}, \tag{4}$$

respectively, where the overdot denotes differentiation with respect to nondimensional time $\tilde{t}$ and the following nondimensional variables and parameters are introduced:

$$\tilde{x} = \frac{x}{x_0}, \qquad \tilde{t} = \omega t, \qquad \tilde{z} = \frac{z}{z_0}, \qquad \delta = \frac{k_e}{k_e + k_d}, \qquad \tilde{k}_3 = \frac{k_3 x_0^2}{k_e + k_d}. \tag{5}$$

In (5), x_0 indicates a characteristic displacement, $z_0 = k_d x_0$, $\omega = \sqrt{N_0/(x_0 m)}$ with $N_0 = (k_e + k_d)x_0$ and m denoting a characteristic mass. The other dimensionless parameters are $(\tilde{\gamma}, \tilde{\beta}) = (\gamma, \beta)x_0 z_0^{n-1}$.

3 The Hysteretic Beam Model

The formulation of the shearable nonlinear beam follows [24]. Let us consider a fixed reference frame $(O, \boldsymbol{e}_1, \boldsymbol{e}_2, \boldsymbol{e}_3)$ and a straight reference configuration for the beam centerline described by the vector $\boldsymbol{r}^o(s) = s\boldsymbol{e}_1$ where $s \in [0, l]$ is the arclength parameter and l denotes the initial beam length. The orientation of the beam cross section in the reference configuration is described by the intrinsic frame $(\boldsymbol{b}_1^o, \boldsymbol{b}_2^o, \boldsymbol{b}_3^o)$ of which $\boldsymbol{b}_1^o$ and $(\boldsymbol{b}_2^o, \boldsymbol{b}_3^o)$ are collinear with $\boldsymbol{e}_1$ and the principal axes of inertia of the cross section, respectively. The reference position of the material points of the beam is defined by the position vector $\boldsymbol{p}^o(s) = \boldsymbol{r}^o(s) + x_2(s)\boldsymbol{b}_2^o + x_3(s)\boldsymbol{b}_3^o$. The cross sections are assumed to be locally rigid implying the preservation of planarity. We consider only planar motions for the beam centerline which can be described by the displacement vector $\boldsymbol{u}(s,t) = u(s,t)\boldsymbol{e}_1 + v(s,t)\boldsymbol{e}_2$ while we let the rotation of the cross sections about $\boldsymbol{e}_3$ be described by $\theta(s,t)$. The actual configuration of the

centerline is given by the position vector $\boldsymbol{r}(s,t) = \boldsymbol{r}^o(s,t) + \boldsymbol{u}(s,t)$ while the actual orientation of the cross sections is described by the triad $(\boldsymbol{b}_1, \boldsymbol{b}_2, \boldsymbol{b}_3)$. The unit vector $\boldsymbol{b}_1$ makes the angle $\theta(s,t)$ with $\boldsymbol{b}_1^o = \boldsymbol{e}_1$. The position vector of a material point in the actual beam configuration is described by $\boldsymbol{p}(s,t) = \boldsymbol{r}(s,t) + x_2(s)\boldsymbol{b}_2 + x_3(s)\boldsymbol{b}_3$ where $\boldsymbol{b}_1 = \cos\theta\boldsymbol{e}_1 + \sin\theta\boldsymbol{e}_2, \boldsymbol{b}_2 = -\sin\theta\boldsymbol{e}_1 + \cos\theta\boldsymbol{e}_2$, and $\boldsymbol{b}_3 = \boldsymbol{e}_3$. The kinematic unknowns are $(u(s,t),\ v(s,t),\ \theta(s,t))$. Denoting by ∂_s differentiation with respect to s, the stretch vector is defined as $\boldsymbol{\nu} := \partial_s \boldsymbol{r}$ and expressed as

$$\boldsymbol{\nu}(s,t) = \nu(s,t)\boldsymbol{b}_1(s,t) + \eta(s,t)\boldsymbol{b}_2(s,t) \tag{6}$$

where ν and η represent the beam stretch and shear strain, respectively. The third generalized strain is the bending curvature μ given by

$$\mu(s,t) = \partial_s\theta. \tag{7}$$

The stretch and the shear strain can be expressed in terms of the displacement gradient and the flexural rotation angle as

$$\nu(s,t) = (1+\partial_s u)\cos\theta + \partial_s v \sin\theta, \qquad \eta(s,t) = -(1+\partial_s u)\sin\theta + \partial_s v\cos\theta. \tag{8}$$

The generalized strains (ν, η, μ) are related through the constitutive relationships to the generalized stress resultants and moment resultant, also referred to as contact forces and contact couple. The contact force vector is $\boldsymbol{n} = N(s,t)\boldsymbol{b}_1(s,t) + Q(s,t)\boldsymbol{b}_2(s,t)$ while the bending moment is $M(s,t)$. The linear constitutive equations for an elastic isotropic beam read

$$N(s,t) = EA(\nu(s,t) - 1), \qquad Q(s,t) = GA^*\eta(s,t), \qquad M(s,t) = EJ\mu(s,t), \tag{9}$$

where E and G represent Young's modulus and the shear modulus, respectively; A is the area of the cross section, A^* is the shear area and J is the area moment of inertia about the principal axis $\boldsymbol{b}_3$.

The equations of motion read

$$\rho A\partial_{tt}\boldsymbol{u} = (\partial_s N - \mu Q)\cos\theta - (\partial_s Q + \mu N)\sin\theta + f_1, \tag{10}$$

$$\rho A\partial_{tt} v = (\partial_s N - \mu Q)\sin\theta + (\partial_s Q + \mu N)\cos\theta + f_2, \tag{11}$$

$$\rho J\partial_{tt}\theta = \partial_s M + \nu Q - \eta N + c, \tag{12}$$

where ρ is the mass density, f_1, f_2, and c indicate the forces and the couple per unit reference length, respectively. Equations (10)–(12) are obtained from the balance of linear and angular momentum in the fixed reference frame. They are supplemented by general boundary and initial conditions expressed as

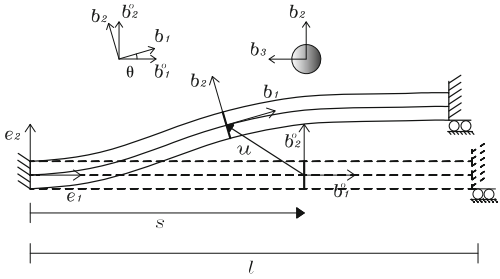

Fig. 2 The planar beam in the reference (*dashed lines*) and actual configurations (*solid lines*)

$$\boldsymbol{u}(0,t) = \overline{\boldsymbol{u}}(t), \quad \theta(0,t) = \overline{\theta}(t), \qquad \boldsymbol{u}(l,t) = \widehat{\boldsymbol{u}}(t), \quad \theta(l,t) = \widehat{\theta}(t) \qquad t \in [0,T], \tag{13}$$

$$\boldsymbol{u}(s,0) = \breve{\boldsymbol{u}}(s), \quad \theta(s,0) = \breve{\theta}(s) \qquad s \in [0,l], \tag{14}$$

where $[0, T]$ denotes the time integration domain. Figure 2 shows the beam in the reference configuration that undergoes a planar motion to the actual configuration.

In the present model, hysteresis is introduced in the constitutive equation $(9)_3$ between the bending moment and the flexural curvature. The hysteretic constitutive equation reads

$$M(s,t) = EJ_e\mu + M_h + k_3\mu^3 \tag{15}$$

where k_3 represents the coefficient of the cubic elastic bending moment, M_h is the hysteretic bending moment whose evolution is governed by the first-order differential equation

$$\partial_t M_h = \left\{EJ_h - \left[\gamma + \beta\,\mathrm{sgn}(M_h\partial_t\mu)\right]|M_h|^n\right\}\partial_t\mu \tag{16}$$

with ∂_t denoting differentiation with respect to time t. The parameters (γ, β, n) are the same as those defined in (1). The tangent stiffness of the bending moment at the origin $\mu = 0$ is $EJ_t = EJ_e + EJ_h$ while the post-elastic bending stiffness is EJ_e, attained when $\partial_t M_h = 0$, $M_h = \pm[EJ_h/(\gamma+\beta)]^{\frac{1}{n}}$ and $k_3 = 0$.

The main objective of the hysteretic beam model is to describe the experimentally obtained hysteretic responses of steel wire ropes subject to bending cycles. The nonlinear beam model can reproduce the actual geometry (length and cross section) of the wire rope, boundary and loading conditions during the tests. The hysteretic bending moment, introduced in the constitutive equation, has the designated function of describing the hysteretic behavior due to the interwire friction within the rope. The beam cross section is assumed as the circular envelope of the actual cross section of the wire rope. However, to take into account the fact that the cross section of a wire rope is not compact but is constituted by an assembly of individual wires, an additional parameter $\psi \in (0, 1]$ is introduced to reduce the bending stiffness EJ of

the compact circular cross section bounding the actual rope cross section. By letting the new parameter $\delta \in (0, 1)$ denote the post-elastic-to-elastic bending stiffness (in the limit $n = \infty$), we set

$$EJ_t = \psi EJ, \qquad \frac{EJ_e}{EJ_t} = \delta, \qquad \frac{EJ_h}{EJ_t} = 1 - \delta. \tag{17}$$

The parts of the bending stiffness indicated by EJ_e and EJ_h, respectively, can be written as

$$EJ_e = \delta EJ_t = \delta\psi EJ, \qquad EJ_h = (1 - \delta)EJ_t = (1 - \delta)\psi EJ. \tag{18}$$

The beam length, Young's modulus, cross section (zeroth and second area moments), boundary and loading conditions are assumed on the basis of the actual wire ropes geometrical and mechanical features. The hysteresis parameters (γ, β, n) and the stiffness parameters (ψ, δ) are calibrated to best fit the experimental measurements. This model has the purpose of describing, among other goals, the applications exploiting the frictional dissipation of wire ropes [4, 5]. The hysteretic features of the response of a given wire rope type under bending can be evaluated carrying out an experimental campaign whose results are used for identifying the parameters of the proposed model. The advantage is that the identified model of a given wire rope can be used during the design process of the specific application which makes use of wire ropes thus drastically reducing the number of experimental tests required and the overall design costs.

Equations (10)–(12) can be rendered nondimensional introducing the following nondimensional variables and parameters [24]: $\tilde{s} = s/l$, $\tilde{t} = \omega_c t$, $\tilde{u} = u/l$, $\tilde{v} = v/l$, $\omega_c = [EJ/(\rho A l^4)]^{1/2}$, $k_a = EAl^2/(EJ)$, $k_s = GA^* l^2/(EJ)$, $\tilde{k}_3 = k_3/(EJ)$, $(\tilde{f}_1, \tilde{f}_2) = (f_1, f_2)l^3/(EJ)$, $\tilde{c} = cl^2/(EJ)$. The nondimensional hysteretic moment is given by

$$\tilde{M}_h = M_h l/EJ \tag{19}$$

whose evolution is described by the following nondimensional equation:

$$\partial_{\tilde{t}}\tilde{M}_h = \left\{(1 - \delta)\psi - \left[\tilde{\gamma} + \tilde{\beta}\,\mathrm{sgn}(M_h \partial_{\tilde{t}}\mu)\right]\left|\tilde{M}_h\right|^n\right\}\partial_{\tilde{t}}\mu \tag{20}$$

where

$$\tilde{\gamma} = \gamma(EJ)^{n-1}/l^n, \qquad \tilde{\beta} = \beta(EJ)^{n-1}/l^n. \tag{21}$$

The nondimensional equations of motion read

$$\partial_{\tilde{t}\tilde{t}}\tilde{u} = [k_a\partial_{\tilde{s}}\nu - k_s\eta\partial_{\tilde{s}}\theta]\cos\theta - [k_s\partial_{\tilde{s}}\eta + k_a(\nu - 1)\partial_{\tilde{s}}\theta]\sin\theta + \tilde{f}_1, \tag{22}$$

$$\partial_{\tilde{t}\tilde{t}}\tilde{v} = [k_a\partial_{\tilde{s}}\nu - k_s\eta\partial_{\tilde{s}}\theta]\sin\theta + [k_s\partial_{\tilde{s}}\eta + k_a(\nu - 1)\partial_{\tilde{s}}\theta]\cos\theta + \tilde{f}_2, \tag{23}$$

$$\partial_{\tilde{t}\tilde{t}}\theta/k_a = (\psi\delta + \tilde{k}_3)\partial_{\tilde{s}\tilde{s}}\theta + \partial_{\tilde{s}}\tilde{M}_h + k_s\nu\eta - k_a(\nu - 1)\eta + \tilde{c} \tag{24}$$

where the assumption that the beam has a uniform cross section along the overall span has been adopted. These equations are supplemented by boundary and initial conditions expressed by (13) and (14). The solution can be obtained via a finite element discretization [24]. The solution at each step is obtained employing a Newton-Raphson iterative scheme.

4 Experimental Bending Tests for Steel Wire Ropes

The complex geometry of the contact areas between the wires of spiral and stranded wire ropes makes the experimental tests necessary for quantifying the dissipation capacity. An experimental campaign was carried out to evaluate the hysteresis cycles of two stranded steel wire ropes subject to bending cycles. The investigated wire ropes have a diameter equal to 10 and 6 mm and are constituted by 7 strands of 19 steel wires and 7 strands of 7 steel wires of diameter equal to 0.65 mm, respectively. Figure 1 shows the wire ropes and their cross sections. The tests were performed employing the Material Testing System (MTS) in the DISG laboratory at Sapienza University of Rome (Italy). Two groups of four parallel 7×19 and 7×7 wire ropes were tested with the experimental setup illustrated in Fig. 3. The wire ropes ends are clamped at the two thick steel bars denoted by B_1 and B_2, the former being connected to the piston P of the MTS machine. Bar B_2 is passed through by two smooth rods (denoted by S_1 and S_2) and one threaded cylindrical rod (denoted by t). The threaded bar does not touch the bar B_2 while between the smooth rods s_1 and s_2 and B_2 two self-lubricated clinched joints are placed to allow a relative frictionless sliding. The rods t, s_1 and s_2 are welded to a third steel bar denoted by B_3 that is, in turn, fixed to a load cell.

A sinusoidal displacement with a relatively low frequency equal to 0.1 Hz is applied to B_1 along the direction orthogonal to the wire ropes whose restoring force is measured by the load cell (see Fig. 3). The wire ropes are subject to pure bending thanks to the free sliding of bar B_2 on rods s_1 and s_2. The two bolts (denoted by b_1 and b_2) on the threaded bar t can be used both for mounting the system and realizing another testing setup in which the sliding of B_2 is prevented. In the latter case, tensile loads arise in the ropes and the measured force-displacement curves exhibit a strong hardening behavior. In this paper only pure bending tests are presented.

Figure 4 shows the experimental setup with the undeformed and some deformed configurations of the specimen. The wire ropes present a deflected shape characterized by a change of curvature through the midspan. Table 1 lists the experimental tests for the 7×19 and 7×7 wire ropes. For each wire rope length and displacement amplitude, 15 hysteresis cycles were measured to obtain a stabilized loop.

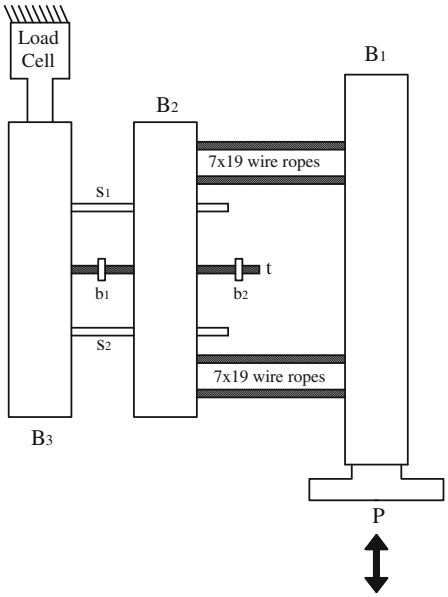

Fig. 3 Experimental setup with the tested wire ropes and their fixtures. The *arrow* indicates the cyclic displacement provided by the MTS testing machine

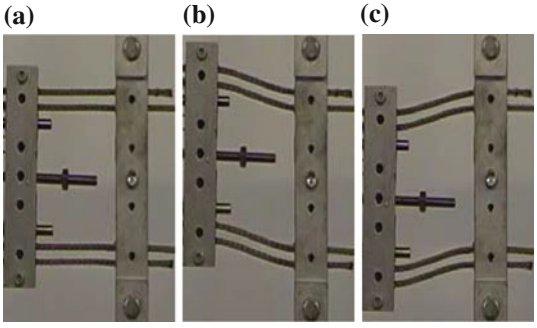

Fig. 4 The experimental setup showing the wire ropes in the undeformed (**a**) and deformed (**b**), (**c**) configurations

Table 1 List of the performed experimental tests in which the wire rope section, the wire rope length and the prescribed displacement are indicated

Wire rope cross section	Length (mm)	Displacement amplitude (mm)			
7 × 19	75	5	10	15	20
7 × 19	85	5	10	15	20
7 × 19	90	5	10	15	–
7 × 7	100	5	10	15	20

5 Particle Swarm Optimization Algorithm

Particle Swarm Optimization (PSO) is a heuristic global optimization method based on the swarm intelligence theory and inspired from the social interactions in bird flocks, schools of fish or swarms of insects. The algorithm starts from an initial population (the particles) formed by several sets of parameters to optimize with respect to an objective function (OF). Each particle is modified iteratively by a velocity vector that is function of the best particle within the population and the best values assumed by the particle itself until the considered iteration.

Here, we seek to identify the model parameters of the hysteretic beam which best fit the experimentally obtained restoring forces as function of the prescribed displacements. The measured restoring force is denoted by $f(y)$ while the model-based restoring force is indicated by $\hat{f}(y)$. The mean square error (MSE) between measured and model-based restoring forces is assumed as objective function to minimize and expressed as

$$OF(\boldsymbol{x}) = \frac{\sum_{k=1}^{N} [f(y_k) - \hat{f}(y_k|\boldsymbol{x})]^2}{N\sigma_f^2} \tag{25}$$

where σ_f^2 and N are the variance and the number of samples of the experimentally obtained restoring force, respectively, $\boldsymbol{x}$ denotes the parameters vector of the model, and y indicates the displacement. Considering the particles $\boldsymbol{x}_i$ $(i = 1, 2, .., p)$ and the lower and upper bounds $\boldsymbol{x}_{LB}$ and $\boldsymbol{x}_{UB}$ for the particle values, respectively, the initial population is a matrix formed by p vectors whose values are drawn by a Gaussian distribution on their ranges of variation. The particles are updated at the jth iteration according to the following expression:

$$\boldsymbol{x}_{i,j+1}^k = \boldsymbol{x}_{i,j} + \boldsymbol{v}_{i,j+1}^k \qquad i = 1, 2, .., p, \quad j = 1, 2, .., q \tag{26}$$

where time is assumed to be equal to unity and q is the number of iterations. The velocity is

$$\boldsymbol{v}_{i,j+1} = w\boldsymbol{v}_{i,j} + c_1\boldsymbol{r}_1 \circ (\boldsymbol{p}_{i,j} - \boldsymbol{x}_{i,j}) + c_2\boldsymbol{r}_2 \circ (\boldsymbol{p}_j - \boldsymbol{x}_{i,j}) \tag{27}$$

where w is the inertia factor; c_1, c_2 are the cognitive and social parameters, respectively. These parameters in the simple PSO algorithm are constant and can be set to $w = 0.8$, $c_1 = 2.8$, and $c_2 = 1.3$. A study about the effect of the values assigned at the inertia factor and cognitive and social parameters can be found in [13]. The vector $\boldsymbol{p}_{i,j}$ represents the ith best ever particle at the jth iteration with respect to the criterion expressed by (25). The vector $\boldsymbol{p}_j$ denotes the best ever particle at the jth iteration between all vectors of the population. The notation $\circ$ indicates element-by-element multiplication and the vectors $\boldsymbol{r}_1$ and $\boldsymbol{r}_2$ are formed by random variables

with uniform distributions in the interval [0, 1]. When a particle element exceeds the assigned range of variation, its value is reset to the value belonging to the closest boundary. The number of iterations q is chosen by the user according to the values achieved by MSE that must be lower than a given tolerance for which the identification is considered acceptable.

6 Identification Results

The experimentally obtained force-displacement hysteresis cycles are identified using the proposed hysteretic beam model. The measured restoring forces are divided by the number of wire ropes according to the fact that they work in parallel and equally contribute to the total restoring force. The tests with the 7×19 wire rope of length equal to 75 mm are identified with an individual parameters set for each displacement amplitude. The set of model parameters, obtained by averaging the thus obtained values, is used to compute the hysteresis cycles for the other wire ropes lengths and compared with the experimental measurements. The test with the 7×7 wire rope for a displacement amplitude equal to 15 mm is identified with a parameters set that is later employed to compute the hysteresis cycles for different displacement amplitudes. Thus, the model-based cycles are compared with the experimentally obtained curves.

The same geometric features and boundary conditions of the wire ropes are assigned to the hysteretic beam. In particular, the beam length and the diameter of the circular cross section are assumed equal to those of the wire ropes. The beam ends are both clamped. The Young modulus and Poisson coefficient are assumed equal to 206 GPa and 0.3, respectively, while the parameters $(\psi, \delta, \gamma, \beta, n, k_3)$ to identify are assigned ranges of variation according to the PSO algorithm. One end of the beam (i.e., that at $s = l$) is subject to the displacement $x = A \sin \omega t$ along $\boldsymbol{e}_2$ (see Fig. 2) where A is the amplitude (equal, in turn, to that of the experimental tests), $\omega = 0.628$ rad/s is the circular frequency, and $t \in (0, T)$ is the time. The generalized force $f(s,t) = N(s,t) \sin\theta(s,t) + Q(s,t) \cos\theta(s,t)$ along $\boldsymbol{e}_2$ at $s = 0$, which coincides with the shear force $Q(0,t)$ (since the clamp implies $\theta(0,t) = 0$), is the restoring force. Therefore, $(x(t),\ f(0,t),\ t \in (t_1, t_2))$ represent the displacement and force to compare with the experimental measurements, t_1 and t_2 are the time instants delimiting a stabilized hysteresis cycle. Time t can be seen as a parameter because the frequency ω is assumed so low that the inertia forces and rotary inertia become negligible. The boundary and initial conditions for the beam can be summarized as follows

$$\boldsymbol{u}(0,t) = \theta(0,t) = 0, \qquad v(l,t) = x(t), \quad \theta(l,t) = 0, \qquad t \in [0,T] \tag{28}$$

$$\boldsymbol{u}(s,0) = \theta(s,0) = 0, \qquad s \in [0,l]. \tag{29}$$

Note that the horizontal displacement $u(t)$ at $s = l$ is not restricted.

The identification task is performed employing concurrently the finite element solver COMSOL Multiphysics [29] and Matlab [42]. The computational architecture is managed by Matlab to which the input data are fed. COMSOL Multiphysics is used for the computation of the hysteretic beam response across the beam span. At each iteration of the PSO algorithm, the beam model parameters, evaluated by Matlab, are given as input to COMSOL that performs the finite element discretization and solves the problem. The vectors $(\boldsymbol{x}, \boldsymbol{f})$ are fed back to Matlab for computing the OF (i.e., MSE) and performing the identification. The number of particles p and iterations q are set to 10 and 75, respectively. Table 2 shows the assigned ranges of variation for the parameters to identify. The coefficient of the cubic term k_3 is set to zero a priori and is not reported in the following results. These initial input data are evaluated by means of some preliminary calculations.

Table 3 summarizes the optimal parameter sets selected by the PSO algorithm for the 7×19 wire rope whose length is 75 mm while in Fig. 5 the comparisons between the model-based and the experimentally obtained hysteresis cycles are shown. The identification is accurately performed and the parameters which exhibit the lowest variation with the displacement amplitude are ψ and δ regulating the elastic and hysteretic stiffnesses. This suggests that the hysteretic beam model is suitable for reproducing the hysteretic wire ropes response. For the displacement amplitude of 20 mm (Fig. 5d), both the experimentally obtained and model-based restoring forces show a slight hardening. This is more pronounced for the model-based curves and is due to the geometric effect of the bending curvature that takes finite values. Figure 6 shows a cycle of (a) the total and (b) the hysteretic bending moments as function of the curvature at $s = 0$ for the beam length equal to 75 mm and the prescribed end

Table 2 Ranges of variation for the parameters to identify

	ψ (–)	δ (–)	γ ($\mathrm{N}^{1-n}\mathrm{m}^{2-n}$)	β ($\mathrm{N}^{1-n}\mathrm{m}^{2-n}$)	n (–)
Min	0.008	0.1	0.8	0.8	1.0
Max	0.025	0.6	2	2	1.3

Table 3 Identified parameters and associated MSEs for the 7×19 wire rope of length equal to 75 mm

A (mm)	ψ (–)	δ (–)	γ ($\mathrm{N}^{1-n}\mathrm{m}^{2-n}$)	β ($\mathrm{N}^{1-n}\mathrm{m}^{2-n}$)	n (–)	MSE (%)
5	0.0159	0.251	1.478	1.729	1.275	0.43
10	0.0162	0.240	1.391	1.103	1.152	0.44
15	0.0166	0.21	1.218	1.151	1.165	0.40
20	0.0168	0.186	1.684	1.989	1.285	0.50

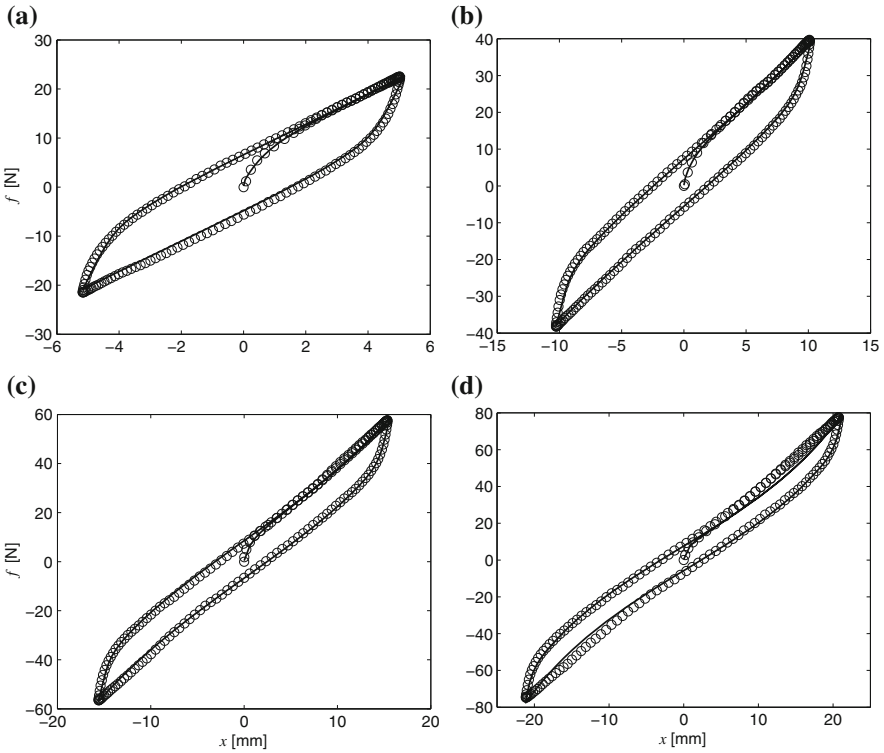

Fig. 5 Comparison between the experimentally obtained (*circles*) and model-based (*solid lines*) hysteresis cycles for displacement amplitudes equal to 5 mm (**a**), 10 mm (**b**), 15 mm (**c**) and 20 mm (**d**); the employed model parameters are reported in Table 3 and the identified tests are those for the 7×19 wire rope of length equal to 75 mm

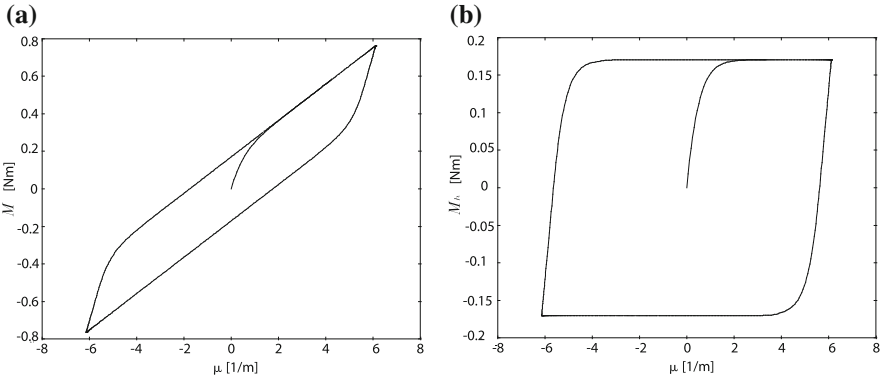

Fig. 6 **a** Total and **b** hysteretic bending moments versus the curvature at $s = 0$ for the beam length of 75 mm with the model parameters of Table 4 and the prescribed end displacement equal to 5 mm

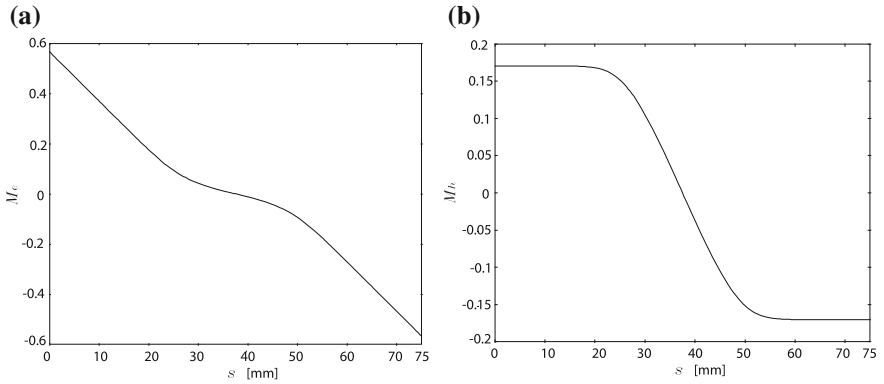

Fig. 7 **a** Elastic and **b** hysteretic bending moments across the beam span whose length is equal to 75 mm with the model parameters of Table 4 and for the prescribed end displacement equal to 5 mm

Table 4 Values of the model parameters obtained as mean values of the parameters in Table 3

ψ (–)	δ (–)	γ ($\mathrm{N}^{1-n}\mathrm{m}^{2-n}$)	β ($\mathrm{N}^{1-n}\mathrm{m}^{2-n}$)	n (–)
0.0164	0.222	1.443	1.493	1.219

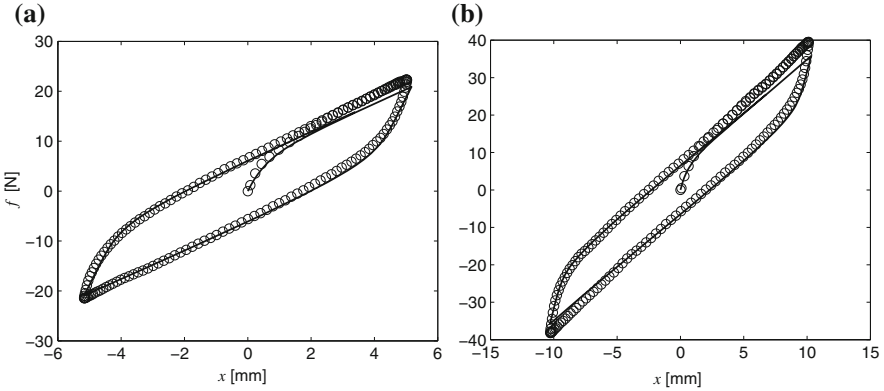

Fig. 8 Comparison between the experimentally obtained (*circles*) and model-based (*solid lines*) hysteresis cycles for displacement amplitudes equal to 5 mm (**a**) and 10 mm (**b**); the employed model parameters are reported in Table 3 and the identified tests are those for the 7 × 19 wire rope whose length is 75 mm

displacement of 5 mm. The elastic and hysteretic bending moments along the beam length are illustrated in Fig. 7. The mean values of the model parameters reported in Table 4 are used to reproduce the hysteresis curves for the other wire rope lengths. Figures 8, 9 and 10 show the comparisons between the model-based and the experimentally obtained hysteresis cycles for the wire rope lengths of 75, 80, and 90 mm, respectively. The associated MSEs are given in Table 5. The mean values of the

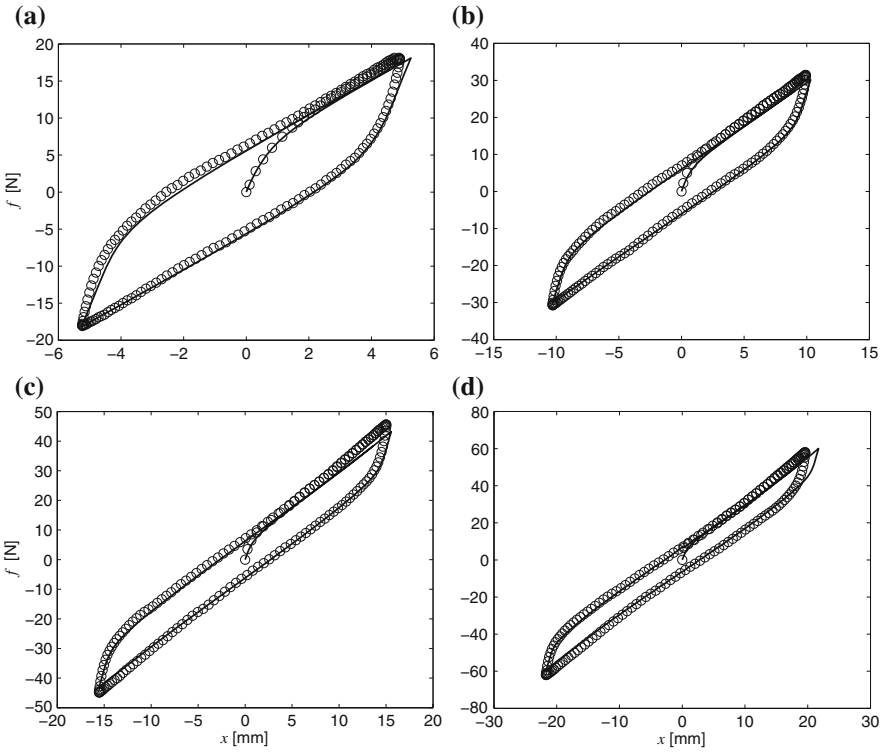

Fig. 9 Comparison between the experimentally obtained (*circles*) and model-based (*solid lines*) hysteresis cycles for displacement amplitudes equal to 5 mm (**a**), 10 mm (**b**), 15 mm (**c**) and 20 mm (**d**); the employed model parameters are reported in Table 4 and the identified tests are those for the 7×19 wire rope whose length is 80 mm

parameters identified for the 7×19 wire rope of length equal to 75 mm are capable of accurately describing the hysteresis curves obtained for the lengths equal to 75, 80, and 90 mm. The best results are achieved for the displacement amplitudes of 5, 10 and 15 mm while for the displacement amplitude of 20 mm some discrepancies are observed. This loss of accuracy is mainly due to the hardening behavior exhibited by both the model-based and experimentally obtained hysteretic cycles for large displacement amplitudes. The hardening is more significant in the model-based response, thus a variation of the constitutive parameters for different displacement amplitudes is required for an accurate description of the experimentally obtained curves. However, the achieved accuracy level is consistent with the practical requirements.

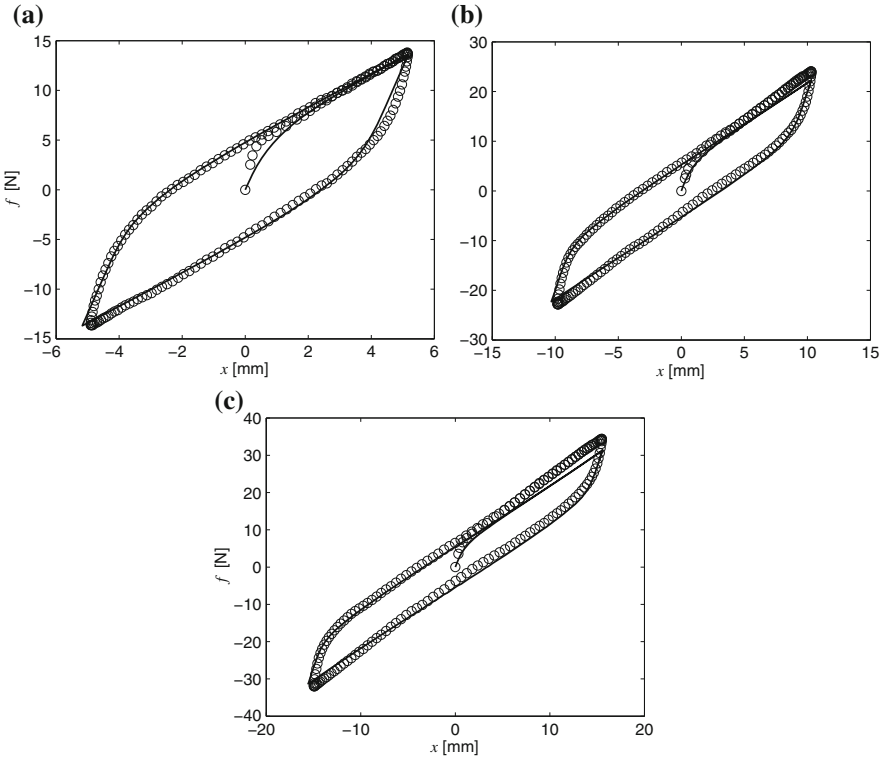

Fig. 10 Comparison between the experimentally obtained (*circles*) and model-based (*solid lines*) hysteresis cycles for displacement amplitudes equal to 5 mm (**a**), 10 mm (**b**) and 15 mm (**c**); the employed model parameters are reported in Table 4 and the identified tests are those for the 7×19 wire rope whose length is 90 mm

The experimentally obtained hysteretic cycles for the 7×7 wire rope can be accurately described identifying the model parameters according to a single displacement amplitude cycle. This is due to the fact that the ratio between the displacement amplitudes and wire rope length is small enough to induce weak nonlinearities and the parameters change with the displacement amplitude is negligible. In Table 6 the parameters identified for fitting the hysteretic curve of the 7×7 wire rope for a displacement amplitude equal to 15 mm are shown. The comparisons between the experimentally obtained and model-based curves are shown in Fig. 11 with the associated MSEs given in Table 7.

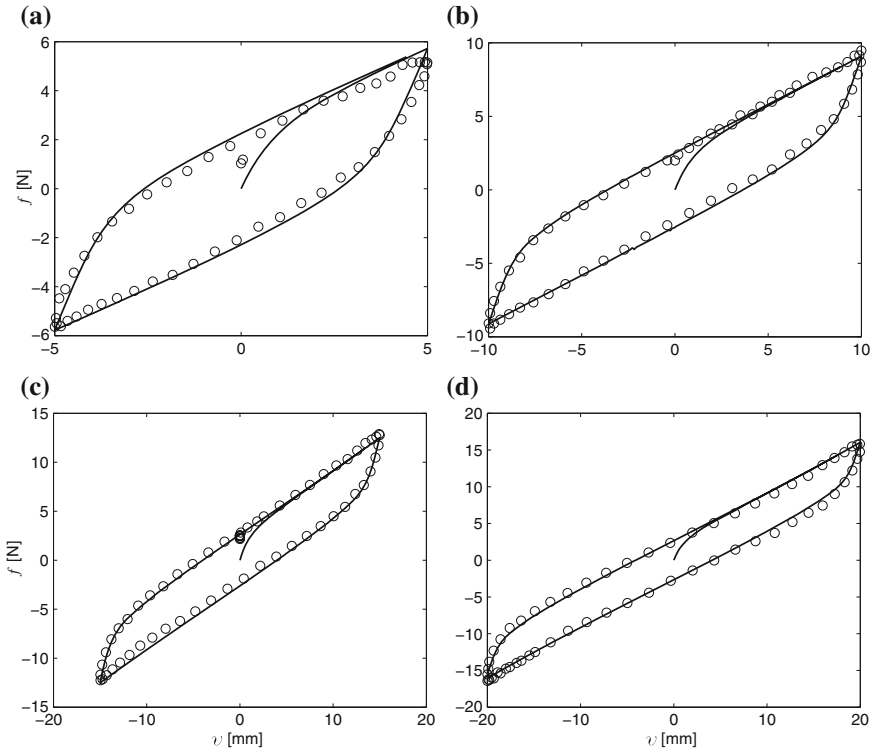

Fig. 11 Comparison between the experimentally obtained (*circles*) and model-based (*solid lines*) hysteresis cycles for displacement amplitudes equal to 5 mm (**a**), 10 mm (**b**), 15 mm (**c**) and 20 mm (**d**); the employed model parameters are reported in Table 6 and the identified tests are those for the 7 × 7 wire rope

Table 5 MSEs between the model-based and experimentally obtained hysteresis cycles of Figs. 8, 9 and 10, identified by the wire rope type, length l and displacement amplitude A

Wire rope type	l (mm)	A (mm)	MSE (%)
7 × 19	75	5	0.63
7 × 19	75	10	0.92
7 × 19	80	5	0.94
7 × 19	80	10	0.89
7 × 19	80	15	0.53
7 × 19	80	20	0.68
7 × 19	90	5	0.71
7 × 19	90	10	0.71
7 × 19	90	15	0.87

Table 6 Identified model parameters which best fit the experimentally obtained hysteretic curve of the 7 × 7 wire rope for a displacement amplitude equal to 15 mm

ψ (–)	δ (–)	γ ($N^{1-n}m^{2-n}$)	β ($N^{1-n}m^{2-n}$)	n (–)
0.0355	0.201	1.987	1.188	1.134

Table 7 MSEs between the model-based and experimentally obtained hysteresis cycles of Fig. 11, identified according to the wire rope type, length l and displacement amplitude A

Wire rope type	l (mm)	A (mm)	MSE (%)
7 × 7	100	5	1.1
7 × 7	100	10	0.68
7 × 7	100	15	0.45
7 × 7	100	20	0.51

7 Conclusions

A nonlinear hysteretic beam model based on the formulation of an equivalent shear deformable beam with geometric nonlinearities and an extension of the Bouc-Wen model of hysteresis to the one-dimensional polar continuum was proposed. Hysteresis is introduced in the constitutive equation for the bending moment given as a direct summation of elastic and hysteretic components. The model aims to describe the hysteretic behavior of steel wire ropes subject to bending cycles. Experimental tests were performed by means of an *ad hoc* setup for evaluating the restoring force exhibited by a group of steel wire ropes clamped at both ends and subject to a quasistatic displacement of one end in the direction orthogonal to the wire ropes rest position. The energy dissipation within the wire ropes is due to the interwire friction. Several tests were executed for three lengths of the wire ropes and for different prescribed displacement amplitudes. The proposed model reduces the actual wire rope to a compact nonlinear beam in which the hysteretic bending moment describes the frictional dissipation in a phenomenological fashion and the Cosserat-type nonlinear beam formulation reproduces the actual mechanics. Thus the geometric and boundary conditions of the beam are assumed as those of the wire ropes while the dissipation properties are identified on the basis of experimental tests. Moreover, the bending stiffness is reduced by an additional parameter denoted by ψ to take into account the lack of compactness of the rope with respect to the equivalent cylindrical rod. The parameters regulating the hysteretic moment and the parameter ψ were identified using the PSO algorithm by best fitting the experimentally obtained curves for the 7 × 19 wire rope of length equal to 75 mm and for the 7 × 7 wire rope subject to a displacement amplitude of 15 mm. Thus, the identified parameters were employed to reproduce the hysteresis curves obtained for different lengths of the 7 × 19 wire rope and for different displacement amplitudes of the 7 × 7 wire rope. These curves show a good agreement with the experimental results confirming that the proposed

model is a valid tool for the design of a wide range of applications based on wire ropes hysteretic behaviors.

Acknowledgments This work was partially supported by the Italian Ministry of Education, University and Scientific Research (2010-2011 PRIN Grant No. 2010BFXRHS-002) and by a FY 2013 Sapienza Grant N. C26A13JPY9.

References

1. Baber, T., Noori, M.: Random vibration of degrading, pinching systems. J. Eng. Mech. **111**(8), 1010–1026 (1985)
2. Baber, T., Wen, Y.: Random vibration hysteretic, degrading systems. J. Eng. Mech. Div. **107**(6), 1069–1087 (1981)
3. Bouc, R.: Forced vibration of mechanical systems with hysteresis. In: Proceedings of the Fourth Conference on Non-linear oscillation, Prague, Czechoslovakia (1967)
4. Carboni, B., Lacarbonara, W.: A new vibration absorber based on the hysteresis of multi-configuration nitinol-steel wire ropes assemblies. In: MATEC Web of Conferences, vol. 16, p. 01004. EDP Sciences (2014)
5. Carboni, B., Lacarbonara, W., Auricchio, F.: Hysteresis of multiconfiguration assemblies of nitinol and steel strands: experiments and phenomenological identification. J. Eng. Mech. **141**, 04014135 (2014)
6. Carpineto, N., Lacarbonara, W., Vestroni, F.: Hysteretic tuned mass dampers for structural vibration mitigation. J. Sound Vib. **333**(5), 1302–1318 (2014)
7. Casciati, F.: Stochastic dynamics of hysteretic media. Struct. Saf. **6**(2), 259–269 (1989)
8. Charalampakis, A., Dimou, C.: Identification of bouc-wen hysteretic systems using particle swarm optimization. Comput. Struct. **88**(21), 1197–1205 (2010)
9. Costello, G.: Theory of Wire Rope. Springer, New York (1990)
10. Crawley, E.F., ODonnell, K.J.: Identification of nonlinear system parameters in joints using the force-state mapping technique. AIAA Pap **86**(1013), 659–667 (1986)
11. Demetriades, G., Constantinou, M., Reinhorn, A.: Study of wire rope systems for seismic protection of equipment in buildings. Eng. Struct. **15**(5), 321–334 (1993)
12. Dimou, C., Koumousis, V.: Reliability-based optimal design of truss structures using particle swarm optimization. J. Comput. Civil Eng. **23**(2), 100–109 (2009)
13. Eberhart, R.C., Shi, Y.: Particle swarm optimization: developments, applications and resources. In: Proceedings of the 2001 Congress on Evolutionary Computation, 2001, vol. 1, pp. 81–86. IEEE (2001)
14. Fourie, P., Groenwold, A.: The particle swarm optimization algorithm in size and shape optimization. Struct. Multi. Optim. **23**(4), 259–267 (2002)
15. Fourie, P., Groenwold, A.A.: Particle swarms in topology optimization. In: Proceedings of the Fourth World Congress of Structural and Multidisciplinary Optimization, Dalian, China (2001)
16. Gerges, R.: Model for the force-displacement relationship of wire rope springs. J. Aerosp. Eng. **21**(1), 1–9 (2008)
17. Gerges, R., Vickery, B.: Parametric experimental study of wire rope spring tuned mass dampers. J. Wind Engi. Ind. Aerodyn. **91**(12), 1363–1385 (2003)
18. Gerges, R., Vickery, B.: Optimum design of pendulum-type tuned mass dampers. Struct. Des. Tall Spec. Build. **14**(4), 353–368 (2005)
19. Gholizadeh, S., Salajegheh, E.: Optimal design of structures subjected to time history loading by swarm intelligence and an advanced metamodel. Comput. Methods Appl. Mech. Eng. **198**(37), 2936–2949 (2009)
20. Gnanavel, B., Gopinath, D., Parthasarathy, N.: Effect of friction on coupled contact in a twisted wire cable. J. Appl. Mech. **77**(2), 024501 (2010)

21. Gnanavel, B., Parthasarathy, N.: Effect of interfacial contact forces in radial contact wire strand. Arch. Appl. Mech. **81**(3), 303–317 (2011)
22. Kennedy, J., Eberhart, R.: Particle swarm optimization. In: Proceedings of IEEE International Conference of Neural Network IV, Perth, Australia
23. Kwok, N., Ha, Q., Nguyen, T., Li, J., Samali, B.: A novel hysteretic model for magnetorheological fluid dampers and parameter identification using particle swarm optimization. Sens. Actuators A: Phys. **132**(2), 441–451 (2006)
24. Lacarbonara, W.: Nonlinear Structural Mechanics: Theory, Dynamical Phenomena and Modeling. Springer, New York (2013)
25. Liu, B., Wang, L., Jin, Y.H., Tang, F., Huang, D.X.: Directing orbits of chaotic systems by particle swarm optimization. Chaos, Solitons Fractals **29**(2), 454–461 (2006)
26. Love, A.E.H.: A Treatise on the Mathematical Theory of Elasticity. Cambridge University Press, Cambridge (2013)
27. Ma, J., Ge, S.R., Zhang, D.K.: Distribution of wire deformation within strands of wire ropes. J. China Univ. Min. Technol. **18**(3), 475–478 (2008)
28. Masri, S., Caughey, T.: A nonparametric identification technique for nonlinear dynamic problems. J. Appl. Mech. **46**(2), 433–447 (1979)
29. Multiphysics, C.: Version 3.5 a (2008)
30. Nucera, C., di Scalea, F.L.: Monitoring load levels in multi-wire strands by nonlinear ultrasonic waves. Struct. Health Monit. **10**(6), 617–629 (2011)
31. Quaranta, G., Monti, G., Marano, G.C.: Parameters identification of van der pol-duffing oscillators via particle swarm optimization and differential evolution. Mech. Syst. Sig. Process. **24**(7), 2076–2095 (2010)
32. Sauter, D., Hagedorn, P.: On the hysteresis of wire cables in stockbridge dampers. Int. J. Nonlinear Mech. **37**(8), 1453–1459 (2002)
33. Schutte, J., Groenwold, A.: Sizing design of truss structures using particle swarms. Struct. Multi. Optim. **25**(4), 261–269 (2003)
34. Simeonov, V.K., Sivaselvan, M.V., Reinhorn, A.M.: Nonlinear analysis of structural frame systems by the state-space approach. Comput. Aided Civil Infrastruct. Eng. **15**(2), 76–89 (2000)
35. Sivaselvan, M.V., Reinhorn, A.M.: Hysteretic models for deteriorating inelastic structures. J. Eng. Mech. **126**(6), 633–640 (2000)
36. Stockbridge, G.: Vibration damper. US patent 1,675,391 (1928)
37. Tinker, M., Cutchins, M.: Damping phenomena in a wire rope vibration isolation system. J. Sound Vib. **157**(1), 7–18 (1992)
38. Triantafyllou, S., Koumousis, V.: Bouc-wen type hysteretic plane stress element. J. Eng. Mech. **138**(3), 235–246 (2011)
39. Triantafyllou, S., Koumousis, V.: Small and large displacement dynamic analysis of frame structures based on hysteretic beam elements. J. Eng. Mech. **138**(1), 36–49 (2011)
40. Triantafyllou, S.P., Koumousis, V.K.: An hysteretic quadrilateral plane stress element. Arch. Appl. Mech. **82**(10–11), 1675–1687 (2012)
41. Venter, G., Sobieszczanski-Sobieski, J.: Multidisciplinary optimization of a transport aircraft wing using particle swarm optimization. Struct. Multi. Optim. **26**(1–2), 121–131 (2004)
42. Version, M.: 7.10. 0.499 (r2010a) (2010)
43. Vestroni, F., Lacarbonara, W., Carpineto, N.: Hysteretic tuned mass damper for passive control of mechanical vibration. Sapienza University of Rome, Italian Patent No. RM2011A000434 (2011)
44. Waisman, H., Montoya, A., Betti, R., Noyan, I.: Load transfer and recovery length in parallel wires of suspension bridge cables. J. Eng. Mech. **137**(4), 227–237 (2010)
45. Wen, Y.: Method for random vibration of hysteretic systems. J. Eng. Mech. Div. **102**(2), 249–263 (1976)
46. Worden, K.: Data processing and experiment design for the restoring force surface method, part i: integration and differentiation of measured time data. Mech. Syst. Sig. Process. **4**(4), 295–319 (1990)

47. Worden, K.: Data processing and experiment design for the restoring force surface method, part ii: choice of excitation signal. Mech. Syst. Sig. Process. **4**(4), 321–344 (1990)
48. Ye, M.: Parameter identification of dynamical systems based on improved particle swarm optimization. In: Intelligent Control and Automation, pp. 351–360. Springer, Berlin (2006)

An Investigation into the Dynamic Interaction Between an Electro-dynamic Shaker and a Test Structure with Cubic Nonlinearity

Gianluca Gatti, Michael J. Brennan and Ivana Kovacic

Abstract This chapter describes the dynamic behaviour of a coupled system where a nonlinear oscillator is attached and driven harmonically by an electro-dynamic shaker. The shaker is modelled as a linear single degree-of-freedom oscillator and the nonlinear attachment is modelled as a hardening Duffing oscillator. The attachment consists of four elastic wires, represented as springs, and its nonlinearity is due to the geometric configuration of the springs, which incline as they extend. The mass of the nonlinear system is much less than the moving mass of the shaker so that the nonlinear system has little effect on the shaker dynamics. The objective is to explore the dynamic behaviour of this system under a range of different conditions. Of particular interest is the situation when the linear natural frequency of the nonlinear system is less than the natural frequency of the shaker such that the frequency response curve of the nonlinear system bends to higher frequencies and thus interacts with the resonance frequency of the shaker. It is found that for some values of the system parameters a two-part frequency response curve can occur: a closed detached curve can appear as a part of the overall amplitude-frequency response, and this detached curve can lie outside or inside the main continuous resonance curve.

1 Introduction

When a nonlinear oscillator is attached to a linear host structure, complex dynamics can occur [1, 2]. In particular, if it is assumed that the linear system is excited by a harmonic force, and that the responses of the two degree-of-freedom (DOF) system

G. Gatti
University of Calabria, 87036 Rende (CS), Italy
e-mail: gianluca.gatti@unical.it

M.J. Brennan
Universidade Estadual Paulista, 15385-000 Ilha Solteira (SP), Brazil
e-mail: mjbrennan0@btinternet.com

I. Kovacic (✉)
Faculty of Technical Sciences, University of Novi Sad, 21125 Novi Sad, Serbia
e-mail: ivanakov@uns.ac.rs

M. Belhaq (ed.), *Structural Nonlinear Dynamics and Diagnosis*,
Springer Proceedings in Physics 168, DOI 10.1007/978-3-319-19851-4_14

are predominantly harmonic at the frequency of excitation, multi-valuedness of the steady-state solution may occur, which affects the shape of the frequency response curve (FRC). Due to the coupling with the attachment, and for some particular combinations of the system parameters, the FRC can have interesting features, such as a detached resonance curve (DRC), lying inside or outside the main continuous FRC. Outer DRCs have been identified in several studies for the case of a purely nonlinear attachment with no linear stiffness term [3–7]. For the same condition, i.e. in the case when the attachment has a quasi-zero-stiffness (QZS) characteristic around the equilibrium position, inner DRCs may also appear with stable and unstable parts. These inner DRCs are of particular interest in this chapter.

For the sake of clarity, some assumptions are adopted in this study. The general aim is to limit the number of system parameters, so that on the one hand, their effect on the main features of the system dynamics are retained, and on the other hand, a quantitative insight is possible without additional cumbersome mathematical formulation. Further, it is assumed that the mass of the nonlinear attachment is small compared to that of the linear system. The effect of this assumption is that the nonlinear system does not have an appreciable effect on the vibration of the forced linear system. Although such an assumption is reasonable for the testing of a nonlinear attachment by a shaker, it excludes the nonlinear absorber as an application example. However, the interested reader can find more on this latter application in [8]. Regarding the type of excitation, it is assumed to be a harmonic force with a constant amplitude as frequency changes. With reference to the test of a nonlinear system using an electro-dynamic shaker, this implies that the shaker is supplied with a constant current at each frequency. This can easily be achieved in practice using commercially available shakers and controllers.

2 Mechanical and Mathematical Model

2.1 System Description

The practical system of interest in this chapter is depicted in Figs. 1 and 2. Photographs of the system are shown in Fig. 1a, b, and a schematic representation is shown in Fig. 2. A small mass m, is attached to a large shaker via a support frame, and the connection between the small mass and the support frame is made by four elastic wires, which can be modelled as four springs of stiffness k and a damper c. The initial tension in the wires can be adjusted upon assembly and has a profound effect on the stiffness of the system attached to the shaker. When the small mass vibrates in the horizontal direction, the springs stretch in tension, thus creating a geometric stiffness nonlinearity. The electro-dynamic shaker, which is used to excite the system, can be modelled as a linear system consisting of a parallel combination of a spring k_s and a damper c_s connected to a mass m_s, which is made up of the moving mass of the shaker and the support frame, and is much larger than the mass

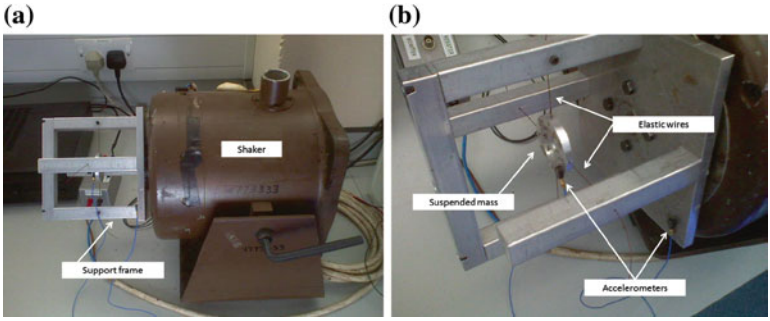

Fig. 1 Practical system under consideration, consisting of a nonlinear system attached to an electrodynamic shaker: **a** photograph of the system, **b** photograph showing the details of the nonlinear system attached to the shaker

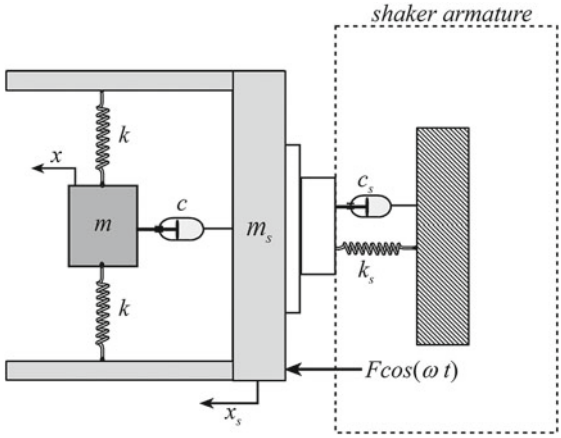

Fig. 2 Schematic view of the shaker and the nonlinear attachment

m. If the shaker is driven by a constant current at each frequency, the excitation can be modelled as a harmonic force with constant amplitude, $F\cos(\omega t)$ as shown in Fig. 2.

2.2 System Modelling

The wires connecting the small mass to the support structure can be modelled as shown in Fig. 3a. The distance d is equal to the length of the springs when they are assembled and the system is at rest. When the mass moves in the z direction, the springs incline to accommodate the motion as shown in the figure and it is the change in their length that causes the nonlinearity. Note that the effect of gravity on the mass is neglected. The relationship between the static restoring force f in Fig. 3a, and the resulting relative displacement z between the mass and the support structure, is given by

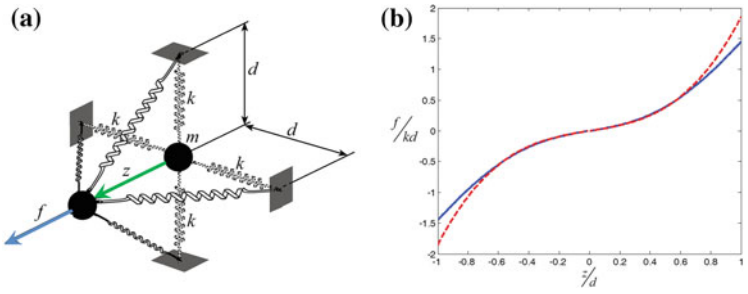

Fig. 3 Nonlinear system attached to the shaker: **a** schematic view; **b** non-dimensional restoring force as a function of the non-dimensional relative displacement for $d_0/d = 0.9$, exact expression (*solid line*), approximate expression (*dashed line*)

$$f = 4kz\left(1 - \frac{d_0}{\sqrt{z^2 + d^2}}\right), \tag{1}$$

where $d_0 \leq d$ is the length of the unstretched spring.

Using the McLaurin expansion to the third order for small z, (1) can be written as

$$f \approx k_1 z + k_3 z^3, \tag{2}$$

where $k_1 = 4k\left(1 - \frac{d_0}{d}\right)$ and $k_3 = 2k\frac{d_0}{d^3}$. The non-dimensional form of (1) and its approximation given by (2) are illustrated in Fig. 3b, for the particular case when $\frac{d_0}{d} = 0.9$. It can be seen that for a relative displacement $z = x_s - x$ less than about 40 % of the length d, the percentage error between (1) and (2) is less than 5 %. Furthermore, this error reduces for decreasing values of $\frac{d_0}{d}$.

Using the approximate expression for the spring restoring force, the equations of motion of the two DOF system depicted in Fig. 2 are given by

$$m_s\ddot{x}_s + c_s\dot{x}_s + k_s x_s + c\dot{z} + k_1 z + k_3 z^3 = F\cos(\omega t), \tag{3a}$$

$$m\ddot{x} - c\dot{z} - k_1 z - k_3 z^3 = 0 \tag{3b}$$

Equations (3a), (3b) correspond to the simplified system depicted in Fig. 4 and can be written in non-dimensional form as

$$y_s'' + 2\zeta_s y_s' + y_s + \mu y'' = \cos(\Omega\tau), \tag{4a}$$

$$w'' + 2\zeta w' + \omega_0^2 w + \gamma w^3 = y_s'' \tag{4b}$$

where $x_0 = F/k_s$ is the static displacement of the primary mass; $y_s = \frac{x_s}{x_0}$, $y = \frac{x}{x_0}$, $w = \frac{z}{x_0}$ are the non-dimensional displacement of the primary and secondary mass, and the corresponding relative displacement, respectively; $\omega_s = \sqrt{\frac{k_s}{m_s}}$, $\omega_1 =$

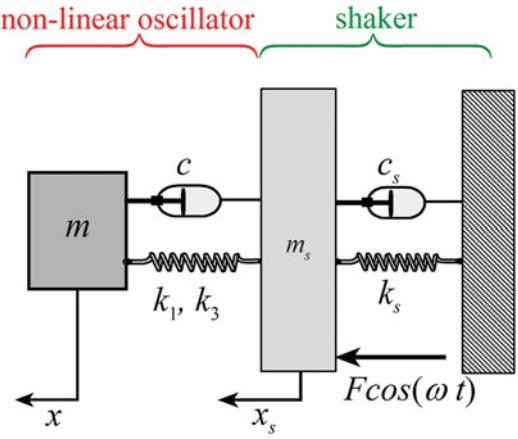

Fig. 4 Simplified model of the nonlinear system attached to the shaker

$\sqrt{\frac{k_1}{m}}$, $\omega_0 = \frac{\omega_1}{\omega_s}$ are the undamped natural frequency of the primary mass alone on its suspension, the linearized undamped natural frequency of the secondary mass alone on its suspension, and the ratio between the two, respectively; $\zeta_s = \frac{c_s}{2m_s\omega_s}$, $\zeta = \frac{c}{2m\omega_s}$ are the damping ratios of the primary and secondary masses, respectively; $\tau = \omega_s t$, $\Omega = \frac{\omega}{\omega_s}$, $\mu = \frac{m}{m_s}$ are the non-dimensional time, non-dimensional frequency and mass ratio, respectively; $\gamma = \frac{k_3}{\mu k_s} x_0^2$ is the nonlinear coefficient; and the primes denote differentiation with respect to the non-dimensional time.

It should be noted that a change in γ can be interpreted as a change in the nonlinearity or in the amplitude of excitation or in the mass ratio, or a combination of the three.

By assuming that the mass of the nonlinear attachment is small compared to that of the linear system, so that $\left|y_s''\right| \gg \left|\mu y''\right|$, as in the practical situation discussed, (4a), (4b) reduce to

$$y_s'' + 2\zeta_s y_s' + y_s = \cos(\Omega\tau) \tag{5a}$$

$$w'' + 2\zeta w' + \omega_0^2 w + \gamma w^3 = y_s''. \tag{5b}$$

Equation (5a) shows that the nonlinear system attached to the shaker has a negligible effect on the shaker vibration so that the shaker vibrates predominantly as a disconnected linear system, while (5b) describes a base-excited hardening Duffing oscillator [2].

3 Steady-State Response: Approximate Analytical Solution

3.1 Primary Resonance Response

Approximate solutions for the equations of motion given by (5a), (5b) are found in terms of the primary resonance responses, assuming that the system responds predominantly at the frequency of excitation, so that

$$y_s \approx Y_s \cos(\Omega\tau + \varphi_s), \tag{6a}$$

$$w \approx W \cos(\Omega\tau + \varphi) \tag{6b}$$

which also means that higher and lower order harmonics are negligible in the system response.

Substituting (6a), (6b) into (5a), (5b) and applying the harmonic balance method [9] results in

$$Y_s^2\left[\left(1-\Omega^2\right)^2 + 4\zeta_s^2\Omega^2\right] = 1 \tag{7a}$$

$$\frac{9}{16}\gamma^2 W^6 + \frac{3}{2}\gamma W^4\left(\omega_0^2 - \Omega^2\right) + W^2\left(\Omega^4 + 4\zeta^2\Omega^2 + \omega_0^4 - 2\omega_0^2\Omega^2\right) - \Omega^4 Y_s^2 = 0. \tag{7b}$$

Equations (7a), (7b) define the amplitude-frequency behaviour of the system response and show that the frequency response of the primary mass, is decoupled from the motion of the mass of the nonlinear attachment. This is due to the assumption adopted that the mass ratio is relatively small. However, (7b) is coupled with (7a) by the amplitude of the response of the primary mass Y_s.

The focus of this chapter is on the amplitude-frequency relationships only, so the expressions for the phases φ_s and φ in (6a), (6b) are not given.

Combining (7a) and (7b), gives the implicit amplitude-frequency equation, which can be written as

$$\frac{9}{16}\gamma^2 W^6 - \frac{3}{2}\gamma W^4\left(\Omega^2 - \omega_0^2\right) + W^2\left(\Omega^4 + 4\zeta^2\Omega^2 + \omega_0^4 - 2\omega_0^2\Omega^2\right) - \frac{\Omega^4}{\left[\left(\Omega^2-1\right)^2 + 4\zeta_s^2\Omega^2\right]} = 0. \tag{8}$$

Equation (8) is used to plot the FRC shown later in this chapter. It is interesting to note that, since it is cubic in W^2, this equation can yield up to three real solutions, and thus a multi-valued response for the steady-state can occur.

3.2 Stability

The stability of the steady-state solutions is calculated following the procedure in [9] and the limits for stability are determined to be

$$\Omega_{1,2} = \sqrt{\left(\frac{3}{2}W^2\gamma - 2\zeta^2 + \omega_0^2\right) \pm \sqrt{\left(-\frac{3}{2}W^2\gamma + 2\zeta^2 - \omega_0^2\right)^2 - \frac{27}{16}W^4\gamma^2 - \omega_0^4 - 3W^2\gamma\omega_0^2}}. \tag{9}$$

Both (8) and (9) involve a relationship between the amplitude of the non-dimensional relative displacement W and the non-dimensional frequency Ω. However, while (8) is an implicit polynomial equation whose roots can be solved numerically in terms of W for each value of Ω and of the system parameters, (9) is explicitly written in terms of Ω as a function of W and of the system parameters. Both (8) and (9) can then be plotted in the $\Omega - W$ plane. The solutions of (8) which are enclosed by the two curves given by (9) correspond to unstable solutions. In the FRCs plotted in this chapter, the unstable solutions are depicted by dashed lines while stable solutions are represented by solid lines.

4 Steady-State Response: Experimental Work

4.1 Setup Configuration

The experimental setup is depicted in Fig. 5. The electro-dynamic shaker was driven by a signal generator supplying a stepped-sine signal. Accelerometers were attached to the support structure and to the small mass, while a signal conditioner and a two-channel oscilloscope were used to observe the system response.

Before collecting data, two tests were carried out to broadly investigate the dynamic behaviour of the system. For each test, the support wires had a different initial tension. In the first test, a slow frequency sweep was applied from zero to

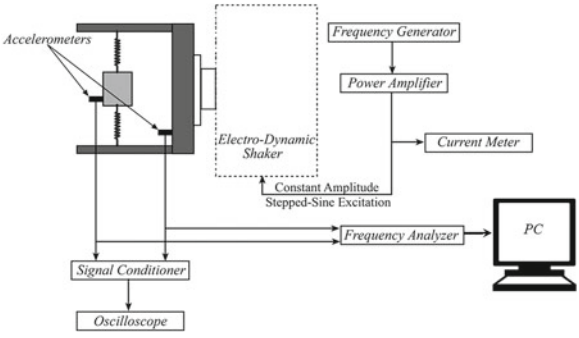

Fig. 5 Experimental set-up configuration

about 28 Hz and the response of the system was monitored using the oscilloscope. The first resonance was observed to be at about 19 Hz, with both masses vibrating with large amplitudes. As the frequency was increased beyond this, a second resonance occurred at about 26 Hz, in which only the vibration of the suspended mass was large. This was followed by a sudden decrease in the motion of the suspended mass (a jump-down). The frequency was then slowly swept down. A sudden increase in the amplitude was observed at a frequency of about 22 Hz, again for the suspended mass only (a jump-up). At about 19 Hz, the resonance response in which there was large motion of both the support structure and the suspended mass was observable. In the second test, similar behaviour was observed, but the jump-up and jump down frequencies were found to occur at about 29 and 34 Hz respectively.

To collect data, the shaker was then driven at discrete frequencies for the system with the wires set with low and high initial tension, corresponding to the cases described above, respectively. The excitation frequency was increased from 10 to 36 Hz, with a 1 Hz increment, and then decreased to 10 Hz with the same frequency increment. As mentioned previously, the amplitude of the excitation force was maintained at a constant level for all excitation frequencies, by manually adjusting the power amplifier so that the current was 0.8 A. At each frequency, once the system was at steady-state, five-second acceleration time histories were captured using a frequency analyser. Subsequently, these data were processed to give the displacement of the support structure and the suspended mass. The data are presented in terms of the absolute displacement x_s of the support structure and the relative displacement $z = x_s - x$ between the support structure and the suspended mass. The Fourier series coefficients are extracted from these two time histories and the amplitude of the first harmonic of each data set is plotted at the corresponding frequency. This can be seen in Fig. 6a, b for the system in which the springs have low initial tension, and in Fig. 6c, d for the high initial tension springs, respectively. The data points in each graph are denoted by a '+' for increasing frequency and a '×' for decreasing frequency.

In Fig. 6a, c, which depict the response of the support structure, it can be seen that, in each case, the FRC is similar, resembling the response of a single DOF linear system. The peak, at about 19.5 Hz corresponds broadly to the resonance frequency of the shaker and the attached mass of the support structure. It is evident, therefore, that the nonlinear system attached to the shaker has only a small effect on its response. This is because the combined mass of the moving part of the shaker and support structure is much greater than that of the suspended mass.

In the FRCs of the relative displacement Z, shown in Fig. 6b, d, in addition to the peak associated with the resonance frequency of the shaker, a jump-down and jump-up frequency can be seen, due to the response of the suspended mass. These are the frequencies where there is a sudden change in the amplitude of the response when the excitation frequency is changed very slowly [10]. The jump-down frequencies occur at approximately 26 and 33 Hz for the low initial tension and high initial tension cases, respectively, and the corresponding jump-up frequencies at about 21 and 31 Hz.

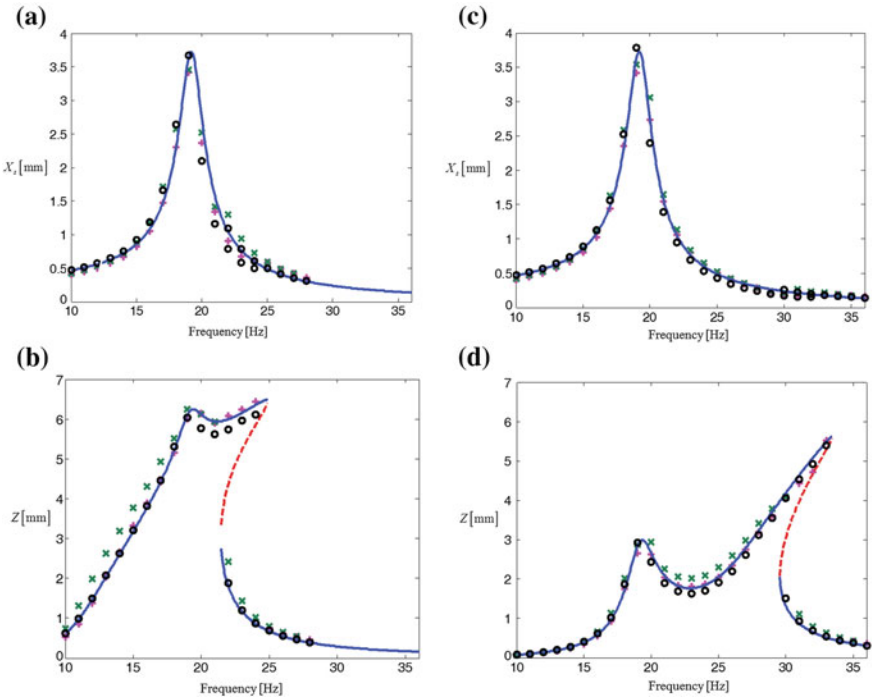

Fig. 6 Analytical, simulated and experimental results for step-sine input to the shaker: **a** and **b** wires with low initial tension; **c** and **d** wires with high initial tension. Analytical solution: stable solution (*solid line*), unstable solution (*dashed line*). Numerical solution ('○'). Experiment: increasing frequency ('+'), decreasing frequency ('×')

4.2 Parameter Estimation and Model Validation

To compare the experimental results with the predictions from the model, the system parameters are required. One group of parameters (m_s, k_s, c_s, m) was measured independently, and the other group (k_1, k_3, c) is considered to be unknown and chosen so that the FRCs are a best fit to the experimental data. Both sets of parameters are given in Table 1. The first group was estimated as follows. The combined mass of the moving part of the shaker and the support structure m_s, together with the stiffness k_s and damping c_s of the shaker were estimated through measurements made from an impact hammer test. With the suspended mass m detached and measured directly, the frequency response function (FRF) of the shaker and attached support structure was measured. The system parameters were estimated by fitting a theoretical single DOF FRF to the experimental FRF. Once these parameters were estimated, the electro-mechanical constant of the shaker, defined as the ratio of the force over the electric current (assumed to be constant), was estimated by measuring the FRF of

Table 1 System parameters for the two different experimental tests[a]

	m_s (kg)	c_s (Ns/m)	k_s (Ns/m)	M (kg)	c (Ns/m)	k_1 (N/m)	k_3 (N/m^3)	F (N)
Wires with low initial tension	1.72	19.12	2.51×10^4	19.4×10^{-3}	(0.234)	(1.3×10^2)	(1.1×10^7)	8.59
Wires with high initial tension	1.72	19.12	2.51×10^4	19.4×10^{-3}	(0.122)	(5.5×10^2)	(1.3×10^7)	8.59

[a]Numerical values in parenthesis are estimated by fitting the FRC to the experimental data

Table 2 Equivalent non-dimensional system parameters

	μ	ω_0	γ	ζ_s	ζ
Wires with low initial tension	0.011	0.677	4.6×10^{-3}	0.046	0.050
Wires with high initial tension	0.011	1.394	5.4×10^{-3}	0.046	0.026

the same system when driven by a random signal from the signal generator through the power amplifier. For a given input current of 0.8A, the force amplitude is calculated and is given in Table 1.

The second group of parameters is chosen to best fit the experimental data as follows. Noting that, for fairly weak nonlinearity, the damping has a negligibly small effect on the jump-up frequency and the corresponding FRC amplitude [11], a first two-parameter fit is performed to match those values, and k_1, k_3 are estimated. The remaining parameter c is then estimated by matching the jump-down frequency, which is affected by the degree of nonlinearity and damping. These three parameters are also listed in Table 1, but in parenthesis to indicate that they are estimated this way. For completeness, Table 2 lists the equivalent system parameters for the equation of motion written in the non-dimensional form of (4a), (4b).

Using the parameters in Table 2 and their relation to the dimensional parameters in Table 1, the FRCs described by (7a), (7b) are plotted in Fig. 6a–d together with the experimental results for comparison.

5 Steady-State Response: Numerical Solution

The FRCs reported in the section above are plotted using the approximate amplitude-frequency equations given in (7a), (7b), which are derived based on the assumption that the system response is predominately harmonic at the frequency of excitation. In this section it is shown how this assumption is verified and the analytical FRCs are validated.

The original equations of motion of the system, given in (4a), (4b), without the assumption for the mass ratio, are numerically integrated for a value of $\mu = 0.001$, which satisfies the assumption $|\mu \ddot{y}| \ll |\ddot{y}_s|$, and the Fourier series coefficients are extracted from the time history of the non-dimensional absolute displacement of the primary mass, y_s, and from the non-dimensional relative displacement between the primary and secondary mass, w. The amplitude of the first Fourier coefficient of the time response of w, which corresponds to the component at the frequency of excitation, is plotted as a circle in the FRCs shown in Fig. 6a–d. For the parameters of the experimental rig, higher- and lower-order harmonics are found to be negligible

compared to the first harmonic; the small differences between the analytical and numerical results around the resonances are due to the fact that the assumption $|\ddot{y}_s| \gg |\mu\ddot{y}|$ does not hold in these frequency regions. Examining Fig. 6a–d it can be seen that there is reasonably good agreement between the approximate analytical solution and the experimental results. Thus, the analytical model qualitatively captures the behaviour of the system.

Furthermore, for the numerical results superimposed on the FRCs reported in the figures of this chapter it is also verified that the amplitudes of the higher- and lower-order harmonics were negligible (less than 5 %) compared to that of the fundamental. A similar validation is performed on the time response of the displacement y_s. Although the FRCs of the corresponding amplitude are not reported here, a verification of the assumption is performed and, also in this case, it is valid for y_s.

6 Frequency-Response Curves for a QZS Attachment

The model developed in the previous sections is used here to investigate the effects of the system parameters on the FRC of the relative displacement W, and in particular on the interaction of the two resonances of the two DOF system depicted in Fig. 4. Of particular interest is the case where the natural frequency of the underlying linear system of the nonlinear attachment is lower than the natural frequency of the primary system. In this case, the FRC of the two DOF system will have a lower resonance frequency which is related to the nonlinear attachment and a higher resonance frequency which is related to the primary system. Due to the hardening characteristics of the nonlinear attachment, the bending of the first resonance peak to higher frequencies interacts with the second resonant peak, yielding the specific shape of the FRC. To limit the number of system parameters, the particular case is considered where the nonlinear attachment has a very small linear stiffness coefficient k_1, which can be practically achieved by a very low tightening of the suspension wires during assembly of the mechanical rig showed in Fig. 1. As a result, the non-dimensional frequency ratio is very small, i.e. $\omega_0 \approx 0$ and this corresponds to a QZS configuration around the equilibrium position [12]. For the results related to the case of the non-QZS configuration, the interested reader is directed to [13].

6.1 Effect of System Parameters: Jumps and Detachments

In this section, the FRCs of the non-dimensional relative displacement amplitude W are illustrated for some particular combinations of the systems parameters, in which ω_0 is set to zero, for the sake of simplicity. To this end, (8) is solved numerically for different values of frequency and for different combinations of the system parameters. The stability of the solution is checked by applying (9). The FRCs of the displacement amplitude of the primary mass, which are governed by (7a) are not shown here, since

this is assumed to be not affected by the nonlinear attachment, due to the assumption of the small mass ratio. The FRC of Y_s thus corresponds to the frequency response of a linear single DOF oscillating system.

In Figs. 7 and 8, two sets of sub-figures are reported, where the effect of the nonlinear parameter γ is shown for a similar value of the damping ζ_s in the primary system and two different values of the damping ζ in the attachment, respectively.

It can be seen from Figs. 7 and 8 that a variety of different shapes of the FRCs are obtained, depending on the values of the system parameters. In both figures, sub-figures a-f correspond to increasing values of the nonlinear parameter γ. It can be seen that the shapes of the FRCs in Figs. 7 and 8 are qualitatively the same, except for sub-plots c.

In particular, Figs. 7a and 8a refer to low values of the nonlinearity, and show a single-valued FRC which is qualitatively similar to that of a linear two DOF system with one of the stiffness equal to zero, since it is QZS. This shape is labelled as Type I (see the upper-right corner of the sub-figure). When the nonlinearity increases, an outer detached resonance curve, having a stable and an unstable branch, appear above the main continuous FRC. This shape is labelled as Type II. The detached resonance curve comes 'from above' in the sense that as the nonlinearity increases from zero to a specific value, it moves downwards until it merges with the main continuous curve. At this stage, two different types of behaviour may occur: the detached curve merges at $\Omega \approx 1$, which occurs in Fig. 7c; or it merges at $\Omega \approx 0$, which occurs in Fig. 8c. These two qualitatively different types of behaviour are labelled, respectively, as Type IIIa and IIIb. If the nonlinearity is increased further, the detached resonance curve appears inside the main continuous resonance curve, and this behaviour is again qualitatively similar for the sub-plots d in Figs. 7 and 8. The appearance of the inner detached resonance curve is associated with a FRC with a shape of Type IV. Such a detached curve decreases in size as the nonlinearity increases, as shown in sub-plots e, until it disappears. The shape of the FRC which is qualitatively similar to those shown in sub-plots f is labelled as Type V.

It is also interesting to note the typical bending of the resonance peak to the right (i.e. to higher frequencies), which is related to a hardening type nonlinearity. Such bending, which is clearly seen in the FRC of Type V, is associated with the jump frequencies. A lower jump-up frequency and a higher jump-down frequency are evident in the FRCs of the sub-plots f.

When an inner detached resonance curve appears, two new jump-up frequencies appear in the FRC, as shown in the sub-plots d and e. They are always lower than $\Omega = 1$. The outer detached resonance curves, shown in sub-plots b, appear above the main continuous FRC and introduce two jump-down frequencies, one of which corresponds to the frequency higher than $\Omega = 1$, while the other one corresponds to the frequency lower than $\Omega = 1$.

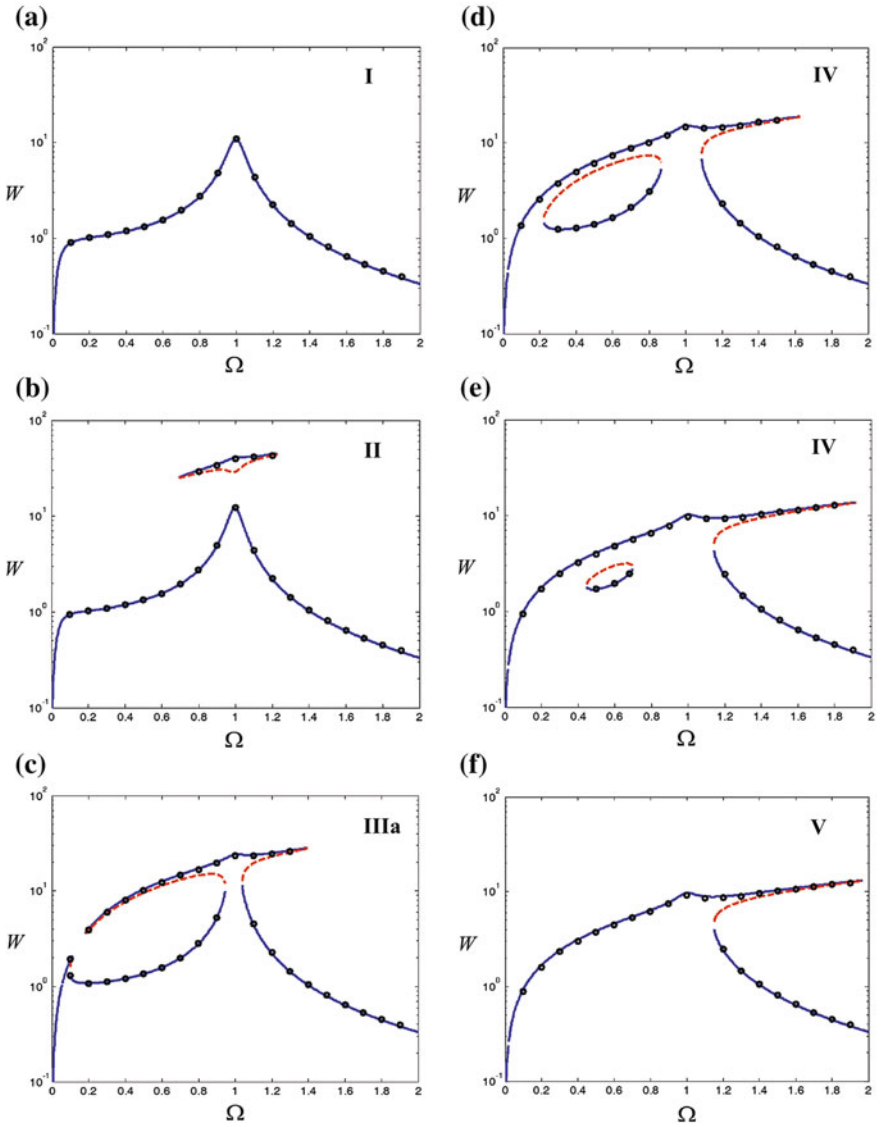

Fig. 7 FRCs of the normalized relative displacement W as a function of the normalized frequency Ω for $\zeta_s = 0.046$, $\zeta = 0.026$, and for different values of the nonlinear parameter γ: **a** $\gamma = 10^{-5}$; **b** $\gamma = 10^{-3}$; **c** $\gamma = 3.3 \times 10^{-3}$; **d** $\gamma = 10^{-2}$; **e** $\gamma = 2.6 \times 10^{-2}$; **f** $\gamma = 3 \times 10^{-2}$. Stable solutions (*solid lines*), unstable solutions (*dashed lines*). Numerical solution ('○')

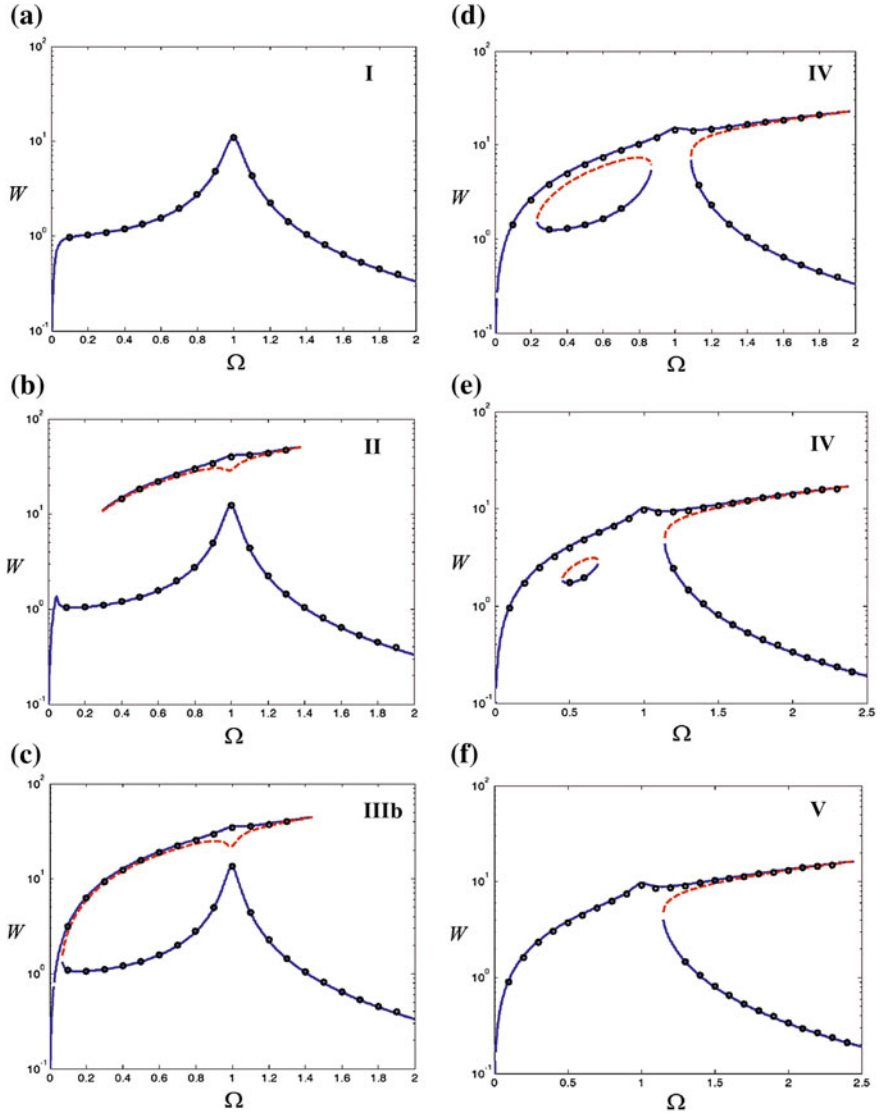

Fig. 8 FRCs of the normalized relative displacement W as a function of the normalized frequency Ω for $\zeta_s = 0.046$, $\zeta = 0.015$, and for different values of the nonlinear parameter γ: **a** $\gamma = 10^{-5}$; **b** $\gamma = 10^{-3}$; **c** $\gamma = 1.4 \times 10^{-3}$; **d** $\gamma = 10^{-2}$; **e** $\gamma = 2.6 \times 10^{-2}$;**f** $\gamma = 3 \times 10^{-2}$. Stable solutions (*solid lines*), unstable solutions (*dashed lines*). Numerical solution ('∘')

6.2 Insight into the FRC Shape

In this section a detailed analysis is performed with the aim of showing the effect of the system parameters on the shapes of the FRC and to categorize the main qualitative features. Again, for the sake of simplicity, the frequency ratio ω_0 is set to zero and (8) is rewritten as

$$\frac{9}{16}\gamma^2 W^6 - \frac{3}{2}\gamma W^4\Omega^2 + W^2\Omega^2\left(\Omega^2 + 4\zeta^2\right) - \frac{\Omega^4}{\left[\left(\Omega^2-1\right)^2 + 4\zeta_s^2\Omega^2\right]} = 0. \quad (10)$$

As mentioned earlier, (10) is cubic in W^2, and depending on the sign of the discriminant of the corresponding polynomial, it can yield up to three real solutions for the steady-state response of the system at a given excitation frequency. In particular, if its discriminant is negative, (10) has one distinct real root and a pair of complex conjugate roots; if it is positive, there are three distinct real roots; and if it is zero, then two roots coincide.

The transition between a single-valued and multi-valued response is determined by setting the discriminant to zero to get a quadratic equation in terms of the nonlinear parameter γ, and solving to give the following two solutions

$$\gamma_{u,l} = \frac{8}{81\Omega}\left[36\zeta^2\Omega + \Omega^3 \pm \left(\Omega^2 - 12\zeta^2\right)^{\frac{3}{2}}\right]\left[\left(\Omega^2-1\right)^2 + 4\zeta_s^2\Omega^2\right], \quad (11)$$

where the sub-scripts u and l stands for *upper* and *lower*, respectively. For values of the nonlinear parameter between γ_u and γ_l, the amplitude-frequency equation in (10) yields three distinct real solutions for the steady-state amplitude response W, while for values of γ equal to γ_u or γ_l, there are two coincident real solutions, and this occurs at the jump-up or jump-down frequencies. Thus, (11) give implicit expressions for the frequencies where a jump occurs. When (11) is plotted in the $\Omega-\gamma$ plane, the curves obtained are referred to as the *transition curves* or *bifurcation curves*. They are plotted in Figs. 9 and 10 to show the effects of the damping ratios in the linear and nonlinear oscillator. It can be seen that the transition curves are not defined for a value of the non-dimensional frequency lower than Ω_C, as indicated in the figures. Point C is obtained by setting $\gamma_u = \gamma_l$ in (11) to give

$$(\Omega_C, \gamma_C) = \left(2\sqrt{3}\zeta, \frac{128}{27}\zeta^2\left[\left(1-12\zeta^2\right)^2 + 48\zeta^2\zeta_s^2\right]\right). \quad (12)$$

It should be observed that Ω_C increases linearly with ζ and does not depend on ζ_s.

In particular, the bifurcation curves in Fig. 9 are shown for a fixed value of $\zeta = 0.03$ and for several values of ζ_s. It can be seen that a change in the value of ζ_s has the same effect on γ_u and γ_l, i.e. only shifting the position of the local minima of these curves, which occur approximately at $\Omega \approx 1$.

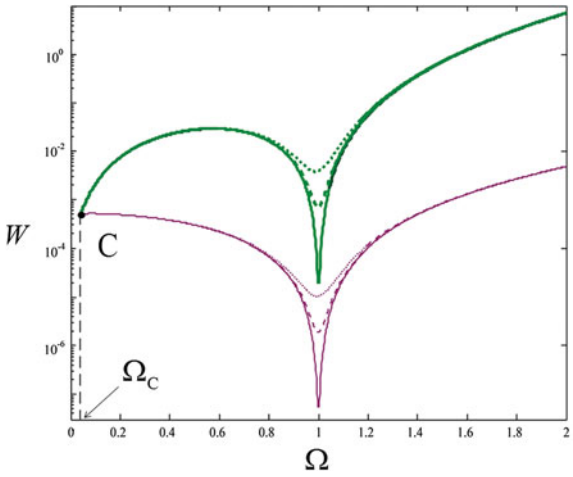

Fig. 9 Effects of the damping parameter ζ_s on the bifurcation curves depicted by a *thick line* (γ_u) and by a *thin line* (γ_l), for $\zeta = 0.03$: $\zeta_s = 0.005$ (*solid curve*); $\zeta_s = 0.03$ (*dash curve*); $\zeta_s = 0.07$ (*dot curve*)

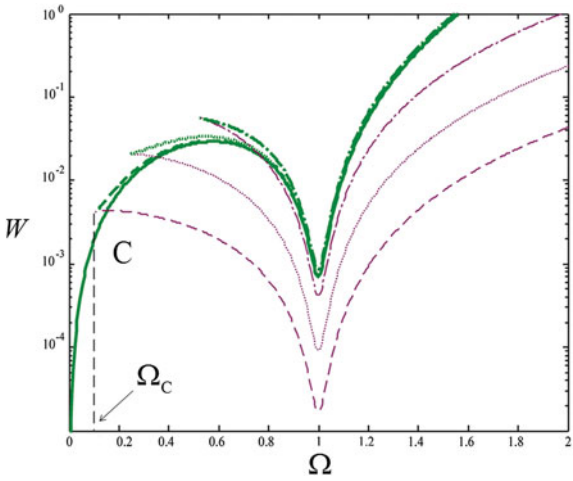

Fig. 10 Effects of the damping parameter ζ on the bifurcation curves depicted by a *thick line* (γ_l) and by a *thin line* (γ_l), for $\zeta_s = 0.03$: $\zeta = 0$ (*solid curve*); $\zeta = 0.03$ (*dash curve*); $\zeta = 0.07$ (*dot curve*); $\zeta = 0.15$ (*dash-dot curve*)

In Fig. 10, the transition curves are shown for a fixed value of $\zeta_s = 0.03$ and for different values of ζ. They illustrate that the damping in the attached nonlinear system has a different effect on γ_u andγ_l. It should be noted that, depending on the value of ζ, both curves can be with or without a local maximum point, which occurs at different frequencies, and may be with or without local minimum points, which occur at $\Omega \approx 1$. This local minimum of the upper curve is slightly affected by ζ.

It is also noted that if Ω_C is greater than unity, which occurs when $\zeta \approx 1/2\sqrt{3}$, no local maxima or minima exists, while in the special case when $\zeta = 0$, (11) reduce to $\gamma_l = 0$ and to

$$\gamma_u = \frac{16}{81}\left[\Omega^2\left(\Omega^2 - 1\right)^2 + 4\Omega^4\zeta_s^2\right]. \tag{13}$$

For the combination of parameters below this curve, depicted by the solid line in Fig. 10, three distinct real roots of (10) exist. In this case, point C coincides with the origin, and a multi-valued response occurs for any value of frequency.

Approximate relationships for the local maxima and minima of the bifurcation curves can be derived analytically by assuming that the damping in the linear oscillator is light, i.e. $\zeta_s \ll 1$. To this end, the local maxima on the upper and lower bifurcation curve are labelled as $\mathrm{U_{max}}$ and $\mathrm{L_{max}}$, respectively, while the local minima on the upper and the lower curve are labelled $\mathrm{U_{min}}$ and $\mathrm{L_{min}}$, respectively.

From Figs. 9 and 10, it can be observed that point C and point $\mathrm{L_{max}}$ are almost indistinguishable from each other, so that

$$\left(\Omega_{\mathrm{L_{max}}}, \gamma_{\mathrm{L_{max}}}\right) \approx \left(\Omega_{\mathrm{C}}, \gamma_{\mathrm{C}}\right) \approx \left(2\sqrt{3}\zeta, \frac{128}{27}\zeta^2\left(1-12\zeta^2\right)^2\right). \tag{14}$$

It can also be observed that the frequency corresponding to the relative maximum of the upper curve, $\mathrm{U_{max}}$, seems not to be greatly affected by either damping ratios. If these are then neglected in (11), a quadratic equation in terms of Ω^2 is obtained. This can be solved to give $\Omega = 1/\sqrt{3}$ and $\Omega = 1$, which correspond approximately to the frequencies where the maximum and minimum points of the upper transition curve occur. If the value $\Omega = 1/\sqrt{3}$ is substituted back into (11), the coordinates of point $\mathrm{U_{max}}$ in the $\Omega - \gamma$ plane are determined to be

$$\left(\Omega_{U_{\mathrm{max}}}, \gamma_{\mathrm{U_{max}}}\right) \approx \left(\frac{1}{\sqrt{3}}, \frac{32}{2187}\left[1+108\zeta^2+\sqrt{-\left(36\zeta^2-1\right)^3}\right]\right). \tag{15}$$

Finally, it can be noted that the frequency corresponding to the relative minima of the upper and lower curves appears at $\Omega \approx 1$. By substituting this value into (11), the coordinates of points $\mathrm{U_{min}}$ and $\mathrm{L_{min}}$ are obtained as

$$\left(\Omega_{U_{\mathrm{min}}}, \gamma_{\mathrm{U_{min}}}\right) \approx \left(1, \frac{32}{81}\zeta_s^2\left[1+36\zeta^2+\sqrt{\left(1-12\zeta^2\right)^3}\right]\right), \tag{16}$$

$$\left(\Omega_{L_{\mathrm{min}}}, \gamma_{\mathrm{L_{min}}}\right) \approx \left(1, \frac{32}{81}\zeta_s^2\left[1+36\zeta^2-\sqrt{\left(1-12\zeta^2\right)^3}\right]\right). \tag{17}$$

Points $\mathrm{U_{max}}$, $\mathrm{L_{max}}$, $\mathrm{U_{min}}$, $\mathrm{L_{min}}$ and C are used to define regions in the $\Omega - \gamma$ plane which characterize the different shapes of the FRCs. These are shown in Fig. 11a, b for two different combinations of ζ and ζ_s. Although Fig. 11a, b appear to be similar, they are different with respect to the relative positions of points $\mathrm{L_{max}}$ and $\mathrm{U_{min}}$. The characteristic regions where a specific shape in the FRC is achieved are indicated as I, II, IIIa, IV and V in Fig. 11a, and as regions I, II, IIIb, IV and V in Fig. 11b. They are also shaded by using different grey-scales. Each region in Fig. 11 is associated with the corresponding type of shape of the FRC, as indicated in the upper-right corners of Figs. 7 and 8 and discussed in the previous section.

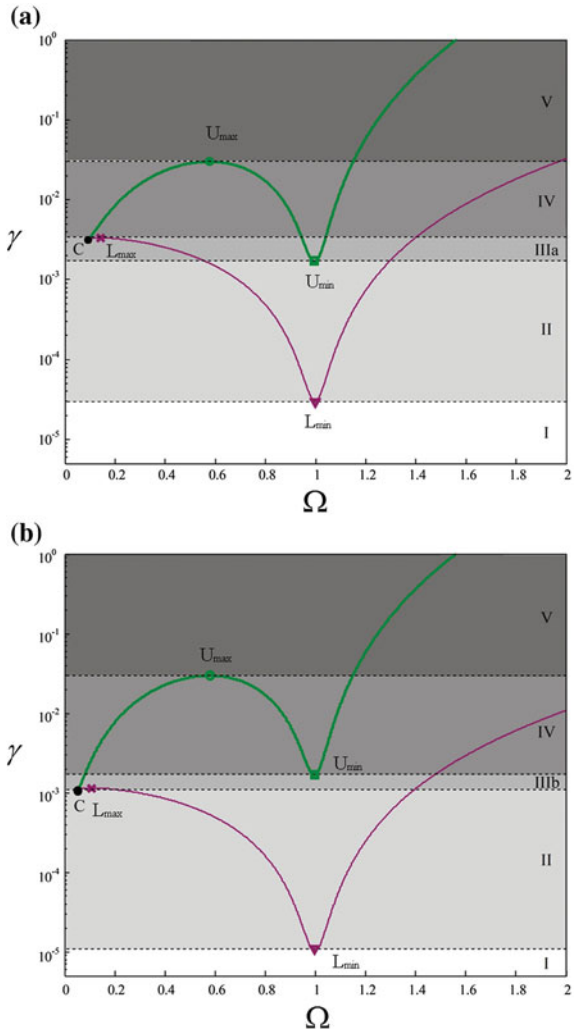

Fig. 11 Characteristic regions *I*–*V* in the $\Omega - \gamma$ plane, where the FRC of *W* exhibits different shapes, for $\zeta_s = 0.046$: **a** $\zeta = 0.026$; **b** $\zeta = 0.015$. Characteristic points U_{max}, L_{max}, U_{min}, L_{min} and C are also labelled

To emphasize the relationship between the bifurcation curves in the $\Omega - \gamma$ plane and the FRCs in the $\Omega - W$ plane, a three-dimensional plot involving the three variables Ω, γ, W is reported in Fig. 12. Two graphs are shown (Fig. 12a, b) to illustrate the relationship between the bifurcation curves in Fig. 11 and the FRCs of Figs. 7 and 8. It can be seen that a straight line, drawn for a particular value of γ, may be interpreted as the projection of the corresponding FRC on the $\Omega - \gamma$ plane. Moreover, the intersections between this straight line and the bifurcation curves give the values of the jump frequencies: jump-up points on the upper bifurcation curve, and jump-down points on the lower bifurcation curve.

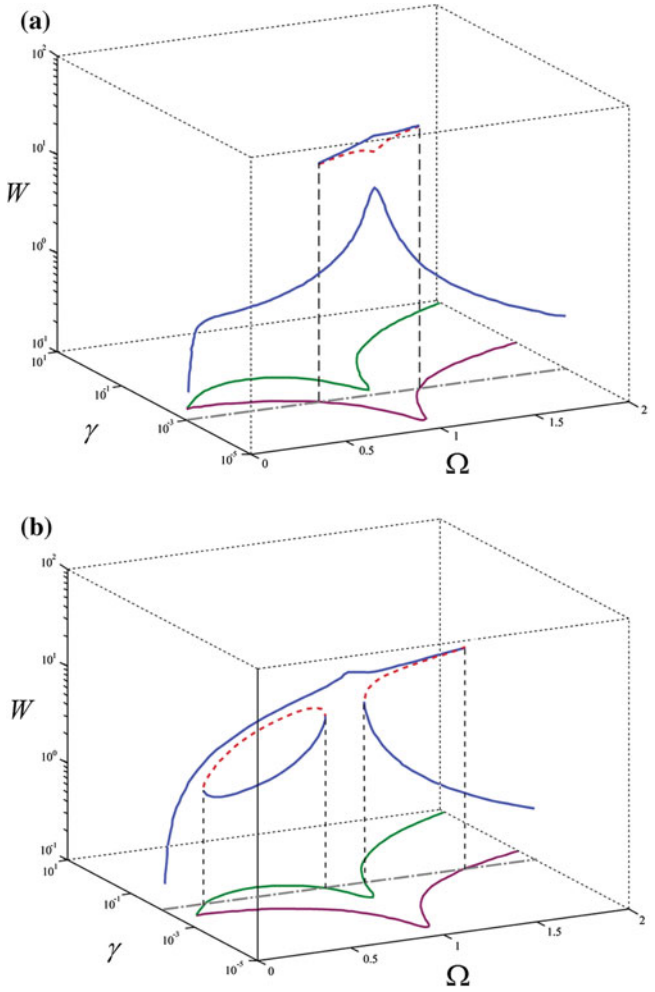

Fig. 12 Three-dimensional plot illustrating the relationship between the bifurcation curves and the FRCs

7 Summary

This chapter has presented an investigation into the dynamics of a nonlinear system attached to a shaker which is driven harmonically, where the mass of the nonlinear system is much less than that of the support structure and the shaker. Consequently, the nonlinear system has a negligible effect on the response of the shaker for the majority of frequencies. The stiffness nonlinearity of the attached system is due to the particular geometrical configuration of the elastic wires, represented as springs. The system has been modelled as a two degree-of-freedom system with a cubic type

nonlinearity and solved using the harmonic balance method to determine the primary frequency response equation and the stability conditions, which define the stable and unstable steady-state solutions. The system of equations has been decoupled and solved in closed-form. Good agreement has been found between the experimental results and the analytical and numerical solutions.

The effect of the system parameters on the frequency response curves was further investigated through simulations and it has been found that they can have different shapes. In particular, of main interest has been the case when the nonlinear attachment has a quasi-zero-stiffness. In this situation, closed detached resonance curves can appear. They can lie outside or inside the main resonance curve, and have stable and unstable parts. Approximate analytical expressions that define the boundaries between the shapes of the frequency response have been determined, enabling the parameters that influence the shape of the frequency response curves to be identified.

References

1. Nayfeh, A.H.: Nonlinear Interactions: Analytical Computational and Experimental Methods. Wiley, New York (2000)
2. Kovacic I, Brennan M.J. (eds): The Duffing Equation: Nonlinear Oscillators and Their Behavior. Wiley (2011)
3. Jiang, X., McFarland, M., Bergman, L.A., Vakakis, A.F.: Steady state passive nonlinear energy pumping in coupled oscillators: theoretical and experimental results. Nonlinear Dyn. **33**, 87–102 (2003)
4. Starosvetsky, Y., Gendelman, O.V.: Response regimes of linear oscillator coupled to nonlinear energy sink with harmonic forcing and frequency detuning. J. Sound Vib. **315**, 746–765 (2008)
5. Starosvetsky, Y., Gendelman, O.V.: Dynamics of a strongly nonlinear vibration absorber coupled to a harmonically excited two-degree-of-freedom system. J. Sound Vib. **312**, 234–256 (2008)
6. Starosvetsky, Y., Gendelman, O.V.: Vibration absorption in systems with a nonlinear energy sink: nonlinear damping. J. Sound Vib. **324**, 916–939 (2009)
7. Alexander, N.A., Schilder, F.: Exploring the performance of a nonlinear tuned mass damper. J. Sound Vib. **319**, 445–462 (2009)
8. Brennan, M.J., Gatti, G.: The characteristics of a nonlinear vibration neutralizer. J. Sound Vib. **331**, 3158–3171 (2012)
9. Hamdan, M.N., Burton, T.D.: On the steady state response and stability of non-linear oscillators using harmonic balance. J. Sound Vib. **166**, 255–266 (1993)
10. Worden, K.: On jump frequencies in the response of the Duffing oscillator. J. Sound Vib. **198**, 522–525 (1996)
11. Brennan, M.J., Kovacic, I., Carrella, A., Waters, T.P.: On the jump-up and jump-down frequencies of the Duffing oscillator. J. Sound Vib. **318**, 1250–1261 (2008)
12. Gatti, G., Kovacic, I., Brennan, M.J.: On the response of a harmonically excited two degree-of-freedom system consisting of a linear and a nonlinear quasi-zero stiffness oscillator. J. Sound Vib. **329**, 1823–1835 (2010)
13. Gatti, G., Brennan, M.J.: On the effects of system parameters on the response of a harmonically excited system consisting of weakly coupled nonlinear and linear oscillators. J. Sound Vib. **330**, 4538–4550 (2011)

Axial Non-linear Dynamic Soil-Pile Interaction

A. Holeyman and V. Whenham

Abstract This chapter describes recent analytical and numerical advances in the modeling of the axial nonlinear dynamic interaction between a single pile and its embedding soil. On one hand, analytical solutions are developed for assessing the nonlinear axial dynamic response of the shaft of a pile subjected to dynamic loads, and in particular to vibratory loads. Radial inhomogeneity arising from shear modulus degradation is evaluated over a range of parameters and compared with those obtained by other authors and by a numerical radial discrete model simulating the pile and soil movements from integration of the laws of motion. New approximate nonlinear solutions for axial pile shaft behaviour developed from general elastodynamic equations are presented and compared to existing linear solutions. The soil nonlinear behaviour and its ability to dissipate mechanical energy upon cyclic loading are shown to have a significant influence on the mechanical impedance provided by the surrounding soil against pile shaft movement. The limitations of over-simplified modelling of pile response are highlighted.

List of Symbols

The following symbols are used in this paper:

a	Dimensionless frequency $\omega \cdot r_0 / V_s$ (–)
a^*	Complex value of dimensionless frequency $a / \sqrt{1 + 2i\xi} = \omega \cdot r_0 / V_s^*$ (–)
a_0	Dimensionless frequency for the pile shaft-soil interface $\omega \cdot r_0 / V_{s0}$ (–)
a_{ff}	Dimensionless frequency in the free field $\omega \cdot r_0 / V_{ff}$ (–)
C_z	Damping coefficient (kPa s^{-1})

A. Holeyman (✉)
Université Catholique de Louvain, iMMC, GeoMEM, 1348 Louvain-la-Neuve, Belgium
e-mail: alain.holeyman@uclouvain.be

V. Whenham
Fugro Geoconsulting Belgium, 1150 Brussels, Belgium

M. Belhaq (ed.), *Structural Nonlinear Dynamics and Diagnosis*,
Springer Proceedings in Physics 168, DOI 10.1007/978-3-319-19851-4_15

$C_{za} = \Im\{I_z\}/(\omega \cdot G_{s0})$	Dimensionless damping parameter (–)
f	"Loading factor" or soil strength mobilization ratio at $r = r_0$ (–)
G	Shear modulus (kPa)
G^*	Complex shear modulus $G \cdot (1 + 2i\xi)$ (kPa)
$G_{\max}$	Initial (maximal) shear modulus (kPa)
G_s	Secant shear modulus (kPa)
G_{s0}	Shear modulus at the pile shaft-soil interface ($r = r_0$) (kPa)
H_n^2	Hankel function $J_\nu - iY_\nu$
I_0	Modified Bessel function of order 0 of first type
I_z	Unit (lineal) shear impedance of the soil against the pile shaft movement in the z direction (kPa)
J_υ	Bessel function of order υ of first type
k	Shear wave number ω/V_s (m^{-1})
k^*	Complex shear modulus ω/V_s^* (m^{-1})
k_{ff}^*	Complex shear modulus in the free field a_{ff}^*/r_0 (m^{-1})
K_0	Modified Bessel function of order 0 of second type
K_z	The stiffness coefficient (kPa)
K_{za}	Dimensionless stiffness $\Re\{I_z\}/G_{s0}$ (–)
r	Distance to the pile shaft (m)
r_0	Pile shaft radius (m)
R_m	Influence radius of shear strain field
t	Time (s)
V_s	Shear wave velocity $\sqrt{G_s/\rho}$ ($m\,s^{-1}$)
V_s^*	Complex value of shear wave velocity $\sqrt{G_s^*/\rho}$ ($m\,s^{-1}$)
V_{s0}	Shear wave velocity at the pile shaft-soil-soil interface $\sqrt{G_{s0}/\rho}$ ($m\,s^{-1}$)
V_{ff}	Shear wave velocity in the free field $\sqrt{G_{\max}/\rho}$ ($m\,s^{-1}$)
w	Displacement (m)
w_c	Time-independent value of displacement (m)
w_o	Displacement at the pile shaft (m)
w_{oc}	Amplitude of imposed displacement at the pile shaft (m)
Y_υ	Bessel function of order υ of second type
γ	Shear strain (–)
$\dot{\gamma}$	Shear strain rate (s^{-1})
γ_c	Amplitude of shear strain (–)
γ_r	Reference strain $\tau_{\max}/G_{\max}$ (–)
ξ	Damping coefficient (–)
ρ	Soil density (T/m^3)
τ	Shear stress (kPa)
τ_c	Amplitude of shear stress (kPa)
τ_0	Shear stress at the pile shaft-soil interface (kPa)
τ_{0c}	Amplitude of shear stress at the pile shaft-soil-soil interface (kPa)

τ_{max}	Maximal shear stress (shear strength) (kPa)
ω	Circular frequency (rad s^{-1})
ς	Dimensionless distance to the pile shaft $r/r_0 > 1$ (–)

The asterisk indicates that the viscous soil behavior (characterized by the Kelvin-Voigt formulation) is taken into consideration.

1 Introduction

1.1 Typical Situations

Piles are used to support civil engineering structures whenever loads are concentrated relative to the soil bearing capacity and thus strength. They consist of elongated structural elements that are embedded in the soil to a depth that will allow bearing layers to develop a safe resistance. Typical situations where piles are used are illustrated on Fig. 1. In the most common case referred to as "active" pile, the pile head receives the load from the superstructure and transmits it to the resisting soil.

Although all 6 load components (forces components and moments about 3 orthogonal axes) need to be considered, the pile axial component generally governs the design of the pile and in particular its embedment depth. In addition to static loads resulting from gravity, operational transient or periodic loads may warrant special design requirements. In response to the quickly expanding market of offshore renewable energy [1], piles have been recently used in several configurations to support wind turbines, as illustrated in Fig. 1.

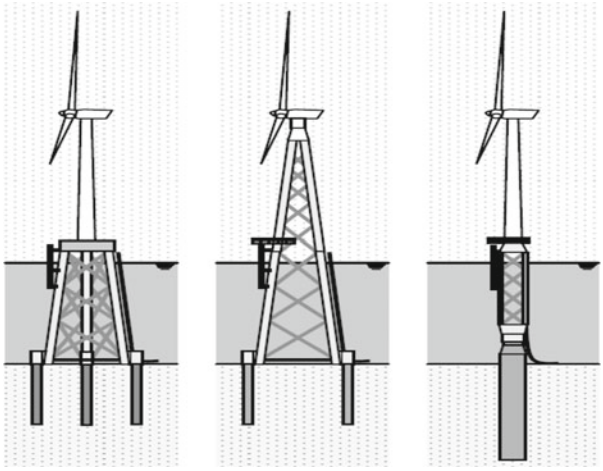

Fig. 1 Typical use of piles to support wind turbines: Tripod, Jacket, and Monopile [1]

Extreme loading cases have also to be considered due to the fact that piles have to be installed at depth: such cases involve pile impact driving as well as vibratory driving.

Due to space and time constraints, this chapter will only focus on the axial response of a pile subjected to a harmonic axial load. Similar contributions can be developed on the pile lateral response, torsional response and would justify a discussion on the coupling. Finally, most of the discussion will revolve about the friction component of the pile resistance, leaving out the singularity brought about by the pile bottom end.

Whatever the mode considered, the engineering picture needs to involve three main ingredients: the complete definition of all actions on the pile, the structural characterization of the pile, and the characterization of the embedding medium, i.e. the soil.

1.2 Pile Characterization

Piles used for large projects are commonly made of concrete or steel. Generally concrete is used for onshore applications while steel is used for offshore applications. In the later case, steel pipes are used to construct "pipe piles". The advantage of that geometry is that the volume of soil to be displaced to accommodate pile insertion into the soil is a very small fraction of the gross pile volume that will govern the geotechnical capacity of the pile. For large diameter piles, the inertia of the soil volume inside the pipe will prevent the soil core from moving down in unison with the pile during driving, leading to what is termed a "coring" mode of driving.

Most tubular piles are driven by impact using special pieces of equipment (hydraulic pile hammers) set on top of the pile during installation. More rarely, piles can be vibrated into the ground using vibratory hammers. Once installed to an appropriate depth, a pile will develop its bearing capacity over time, moving from its end-of-installation capacity towards its long-term capacity. The pile geotechnical capacity will come from contact stresses generated by the soil along two interfaces: a shear stress along the pile lateral surface (called shaft) and a normal stress against the pile end bearing area (called toe).

The axial bearing performance of a pile can be characterized by its response under axial static loading. As illustrated in Fig. 2a, the pile load-settlement curve provides the overall relationship between the applied load F and the pile settlement s. One can notice that under limited loads, the pile responds linearly, but endures non recoverable displacements under larger loads, with the ultimate limit state being defined by unlimited displacements under an asymptotic load. This reflects the nonlinear behaviour of the soil while the pile material remains well within its elastic realm. This forces us to address an essential feature of the system, namely the soil behaviour that will be characterized in Sect. 2.

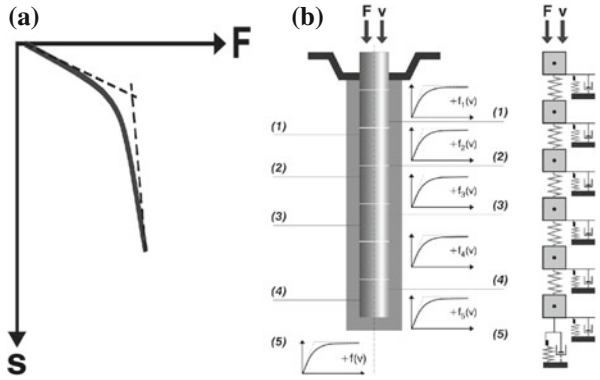

Fig. 2 **a** Global load-settlement curve at top of pile. **b** Embedded pile as continuously supported column

1.3 Simplified Soil-Pile Interaction

Engineering methods that are commonly applied to assess pile response under a static load applied at the head of the pile treat the pile as a column collecting reactions along its shaft and at the pile toe. Assuming that the embedding medium is elastic, it would appear possible to model each local reaction as proportional to the local displacement. Further assuming that each equivalent spring is independent from its neighbours allows one to treat each soil layer with its own properties.

This simplification known as a "Winkler" model has been extended to cope with nonlinear behaviour, leading to what is known in the geotechnical jargon as "t-z" and "Q-z" curves. A "t-z" curve models the nonlinear development of the local shear stress along the pile shaft versus local vertical displacement while a "Q-z" curve models the nonlinear development of the pile toe resistance versus the pile base displacement. Figure 2b schematizes such simplified modelling of the soil-pile interaction.

By extending Winkler approach initially developed in the static domain, the dynamic response of pile shafts embedded in an elastic medium can be studied by replacing the soil surrounding the pile with a series of independent springs and dashpots. Notably, Smith [2] used that approach to model soil resistance to pile driving, leading to the emergence of soil-pile dynamic interaction parameters known as "quake" and "damping", as illustrated as Q and J in Fig. 3.

For a pile undergoing harmonic axial motion, coefficients of the Winkler springs and dashpots depend on the frequency. Such coefficients can be obtained by considering the elastodynamic problem of an infinitely long pile subjected to harmonic vertical displacements.

An alternative approach consists in modelling fully coupled 3D pile-soil interactions, for example by means of the finite element method. However because of the complexity of the problem, especially when the pile is subjected to high strain

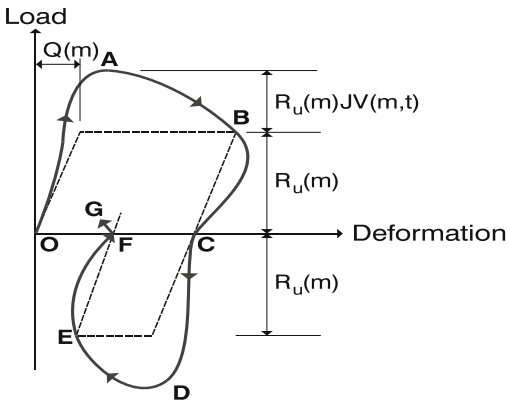

Fig. 3 Smith visco-elasto-plastic load-deformation curve for local slice of pile shaft (adapted from [2])

loading conditions, this approach makes it difficult to properly simulate the essential phenomena at play and is faced with the challenge to harness adequate model parameters. Practical use of the full 3D finite element approach is further hampered by its high demand for computer resources.

While structural engineers are quite fond of simplifications of the pile behaviour boiling it down to a single spring and sometimes a dashpot, they tend to overlook that a pile is a complex infrastructural system that interacts with the soil surrounding and with the superstructure. Furthermore soil is a medium that is far from behaving linearly, as can be summarized below.

2 Soil Characterization

Soil is a multiphase medium made of solid particles whose composite behaviour depends on many factors: attributes of particles, fluid filling the voids left between the solids, stress history, just to name a few. While the particles can be characterized by their nature, size, and shape, their overall behaviour with respect to the water content can be characterized by their plasticity index (PI). The PI of sand is zero while clay minerals can exhibit values in excess of 50, with silts having intermediate values.

Volume variations and distortion of soil depend solely on the soil "effective" stress, i.e. the stress between particles, the pore pressure having no intrinsic role other than taking a part of the total stress. One rather unique feature of soil behaviour is its tendency to change volume when sheared. Loosely packed soils tend to contract while densely packed soils tend to dilate. Soil shear strength essentially comes from friction, which is controlled by effective stress while the effective internal friction angle generally assumes a value close to 30°.

When saturated with water, a contractant assemblage of particles can only modify its volume inasmuch water has the time to drain away from it. This means that low

permeability soils or soils undergoing fast loading have to deform without changing their volume, which implies a substantial change in their effective stress. Such a volumetric constraint explains why the strength of a soil depends so drastically upon its loading rate. At one extreme, loading is so slow that volume changes can be accommodated without any interference from the pore fluid, and the soil will behave as "drained". At the other extreme, loading is so fast that volume remains constant and the material will behave as undrained.

Whether drained or undrained, the latter case being more common under dynamic loading, soil behavior exhibits several features that are characterized in the following section, namely, stiffness, strain hardening and yield criteria, implying material damping upon cyclic loading.

2.1 Key Attributes of Soil Behavior

2.1.1 Small Strain Stiffness

An initial (or maximum) shear modulus can be calculated for rounded grained sands using the relation of Hardin and Black [3]:

$$G_{\max} = 6908 \frac{(2.17 - e)^2}{1 + e} \sigma'^{0.5} (\text{kPa}) \tag{1}$$

where e is the soil void ratio and σ' is the effective confining mean stress usually calculated as:

$$\sigma' = \frac{\sigma'_v + 2\sigma'_{r,0}}{3} \tag{2}$$

where σ'_v is the easily calculated effective initial vertical stress, $\sigma'_{r,0} = k\sigma'_v$ is the effective horizontal stress, with k being the coefficient of horizontal stress in the soil. For a "wished-in-place" pile assumption, an at rest coefficient is estimated herein using Jacky's formula $k = 1 - \sin\varphi\prime$ wherein $\varphi\prime$ is the soil internal friction angle.

2.1.2 Strain Hardening

Thanks to numerous forms of soil testing, the relationship between shear stress and shear strain has been shown to deviate from the initial tangent value G_{max} defined above as shear strain increases, as shown in Fig. 4. This can be viewed as "strain hardening" since the shear stress increases beyond an "elastic" limit to be identified. In soil mechanics, this feature is preferably described in terms of shear modulus degradation [4] inasmuch the secant modulus G_s degrades with strain. Two examples of models commonly accepted to characterize the shear modulus degradation are

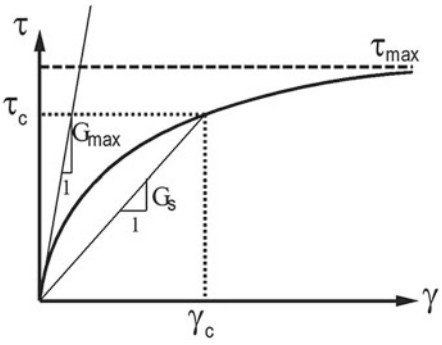

Fig. 4 Hyperbolic shear stress—shear strain model for soils [4]

discussed in Sects. 2.2 and 2.3. Densely packed soils, such as stiff clays can also exhibit some form of strain softening, which will not be covered in this chapter.

At large strains, the soil reaches a "critical state" shear strength characterized by a constant volume and mean stress. That ultimate limit state will be characterized by the value of $\tau_{\max}$ shown on Fig. 4.

2.1.3 Material Damping and Viscous Equivalent

According to Masing rules [5] which will be deemed applicable, if the loading curve is characterized by the relationship $f(F, \delta) = 0$ with F the load and δ the displacement, then for a cycle between points (δ_c, F_c) and $(-\delta_c, -F_c)$, the loading-unloading curves are:

$$f\left(\frac{\delta - \delta_c^*}{2}, \frac{F - F_c^*}{2}\right) = 0 \tag{3}$$

where (δ_c^*, F_c^*) is the point of loading inversion. Figure 5 provides an illustration of Masing's rules, showing how the backbone loading curve can be expanded and rotated to generate the unloading and reloading curves.

The loop developed within this stress-strain plane highlights the dissipation of mechanical energy during a complete loading cycle. Such a material dissipation is characterized by the soil "damping coefficient", a relative measure of the dissipated energy ΔW within one cycle to the maximum accumulated elastic energy. If τ_c is the amplitude of the shear stress and γ_c the amplitude of the shear strain, the soil damping coefficient is defined as $\xi = \Delta W/(4\pi W)$, with $W = \gamma_c \cdot \tau_c/2$.

It should be noted that for a given $\tau_{\max}$ the material damping depends on γ_c but not on the frequency of a potentially considered harmonic movement. Harmonic displacements prescribed by the pile generate cyclic deformations and stresses within the influenced soil zone that can be conveniently expressed by:

$$\tau = \tau_c \cdot e^{i\omega t} = G \cdot (1 + 2i\xi) \cdot \gamma_c \cdot e^{i\omega t} = G^* \cdot \gamma_c \cdot e^{i\omega t}$$

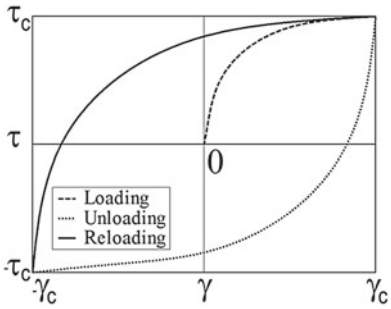

Fig. 5 Masing's rules [5] applied to stress-strain curves

where G^* is the complex shear modulus.

Such an expression postulates that energy losses can be attributed to an out of phase term treating the soil as visco-elastic. In that case, a so called "linear equivalent" soil model is invoked, although strictly speaking, it is linear only under static conditions.

Assuming hysteretic energy losses can be handled at a given frequency by an equivalent viscous-elastic shear modulus $G^* = G \cdot (1 + 2i\xi)$, the equivalent soil viscosity can be expressed under harmonic conditions at frequency ω as $\eta = \partial\tau/\partial\dot{\gamma} = 2G\xi/\omega$, with $\dot{\gamma}$ being the shear strain rate. Although it does not respect the shape of the stress-strain loop, the assumption of the "linear equivalent" medium is generally accepted because of its mathematical convenience, as will be shown in Sect. 3.3.

2.1.4 Cyclic Degradation and Liquefaction

Beyond strain related shear modulus "degradation" discussed above, soil is subject to fatigue whenever strain cycles of sufficient amplitude accumulate. In loose granular soils that are saturated, the cyclic degradation can be compounded by the onset of "liquefaction". This phenomenon occurring in contractive materials involves the increase of the pore pressure to the point that effective stresses vanish. Since soil strength is intrinsically related to friction, the removal of any effective stress actually transforms the soil into a medium unable to resist to shear stress, i.e. a fluid.

2.2 Hardin and Drnevich [4] Model

The relationship between shear stress and shear strain under undrained conditions can be assumed to follow the soil model suggested by Hardin and Drnevich [4] and based on Kondner [6] formulation.

$$\tau = \frac{\gamma}{1/G_{\max} + \gamma/\tau_{\max}} = \tau_{\max} \cdot \frac{\gamma}{\gamma + \gamma_r} \tag{4}$$

where τ is the shear stress, γ is the shear strain, τ_{max} is the maximal shear stress (shear strength), G_{max} is the initial shear modulus and $\gamma_r = \tau_{max}/G_{max}$ is the reference strain. Degradation of the secant shear modulus with the shear strain can therefore be defined by:

$$G = \frac{\tau}{\gamma} = \frac{\tau_{max}}{\gamma + \gamma_r} = G_{max} \cdot \frac{\gamma_r}{\gamma + \gamma_r} = G_{max} \cdot \left(1 - \frac{\tau}{\tau_{max}}\right) \tag{5}$$

Applying Masing's rules to the Hardin and Drnevich [4] loading curve leads to the following expression of the damping coefficient as a function of γ_c:

$$\xi = \frac{2}{\pi} \cdot \left(2\frac{\gamma_r}{\gamma_c^2} \cdot (\gamma_r + \gamma_c) \cdot \ln\left(\frac{\gamma_r}{\gamma_r + \gamma_c}\right) + 2\frac{\gamma_r}{\gamma_c} + 1\right) \tag{6}$$

Illustrations of the Hardin and Drnevich [4] formulation and Masing's rules [5] are provided in Figs. 4, 5 and 6.

2.3 Ishibashi and Zhang [7] Model

Alternatively, the stress-strain relation suggested by Ishibashi and Zhang [7] can be considered to characterize soil nonlinearity, especially in the weakened zone close to the pile shaft. The degradation of the secant shear modulus is expressed as a function of the shear strain γ, of the effective confining mean stress σ', and of the plasticity index IP:

$$\frac{G}{G_{max}} = 0.5\left\{1 + \tanh\left(0.492 \ln \frac{0.000102 + n}{\gamma}\right)\right\} \sigma'^{m} \tag{7a}$$

where

$$m = 0.272\left\{1 - \tanh\left(0.4 \ln \frac{0.000556}{\gamma}\right)\right\} e^{-0.0145IP^{1.3}} \tag{7b}$$

$$n = \begin{cases} 0.0 & \text{for IP} = 0 \\ 3.37 \times 10^{-6} IP^{1.404} & \text{for } 0 < \text{IP} \leq 15 \\ 7 \times 10^{-7} IP^{1.976} & \text{for } 15 < \text{IP} \leq 70 \\ 2.7 \times 10^{-5} IP^{1.115} & \text{for IP} > 70 \end{cases} \tag{7c}$$

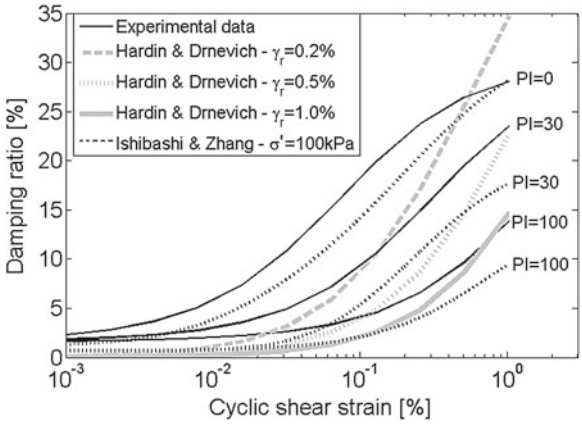

Fig. 6 Soil damping coefficient ξ as a function of cyclic shear strain γ_c: experimental curves versus models [4, 7]

The hysteretic damping coefficient resulting from (7a), (7b), (7c) can be expressed as [7]:

$$\xi = \frac{1 + e^{-0.0145IP^{1.3}}}{6}\left[0.586\left(\frac{G}{G_{\max}}\right)^2 - 1.547\frac{G}{G_{\max}} + 1\right] \tag{8}$$

The asymptotic value of ξ depends on the plasticity index $\left(\xi_{IP}^{\max} = \frac{1 + e^{-0.0145IP^{1.3}}}{6}\right)$, reaching a maximum of 33 % for IP = 0 and 18.3 % for IP = 50. This feature makes the Ishibashi and Zhang's model more flexible than the basic hyperbolic model [4] and applicable to several types of soils according to their plasticity attributes.

2.4 Experimental Evidence and Complicating Factors

Figure 6 presents a comparison between experimental curves established by Vucetic and Dobry [8] for soils of varying PI and the above theoretical formulations of the damping coefficient (6 and 8), for various reference strains. It can be noted that experimental values of ξ can typically range between 0 and 0.4.

In soils that are subject to cyclic degradation, such as loose sands or sensitive clays, the maximum shear stress (shear strength) $\tau_{\max}$ evolves as cycles accumulate. Such an evolution is not explicitly accounted for in the analytical models presented hereafter; rather it is accounted in the choice of an equivalent $\tau_{\max}$ that takes a representative number of cycles and degradability into account. That refinement can however be explicitly accounted for in the numerical models developed by Holeyman [9], where several degradation laws of $\tau_{\max}$ are implemented according to the local shear strain history.

2.5 More Advanced Models

Many more models have been developed by researchers attempting to capture various features of the complex soil behaviour. These can be approached by separating recoverable and non recoverable deformations, the latter being handled through plastic theory. Three-dimensional representations of the yield function in the stress space and the choice of flow rules in the strain space are then necessary, requiring the knowledge of up to tens of parameters that are difficult to determine experimentally for many engineering projects.

The separation between elastic and plastic domains can be circumvented by the use of so-called "Hypoplasticity", which appears to gain popularity thanks to a more reasonable number of parameters. While the initial hypoplastic model [10] required 8 parameters, those incorporating the intergranular concept and cyclic features [11] can go up to 13. That number contrasts with the more manageable 2 or 3 parameters necessary to understand what are believed to be the essentials of pile response used in the remainder of this invited contribution. Moreover the basic parameters used (e and PI or $G_{\max}$ and $\tau_{\max}$) are standard geotechnical parameters widely available from customary site characterization.

3 Problem Statement and Linear Solution

3.1 Idealized Conditions

The problem considered in this chapter involves a vertical cylindrical floating pile shaft of infinite length and rigidity, embedded within an infinite homogeneous soil medium. The pile shaft is subjected to a purely harmonic axial displacement prescribed by $w_0 = w_{0c} \cdot \cos \omega t$ where w_{0c} is the amplitude of displacement of the pile shaft, and ω is the circular frequency, and t the time. The examined system is a unit slice of the problem as shown on Fig. 7, isolating a single pile shaft segment and associated unit thickness soil layer of infinite radial extent. Plane strain conditions prevail across any horizontal slice because of the infinite extent of the considered problem in the axial direction and uniformity of the prescribed movement along the vertical direction. The layer outside the pile can be viewed as an infinite shear plate with a circular hole about which the harmonic vertical motion is prescribed.

The prescribed dynamic displacement generates cyclic deformations and stresses within the analyzed soil layer shown on Fig. 7 that can be represented by $\tau_c \cdot \cos(\omega t - \theta)$ where τ_c is the stress at radial distance r and θ is the phase difference with respect to the displacement applied at the soil-shaft interface.

In practice, stress anisotropy induced due to the weight of the soil will result in a specific distribution of the shear modulus with depth. Furthermore, soil layering is not homogeneous as the pile can endure axial compression, making the infinite

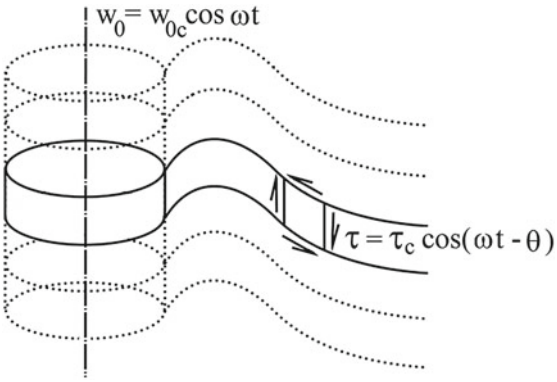

Fig. 7 Unit layer considered within infinite pile shaft and embedding soil

extent of the pile and surrounding soil assumption less legitimate. Averaging of soil properties along the depth of the pile shaft should be considered prior to using a single layer model.

Relationship between shear stress and shear strain under undrained conditions will be assumed to follow the soil model suggested by Hardin and Drnevich [4] and based on Kondner [6] formulation.

3.2 Soil Impedance to Pile Shaft Movement

Under the assumption of small deformations and absence of slippage at the pile shaft-soil interface, and provided radial deformations as well as the pile mass effect can be neglected in the analysis, the differential equation describing the vertical motion $w(r, t)$ of a floating rigid pile shaft embedded in a homogeneous isotropic elastic soil medium of shear modulus G and volumetric mass ρ is given by:

$$G\frac{\partial^2 w}{\partial r^2} + \left(\frac{G}{r} + \frac{\partial G}{\partial r}\right) \cdot \frac{\partial w}{\partial r} = \rho \cdot \frac{\partial^2 w}{\partial t^2} \tag{9}$$

Let us consider further that the vertical movement is harmonic and stationary; it can be characterized by the following relationship: $w(r, t) = w_c \cdot e^{i\omega t}$, where w_c is the amplitude of the soil displacement that solely depends on the radial distance r. Assuming hysteretic energy losses can be handled at a given frequency by an equivalent viscous-elastic shear modulus $G^* = G.(1 + 2i\xi)$, the equation of movement becomes:

$$G^*\frac{\partial^2 w}{\partial r^2} + \left(\frac{G^*}{r} + \frac{\partial G^*}{\partial r}\right) \cdot \frac{\partial w}{\partial r} = \rho \cdot \frac{\partial^2 w}{\partial t^2} \tag{10}$$

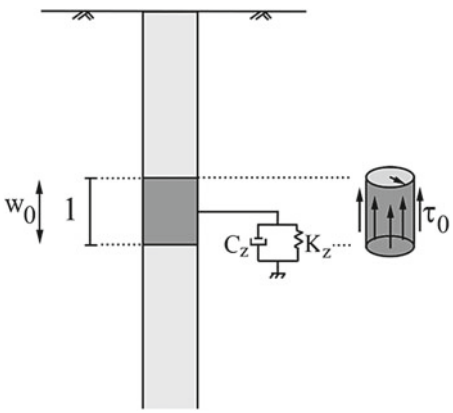

Fig. 8 Equivalent Winkler spring-dashpot soil model supporting the pile shaft

Extending the Winkler concept introduced in Sect. 1.3, the dynamic reaction of the soil surrounding the pile shaft may be expressed with reference to an equivalent spring-dashpot system anchored to a stationary point, as illustrated by Fig. 8. The dynamic soil reaction opposing the prescribed pile shaft movement can then be expressed as

$$P_z(r,t) = C_z \cdot \dot{w}(r,t) + K_z \cdot w(r,t) \tag{11}$$

with P_z the soil reaction per unit length of shaft, C_z the damping coefficient and K_z the stiffness coefficient. Since the problem has been stated within a unit thickness soil layer, it should be noted that P_z, C_z, and K_z are expressed per unit length of pile shaft, and thus typically in the following respective units (kN/m), (kPa/s), and (kPa).

Assuming $P_z(r,t)$ is harmonic, we can define the unit (lineal) shear impedance of the soil against the pile shaft movement in the z direction as:

$$\begin{aligned} I_z &= \tfrac{P_{zc}}{w_c} = (C_z \cdot i \cdot \omega + K_z) \\ &= G_{s0}(C_{za} \cdot i + K_{za}) = \tfrac{2\pi \cdot r_0}{w_c(r_0)} \cdot \tau_c(r_0) \end{aligned} \tag{12}$$

with G_{s0} the shear modulus at the pile shaft-soil interface ($r = r_0$), and

$$K_{za} = \Re\{I_z\}/G_{s0} \tag{13}$$

$$C_{za} = \Im\{I_z\}/(\omega \cdot G_{s0})$$

are the dimensionless stiffness and damping parameters, respectively.

3.3 Analytical Solution for Equivalent Medium

Assuming that the shear modulus is independent of the radial distance r to the pile shaft, a unique shear wave velocity can be defined as: $V_s = \sqrt{G_s/\rho}$ for a purely elastic medium (or $V_s^* = \sqrt{G_s^*/\rho}$ for the equivalent visco-elastic medium) (10) can be thus expressed as:

$$\frac{\partial^2 w_c}{\partial r^2} + \frac{1}{r} \cdot \frac{\partial w_c}{\partial r} + (k^*)^2 \cdot w_c = 0 \tag{14}$$

where $k = \omega / V_s$ is the shear wave number, the asterisk indicating that the viscous soil behavior (characterized by the Kelvin-Voigt formulation) is taken into consideration, i.e. $k^* = \omega / V_s^*$.

Defining the dimensionless frequency for the pile shaft-soil interface as $a = \omega \cdot r_0 / V_s$ or $a^* = \omega \cdot r_0 / V_s^*$, the general solution of (14) is given by

$$w_c = w_{0c} \cdot H_0^{(2)} \left(a^* . \frac{r}{r_0} \right) / H_0^{(2)} \left(a^* \right) \tag{15}$$

with $H_\upsilon^{(2)} = J_\upsilon - i \cdot Y_\upsilon$ the Hankel function and J_ν, Y_ν, Bessel functions of order υ of the first and second type, respectively. Based on the $\tau(r,t) = G^* \cdot \partial w(r,t)/\partial r$ relationship, the solution can also be expressed in terms of stress amplitudes:

$$\tau_c = G_s \cdot (1 + 2i\xi) \cdot \frac{a^* \cdot w_{0c}}{r_0} \cdot H_1^{(2)} \left(a^* \cdot \frac{r}{r_0} \right) / H_0^{(2)} \left(a^* \right) \tag{16}$$

Particular solutions can be obtained by applying adequate boundary conditions. A first boundary condition corresponds to the imposed displacement at the pile shaft-soil interface, i.e. $w_c = w_{0c}$ for $r = r_0$. The second boundary condition is a radiation condition imposing that the wave should only propagate away from the vibration source at the outer boundary ($w(r \to \infty, t)$, also known as "Sommerfeld" condition [12]).

$$\begin{aligned} &\to \bar{w}_c(r) = \sqrt{\Re^2 \{w_c(r)\} + \Im^2 \{w_c(r)\}} \\ &= w_{0c} \sqrt{\frac{J_0^2 \cdot \left(a \cdot \frac{r}{r_0} \right) + Y_0^2 \cdot \left(a \frac{r}{r_0} \right)}{J_0^2 \cdot (a) + Y_0^2 \cdot (a)}} \end{aligned} \tag{17}$$

$$\begin{aligned} &\to \bar{\tau}_c(r) = \sqrt{\Re^2 \{\tau_c(r)\} + \Im^2 \{\tau_c(r)\}} \\ &= G_s \cdot \frac{a \cdot w_{0c}}{r_0} \cdot \sqrt{\frac{J_1^2 \cdot \left(a \cdot \frac{r}{r_0} \right) + Y_1^2 \cdot \left(a \cdot \frac{r}{r_0} \right)}{J_0^2 \cdot (a) + Y_0^2 \cdot (a)}} \end{aligned} \tag{18}$$

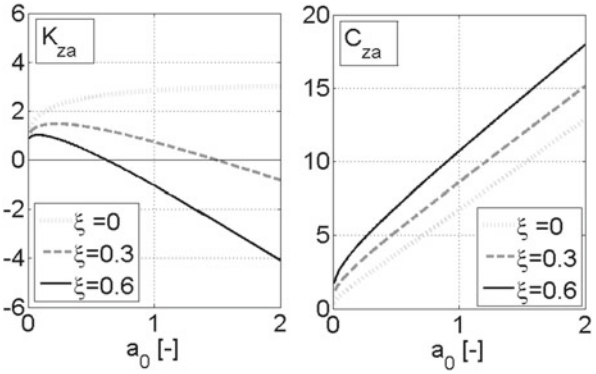

Fig. 9 Impedance parameters for homogeneous shear modulus

Using (8) we deduce the equivalent impedance:

$$I_z = -2\pi \cdot a^* \cdot G_s(1 + 2i\xi) \cdot \frac{H_1^{(2)}(a^*)}{H_0^{(2)}(a^*)} \tag{19}$$

Dimensionless impedance parameters defined by (12) and (13) are depicted in Fig. 9, emphasizing the influence of the hysteretic damping coefficient. In the absence of viscous damping ($\xi = 0$) only radiation or geometrical damping prevails. In that case, the stiffness parameter (real part $K_{z,a}$ of impedance) tends toward π for increasing frequencies ($a \to \infty$), per (9). Except for low a values, the dimensionless damping term $C_{z,a}$ linearly increases with frequencies at a rate of $\Delta C_{z,a} = 2\pi\,\Delta a$. An increased hysteretic damping coefficient enhances the quasi-linear increase of the total (hysteretic and radiation) damping term, but decreases the in-phase stiffness component. Figure 9 also shows that $K_{z,a}$ can become equal to 0 at particular values of a $\left(a_{(K_{z,a}=0)}\right)$, implying a potential for some form of 'resonance' effect. Influence of the hysteretic damping on the infinite annular shear plate apparent 'resonant' frequency can be appreciated in Fig. 10. The physical reason for that effect remains unclear, despite the fact that similar phenomena have been experimentally observed on model tests [13].

Typical results expressed in terms of dimensionless displacement and stress amplitudes profiles are presented in Fig. 11 for two dimensionless frequency values and two damping coefficients. The dimensionless displacement (stress) amplitude is the ratio between the displacement (stress) amplitude w_c (τ_c) at a given radial distance to that w_{0c} (τ_{0c}) at the pile shaft-soil interface.

For $\xi = 0$ and high a values, displacement amplitudes attenuate according to the inverse of the square root of the radial distance, while for $\xi = 0$ and low a values, shear stress amplitudes attenuate according to the inverse of the radial distance. These

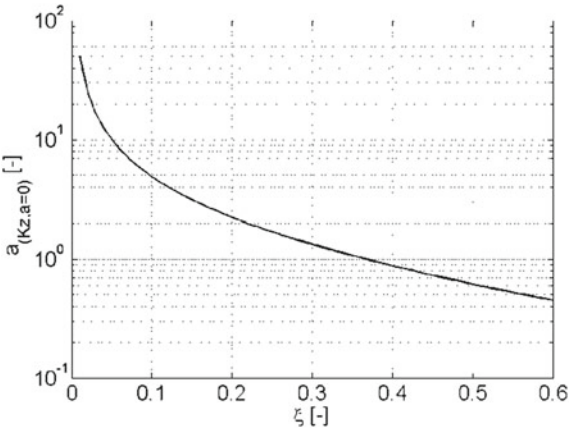

Fig. 10 Dimensionless "resonant" frequency of the soil annular shear plate versus hysteretic damping coefficient

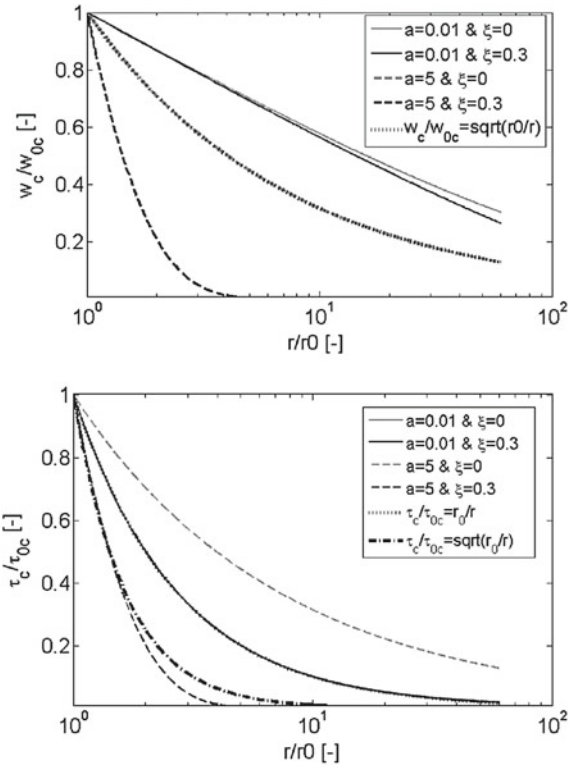

Fig. 11 Radial distribution of displacement and shear stress amplitudes

results can be demonstrated by considering the asymptotic behavior of the Bessel functions for $a \rightarrow \infty$ (17) and (18). It can also be noted that material damping enhances the radial attenuation of both displacement and stress amplitudes.

Impedance parameters for use in the Winkler approach have been studied by many researchers in the past. First models (e.g. Novak [14]) were based on the assumptions that the soil behavior is governed by the laws of (viscous-) elasticity and the soil is perfectly bonded to the pile. In practice however the soil region immediately adjacent to the pile can undergo a large degree of straining which causes the soil-structure system to behave non-linearly and even degrade under cyclic loading. Slippage can also occur about the contact area.

4 Nonlinear Aspects

4.1 Literature Review

Nonlinear models of axial pile-soil vibration started with the works of Novak and Sheta [15], Mitwally and Novak [16], Han and Sabin [17], and El Naggar and Novak [18, 19] who suggested distinguishing two separate radial soil zones around the pile shaft: an inner zone with reduced shear stiffness and an outer zone where the elastic solution is considered.

To eliminate undulations in the impedance functions due to wave reflections from the interface between the two media, some researchers proposed a continuously increasing modulus with radial distance to the pile shaft. Gazetas and Dobry [20] and Veletos and Dotson [21] suggested schemes in which the modulus increased unboundedly. Han and Sabin [17] formulated impedances based on a parabolic variation of the medium properties so that the inner zone has properties smoothly approaching those of the outer zone.

These contributions however address the problem of lateral soil heterogeneity with only qualitative reference to the nonlinear soil response, since the variations of soil properties invoked are merely hypothetical. To aid practical applications, Michaelides et al. [22, 23] utilized experimental data (e.g. Vucetic and Dobry [8]) characterizing the dependence of the secant shear modulus and hysteretic damping of soil on the shear strain amplitude and the nature of the soil (the latter represented by the plasticity index PI). The variation of modulus and damping is then related to the magnitude of the applied load through the amplitude of the shear strains induced within a succession of co-axial cylinders. Such an approach involves assumptions related to the shear stress distribution and implies the use of an iterative procedure to calculate the variation of modulus as a function of the distance to the pile shaft.

Some modifications to the Michaelides et al.'s model have been proposed by Holeyman et al. [24] to simplify definitions of the model parameters as well as calculation procedures. Using the modified method, a refined soil discretization can be achieved based on more rigorous soil behavior description and without a priori assumptions about the shear modulus or shear stress radial distributions.

The following sections describe analytical solutions assuming various theoretical radial variations of shear modulus. The results are evaluated over a range of parameters and compared with those obtained from the semi-analytical model derived from [22, 23], and from a radial discrete model simulating the pile shaft and soil movements by integrating of the laws of motion [25–27] (pile driving model), [9, 28, 29] (Vibratory pile driving).

4.2 Radius-Dependent Shear Modulus

Assuming that the stress developed into the soil attenuates according to the inverse of the radial distance, which is exact in the static case, the following can be established: $\tau/\tau_0 = r_0/r$. If we further consider that the stress τ_0 is a fraction f of the shear strength $\tau_{\max}$, i.e. $\tau/\tau_{\max} = f \cdot r_0/r$, (5) becomes:

$$G_s = G_{\max} \cdot \left(1 - f \cdot \left(\frac{r_0}{r}\right)\right) \tag{20}$$

where f can be viewed as a "loading factor" or soil strength mobilization ratio at $r = r_0$: it is actually the inverse of the factor of safety of the pile shaft capacity.

Because of the variation of the shear modulus with the radial distance, two extreme shear wave velocities can be distinguished: $V_{s0} = \sqrt{G_{s0}/\rho}$ at the pile shaft-soil interface and $V_{ff} = \sqrt{G_{\max}/\rho}$ in the free field at the furthest distance away from the pile. Dimensionless frequencies can thus be defined respectively for the pile shaft-soil interface: $a_0 = \omega \cdot r_0/V_{s0}$ (or $a_0^* = a_0/\sqrt{1+2i\xi} = \omega \cdot r_0/V_{s0}^*$) and the free-field: $a_{ff} = \omega \cdot r_0/V_{ff}$ (or $a_{ff}^* = a_{ff}/\sqrt{1+2i\xi}$). Defining $\varsigma = r/r_0 > 1$ the dimensionless distance to the pile shaft, the general equation of movement becomes:

$$\frac{\partial^2 w_c}{\partial \zeta^2} + \frac{1}{\zeta} \cdot \frac{\zeta}{\zeta - f} \cdot \frac{\partial w_c}{\partial \zeta} + (a_{ff}^*)^2 \cdot \frac{\zeta}{\zeta - f} \cdot w_c = 0 \tag{21}$$

Analytical solutions of (21) are presented in [24] and discussed below. Influence of the 'f' parameter on the shear modulus distribution is depicted in Fig. 12. The reader is referred to Bertin [30] for solutions based on other assumptions of shear modulus distributions.

4.3 Semi-analytical Solutions

Michaelides et al. [22, 23] suggested the use of a radial discretization and approximation of the shear modulus G_s distribution within each zone using the following expression

$$G = G_{s0}^* \cdot \left(\frac{r}{r_0}\right)^m \tag{22}$$

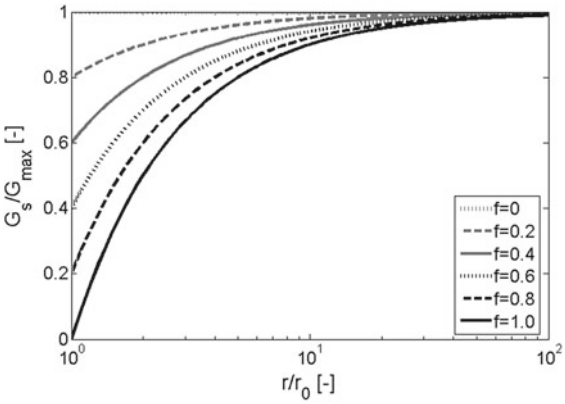

Fig. 12 Influence of 'f' parameter on the shear modulus distribution, assuming stress attenuation according to r^{-1}

with m values decreasing with the distance to the pile shaft. This discretization also allows taking into account damping coefficients ξ varying with r, albeit through a piecewise approximation.

Michaelides et al. assume that the shear stress distribution is independent from the shear modulus distribution, in order to alleviate interdependence between G_s, τ_c and γ_c. Based on this assumption and the use of empirical rules for the shear modulus distribution, they proposed following equation:

$$G_s = G_{\max} \cdot \left(1 - \left\{\Lambda \cdot \frac{r_0}{r} \cdot h(a_r)\right\}^{0.72}\right) \tag{23}$$

where $\Lambda = \tau/\tau_{\max}$ is a loading intensity factor and $h(a_r)$ a shape function. Since the method imposes the use of iterations to determine $h(a_r)$ values, Michaelides limited the number of radial increments to four. That approximation has been further enhanced by Bertin [30], who developed a special routine able to iterate on many more radial increments.

Because of the limitations of the Michaelides et al.'s method, Bertin [30] suggested another approach based on analytical elements to discretize the radial coordinate. The shear modulus distribution is still described by a set of parabolas, but based on the Hardin and Drnevich [4] functions and Masing rules [5]. Furthermore, a higher number of radial steps, up to 270, is considered. Because values of m and ξ are different for each element, displacements and stresses are obtained by assuring continuity of displacement and stress equilibrium. For each discretization step, the following (24) are used:

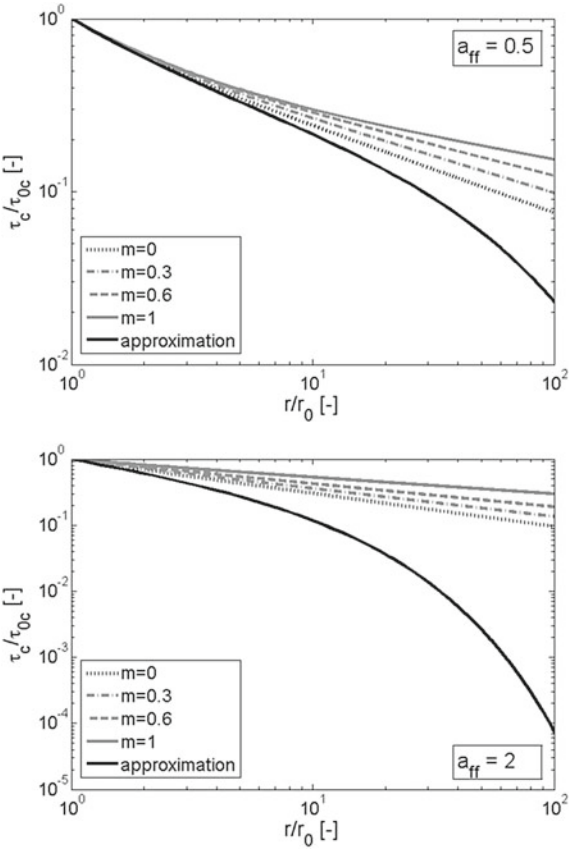

Fig. 13 Shear stress radial distributions for different values of m exponent compared to [30] enhanced approximation

$$w_c(r) = \begin{cases} \zeta_{(i-1)}^{m_0/2} \cdot \begin{bmatrix} A_{(i-1)} \cdot J_{\chi_{(i-1)}-1} \cdot \left(\chi_{(i-1)} \cdot \lambda_{0_{(i-1)}} \cdot \zeta_{(i-1)}^{1/\chi_{(i-1)}}\right) \\ +B_{(i-1)} \cdot Y_{\chi_{(i-1)}-1} \cdot \left(\chi_{(i-1)} \cdot \lambda_{0_{(i-1)}} \cdot \zeta_{(i-1)}^{1/\chi_{(i-1)}}\right) \end{bmatrix} & if\ r \le r_i \\ \zeta_{(i)}^{m_1/2} \cdot \begin{bmatrix} A_{(i)} \cdot J_{\chi_{(i)}-1} \cdot \left(\chi_{(i)} \cdot \lambda_{0_{(i)}} \cdot \zeta_{(i)}^{1/\chi_{(i)}}\right) \\ +B_{(i)} \cdot Y_{\chi_{(i)}-1} \cdot \left(\chi_{(i)} \cdot \lambda_{(i)} \cdot \zeta_{(i)}^{1/\chi_{(i)}}\right) \end{bmatrix} & if\ r_i \le r \le r_{i+1} \end{cases} \tag{24}$$

The four integration constants $A_{(i-1)}, A_{(i)}, B_{(i-1)}$ and $B_{(i)}$ are deduced from continuity and equilibrium conditions, adopting previously described boundary conditions (imposed displacement and outer radiation).

As illustrated by Fig. 13, Bertin analytical elements approximation [30] emulating Michaelides et al.'s concept is correct for low values of the dimensionless frequency, but is more questionable for higher values.

4.4 Numerical Solution

4.4.1 Model

Holeyman [26–29] has suggested the use of a radial discrete model (see Fig. 14) to calculate the vertical shear waves propagating away from the pile shaft. The pile is considered as a rigid body and the soil is represented by discretizing the medium into concentric rings that have their own individual masses and that transmit forces to their neighbouring ones. The movement of the pile and the rings is calculated from time integration of the law of motion: the equations of movement are integrated for each cylinder based on their dynamic shear equilibrium in the vertical direction. An energy absorbing boundary condition in accordance with plane-strain elasticity theory [14] limits the lateral extent of the model.

The model makes use of constitutive relationships representing the large-strain, dynamic and cyclic shear stress-strain strength behavior of the medium surrounding the pile shaft. Initially implemented for vibratory driving modeling in a Basic computer code "Hipervib-II" [9], it applied the hyperbolic Kondner law (4) and Masing rules [5] to model the shear force-displacement relationships between successive rings.

The program was further developed using Matlab® routines [30] to produce the results presented herein with a view to compare them with the above described semi-analytical methods. Strain rate effects as well as cyclic degradation effects which are accounted for in the Hipervib-II program were however disabled to produce results compatible with the assumptions adopted in the other methods discussed in this paper.

When comparing Hipervib-II with the (semi-) analytical methods, following considerations are made: (a) only results corresponding to the steady state (after a few second of simulations) are presented herein, (b) impedance parameters are calculated as follows:

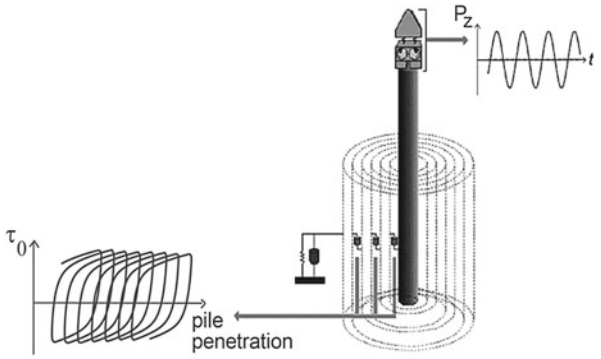

Fig. 14 Numerical model geometry (adapted from [28])

$$I_z = 2\pi \cdot r_0 \cdot \frac{\int_0^{2\pi/\omega} \tau(r_0, t)dt}{\int_0^{2\pi/\omega} w(r_0, t)dt} \tag{25}$$

with $w(t)$ imposed at the pile shaft boundary and $\tau(t)$ calculated by Hipervib-II at the pile shaft-soil interface. In order to compare the numerical results with the analytical ones presented herein for the shaft only, the base resistance that can be modeled in Hipervib-II has been set to zero.

4.4.2 Radial Distribution of Shear Modulus

Relevant results are related to the evolution of the shear modulus as a function of the radial distance, by reference to its value at the pile shaft-soil interface. Figure 15 shows results obtained with three methods: the analytical solution to (21), Michaelides et al. original approximation (4 increments, labelled as "M-4"), and Hipervib-II program.

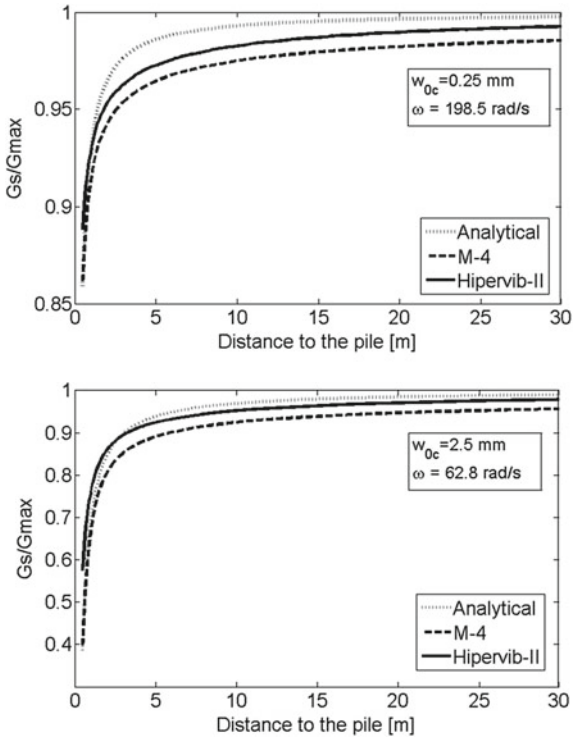

Fig. 15 Shear modulus distributions according to different approaches for same acceleration amplitude of 9.9 m/s^2

Table 1 Reference parameters for comparative study

Soil density (ρ)	1.8	T/m^3
Maximum shear modulus (G_{max})	60	MPa
Free field shear wave celerity (V_{ff})	183	m/s
Shear strength ($\tau_{\max}$)	0.15	MPa
Reference shear strain (γ_r)	1.25	10^{-3}
Hysteretic damping value (ξ)	0	–
Pile shaft radius (r_0)	0.5	m

Reference parameters used to that end are summarized in Table 1, for two different combinations of imposed displacement amplitude and frequency leading to a given acceleration amplitude of 9.9 m/s^2.

For the same imposed acceleration amplitude ($w_{0c} \cdot \omega^2$), all three methods indicate a more heavily degraded shear modulus at the pile shaft-soil interface for a larger displacement amplitude. When however compared to the Michaelides original method, the analytical results [30] better match those of the numerical model.

4.5 Comparison of Calculated Impedance Parameters

Impedance parameters deduced from application of the semi-analytical method using Table 1 parameters are presented in Fig. 16 with a view to emphasize the influence of the imposed displacement amplitude. Figure 16 represents the real and imaginary parts of the impedance versus the dimensionless frequency a_{ff} for three displacement amplitudes.

Comments made for the homogeneous model in Sect. 3.3 are also applicable to the non-homogeneous models, as far as the evolution of the impedance curves as functions of the dimensionless frequency is concerned, when trading the hysteretic damping coefficient for the amplitude of displacement. A comparison between semi-analytical and analytical results is presented in Fig. 17, indicating some quantitative variations in the impedance results that mainly depend on the free field dimensionless frequency. In the above example, analytical results are quite close to the Bertin [30] approximation. If that observation could be extended to other values of w_{oc}/r_o *and* ξ, it would mean that the simplest form of stress attenuation (corresponding to the static case) could be adopted for the dynamic cases.

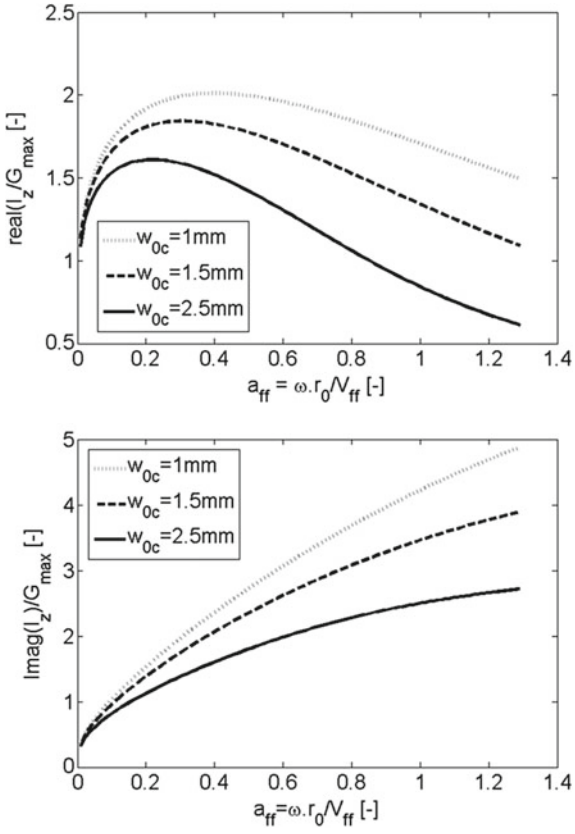

Fig. 16 Stiffness and damping parameters deduced from the semi-analytical method (see Table 1 for reference parameters)

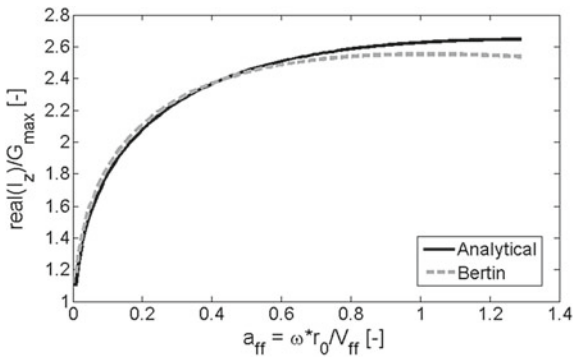

Fig. 17 Comparison of analytical and semi-analytical solutions for $w_{oc}/r_o = 0.4\ 10^{-3}$ (see Table 1 for reference parameters)

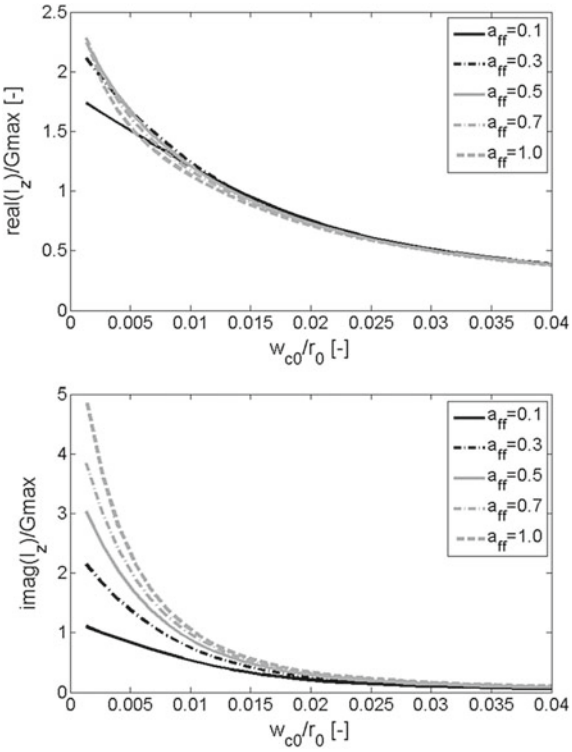

Fig. 18 Impedance parameters as functions of the imposed displacement (analytical model for Table 1 parameters)

Combined influences of frequency and imposed displacement amplitudes are represented in Fig. 18 for the analytical method. Both real and imaginary parts of the impedance decrease as the imposed displacement increases, whatever the frequency. Inspection of (12) and Fig. 19 shows how the stress value at the pile shaft-soil interface naturally tends towards the shear strength with increasing displacements, evidencing another manifestation of stiffness degradation.

The evolutions of the pile shaft friction mobilization ratio ($\tau_{oc}/\tau_{\max}$) versus dimensionless displacement (w_{oc}/r_o) shown in Fig. 19 can be compared to so-called "t-z curves" published in the literature to evaluate the pile shaft load-displacement behavior under axial static ($a_{ff} = 0$) conditions. As an example, static friction mobilization curves adopted by Holeyman [25] based on an extension of the influence radius R_m approach suggested by Randolph and Wroth [31] to incorporate a hyperbolic stress-strain law are also plotted in Fig. 19 for two values of the boundary radius R_m. Confirmation of the effective reduction of the apparent "quake" value as velocity increases, observed by Holeyman [7] can be found in Fig. 19 for increasing values of a_{ff}.

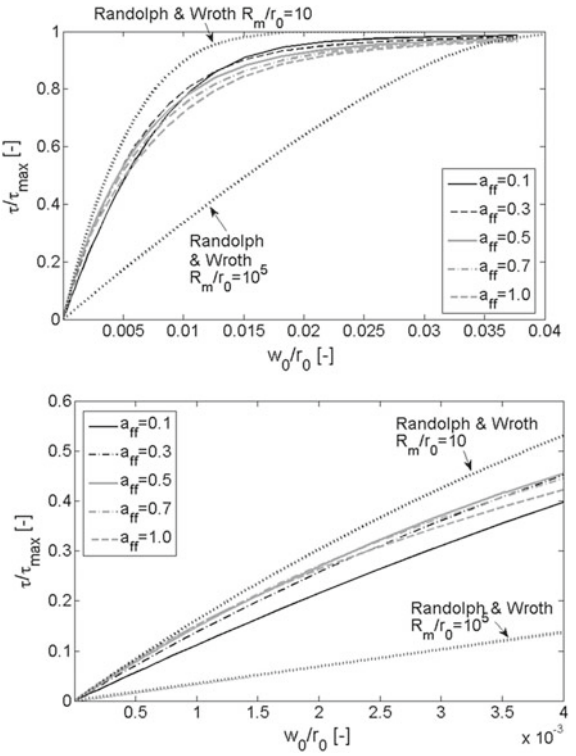

Fig. 19 Shear stress developed at the pile shaft-soil interface as a function of the imposed cyclic displacement amplitude (analytical model with Table 1 parameters vs. typical static t-z curve)

5 Conclusions

The dynamic axial response of pile shafts can be approached using the concept of a continuously distributed mechanical impedance replacing the embedding medium. Equivalent impedance parameters can be defined to characterize the equivalent in-phase 'spring' and the equivalent out-of-phase 'dashpot'. When considering a pile shaft undergoing axial oscillations, shear strains (and shear stresses) are induced in the surrounding soil, the amplitude of which attenuates radially away from the pile shaft. Analytical equivalent linear methods and a numerical method are shown to adequately derive those amplitudes of shear stresses and shear strains as functions of the radial distance r to the pile shaft. The corresponding dynamic impedance components are then readily determined.

The analytical solution proposed herein accommodates a continuous variation of soil properties alleviating wave reflections and avoiding numerical convergence problems. By contrast, the semi-analytical method suffers from numerical limitations arising from the radial soil discretization. The semi-analytical method correctly models a radial variation of the soil hysteretic damping, contrary to the analytical method which assumes a homogeneous hysteretic damping.

Similar approaches can be used to address the dynamic nonlinear response of piles under a lateral mode of deformation [32], as well as coupling effects between the axial and lateral modes of deformation [33].

References

1. Upwind—Integrated Wind Turbine Design. Project funded by the European Commission under the 6th (EC) RTD Project No. 019945 (SE6), (2010)
2. Smith, E.A.L.: Pile driving analysis by the wave equation. J. Soil Mech. Found. **86**(4), 35–61 (1960)
3. Hardin, B.O., Black, W.L.: Vibration modulus of normally consolidated clay. J. Soil Mech. Found. Div. ASCE **92**(2), 353–369 (1968)
4. Hardin, B.O., Drnevich, V.P.: Shear modulus and damping in soils: design equations and curves. J. Soil Mech. Found. Div. ASCE **98**(7), 667–692 (1972)
5. Masing, G., Eigenspannungen und Verfeistigung beim Messing. In: Proceedings of the 2nd International Congress of Applied Mechanics, pp. 332–335 (1926)
6. Kondner, R.L.: Hyperbolic stress-strain response: cohesive soils. J. Soil Mech. Found. Div. ASCE **89**(SM1), 115–143 (1963)
7. Ishibashi, I., Zhang, X.: Unified dynamic shear moduli and damping ratios of sand and clay. Soils Found. **33**(1), 182–191 (1993)
8. Vucetic, M., Dobry, R.: Effect of soil plasticity on cyclic response. J. Geotech. Eng. ASCE **117**(1), 89–107 (1991)
9. Holeyman, A.: HIPERVIB-II, A detailed numerical model proposed for future computer implementation to evaluate the penetration speed of vibratory driven sheet Piles Research report for BBRI. EarthSpectives, Irvine, CA, USA, 54p (1993)
10. Bauer, E.: Calibration of a comprehensive hypoplastic model for granular materials. Soils Found. **36**(1), 13–26 (1996)
11. Von Wolffersdorff, P.A.: A hypoplastic relation for granular materials with a predefined limit state surface. Mech. Cohesive-Frictional Mater. **1**, 251–271 (1996)
12. Sommerfeld, A.: Mechanics, Lectures on Theoretical Physics. Academic press Inc., New York (1952)
13. Storz, M.: Chaotic motion in pile-driving. First International Conference Soil Dynamics and Earthquake Engineering. Southhampton, England: Computational Mechanics, pp. 503–512 (1991)
14. Novak, M.: Dynamic stiffness and damping of piles Can. Geotech. J. **11**(4), 574–598 (1974)
15. Novak, M., Sheta, M.: Approximate approach to contact effects of piles. In: O'Neill M. W., Dobry R. (eds.) Special technical publication on dynamic response of pile foundations: analytical aspects. New York, ASCE (1980)
16. Mitwally, H., Novak, M.: Pile driving analysis using shaft and FEM. In: Proceedings of the third international conference on the application of stress wave theory to piles. Bitech Publishers, Vancouver (1988)
17. Han, Y.C., Sabin, G.C.: Impedances for radially inhomogeneous viscoelastic soil media. J. Eng. Mech. **121**(9), 939–947 (1995)
18. El Naggar, M., Novak, M.: Nonlinear axial interaction in pile dynamics. J. Geotech. Eng. **120**(4), 678–696 (1994)
19. El Naggar, M., Novak, M.: Nonlinear model for dynamic axial pile response. J. Geotech. Eng. **120**(2), 308–329 (1994)
20. Gazetas, G., Dobry, R.: Simple radiation damping model for piles and footings. J. Eng. Mech. ASCE **10**(6), 937–956 (1984)
21. Veletsos, A.S., Dotson, K.W.: Vertical and torsional vibration of foundations in inhomogeneous media. J. Geotech. Eng. Div. ASCE **114**(9), 1002–1021 (1988)

22. Michaelides, O., Gazetas, G., Bouckovalas, G., Chrysikou, E.: Approximate nonlinear dynamic axial response of piles. Geotechnique **48**(1), 33–53 (1997)
23. Michaelides, O., Bouckovalas, G., Gazetas, G.: Non-linear soil properties and impedances for axially vibrating pile elements. Soils Found. **38**(3), 129–142 (1988)
24. Holeyman, A., Bertin, R., Whenham, V.: Impdedance of pile shafts under axial vibratory loads. Soil Dyn. Earthq. Eng. **44**, 115–126 (2013). doi:10.1016/j.soildyn.2012.09.006
25. Holeyman, A.: Contribution à l'étude du comportement transitoire non-linéaire des pieux pendant leur battage. Doctoral thesis, Université Libre de Bruxelles, April 1984, 584p (1984)
26. Holeyman, A.: Dynamic non-linear skin friction of piles. In: Proceedings of the International Symposium on Penetrability and Drivability of Piles, vol. 1, San Francisco, 10 Aug, pp. 173–176 (1985)
27. Holeyman, A.: Technology of pile dynamic testing. In: Barends, F. (ed.) Application of Stress-Wave Theory to Piles, pp. 195–215. Rotterdam, Balkema (1992)
28. Holeyman, A., Legrand, C.: Soil modeling for pile vibratory driving. In: U.S. FHWA International Conference on Design and Construction of Deep Foundations, Orlando, Florida, Dec 1994, vol. II, pp. 1165–1178 (1994)
29. Holeyman, A.: Vibratory Pile Driving. In: Nyyama S., Beim J. (eds.) Quality Assurance on Land and Offshore Piling, Balkema Publishers, Rotterdam, pp. 479–494 (2000)
30. Bertin, R.: Modélisation de l'interaction axiale sol-pieu—Détermination des paramètres d'impédance d'un milieu non-homogène, MS thesis, Université Catholique de Louvain (2009)
31. Randolph, M.F., Wroth, C.P.: Analysis of deformation of vertically loaded piles. J. Geotech. Eng. Div. ASCE **104**(GT12), 1465–1488 (1978)
32. Malek, A., Holeyman, A.: Flexural analysis in dynamic pinned head pile testing. Geotech. Geol. Eng. **32**, 59–70 (2014)
33. Malek, A., Holeyman, A.: Numerical evaluation of nonlinear lateral pile vibrations on nonlinear axial response of pile shaft. Soils Found. (2013). doi:10.1016/j.sandf.2013.04.002

Linear and Nonlinear Damping Effects on the Stability of the Ziegler Column

Angelo Luongo and Francesco D'Annibale

Abstract The destabilizing effect of damping on both linear and nonlinear behavior of the Ziegler column is discussed. The paper addresses classical and non-classical aspects related to the 'Ziegler paradox'. First, the linear problem is illustrated in a new perspective, according to which no discontinuities in the critical load exist between undamped and damped systems. Second, it furnishes a first overview of the mechanical behavior of the system in the post-critical range. The equations of motion for the system are derived via the extended Hamilton's principle. Then a linear stability analysis is performed via a perturbation approach, in which, however, simple and not double eigenvalues are perturbed, in contrast with a commonly pursued strategy in the literature. According to this idea, a series expansion around the distinct purely imaginary eigenvalues of the undamped and under-critically loaded system is carried out, with the load kept as a fixed, although unknown, parameter. By pursuing the same idea, an algorithm based on the Multiple Scale Method is developed to investigate the post-critical behavior of the system. The role played by the nonlinear damping on the existence of limit-cycles is discussed.

1 Introduction

The Ziegler Paradox is a well-known mechanical phenomenon, according to which when a strictly dissipative and vanishing damping is added to a linear *circulatory* system (i.e. to an undamped system loaded by a positional nonconservative force) a finite lowering of the critical load is experienced. Thus, in spite of the confidence we have with damping, when added to conservative system, the same damping could have a detrimental effect when added to nonconservative systems [1–6].

A. Luongo (✉) · F. D'Annibale
M&MoCS - University of L'Aquila, Via Giovanni Gronchi, 67100 L'Aquila (AQ), Italy
e-mail: angelo.luongo@univaq.it

F. D'Annibale
e-mail: francesco.dannibale@univaq.it

M. Belhaq (ed.), *Structural Nonlinear Dynamics and Diagnosis*,
Springer Proceedings in Physics 168, DOI 10.1007/978-3-319-19851-4_16

The paradox attracted the attention of dozens of researchers. An exhaustive review of the argument is given in [7], which the reader is referred to. Recently, the authors of the present paper gave a new key for an understanding of the problem [8, 9], using a perturbation method in a way which is *not* the usual way followed in the literature (e.g. [10–12]). It was shown there, that the best way of looking at the phenomenon consists in considering the damped critical system *not* as a perturbation of the (unique and known) undamped critical system (a point of view which leads to the amazing paradox), but rather as a perturbation of one of the infinitely many (and therefore unknown) undamped *stable* systems (a point of view for which no surprises arise at all). In other words the destabilization paradox is caused by the transformation of a marginally stable circulatory system (which cannot be rendered unstable below the critical load) into an incipiently unstable system, when it is embedded in a larger class of damped system (where destabilization is instead possible at this lower load).

After having accepted the idea that damping can be destabilizing, one should ask to himself if such a destabilization has 'practical' effects on the mechanical system. Since the previous reasoning revealed us that the system loses stability through a (simple) Hopf bifurcation, we expect that a limit-cycle exists around the bifurcation point, so that, if this is supercritical, the motion is confined to a neighborhood of the equilibrium. To check this property, a nonlinear analysis has to be carried out. However, in spite of the obvious curiosity a researcher should have about this question, it seems, at the best of the author's knowledge, that this problem has not been exhaustively addressed in the literature, yet (except for [13] where a particular system has been studied).

In this paper, a first analysis of the nonlinear problem is attempted. Guided by the considerations developed for the linear stability analysis, a perturbation procedure, based on a proper use of the Multiple Scale Method, is developed here, leading to a bifurcation equation governing the formation and stability of a limit-cycle close to the Hopf bifurcation point. Qualitative and quantitative information is drawn from this equation.

The paper is organized as follows. In Sect. 2, the nonlinear model of the Ziegler column is derived. In Sect. 3, a synthesis of previous results of the literature concerning the linear stability analysis is given. In Sect. 4 the nonlinear problem is addressed via the Multiple Scale Method, and numerical results are presented. Section 5 resumes the main conclusions and an Appendix furnishes details.

2 The Model

The equations of motion of the upward double-pendulum depicted in Fig. 1, are derived for finite rotations. The system consists of a two hinged weightless rigid bars of equal length ℓ, carrying two concentrated masses, $m_1 := 2m$ at the common hinge (point B in the figure), and $m_2 := m$ at the tip (point C in the figure), viscoelastically constrained at the hinges by: (a) two linear springs of stiffness $k_1 := k$ and $k_2 := k$ and (b) two nonlinear (cubic) dashpots of Van der Pol type, having linear

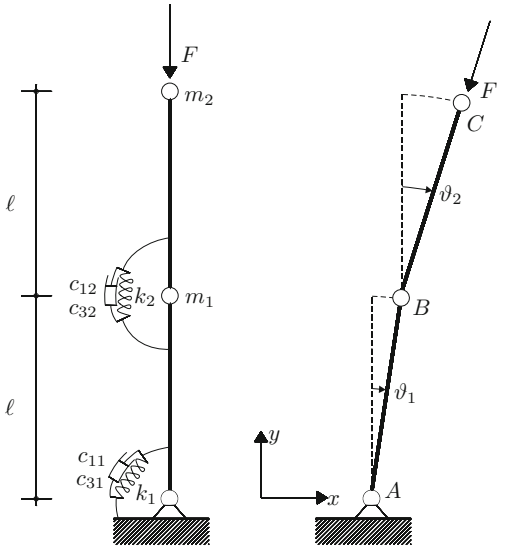

Fig. 1 Nonlinear Ziegler column

viscosity coefficients c_{11} and c_{12}, respectively, and cubic viscosity coefficients c_{31} and c_{32}. The system is loaded at the free end by a follower force of intensity F, which keeps his direction parallel to the upper bar. When infinitesimal rotations of the two bars are considered and when nonlinear viscous damping is neglected, the system degenerates into the well-known Ziegler column [1].

By following the Extended Hamilton's approach, the following variational principle must be satisfied:

$$\delta\mathcal{H} := \int_{t_1}^{t_2} (\delta\mathcal{T} - \delta\mathcal{W}_{int} + \delta\mathcal{W}_{ext})\,\mathrm{d}t = 0 \tag{1}$$

for any kinematically admissible motions. Here $\delta\mathcal{T}$ is the variation of the kinetic energy, $\delta\mathcal{W}_{int}$ is the virtual internal work done by the visco-elastic constraints and $\delta\mathcal{W}_{ext}$ is the virtual external work done by the follower force.

By taking the rotations of the two bars as Lagrangian coordinates, viz. ϑ_1 and ϑ_2, the following kinematic relations hold:

$$\begin{aligned} u_B &= \ell \sin(\vartheta_1) \\ v_B &= -\ell\,[1 - \cos(\vartheta_1)] \\ u_C &= \ell\,[\sin(\vartheta_1) + \sin(\vartheta_2)] \\ v_C &= -\ell\,[2 - \cos(\vartheta_1) - \cos(\vartheta_2)] \\ \chi_1 &= \vartheta_1 \\ \chi_2 &= \vartheta_2 - \vartheta_1 \end{aligned} \tag{2}$$

being u_H and v_H ($H = B, C$) the horizontal and vertical displacements of the hinges, respectively, and χ_j ($j = 1, 2$) the 'lumped curvatures' (i.e. the relative rotations) at the hinges.

The constitutive behavior of the visco-elastic devices is taken in the following form:

$$M_j = k_j \chi_j + c_{1j} \dot{\chi}_j + c_{3j} \chi_j^2 \dot{\chi}_j, \quad j = 1, 2 \tag{3}$$

where M_j ($j = 1, 2$) are the internal couples, k_j, c_{1j}, c_{3j} ($j = 1, 2$) are the constitutive constants referred to elasticity of the springs, linear and cubic (Van der Pol) part of viscous damping.

The first variation $\delta\mathcal{T}$, and the virtual works $\delta\mathcal{W}_{int}$ and $\delta\mathcal{W}_{ext}$, appearing in (1), can be, therefore, written as:

$$\begin{aligned} \delta\mathcal{T} &:= m_1 \left(\dot{u}_B \delta\dot{u}_B + \dot{v}_B \delta\dot{v}_B\right) + m_2 \left(\dot{u}_C \delta\dot{u}_C + \dot{v}_C \delta\dot{v}_C\right) \\ \delta\mathcal{W}_{int} &:= M_1 \delta\chi_1 + M_2 \delta\chi_2 \\ \delta\mathcal{W}_{ext} &:= -F \left[\sin\left(\vartheta_2\right) \delta u_C + \cos\left(\vartheta_2\right) \delta v_C\right] \end{aligned} \tag{4}$$

By using (4) and (2) in (1) and integrating by parts, the following balance equations are obtained:

$$\begin{cases} \left(m_1 + m_2\right) \ell^2 \ddot{\vartheta}_1 + m_2 \ell^2 \ddot{\vartheta}_2 \cos\left(\vartheta_1 - \vartheta_2\right) + m_2 \ell^2 \dot{\vartheta}_2^2 \sin\left(\vartheta_1 - \vartheta_2\right) + M_1 \\ \quad - M_2 - F\ell \sin\left(\vartheta_1 - \vartheta_2\right) = 0 \\ m_2 \ell^2 \ddot{\vartheta}_2 + m_2 \ell^2 \ddot{\vartheta}_1 \cos\left(\vartheta_1 - \vartheta_2\right) - m_2 \ell^2 \dot{\vartheta}_1^2 \sin\left(\vartheta_1 - \vartheta_2\right) + M_2 = 0 \end{cases} \tag{5}$$

Then, by substituting (3) in (5) and by introducing the following quantities (accounting for $m_1 = 2m, m_2 = m, k_1 = k_2 = k$):

$$\begin{aligned} &\tau = \omega t, \quad \omega^2 = \frac{k}{m\ell^2}, \quad \mu = \frac{F}{m\ell\omega^2} \\ &\xi_1 = \frac{c_{11}}{m\ell^2\omega}, \quad \xi_2 = \frac{c_{12}}{m\ell^2\omega}, \quad \zeta_1 = \frac{c_{31}}{m\ell^2\omega}, \quad \zeta_2 = \frac{c_{32}}{m\ell^2\omega} \end{aligned} \tag{6}$$

the nondimensional form of the equations of motion is finally obtained:

$$\begin{cases} 3\ddot{\vartheta}_1 + \ddot{\vartheta}_2 \cos\left(\vartheta_1 - \vartheta_2\right) + \dot{\vartheta}_2^2 \sin\left(\vartheta_1 - \vartheta_2\right) + \left(\xi_1 + \xi_2\right) \dot{\vartheta}_1 - \xi_2 \dot{\vartheta}_2 \\ \quad + 2\vartheta_1 - \vartheta_2 - \mu \sin\left(\vartheta_1 - \vartheta_2\right) + \zeta_1 \vartheta_1^2 \dot{\vartheta}_1 - \zeta_2 \left(\vartheta_2 - \vartheta_1\right)^2 \left(\dot{\vartheta}_2 - \dot{\vartheta}_1\right) = 0 \\ \ddot{\vartheta}_2 + \ddot{\vartheta}_1 \cos\left(\vartheta_1 - \vartheta_2\right) - \dot{\vartheta}_1^2 \sin\left(\vartheta_1 - \vartheta_2\right) + \xi_2 \left(\dot{\vartheta}_2 - \dot{\vartheta}_1\right) + \left(\vartheta_2 - \vartheta_1\right) \\ \quad + \zeta_2 \left(\vartheta_2 - \vartheta_1\right)^2 \left(\dot{\vartheta}_2 - \dot{\vartheta}_1\right) = 0 \end{cases} \tag{7}$$

where $0 < \mu \in \mathbb{R}$ is the load parameter. In view of a perturbation solution, we need to expand (7) in series; by retaining up to the cubic terms in displacements and velocities, we have:

$$\begin{cases} 3\ddot{\vartheta}_1 + \ddot{\vartheta}_2 + (\xi_1 + \xi_2)\,\dot{\vartheta}_1 - \xi_2\dot{\vartheta}_2 + 2\vartheta_1 - \vartheta_2 + \mu\,(\vartheta_2 - \vartheta_1) \\ + \dfrac{1}{6}\mu\,(\vartheta_1 - \vartheta_2)^3 + \zeta_1\vartheta_1^2\dot{\vartheta}_1 - \zeta_2\,(\vartheta_2 - \vartheta_1)^2\left(\dot{\vartheta}_2 - \dot{\vartheta}_1\right) \\ - \dfrac{1}{2}\,(\vartheta_1 - \vartheta_2)^2\ddot{\vartheta}_2 + (\vartheta_1 - \vartheta_2)\,\dot{\vartheta}_2^2 = 0 \\ \ddot{\vartheta}_1 + \ddot{\vartheta}_2 + \xi_2\left(\dot{\vartheta}_2 - \dot{\vartheta}_1\right) + (\vartheta_2 - \vartheta_1) - \dfrac{1}{2}\,(\vartheta_1 - \vartheta_2)^2\ddot{\vartheta}_1 - (\vartheta_1 - \vartheta_2)\,\dot{\vartheta}_1^2 \\ + \zeta_2\,(\vartheta_2 - \vartheta_1)^2\left(\dot{\vartheta}_2 - \dot{\vartheta}_1\right) = 0 \end{cases} \tag{8}$$

Finally, these latter can be written in matrix form as (see the Appendix A for further details):

$$\begin{aligned} &\mathbf{M}\ddot{\mathbf{q}} + \mathbf{C}\dot{\mathbf{q}} + (\mathbf{K} + \mu\mathbf{H})\,\mathbf{q} = \mu\mathbf{F}_1\,(\mathbf{q}, \mathbf{q}, \mathbf{q}) + \mathbf{F}_2\,(\mathbf{q}, \dot{\mathbf{q}}, \dot{\mathbf{q}}) \\ &+ \mathbf{F}_3\,(\mathbf{q}, \mathbf{q}, \ddot{\mathbf{q}}) + \mathbf{F}_4\,(\mathbf{q}, \mathbf{q}, \dot{\mathbf{q}}) \end{aligned} \tag{9}$$

where the following definitions hold:

$$\begin{aligned} &\mathbf{q} := \begin{bmatrix} \vartheta_1 \\ \vartheta_2 \end{bmatrix}, \quad \mathbf{M} := \begin{bmatrix} 3 & 1 \\ 1 & 1 \end{bmatrix}, \quad \mathbf{C} := \begin{bmatrix} \xi_1 + \xi_2 & -\xi_2 \\ -\xi_2 & \xi_2 \end{bmatrix} \\ &\mathbf{K} := \begin{bmatrix} 2 & -1 \\ -1 & 1 \end{bmatrix}, \quad \mathbf{H} := \begin{bmatrix} -1 & 1 \\ 0 & 0 \end{bmatrix} \end{aligned} \tag{10}$$

while $\mathbf{F}_j\,(\cdot)$, $j = 1, \cdots, 4$ are trilinear vector functions with respect to their arguments. Among them, $\mathbf{F}_4$ accounts for nonlinear damping, the remaining describing geometrical nonlinearities related to the follower force, viz. $\mathbf{F}_1$, and inertial forces, viz. $\mathbf{F}_2$, $\mathbf{F}_3$.

3 Linear Stability Analysis

Here, we briefly present the linear bifurcation scenario of the (linear) Ziegler column. We first recall the well-known results of the exact analysis; then we resume the main achievements of the asymptotic analysis developed in [8, 9].

Let us consider the linear part of (9), for which the trivial equilibrium position $\mathbf{q} = \mathbf{0}$ is asymptotically stable when $\mu = 0$; the goal of the analysis is to find the smallest (critical) value μ_d of μ at which the equilibrium manifests incipient instability. To solve the problem, $\mathbf{q} = \mathbf{w}\exp(\lambda t)$ is posed in the linearized (9), and the following algebraic eigenvalue problem is obtained:

$$\left[\lambda^2\mathbf{M} + \lambda\mathbf{C} + (\mathbf{K} + \mu\mathbf{H})\right]\mathbf{w} = \mathbf{0} \tag{11}$$

When the system is undamped (usually referred as circulatory [1, 2]), and $\mu = 0$, all the (distinct) eigenvalues lie on the imaginary axis in pairs of complex conjugate, so that the system is (marginally) stable. If μ is increased from zero, the eigenvalues move on the imaginary axis, assuming the values $\pm i\omega_j$ and still remaining distinct. When the load reaches a critical value, namely $\mu = \mu_c$, a couple of them (e.g. $i\omega_1$, $i\omega_2$), together with their complex conjugate, collide (*circulatory or reversible Hopf bifurcation*) and if an infinitesimal increment $\delta\mu > 0$ is given, they separate, one on the left, the other on the right of the complex plane, thus entailing instability.

When the system is damped, namely $\mathbf{C}$ is positive definite, the eigenvalue analysis furnishes the eigenvalues $\lambda = \lambda(\mu)$. The critical load μ_d is the smallest μ at which an eigenvalue, viz. the j-th (together with its complex conjugate), crosses from the left the imaginary axis, i.e. $\mathrm{Re}\left[\lambda_j(\mu_d)\right] = 0$, $(\mathrm{d}/\mathrm{d}\mu)\,\mathrm{Re}\left[\lambda_j(\mu)\right]_{\mu=\mu_d} > 0$. It has been shown in the literature (see e.g. [1, 2, 12, 14]) that, when the damping is vanishingly small, $\mu_d < \mu_c$. Therefore small damping has a detrimental effect on stability of circulatory systems. The phenomenon is known in the literature as the 'Ziegler paradox', or the 'destabilizing effect of damping'.

3.1 Exact Analysis

First, we tackle the problem throughout an exact analysis. When damping is zero, the characteristic equation of the problem (11) is bi-quadratic; it admits purely imaginary eigenvalues of modulus:

$$\omega_{1,2} = \frac{1}{2}\left(7 - 2\mu \mp \Delta(\mu)\right)^{\frac{1}{2}}, \qquad \Delta(\mu) := \sqrt{4\mu^2 - 28\mu + 41} \tag{12}$$

together with their complex conjugate. A circulatory Hopf bifurcation occurs when $\mu = \mu_c := 7/2 - \sqrt{2}$. On the other side, when damping is different from zero, the characteristic equation is a complete degree-4 polynomial equation and, by using the Routh-Hurwitz criterion, a piecewise critical locus in the (μ, ξ_1, ξ_2)-space of parameter (Fig. 2a) can be found.

The effect of damping on the stability of the Ziegler column is mostly detrimental, since the critical load of the damped system is lower with respect to the undamped one, except for a small region (Fig. 2b) in the neighborhood of an *optimal* direction (dashed line in the figure): on the left side of this latter the stability is governed by the first mode; on the right side, by the second mode.

3.2 Asymptotic Analysis

In this section we will briefly resume the theory developed in [8, 9], where an asymptotic method is discussed in order to evaluate the eigenvalue sensitivities of a general circulatory system, when a small damping is introduced as a perturbation.

Differently from the common approach followed in the literature [10], in which a perturbation of the (defective) double eigenvalue at μ_c is performed, here the starting point of the asymptotic expansion is a simple eigenvalue of a sub-critically loaded undamped system ($\mu < \mu_c$), where the parameter μ is arbitrary and unknown in the interval $(0, \mu_c)$. Then, the rescaling $\mathbf{C} \to \varepsilon\mathbf{C}$, where $0 < \varepsilon \ll 1$ is a perturbation parameter, and the following series expansions for the eigenpairs are introduced:

$$\begin{aligned} \lambda &= \lambda_0 + \varepsilon\hat{\lambda}_0 + \varepsilon^2\hat{\hat{\lambda}}_0 + \dots \\ \mathbf{w} &= \mathbf{w}_0 + \varepsilon\hat{\mathbf{w}}_0 + \varepsilon^2\hat{\hat{\mathbf{w}}}_0 + \dots \end{aligned} \tag{13}$$

By substituting (13) in the eigenvalue problem (11) and by requiring it is satisfied for any ε, we obtain the following perturbation equations:

$$\begin{aligned} \varepsilon^0 &: \left[\lambda_0^2\mathbf{M} + (\mathbf{K} + \mu\mathbf{H})\right]\mathbf{w}_0 = \mathbf{0} \\ \varepsilon^1 &: \left[\lambda_0^2\mathbf{M} + (\mathbf{K} + \mu\mathbf{H})\right]\hat{\mathbf{w}}_0 = -\lambda_0\left(\mathbf{C} + 2\hat{\lambda}_0\mathbf{M}\right)\mathbf{w}_0 \end{aligned} \tag{14}$$

Generating solution of the ε^0-order problem is represented by the eigenpairs of the sub-critically loaded undamped system, namely $(\lambda_0(\mu), \mathbf{w}_0(\mu)) = \left(\pm i\omega_j(\mu), \mathbf{u}_j(\mu)\right)$, with $\mathbf{u}_j \in \mathbb{R}^n$. Due to the non-self-adjointness of the problem, the left eigenvectors $\mathbf{v}_j(\mu) \in \mathbb{R}^n$, which form the dual basis, are also of interest. Right and left eigenvectors satisfy, respectively:

$$\begin{aligned} &\left[(\mathbf{K} + \mu\mathbf{H}) - \omega_j^2\mathbf{M}\right]\mathbf{u}_j = \mathbf{0} \\ &\left[\left(\mathbf{K} + \mu\mathbf{H}^T\right) - \omega_j^2\mathbf{M}\right]\mathbf{v}_j = \mathbf{0} \end{aligned} \tag{15}$$

Moreover, they are bi-orthogonal with respect the mass matrix, according to $\mathbf{v}_k^T\mathbf{M}\mathbf{u}_j = 0$ if $k \neq j$, and can be normalized to satisfy $\mathbf{v}_j^T\mathbf{M}\mathbf{u}_j = 1$.

Compatibility of the ε-order problem furnishes the first sensitivity of $i\omega_j$ to the damping, which turns out to be [8, 9]:

$$\hat{\lambda}_j = -\frac{1}{2}\mathbf{v}_j^T(\mu)\,\mathbf{C}\mathbf{u}_j(\mu) \tag{16}$$

Therefore, the first sensitivity is found to be real and implicitly dependent of μ by the way of the eigenvectors. It is important to remark that $\hat{\lambda}_j$ can be either negative or positive; hence, differently to what happens in conservative systems, damping can

have a stabilizing as well as a destabilizing effect. Moreover, the previous analysis only holds for $\mu < \mu_c$: indeed when $\mu = \mu_c$ a special perturbation analysis must be carried out (see, e.g. [10, 12]).

By coming back to the Ziegler column, right and left eigenvectors associated with the frequencies (12) are:

$$\begin{aligned}
\mathbf{u}_1 &= b_1 \left\{ \frac{-\Delta(\mu) - 6\mu + 11}{3\Delta(\mu) + 2\mu - 13}, 1 \right\}^T, \quad \mathbf{u}_2 = b_2 \left\{ -\frac{\Delta(\mu) - 6\mu + 11}{3\Delta(\mu) - 2\mu + 13}, 1 \right\}^T \\
\mathbf{v}_1 &= d_1 \left\{ 1, \frac{-\Delta(\mu) - 6\mu + 11}{\Delta(\mu) + 2\mu - 3} \right\}^T, \quad \mathbf{v}_2 = d_2 \left\{ 1, -\frac{\Delta(\mu) - 6\mu + 11}{\Delta(\mu) - 2\mu + 3} \right\}^T
\end{aligned} \tag{17}$$

where the coefficients b_j and d_j, not reported here, are evaluated by the normalization conditions $\|\mathbf{u}_j\| = 1$ and $\mathbf{v}_j^T \mathbf{M} \mathbf{u}_j = 1$. Then, (16) provides the first-order sensitivities of the two eigenvalues, namely:

$$\begin{aligned}
\hat{\lambda}_1 &= -\frac{\xi_1(\Delta(\mu) + 2\mu - 3) + 6\xi_2(\Delta(\mu) + 2\mu) - 38\xi_2}{8\Delta(\mu)} \\
\hat{\lambda}_2 &= -\frac{\xi_1(\Delta(\mu) - 2\mu + 3) + 6\xi_2(\Delta(\mu) - 2\mu) + 38\xi_2}{8\Delta(\mu)}
\end{aligned} \tag{18}$$

By equating to zero $\hat{\lambda}_1$ and $\hat{\lambda}_2$, two surfaces in the (μ, ξ_1, ξ_2)-parameter space are found. The lower envelope of the two graphs is the critical locus which is represented in the (μ, ξ_1, ξ_2)-parameter space in Fig. 2a and by μ-isolines in the plane of the

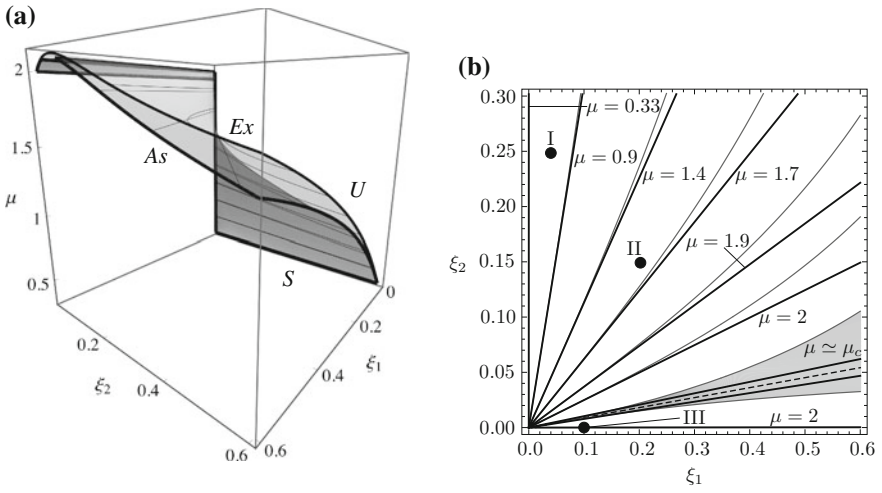

Fig. 2 Exact versus asymptotic stability boundaries for the Ziegler column: **a** critical manifolds in the (μ, ξ_1, ξ_2)-parameter space: *S* stable region, *U* unstable region, *Ex* exact boundary, *As* asymptotic boundary; **b** μ-isolines

damping parameters (Fig. 2b). These latter are straight lines outgoing from the origin, for μ spanning the range $(1/3,\ 2)$: when they are compared with the isolines of the exact solution, it is seen that for small damping the approximation is excellent far from the optimal direction, progressively worsening while moving close to it. In the shaded region in the figure, it is $\mu > \mu_c$, i.e. damping stabilizes the circulatory system, provided it is not evanescent.

4 Post-critical Behavior

To investigate the mechanical behavior of the system in the post-critical range (i.e. for $\mu > \mu_d$), we aim to approach the nonlinear problem by using the Multiple Scale Method [15–19]. The bifurcation equations are first built-up, and then they are analytically studied. Numerical results are finally illustrated.

4.1 Bifurcation Equations

Guided by the linear analysis, the starting point of perturbation is a sub-critically loaded undamped system ($\mu < \mu_c$) for which μ is a unknown critical load. First, we perform the rescaling: $\mathbf{q} \to \varepsilon^{1/2}\tilde{\mathbf{q}}$, $\mathbf{C} \to \varepsilon\tilde{\mathbf{C}}$, where $0 < \varepsilon \ll 1$ is a perturbation parameter; by omitting the tilde, (9) reads:

$$\begin{aligned}&\mathbf{M}\ddot{\mathbf{q}} + \varepsilon\mathbf{C}\dot{\mathbf{q}} + (\mathbf{K} + \mu\mathbf{H})\,\mathbf{q} = \varepsilon\mu\mathbf{F}_1\,(\mathbf{q}, \mathbf{q}, \mathbf{q}) + \varepsilon\mathbf{F}_2\,(\mathbf{q}, \dot{\mathbf{q}}, \dot{\mathbf{q}})\\ &+ \varepsilon\mathbf{F}_3\,(\mathbf{q}, \mathbf{q}, \ddot{\mathbf{q}}) + \varepsilon\mathbf{F}_4\,(\mathbf{q}, \mathbf{q}, \dot{\mathbf{q}})\end{aligned} \tag{19}$$

Then, by introducing in (19) several independent time scales, namely $t_0 = t$, $t_1 = \varepsilon t, \cdots$ so that $\mathrm{d}/\mathrm{d}t = \mathrm{d}_0 + \varepsilon\mathrm{d}_1 + \cdots$, and by expanding the unknown vector $\mathbf{q}$ in series of integer powers of ε, namely $\mathbf{q} = \mathbf{q}_0 + \varepsilon\mathbf{q}_1 + \cdots$, we get the following perturbation equations:

$$\begin{aligned}\varepsilon^0 &: \left[\mathbf{M}\mathrm{d}_0^2 + (\mathbf{K} + \mu\mathbf{H})\right]\mathbf{q}_0 = \mathbf{0}\\ \varepsilon &: \left[\mathbf{M}\mathrm{d}_0^2 + (\mathbf{K} + \mu\mathbf{H})\right]\mathbf{q}_1 = -\left(\mathbf{C} + 2\mathbf{M}\mathrm{d}_1\right)\mathrm{d}_0\mathbf{q}_0 + \mu\mathbf{F}_1\,(\mathbf{q}_0, \mathbf{q}_0, \mathbf{q}_0)\\ &+ \mathbf{F}_2\,(\mathbf{q}_0, \mathrm{d}_0\mathbf{q}_0, \mathrm{d}_0\mathbf{q}_0) + \mathbf{F}_3\left(\mathbf{q}_0, \mathbf{q}_0, \mathrm{d}_0^2\mathbf{q}_0\right) + \mathbf{F}_4\,(\mathbf{q}_0, \mathbf{q}_0, \mathrm{d}_0\mathbf{q}_0)\end{aligned} \tag{20}$$

Solution of the ε^0-order problem reads:

$$\mathbf{q}_0 = A_j\,(t_1, \cdots)\,\mathbf{u}_j e^{i\omega_j t_0} + c.c. \tag{21}$$

where A_j is the unknown (complex) amplitude and $\left(\omega_j\,(\mu)\,, \mathbf{u}_j\,(\mu)\right) \in \mathbb{R}$ are the eigenpairs of problem (15)a, $j = 1, 2$. Since just one eigenvalue is critical, $j = 1$ or $j = 2$ must alternatively be taken.

By substituting (21) into the ε-order problem, this latter reads:

$$\begin{aligned}\varepsilon:&\left[\mathbf{M}\mathrm{d}_0^2+(\mathbf{K}+\mu\mathbf{H})\right]\mathbf{q}_1=-i\omega_j\left(\mathbf{C}+2\mathbf{M}\mathrm{d}_1\right)A_j\mathbf{u}_j e^{i\omega_j t_0}\\&+3A_j^2\bar{A}_j\mu\mathbf{F}_1\left(\mathbf{u}_j,\mathbf{u}_j,\mathbf{u}_j\right)e^{i\omega_j t_0}+i\omega_j A_j^2\bar{A}_j\mathbf{F}_4\left(\mathbf{u}_j,\mathbf{u}_j,\mathbf{u}_j\right)e^{i\omega_j t_0}\\&+\omega_j^2A_j^2\bar{A}_j\left[\mathbf{F}_2\left(\mathbf{u}_j,\mathbf{u}_j,\mathbf{u}_j\right)-3\mathbf{F}_3\left(\mathbf{u}_j,\mathbf{u}_j,\mathbf{u}_j\right)\right]e^{i\omega_j t_0}+c.c.+NRT\end{aligned}\tag{22}$$

where NRT denotes 'non-resonant terms'. This is a non-homogeneous problem in the unknown $\mathbf{q}_1$. In order it can be solved, the known term must belong to the range of the operator; this solvability condition requires that:

$$\begin{aligned}&-i\omega_j\mathbf{v}_j^T\left(\mathbf{C}+2\mathbf{M}\mathrm{d}_1\right)A_j\mathbf{u}_j+\omega_j^2A_j^2\bar{A}_j\mathbf{v}_j^T\left[\mathbf{F}_2\left(\mathbf{u}_j,\mathbf{u}_j,\mathbf{u}_j\right)-3\mathbf{F}_3\left(\mathbf{u}_j,\mathbf{u}_j,\mathbf{u}_j\right)\right]\\&+3A_j^2\bar{A}_j\mu\mathbf{v}_j^T\mathbf{F}_1\left(\mathbf{u}_j,\mathbf{u}_j,\mathbf{u}_j\right)+i\omega_jA_j^2\bar{A}_j\mathbf{v}_j^T\mathbf{F}_4\left(\mathbf{u}_j,\mathbf{u}_j,\mathbf{u}_j\right)=0\end{aligned}\tag{23}$$

that furnishes:

$$\mathrm{d}_1A_j=-\frac{1}{2}cA_j+\frac{1}{2}n_4A_j^2\bar{A}_j-\frac{3}{2\omega_j}i\mu n_1A_j^2\bar{A}_j-\frac{1}{2}i\omega_j\left(n_2-3n_3\right)A_j^2\bar{A}_j\tag{24}$$

where the following (real) scalar quantities, depending on μ, have been introduced.

$$\begin{aligned}&c\left(\mu\right):=\mathbf{v}_j^T\mathbf{C}\mathbf{u}_j,\quad n_1\left(\mu\right):=\mathbf{v}_j^T\mathbf{F}_1\left(\mathbf{u}_j,\mathbf{u}_j,\mathbf{u}_j\right),\quad n_2\left(\mu\right):=\mathbf{v}_j^T\mathbf{F}_2\left(\mathbf{u}_j,\mathbf{u}_j,\mathbf{u}_j\right)\\&n_3\left(\mu\right):=\mathbf{v}_j^T\mathbf{F}_3\left(\mathbf{u}_j,\mathbf{u}_j,\mathbf{u}_j\right),\quad n_4\left(\mu\right):=\mathbf{v}_j^T\mathbf{F}_4\left(\mathbf{u}_j,\mathbf{u}_j,\mathbf{u}_j\right)\end{aligned}\tag{25}$$

Finally, by reabsorbing the ε-parameter and coming back to the true time, (24) can be written in real variables as:

$$\begin{aligned}\dot{a}_j&=-\frac{1}{2}ca_j+\frac{1}{8}n_4a_j^3\\a_j\dot{\phi}_j&=-\frac{a_j^3\left(3\mu n_1+n_2\omega_j^2-3n_3\omega_j^2\right)}{8\omega_j}\end{aligned}\tag{26}$$

where $a_j\left(t\right)$ and $\phi_j\left(t\right)$ are the (real) amplitude and phase, respectively (i.e. $A_j:=a_j/2\ \exp(i\phi_j)$). They constitute the bifurcation equations sought for.

4.2 Qualitative Analysis

The bifurcation equation (26)a governs the modulation of the amplitude of the (at this order) harmonic evolution (21) of the system. Amplitude a_j depends on the load parameter μ by the way of the coefficients $c=c\left(\mu\right)$ and $n_4=n_4\left(\mu\right)$. It should be remarked, that the eigenvalue associated to the linear part of (26)a, coincides with

that furnished by the sensitivity analysis, since $-c/2 = \hat{\lambda}_j$ (see (16)). Therefore, when $\mu < \mu_d$, since $c(\mu) > 0$, the equilibrium point $a_j = 0$ is asymptotically stable; when, $\mu > \mu_d$, since $c(\mu) < 0$, the equilibrium is unstable. A limit-cycle of amplitude $a_j = a_{je} = \text{const}$ however exists, *provided* $n_4 \neq 0$; it is given by:

$$a_{je} := \pm 2\sqrt{\frac{c(\mu)}{n_4(\mu)}} \tag{27}$$

This limit-cycle is supercritical ($\mu > \mu_d$), and therefore stable, if $n_4(\mu_d) < 0$ and subcritical ($\mu < \mu_d$), and therefore unstable, if $n_4(\mu_d) > 0$. If, in contrast, $n_4 = 0$, i.e. if the system does not possess nonlinear damping at all, then, no limit-cycle does exist around the bifurcation. This, of course, does not mean that the motion increases unbounded once the critical load has been overcame, since the asymptotic analysis loses its validity far from bifurcation. However, this circumstance signals that if a limit-cycle does exist, it occurs at large amplitudes.

Since $n_4(\mu_d)$ is a degree-1 homogeneous function of the nonlinear damping coefficients (see (25)e and (31)d), i.e. it is $n_4(\mu_d) = b_1\zeta_1 + b_2\zeta_2$, with b_1, b_2 coefficients, it exists in the plane (ζ_1, ζ_2) a straight line outgoing from the origin, which separates systems undergoing supercritical from subcritical Hopf bifurcations. Therefore, nonlinear damping has a beneficial effect in a half-plane, and a detrimental effect in the other half-plane. If this line crosses the first quadrant of the plane, where one would expect that $\zeta_1 > 0$, $\zeta_2 > 0$ always increase the dissipation capability of the system, one finds that this is not the case. In other words, another aspect of the Ziegler paradox exists even in the nonlinear range, where 'presumed' dissipation sources, cause, indeed, worsening of the mechanical performances.

It is interesting to note that the other nonlinear effects, of geometrical nature, encompassed by the coefficients n_1, n_2, n_3, are ineffective at this order on the formation of the limit-cycle, since they only affect its frequency, ruled by (26)b.

It can be concluded that the Ziegler column calls for an accurate description of damping, since its linear part is responsible for the critical load, and its nonlinear part for the existence and position of a limit-cycle.

4.3 Numerical Results

Some numerical results are illustrated concerning the post-critical behavior of the Ziegler column. Results from asymptotic analysis are compared with direct numerical integrations of the equations of motion. To this end, we first introduce the moduli ρ_L, ρ_{NL} and ratios φ_L, φ_{NL}, for the linear (subscript L) and nonlinear (subscript NL) part of damping, respectively, such as: $\xi_1 = \rho_L \cos(\varphi_L)$, $\xi_2 = \rho_L \sin(\varphi_L)$, $\zeta_1 = \rho_{NL} \cos(\varphi_{NL})$, $\zeta_2 = \rho_{NL} \sin(\varphi_{NL})$, where φ_L, φ_{NL} span the range $(0, \pi/2)$ (positive damping coefficients). Then, three case studies, labeled with black circles in Fig. 2b, are considered, namely:

- case study I: $\rho_L = 0.25$, $\varphi_L = 9\pi/20$, $\rho_{NL} = 25$, $\varphi_{NL} = 3\pi/8$, for which the asymptotic analysis developed in Sect. 3.2 furnishes $\mu_d \simeq 0.654$ ($\mu_d \simeq 0.658$ exact), and where the critical mode is the first one;
- case study II: $\rho_L = 0.25$, $\varphi_L = \pi/5$, $\rho_{NL} = 25$, $\varphi_{NL} = \pi/24$, for which the asymptotic analysis developed in Sect. 3.2 furnishes $\mu_d \simeq 1.626$ ($\mu_d \simeq 1.641$ exact), and where the critical mode is again the first one;
- case study III: $\rho_L = 0.1$, $\varphi_L = 0$, $\rho_{NL} = 30$, $\varphi_{NL} = \pi/8$, for which the asymptotic analysis developed in Sect. 3.2 furnishes $\mu_d \simeq 2$ ($\mu_d \simeq 2$ exact), and where the critical mode is the second one.

First, the system deprived of the nonlinear damping, namely with $\rho_{NL} = 0$, is analyzed. Since the asymptotic analysis fails in this case, numerical integrations in time of the third-order equations of motion are performed for (I) $\mu = 0.758$, (II) $\mu = 1.741$, (III) $\mu = 2.08$, displayed in Fig. 3. It can be seen that, in all the cases, after a transient has been exhausted, a limit-cycle is reached, in which at least one of the rotations is large. In particular, the following maximum values (amplitudes) are found: (I) $\vartheta_1 \simeq 0.80$ rad, $\vartheta_2 \simeq 1.2$ rad; (II) $\vartheta_1 \simeq 0.37$ rad, $\vartheta_2 \simeq 0.71$ rad; (III) $\vartheta_1 \simeq 0.007$ rad, $\vartheta_2 \simeq 0.73$ rad.

The effects of nonlinear damping on the post-critical behavior of the system are then studied. As discussed in Sect. 4.2, the qualitative influence of the nonlinear damping can be conveniently represented in the plane (ζ_1, ζ_2), where the sign of n_4 (μ_d) is analyzed. For the three cases under study, results are displayed in Fig. 4, where a straight line outgoing from the origin separates systems undergoing supercritical (shaded region in the figure) from subcritical bifurcations. The angle that this line forms with the ζ_1-axis is defined as the *critical angle* φ^c_{NL}, since a transition

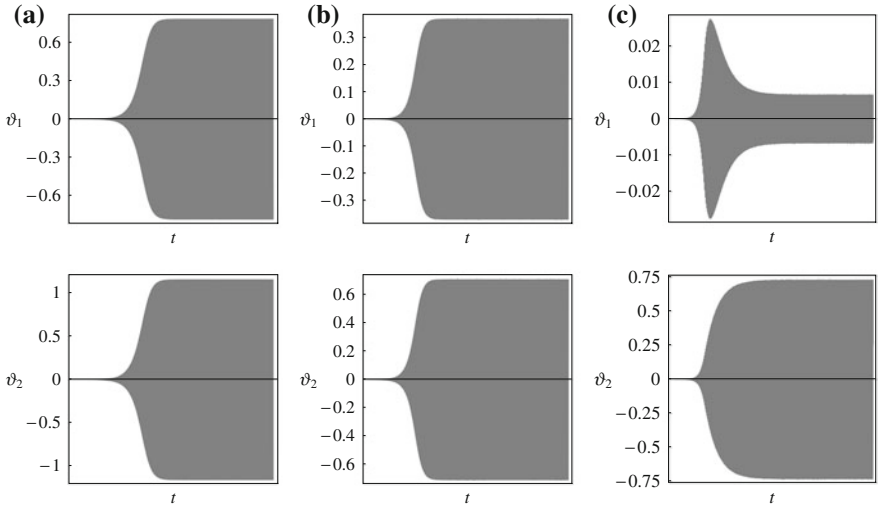

Fig. 3 Time-histories $\vartheta_1(t)$, $\vartheta_2(t)$ for linearly damped systems ($\rho_{NL} = 0$), from numerical integrations of the third-order equations of motion: **a** case study I; **b** case study II; **c** case study III

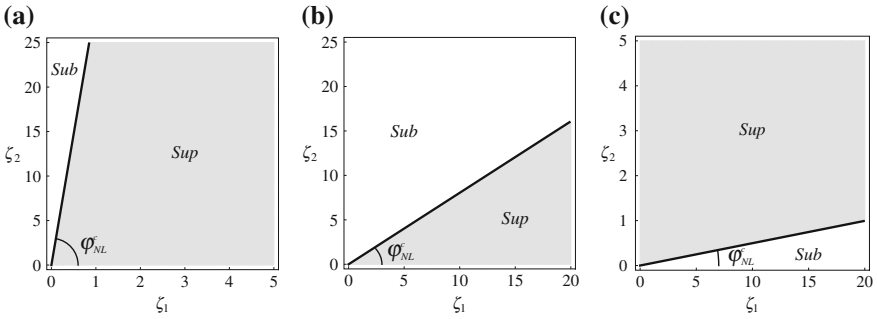

Fig. 4 Supercritical (*shaded*) and subcritical (*white*) regions in the (ζ_1, ζ_2)-plane: **a** case study I; **b** case study II; **c** case study III

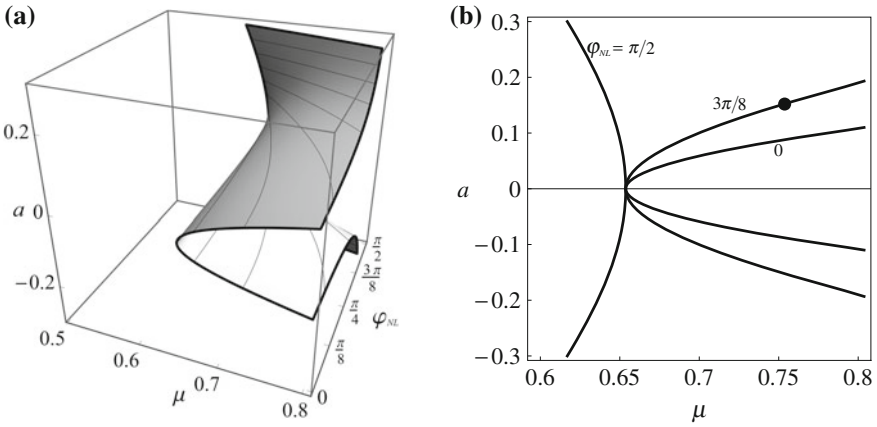

Fig. 5 Asymptotic bifurcation diagram for the case study I: **a** critical locus in the (μ, φ_{NL}, a)-parameter space; **b** φ_{NL}-isolines

from a supercritical to a subcritical Hopf bifurcation occurs there. The following values are found: (I) $\varphi_{NL}^c = 1.537$ rad; (II) $\varphi_{NL}^c = 0.677$ rad; (III) $\varphi_{NL}^c = 0.050$ rad. It is noticed that a qualitative exchange occurs between cases (I) (II), in which the critical mode is the lowest, and case (III), in which the critical mode is the highest. Indeed, supercritical bifurcations occur when $\varphi_{NL} < \varphi_{NL}^c$ in the former case, and when $\varphi_{NL} > \varphi_{NL}^c$ in the latter case.

To investigate the dependence of the amplitude of the limit-cycles on both the load and the nonlinear damping ratio, we plot bifurcation diagrams in the (μ, φ_{NL}, a)-parameter space, as furnished by the asymptotic analysis (see Figs. 5, 6, 7 for the three case studies, respectively). In the same figures, some cross-sections of the surface for selected values of φ_{NL} are shown. Both the representations show the sub-supercritical transition, when the nonlinear damping ratio is varied, and how the amplitude of the relevant unstable/stable limit-cycle, also varies with the load. It is seen that, consistently with the previous analysis, case I (Fig. 5) and case II (Fig. 6)

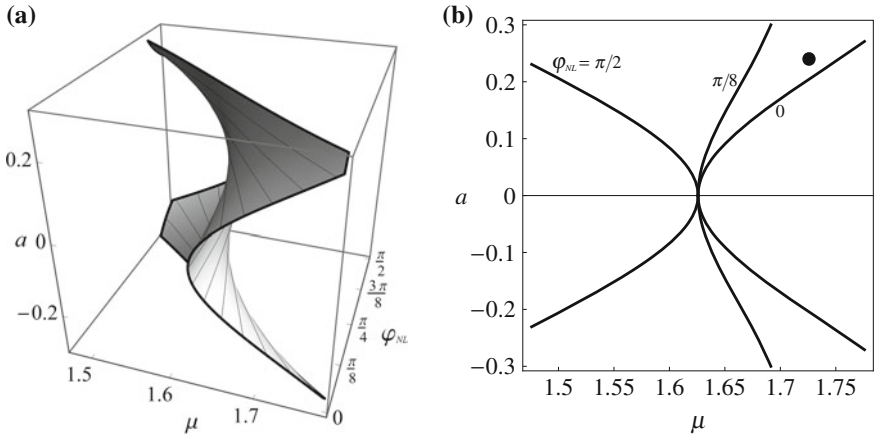

Fig. 6 Asymptotic bifurcation diagram for the case study II: **a** critical locus in the (μ, φ_{NL}, a)-parameter space; **b** φ_{NL}-isolines

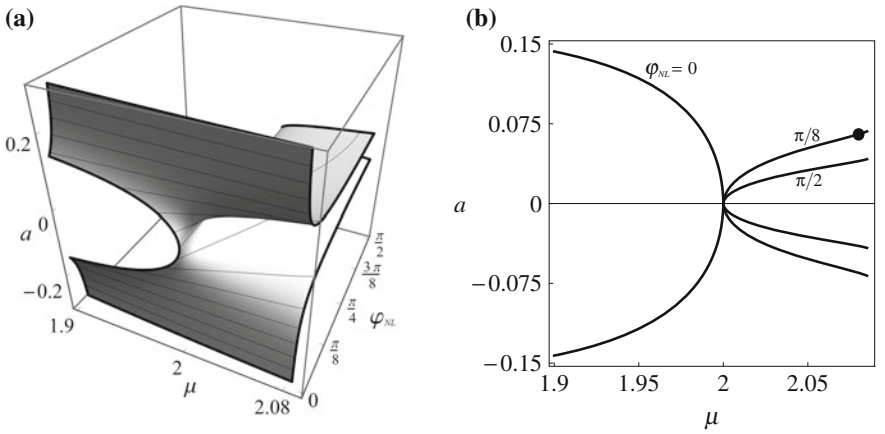

Fig. 7 Asymptotic bifurcation diagram for the case study III: **a** critical locus in the (μ, φ_{NL}, a)-parameter space; **b** φ_{NL}-isolines

are qualitatively similar, although the subcritical bifurcation region is greater in latter case II. In contrast, case III (Fig. 7) exhibits 'reversed' aspects.

Finally, the previous findings have been corroborated by numerical integrations of the third-order equations of motion, shown in Figs. 8, 9, 10 for the three cases, respectively. In particular, the asymptotic amplitudes modulation equations have been numerically integrated for $\mu = \mu_d + \delta\mu$, with $\delta\mu = 0.1$ (for cases I and II) and with $\delta\mu = 0.08$ (case III), which have been labeled with black circles in Figs. 5b, 6b, 7b. It is found that, the obtained asymptotic results (black curves in the figures), compared with numerical integrations (gray curves in the figures), are all in good qualitative accordance. However, while in the cases I and II also an excellent quantitative accordance is found, in the case III quite significant numerical differences

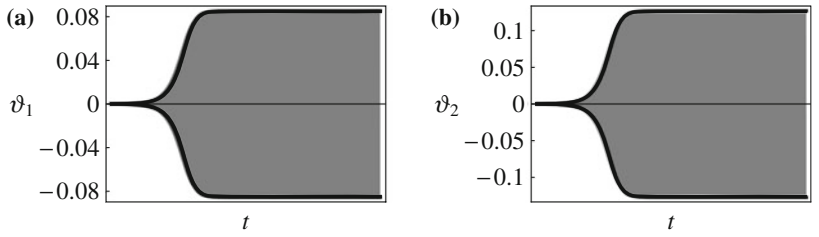

Fig. 8 Numerical versus asymptotic amplitudes ϑ_1, ϑ_2 for the case study I

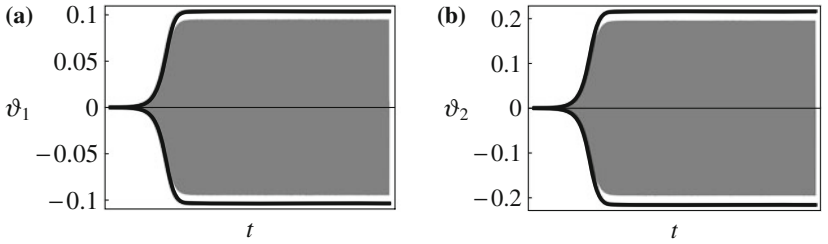

Fig. 9 Numerical versus asymptotic amplitudes ϑ_1, ϑ_2 for the case study II

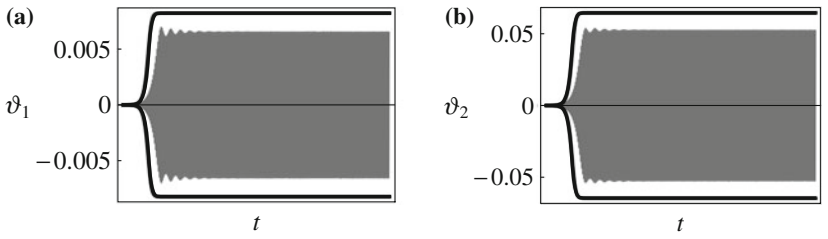

Fig. 10 Numerical versus asymptotic amplitudes ϑ_1, ϑ_2 for the case study III

are present. This circumstance is tentatively attributed to the fact that, in case III, the stable (lower) mode is associated with eigenvalues which, although are on the left side of the complex plane, are quite close to the imaginary axis, i.e. they are not well-separated by the critical ones, as instead supposed in the asymptotic analysis (and, in general, by the Center Manifold approach). Therefore, an interaction between the two modes is suspected to occur, that would require further and much more complex investigation along the lines, e.g., of [20–22].

5 Conclusions

The mechanical behavior of a nonlinear, nonconservative two-degree-of freedom system, known in the linear range as the Ziegler column, has been analyzed. The 'destabilization paradox', according to which a small, strictly dissipative, damping has a detrimental effect on linear stability of the column, has been explained in a new

perspective. According to it, the critical damped system is not a (finite) perturbation of the known critical undamped system, but rather an infinitesimal perturbation of an unknown undamped (circulatory) system, which is loaded below the critical value, and therefore is stable. Thus, the paradox is the result of destabilization of a marginally stable circulatory system. A perturbation method has been consistently developed.

Then the analysis of the nonlinear problem has been carried out, aimed to investigate the evolution of the column, once its critical load is exceeded. An asymptotic analysis, carried out via the Multiple Scale Method, consistently with the ideas springing from the linear study, has been performed. The analysis provides bifurcation equations governing the evolution of amplitude and phase of the motion. It has been found that a supercritical limit-cycle, limiting the motion of the unstable column, does exist, provided a *suitable nonlinear damping* is present in the system. In contrast, geometrical nonlinearities related to the load and the inertia forces are unable (at the first order) to lead the system onto a nearby periodic orbit. Such main result has been confirmed by numerical integrations of the equations of motion, who have revealed: (a) the existence of small-amplitude limit-cycle, when the system is endowed with a proper nonlinear damping, and, (b) large-amplitude limit-cycle (not captured by the first-order asymptotic analysis), when nonlinear damping is removed from the system.

The analysis has shown that nonlinear damping can have a beneficial effect on the nonlinear behavior of the system, rendering supercritical the Hopf bifurcation, but also a detrimental effect, rendering subcritical the same bifurcation, thus revealing a new aspect of the Ziegler paradox, existing also in the nonlinear field.

Further analysis has to be carried out to (a) investigate the proper form of the nonlinear damping, able to optimize the performances of the column, (b) its relationships with the linear damping, and (c) possible interactions among two modes (multiple Hopf bifurcation).

Acknowledgments This work was granted by the Italian Ministry of University and Research (MIUR), under the PRIN10-11 program, project N. 2010MBJK5B.

Appendix A: Nonlinear Vector Functions

Equations of motion (8) can be written as:

$$\begin{aligned}&\mathbf{M}\ddot{\mathbf{q}} + \mathbf{C}\dot{\mathbf{q}} + (\mathbf{K} + \mu\mathbf{H})\,\mathbf{q} = \mu\mathbf{f}_1\left(\vartheta_1, \vartheta_2\right) + \mathbf{f}_2\left(\vartheta_1, \vartheta_2, \dot{\vartheta}_1, \dot{\vartheta}_2\right)\\ &+ \mathbf{f}_3\left(\vartheta_1, \vartheta_2, \ddot{\vartheta}_1, \ddot{\vartheta}_2\right) + \mathbf{f}_4\left(\vartheta_1, \vartheta_2, \dot{\vartheta}_1, \dot{\vartheta}_2\right)\end{aligned} \tag{28}$$

where $\mathbf{q}$, $\mathbf{M}$, $\mathbf{C}$, $\mathbf{K}$ and $\mathbf{H}$ have been defined in (10) and:

$$
\begin{aligned}
\mathbf{f}_1\left(\vartheta_1,\vartheta_2\right) &:= \begin{bmatrix} -\frac{1}{6}\left(\vartheta_1-\vartheta_2\right)^3 \\ 0 \end{bmatrix} \\
\mathbf{f}_2\left(\vartheta_1,\vartheta_2,\dot{\vartheta}_1,\dot{\vartheta}_2\right) &:= \begin{bmatrix} -\left(\vartheta_1-\vartheta_2\right)\dot{\vartheta}_2^2 \\ \left(\vartheta_1-\vartheta_2\right)\dot{\vartheta}_1^2 \end{bmatrix} \\
\mathbf{f}_3\left(\vartheta_1,\vartheta_2,\ddot{\vartheta}_1,\ddot{\vartheta}_2\right) &:= \begin{bmatrix} \frac{1}{2}\left(\vartheta_1-\vartheta_2\right)^2\ddot{\vartheta}_2 \\ \frac{1}{2}\left(\vartheta_1-\vartheta_2\right)^2\ddot{\vartheta}_1 \end{bmatrix} \\
\mathbf{f}_4\left(\vartheta_1,\vartheta_2,\dot{\vartheta}_1,\dot{\vartheta}_2\right) &:= \begin{bmatrix} -\zeta_1\vartheta_1^2\dot{\vartheta}_1+\zeta_2\left(\vartheta_2-\vartheta_1\right)^2\left(\dot{\vartheta}_2-\dot{\vartheta}_1\right) \\ -\zeta_2\left(\vartheta_2-\vartheta_1\right)^2\left(\dot{\vartheta}_2-\dot{\vartheta}_1\right) \end{bmatrix}
\end{aligned}
\tag{29}
$$

are the nonlinear (cubic) vector functions. These latter can be suitably re-written as trilinear vector functions with respect to their arguments, namely:

$$
\mathbf{F}_j\left(\mathbf{u},\mathbf{v},\mathbf{w}\right) = \frac{1}{6}\mathbf{f}^0_{j\mathbf{uvw}}\mathbf{uvw}, \quad j=1,\cdots,4 \tag{30}
$$

being $\mathbf{u} := (u_1,u_2)^T$, $\mathbf{v} := (v_1,v_2)^T$, $\mathbf{w} := (w_1,w_2)^T$ three dummy vectors and $\mathbf{f}^0_{j\mathbf{uvw}}\mathbf{uvw}$ the third variation (evaluated at the origin) of each of $\mathbf{f}_j(\cdot)$ $(j=1,\cdots,4)$ with respect to its arguments. In particular:

$$
\begin{aligned}
\mathbf{f}^0_{1\mathbf{uvw}}\mathbf{uvw} &:= \begin{bmatrix} -\left(u_1-u_2\right)\left(v_1-v_2\right)\left(w_1-w_2\right) \\ 0 \end{bmatrix} \\
\mathbf{f}^0_{2\mathbf{uvw}}\mathbf{uvw} &:= 2\begin{bmatrix} \left(w_2-w_1\right)\dot{u}_2\dot{v}_2+\left(v_2-v_1\right)\dot{u}_2\dot{w}_2+\left(u_2-u_1\right)\dot{v}_2\dot{w}_2 \\ \left(w_1-w_2\right)\dot{u}_1\dot{v}_1+\left(v_1-v_2\right)\dot{u}_1\dot{w}_1+\left(u_1-u_2\right)\dot{v}_1\dot{w}_1 \end{bmatrix} \\
\mathbf{f}^0_{3\mathbf{uvw}}\mathbf{uvw} &:= \begin{bmatrix} \left(v_1-v_2\right)\left(w_1-w_2\right)\ddot{u}_2+\left(u_1-u_2\right)\left(w_1-w_2\right)\ddot{v}_2 \\ \quad +\left(u_1-u_2\right)\left(v_1-v_2\right)\ddot{w}_2 \\ \left(v_1-v_2\right)\left(w_1-w_2\right)\ddot{u}_1+\left(u_1-u_2\right)\left(w_1-w_2\right)\ddot{v}_1 \\ \quad +\left(u_1-u_2\right)\left(v_1-v_2\right)\ddot{w}_1 \end{bmatrix} \\
\mathbf{f}^0_{4\mathbf{uvw}}\mathbf{uvw} &:= 2\begin{bmatrix} -\zeta_1\left(u_1\dot{v}_1w_1+\dot{u}_1v_1w_1+u_1v_1\dot{w}_1\right) \\ +\zeta_2\left[\left(\dot{u}_2-\dot{u}_1\right)\left(v_2-v_1\right)\left(w_2-w_1\right)\right] \\ +\zeta_2\left[\left(u_2-u_1\right)\left(\dot{v}_2-\dot{v}_1\right)\left(w_2-w_1\right)\right] \\ +\zeta_2\left[\left(u_2-u_1\right)\left(v_2-v_1\right)\left(\dot{w}_2-\dot{w}_1\right)\right] \\ \zeta_2\left[\left(u_1-u_2\right)\left(w_1-w_2\right)\left(\dot{v}_1-\dot{v}_2\right)\right] \\ +\zeta_2\left[\left(v_1-v_2\right)\left(w_1-w_2\right)\left(\dot{u}_1-\dot{u}_2\right)\right] \\ +\zeta_2\left[\left(u_1-u_2\right)\left(v_1-v_2\right)\left(\dot{w}_1-\dot{w}_2\right)\right] \end{bmatrix}
\end{aligned}
\tag{31}
$$

Finally, by substituting (30) and (31) in (28), this latter assumes the form of (9).

References

1. Ziegler, H.: Die stabilitätskriterien der elastomechanik. Ingenieur Archiv **20**(1), 49–56 (1952)
2. Bolotin, V.V.: Nonconservative problems of the theory of elastic stability. Macmillan, New York (1963)
3. Herrmann, G., Jong, I.C.: On the destabilizing effect of damping in nonconservative elastic systems. J. Appl. Mech. **32**(3), 592–597 (1965)
4. Herrmann, G.: Stability of equilibrium of elastic systems subjected to non-conservative forces. Appl. Mech. Rev. **20**, 103–108 (1967)
5. Hagedorn, P.: On the destabilizing effect of non-linear damping in non-conservative systems with follower forces. Int. J. Non-Linear Mech. **5**(2), 341–358 (1970)
6. Bigoni, D., Noselli, G.: Experimental evidence of flutter and divergence instabilities induced by dry friction. J. Mech. Phys. Solids **59**(10), 2208–2226 (2011)
7. Kirillov, O.N., Verhulst, F.: Paradoxes of dissipation-induced destabilization or who opened Whitney's umbrella? Zeitschrift für Angewandte Mathematik und Mechanik **90**(6), 462–488 (2010)
8. Luongo, A., D'Annibale, F.: A paradigmatic minimal system to explain the Ziegler paradox. Continuum Mech. Thermodyn. **27**(1), 211–222 (2015)
9. Luongo, A., D'Annibale, F.: On the destabilizing effect of damping on discrete and continuous circulatory systems. J. Sound Vibration **333**, 6723–6741 (2014)
10. Kirillov, O.N.: A theory of the destabilization paradox in non-conservative systems. Acta Mechanica **174**(3–4), 145–166 (2005)
11. Kirillov, O.N., Seyranian, A.P.: The effect of small internal and external damping on the stability of distributed non-conservative systems. J. Appl. Math. Mech. **69**(4), 529–552 (2005)
12. Seyranian, A.P., Mailybaev, A.A.: Multiparameter Stability Theory With Mechanical Applications, vol. 13. World Scientific, Singapore (2003)
13. Thomsen, J.J.: Chaotic dynamics of the partially follower-loaded elastic double pendulum. J. Sound Vibration **188**(3), 385–405 (1995)
14. Kirillov, O.N., Seyranian, A.P.: Stabilization and destabilization of a circulatory system by small velocity-dependent forces. J. Sound Vibration **283**, 781–800 (2005)
15. Nayfeh, A.H., Mook, D.T.: Nonlinear Oscillations. Wiley, New York (2008)
16. Piccardo, G., D'Annibale, F., Zulli, D.: On the contribution of Angelo Luongo to Mechanics: in honor of his 60th birthday, Continuum Mech. Thermodyn. doi:10.1007/s00161-014-0388-z
17. Luongo, A., Di Egidio, A.: Divergence, Hopf and double-zero bifurcations of a nonlinear planar beam. Comput. Struct. **84**(24), 1596–1605 (2006)
18. Di Egidio, A., Luongo, A., Paolone, A.: Linear and non-linear interactions between static and dynamic bifurcations of damped planar beams. Int. J. Non-Linear Mech. **42**(1), 88–98 (2007)
19. Luongo, A., D'Annibale, F.: Double zero bifurcation of non-linear viscoelastic beams under conservative and non-conservative loads. Int. J. Non-Linear Mech. **55**, 128–139 (2013)
20. Luongo, A., Paolone, A.: Perturbation methods for bifurcation analysis from multiple nonresonant complex eigenvalues. Nonlinear Dyn. **14**(3), 193–210 (1997)
21. Luongo, A., Paolone, A., Di Egidio, A.: Multiple timescales analysis for 1: 2 and 1: 3 resonant Hopf bifurcations. Nonlinear Dyn. **34**(3–4), 269–291 (2003)
22. Luongo, A., Di Egidio, A., Paolone, A.: Multiscale analysis of defective multiple-Hopf bifurcations. Comput. Struct. **82**(31), 2705–2722 (2004)

Pseudoelastic Shape Memory Alloys to Mitigate the Flutter Instability: A Numerical Study

Arnaud Malher, Olivier Doaré and Cyril Touzé

Abstract A passive control of aeroelastic instabilities on a two-degrees-of-freedom (dofs) system is considered here using shape memory alloys (SMA) springs in their pseudo-elastic regime. SMA present a solid-solid phase change that allow them to face strong deformations ($\sim$10 %); in the pseudo-elastic regime, an hysteresis loop appears in the stress-strain relationship which in turn gives rise to an important amount of dissipated energy. This property makes the SMA a natural candidate for mitigating undesired vibrations in a passive manner. A 2-dofs system is used here to model the classical flutter instability of a wing section in a uniform flow. The SMA spring is selected to act on the pitch in order to dissipate energy of the predominant motion. A simple phenomenological model for the SMA hysteresis loop is introduced, allowing for a quantitative study of the important parameters to optimize in view of an experimental design. Thanks to a simple phenomenological model for the SMA hysteresis loop, a quantitative numerical study is performed in order to exhibit the best tuning of the material parameters for controlling the flutter instability.

1 Introduction

Aeroelastic instabilities are an important issue in aeronautics, especially regarding the wing motions. Indeed, for a coupled system airflow—flexible structure, like aircraft wing, turbojet or bridge, a limit velocity exists above which the flexible structure cannot evacuate the energy received from the airflow anymore, then giving rise to strong or even fatal deformations. These instabilities, usually described under the generic term flutter instability, result from interaction between aerodynamic, inertia and elastic forces [3]. In this contribution, we focus on a passive control device for mitigating the flutter instability by using springs composed of shape memory alloys (SMA). In their pseudo-elastic regime, SMA are known for showing the ability of

A. Malher (✉) · O. Doaré · C. Touzé
Unité de Mécanique (UME), ENSTA-ParisTech, 828 Boulevard des Maréchaux,
91762 Palaiseau Cedex, France
e-mail: arnaud.malher@ensta-paristech.fr

O. Doaré
e-mail: olivier.doare@ensta-paristech.fr

C. Touzé
e-mail: cyril.touze@ensta-paristech.fr

M. Belhaq (ed.), *Structural Nonlinear Dynamics and Diagnosis*,
Springer Proceedings in Physics 168, DOI 10.1007/978-3-319-19851-4_17

dissipating an important amount of energy thanks to the hysteresis loop appearing in their stress-strain relationship [11], and has thus already been used in numerous applications ranging from civil engineering, aeronautics to medical industry [13, 14]. The goal of this study is, in a first step, not to describe the system as accurately as possible but to exhibit the interest of using an hysteretic phenomenon in the view of controlling an aeroelastic instability and studying the influence of different SMA parameters for the flutter control.

Recent contributions have considered the dynamical responses of SMA springs from the theoretical viewpoint [1, 7, 11] in order to properly quantify the most prominent features of the vibrations of simple single dof systems. Experimentally, a torsion pendulum has recently been used in order to clearly exhibit the softening effect of SMA oscillators [4].

The aim of this paper is to investigate the effect of a SMA spring on the flutter instability. More particularly, the most relevant parameters of a pseudo-elastic regime on the amplitudes of the limit cycle oscillations (LCO) are analyzed, in order to quantify the effect of the dissipation brought by the hysteresis loop. The airfoil is modeled using the classical 2-dofs system coupling pitch and heave motions [5]. In order to exchange energy and create the possibility of a Hopf bifurcation in the system, the minimal model should contain at least a flexural (heave) and a torsional (pitch) mode. The SMA nonlinear behaviour is described by an heuristic model where the prominent parameters are left free to vary. The structural nonlinearities that may appear in the wing motion are here described thanks to the addition of a cubic nonlinearity in the restoring force [6, 8, 9, 12]. Numerical simulations are then conducted in order to investigate the effect of the SMA on the LCO. In particular, it is shown that for certain parameter range, the SMA spring can lead to a significant decrease of the amplitude of the LCO.

2 2DOFs Airfoil Model

2.1 Linear Model and Flutter Velocity

The system under consideration is shown in Fig. 1. A Lagrangian formulation is used to express the evolution of the altitude h (heave) and the angle of attack α (pitch) [5]. The kinetic energy reads $\mathcal{T} = \frac{1}{2}m\dot{h}^2 + \frac{1}{2}I_\alpha\dot{\alpha}^2 + S_\alpha\dot{h}\dot{\alpha}$, and the potential energy reads $\mathcal{V} = \frac{1}{2}k_\alpha\alpha^2 + \frac{1}{2}k_h h^2$. In these expressions, I_α is the inertia moment and S_α the static moment which is directly related to the position of the airfoil gravity center and is the cause of the coupling. The source terms F and M (aerodynamic force and moment) are classically derived from the lift coefficient C_L such as $F = \frac{1}{2}\rho U^2 S C_L$ and $M = eF$, where ρ is the fluid density, U the upstream airspeed and S the airfoil section. We assume that the angle of attack remains small, so that the lift coefficient depends linearly on α_{app} the apparent angle of attack, so that $C_L = (\partial C_L/\partial\alpha)\alpha_{app}$ ($C_L|_{\alpha=0} = 0$ because the airfoil is symmetric). A pseudo-static approach is used,

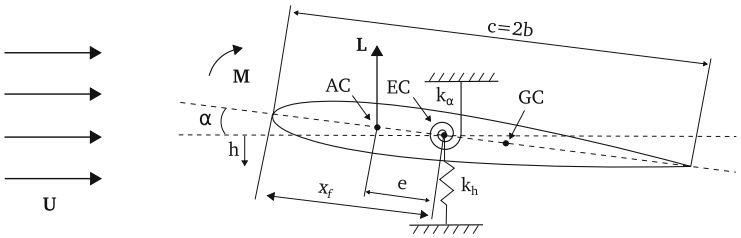

Fig. 1 Sketch of the airfoil model as a rigid body in uniform flow U with two dof: pitch (α) and heave (h)

i.e. the airfoil speed $\dot{h}$ is not neglected as compared to the upstream airspeed U and $\alpha_{app} = \alpha + \dot{h}/U$ [5].
Lagrange equations lead to the following dynamical system:

$$\begin{bmatrix} m & S_\alpha \\ S_\alpha & I_\alpha \end{bmatrix} \begin{bmatrix} \ddot{h} \\ \ddot{\alpha} \end{bmatrix} + \begin{bmatrix} \frac{1}{2}\rho U S C_{L,\alpha} & 0 \\ -\frac{1}{2}e\rho U S C_{L,\alpha} & 0 \end{bmatrix} \begin{bmatrix} \dot{h} \\ \dot{\alpha} \end{bmatrix} + \begin{bmatrix} K_h & \frac{1}{2}\rho U^2 S C_{L,\alpha} \\ 0 & K_\alpha - \frac{1}{2}e\rho U^2 S C_{L,\alpha} \end{bmatrix} \begin{bmatrix} h \\ \alpha \end{bmatrix} = 0. \tag{1}$$

In nondimensional form (1) reads

$$\begin{bmatrix} 1 & x_\alpha \\ x_\alpha & r_\alpha^2 \end{bmatrix} \begin{bmatrix} y'' \\ \alpha'' \end{bmatrix} + \begin{bmatrix} \mu C_{L,\alpha}\Theta & 0 \\ -\mu\gamma C_{L,\alpha}\Theta & 0 \end{bmatrix} \begin{bmatrix} y' \\ \alpha' \end{bmatrix} + \begin{bmatrix} \Omega^2 & \mu C_{L,\alpha}\Theta^2 \\ 0 & r_\alpha^2 - \mu\gamma C_{L,\alpha}\Theta^2 \end{bmatrix} \begin{bmatrix} y \\ \alpha \end{bmatrix} = 0, \tag{2}$$

$$\begin{aligned} y &= \tfrac{h}{b}, & \tau &= \tfrac{K_\alpha t}{I_\alpha}, & (\,)' &= \tfrac{d}{d\tau}, \\ r_\alpha &= \sqrt{\tfrac{I_\alpha}{mb^2}}, & \mu &= \tfrac{\rho b S}{2m}, & x_\alpha &= \tfrac{S_\alpha}{mb}, \\ \Theta &= \tfrac{U}{b}\sqrt{\tfrac{I_\alpha}{K_\alpha}}, & \Omega &= \sqrt{\tfrac{K_h I_\alpha}{m K_\alpha}}, & \gamma &= \tfrac{e}{b}. \end{aligned}$$

In order to gain insight on the critical parameter values, the flutter speed Θ_f can be derived analytically. Indeed, assuming that the airfoil motion is harmonic, $y = \Re\,(\tilde{y}\exp(pt))$ and $\alpha = \Re\,(\tilde{\alpha}\exp(pt))$ with $(p, \tilde{\alpha}, \tilde{y}) \in \mathcal{C}$, replacing α and y by their new expressions in (2) it yields

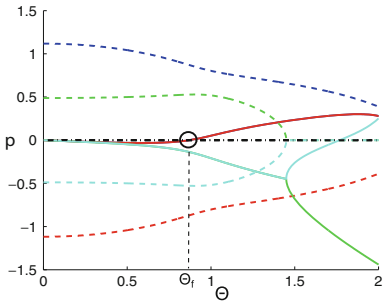

Fig. 2 Real (*solid lines*) and imaginary (*dotted lines*) parts of the solutions of $\det(\mathbf{A}) = 0$, with $\mathbf{A}$ defined in (3). Parameters of the problem are listed in Table 1

$$\mathbf{A}\begin{bmatrix}\tilde{y}\\ \tilde{\alpha}\end{bmatrix} = 0, \quad \text{with} \tag{3}$$

$$\mathbf{A} = \begin{bmatrix} p^2 + \mu C_{L,\alpha}\Theta p + \Omega^2 & x_\alpha p^2 + \mu C_{L,\alpha}\Theta^2 \\ x_\alpha p^2 - \mu\gamma C_{L,\alpha} p & r_\alpha^2 p^2 + r_\alpha^2 - \mu\gamma C_{L,\alpha}\Theta^2 \end{bmatrix}.$$

Equation (3) has non trivial solutions p_i when $\det(\mathbf{A}) = 0$. Using the parameter values of Table 1, the solutions p_i versus the flow speed Θ is plotted in Fig. 2. At the flutter velocity Θ_f, the real part of one of the solutions p_i vanishes. Assuming then p purely imaginary, separating real and imaginary parts in the equation $\det(\mathbf{A}) = 0$, and grouping the terms to eliminate p, the following expression is found for which Θ_f is solution

$$(A_1\Theta^2 - A_2)(A_3\Theta^2 + A_4) = 0,$$

$$\text{with} \begin{cases} A_1 = \mu C_{L,\alpha}(r_\alpha^2 + \gamma x_\alpha) \\ A_2 = r_\alpha^2 x_\alpha \end{cases},$$

$$\text{thus} \quad \Theta_f = \sqrt{\frac{A_2}{A_1}} = \sqrt{\frac{r_\alpha^2 x_\alpha}{\mu C_{L,\alpha}(r_\alpha^2 + \gamma x_\alpha)}}. \tag{4}$$

Using values of Table 1 we find $\Theta_f = 0.87$.

2.2 SMA Model

The SMA spring is assumed to have pseudo-elastic behaviour, which is briefly recalled in Fig. 3. This nonlinear behaviour is characterized by a solid-solid phase change between two different states. The first one called *austenite* is stable at large

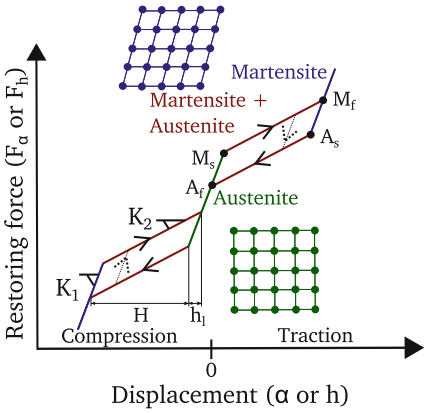

Fig. 3 Pseudo-elastic behaviour of SMA and its microstructure for each phase

temperatures and is the natural state of the spring at rest. The microstructure of the austenite phase is also sketched in Fig. 3. When deformed, the microstructure of the SMA turns into a new phase called *martensite*, energetically stable at small temperatures and for which the microstructure is now oriented. The points in the stress-strain space where the transformations start and finish are usually denoted with the subscripts s (start) and f (finish), so that for instance M_f refers to the point where the martensitic transformation has been fully accomplished in the SMA structure.

The path followed in the stress-strain relationship is not the same when the material is loaded or unloaded, thus an hysteresis loop appears as illustrated in Fig. 3. This hysteretic phenomena is the most salient feature of the pseudo-elastic behaviour of SMA. The dissipated energy during a cycle is proportional to the area of the hysteresis loop so that the more the loop area is large, the more energy is prone to be dissipated in the device.

The nonlinear behaviour of single dof SMAs can be derived from a general, three-dimensional model inferred from thermodynamical laws and then reduced by considering ad-hoc assumptions, see e.g. [2, 7, 10, 11]. In this case the model contains, in-built within the oscillator equation, additional equations governing the evolution of the fraction of martensite, the description of heat transfer, and the thermodynamic force, which expression is derived from a pseudopotential of dissipation that can include yields functions in order to express the phase transformations [11]. These modeling features are typical of hysteretic systems [15] and give rise to a complex formulation which, in turn, induces numerical difficulties for solving the whole system. Contrary to this general approach, we use in this contribution a simple heuristic model instead, as it has the capacity to retrieve the main features of the dynamical behaviour within a light computational framework. It is built following the sketch in Fig. 3 by approximating each part of the diagram by a linear relationship, h_l modelize the beginning of the martensitic transformation and H the end of the martensitic transformation. An internal auxiliary variable playing the role of the fraction of martensite is defined so as to keep the memory of the precedent state of the material in a dynamical simulation. For simplification, it is assumed that the slopes of

Table 1 Nondimensional aeroelastic parameters

r_α	μ	x_α	Ω	γ	$C_{L,\alpha}$
0.5	$1/10\pi$	0.2	0.5	0.4	2π

the purely austenitic and purely martensitic phases are equal, as well as the slopes during the reverse or transverse transformations, so that the stiffness of the SMA are defined by K_1 and K_2, only as shown in Fig. 3. It is also assumed that the behaviour of the spring is symmetric in traction and compression. Internal loops are described following the sketch in Fig. 3 and we call A_{SMA} the area of the maximal internal loop. The area A_{SMA} is completely defined by the four parameters K_1, K_2, h_l and H with the following relationship

$$A_{SMA} = h_l H \sqrt{1 + K_1^2}\sqrt{1 + K_2^2}\cos(\tan^{-1}(1/K_1) + \tan^{-1}(K_2)).$$

For the remainder of the study, the four parameters that will be considered are A_{SMA}, K_1, K_2 and h_l (A_{SMA} instead of H as it is more physically meaningful).

After the flutter instability, with the physical parameters from Table 1 the wing experiences large-amplitude motions especially on the pitch mode, whereas the amplitude of the motion of the heave mode remains fairly small. In order to take advantage of the dissipative properties of the SMA, it appears logical to include a SMA spring on the torsional motion, whereas the flexural spring is left unchanged with a linear behaviour law.

2.3 Final Model

To ensure a LCO after bifurcation occurs (no matter using SMA or not) a cubic stiffness is added on both modes (ξ_y for heave and ξ_α for pitch). The final model with a SMA torsional spring is then derived by replacing $r_\alpha^2\alpha$ from (2) with the nonlinear behaviour of the SMA spring f_{NL}^{SMA} depicted in Fig. 3. It reads:

$$\begin{bmatrix} 1 & x_\alpha \\ x_\alpha & r_\alpha^2 \end{bmatrix}\begin{bmatrix} y'' \\ \alpha'' \end{bmatrix} + \begin{bmatrix} \mu C_{L,\alpha}\Theta & 0 \\ -\mu\gamma C_{L,\alpha}\Theta & 0 \end{bmatrix}\begin{bmatrix} y' \\ \alpha' \end{bmatrix} + \begin{bmatrix} \Omega^2 & \mu C_{L,\alpha}\Theta^2 \\ 0 & -\mu\gamma C_{L,\alpha}\Theta^2 \end{bmatrix}\begin{bmatrix} y \\ \alpha \end{bmatrix} = \begin{bmatrix} -\xi_y y^3 \\ -f_{NL}^{SMA}(\alpha) - \xi_\alpha \alpha^3 \end{bmatrix}. \tag{5}$$

3 Results and Discussion

The aeroelastic parameters for the two-dofs system have been selected according to [5], they are listed in Table 1. Equation (5) is integrated in time with a fourth-order Runge-Kutta scheme. The initial condition is generally prescribed as a small perturbation on the heave mode. The results shown in Fig. 4 are made for $\xi_y = \xi_\alpha = 0$, thus the nonlinearity is exclusively due to the SMA.

When $\Theta < \Theta_f$, the airfoil motion decreases and tends to zero, see Fig. 4a. When $\Theta \geq \Theta_f$, the flutter instability occurs and the position at rest is not stable anymore. However, the energy of the LCO can be dissipated by the SMA, so that for a certain range of reduced velocity, the amplitude of the motion saturates thanks to the nonlinear behaviour of the SMA, as illustrated in Fig. 4b. When the motion amplitudes of the LCO are beyond the end of the martensitic transformation, the potential of dissipation of the SMA is reached, so that divergent motions are retrieved. The critical speed above which the motion diverges is denoted Θ_c. The first observed and awaited effect of adding the SMA is to increase Θ_c thanks to the damping property of the hysteresis loop, an intermediate stage where LCO with small amplitude is present. In a first step the energy evolution is investigated to ensure the LCO is entirely due to the hysteresis loop of the SMA and in a second step, a parametric study of the SMA is made to understand its influence on the LCO.

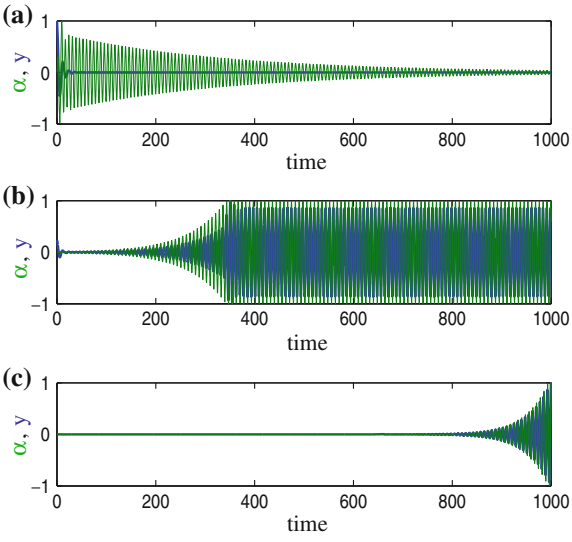

Fig. 4 Effect of the SMA on the linear flutter instability ($\xi_y = \xi_\alpha = 0$) for three different reduced velocities: **a** Linear stability case, $\Theta = 0.86$ **b** Instability case, with LCO due to SMA dissipation, $\Theta = 0.91$ **c** Instability case where SMA cannot dissipate enough energy, and an exponential growth is observed, $\Theta = 0.93$ ($\Theta_f = 0.87$ and $\Theta_c = 0.926$). *Blue* heave motion y, *green* pitch α. The *curves* are normalized to their maximal value

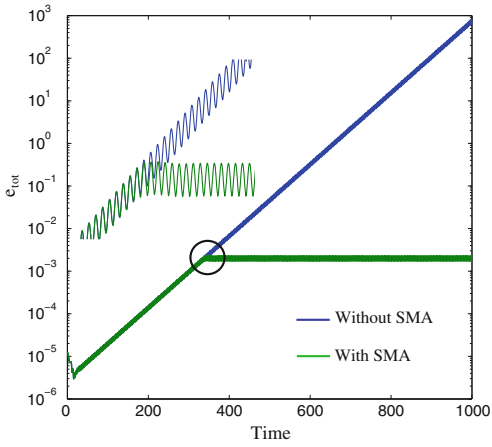

Fig. 5 Total energy e_{tot} versus time for the aeroelastic system (parameters of Table 1), with and without SMA, and for $\Theta = 0.9$

3.1 Energy Exchange

We investigate the energy evolution with time for the case $\Theta_f < \Theta < \Theta_c$. The energy contained in the airfoil reads

$$E_{tot} = \mathcal{T} + \mathcal{V} = \frac{1}{2}\left(m\dot{h}^2 + I_\alpha\dot{\alpha}^2 + K_\alpha\alpha^2 + K_h h^2\right) + S_\alpha\dot{h}\dot{\alpha}.$$

Then the nondimensional energy is

$$e_{tot} = \frac{1}{2}\left(\dot{y}^2 + r_\alpha^2\dot{\alpha}^2 + k_\alpha\alpha^2 + \Omega^2 y^2\right) + x_\alpha\dot{y}\dot{\alpha}. \tag{6}$$

Its evolution is plotted in Fig. 5 for system with and without SMA. For each cycle the energy increase of the system without SMA corresponds exactly to the energy dissipated by the SMA in its internal loop (for example right after the system with SMA enters in its first internal loop this loop dissipates $1.198\,10^{-4}$ and during this time the system without SMA grew $1.189\,10^{-4}$). Hence in this regime, the energy saturates to a finite value. This clearly shows that the LCO appearing when $\Theta_f < \Theta < \Theta_c$ is entirely due to the SMA hysteresis loop. We now explore the influence of the SMA parameters on the LCO.

3.2 Influence of SMA Parameters

The global effect of the SMA parameters on the behaviour of the flutter instability is studied through the bifurcation diagram for varying flow velocities Θ. Fig. 6 shows such a bifurcation diagram for a given SMA spring (the amplitude of pitch motion

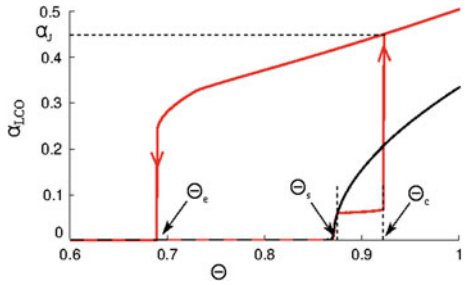

Fig. 6 Bifurcation diagram of the 2 dof aeroelastic system with cubic stiffness ($\xi_y = \xi_\alpha = 1$). *Black* Without SMA spring. *Red* With SMA spring (selected values: $h_l = 0.05$, $K_1 = 10\,K_2$ and $A_{SMA} = 2.35 \times 10^{-3}$)

LCO is represented versus Θ). The diagram is obtained numerically by direct integration in time of (5). The flow velocity is increased step by step, one time forward and one time backward, in order to get all the solution branches. When changing Θ to $\Theta + \delta\Theta$, the initial condition for $\Theta + \delta\Theta$ is selected as the steady state of the previous simulation launched for Θ. The black line in Fig. 6 shows the bifurcation diagram when only a cubic nonlinear restoring force is considered, no SMA is added to the system. In this case the classical supercritical bifurcation is retrieved. The diagram with a given SMA is represented with the red line.

The first striking feature one can observe is that due to the softening effect brought by the SMA, the bifurcation is now subcritical. The gain in using enhanced damping properties thanks to the hysteresis loop is illustrated through the appearance of the points denoted Θ_s (flow velocity for which the oscillations enters the loop and thus the enhanced damping capacity is present) and Θ_c (the point for which the martensitic transformation is finished so that the damping capacity has been fully exploited). Above Θ_c, a jump is observed to a branch parameterized by α_J (amplitude at Θ_c) where the LCO amplitudes are larger than without SMA. Hence the advantage of the enhanced damping capacity is here completely lost due to the appearance of this subcritical branch where large-amplitude motions are observed. Finally, the point where this subcritical branch disappears when decreasing the flow velocity, denoted Θ_e, defines a dangerous range of flow velocities where the system could jump to the higher branch.

The SMA parameters can be optimized in order to fulfill the following targets:

- decrease the amplitude α_J of the secondary branch as much as possible. In the best case, avoid subcriticality,
- decrease Θ_s so as to bring this point as close as possible to the flutter velocity,
- increase Θ_c as much as possible so as to take full advantage of the enhanced damping capacity of the SMA,
- increase Θ_e so as to avoid the large range of subcriticality where the two solution branches coexist.

Numerous simulations have been done to obtain the best parameters h_l and K_1/K_2, in order to fulfill at best these objectives. Figure 7c sums up some of the results obtained for illustration. One can conclude that in order to decrease the value α_J describing the upper branch, one has to select a large value for h_l, and in this case

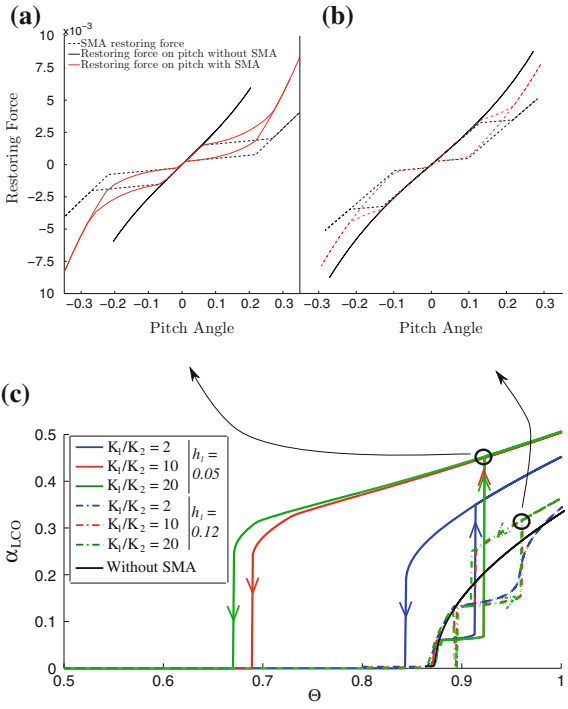

Fig. 7 **a** LCO amplitude versus flow speed for different SMA parameters ($\xi_h = \xi_\alpha = 1$ and A_{SMA} constant). **b** Corresponding restoring force for $\Theta = \Theta_c$, on the *left* $h_l = 0.05$ and $K_1/K_2 = 10$ and on the *right* $h_l = 0.12$ and $K_1/K_2 = 10$

it appears then more appropriate to take smaller values for the ratio K_1/K_2. One can also observe the advantageous effect of using a small value for K_1/K_2 when h_l has been selected small, as it increases substantially the value of Θ_e. Table 2 summarizes the effect of the coefficients with respect to the targeted objectives relative to the different remarkable points Θ_s, Θ_e, Θ_c and α_J. A simple plus/minus sign code is used for a quick understanding of the effect of each coefficients: a plus sign indicates an advantageous effect whereas a minus sign indicates a detrimental effect with respect to the target. From this table and Fig. 7c it appears clear that the best choice is a large h_l together with a small ratio K_1/K_2.

Figure 7a, b show the restoring force at two particular points in order to get physical insight in the results obtained. In Fig. 7a, a disadvantageous case is selected and one can observe that the softening effect is the dominating feature of the nonlinear restoring force of the SMA, explaining the enforced subcriticality observed on the bifurcation diagram. This adverse case helps also in understanding that increasing blindly the hysteresis loop area A_{SMA} is not a solution as it may have no effect on the subcriticality. When K_2 is too small, the sudden jump in amplitude observed for a small variation of force is detrimental as the system jumps to large amplitude motions and the energy of this vibratory state is too important. Figure 7b illustrates an advantageous case where the softening effect is not too important and thus leads to an improved global behaviour in the bifurcation diagram.

Table 2 Influence of the SMA constants on the identified points in the bifurcation diagram

SMA parameters	K_1/K_2		h_l	
Bif. pt	Small	Large	Small	Large
Θ_s	=	=	+++	−−−
Θ_e	+++	−−−	−−−	+++
Θ_c	−	+	−−−	+++
α_J	++	− −	−−−	+++

A plus sign shows an advantageous effect, whereas a minus sign indicates a detrimental effect on the targeted behaviour, while an equal sign shows no effect. The number of the sign is proportional to the magnitude of the effect

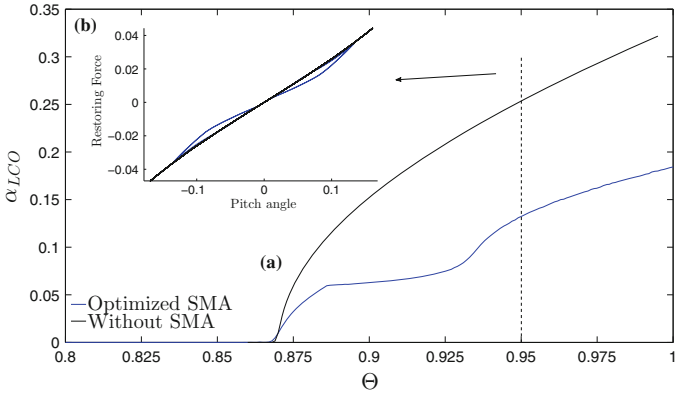

Fig. 8 **a** Bifurcation diagram with $h_l = 0.05$, $K_1/K_2 = 1.5$ and $\xi_\alpha = 3.4$. **b** Restoring force at $\Theta = 0.95$

This analysis shows undoubtedly that the best choice would be to have both the case of the hysteresis loop together with a stronger hardening effect at very large amplitude. To fulfill these requests, the full martensite branch should have a hardening behaviour stronger that the one of the reference case (without SMA). Such a configuration is obtained for example with $h_l = 0.05$, $K_1/K_2 = 1.5$ and $\xi_\alpha = 3.4$. Figure 8 shows the bifurcation diagram obtained in this case. One can observe that supercriticality is enforced. Secondly a large range of small amplitudes of LCOs are observed between 0.875 and 0.93, where the enhanced damping capacity of the SMA plays its role. Finally the improved hardening effect at large amplitude gives rise to a branch where amplitudes of LCOs are smaller, even when the transformation has been completed.

4 Conclusion

Whether one wants to harvest energy or avoid devastating intabilities, the control of aeroelastic flutter is a critical issue. An option is discussed here by using SMA springs in pseudo-elastic behaviour, in order to use the potential of dissipation of such materials. A numerical study with a simple heuristic model for the behaviour of the SMA has shown that the amplitude of the LCO after the flutter velocity can be significantly reduced by adding a SMA spring on the pitch mode of the two-dofs aeroelastic system. More precisely, the study of the bifurcation diagram clearly exhibits an advantageous effect of using the enhanced damping capacity of the SMA with the appearance of a branch of small amplitudes LCOs. However a detrimental effect appears because of the softening effect created by the solid-solid phase change. The optimized case is obtained by hardening the stiffness of the martensite phase. In this case it has been shown that subcriticality together with small amplitudes LCOs can be obtained.

The next steps of this research is to confront these preliminary findings with experiments. Complicating effects such as the dependence of the hysteresis loop on frequency, asymmetry of the SMA restoring force, aeroelastic nonlinearities due to stall phenomenon, will be studied and included in the model in order to obtain a global picture of the passive control of the flutter instability with SMA springs.

Acknowledgments This work is supported by Direction Générale de l'Armement (DGA) from French Ministry of Defense.

References

1. Bernardini, D., Rega, G.: The influence of model parameters and of the thermomechanical coupling on the behavior of shape memory devices. Int. J. Non-Linear Mech. **45**(10), 933–946 (2010)
2. Bernardini, D., Vestroni, F.: Non-isothermal oscillations of pseudoelastic devices. Int. J. Non-Linear Mech. **38**(9), 1297–1313 (2003)
3. Bisplinghoff, R.L., Ashley, H., Halfman, R.L.: Aeroelasticity. Courier Dover Publications, New York (2013)
4. Doaré, O., Sbarra, A., Touzé, C., Moussa, M.O., Moumni, Z.: Experimental analysis of the quasistatic and dynamic torsional behaviour of shape memory alloys. Int. J. Solids Struct. (2011)
5. Dowell, E.H. et al. A Modern Course in Aeroelasticity. Kluwer Academic, Dordrecht (1994)
6. Ko, J., Strganac, T.W., Kurdila, A.J.: Adaptive feedback linearization for the control of a typical wing section with structural nonlinearity. Nonlinear Dyn. **18**(3), 289–301 (1999)
7. Lacarbonara, W., Bernardini, D., Vestroni, F.: Nonlinear thermomechanical oscillations of shape-memory devices. Int. J. Solids Struct. **41**(5–6), 1209–1234 (2004)
8. Lee, Y.S., Kerschen, G., McFarland, D.M., Hill, W.J., Nichkawde, C., Strganac, T.W., Bergman, L.A., Vakakis, A.F.: Suppressing aeroelastic instability using broadband passive targeted energy transfers, part 2: experiments. AIAA J. **45**(10), 2391–2400 (2007)
9. Lee, Y.S., Vakakis, A., Bergman, L., McFarland, D.M., Kerschen, G.: Suppression aeroelastic instability using broadband passive targeted energy transfers, part 1: Theory. AIAA J. **45**(3), 693–711 (2007)

10. Moussa, M.O.: Modélisation du comportement dynamique non-linéaire des structures en matériaux à mémoire de forme. PhD thesis, Ecole Polytechnique (2012)
11. Moussa, M.O., Moumni, Z., Doaré, O., Touzé, C., Zaki, W.: Non-linear dynamic thermomechanical behaviour of shape memory alloys. J. Intell. Mater. Syst. Struct. **23**(14), 1593–1611 (2012)
12. Platanitis, G., Strganac, T.W.: Control of a nonlinear wing section using leading-and trailing-edge surfaces. J. Guidance Control Dyn. **27**(1), 52–58 (2004)
13. Saadat, S., Salichs, J., Noori, M., Hou, Z., Davoodi, H., Bar-On, I., Suzuki, Y., Masuda, A.: An overview of vibration and seismic applications of niti shape memory alloys. Smart Mater. Struct. (2002)
14. Strelec, J.K., Lagoudas, D.C., Kahn, M.A., Yen, J.: Design and implementation of a shape memory alloy actuated reconfigurable airfoil. J. Intell. Mater. Syst. Struct. (2003)
15. Visintin, A.: Differential Models of Hysteresis, vol. 1. Springer, Berlin (1994)

Using Steady-State Response for Predicting Stability Boundaries in Switched Systems Under PWM with Linear and Bilinear Plants

A. El Aroudi, M. Al-Numay, K. Al Hosani and N. Al Sayari

Abstract Switching systems under Pulse Width Modulation (PWM) are commonly utilized in many industrial applications. Due to their associated nonlinearities, such systems are prone to exhibit a large variety of complex dynamics and undesired behaviors. In general, slow dynamics in these systems can be predicted and analyzed by conventional averaging procedures. However, fast dynamics instabilities such as period doubling (PD) and saddle-node (SN) bifurcations cannot be detected by average models and analyzing them requires the use of additional sophisticated tools. In this chapter, closed-form conditions for predicting the boundary of these bifurcations in a class of PWM systems with linear and bilinear plants are obtained using a time-domain asymptotic approach. Previous studies have obtained similar boundaries by either solving the eigenvalue problem of the monodromy matrix of the Poincaré map or performing a Fourier series expansion of the feedback signal. While the former approach is general and can be applied to linear as well as bilinear plants, the later approach is applicable only to PWM systems with linear plants. The conditions for fast scale instability boundaries presented in this chapter are obtained from the steady-state analysis of the Poincaré map using an asymptotic approach without resorting to frequency-domain Fourier analysis and without using the monodromy matrix of the Poincaré map. The obtained expressions are simpler than the previously reported ones and allow to understand the effect of different system's

A. El Aroudi (✉)
University Rovira i Virgili, Tarragona, Spain
e-mail: abdelali.elaroudi@urv.cat

M. Al-Numay
King Saud University, Riyadh, KSA
e-mail: alnumay@ksu.edu.sa

K. Al Hosani · N. Al Sayari
The Petroleum Institute, Abu Dhabi, UAE
e-mail: khalhosani@pi.ac.ae

N. Al Sayari
e-mail: nalsayari@pi.ac.ae

M. Belhaq (ed.), *Structural Nonlinear Dynamics and Diagnosis*,
Springer Proceedings in Physics 168, DOI 10.1007/978-3-319-19851-4_18

parameters on its stability. In PWM systems with linear plants, under certain practical conditions concerning these parameters, the matrix form expression can be approximated by standard polynomial functions expressed in terms of the operating duty cycle weighted by the Markov parameters of the linear part of the system.

1 Introduction

Switched systems constitute a special class of nonlinear dynamical systems [1] and arise often in many practical engineering systems when some switching elements such as switches or diodes, block with dead-zone, saturated amplifiers, relays and comparators in electrical systems are present. This is also the case of mechanical systems where impacts or nonsmooth friction take place. A particular class of switched systems are those characterized by linear differential equations between switching events. These systems are called therefore piecewise linear (PWL) or piecewise affine (PWA) systems [2]. Most of the PWL systems studied in the literature are characterized by switching among linear subsystems when certain time-varying and T—periodic boundaries in the state-space are reached. This is the case of Pulse Width Modulation (PWM) systems like switching DC-DC power converters [3–8], DC-AC inverters [9], temperature control systems [10], switched capacitor networks and chaos generators [11] and hydraulic and fluid valve drivers [12, 13]. Nonlinearity arises from the feedback which imposes a constraint relating the duty cycle nonlinearly and in general implicitly to the vector of the system state variables. Despite their engineering use, one of the main drawbacks of switched systems under PWM is this nonlinearity making them prone to exhibit a large variety of complex dynamics and undesired behaviors [6, 10, 11]. Although each subsystem is linear and its describing differential equations can be solved in closed-form, the dynamics of the complete switched system is highly nonlinear and its accurate stability analysis requires sophisticated computational tools [14].

Switched systems under PWM employ switching devices to control a suitable output variable by using a T—periodic external modulating signal. Therefore, the only acceptable nominal operation of any switched system under PWM is a T—periodic oscillation around the desired level. When the stability of this periodic operation is lost, different slow scale-time or fast scale-time nonlinear phenomena can take place [15].

The dynamical behavior and the accurate stability analysis of this kind of systems can either be tackled by long-time integration of the continuous-time switched model, discrete-time model and its Jacobian matrix or Floquet theory with Fillipov technique to compute the mondromy matrix [16]. Other methods leading to the same matrix and based on trajectory sensitivity analysis are also available [17]. After obtaining the Jacobian or monodromy matrix, critical boundary conditions for some singularities like saddle-node (SN) bifurcation or period-doubling (PD) can be obtained by imposing that one eigenvalue is equal to $+1$ or -1, respectively [4]. It is in general

very cumbersome to compute the stability boundary of a PWM system using the previous methods.

Another approach, which was called *harmonic balance*,[1] used for the first time in [18] and recently in [5] for locating these boundaries is by expanding the feedback signal into a Fourier series to obtain the steady-state trajectory in certain periodic regimes and imposing critical conditions for the occurrence of the corresponding singularities like PD and SN bifurcations.

The conditions for fast scale instability boundaries presented in this chapter are obtained from the steady-state analysis of the Poincaré map using a time domain asymptotic approach without resorting to frequency-domain Fourier analysis and without using the monodromy matrix of the Poincaré map. The obtained expressions are simpler than the previously reported ones and allow to understand the effect of different system's parameters on its stability. Examples of PWM systems that can be studied by the approach of this chapter are DC-DC switching power electronics converters [3, 5, 6], DC-AC inverters [9], temperature control systems [10] and switched capacitor chaos generators [11], among others.

The rest of the chapter is organized as follows. Section 2 presents the switched model of systems with bilinear plants under PWM. A review of Poincaré map modeling approach is explained in Sect. 3 together with its steady-state solution. Subsequently, Sect. 4 deals with the steady-state approach for predicting the boundary of SN and PD instabilities in this kind of systems by imposing boundary conditions in the time-domain on the steady-state T-periodic and the $2T$—periodic orbits together with their respective switching conditions imposed by the PWM process. Finally, some concluding remarks are drawn in the last section.

2 Bilinear Modeling of PWM Switched Systems

2.1 Pulse Width Modulation

Pulse-width modulation is a technique used, among others, to control switched systems. This modulation technique is one of the mostly used methods in switched mode power supply for different applications. In this kind of systems, the average value of voltage or current fed to the load is controlled by turning ON and OFF some switching devices such as MOSFETs and IJBTs. The PWM switching frequency has to be much higher than the time constants of the plant to be controlled to minimize the ripple of the voltage or current applied to the load. The term duty cycle is defined as the proportion of ON-time duration of the switching element to the complete switching period. In the traditional PWM strategy, the duty cycle of the pulse driving signal $u(t)$ is varied according to the control signal $x_c(t)$ which correspond to

[1] In [5] this type of analysis was called *Harmonic Balance*. Here this term was conserved but to the opinion of the authors only a steady-state analysis of the feedback signal expressed in Fourier series has been used and no harmonic balance has been performed since the system loop is linear.

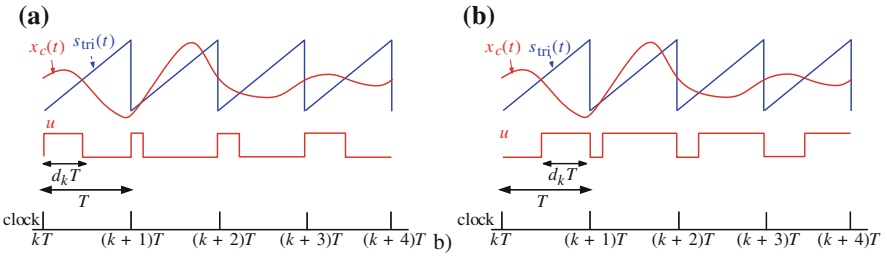

Fig. 1 Waveforms of the T—periodic external signal $s_{\text{tri}}(t)$ and the control signal **a** TEM $x_c = \mathbf{C}^{\intercal}(\mathbf{X}_{\text{ref}} - \mathbf{x}(t))$, **b** LEM $x_c = \mathbf{C}^{\intercal}(\mathbf{x}(t) - \mathbf{X}_{\text{ref}})$

a compensated version of the error between the output variable (voltage or current) and its desired reference x_{ref}. This error is processed through an error compensator to provide the control signal $x_c(t)$. In direct duty cycle control, the simplest analog form of generating a fixed frequency PWM is by comparing the control voltage with a ramp periodic signal $s_{\text{tri}}(t)$ in such a way that the pulse signal $u(t)$ goes high/low at switching instants t_s when the control signal $x_c(t)$ is higher/lower than the triangular signal $s_{\text{tri}}(t)$ (Fig. 1). In other constant frequency modulation schemes, the switch is turned ON (resp. OFF) periodically while it is turned OFF (resp. ON) whenever the peak (resp. valley) control signal x_c reaches the ramp compensator. The ratio of the first interval duration $t_{s,k}$ to the complete period T $((t_{s,k})/T)$ during the switching cycle $(kT, (k+1)T)$ is the duty cycle d_k in that cycle for Trailing Edge Modulation (TEM) strategies while it is its complementary $\overline{d}_k = 1 - d_k$ for Leading Edge Modulation (LEM) strategies. The control signal for TEM strategies can be expressed as $x_c = \mathbf{C}^{\intercal}(\mathbf{X}_{\text{ref}} - \mathbf{x})$ while it is $x_c = \mathbf{C}^{\intercal}(\mathbf{x} - \mathbf{X}_{\text{ref}})$ for LEM schemes, where $\mathbf{x} \in \mathbb{R}^n$ is the vector of the state variables including the power stage and the controller parameters and n is the order of the system after excluding any existing integrator in the loop. $\mathbf{C}$ is an appropriate feedback vector and $\mathbf{X}_{\text{ref}}$ is a suitable reference vector. In both strategies, the generation of the PWM driving signal is carried out by comparing the control signal x_c with the T—periodic signal s_{tri}.

2.2 The Bilinear Switched Model

Let us focus on TEM strategy. The results corresponding to LEM can be deduced from those of TEM strategy by just a change of variable $d_k \to 1 - d_k$. During a switching period of length T, an orbit of a switched system under PWM starting at time instant kT $(k \in \mathbb{Z})$ is forced, using a clocked latch, to be governed by the vector field

$$\mathbf{f}_1(\mathbf{x}, \mathbf{w}) = \mathbf{A}_1\mathbf{x} + \mathbf{B}_1\mathbf{w} \tag{1}$$

This orbit intersects with a switching boundary, at a certain switching instant $t_s = d_kT$ decided by the modulation strategy. The switching occurs when the external

periodic ramp signal s_{tri} intersects with the control signal x_c. The orbit then goes to another different linear system described by the vector field

$$\mathbf{f}_2(\mathbf{x}, \mathbf{w}) = \mathbf{A}_2\mathbf{x} + \mathbf{B}_2\mathbf{w} \tag{2}$$

where $\mathbf{A}_i \in \mathbb{R}^{n\times n}$ and $\mathbf{B}_i \in \mathbb{R}^{n\times m}$, $i = 1, 2$ are the system state matrices for phase i and $\mathbf{w} \in \mathbb{R}^m$ is the vector of the external parameters of the plant and controller, m being the number of the external inputs to the system which are supposed to be constant within a switching cycle. The system is forced periodically and synchronously to the first phase ($i = 1$) characterized by the vector field $\mathbf{f}_1$ while it is switched to the second phase ($i = 2$) characterized by the vector field $\mathbf{f}_2$ whenever the condition $\sigma(\mathbf{x}, t) := \mathbf{C}^\intercal(\mathbf{X}_{\text{ref}} - \mathbf{x}) - s_{\text{tri}} = 0$ holds. In compact form, the model of a switched system under PWM can be written in the following general *bilinear* form

$$\dot{\mathbf{x}} = u\mathbf{f}_1(\mathbf{x}, \mathbf{w}) + (1 - u)\mathbf{f}_2(\mathbf{x}, \mathbf{w}) \tag{3a}$$

where $\mathbf{f}_1(\mathbf{x}, \mathbf{w}) = \mathbf{A}_1\mathbf{x} + \mathbf{B}_1\mathbf{w}$, $\mathbf{f}_2(\mathbf{x}, \mathbf{w}) = \mathbf{A}_2\mathbf{x} + \mathbf{B}_2\mathbf{w}$ and $u \in \{0, 1\}$ is the driving signal which is generated by the PWM process by which the system is forced to one phase cyclically while it is switched to the other phase whenever the control signal x_c crosses the periodic signal $s_{\text{tri}}(t)$. In TEM strategies, the switching condition $\mathbf{C}^\intercal(\mathbf{X}_{\text{ref}} - \mathbf{x}) = s_{\text{tri}}$ can be written as $-\mathbf{C}^\intercal\mathbf{x} = r$, where $r = -\mathbf{C}^\intercal\mathbf{X}_{\text{ref}} + s_{\text{tri}}$.

3 Review of Poincaré Map Modeling of PWM Systems

3.1 Closed-Form Solution of the State Variables

The trajectory $\mathbf{x}(t)$ at time t of the system starting from an initial condition $\mathbf{x}(t_0)$ at time instant t_0 can be expressed as follows

$$\mathbf{x}(t) = e^{\mathbf{A}_i(t-t_0)}\mathbf{x}(t_0) + \mathbf{A}_i^{-1}(e^{\mathbf{A}_i(t-t_0)} - \mathbf{I})\mathbf{B}_i\mathbf{w} \tag{4}$$

It is assumed that the matrix $\mathbf{A}_i$ is nonsingular. It should be noted that two kinds of singularities may arise in this kind of switched systems which are detailed below:

1. A singularity which takes place only theoretically and that can be avoided by just adding parasitic elements [19].
2. A structural singularity that cannot be avoided by just adding parasitics. In this case, the previous expression for the solution of the system state variables cannot be used if the integrator was taken into account despite the fact that this solution exists and it is well defined even in the case when the matrix $\mathbf{A}_i$ is not invertible. However, the integral action has no meaning without closing the loop by the feedback and the PWM process. Having said that, the switched model used in this study and the expression of the trajectories in (4) do not take into account the

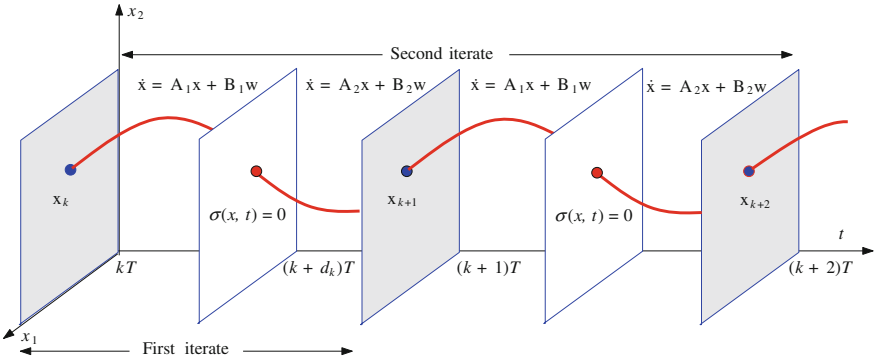

Fig. 2 State-space representation of a switched system under PWM

integral variable. However, while the integral action could have an effect on the slow scale dynamics, its effect on the fast scale dynamics is negligible [6].

3.2 Local Mappings

Since the vector fields between the switching events are linear we can use the exact analytical solution to express the value of the state vector at the end of a switching cycle in terms of its value at the beginning of that cycle, Fig. 2. The local Poincaré map of the system within switching sub-intervals can be obtained by using (4) during the corresponding interval [2]. Let us define $\mathbf{x}_k = \mathbf{x}(kT)$, $\mathbf{x}_d = \mathbf{x}((k + d_k)T)$, $\mathbf{x}_{k+1} = \mathbf{x}((k + 1)T)$ where d_k is the duty cycle during the cycle $(kT, (k + 1))T$. Therefore, the local mappings are given by

$$\mathbf{x}_d := P_1(\mathbf{x}_k) = \mathbf{\Phi}_1(d_kT)\mathbf{x}_k + \mathbf{\Psi}_1(d_kT) \tag{5a}$$

$$\mathbf{x}_{k+1} := P_2(\mathbf{x}_d) = \mathbf{\Phi}_2((1 - d_k)T)\mathbf{x}_d + \mathbf{\Psi}_2((1 - d_k)T) \tag{5b}$$

where, according to (5a) and (5b), $\mathbf{\Phi}_k(t)$ and $\mathbf{\Psi}_k(t)$ are defined by:

$$\mathbf{\Phi}_k(t) = e^{\mathbf{A}_kt} \quad \text{and} \quad \mathbf{\Psi}_k(t) = \mathbf{A}_i^{-1}(e^{\mathbf{A}_it} - \mathbf{I})\mathbf{B}_i\mathbf{w} \tag{6}$$

Most parts of this chapter require only a very moderate knowledge of mathematics. What is importantly required is just an understanding of the previous solution and simple algebraic matrix arrangements as it will be shown later.

3.3 Linear Poincaré Map for the Open Loop System

The mapping describing the system behavior between the time instants kT and $(k+1)T$ can be obtained by composing the two previously presented local mappings [2], i.e., the Poincaré map $P = P_2 \circ P_1$ of the switched PWM system described by the vector fields given in (1) and (2) can be written in the following form

$$\mathbf{x}_{k+1} = \boldsymbol{\Phi}(d_k)\mathbf{x}_k + \boldsymbol{\Psi}(d_k) \tag{7}$$

where $\boldsymbol{\Phi}(d_k)$ and $\boldsymbol{\Psi}(d_k)$ are given by:

$$\boldsymbol{\Phi}(d_k) := \boldsymbol{\Phi}_2((1-d_k)T)\boldsymbol{\Phi}_1(d_kT) \tag{8a}$$

$$\boldsymbol{\Psi}(d_k) := \boldsymbol{\Phi}_2((1-d_k)T)\boldsymbol{\Psi}_1(d_kT) + \boldsymbol{\Psi}_2(d_kT) \tag{8b}$$

3.4 Closing the Loop: The Source of Nonlinearity

For appropriate operation of PWM systems and regulation of some suitable outputs in the presence of parameter changes, output feedback is used. Often an integrative action is necessary in order to regulate a certain output variable x_o to get a zero steady-state error between this output variable and the desired reference x_{ref}. First, the error $e := x_{\text{ref}} - x_o$ is computed and then it is processed through a compensator containing an integrator to increase, in average, the DC gain of the system while other poles and zeroes of the compensator are selected with the aim to meet some design specifications like maximum allowed overshoot and system response speed and settling time due to step changes. As it has been mentioned before, this integral action has a negligible effect on the fast scale instability [6]. Therefore, we exclude the integral variable from the analysis. The feedback loop together with the PWM process imposes the following constraint between the state variables $\mathbf{x}(d_kT)$ and the duty cycle d_k at the kth switching cycle

$$\begin{aligned}\sigma(\mathbf{x}(d_kT), d_k) :&= -\mathbf{C}^{\intercal}\mathbf{x}_d - r(d_kT) \\ &= -\mathbf{C}^{\intercal}\boldsymbol{\Phi}_1(d_kT)\mathbf{x}_k + \boldsymbol{\Psi}_1(d_kT) - r(d_kT) = 0\end{aligned} \tag{9}$$

The expression in (9) is nonlinear in d_k and it is responsible for many nonlinear phenomena that could take place in PWM systems.

3.5 Steady-State Response of the Poincaré Map

In this section, let D be the steady-state duty cycle. Let also $\boldsymbol{\Phi}_1 = e^{\mathbf{A}_1 DT}$ and $\boldsymbol{\Phi}_2 = e^{\mathbf{A}_2(1-D)T}$, $\boldsymbol{\Psi}_1 = \mathbf{A}_1^{-1}(e^{\mathbf{A}_i DT} - \mathbf{I})\mathbf{B}_1\mathbf{w}$ and $\boldsymbol{\Psi}_2 = \mathbf{A}_2^{-1}(e^{\mathbf{A}_i((1-D)T)} - \mathbf{I})\mathbf{B}_2\mathbf{w}$. Let $\mathbf{x}_{ss}(0)$ be the steady-state value of the periodic orbit of the system at the beginning

of the switching period and $\mathbf{x}_{ss}(DT)$ be the steady-state value of this orbit at time instant DT. Therefore, in steady-state, according to (4), the vector of state variables at the beginning of the switching period is given by (Fig. 1)

$$\mathbf{x}_{ss}(0) = \mathbf{x}_{ss}(T) = \mathbf{\Phi}_2 \mathbf{x}_{ss}(DT) + \mathbf{\Psi}_2 \tag{10}$$

In turn, the vector of state variables at the switching time DT within the same period can be expressed as follows

$$\mathbf{x}_{ss}(DT) = \mathbf{\Phi}_1 \mathbf{x}_{ss}(0) + \mathbf{\Psi}_1 \tag{11}$$

Using (10) in (11), one obtains

$$\mathbf{x}_{ss}(DT) = \mathbf{\Phi}_1 \mathbf{\Phi}_2 \mathbf{x}_{ss}(DT) + \mathbf{\Phi}_1 \mathbf{\Psi}_2 + \mathbf{\Psi}_1 \tag{12}$$

Therefore, the steady-state value of the state variables $\mathbf{x}_{ss}(DT)$ at the time instant DT is given by

$$\mathbf{x}_{ss}(DT) = (\mathbf{I} - \mathbf{\Phi}_1 \mathbf{\Phi}_2)^{-1} (\mathbf{\Phi}_1 \mathbf{\Psi}_2 + \mathbf{\Psi}_1) \tag{13}$$

Let $\mathbf{\Phi} = \mathbf{\Phi}_1 \mathbf{\Phi}_2$ and $\mathbf{\Psi} = \mathbf{\Phi}_1 \mathbf{\Psi}_2 + \mathbf{\Psi}_1$. Then, (13) can be simplified as follows

$$\mathbf{x}_{ss}(DT) = (\mathbf{I} - \mathbf{\Phi})^{-1} \mathbf{\Psi} \tag{14}$$

where the matrix $(\mathbf{I} - \mathbf{\Phi})$ is assumed to be nonsingular. It should be noted that the previous system is open loop stable if the integral state variable is excluded because the matrices $\mathbf{A}_i$ are supposed to represent dissipative linear system configuration. The monodromy matrix of the open loop system is the product of the monodromy matrices corresponding to the two linear configurations. Both monodromy matrices are stable because they are exponential matrix functions of Hurwitz matrices. Therefore, the product of both monodromy matrices is a Jury matrix and then the open loop system is stable. Note also that if the integrator was included in the model, the open loop system response would be unbounded unless the input to the integrator is zero.

The stability of periodic orbits of a closed loop PWM system can be analyzed by checking the evolution of a small perturbation in the state variable within one period. This problem can be tackled by different ways. One of the most used techniques is to analyze the stability of the fixed points of the Poincaré map of the closed loop system by using its Jacobian matrix. The periodic orbit will be stable if this matrix evaluated at the associated fixed point has eigenvalues with modulus less than 1. Another technique is by using Floquet theory and Filippov method which leads to the same results [6]. In this chapter a different approach will be used which is based on the analysis of the steady-state response of the Poincaré map to periodic and subharmonic excitations [26].

4 A Steady-State Approach for Predicting Fast Time-Scale Instabilities

Using the steady-state response for predicting fast-scale instability in the form of subharmonic oscillation has been first introduced in [17] for a simple case of a PWM system with linear plant which consists of a DC-DC buck converter under voltage mode control. Years later, this method has been re-considered in [3, 5]. The method in both works consists of a Fourier series expansion of the feedback signal and its use for predicting stability boundaries after imposing a certain system periodic regime by the PWM process. With that approach an effort to transform the results from the Fourier frequency-domain into the time-domain must be done. In [5], the transformation from the Fourier frequency-domain to the time-domain is based on elementary partial fraction decomposition after defining some elementary cases of the system *transfer function* in the $s-$domain and listing them in the form of tables. However, this transfer function cannot be directly defined for systems with $\mathbf{A}_2 \neq \mathbf{A}_1$ making the approach only applicable for a limited class of PWM systems like the ones considered in [5]. In particular, those can be formulated in the form of a linear subsystem and a square-wave signal generated by a comparator like the PWM process. It should be noted that in [5] the approach is based on the Fourier series expansion to a system with theoretically $\mathbf{A}_2 \neq \mathbf{A}_1$ was applied but by making an approximation and an order reduction leading finally to the simple linear case $\mathbf{A}_1 = \mathbf{A}_2$. Another different type of approximation leading to the same consequence $\mathbf{A}_1 = \mathbf{A}_2$ has been used and justified in [7] for this kind of systems. In [20], the Poisson sum formulae and some related Fourier series properties have been used to transform the condition for PD occurrence derived in [5] from the Fourier frequency-domain to a matrix-form state-space time-domain condition. It was shown in this study that a steady-state analysis of the trajectory of the system in the time-domain without any order reduction, except from excluding the integrator, will lead to new equivalent simple expressions without need to use the Fourier series expansion and without having to perform any transformation nor needing the calculation of the Jacobian or the monodromy matrix.

4.1 Predicting SN Bifurcation

SN bifurcation or *tangent* bifurcation is a type of local bifurcations that can take place in nonlinear continuous-time dynamical systems. This nonlinear phenomenon is characterized by the fact that two solutions of a continuous system collide and annihilate each other at a certain critical value of the system bifurcation parameter. When the system is represented by a Poincaré mapping obtained by sampling a continuous-time system as it is the case in PWM systems, these solutions correspond to periodic orbits of the original system and the phenomenon is also called *cyclic fold* bifurcation.

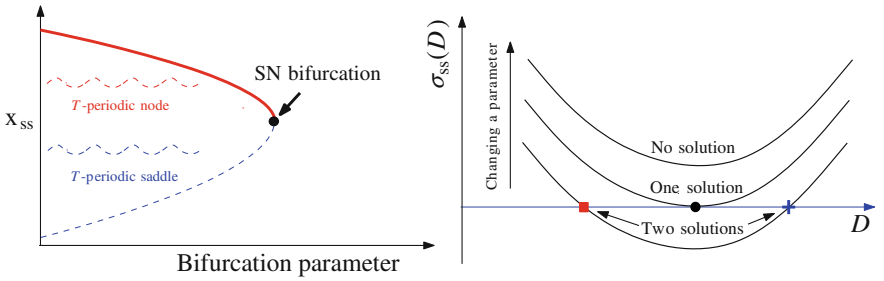

Fig. 3 SN bifurcation in a nonlinear dynamical system

In steady state the feedback loop together with the PWM process imposes the following constraint between the state variables $\mathbf{x}_{ss}(DT)$ and the steady-state duty cycle D

$$\sigma_{ss}(D) := \sigma(\mathbf{x}_{ss}(DT), DT) := -\mathbf{C}^{\intercal}\mathbf{x}_{ss}(DT) - r(DT) = 0 \tag{15}$$

If a SN bifurcation takes place at a certain critical value of the system bifurcation parameter, there must be a tangency between the feedback signal—$\mathbf{C}^{\intercal}x_{ss}(DT)$ and the ramp signal $r(DT)$ for the imposed steady-state duty cycle D in such a way that two solutions of (15) coalesce and disappear (Fig. 3). The number of solutions of (15) equals to the number of T—periodic orbits that exist for a specific set of parameters. Therefore, from (15), the following equality holds at this critical point

$$\frac{\partial \sigma_{ss}(D)}{\partial D} = 0 \Rightarrow -\frac{\partial \mathbf{C}^{\intercal}\mathbf{x}_{ss}(DT)}{\partial D} = \frac{\partial r(DT)}{\partial D} \tag{16}$$

Let $\sigma_e(D) = 1/T \times \partial r/\partial D$ be the slope of the external T—periodic signal $r(t)$ at time instant DT. Therefore, (16) becomes

$$-\frac{1}{T}\mathbf{C}^{\intercal}\frac{\partial \mathbf{x}_{ss}(DT)}{\partial D} = \sigma_e(D) \tag{17}$$

The derivative of the left side of (17) can be obtained by using (14) and differentiating the involved matrix functions. Let us calculate the derivative $\partial \mathbf{x}_{ss}(DT)/\partial D$. Using (14) one obtains

$$\frac{\partial \mathbf{x}_{ss}(DT)}{\partial D} = \frac{\partial}{\partial D}(\mathbf{I} - \mathbf{\Phi})^{-1}\mathbf{\Psi} + (\mathbf{I} - \mathbf{\Phi})^{-1}\frac{\partial \mathbf{\Psi}}{\partial D} \tag{18}$$

Using known chain rules for matrix derivative, (18) can be written as follows

$$\frac{\partial \mathbf{x}_{ss}(DT)}{\partial T} = (\mathbf{I} - \mathbf{\Phi})^{-1}\frac{\partial \mathbf{\Phi}}{\partial D}(\mathbf{I} - \mathbf{\Phi})^{-1}\mathbf{\Psi} + (\mathbf{I} - \mathbf{\Phi})^{-1}\frac{\partial \mathbf{\Psi}}{\partial D} \tag{19}$$

Making the term $(\mathbf{I}-\mathbf{\Phi})^{-1}$ as a common factor results in the following equation

$$\frac{\partial \mathbf{x}_{\mathrm{ss}}(DT)}{\partial D} = (\mathbf{I}-\mathbf{\Phi})^{-1}\left(\frac{\partial \mathbf{\Phi}}{\partial D}(\mathbf{I}-\mathbf{\Phi})^{-1}\mathbf{\Psi} + \frac{\partial \mathbf{\Psi}}{\partial D}\right) \tag{20}$$

then by using (14), the expression (20) becomes

$$\frac{\partial \mathbf{x}_{\mathrm{ss}}(DT)}{\partial D} = (\mathbf{I}-\mathbf{\Phi})^{-1}\left(\frac{\partial \mathbf{\Phi}}{\partial D}\mathbf{x}(DT) + \frac{\partial \mathbf{\Psi}}{\partial D}\right) \tag{21}$$

The derivative of the involved matrix function $\partial\mathbf{\Phi}(D)/\partial D$ can be calculated as follows

$$\begin{aligned}\frac{\partial \mathbf{\Phi}}{\partial D} &= \frac{\partial}{\partial D}(\mathbf{\Phi}_1\mathbf{\Phi}_2)\\ &= \mathbf{\Phi}_1(\mathbf{A}_1-\mathbf{A}_2)\mathbf{\Phi}_2 T\end{aligned} \tag{22}$$

Likewise, the derivative of $\partial\mathbf{\Psi}(D)/\partial D$ can be obtained by

$$\begin{aligned}\frac{\partial \mathbf{\Psi}}{\partial D} &= \frac{\partial}{\partial D}(\mathbf{\Phi}_1\mathbf{\Psi}_2+\mathbf{\Psi}_1)\\ &= \frac{\partial}{\partial D}(\mathbf{\Phi}_1)\mathbf{\Psi}_2 + \mathbf{\Phi}_1\frac{\partial}{\partial D}(\mathbf{\Psi}_2) + \frac{\partial}{\partial D}(\mathbf{\Psi}_1)\\ &= \mathbf{\Phi}_1((\mathbf{A}_1-\mathbf{A}_2)\mathbf{\Psi}_2 + \mathbf{B}_1-\mathbf{B}_2)T\end{aligned} \tag{23}$$

Let $\Delta\mathbf{A} = \mathbf{A}_1-\mathbf{A}_2$ and $\Delta\mathbf{B} = \mathbf{B}_1-\mathbf{B}_2$. Substituting (22) and (23) in (21), the critical boundary condition for SN bifurcation boundary in (17) becomes

$$\sigma_{e,\mathrm{SN}}(D) = \sigma_e(D) \tag{24}$$

where $\sigma_{e,\mathrm{SN}}(D)$, the critical slope of the external function $r(t)$ for SN bifurcation occurrence, can be expressed by

$$\sigma_{e,\mathrm{SN}}(D) = -\mathbf{C}^{\intercal}(\mathbf{I}-\mathbf{\Phi})^{-1}\mathbf{\Phi}_1(\Delta\mathbf{A}\mathbf{x}_{ss}(0)+\Delta\mathbf{B}) \tag{25}$$

Taking into account that $\mathbf{A}_1\mathbf{x}(t)+\mathbf{B}_1 = \dot{\mathbf{x}}(t^-) = \mathbf{f}_1(\mathbf{x},\mathbf{w})$ and that $\mathbf{A}_2\mathbf{x}(t)+\mathbf{B}_2 = \dot{\mathbf{x}}(t^+) = \mathbf{f}_2(\mathbf{x},\mathbf{w})$, the critical value of the slope of the external T—periodic function at the boundary of a SN bifurcation is

$$\sigma_{e,\mathrm{SN}}(D) = -\mathbf{C}^{\intercal}(\mathbf{I}-\mathbf{\Phi})^{-1}\mathbf{\Phi}_1\Delta\mathbf{f}(\mathbf{x}_{\mathrm{ss}}(0)) \tag{26}$$

where $\Delta\mathbf{f}(\mathbf{x}) = \mathbf{f}_1(\mathbf{x},\mathbf{w}) - \mathbf{f}_2(\mathbf{x},\mathbf{w})$. It has to be mentioned here that in [4, 8] a slightly differently expressed condition has been obtained for the same boundary condition which is reported and adapted here for comparison

$$\sigma_{e,\mathrm{SN}}(D) = -\mathbf{C}^{\mathsf{T}}[\mathbf{f}_1(\mathbf{x}_{\mathrm{ss}}(D^-T)) + \mathbf{\Phi}_1(\mathbf{I} - \mathbf{\Phi}_2\mathbf{\Phi}_1)^{-1}])\mathbf{\Phi}_2\Delta\mathbf{f}(\mathbf{x}_{\mathrm{ss}}(DT)) \quad (27)$$

Although apparently the condition (27) derived in [4, 8] and that in (26) do not coincide, they just happen to be the same conditions but expressed differently. Note however that the expression (26) is simpler than (27). To illustrate the use of the previous expression, let us consider the following three different cases of compensating external signals:

- Case of a linear compensating ramp signal

$$r(t) = r_0 + \sigma_e t \quad (28)$$

where r_0 is the initial value of the external signal at $t = 0$ and σ_e is its constant slope. This is the ideal case of most PWM systems. Since the slope is constant, the right-hand side of (24) is given by

$$\sigma_e(D) = \sigma_e \ \forall D \quad (29)$$

- Case of a quadratic modulating signal. For improving the performances of some switching PWM systems, a quadratic modulating signal can be used [21, 22]. Let σ_0 be the initial slope of the external signal at $t = 0$ and let σ_T be its final slope at $t = T$. Therefore, this signal can be expressed as follows

$$r(t) = r_0 + \sigma_0 t + \frac{1}{2T}(\sigma_T - \sigma_0)t^2 \quad (30)$$

In this case, the slope is linearly dependent on the duty cycle D and the right-hand side of (24) can be expressed as follows

$$\sigma_e(D) = \sigma_0 + (\sigma_T - \sigma_0)D \quad (31)$$

- In a practical implementation, the external modulating signal is implemented by a first order low pass filter system making its shape more exponential than linear. In this case, the ramp signal $r(t)$ can be expressed as follows

$$r(t) = r_0 + \sigma_0\tau(1 - e^{-\frac{t}{\tau}}) \quad (32)$$

where τ is a suitable time constant and σ_0 is the initial slope at the beginning of the switching cycle. The slope is exponentially depending on the duty cycle D and the right-hand side of (24) is given by

$$\sigma_e(D) = \sigma_0 e^{-\frac{DT}{\tau}} \quad (33)$$

4.2 Application Examples for Predicting SN Bifurcation

4.2.1 General Bilinear Plants

Example 1: Consider a boost converter under state feedback control with the parameter values considered in [23] (Fig. 4). These are: input voltage $v_g = 5$ V, inductance $L = 50$ μH, capacitance $C = 4.4$ μF, voltage feedback gain $k_v = -0.0435$, current feedback gain $k_i = 0.174$ Ω, voltage reference $V_{\text{ref}} = 0.13$ V, load resistance $R = 28$ Ω. Three different values of switching frequency are used to illustrate the occurrence of SN bifurcation. The system matrices and vectors are as follows

$$\mathbf{A}_1 = \begin{pmatrix} -\frac{1}{RC} & 0 \\ 0 & 0 \end{pmatrix}, \mathbf{A}_2 = \begin{pmatrix} -\frac{1}{RC} & \frac{1}{C} \\ -\frac{1}{L} & 0 \end{pmatrix}$$

$$\mathbf{B}_1 = \mathbf{B}_2 = \begin{pmatrix} 0 \\ \frac{1}{L} \end{pmatrix}, \quad \mathbf{x} = \begin{pmatrix} v_{C_1} \\ i_{L1} \end{pmatrix}, \quad \mathbf{w} = v_g, \quad \mathbf{C} = \begin{pmatrix} k_v \\ k_i \end{pmatrix}$$

All the parameters appearing in the matrices can be identified in the circuit diagram of Fig. 4.

Numerical simulations in [23] confirm that the system is stable for switching frequencies greater than $f_s = 500$ kHz and unstable for lower frequencies. For f_s =500 kHz, it was shown in [24] that the system has one stable operating solution with duty

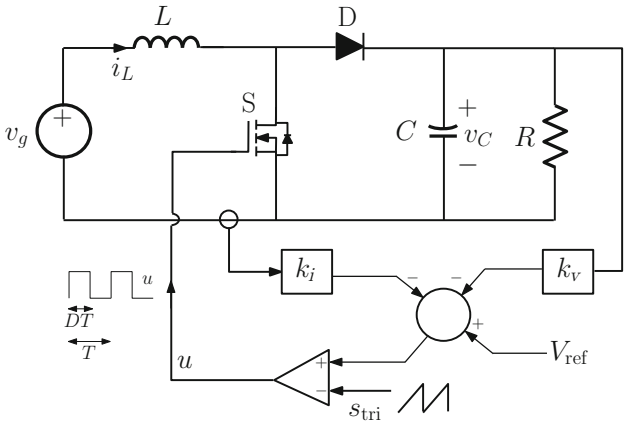

Fig. 4 Boost converter under a state feedback control

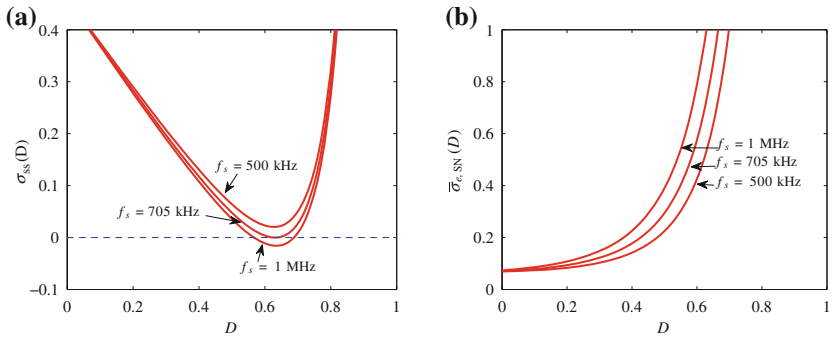

Fig. 5 The switching function $\sigma_{ss}(D)$ showing the disappearance of two solutions near a SN bifurcation (**a**) and the stability map in terms of the duty cycle and the normalized slope ($\overline{\sigma}_e = \sigma_e/(v_g/L)$) of the signal r (**b**)

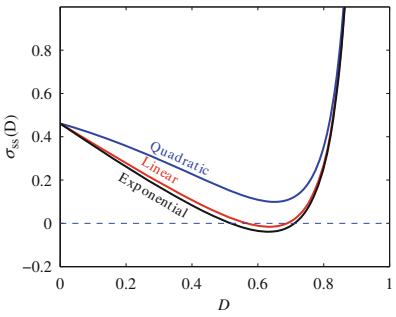

Fig. 6 The effect of the type of the modulator on the SN bifurcation

cycles $D \approx 0.58$ and one unstable solution with $D \approx 0.70$. This instability has been explained numerically by expanding the system waveforms in the form of a Fourier series and a Picard iterative process applied to the function $f(D) = -\mathbf{C}^{\mathrm{T}}\mathbf{x}(DT)$. The statement in [23] that the system is unstable has been refined using the concept of the basin of attraction. It has been stated that starting in the (possibly small) basin of attraction of the behavior corresponding to the stationary duty cycle $D \approx 0.58$ the system converges to a periodic regime characterized by this duty cycle value. Hence, starting in this domain of attraction the system exhibits a stable behavior. However, transient solutions outside this basin are unstable and the system do not converge to the desired periodic regime. Here we confirm the result reported in [24] by using the new derived expression (26) and we show that the critical value for occurrence of SN bifurcation is $f_s \approx 705$ kHz.

Figure 5a shows the boundary of SN in the parameter space (D, σ_e) by considering a linear ramp modulator for different values of switching frequency f_s. Figure 5b shows the steady-state switching function $\sigma_{ss}(D)$ for the same values of the switching frequency where it can be observed that for $f_s \approx 705$ kHz the system is indeed at the boundary of SN bifurcation. In order to show the effect of the type of the modulator signal on the system behavior, Fig. 6 shows the switching function $\sigma_{ss}(D)$ in term

of the steady-sate duty cycle D. The switching frequency is fixed at $f_s = 1$ MHz. It can be observed that while the stability is improved with an exponential modulator, it is worsened in the case of a quadratic modulator. For a fair comparison, the same value of ramp amplitude $V_M = 1$ V is used for the three modulators.

4.2.2 Special Linear Plants

Example 2: The second example that will be considered in this study is a buck converter driving another converter both under current mode control. The second converter can be approximated by a constant current sink [25]. All the parameters appearing in the matrices can be identified in the circuit diagram of Fig. 7. Because $\mathbf{A}_1 = \mathbf{A}_2$, the plant is linear. The used parameter values are the same ones of [25] and are as follows: input voltage $v_g = 120$ V, inductance $L = 37.5\,\mu$H, DC parasitic of the inductance $r_L = 0.01\ \Omega$, capacitance value $C = 420\,\mu$F, equivalent series resistance of the capacitor $r_C = 0.01\ \Omega$, output current $i_o = 38$ A and switching frequency $f_s = 50$ kHz. The system matrices and vectors are as follows

$$\mathbf{A}_1 = \mathbf{A}_2 = \begin{pmatrix} 0 & \frac{1}{C} \\ -\frac{1}{L} & -\frac{r_L + r_C}{L} \end{pmatrix},$$

$$\mathbf{B}_1 = \begin{pmatrix} \frac{1}{C} & 0 \\ \frac{1}{L} & \frac{r_C}{L} \end{pmatrix}, \quad \mathbf{B}_2 = \begin{pmatrix} \frac{1}{C} & 0 \\ 0 & \frac{r_C}{L} \end{pmatrix},$$

$$\mathbf{x} = \begin{pmatrix} v_C \\ i_L \end{pmatrix}, \quad \mathbf{w} = \begin{pmatrix} v_g \\ i_o \end{pmatrix}, \quad \mathbf{C_1} = \begin{pmatrix} 1 \\ 0 \end{pmatrix}$$

Figure 8 shows $\sigma_{\text{ss}}(D)$ which gives the possible operating steady-state duty cycles for different values of i_{ref} just below and just above the SN critical point. This figure also shows the stability map of the system in the parameter space (D, σ_e). For $D < 0.5$, the system has only one solution. For $D > 0.5$, three different regions can be identified. The first one is $\sigma_e < \sigma_{e,\text{SN}}$ where the system presents no solution. The second one is $\sigma_{e,\text{SN}} < \sigma_e < V_g/(2L)$ where the system presents one stable solution and one saddle. The last one where $\sigma_e > V_g/(2L)$ and the system presents one stable solution. For this particular example it turns out that the boundary of the SN bifurcation in the parameter space (D, σ_e) is approximately a straight line whose slope is V_g/L and passing from $D = 0.5$ and its maximum value is $V_g/(2L)$ for $D = 1$. Therefore, by choosing $\sigma_e = V_g/(2L)$ will guarantee that the system to have only one solution independently on the value of the steady-state cycle.

4.3 A Steady-State Approach for Predicting PD Bifurcation

4.3.1 Steady-State Response of the Second Iterate Poincaré Map

Consider a switched dynamical system under PWM exhibiting a PD bifurcation as shown in Fig. 9. After this phenomenon takes place, a $2T$-periodic solution develops at the critical point while in contrast to the SN bifurcation case, the T-periodic solution loses its stability but it continues to exist. During the switching cycle of duration T, a PWM system has two phases defined by the system matrices $(\mathbf{A}_1, \mathbf{B}_1)$ and $(\mathbf{A}_2, \mathbf{B}_2)$, respectively. During the switching cycle of duration $2T$, this system has four phases defined by the system matrices $(\mathbf{A}_1, \mathbf{B}_1)$, $(\mathbf{A}_2, \mathbf{B}_2)$, $(\mathbf{A}_1, \mathbf{B}_1)$ and $(\mathbf{A}_2, \mathbf{B}_2)$, respectively. Let us assume that the system behavior in steady-state is a $2T$-periodic orbit. Therefore, during two consecutive switching periods in the interval $(kT, (k+2)T)$, let the crossing between the signals $-\mathbf{C}^\intercal\mathbf{x}(t)$ and $r(t)$ occurs at $t = (D - \varepsilon_t + k)T$ and at $t = (1 + D + \varepsilon_t + k)T$, $k \in \mathbb{Z}$ (see Fig. 10). The parameter ε_t is a small quantity that vanishes at the boundary between T—periodic and $2T$-periodic behavior. At this point, the T-periodic solution and the $2T$-periodic solution are coincident (Fig. 9). By obtaining the expression of the $2T$-periodic steady-state solutions at the switching instants, imposing the corresponding feedback constraints imposed by the PWM process and equating them at the critical point ($\varepsilon_t \to 0$), a condition for predicting PD bifurcation is obtained in terms of the system matrices containing all the parameters.

From the switching conditions at the two switching instants $t = (D + \varepsilon_t)T$ and $t = (1 + D + \varepsilon_t)T$, the following equalities hold

$$-\mathbf{C}^\intercal\mathbf{x}_{ss}((D - \varepsilon_t)T) = r((D - \varepsilon_t)T) \tag{34a}$$

$$-\mathbf{C}^\intercal\mathbf{x}_{ss}((D + \varepsilon_t + 1)T) = r((D + \varepsilon_t)T) \tag{34b}$$

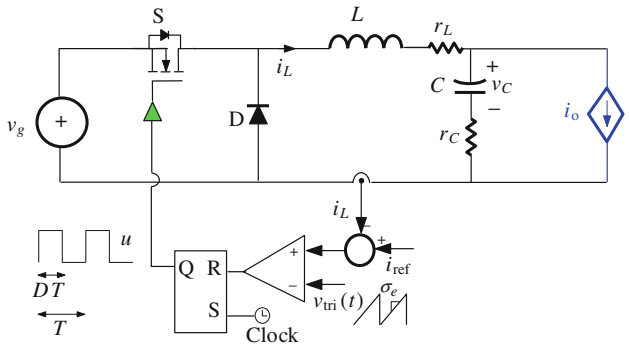

Fig. 7 Schematic circuit diagram of a buck converter under a current mode control loaded by a constant current source as a load representing a downstream converter also under current mode control

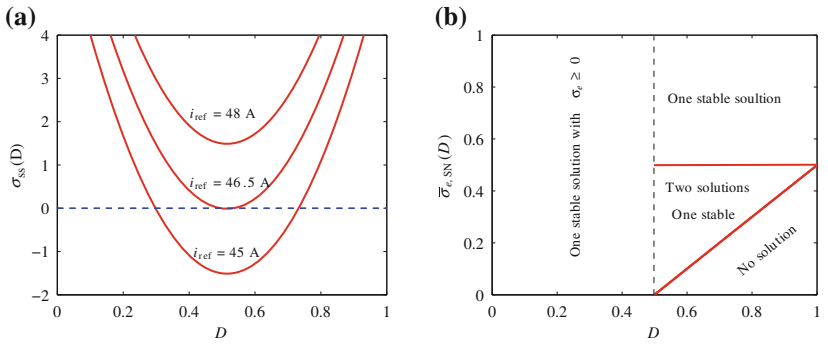

Fig. 8 The switching function $\sigma_{ss}(D)$showing the disappearance of two solutions near a SN bifurcation (**a**) and the stability map in terms of the duty cycle and the slope of the signal r (**b**)

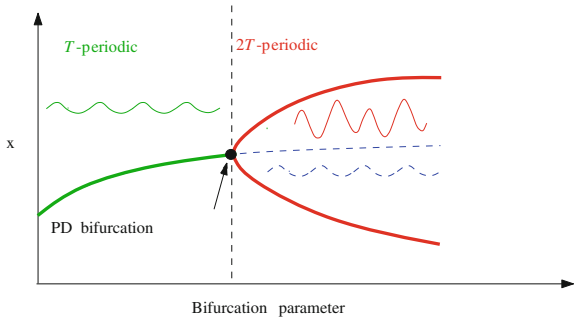

Fig. 9 Sketch of a PD bifurcation in a switched dynamical system under PWM and the corresponding waveforms before and after the bifurcation takes place by sweeping a parameter

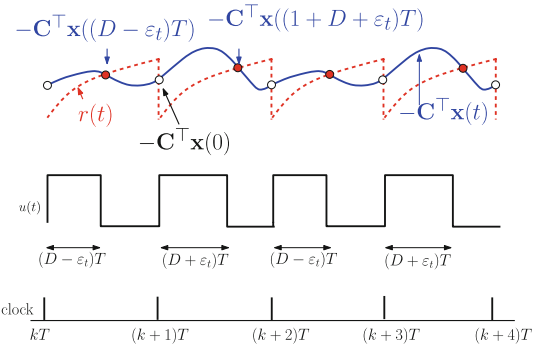

Fig. 10 Waveforms of the T—periodic external signal $r(t)$ and the feedback signal $-\mathbf{C}^\top\mathbf{x}_{ss}(t)$ at $2T$—periodic regime in steady-state

While in [5], the previous equations are expressed in the Fourier frequency domain in the case of an example of PWM systems with linear plant for which $\mathbf{A}_1 = \mathbf{A}_2$, in this chapter these two equations are treated generally for the bilinear case directly in the time-domain without any extra effort to go back from the Fourier frequency-domain into the time-domain. Exhibiting a $2T$-periodic regime, the sampled value of the steady-state variables of the system at the switching instants $(D - \varepsilon_t)T$ and

$(D+\varepsilon_t+1)T$ can be obtained by using (4) and forcing $2T$—periodicity. By doing so, it can be expressed as follows

$$\mathbf{x}_{ss}((D-\varepsilon_t)T) = (\mathbf{I}-\boldsymbol{\Phi}_-(\varepsilon_t))^{-1}\boldsymbol{\Psi}_-(\varepsilon_t) \tag{35a}$$

$$\mathbf{x}_{ss}((D+\varepsilon_t+1)T) = (\mathbf{I}-\boldsymbol{\Phi}_+(\varepsilon_t))^{-1}\boldsymbol{\Psi}_+(\varepsilon_t) \tag{35b}$$

where all the matrices and vectors appearing in the previous equations are given by

$$\boldsymbol{\Phi}_-(\varepsilon_t) = \bar{\boldsymbol{\Phi}}_1\bar{\boldsymbol{\Phi}}_4\bar{\boldsymbol{\Phi}}_3\bar{\boldsymbol{\Phi}}_2 \tag{36a}$$

$$\boldsymbol{\Phi}_+(\varepsilon_t) = \bar{\boldsymbol{\Phi}}_3\bar{\boldsymbol{\Phi}}_2\bar{\boldsymbol{\Phi}}_1\bar{\boldsymbol{\Phi}}_4 \tag{36b}$$

$$\boldsymbol{\Psi}_-(\varepsilon_t) = \bar{\boldsymbol{\Phi}}_1\bar{\boldsymbol{\Phi}}_4\bar{\boldsymbol{\Phi}}_3\bar{\boldsymbol{\Psi}}_2 + \bar{\boldsymbol{\Phi}}_1\bar{\boldsymbol{\Phi}}_4\bar{\boldsymbol{\Psi}}_3 + \bar{\boldsymbol{\Phi}}_1\bar{\boldsymbol{\Psi}}_4 + \bar{\boldsymbol{\Psi}}_1 \tag{36c}$$

$$\boldsymbol{\Psi}_+(\varepsilon_t) = \bar{\boldsymbol{\Phi}}_3\bar{\boldsymbol{\Phi}}_2\bar{\boldsymbol{\Phi}}_1\bar{\boldsymbol{\Psi}}_4 + \bar{\boldsymbol{\Phi}}_3\bar{\boldsymbol{\Phi}}_2\bar{\boldsymbol{\Psi}}_1 + \bar{\boldsymbol{\Phi}}_3\bar{\boldsymbol{\Psi}}_2 + \bar{\boldsymbol{\Psi}}_3 \tag{36d}$$

and

$$\bar{\boldsymbol{\Phi}}_1 = \boldsymbol{\Phi}_1 e^{-\mathbf{A}_1\varepsilon_t T},\quad \bar{\boldsymbol{\Psi}}_1 = \int_0^{(D-\varepsilon_t)T} e^{\mathbf{A}_1\tau}\mathrm{d}\tau\mathbf{B}_1\mathbf{w} \tag{37a}$$

$$\bar{\boldsymbol{\Phi}}_2 = \boldsymbol{\Phi}_2 e^{\mathbf{A}_2\varepsilon_t T},\quad \bar{\boldsymbol{\Psi}}_2 = \int_0^{(1-D+\varepsilon_t)T} e^{\mathbf{A}_2\tau}\mathrm{d}\tau\mathbf{B}_2\mathbf{w} \tag{37b}$$

$$\bar{\boldsymbol{\Phi}}_3 = \boldsymbol{\Phi}_1 e^{\mathbf{A}_1\varepsilon_t T},\quad \bar{\boldsymbol{\Psi}}_3 = \int_0^{(D+\varepsilon_t)T} e^{\mathbf{A}_1\tau}\mathrm{d}\tau\mathbf{B}_1\mathbf{w} \tag{37c}$$

$$\bar{\boldsymbol{\Phi}}_4 = \boldsymbol{\Phi}_2 e^{-\mathbf{A}_2\varepsilon_t T},\quad \bar{\boldsymbol{\Psi}}_4 = \int_0^{(1-D-\varepsilon_t)T} e^{\mathbf{A}_2\tau}\mathrm{d}\tau\mathbf{B}_2\mathbf{w} \tag{37d}$$

Subtracting (34a) from (34b), one obtains

$$-\mathbf{C}^{\mathsf{T}}(\mathbf{x}_{ss}((D+1+\varepsilon_t)T) - \mathbf{x}_{ss}((D-\varepsilon_t)T)) = r((D+\varepsilon_t)T) - r((D-\varepsilon_t)T) \tag{38}$$

The boundary of PD bifurcation can be located by taking the limit in (38) when the parameter $\varepsilon_t \to 0$. Therefore, at the onset of this instability the following equality holds

$$-\lim_{\varepsilon_t\to 0}\mathbf{C}^{\mathsf{T}}(\mathbf{x}_{ss}((D+1+\varepsilon_t)T) - \mathbf{x}_{ss}((D-\varepsilon_t)T)) = \lim_{\varepsilon_t\to 0} r((D+\varepsilon_t)T) - r((D-\varepsilon_t)T) \tag{39}$$

While the right-hand side of (39) is generally easy to obtain, the left-hand side of the previous equation is mathematically more involved. Let us first focus on the right-hand side of (39) and let us obtain it for three different cases of PWM signals:

- In the case of a linear ramp compensating signal, the right-hand side of (39) is given by

$$\lim_{\varepsilon_t \to 0} r((D+\varepsilon_t)T) - r((D-\varepsilon_t)T) = 2\sigma_e T \tag{40}$$

- In the case of a quadratic modulating signal, the right-hand side of (39) can be easily expressed as follows

$$\lim_{\varepsilon_t \to 0} r((D+\varepsilon_t)T) - r((D-\varepsilon_t)T) = 2T(\sigma_0 + (\sigma_T - \sigma_0)D) \tag{41}$$

- In a practical implementation, the slope is exponentially depending on the duty cycle D and the right-hand side of (39) is given by

$$\lim_{\varepsilon_t \to 0} r((D+\varepsilon_t)T) - r((D-\varepsilon_t)T) = 2\sigma_0 T e^{-\frac{DT}{\tau}} \tag{42}$$

As it was mentioned previously, the left-hand side of the previous equation is mathematically more involved. For simplicity let us consider that the external T—periodic function is linear during the switching period in such a way that its slope σ_e is constant and that (39) can be written as follows

$$\sigma_{e,\mathrm{PD}}(D) = \sigma_e \tag{43}$$

where $\sigma_{e,\mathrm{PD}}(D)$, the critical slope for PD bifurcation boundary, is given by

$$\sigma_{e,\mathrm{PD}}(D) = -\lim_{\varepsilon_t \to 0} \frac{1}{2\varepsilon_t T} \mathbf{C}^{\intercal}(\mathbf{x}_{ss}((D+1+\varepsilon_t)T) - \mathbf{x}_{ss}((D-\varepsilon_t)T)) \tag{44}$$

By using (35a)–(35b), the limit expression in (44) becomes

$$\sigma_{e,\mathrm{PD}}(D) = -\lim_{\varepsilon_t \to 0} \frac{1}{2\varepsilon_t T}((\mathbf{I} - \Phi_+(\varepsilon_t))^{-1}\boldsymbol{\Psi}_+(\varepsilon_t) - (\mathbf{I} - \boldsymbol{\Phi}_-(\varepsilon_t))^{-1}\boldsymbol{\Psi}_-(\varepsilon_t)) \tag{45}$$

By calculating the limit in the previous expression, the following condition is obtained at the boundary of subharmonic oscillation

$$\sigma_{e,\mathrm{PD}}(D) = -\mathbf{C}^{\intercal}[(\mathbf{I} - \boldsymbol{\Phi})^{-1}\boldsymbol{\Phi}_1(\mathbf{f}_1(\mathbf{x}_{\mathrm{ss}}(0)) + \mathbf{f}_2(\mathbf{x}_{\mathrm{ss}}(0)))] \tag{46}$$

More calculation details can be found in [26]. It is worth mentioning here that in [4], a slightly differently expressed condition has been obtained using a different approach based on solving the eigenvalue problem of the z-domain characteristic equation, for the same boundary condition which is reported and adapted here for comparison

$$\sigma_{e,\mathrm{PD}}(D) = -\mathbf{C}^{\mathsf{T}}[\mathbf{f}_1(\mathbf{x}_{\mathrm{ss}}(DT^-)) - \boldsymbol{\Phi}_1(\mathbf{I} - \boldsymbol{\Phi}_2\boldsymbol{\Phi}_1)^{-1}]\boldsymbol{\Phi}_2\Delta\mathbf{f}(\mathbf{x}_{\mathrm{ss}}(DT)) \quad (47)$$

Although they are expressed differently, the critical ramp slope for PD bifurcation given in (46) and the one derived in [4] and shown in (47), are coincident. Note however that (46) is simpler than (47).

4.4 Application Examples for Predicting PD Bifurcation

4.4.1 General Bilinear Plants

Example 3: The system which will be considered in this section is a boost converter under a current mode peak controller. The state variables are the capacitor voltage v_C and the inductor current i_L. The system matrices and vectors are as follows

$$\mathbf{A}_1 = \begin{pmatrix} -\frac{1}{RC} & 0 \\ 0 & -\frac{r_L}{L} \end{pmatrix}, \quad \mathbf{A}_2 = \begin{pmatrix} -\frac{1}{RC} & \frac{1}{C} \\ \frac{1}{C} & -\frac{r_L}{L} \end{pmatrix}$$

$$\mathbf{B}_1 = \mathbf{B}_2 = \begin{pmatrix} 0 \\ \frac{1}{L} \end{pmatrix}, \quad \mathbf{x} = \begin{pmatrix} v_C \\ i_L \end{pmatrix}, \quad \mathbf{w} = v_g, \quad \mathbf{C} = \begin{pmatrix} 0 \\ 1 \end{pmatrix}$$

where R is the load resistance, L is the inductance with equivalent series resistance r_L, C is the output filtering capacitance and v_g is the input voltage. The peak current is i_{ref}. The duty cycle D is varied by varying i_{ref}. The used parameter values are as follows: input voltage $v_g = 5\,\mathrm{V}$, inductance $L = 200$ $\mu\mathrm{H}$, DC parasitic of the inductance $r_L = 0.1\ \Omega$, capacitance value $C = 10\,\mu\mathrm{F}$, load resistance $R = 15\ \Omega$ and switching frequency $f_s = 10\,\mathrm{kHz}$.

It can be demonstrated that SN bifurcation is not possible in this case because the switching function $\sigma_{ss}(D)$ is monotone with respect to the duty cycle D. However, PD can take place in this converter if a suitable parameter is varied. One would be interested on determining the boundary in the parameter space of this instability. Figure 11 shows such a boundary in the parameter space (D, σ_e) for the system. It is worth noting that a traditional approximated approach will predict PD instability for duty cycle values larger than 0.5 in the case of not using a compensating ramp ($\sigma_e = 0$). Note that the exact closed-form expression predicts a lower critical value of the duty cycle ($D_c \approx 0.43$). Therefore, the approximated conventional approach could predict stability for a PWM system while it exhibits subharmonic oscillation due to PD bifurcation.

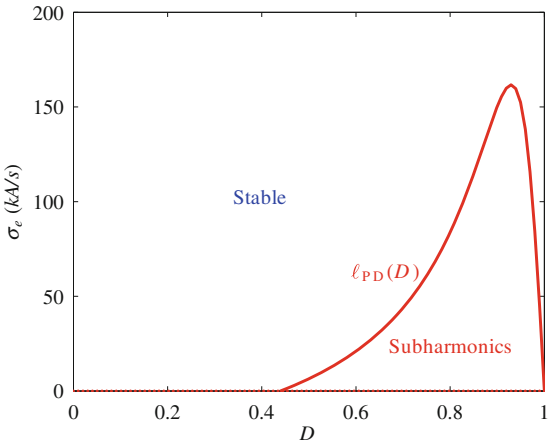

Fig. 11 PD bifurcation curve in terms of the duty cycle D and the slope σ_e of the compensating ramp for a boost converter under peak current mode control. The *curve* $\ell_{\mathrm{PD}}(D)$ represents the boundary

4.4.2 Special Linear Plants

The switched model for a PWM system with linear plant can be expressed in compact form as follows

$$\dot{\mathbf{x}} = \mathbf{A}\mathbf{x} + \mathbf{B}u + \mathbf{B}_2\mathbf{w}, \quad x_c = \mathbf{C}^{\mathsf{T}}(\mathbf{X}_{\mathrm{ref}} - \mathbf{x}) \tag{48}$$

where $\mathbf{B} = (\mathbf{B}_1 - \mathbf{B}_2)\mathbf{w}$. Let the Markov parameters of the system described by the 3-tuple $(\mathbf{A}, \mathbf{B}, \mathbf{C})$ as follows [27]

$$\mu_k = \mathbf{C}^{\mathsf{T}}\mathbf{A}^{k-1}\mathbf{B}, k = 1, 2.... \tag{49}$$

Hence, performing a Taylor series expansion on (46), the following equality holds at the onset of subharmonic instability

$$\begin{aligned}\sigma_{e,\mathrm{PD}}(D) &= \sum_{k=1}^{\infty} \mu_{k-1}\mathcal{S}_k(D)T^{k-1} \\ &\approx \mu_0(D - \frac{1}{2}) + \mu_1 T\left(\frac{D^2}{2} - \frac{D}{2} + \frac{1}{4}\right)\end{aligned} \tag{50}$$

The functions $\mathcal{S}_k(D)$ are related to the kth order Clausen polynomials $\mathrm{cl}_k(\theta)$ shown in Table 1 and having the following property [28].

$$\frac{\mathrm{d}}{\mathrm{d}\theta}\mathrm{cl}_k(\theta) = (-1)^k \mathrm{cl}_{k-1}(\theta) \quad \text{for } k = 2, 3\ldots \tag{51}$$

Moreover, the presence of these terms in (50) is largely dependent on the relative degree of the system (48) where the input is the command driving signal u and the

Table 1 Polynomial functions $\mathrm{cl}_k(\theta)$ and $\mathcal{S}_k(D)$

k	$\mathrm{cl}_k(\theta)$	$\mathcal{S}_k(D)$
1	$\frac{1}{2}(\pi-\theta)$	$D-\frac{1}{2}$
2	$\frac{\pi^2}{6}-\frac{\pi\theta}{2}+\frac{\theta^2}{4}$	$\frac{D^2}{2}-\frac{D}{2}+\frac{1}{4}$
3	$\frac{\pi^2\theta}{6}-\frac{\pi\theta^2}{4}+\frac{\theta^3}{12}$	$\frac{D^3}{6}-\frac{D^2}{4}+\frac{D}{12}$

output is the control signal x_c. The relative degree rd of a single-input single-output system is the smallest integer such that the Markov parameter $\mathbf{C}^\intercal\mathbf{A}^{rd-1}\mathbf{B}\neq 0$, i.e.,

$$rd=\inf\{k\geq 0:\mu_k\neq 0\} \tag{52}$$

The PWM system (plant including the controller) will have therefore a relative degree rd such that [27]

$$rd=1 \text{ if } \mu_0=\mathbf{C}^\intercal\mathbf{B}\neq 0, \tag{53a}$$

$$rd=2 \text{ if } \mu_0=\mathbf{C}^\intercal\mathbf{B}=0 \text{ and } \mu_1=\mathbf{C}^\intercal\mathbf{A}\mathbf{B}\neq 0 \tag{53b}$$

$$\vdots$$

Example 4: Let us apply the previous theoretical results to a buck converter with a simple proportional-integral (PI) control. The expressions of the matrix $\mathbf{A}$ and vector $\mathbf{B}$ are given by

$$\mathbf{A}=\begin{pmatrix}-\frac{1}{RC} & \frac{1}{C} & 0\\ -\frac{1}{L} & 0 & 0\\ -1 & 0 & 0\end{pmatrix},\quad \mathbf{B}=\begin{pmatrix}0\\ \frac{1}{L}\\ 0\end{pmatrix},\quad \mathbf{w}=v_g$$

The vector of the state variables after excluding the integrator is $\mathbf{x}(t)=(v_C,\ i_L)^\intercal$. Therefore, the vector $\mathbf{C}^\intercal=(k_v\ \ 0)$, where k_v is a voltage feedback gain. Figure 12 shows a schematic circuit diagram of a DC-DC buck converter under voltage mode PI control. All the parameters appearing in the matrices can be identified in the circuit diagram of Fig. 12. Because $\mathbf{A}_1=\mathbf{A}_2$, the plant is linear. The parameter values used are inductance $L=20$ mH, capacitance $C=47$ μF, lower value of the ramp modulator signal $V_l=3.8$ V, its amplitude $V_M=4.4$ V, switching period $T=400$ μs, voltage reference, $v_{\mathrm{ref}}=11.3$ V and voltage feedback gain $k_v=8.4$, [6, 19, 29].

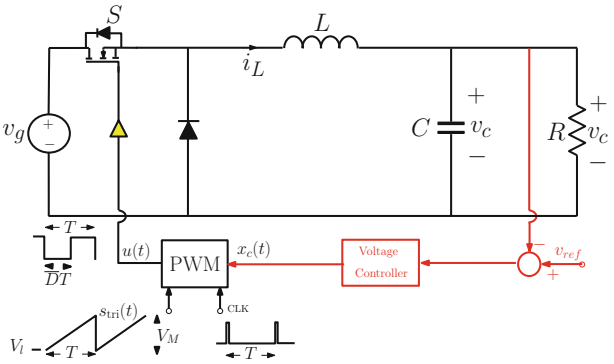

Fig. 12 Block circuit diagram of a DC-DC buck converter under PI voltage mode control

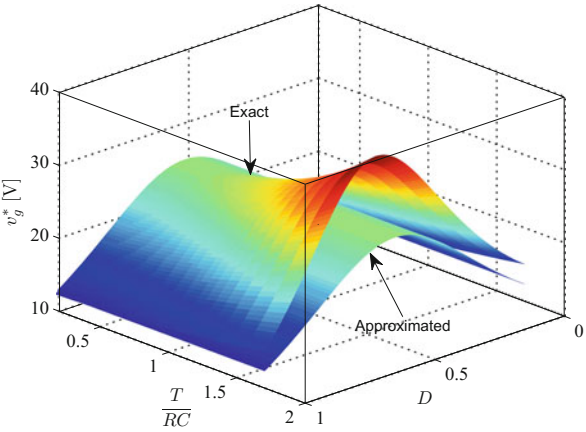

Fig. 13 Exact and approximated stability surface $v_g^*(T/(RC), D)$ in terms of the duty cycle D and $T/(RC)$ showing that only for high values of $T/(RC) \gg 1$ (not practical), (50) is not accurate enough

The control signal can be expressed as $x_c = \mathbf{C}^\intercal(\mathbf{X}_{\text{ref}} - \mathbf{x}) = k_v(v_{\text{ref}} - v_c)$. The time constant of the integrator is selected to be $\tau = 0.01$ s which is much larger than the switching period to ensure slow time-scale and to reduce its effects on the fast scale instability. Traditionally, the dynamic behavior of the system in this example has been studied in terms of the input voltage v_g and the load resistance R [6, 19, 29]. In Fig. 13, the exact mesh plot of the critical value of the input voltage $v_g^*(T/(RC), D)$ from (46) is shown together with the approximated plot from (50) using the first two terms in the expansion. From this figure, it can be observed that for $T/(RC) \ll 1$, a good concordance between the exact and the approximated expressions is obtained, while a discrepancy exists between their corresponding plots for relatively large values of $T/(RC)$. This discrepancy becomes significant for time constant RC approaching the switching period T. Only for $T/(RC) \gg 1$, (50) will give inaccurate results. However, this is not a practical case since the time constant of the converter filter must be much larger than the switching period in all practical implementations of switching converters in particular and PWM systems in general.

Finally, it should be noted that this example uses a LEM strategy and a change of variable $D \rightarrow (1 - D) := \overline{D}$ must be done in (46) together with a sign inversion in the voltage feedback gain.

5 Conclusions

In this chapter closed-form conditions for predicting the fast-scale stability boundaries corresponding to both saddle-node (SN) and period-doubling (PD) bifurcations have been derived for a class of PWM switching systems with bilinear plants. The results presented in this chapter can also be applied to the special case of switched systems with linear plants. Hence, for both cases, the effect of the different parameters of the system upon the stability boundary can be easily unveiled. The general-purpose derived expressions can be applied to different examples of PWM systems such as switching power converters, switched capacitor chaos generators, temperature control systems and hydraulic valve drive control among others. The stability boundaries have been derived without the need of the Jacobian matrix and without expressing the system trajectories in the Fourier frequency-domain and without any order reduction apart from excluding the integrator which has negligible effect on the fast scale instabilities. The simple asymptotic time-domain approach used in this chapter can be better understood by practitioners than those based in frequency-domain approach or on the eigenvalue problem of the Jacobian or the monodromy matrix.

Acknowledgments This work was supported by the Spanish *ministerio de Economía y Competitividad* under grant DPI2013-47437-R, the VPP of King Saud University, Riyadh, KSA and The Petroleum Institute, Abu Dhabi, UAE.

References

1. Liberzon, D. Switching in Systems and Control, Springuer, 2003
2. El Aroudi, A., Debbat, M., Martinez-Salamero, L.: Poincaré maps modelling and local orbital stability analysis of discontinuous piecewise affine periodically driven systems. Nonlinear Dyn. **50**(3), 431–445 (2007)
3. El Aroudi, A.: Prediction of subharmonic oscillation in switching converters under different control strategies. IEEE Trans. Circuits Syst. II: Express Briefs **62**(11), 910–914 (2014)
4. Fang, C.-C.: Using byquist or nyquist-like plot to predict three typical instabilities in DC-DC converters. J. Franklin Inst. **350**(10), 3293–3312 (2013)
5. Fang, C.-C.: Critical conditions for a class of switched linear systems based on harmonic balance: applications to DC-DC converters. Nonlinear Dyn. **70**(3), 1767–1789 (2012)
6. Giaouris, D., Maity, S., Banerjee, S., Pickert, V., Zahawi, B.: Application of Filippov method for the analysis of subharmonic instability in DC-DC converters. Int. J. Circuit Theory Appl. **37**(8), 899–919 (2009)
7. El Aroudi, A., Calvente, J., Giral, R., Martinez-Salamero, L.: Effects of non-ideal current sensing on subharmonic oscillation boundary in DC-DC switching converters under CMC.

In: Industrial Electronics Society, IECON 2013–39th Annual Conference of the IEEE, pp. 8367–8372, 10–13 Nov 2013
8. Fang, C.-C.: Critical conditions of saddle-node bifurcations in switching DC-DC converters. Int. J. Electron. **100**(8), 1147–1174 (2013)
9. Robert, B., Robert, C.: Border collision bifurcations in a one-dimensional piecewise smooth Map for a PWM current-programmed H-bridge Inverter. Int. J. Control **7**(16), 1356–1367 (2002)
10. Miladi, Y., Feki, M., Derbel, N.: On the model identification of an incubator based on genetic algorithms. In: 9th International Multi-Conference on Systems. Signals and Devices, Chemnitz, Germany (2012)
11. Gardini, L., Tramontana, F., Banerjee, S.: Bifurcation analysis of an inductorless chaos generator using 1D piecewise smooth map. Math. Comput. Simul. **95**, 137–145 (2014)
12. Huh J.-Y., Wennmacher, G.: A study on the stability analysis of a PWM controlled hydraulic equipment. KSME Int. J. **11**(4), 397–407 (1997)
13. Liu, G., Xia, W., Qi, D., Hu, R.: Analysis of Dither in electro-hydraulic proportional control. Telekominika **11**(11), 6808–6814 (2013)
14. Mandal, K., Chakraborty, C., Abusorrah, A., Al-Hindawi, M., Al-Turki, Y., Banerjee, S.: An automated algorithm for stability analysis of hybrid dynamical systems. Eur. Phys. J. Special Topics **222**, 757–768 (2013)
15. Mazumder, S.K., Nayfeh, A.H., Boroyevich, D.: Theoretical and experimental investigation of the fast- and slow-scale instabilities of a DC-DC converter. IEEE Trans. Power Electron. **16**(2), 201–216 (2001)
16. Leine, R.L., Nijemeijer, H.: Dynamics and Bifurcations of Non-smooth Mechanical Systems. Lecture Notes in Applied and Computational Mechanics, vol. 18. Springer, Heidelberg (2004)
17. Fang, C.-C., Abed, E.H.: Harmonic balance analysis and control of period doubling bifurcation in buck converters. IEEE Int. Symp. Circuits Syst. **3**, 209–212 (2001)
18. Hiskens, I.A., Pai, M.A.: Trajectory sensitivity analysis of hybrid systems. IEEE Trans. Circuits Syst. I: Fundam. Theory Appl. **47**(2), 204–220, (2000)
19. Fossas, E., Olivar, G.: Study of Chaos in the buck converter. IEEE Trans. Circuits Syst. I: Fundam. Theory Appl. **43**(1), 13–25 (1996)
20. El Aroudi, A.: A closed form expression for predicting fast scale instability in switching buck converters. In: The International Conference on Structural Nonlinear Dynamics and Diagnosis, Marrakech, Morocco (2012)
21. Tanitteerapan, T., Mori, S.: Fundamental frequency parabolic PWM controller for lossless soft-switching boost power factor correction. In: The 2001 IEEE International Symposium on Circuits and Systems, ISCAS 2001, vol. 3, pp. 57–60 (2001)
22. Fang, C.-C. Exact orbital stability analysis of static and dynamic ramp compensations in DC-DC converters. In: Proceedings IEEE International Symposium on Industrial Electronics, ISIE 2001, vol. 3, pp. 2124–2129 (2001)
23. Lehman, B., Bass, R.M.: Switching frequency dependent averaged models for PWM DC-DC converters. IEEE Trans. Power Electron. **11**(1), 89–98 (1996)
24. van der Woude, J.W., De Koning, W., Fuad, Y.: On the periodic behavior of PWM DC-DC converters. IEEE Trans. Power Electron. **17**(4), 585–595 (2002)
25. El Aroudi, A., Giaouris, D., Martinez-Salamero, L., Banerjee, S., Voutetakis, S., Papadopoulou, S.: Bifurcation behavior in switching converters driving other downstream converters in DC distributed power systems applications. In: MEDYNA'2013 Marrakech Morocco (2013)
26. El Aroudi, A.: A time-domain asymptotic approach to predict saddle-node and period doubling bifurcations in pulse width modulated piecewise linear systems. In: The International Conference on Structural Nonlinear Dynamics and Diagnosis, Agadir, Morocco (2014)
27. Corriou, J.-P.: Process control: theory and applications. Springer, London (2014). ISBN 978-1-4471-3848-8
28. Lewin, L.: Polylogarithms and Associated Functions. North-Holland, New York (1981)
29. Hamill, D.C., Deane, J.H.B., Jefferies, D.J.: Modelling of chaotic DC-DC converters by iterated nonlinear mapping. IEEE Trans. Power Electron. **7**(1), 25–36 (1992)

Reliability Analysis of a Vibro-acoustique System: Application to a Marine Propeller

B. Radi and A. El Hami

Abstract In this chapter, we focus on the interaction between fluid and structure and specifically the vibro-acoustic problem which is generally defined as the contact between bodies interacting according to the principles of continuum mechanic. The comprehension of the mechanisms of these interaction has a capital importance in several industrial applications (aerospace, automotive, civil engineering areas as well as in biomechanics ...). When a structure vibrates in the presence of a fluid, there is interaction between the natural waves of each media: the fluid flow generates a structural deformation and/or the movement of a solid causes the displacement of the fluid. These applications require an effective coupling. For the coupling fluid structure finite elements models, the importance of the size reduction becomes obvious because the fluid degrees of freedom will be added to those of the structure. A method of condensation will be used to reduce the matrixes size. One of the principal hypotheses in the use of component mode synthesis method is that the model is deterministic; it is to say that parameters used in the model have a defined and fixed value. In fact, all aspects of an analysis model are uncertain. However, the fluctuations in input parameters generate significant degradation of the quality of the deterministic solution. So it is neither financially feasible nor physically possible to eliminate the dispersion of the input parameters. A numerical vibratory study is leaded on a structure 3D immersed in water taking the acoustic aspect. In this context, we focused very specifically on a deterministic and stochastic analysis through numerical simulations in 3D dynamic fluid-structure interaction problems. The results of the reliability based design optimization (RBDO) study of the marine propeller tend to show the effectiveness of the step followed to condense the system and to take into account the uncertain parameters.

B. Radi (✉)
LIMMII, FST Settat, Settat, Morocco
e-mail: bouchaib.radi@yahoo.fr

A. El Hami
LOFIMS, INSA de Rouen, Rouen, France
e-mail: aelhami@insa-rouen.fr

M. Belhaq (ed.), *Structural Nonlinear Dynamics and Diagnosis*,
Springer Proceedings in Physics 168, DOI 10.1007/978-3-319-19851-4_19

1 Introduction

The comprehension of the mechanisms of interactions between a fluid and an elastic solid has a capital importance in several industrial applications. When a structure vibrates in the presence of a fluid, there is interaction between the natural waves of each media: the fluid flow generates a structural deformation and/or the movement of a solid causes the displacement of the fluid. These applications require an effective coupling. In [1], many methods to resolve fluid-structure interaction problems can be found. Furthermore, the dynamic analysis of the industrial systems is often expensive from the numerical (CPU) point of view. For the coupling fluid structure finite elements models, the importance of the size reduction becomes obvious because the fluid degrees of freedom will be added to those of the structure. A method of condensation will be used to reduce the matrixes size.

One of the main assumptions in the study of mechanical systems is that the model is deterministic. That means that the parameters used in the model are constant. However, the experimental works show the limitations of such assumptions. This is because there are always differences between what we calculate and what we measure due mainly to the uncertainties in geometry, the material properties, the boundary conditions or the load, which has a considerable impact on the vibrating behavior of mechanical systems. This is why it is important to use numerical methods in order to take these uncertainties into account. In [2–4], various approaches to treat mechanical systems with uncertain parameters can be found.

The numerical approach has been to propose a finite element model of the structure coupled with the fluid and has validated the use of a general computer code for numerical modeling of coupled fluid/structure problems. The method is illustrated by an example of a solid 3D immersed in water with properties that both materials are random. We present in this chapter a stochastic numerical modal analysis of a solid 3D immersed in water to simulate the stochastic response, in medium frequencies, by considering the random parameters. In this case, the presence of several parameters to random characters, namely the Young's modulus of the structure the structure density which fluid density, and often show a great variability, and inevitably leads to lose important computational precision. Better control of these parameters is thus based on the use of stochastic methods whose main objective is to improve the quality and the reinterpretation of results from simulations. To do so, a good understanding and formulation of the main phenomena involved in the coupling problem are needed. The RBDO analysis of the marine propeller shows the efficiency of such approach coupling optimization and reliability.

This chapter is organized as follows. The problem of the interaction between a fluid and an elastic body is presented in Sect. 1. The validation of the adopted approach is given in Sect. 2 by the study of an immersed plate. Section 3 deals with reliability

analysis and the application to the marine propeller is given. The RBDO analysis is presented in Sect. 4 and the numerical results relative to the marine propeller are given.

2 Fluid Structure Interaction

In the context of this study of fluid-structure interaction, we focus on the vibro-acoustic problem where the fluid makes an elastic potential energy in contact with an elastic structure. The two media have their own degrees of freedom, and the coupled dynamic system is governed by the vibratory equations of the structure and the fluid coupled with each other. The numerical results are deduced from a finite element approach of the coupled problem with a non symmetric pressure/displacement formulation. These numerical techniques are based on a finite element discretization for solving the equations of fluid/structure interaction problems [5]. These methods are applicable to general computer codes.

The modelization of the problem is carried out by using a non-symmetric formulation: a displacement and a pressure (u, p) which presents the advantage of being easily treated by finite elements methods, because it leads to a representation incorporating only one unknown by knot. This formulation presents in fact the interest of being easily manipulated from a IT (Information Technology) perspective. Moreover, the finite element codes which allow us to generate stiffness and mass matrices of coupled systems treat this type of formulation in a particularly efficient way, especially from a matrices conditioning.

2.1 Problem Statement

We consider here the assumption of small perturbations and it is assumed that the structure is elastic and it is characterized by the mechanical properties of materials that are Young's modulus E, the density ρ_s and the Poisson's ratio ν. The structure is immersed in fluid which is supposed to be perfect, homogeneous, linear and at rest (stagnant fluid) characterized by its density ρ_f and its sonic velocity c.

The structure occupies the area Ω_s, of Σ_s boarder, free from any exterior effort and blocked from one side Γ_s. The fluid occupies the field Ω_f of border Σ_f. They are coupled through the interface noted $\Sigma = \Sigma_s \cap \Sigma_f$. n^s and n^f are respectively, the exterior normal to a solid area Ω_s and the exterior normal to a fluid area Ω_f. The problem of the fluid/structure interaction is thus to resolve two problems simultaneously: The first problem concerns the structure which undergoes a pressure imposed by the fluid in the boarder Σ. The second one concerns the fluid which undergoes a field displacement u imposed by Σ interface [6].

With the previous hypotheses, the equations of the vibro-acoustic problem governing the movement of the coupled system in function of displacement u of the structure and the pressure p of fluid are:

$$\sigma_{ij,j}(u) + \omega^2 \rho_s u = 0 \quad \text{in} \quad \Omega_s. \tag{1}$$

$$\Delta p + \frac{\omega^2}{c^2} p = 0 \quad \text{in} \quad \Omega_f. \tag{2}$$

$$u = 0 \quad \text{on} \quad \Gamma_s. \tag{3}$$

$$\sigma_{ij}(u) n_j^s = p n_i^f \quad \text{on} \quad \Sigma. \tag{4}$$

$$\frac{\partial p}{\partial n^f} = \omega^2 \rho_f u n^f \quad \text{on} \quad \Sigma. \tag{5}$$

The angular frequency of vibration is denoted as ω, the linearized strain tensor is denoted as ε_{ij} and the corresponding stress tensor is denoted as σ_{ij}.

2.2 Variational Formulation

By introducing the spaces of functions-test "sufficiently" regular and independent of time $C_u^* = \{u | u = 0 \text{ on } \Gamma_s\}$ et C_p^*, the variational formulation of the coupled problem fluid-structure is to find $u \in C_u^*$ et $p \in C_p^*$ such as $\forall v \in C_u^*$ et $\forall q \in C_p^*$:

Taking into account the boundaries conditions (4) the variational formulation of the structure is obtained by writing for each field of virtual displacement v, c and a.

$$\int_{\Omega_s} \sigma_{ij}(u) \cdot \varepsilon_{ij}(v) dV - \omega^2 \int_{\Omega_s} \rho_s \cdot u_i v_i dV = \int_{\Sigma} p \cdot n_i \cdot v_i \cdot d\Sigma \quad \forall v \tag{6}$$

The variational formulation is obtained for the field of pressure p by using (5) and whatever the virtual field pressure q statically admissible:

$$\int_{V_f} \frac{\partial p}{\partial x_i} \cdot \frac{\partial q}{\partial x_i} dV - \omega^2 \int_{V_f} \frac{1}{c^2} \cdot p \cdot q dV = \omega^2 \cdot \rho_f \int_{\Sigma} u_i \cdot n_i q \cdot d\Sigma \quad \forall q \tag{7}$$

The variational formulation of the system is the sum of the two variational equations (6) and (7):

$$F(u, p) = \frac{1}{2} \int_{\Omega_s} \left(\sigma_{ij}(u) \varepsilon_{ij}(u) - \rho_s \cdot \omega^2 \cdot (u, u) \right) dV - \int_{\Sigma} p \cdot u \cdot d\Sigma - \frac{1}{2\rho_f \cdot \omega^2} \cdot \int_{V_f} \left[\left(\frac{\partial p}{\partial x_i}, \frac{\partial p}{\partial x_i} \right) + k^2 \cdot p^2 \right] dV \tag{8}$$

2.3 Finite Elements Approximation

The interaction of the fluid and the structure at a mesh interface causes the acoustic pressure to exert a force applied to the structure and the structural motions produce an effective "fluid load." The governing finite element matrix equations become as follows:

- For the structure

$$[\mathbf{M}]\{\ddot{\mathbf{u}}\} + [\mathbf{K}]\{\mathbf{u}\} = [\mathbf{L}]\{\mathbf{P}\} \tag{9}$$

- For the fluid:

$$[\mathbf{E}]\{\ddot{\mathbf{P}}\} + [\mathbf{H}]\{\mathbf{P}\} = -\rho[\mathbf{L}]^{\mathbf{t}}\{\ddot{\mathbf{u}}\} \tag{10}$$

where $[L]$ is a "coupling" matrix that represents the effective surface area associated with each node on the fluid-structure interface (FSI). Both the structural and fluid load quantities that are produced at the fluid-structure interface are functions of unknown nodal degrees of freedom. Placing these unknown "load" quantities on the left hand side of the equations and combining the two equations into a single equation produces the following:

$$\begin{bmatrix} \mathbf{M} & \mathbf{0} \\ \rho_{\mathbf{f}}\mathbf{L}^{\mathbf{t}} & \mathbf{E} \end{bmatrix} \begin{Bmatrix} \ddot{\mathbf{u}} \\ \ddot{\mathbf{P}} \end{Bmatrix} + \begin{bmatrix} \mathbf{K} & -\mathbf{L} \\ \mathbf{0} & \mathbf{H} \end{bmatrix} \begin{Bmatrix} \mathbf{u} \\ \mathbf{P} \end{Bmatrix} = \begin{Bmatrix} \mathbf{0} \\ \mathbf{0} \end{Bmatrix} \tag{11}$$

we can still write as follows:

$$\left(-\omega^2 \begin{bmatrix} \mathbf{M} & \mathbf{0} \\ \rho_{\mathbf{f}}\mathbf{L}^{\mathbf{t}} & \mathbf{E} \end{bmatrix} + \begin{bmatrix} \mathbf{K} & -\mathbf{L} \\ \mathbf{0} & \mathbf{H} \end{bmatrix}\right) \begin{Bmatrix} \mathbf{u}(\omega) \\ \mathbf{p}(\omega) \end{Bmatrix} = \begin{Bmatrix} \mathbf{0} \\ \mathbf{0} \end{Bmatrix} \tag{12}$$

The foregoing equation implies that nodes on a fluid-structure interface have both displacement and pressure degrees of freedom. The numerical techniques based on a discretization of the type of finite elements allow us to resolve the equations of the fluid/structure interaction problem (12). This method is applicable with the codes of generalist calculation. In this work we are interested in the validation of the code of ANSYS© calculation by implementing coupled calculation in elementary cases. We follow here this measure of validation by proposing a comparison of the results within the framework of a numerical and experimental modal analysis of submerged structures. To determine the eigenfrequencies of the coupled system, the matrix must be symmetrical which is not the case. Therefore, a symmetrization procedure such as Irons method will be used [7].

3 Study of an Immersed Plate

3.1 Deterministic Case

We begin by the validation of the fluid-structure interaction in the deterministic case. The numerical study considered in this section consists of a solid 3D coupled with a compressible fluid which is modeled using ANSYS code. This application aims at illustrating the methodology proposed in a deterministic analysis. Geometrical and material properties are:

- For the structure: density = 7860 kg m^{-3}; Young's modulus = 2.1×10^{11} Pa; Poisson's ratio = 0.3; Length= 2 m; Width = 1 m; Height = 0.2 m.
- For the fluid: density = 1000 kg m^{-3}; Speed of sound = 1500 m s^{-1}; Length = 20 m; Width = 10 m; Height = 10 m.

For the finite elements calculation: SOLID45 is used for the 3D modeling of solid, the element is defined by eight nodes having three degrees of freedom at each node: translations in the nodal x, y, and z directions. FLUID30 is used for modeling the fluid medium and the interface in fluid/structure interaction problems. Typical applications include sound wave propagation and submerged structure dynamics. The governing equation for acoustics, namely the 3D wave equation, has been discretized taking into account the coupling of acoustic pressure and structural motion at the interface. The element has eight corner nodes with four degrees of freedom per node: translations in the nodal x, y and z directions and pressure. The translations, however, are applicable only at nodes that are on the interface.

This problem demonstrates the use of FLUID30 and SOLID45 to predict the acoustic standing wave pattern of a solid submerged in fluid. Figure 1 shows a diagram of the types elements used in this study and the finite elements discretization of this immersed structure.

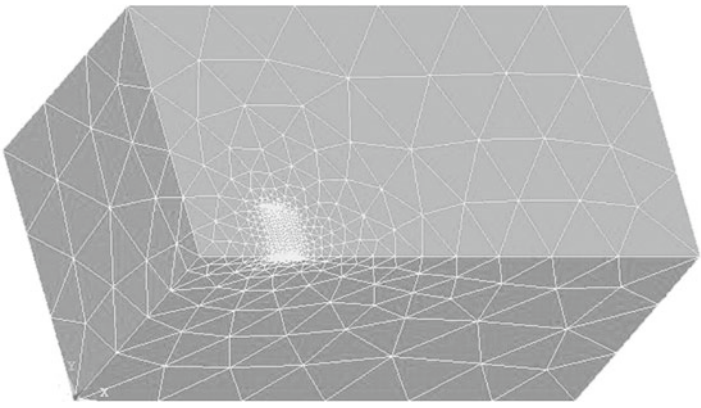

Fig. 1 Finite element model

Table 1 The first 5 frequencies of submerged structure (modal synthesis)

Deterministic case	ANSYS
R_1	23.395
R_2	67.646
R_3	91.626
R_4	131.76
R_5	210.458

Table 2 Moments of the parameters of the problem and distribution laws

Parameters	Means	Standard deviation	Distribution
Young modulus (Pa)	2.1×10^{11}	0.05×10^{11}	Gaussian (μ, σ)
Structure's density (kg/m^3)	7860	250	Uniform (a,b)
Fluid's density (kg/m^3)	1000	40	Uniform (a,b)

The founding results in the immersed structure and the comparison results between the ANSYS results is given in Table 1. The adopted vibro-acoustic model gives a good predictions.

There is a substantial drop in natural frequencies of the structure after its immersion in the fluid which changes the vibration behavior of the structure.

3.2 Probabilistic Case

The choice of the random variables is a central point [8]. In the three dimensions case, the following variables are taking as random one (see Table 2).

The stochastic calculation was carried out using probabilistic design system of the ANSYS and MATLAB code. This tool is based on a calculation with Monte Carlo simulation (for 100 samples) and the response surface method (for 40 samples). The Table 3 shows means and standard deviations of the natural frequencies as well as the finding results using the immersed structure.

4 Reliability Analysis

Physical tests or measures show that the mechanical properties, the geometrical characteristics of structure elements or applied loads could be random and follow statistical distributions. This leads to define a probabilistic model. In general, random variables give a good representation of structural stochastic parameters. Let $X = (X_1, X_2, \ldots, X_m)^t$ be the random vector of the probabilistic analysis. To preserve

Table 3 Means and standard deviations of the natural frequencies for the immersed structure

Modes	R_1	R_2	R_3	R_4	R_5
Deterministic	23.39	67.64	91.62	131.76	210.45
MC	21.21	70.51	90.98	129.23	215.43
RSM	22.14	68.13	91.01	130.87	211.99
FORM	22.78	67.04	91.11	131.52	212.62
SORM	22.78	67.04	91.11	131.52	212.62
St. dev	2.63	3.24	4.15	6.07	10.68

the integrity of the structure, the failure mode must be defined and the corresponding limit state function $G(X)$ established. The structure is situated in its safe domain D_s if $\{G(X) > 0\}$ and it is situated in its failure domain D_f if $\{G(X) \leq 0\}$. Then, the failure probability is:

$$P_f = Prob(G(X) \leq 0). \tag{13}$$

In our situation, the analytical expressions of the limit state function G and its derivatives are often not available in function of the physical random variables $X_1, X_2, \ldots, X_m$. Then, it is only possible to obtain the failure probability under an implicit numerical form. The response surface methods have been widely developed in nonlinear reliability analysis. Several authors have proposed solutions to improve the accuracy of results, to decrease the number of necessary numerical calculations on FEM codes and to increase the robustness of the algorithms. In this nonlinear study, we propose an adaptive surface method coupled with the first order reliability method (FORM) [9, 10]. The sets of design points and the response surfaces are generated in the space of standard Gaussian variables. The scheme of the adaptive process is given as follows:

- $k = 1$, the generated set of points is a central composite design. Its center coordinates are the mean values of random variables. $d^{(1)}$ is a fixed real number and the distance from the central point to a 'corner' in the design is equal to $\sqrt{m}d^{(1)}$. So

$$\begin{cases} u^{(k,1)} = (0, 0, \ldots, 0)^T \\ u^{(k,r)} = (0, \ldots, \pm d^{(k)}, \ldots, 0)^T, \qquad r = 2, \ldots, 2m+1 \\ u^{(k,r)} = (\pm d^{(k)}, \pm d^{(k)}, \ldots, \pm d^{(k)})^T, \; r = 2m+2, \ldots, 2^m + 2m + 1 \end{cases} \tag{14}$$

- The response surface $\tilde{h}^{(k)}(u)$ is a second order polynomial with crossed terms:

$$\tilde{h}^{(k)}(u) = a_0 + \sum_{i=1}^{n} a_i u_i + \sum_{i=1}^{n} \sum_{j=1}^{n} a_{ij} u_i u_j \tag{15}$$

- The polynomial coefficients identification is done by the least square method

$$E^{(k)} = \sum_{r=1}^{p} w_i [\tilde{h}^{(k)}(u^{(k,r)}) - h(u^{(k,r)})]^2 \tag{16}$$

$$\frac{\partial E^{(k)}}{\partial a_i} = 0 \quad i = 0, \ldots, N_h \tag{17}$$

where $p = 2^m + 2m + 1$ and $N_h = (m+1)(m+2)/2$ is the number of coefficients of the function $\tilde{h}^{(k)}(u) \cdot w_i = 1$.

- The SQP optimization algorithm is used to compute the reliability index $\beta_{HL}^{(k)}$ and the design point $u^{(k,r)}$, solutions of the following minimization problem:

$$\beta_{HL}^{(k)} = \min \sqrt{u^t \cdot u} \quad \text{subjected to: } \tilde{h}^{(k)} = 0 \tag{18}$$

- $k = k + 1$, generation of a new set of points. Its center is the point $u^{(k-1,r)}$ and the distance from the central point to a "corner" in the design is equal to $\sqrt{m} d^k$ with

$$d^{(k)} = \frac{d^{(k-1)}}{q} \tag{19}$$

$q > 1$ is a real number which plays the role of a zoom factor.

Repeat (13)–(17) until a test of convergence on $\beta_{HL}^{(k)}$ stops the iterative algorithm. Then the failure probability is evaluated by the first order reliability method

$$P_f \approx \Phi(-\beta_{HL}) \tag{20}$$

where $u = (u_1, u_2, \ldots, u_m)^T$ is a realization of the random vector U and $\tilde{h}^{(k)}(u)$ is the approximated limit state function in the space of standard Gaussian variables [11]. U is the image of X by the probabilistic transformation and Φ is the standard normal distribution function. This iterative scheme is particularly efficient. The adaptive central composite designs give a very good representation of the random variables domain. The second order polynomial and the least square method ensures a good compromise between the computational effort and the approximation accuracy of the real limit state function $h(u)$. The number of necessary calculations is reasonable and depends on the number of variables. The SQP algorithm is robust and efficient for this application in nonlinear finite-element reliability analysis. For more details, see [3, 12, 13] (Fig. 2).

4.1 Reliability Analysis of the Marine Propeller

Following our deterministic study applied to a boat propeller and a single blade in air and in water, we have noticed a variation of the numerical results compared to the

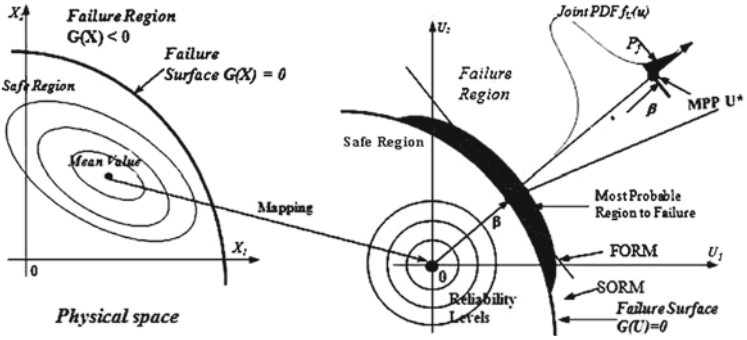

Fig. 2 Reliability approach

Table 4 Material properties of the structure

Young's modulus	Poisson's ratio	Density
9.6×10^10	0.3	9200

Table 5 Material properties of the fluid

Density ($kg\,m^{-3}$)	Speed of sound ($m\,s^{-1}$)
1000	1500

experimental results, and want to extend this study to the stochastic and reliability study to take account of uncertainties in the entered variables. Figure 3 shows the finite element model of the structure. The fluid and the propeller are defined by their properties shown in the Tables 6 and 7. To check the reliability of this structure, the first natural frequency R1 is analyzed. The objective of this study is the demonstration of the interest of the proposed method. The numerical development has been realized by a code which couples MATLAB© and ANSYS©. The learning methods are validated against different criteria, the value of the failure's probability and the calculation of the reliability index. The method of reduction is applied to a given simplified model of the propeller composed of four substructures [14, 15] and the acoustic cavity is divided into four subdomains containing each approximately the same number of elements, see Fig. 3. The deterministic numerical calculations are performed on the whole structure and on the single blade and they are compared with experimental results [16] (Tables 4 and 5).

The highlighting of the important dispersion of material properties of vibro-acoustic problems has incited us to turn towards stochastic methods for their analysis. Front of the complexity of the problem, we have chosen to consider in this work only the sources of uncertainties related to the material properties and we will be limited to the study of a single blade in air and in water. But the uncertainties regarding the other elements of the structure (geometry, boundary conditions and mechanical behavior) have not been taken into account in a perspective of simplification. The choice of standard deviations and the means of random variables were chosen based on deterministic and experimental analyzes. The considered standard devia-

Table 6 Moments of the parameters of the problem and distribution laws

Parameters	Young's modulus (Pa)	Structure's density ($kg\,m^{-3}$)	Fluid's density ($kg\,m^{-3}$)
Distribution	Gaussian	Uniform	Uniform
Means	9.6×10^10	9200	1000
Standard deviation	0.5×10^10	2669.6	295.72

Fig. 3 Finite elements discretization of this immersed structure

tions were also adjusted to maintain realistic ranges of materials involved. Table 6 contains the means of random variables, their standard deviations used in this study and the distributions laws chosen [17].

In this context the stochastic calculation was carried out using probabilistic design system of the ANSYS©. This tool is based on a calculation with Monte Carlo simulation (MC) for 100 samples and the response surface method (RSM) for 40 samples. Tables 7 and 8 show means and standard deviations of the natural frequencies. The first one gives the finding results using the propeller blade in air and the second one gives the finding results using the propeller blade in water.

The finite element code ANSYS© presents the probabilistic modules but it does not allow access to the source files, which is a major handicap in the perspective of implementation of the coupled model. To overcome this difficulty, we have chosen to implement a direct coupling between a reliability code developed in MATLAB and ANSYS. These two codes in fact answer our needs in terms of calculation

Table 7 Means and standard deviations of the natural frequencies for the propeller in air

Modes	R_1 (Hz)	R_2 (Hz)	R_3 (Hz)
ANSYS	74.863	119.82	205.58
Experimental	73	117	201
MC	72.46	115.8	199.6
RSM	73.58	118.5	194.7
SD	12.5	23.5	37.1

Table 8 Means and standard deviations of the natural frequencies for the propeller in water

Modes	R_1 (Hz)	R_2 (Hz)	R_3 (Hz)
ANSYS	37.71	67.54	126.32
Experimental	36	65	123
MC	35.671	66.34	124.12
RSM	34.22	67.45	121.93
SD	5.62	11.16	25.871

capacity and the possibility of dialogue. The first step consists of the declaration in the MATLAB code of the random variables of the model (laws of distribution and associated parameters), the failure function G and all the necessary parameters to solve the reliability calculation. From this information, this probabilistic code can generate achievements of vector $\{X\}$ of random variables. In the second step we appeal to ANSYS to deduce through the finite element calculation the first frequencies of the propeller induced in the different elements of the structure for the draw $\{X\}$. MATLAB code shall then have all the information to assess the quantity $G(\{X\})$. These different steps are repeated until convergence of the optimization algorithm for obtaining the reliability index and the probability of failure [18].

In this numerical study, the analysis of the reliability of the propeller in air and in water was based on an implicit limit state function G based on the first natural frequency R_1:

- For the propeller in air:

$$G(E, \rho_s) = R_1 - R_0, \quad \text{with } R_0 = 73 \text{ Hz} \tag{21}$$

- For the propeller in water:

$$G(E, \rho_s, \rho_f) = R_1 - R_0, \quad \text{with } R_0 = 36 \tag{22}$$

The mean values of random variables and their standard deviations as well as distributions chosen for this study are shown in Table 6.

Table 9 Design parameters and their statistical moments considered in the propeller in air

Parameters	Young's modulus	Structure's density	Reliability index	P_f
FORM	8.5×10^{10}	9030	3.68	0.083
SORM	8.5×10^{10}	9030	3.68	0.012

Table 10 Design parameters and their statistical moments considered in the propeller in water

Parameters	Young's modulus	Structure's density	Fluid's density	β	P_f
FORM	8.37×10^{10}	8980	890	3.54	0.11
SORM	8.37×10^{10}	8980	890	3.54	0.087

Tables 9 and 10 summarize the design parameters and their statistical moments considered in the uncoupled and coupled structure for this example, and they illustrate a comparison between the results obtained from FORM and SORM approaches.

In the deterministic case the numerical results are little far from those obtained by experimentation, with an uncertainty compared to that given by other authors [19]. To overcome this problem, we extend our study to a stochastic study (Tables 7 and 8) which consists, firstly, to implement a simulation technique based on the Monte Carlo method and response surface method, then secondly, to make a reliability analysis. This technique involves a particular treatment of inputs and outputs random variables in order to build a trusted domain on the parameters of the studied system. On the basis of preliminary deterministic study, the reliability analysis based on FORM and SORM was conducted for the blade in air and in water. Precisely, given the low values of probability of failure P_f, it is convenient to reasoning in terms of reliability index β, in order to build a trust domain of the input parameters chosen, as defined in Table 6.

By comparing the probabilities of failure and reliability index calculated and displayed in Tables 9 and 10 with the ranges of values of probability of failure and reliability index β accepted in various industrial sectors, in particular for the marine structures ($P_f \in [10^{-2}, 10^{-4}]$ and $\beta \in [2.33, 3.72]$), we find that there is a very important level of reliability of the blade. A prior study of the sensitivity of material parameters was performed to identify the dominant parameters at the behavior of materials. By a more rational treatment of uncertainties, the reliability approach allows a better appreciation of the safety margins with the aid of the objectives indicators of confidence, and in this sense is an appropriate tool to help to the decision in phases of design and maintenance (Tables 11 and 12).

Table 11 Natural frequencies for the propeller in air calculated by FORM and SORM

Modes	R_1	R_2	R_3
FORM	70.35	116.44	201.24
SD	3.44	5.78	7.39
SORM	69.87	115.63	201.09
SD	3.18	5.36	7.21

Table 12 Natural frequencies for the propeller in water calculated by FORM and SORM

Modes	R_1	R_2	R_3
FORM	36.56	65.73	123.49
SD	1.48	3.65	4.18
SORM	35.67	65.58	123.24
SD	1.56	3.83	4.21

5 Reliability Based Design Optimization

Optimization in mechanical structures aims to determine the best possible design in terms of cost and quality. In general, the designer considers an optimization criterion, restrictions and numerical variables, either real or integer and uses determinist procedures. We can, for example, cite the common methods of descent of stochastic or hybrid algorithms. However, even in these two latter cases, the variables are most often considered as numbers, i.e. determinist variables. This widely used approach can be incorrect when there is variation in parameters or random phenomena must be taken into account. For example, the optimal structure must be highly sensitive to significant disruptions and present, therefore, a low level of reliability.

Due to errors in modeling, the uncertainties inherent to mechanical characteristics, geometric dimensions and manufacturing and assembly procedures, design models for mechanical structures must be constructed whilst taking into account uncertainty in the design parameters during multi-objective optimization. This raises the question of optimization robustness with regards to uncertainties in the design parameters and calls into question the solutions found by determinist optimization methods.

A first approach for accounting for what we call the general form of uncertainties entails using security coefficients i.e. not considering the result of optimization as being the design to be proposed but to modify it in order to ensure greater reliability in general, using a multiplying coefficient. This approach, however, suffers from a lack of generality: security coefficients, also known as security factors, are closely linked to the specific situation being studied and the engineer's experience can therefore not be extended to new situations, notably when the accumulated experience is low and the record of faults is not sufficiently detailed [20].

In response to these difficulties, analysis methods which attempt to account for the random or, more generally, uncertain nature of parameters have been developed.

With this in mind, one of the first aspects considered is the control of the level of reliability or, its equivalent, the solution to the optimization problem's probability of failure. As a result, it is common to seek to determine an optimal design which satisfies a minimum level of reliability: we therefore speak of optimization which accounts for reliability or reliability optimization.

Optimization relates to minimizing a function $F(X)$ (which could represent a geometry, cost, etc.) which is subject to a performance constraint (also known as a limited state function) $G_i(X, Y)$ composed of the determinist variable vector X and the random variable vector Y representing the mechanical resistance, the number of admissible cycles and one or several geometric or physical constraints $H_j(X)$ (maximum admissible limits).

Determinist optimization can be carried out using several limited state with in this case, i represents the number of the limited state function considered. There is another formulation of optimization emphasized more on its immediately evident performance by its formulation:

$$\begin{cases} \max_X : G(X, Y) \\ \text{s. t.} \begin{cases} F(X) \geq 0 \\ H_j(X) \geq 0 \ j = 1, \ldots, n \end{cases} \end{cases} \tag{23}$$

This type of formulation is not very well suited to topological optimization with, for example, lattice type structures for bridges, pylons, etc. Optimization itself, as with any method, its Achilles heel in the sense that we rapidly see in this form that it does not provide reliability.

This, however, is not completely true because reliability is underpinned by partial security coefficients but pure optimization cannot control this in any case, hence the need to improve the formulation to result in reliability optimization. This is composed of two problems: the first entails minimizing an objective function under performance deterministic constraints. The reliability associated with optimization balances out the role of each of these two methods and therefore results in the desired objective. The reliability optimization formulation can be expressed as follows:

$$\begin{cases} \min_X \ F(X) \\ \text{s.c.} \begin{cases} Pr[G_i(X, Y) \leq 0] \leq P_f \ i = 1, 2, \ldots, n \\ H_j(X) \geq 0 \qquad\qquad j = n+1, \ldots, N \end{cases} \end{cases} \tag{24}$$

The objective of RBDO is to find an optimal solution which verifies a probability of failure lower or equal to the target probability, expressed as P_f^c. The basic formulation of RBDO can be written as:

$$\begin{array}{l} \min_d \ C_I(d) \\ \text{s.c.} \begin{cases} Pr[G_i(d, X) \leq 0] \leq P_f^c \ i = 1, \ldots, m \\ \qquad h_j(d) \geq \qquad\quad j = m+1, \ldots, n_h \end{cases} \end{array} \tag{25}$$

with C_I being the cost function, G_i the limited state functions, d the determinist variable vector to be optimized, X the random variable vector and h_j the determinist limitations.

5.1 Optimal Safety Factor

We initially use a single constraint optimization problem with two normal variables $U = (u_1, u_2)$ (see Fig. 4). In this case, the design point P^* is calculated by the following optimization procedure:

$$\min_u \ : \ d^2 = u_1^2 + u_2^2 \text{ s.t. } H(u_1, u_2) \leq 0. \tag{26}$$

The Lagrangian L introduces the constraint into the objective function with a penalty λ. We then need to minimize an unconstrained three variable function:

$$L(u, \lambda, s) = d^2(u) + \lambda \times [H(u) + s^2] \tag{27}$$

where λ is the Lagrange multiplier on the limited state function and s is a real variable.

If we find the stationary points (u^*, λ^*, s^*) in the Lagrangian $L(u, \lambda, s)$, this means that we find (u^*, λ^*, s^*) such that $\nabla L(u^*, \lambda^*, s^*) = (0, 0, 0)$. We therefore deduce the following system:

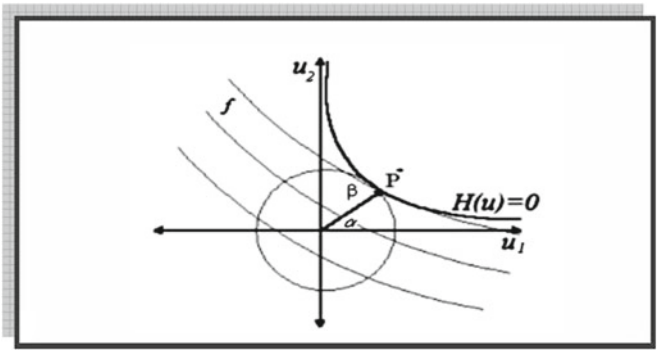

Fig. 4 Design point for a simple limit state function

$$\frac{\partial L}{\partial u_i} = \frac{\partial d^2}{\partial u_i} + \lambda \frac{\partial H}{\partial u_i} = 0,\ i = 1, 2 \tag{28}$$

$$\frac{\partial L}{\partial \lambda} = H(u) + s^2 \tag{29}$$

$$\frac{\partial L}{\partial s} = 2s\lambda = 0 \tag{30}$$

From the third equation $s\lambda = 0$, we can state that the Lagrange multiplier λ is non negative $\lambda \geq 0$ ($\partial^2 L/\partial s^2 \geq 0$). Due to this condition, we can identify the two following cases:

1st example: If the variable s is different from zero ($s \neq 0$), the Lagrange multiplier is equal to zero and the limit state constraint is less than zero ($H(u) < 0$). This scenario corresponds to the state of failure.

2nd example: If the variable s is equal to zero ($s = 0$), the Lagrange multiplier is positive ($\lambda \geq 0$) and the limited state is defined by the equality constraint ($H(u) = 0$). The resulting solution represents the design point.

The first example is not suitable for a reliability study in direct contrast to the second example which is the basis of this new approach. By replacing d^2 by $(u_1^2 + u_2^2)$ in the first condition (28), we obtain:

$$2u_1 + \lambda \frac{\partial H}{\partial u_1} = 0 \leftrightarrow u_1 = -\frac{\lambda}{2} \frac{\partial H}{\partial u_1} \tag{31}$$

$$2u_2 + \lambda \frac{\partial H}{\partial u_2} = 0 \leftrightarrow u_2 = -\frac{\lambda}{2} \frac{\partial H}{\partial u_2} \tag{32}$$

In Fig. 4, P^* indicates the design point and α the direct cosine defined by:

$$\tan \alpha = \frac{u_2}{u_1} = \frac{\frac{\partial H}{\partial u_2}}{\frac{\partial H}{\partial u_1}} \tag{33}$$

β is evaluated following an optimization procedure under the constraint of belonging to the failure problem domain (26), where β represents the minimum distance between the start of the space and the limited state function. The reliability index can be lower or greater at the target reliability β_t. Our objective is to satisfy the target level of reliability which we can express in the following form: $\beta_t^2 = u_1^2 + u_2^2$, referring to this equation in (33), we obtain:

$$u_2^2 \left(\frac{\left(\frac{\partial H}{\partial u_1}\right)^2}{\left(\frac{\partial H}{\partial u_2}\right)^2} + 1 \right) = \beta_t^2 \Rightarrow u_2 = \pm \beta_t \sqrt{\frac{\left(\frac{\partial H}{\partial u_2}\right)^2}{\left(\frac{\partial H}{\partial u_1}\right)^2 + \left(\frac{\partial H}{\partial u_2}\right)^2}} \tag{34}$$

For a normal distribution, the normalized variable u_i has the following form:

$$u_i = \frac{y_i - m_{yi}}{\sigma_i},\ i = 1, \ldots, n \tag{35}$$

where the average m_{yi} and the standard deviation σ_i are two distribution parameters of the normal law with $x_i = m_{yi}$, $i = 1, \ldots, n$ and $\sigma_i = \gamma_i \times x_i$, $i = 1, \ldots, n$.

By introducing the partial safety factor S_{fi} to each component of the design variable vector x_i:

$$y_i = S_{fi} \cdot x_i,\ i = 1, \ldots, n \tag{36}$$

and by referring to the components y_i in (35), we have:

$$u_i = \frac{S_{fi} - 1}{\gamma_i},\ i = 1, \ldots, n \tag{37}$$

From (37) and (34), we can write the security factor S_{f2} in the following form:

$$S_{f_2} = 1 \pm \gamma_2 \times \beta_c \sqrt{\frac{\left(\frac{\partial H}{\partial u_2}\right)^2}{\left(\frac{\partial H}{\partial u_1}\right)^2 + \left(\frac{\partial H}{\partial u_2}\right)^2}}. \tag{38}$$

The calculation of the normal gradient $\frac{\partial H}{\partial u}$ is not accessible because the structures mechanical analysis is carried out in the physical space rather than the standard space. By applying the chain rule to the physical gradient $\frac{\partial G}{\partial y}$, the following expression can be established:

$$\frac{\partial H}{\partial u_i} = \frac{\partial G}{\partial y_k} \frac{\partial T_k^{-1}(x, u)}{\partial u_i},\ i = 1, \ldots, n;\ k = 1, \ldots, K \tag{39}$$

$$\Rightarrow \frac{\partial H}{\partial u_i} = \sqrt{\left|\frac{\partial G}{\partial y_i}\right|},\ i = 1, \ldots, n \tag{40}$$

where $T^{-1}(x, u)$ is an iso-probabilistic transformation defined for the movement between the physical and normed spaces.

By introducing expression (39) into (38), we write:

$$S_{f_2} = 1 + \gamma_2 u_2 = 1 \pm \gamma_2 \times \beta_t \sqrt{\frac{\left|\sum_{j=1}^{2} \frac{\partial G_j}{\partial y_2}\right|}{\sum_{i=1}^{2} \left|\sum_{j=1}^{2} \frac{\partial G_j}{\partial y_2}\right|}} \tag{41}$$

For a problem with a single (simple) limited state with n design variables, (42) can be written in the general form:

$$S_{f_i} = 1 + \gamma_i u_i = 1 \pm \gamma_i \times \beta_t \sqrt{\frac{\left|\sum_{j=1}^{2} \frac{\partial G_j}{\partial y_j}\right|}{\sum_{i=1}^{2}\left|\sum_{j=1}^{2} \frac{\partial G_j}{\partial y_i}\right|}} \tag{42}$$

The sign ($\pm$) depends on the sign of the derivative $\partial G/\partial y_i$ i.e.:

$$\frac{\partial G}{\partial y_i} > 0 \leftrightarrow u_i > 0 \text{ et } S_{fi} > 1,\ i = 1, \ldots, n \tag{43}$$

$$\frac{\partial G}{\partial y_i} < 0 \leftrightarrow u_i < 0 \text{ and } S_{fi} < 1,\ i = 1, \ldots, n \tag{44}$$

By using these safety factors, we can respond to the target reliability whilst avoiding the problem's complexity.

The OSF approach is carried out in three steps:

Step 1: Identify the design point (or the most probable point of failure): we consider the limit state function $G(x, y)$ as the most active constraint. The optimization problem carried out in the physical space entails minimizing the objective function under the limit state constraint and under the determinist constraints. The resulting solution is considered as the most probable point of failure and is termed the design point.

Step 2: Calculate the safety factors: in order to calculate these factors, a sensitivity analysis of the limit state function in relation to the determinist variables is required. When the number of determinist variables is equal to that of the random variables, there is no additional numerical cost because the gradient is calculated during the optimization process. If the number of determinist variables is different from that of the random variables, we can only evaluate the sensitivity of the limit state function which concerns these random variables not associated with determinist variables (low computational cost).

Step 3: Calculate the optimal solution: In the last step, we include the safety factors' values to evaluate the design variables values and we then determine the structure's optimal design.

5.2 RBDO of Marine Propeller

In this application, we have two objectives:

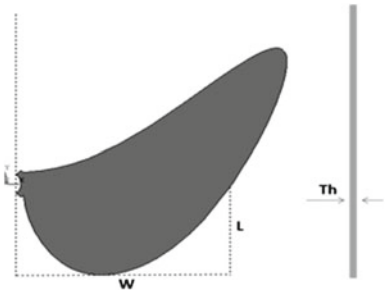

Fig. 5 Scheme of the marine propeller

Table 13 Data of the problem

	Parameter	Value
Plate	W	4.5 m
	L	1.5 m
	Thickness	0.1 m
	Outer radius	0.50 m
	Inner radius	0.35 m
	Density	7860 kg/m^3
	Young modulus	$2.0e11$ Pa
	Poisson ratio	0.3
Water	Density	1000 kg/m^3

1. To show the difference between the deterministic design optimization and the reliability-based design optimization.
2. To demonstrate the efficiency of the proposed safest point method relative to the hybrid method.

Scheme and data problem are presented, respectively, in Fig. 5 and Table 13.

The objective is to find the eigen-frequency for a given interval [13, 19], that is located on the safest position of this interval. So $fa = 14$ Hz, $fb = 20$ Hz and $fn = ?$ Hz, where fn must verify the equality of reliability indices: $\beta_a = \beta_b$. We can deal with three models: The first structure must be optimized subject to the first frequency value of the given f_a, the second one must be optimized at the end frequency value of the interval f_b, and the third structure must be optimized subject to a frequency value f_n that verifies the equality of reliability indices relative to both sides of the given interval (see Fig. 6) [21].

Here, we can deal with two reliability-based design optimization methods: hybrid and safest point methods. The hybrid method (HM) simultaneously optimizes the three structures but the safest point method consists in optimizing three simple problems.

HM procedure: We minimize the weight of one pale of the objective function subject to the different frequencies constraint and the reliability one as follows:

$$\begin{array}{l} \min\limits_{Th_1,\ldots,m_{Th},\ldots,Th_2,\ldots} : Weight_n\,(m_{Th}, m_W, m_L)\,.\,d_{\beta_1}\left(Th_1, W_1, L_{1_1}, m_{Th}, m_W, m_L\right)\,. \\ \qquad d_{\beta_2}\,(Th_2, W_2, L_2, m_{Th}, m_W, mL) \\ subject\ to\ : f^1_{\max}(Th_1, W_1, L_1) - f_a \le 0\,,\, f^2_{\max}(Th_2, W_2, L_{22}) - f_b \le 0 \\ \qquad : d_{\beta_1}\,(Th_1, W_1, L_1, m_{Th}, m_W, mL) - d_{\beta_2}\,(Th_2, W_2, L_2, m_{Th}, m_W, m_L) \le 0 \\ : u_i^a + u_i^b = 0, \end{array} \tag{45}$$

SP procedure: We have two simple optimization problems:

- The first is to minimize the objective function of the first model subject to the frequency f_a constraint as follows:

$$\min_{Th_1,\ldots} : Weight_a\,(Th_1, W_1, L_1)\ subject\ to\ : f^1_{\max}(Th_1, W_1, L_1) - f_a \le 0 \tag{46}$$

- The second is to minimize the objective function of the second model subject to the frequency f_b constraint as follows:

$$\min_{Th_2,\ldots} : Weight_b\,(Th_2, W_2, L_2)\ subject\ to\ : f^2_{\max}(Th_2, W_2, L_2) - f_b \le 0 \tag{47}$$

Let consider a given interval $[f_a, f_b]$ (see Fig. 6). For the first shape mode, to get the reliability-based optimum solution for a given interval, we consider the equality of the reliability indices:

$$\beta_a = \beta_b \quad \text{or} \quad \beta_1 = \beta_2 \tag{48}$$

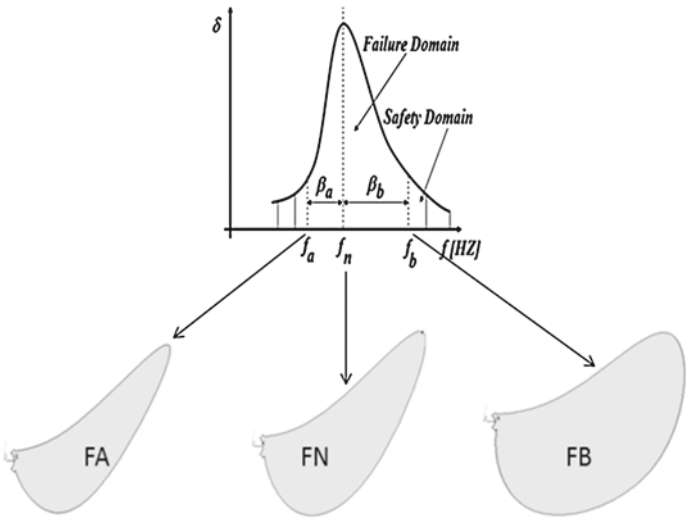

Fig. 6 Marine propeller optimization models for both cases

Table 14 Results for the marine propeller

	Variables	Initial	Optimum design with HM	Optimum design with SP
f_n	Th (m)	0.2	0.175	0.20
	L (m)	2.00	2.253	2.55
	W (m)	4.00	4.151	4.50
f_a	Th_1 (m)	0.1	0.115	0.120
	L_1 (m)	1.5	1.65	1.750
	W_1 (m)	3.5	3.55	3.750
f_b	Th_2 (m)	0.3	0.286	0.278
	L_2 (m)	3.5	3.485	3.353
	W_2 (m)	5.5	5.175	5.246
	f_a (Hz)	13	14.22	14.10
	f_n (Hz)	21	18.29	18.90
	f_b (Hz)	22	19.89	19.90
	Volume (m^3)	2.95	2.836	3.05
	Times (s)	–	4125	995

with

$$\beta_a = \sqrt{\sum_{i=1}^{n} \left(u_i^a\right)^2} \text{ and } \beta_b = \sqrt{\sum_{i=1}^{n} \left(u_i^b\right)^2} i = 1, \ldots, n. \tag{49}$$

To verify the equality (49), we propose the equality of each term. So we have:

$$u_i^a = -u_i^b, i = 1, \ldots, n \tag{50}$$

According to the normal distribution law, the normalized variable u_i is given by (50), we get:

$$\frac{y_i^a - m_i}{\sigma_i} = -\frac{y_i^b - m_i}{\sigma_i}, \text{ or } \frac{y_i^a - x_i}{\sigma_i} = -\frac{y_i^b - x_i}{\sigma_i}, i = 1, \ldots, n \tag{51}$$

To obtain equality between the reliability indices (see (5)), the mean value of variable corresponds to the structure at f_n. So the mean values of safest solution are located in the middle of the variable interval $[y_i^a, y_i^b]$ as follows:

$$m_i = x_i = \frac{y_i^a + y_i^b}{2}, i = 1, \ldots, n \tag{52}$$

The coordinates of the third model corresponds to f_n according to (52).

Table 14 shows the results of the SP method and presents the reliability-based optimum point for a given interval [14 Hz, 20 Hz]. The value of f_n presents

the equality of reliability indices. The SP method reduces the computing time by 75 % relative to the hybrid method. The advantage of the SP method is simple to be implemented on the machine and to define the eigen frequency of a given interval and provides the designer with reliability-based optimum solution with a small tolerance relative to the hybrid method.

6 Conclusion

This work proposes a probabilistic numerical method of modal synthesis extended to reliability study based on FORM and SORM approaches for solving large size vibro-acoustic problem of coupled fluid-structure systems modeled by the finite element method. To take into account uncertainties related to parameters of the two domains, a reliability analysis was subsequently conducted. For this purpose, an integrated approach combining the methods of reliability and finite element modeling has been proposed to account for the failure of submerged structures. From the point of sight of designers, this approach provides an adequate framework for the analysis of the reliability of structures in contact with the fluid which confers a physical significance to the uncertainties introduced.

The used numerical method takes into account the uncertainties of input parameters such as properties of the two domains fluid and solid. The application of the proposed method is performed on a propeller boat in air and water. The numerical study is performed using a code developed which couples MATLAB and ANSYS to evaluate the reliability of the structure. The comparison of the numerical results allows us to validate jointly the process of calculation and the method proposed in the domain of frequency analysis and the reliability of submerged structures in order to build a reliable and robust model for the problems of fluid-structure interaction.

The obtained results through the study of the marine propeller are very encouraging. The proposed model, whose choices have been dictated by the physical phenomena involved, the deterministic results and available experimental data. This model seems indeed capable to account for the reliability of these submerged structures at different scales. If the deterministic study has shed light on the effect of coupling between the fluid and the structure, the stochastic study has demonstrated the relevance of this approach with a view to improve the robustness of the forecast results in the probabilistic approach. RBDO analysis has given an other conception of the marine propeller taking into account optimization and reliability.

References

1. Morand, H.J.-P., Ohayon, R.: Fluid Structure Interaction. Wiley, New York (1995)
2. Ditlevson, O., Madsen, H.: Structural Reliability Methods. Wiley, New York (1996)

3. El Hami, A., Radi, B.: Incertitudes, Optimisation et Fiabilité des Structures. Hermès, Paris (2013)
4. Radi, B., El Hami, A.: Reliability analysis of the metal forming process. Int. J. Math. Comput. Model. **45**(3–4), 431–439 (2007)
5. Souli, M., Sigrist, J.F.: Interaction fluide-structure: modélisation et simulation numérique. Lavoisier (2009)
6. El Hami, A., Borza, D., Eduardo, J.: Souza de Cursi, Vibroacoustic analysis of cyclic structures by using dof's size reduction and holographic measurements. Int. J. Shock Vib. **13**(4–5), 355–366 (2006)
7. Mansouri, M., Radi, B., El Hami, A., Borza, D.: Reliability analysis of the vibro-acoustic problem. Numerical an experimental study, uncertainties proceedings, Brasil (2012)
8. Impollonia, N., Ricciardi, G.: Explicit solutions in the stochastic dynamics of structural systems. Probab. Eng. Mech. **21**, 171–181 (2005)
9. Der Kuireghian, A., Zhang, Y.: Space-variant finite element reliability analysis. Comput. Methods Appl. Mech. Eng. **168**(1–4), 173–183 (1999)
10. El Hami, A., Radi, B. (eds.): Uncertainty and Optimization in Structural Mechanics, Wiley & Sons, New York (2013)
11. Hasofer, A.M., Lind, N.: An exact and invariant first-order reliability format. J. Eng. Mech. **100**, 111–121 (1974)
12. Liu, P.-L., Der Kiureghian, A.: Optimization algorithms for structural reliability. Struct. Saf. Eng. **168**, 173–183 (1991)
13. Shinozuka, M.: Basic analysis of structural safety. J. Struct. Div. ASCE **109**(3), 721–740 (1983)
14. Treyssede, F., El Hami, A.: Une méthode couplée de sous-structuration/sous-domaines acoustiques pour des problémes d'interactions fluide-structure de grande taille. XIVe Colloque Vibrations Chocs et Bruits, Lyon, 16–18 juin (2004)
15. Pavanello, R.: "Contribution à l'étude hydro-élastique des structures à symétrie cyclique," PhD thesis, INSA de Lyon France (1991)
16. Sigrist, J.F.: Interaction fluide-structure: Analyse vibratoire par éléments finis. Ellipses Edition Marketing S.A., France (2011)
17. Mansouri, M., Radi, B., El Hami, A.: Contribution to the analysis and numerical solution of vibro-acoustic phenomena by the modal synthesis. Adv. Mater. Res. **682**, 73–83 (2013)
18. El Maani, R., Radi, B., El Hami, A.: Mechanical reliability study of a coupled three-dimensional system with uncertain parameters. In: Proceeding of the Second International Conference on Structural Nonlinear Dynamics and Diagnosis (CSNDD'14), 19–21 May, Agadir, Morocco (2014)
19. Castellini, P., Santolini, C.: Vibration measurements on blades of a naval propeller rotating in water with tracking laser vibrometer. Measurement **24**(1), 43–54 (1998)
20. Kharmanda, G., Olhoff, N.: An extension of optimum safety factor approach to nonlinear reliability-based design optimization. Struct. Multi. Optim. **34**, 367–380 (2007)
21. Mansouri, M., Makhloufi, A., Radi, B., El Hami, A.: Reliability based design optimization framework for boat propeller. In: Proceeding of the Second International Conference on Structural Nonlinear Dynamics and Diagnosis (CSNDD'14), 19–21 May, Agadir, Morocco (2014)

Localized Structures in Broad Area VCSELs: Experiments and Delay-Induced Motion

Mustapha Tlidi, Etienne Averlant, Andrei Vladimirov, Alexander Pimenov, Svetlana Gurevich and Krassimir Panayotov

Abstract We investigate the space-time dynamics of a Vertical-Cavity Surface-Emitting Laser (VCSEL) subject to optical injection and to delay feedback control. Apart from their technological advantages, broad area VCSELs allow creating localized light structures (LSs). Such LSs, often called Cavity Solitons, have been proposed to be used in information processing, device characterization, and others. After a brief description of the experimental setup, we present experimental evidence of stationary LSs. We then theoretically describe this system using a mean field model. We perform a real order parameter description close to the nascent bistability and close to large wavelength pattern forming regime. We theoretically characterize the LS snaking bifurcation diagram in this framework. The main body of this chapter is devoted to theoretical investigations on the time-delayed feedback control of LSs in VCSELs. The feedback induces a spontaneous motion of the LSs, which we characterize by computing the velocity and the threshold associated with such motion. In the nascent bistability regime, the motion threshold and the velocity of moving LSs depend only on the feedback parameters. However, when considering the

M. Tlidi (✉) · E. Averlant
Faculté des Sciences de l'Université Libre de Bruxelles, Brussels, Belgium
e-mail: mtlidi@ulb.ac.be

E. Averlant · K. Panayotov
IR-TONA, Vrije Universiteit Brussel, Brussels, Belgium
e-mail: eaverlan@ulb.ac.be

K. Panayotov
e-mail: kpanajot@b-phot.org

A. Vladimirov · A. Pimenov
Weierstrass Institute, Berlin, Germany
e-mail: vladimir@wias-berlin.de

A. Pimenov
e-mail: Alexander.Pimenov@wias-berlin.de

S. Gurevich
Institut Für Theoretische Physik, Münster, Germany
e-mail: gurevics@uni-muenster.de

K. Panayotov
Institute of Solid State Physics, Sofia, Bulgaria

M. Belhaq (ed.), *Structural Nonlinear Dynamics and Diagnosis*,
Springer Proceedings in Physics 168, DOI 10.1007/978-3-319-19851-4_20

previously introduced mean-field model, theoretical predictions indicate that both motion threshold and velocity are strongly affected by the phase of the delay and by the carrier relaxation rate.

Keywords VCSEL · Localized light structures · Cavity soliton · Pattern formation · Time-delayed feedback

1 Introduction

Spontaneous symmetry breaking and self-organization phenomena have been observed in various fields of nonlinear science such as nonlinear optics, fibre optics, fluid mechanics, granular matter or plant ecology. The link between the well known Turing instability and transverse patterns formation in nonlinear optics was established for the first time by Lugiato and Lefever [1]. In their seminal paper, they considered an optical resonator filled with a passive nonlinear medium and driven by a coherent radiation beam. Since then, many driven systems have proven to allow periodic patterns in the transverse section of their output beam. Besides a periodic distribution of light, LSs may form in the plane perpendicular to the propagation axis. They are often called localized spots and localized patterns, or cavity solitons which appear either isolated, randomly distributed or self-organized in clusters forming a well-defined spatial pattern [2, 3]. When LSs are sufficiently separated from each other, localized peaks are independent and randomly distributed in space. However, when the distance between peaks decreases they start to interact via their oscillating, exponentially decaying tails [4–7]. LSs have been reported in nonlinear resonators such as lasers with saturable absorbers [8–10], in passive nonlinear resonators [2, 3, 11], optical parametric oscillators [12, 13], in left-handed materials [14–17], in exciton-polariton patterns in semiconductor microcavities [18, 19] and in the framework of the Ginzburg-Landau equation [20–24]. Phase solitons have been demonstrated far from any pattern forming instability [25–30].

Localized structures are homoclinic solutions (solitary or stationary pulses) of partial differential equations. The conditions under which LSs and periodic patterns appear are closely related. Typically, when the Turing instability becomes subcritical, there exists a pinning domain where LSs are stable. This is a universal phenomenon and a well-documented issue in various fields of nonlinear science. The experimental observation of LSs in driven nonlinear optical cavities has further motivated the interest in this field of research. In particular, LSs could be used as bits for information storage and processing. Several overviews have been published on this active area of research [9, 31–48].

Many theoretical and experimental studies on LS formation in VCSELs have been realized [49, 50]. They have been experimentally observed in broad area VCSELs both below [49, 51] and above [52] the lasing threshold when injecting a holding beam with appropriate frequency and power. A spatially LS has also been found in a medium size VCSEL, but only by using its particular polarization properties [53]. Cavity soliton lasers (CSLs) in a VCSEL system without a holding beam have been demonstrated both experimentally [54] and theoretically [55] in VCSELs subject to

frequency selective optical feedback and in face to face coupled VCSELs [56, 57]. In these systems, the VCSELs are placed in self imaging optical systems with either an external grating or another VCSEL biased below lasing threshold, so that the system becomes bistable. Lasing spots spontaneously appear in these systems and can be switched on and off by another laser beam. As a matter of fact a broad area VCSEL with saturable absorber has been the first system in which LSs have been predicted and studied theoretically [58–60]. LSs in a monolithic optically pumped VCSEL with a saturable absorber have been demonstrated in [61] and their switching dynamics studied in [62]. Several applications of LSs in VCSELs have been demonstrated: optical memory [63], optical delay line [64] and optical microscopy [50].

In this chapter, we investigate the formation of LSs in VCSELs subject to both optical injection and delay feedback control. These lasers are characterized by a large Fresnel number and a short cavity. VCSELs are the best candidate for localized structures formation in their transverse section. The first VCSELs were fabricated in 1979 [65] and later on they reached performances comparable to those of edge-emitting lasers [66, 67]. Nowadays VCSELs are replacing edge-emitting lasers in short and medium distance optical communication links thanks to their inherent advantages: much smaller dimensions, circular beam shape that facilitates coupling to optical fibres, two-dimensional array integration and on wafer testing that brings down the production cost [67]. As VCSELs emit light perpendicular to the surface and the active quantum wells, their cavity length is of the order of 1 μm—the wavelength of the generated light. Thanks to the maturity of the semiconductor technology VCSELs can be made homogeneous over a size of hundreds of μm while the characteristic LS size is about 10 μm. The timescales of the semiconductor laser dynamics and LS formation are in the ns scale, which allows for fast and accurate gathering of data. Finally, VCSEL physics and dynamics are quite well understood [67–69].

We investigate experimentally and theoretically the formation of stationary LSs in VCSELs and we describe theoretically the effect of a time delayed feedback on the stability of LSs. For this purpose, we adopt the Rosanov-Lang-Kobayashi approach for modelling of delay feedback [70, 71].

This chapter is organized as follows. After an introduction, we provide a description of the VCSELs in Sect. 2, the experimental setup and the observation of localized structures in a medium size VCSEL are described in Sect. 3. A theoretical description based on mean field model and the derivation of the generalized Swift-Hohenberg equation are given in Sect. 4. Stationary LSs and their bifurcation diagram are presented in Sect. 5. LSs brought into motion under the effect of delay feedback are discussed in Sect. 6. We conclude and draw some perspectives of the present work in Sect. 7.

2 Vertical-Cavity Surface-Emitting Lasers

The structure of a VCSEL is by far more complex than the one of an edge-emitting semiconductor laser. But this complexity, and the inherent fabrication costs, did

not keep VCSELs from becoming the second most produced laser type [72–74]. The biggest advantages of this structure are the circular emission pattern and low divergence, which allow to easily couple the light to an optical fibre for optical interconnects. Moreover, the high reflectivity of the Bragg mirrors provide a low lasing threshold, which makes VCSELs the choice lasers for low power applications (such as optical mice for example). For high power applications, VCSELs can easily be coupled into arrays [75], which provides a high power coherent low divergence beam.

The emission surface of a VCSEL can be made from a few μm to some 200 μm—the first ones are best suited for low power applications, whereas the second category is typically used for spectroscopy. Apart of their use in spectroscopy, broad area VCSELs are best suited for LSs studies. They have several characteristics that makes them a choice material:

- Their use in information technologies provides a mastering of the fabrication process, leading to à la carte properties;
- The response time is much faster than the one in liquid crystals or photorefractive media, which makes them more likely to be used in potential high speed applications;
- Experiments can be carried out on a single one hundred micrometer chip, in comparison with some meter needed for creating LSs in gas cells;

The broad-area bottom emitting VCSEL structure we use in our experiments is described in Fig. 1. The top and bottom distributed Bragg reflectors consist of 30 and 20.5 $Al_{0.88}Ga_{0.12}As$–GaAs layer pairs, respectively. The active region consists of three $In_{0.2}Ga_{0.8}As$ quantum wells embedded in GaAs barriers and AlGaAs cladding layers [75]. The bottom-emitting configuration allows the stand-alone VCSEL to have a better (more homogeneous) current distribution in the transverse plane and, therefore, is more suitable for producing LSs. Moreover a heat sink can be directly mounted on top of the *p*-contact and the *p*-doped DBR, which is the main source of heat. The temperature distribution is hence more homogeneous as well.

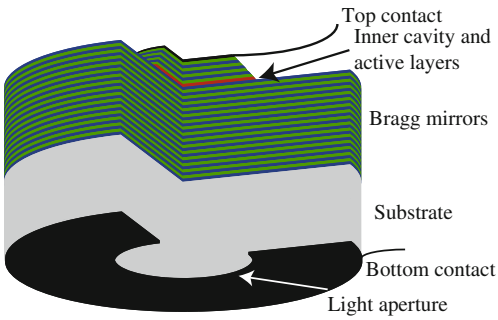

Fig. 1 View of a bottom-emitting VCSEL. The *blue* and *green* layers constitute the pairs in the Bragg mirrors. The *red* element is the cavity containing the quantum wells. The *grey* part is the substrate on which the structure has been grown and through which the light is emitted

3 Experimental Observations

3.1 Description of the Experimental Setup

The experimental setup used for the generation of two-dimensional LSs is shown in Fig. 2. The injection part consists of a tunable External Cavity Diode Laser (Master) in a Littrow configuration, optically isolated from the rest of the experiment. The linear polarization of the injected light is tuned to match the one of the VCSEL. In order to produce LSs, both the optical injection power and the detuning between the injection frequency and the VCSEL resonance frequency are adjusted.

The VCSEL we use is a 80 μm diameter, bottom emitting InGaAs multiple quantum well VCSEL, as described in Sect. 2 which has a threshold current of 42.5 mA at 25.0 °C.

We analyse the optical spectrum, near field and output power of the VCSEL.

A photography of the actual setup is shown in Fig. 3.

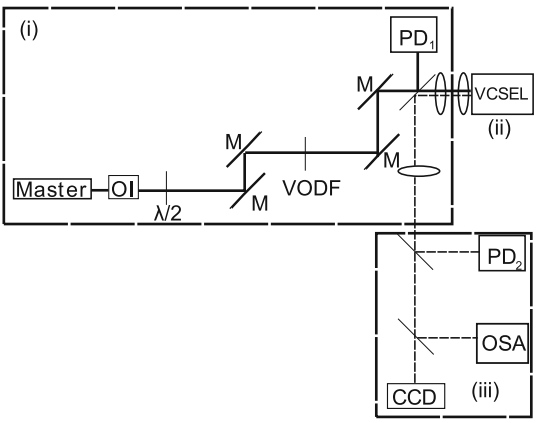

Fig. 2 Experimental setup schematic. The full line is the path of the light from the master laser, whereas the dashed line is the path followed by the light from the VCSEL. (i) injection preparation and monitoring; *Master* master laser, *OI* optical isolator, $\lambda/2$: half wave plate, *M* mirror, *VODF* variable optical density filter; (ii) VCSEL; (iii) analysis branch; *PD* photodiode, *OSA* optical spectrum analyser. Reprinted from [76]

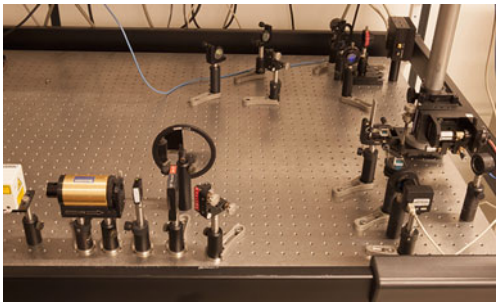

Fig. 3 Photography of the experimental setup. *Left down* side of the picture: injection preparation with external cavity laser diode, optical isolator, half-wave plate and variable optical density filter. *Top right* injection monitoring and VCSEL. *Down right* analysis branch; optical spectrum analyser, CCD camera and photodiode

3.2 Experimental Observations

Tuning the width of the injection beam to 100 μm, the detuning to −174 GHz, the VCSEL driving current to 45.013 mA and its substrate temperature to 25.01 °C, we obtain the bistability curve depicted in Fig. 4. We continuously varied the optical injection power by increasing it, before decreasing it. The hysteresis phenomenon associated with this experiment is evidenced in Fig. 4a. The insets represent near field profiles on the higher and lower branch of the hysteresis curve. One dimensional profiles along the horizontal lines drawn on the insets are shown in Fig. 4b(up),

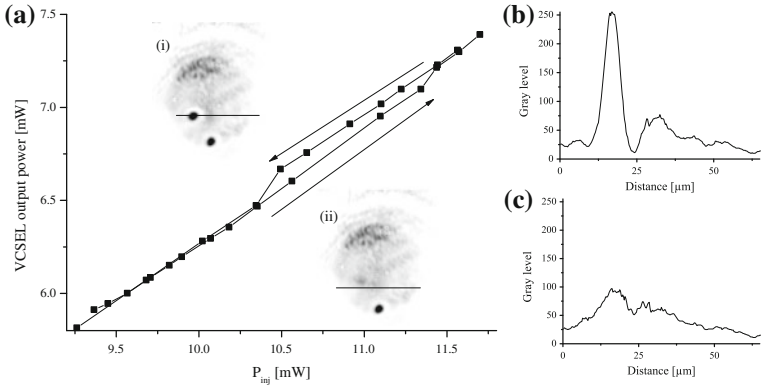

Fig. 4 Bistability between one and two-peaked LSs inside the near field of the VCSEL as a function of the optical injection power. **a** Power emitted by the VCSEL as a function of the optical injection power for $\theta = -174$ GHz and a beam waist of 100 μm. The *insets* (*i*) and (*ii*) respectively represent near field profiles on the higher and lower branch of the hysteresis curve. **b** and **c** One dimensional profiles along the horizontal line drawn on the aforementioned insets. Redrawn from [76]

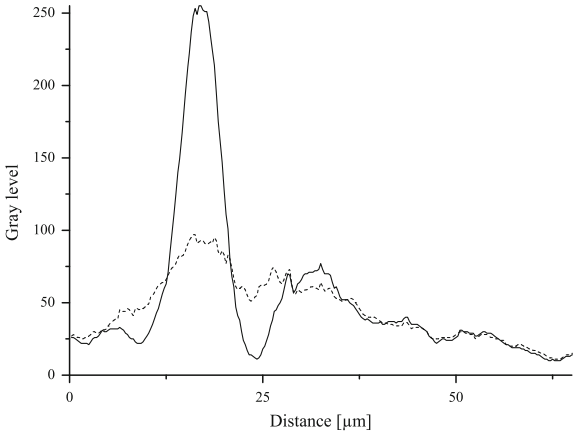

Fig. 5 Cross sections along the solid lines indicated in Fig. 4a, (*i*) and (*ii*). The *dashed line* is the state (*ii*) (lower branch of the hysteresis), whereas the full line is the system with a LS (upper branch of the hysteresis). Redrawn from [76]

c(down). The lower branch corresponds to the "homogeneous" steady state. In Fig. 5, the difference between these two states is evidenced. On the higher branch, there is not only a peak, but a clearly noticeable oscillating tail around this peak, which is characteristic of a LS.

4 Mean Field Model

In this section, we describe the dynamics of a VCSEL submitted to optical injection and delayed feedback. To do so, we assume an external cavity (i) in which the diffraction is compensated (ii) much longer than the characteristic diffraction length of the field. We further apply (i) a paraxial approximation (ii) a slowly varying envelope approximation. The mean field model describing the space-time evolution of the electric field envelope E and the carrier density N in a VCSEL subjected to optical injection and time-delayed feedback is then given by the following set of dimensionless partial differential equations

$$\frac{\partial E}{\partial t} = -(\mu + i\theta)\, E + 2C(1 - i\alpha)(N-1)E + E_i - \eta e^{i\varphi} E(t-\tau) + i\nabla^2 E\,, \tag{1}$$

$$\frac{\partial N}{\partial t} = -\gamma \left[N - I + (N-1)\,|E|^2 - d\nabla^2 N \right]. \tag{2}$$

The parameter α describes the linewidth enhancement factor, μ and θ are the cavity decay rate and the cavity detuning parameter, respectively. The parameter E_i is the amplitude of the injected field which we assume to be positive in order to fix the origin of the phase. C is the bistability parameter, γ is the carrier decay rate, I is the injection current, and d is the carrier diffusion coefficient. The light diffraction

and the carrier diffusion are described by the terms $i\nabla^2 E$ and $d\nabla^2 N$, respectively, where ∇^2 is the Laplace operator acting in the transverse plane $(x,\ y)$. Below we consider the case when the laser is subjected to coherent delayed feedback from an external mirror. To minimize the effect of diffraction on the feedback field we assume that the external cavity is self-imaging [77]. The feedback is characterized by the delay time $\tau = 2L_{ext}/c$, the feedback rate $\eta \geq 0$, and phase φ, where L_{ext} is the external cavity length, and c is the speed of light. The link between dimensionless and physical parameters is provided in [78]. Using the expression for the feedback rate $\eta = r^{1/2}(1-R)/R^{1/2}\tau_{in}$ given in [79], where r (R) is the power reflectivity of the feedback (VCSEL top) mirror and τ_{in} is the VCSEL cavity round trip time, we see that the necessary condition for the appearance of the soliton drift instability $\eta\tau > 1$ [77] can be rewritten in the form $r > \frac{R\tau_{in}^2}{(1-R)^2\tau^2}$. In particular, for $R = 0.3$ and $\tau = 20\tau_{in}$ the latter inequality becomes $r > 1.5 \cdot 10^{-3}$.

To reduce the number of parameters, we introduce the following change of variables: $n = [2C(N-1)-1]/2$ and $e = E^*/\sqrt{2}$. The model (1, 2) of a VCSEL driven by an injected field $Y = E_i/(2\sqrt{2})$ take the following form:

$$\partial_t e = i\theta' e + (1+i\alpha)ne + Y + \eta' e^{-i\psi} e(t-\tau) - i\nabla^2 e, \tag{3}$$

$$\partial_t n = \gamma[P - n - (1+2n)|e|^2 + D\nabla^2 n]. \tag{4}$$

The pump parameter P is $P = C(I-1) - 1/2$, $\gamma = \gamma'/2$, $D = 2d$, $\eta' = \xi/2$, and $\theta' = (\theta+\alpha)/2$. The new time and space scales are $(t, \tau) = 2(t', \tau')$ and $\nabla_\perp^2 = 2\nabla_\perp'^2$. Let us assume for simplicity that the detuning is $\theta' = 0$ and the feedback phases are $\psi = 0$ or $\psi = \pi$.

The homogeneous steady states of (3, 4) are $Y = -e_s(1+i\alpha)(P - |e_s|^2)/(1 + 2|e_s|^2)$ and $n_s = (P - |e_s|^2)/(1 + 2|e_s|^2)$. We explore the vicinity of the nascent optical bistability regime where there exists a second order critical point marking the onset of a hysteresis loop. The critical point associated with bistabilty is obtained when the output intensity as a function of the injection parameter Y has an infinite slope, i.e., $\partial Y/\partial|e_s| = \partial^2 Y/\partial|e_s|^2 = 0$. The coordinates of the critical point are $e_c = (1-i\alpha)\sqrt{3/2(1+\alpha^2)}$, $n_c = -3/2$, $P_c = -9/2$, $D_c = 8\alpha/[3(1+\alpha^2)]$ and $Y_c = (3/2)^{(3/2)}(1+\alpha^2)^{1/2}$. Our objective is to determine a slow time and slow space amplitude equation which is valid under the following approximations: (i) close to the onset of bistabilty (ii) close to large wavelength symmetry breaking instability. Starting from (3, 4), the deviation u of the electric field from its value at the onset of bistablity is shown to obey [80]

$$\begin{aligned}\partial_t u = {} & y - u(p+u^2) + \eta u(t-\tau) \\ & + (d - \frac{5u}{2})\nabla^2 u - a\nabla^4 u - 2(\nabla u)^2,\end{aligned} \tag{5}$$

where $a = (1-\alpha^2)/(4\alpha^2)$. The parameter y denotes the deviation of the injected field amplitude from Y_C. The real variable u, the parameters p and d are the deviations of the electric field, the pump parameter and the carrier diffusion coefficient from their

values at the onset of the critical point, respectively. In the absence of delay; i.e., $\eta = 0$, (5) is the generalized Swift-Hohenberg equation that has been derived for many far from equilibrium systems [81–83]. Even in absence of the delay feedback term, the terms $u\nabla^2 u$ and $(\nabla u)^2$ render (5) nonvariational.

5 Stationary Localized Structures

LSs are nonlinear bright or dark peaks in spatially extended systems. Such structures have been observed in the transverse section of coherently driven optical cavities, and are often called cavity solitons. Currently they attract growing interest in optics due to potential applications for all-optical control of light, optical storage, and information processing [2, 3]. When they are sufficiently separated from each other, localized peaks are independent and randomly distributed in space. However, when the distance between peaks decreases they start to interact via their oscillating, exponentially decaying tails. This interaction then leads to the formation of clusters [4–7]. Mathematically speaking, LSs are homoclinic solutions (solitary or stationary pulses) of partial differential equations. The conditions under which LSs and periodic patterns appear are closely related. Typically, when the Turing instability becomes sub-critical, there exists a pinning domain where localized structures are stable. This is a universal phenomenon and a well documented issue in various fields of nonlinear science, such as chemistry, plant ecology, or optics (see some recent overviews on this multidisciplinary issue [41, 42, 48]).

In this section we describe some basic properties of stationary LS and their bifurcation diagrams in a one dimensional setting. In the absence of delay feedback, (5) admits a variety of LSs. The generalized Swift-Hohenberg equation (5) is numerically integrated using a classical spatial finite-difference method with forward temporal Euler integration. The boundary conditions are periodic in both transverse directions and the initial condition consists of a large amplitude peaks added to the unstable homogeneous steady state. We fix all the parameters except the amplitude of the injected field y. Examples of localized clusters having an odd or an even number of peaks are shown in Fig. 1b, c. They are obtained for the same parameter values and differ only by the initial condition.

We examine the case of one-dimensional monostable system in the subcritical regime where the homogeneous steady state coexists with a spatially periodic structure. In addition, the system exhibits a high degree of multistability in a finite range of y values often called the pinning region [84]. More precisely, (5) then admits an infinite set of odd and even cavity solitons as shown in Fig. 6a, i.e., a set of stationary solutions that exhibit $n = 2p - 1$ or $n = 2p$ peaks, where p is a positive integer. The limit $p \to \infty$, corresponds to the infinitely extended periodic pattern distribution. In the pinning region, the width of LS is close to the half of the periodic wavelength structure. Since the amplitudes of localized patterns having different number of peaks are close to one another, in order to visualize the clusters properties, it is convenient to plot the "L_2-norm"

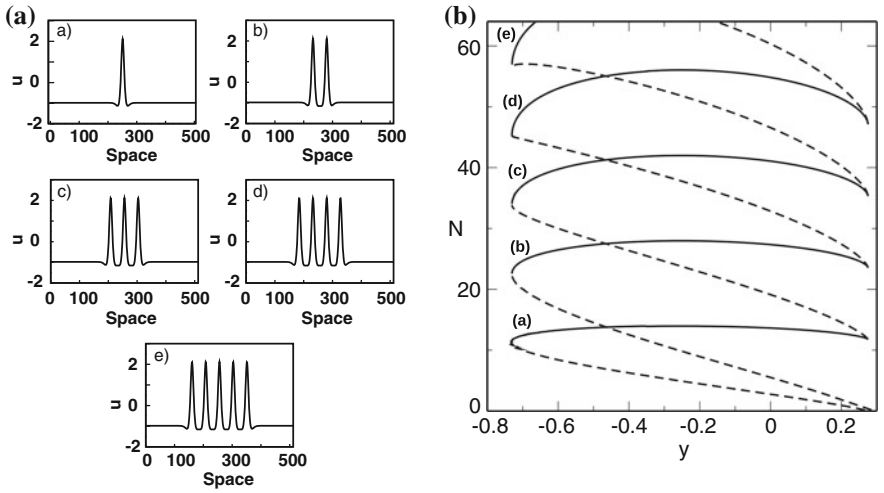

Fig. 6 One dimensional LSs. **a** Multiple peaks localized structures with odd or even number of peaks obtained for $y = -0.35$. **b** Snaking bifurcation diagram showing two inter-weaved snaking curves: the branches (a), (b), (c), (d) and (e) correspond to states having 1, 2, 3, 4 and 5 peaks in Fig. 6a. Redrawn from [80]. The full and the broken lines correspond, respectively, to stable and unstable localized branches of LSs. The parameters are $p = -0.7$, $d = -1.2$, $a = 0.75$, and $\tau = \eta = 0$

$$\mathcal{N} = \int dxdy|u - u_s|^2 \tag{6}$$

as a function of the injected field y. This yields the two snaking curves with odd or even number of peaks as shown in bifurcation diagram of Fig. 6b. As $\mathcal{N}$ increases, at each turning point where the slope becomes infinite, a pair of additional peaks appears in the cluster. One sees that this behavior, referred to as homoclinic snaking phenomenon [85–91], and recently observed experimentally [92, 93], corresponds to back and forth oscillations inside the pinning region. In two spatial dimensions, the variety of stable localized patterns is much larger than in one dimensional system.

6 Moving Localized Structures

In this section we investigate the effect of a time-delayed feedback control on the stability of LSs in VCSELs. This delayed feedback loop compares the electric field at the current moment of time and its values at some time in the past. Recent studies that combined analytical and numerical analysis of the two-dimensional Swift–Hohenberg equation suggested that steady LSs can become mobile when $\eta\tau < 1$ [77, 80, 94].

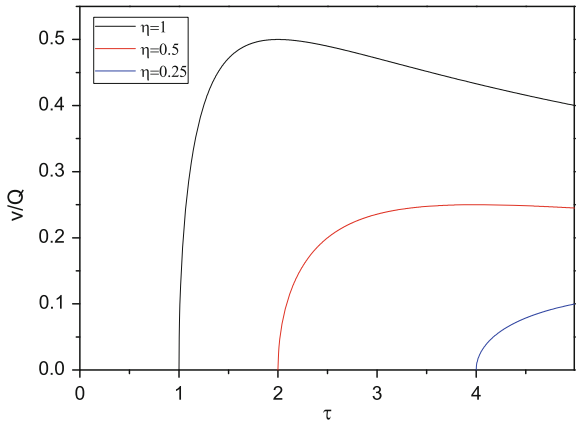

Fig. 7 Velocity by unit of the factor Q of moving localized structures as a function of the time delay τ for different values of the delayed feedback strength η

$$v = \frac{Q}{\tau}\sqrt{-(1-\eta\tau)}, \tag{7}$$

with

$$Q = \sqrt{6\frac{\int_{-\infty}^{+\infty} u_1^2 dxdy}{\int_{-\infty}^{+\infty} u_2^2 dxdy}}$$

Due to the rotational symmetry of the generalized Swift-Hohenberg equation (5), there is no preferred direction for the motion of a circularly symmetric localized structure. The instability leading to the spontaneous motion of a LS solution is a circle pitchfork type of bifurcation. Therefore, the x axis can be chosen for the estimation of the velocity $\mathbf{v}$. In this case we obtain $u_1 = \partial u_0(\mathbf{r})/\partial x$ and $u_2 = \partial^2 u_0(\mathbf{r})/\partial x^2$ where $u_0(\mathbf{r})$ is the stationary localized structure solution. We recover the expression for the soliton velocity (7) that was obtained first in the case of the Swift-Hohenberg equation [77]. The speed formula (7) is valid for any localized pattern, regardless of the number of peaks it contains. The factor Q describes the spatial form of the localized pattern. This factor can be be calculated only numerically. In particular, for the parameter values $y = -0.35$, $p = -0.7$, $d = -1.2$, $a = 0.75$, we obtain $Q = 1.44$. The velocity (7) divided by the factor Q is plotted as a function the delay time for a fixed value of the feedback strength as shown in Fig. 7. The curve of the velocity has a maximum at $\tau = 2/\eta$, which corresponds to the maximal velocity $v_{max} = Q\eta/2$. Note that the threshold $\eta\tau = 1$ and the expression for the formula (7) have been found later on for the chemical reaction-diffusion type of equations [95–97].

Numerical simulations of (5) show indeed that single and many peaked LSs exhibit a spontaneous motion as predicted by the above theoretical analysis, as shown in Fig. 8.

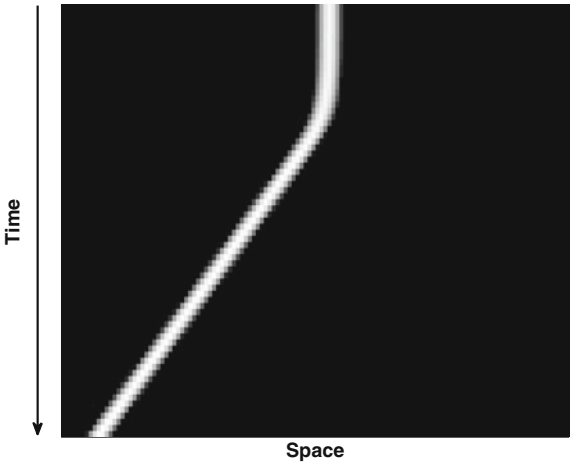

Fig. 8 Space time map of a single-peaked localized structure solution to (5). Parameters are $p = -0.9$, $d = -1.5$, $y = -0.5$, $\eta = 0.15$ and $\tau = 15$. Redrawn from [100]

The velocity and the threshold $\eta\tau = 1$ associated with the LS motion depend only on the delay parameters η and τ. This statement is valid only in nascent optical bistability regime, where the dynamics of the system are described by the real order parameter (5), and for a fixed feedback phase of $\psi = 0$ or $\psi = \pi$. In what follows we will examine the combined role of the phase of the delay feedback ψ and the carrier relaxation rate γ in the framework of the full mean field model.

Since our system is isotropic, the motion of localized structures occurs in an arbitrary direction. At the pitchfork bifurcation the stationary LS loses stability and a branch of moving LSs with the velocity $v = |\mathbf{v}|$ bifurcates from the stationary LS branch of solutions. The bifurcation point can be obtained from the first order expansion of the uniformly moving LS in power series of the small velocity v. Close to the bifurcation point, the uniformly moving LS can be expanded in power series in the small velocity v and through the solvability condition, we obtain the drift instability threshold [98, 99]

$$\eta\tau = \frac{1 + \gamma^{-1}(b/c)}{\sqrt{1 + (a/c)^2}\cos[\varphi + \arctan(a/c)]} \tag{8}$$

with

$$\begin{aligned} a &= \langle \psi_1^\dagger, \psi_2 \rangle - \langle \psi_2^\dagger, \psi_1 \rangle, \\ b &= \langle \psi_3^\dagger, \psi_3 \rangle, \\ c &= \langle \psi_1^\dagger, \psi_1 \rangle + \langle \psi_2^\dagger, \psi_2 \rangle, \end{aligned} \tag{9}$$

and

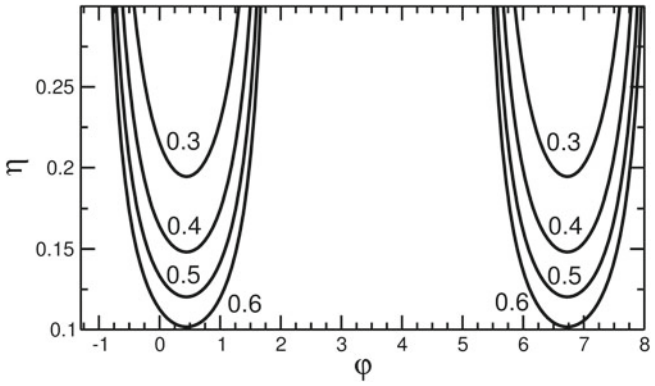

Fig. 9 Threshold associated with the drift bifurcation as a function of the feedback phase φ is plotted for different values of the carrier relaxation rate γ. Parameters are $\mu = 1.0$, $\theta = -2.0$, $C = 0.45$, $\alpha = 5.0$, $\tau = 100$, $d = 0.052$, $E_i = 0.8$, $I = 2$. The values of the parameter γ are shown in the figure. Redrawn from [99]

$$\psi = (\psi_1,\ \psi_2,\ \psi_3)^T = \partial_x\ (X_0,\ Y_0,\ N_0)^T \tag{10}$$

a translational neutral mode of the linear operator L, $L\psi = 0$, while $\psi^\dagger = \left(\psi_1^\dagger,\ \psi_2^\dagger,\ \psi_3^\dagger\right)^T$ is the corresponding solution of the homogeneous adjoint problem $L^\dagger\psi^\dagger = 0$. The real $X_0(x, y)$ and the imaginary $Y_0(x, y)$ parts of the electric field E_0 and the carrier density $N_0(x, y)$ are the stationary axially symmetric LS profiles. They correspond to the time-independent solutions of (1) and (2) with $\tau = 0$. The coefficients a and b are calculated numerically using the relaxation method in two transverse dimensions.

From the expression of the threshold associated with the drift instability (8), we see that the product $\eta\tau$ is not unity as in the case of the generalized Swift-Hohenberg equation, but depends strongly on the feedback phase φ and carrier relaxation rate γ. We plot in Fig. 9, the threshold η associated with the drift instability as a function of the phase of the delay feedback. The numbers on top of the different curves are the different values of the carrier decay rate γ. The carrier relaxation rate strongly affects the threshold associated with the drift instability as shown in Fig. 9. When we increase the carrier relaxation rate, the threshold associated with the moving LS gets higher. In addition, we see from Fig. 9 that, whatever the value of the carrier relaxation rate, the drift instability occurs only within the subinterval $(\varphi_{min} - \pi/2, \varphi_{min} + \pi/2)$ of the interval $(\varphi_{min} - \pi, \varphi_{min} + \pi)$, where $\varphi_{min} = -\arctan a$ is the delay feedback phase, corresponding to the lowest critical feedback rate $\eta_0^{min} = (1 + \gamma^{-1}b)/(\tau\sqrt{1 + a^2})$. Note that η_0 increases very rapidly when approaching the boundaries of these subintervals. In the limit of fast carrier response, $\gamma \gg 1$, and for zero feedback phase, $\varphi = 0$, we recover the expression (8), the threshold formula $\eta\tau = 1$ that has been obtained in both variational Swift-Hohenberg equation [77], and in a modified non-variational one [80]. Note that at $\gamma \to \infty$, $a \neq 0$, and $\varphi = -\arctan a$ the critical

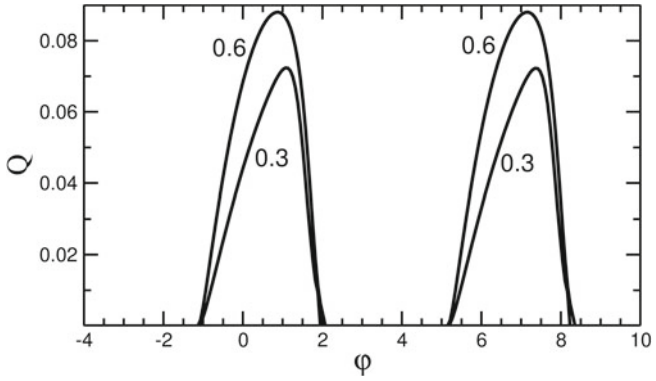

Fig. 10 Q factor as a function of the feedback phase φ , for different values of the carrier relaxation rate γ. The Q factor describes the growth rate of the LS velocity with the square root of the deviation from the critical feedback rate. Parameters are $\mu = 1.0$, $\theta = -2.0$, $C = 0.45$, $\alpha = 5.0$, $\tau = 100$, $d = 0.052$, $E_i = 0.8$, $I = 2$. The values of the parameter γ are shown in the figure. Redrawn from [99]

feedback rate appears to be smaller than that obtained for the real Swift-Hohenberg equation, $\eta\tau = (1 + a^2)^{-1/2} < 1$.

To estimate the velocity of moving localized structure, we expand the slowly moving localized solution in the limit of a small velocity v. The detailed calculations can be found in [99]. The velocity v of LSs then obeys

$$v = \sqrt{\delta\eta}Q \text{ with } Q = (1/\tau)\sqrt{q/(r\eta)}. \tag{11}$$

The factor Q is important since it determines how fast the LS speed increases with the square root of the distance from the critical feedback rate. The Q factor depends on the delay feedback phase as shown Fig. 10. The $\delta\eta$ denotes the deviation of the feedback strength from the bifurcation point associated with the moving LS. The coefficients r and q are $q = a\sin\varphi + c\cos\varphi$, and $r = f\sin\varphi + g\cos\varphi + \mathcal{O}(\tau^{-1})$ with $f = \langle\psi_1^\dagger, \partial_{xxx}Y_0\rangle - \langle\psi_2^\dagger, \partial_{xxx}X_0\rangle$, $h = \langle\psi_3^\dagger, \partial_{xxx}N_0\rangle$, $g = \langle\psi_1^\dagger, \partial_{xxx}X_0\rangle + \langle\psi_2^\dagger, \partial_{xxx}Y_0\rangle$. The coefficients a and c are defined in (10).

Numerical simulations of the full model (1, 2) and the generalized Swift-Hohenberg equation (5) agree with the above theoretical predictions. Indeed, when we choose parameter values such as the system operates above the threshold associated with the motion of LS, a single-peaked LS exhibits a regular motion in the transverse plane of the cavity as shown in Fig. 8 (1-dimensional setting, (5)) and 11 (2-dimensional setting, (1) and (2)).

Note, however, that the motion of LS under the effects of delay feedback is not always regular. It has been shown recently that LSs can exhibit a temporal chaos: numerical simulations of a broad area VCSEL with saturable absorber subjected to time-delayed optical feedback have shown evidence of complex temporal dynamics of LSs [101]. This spatio-temporal chaos is localized in space. More recently, in the

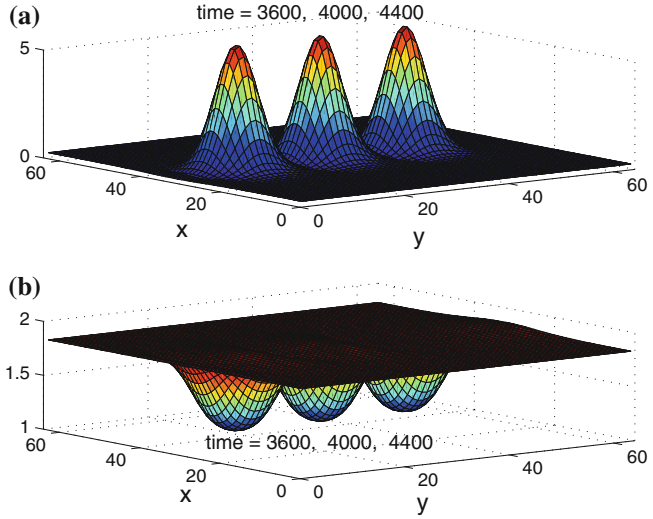

Fig. 11 Field intensity $|E|^2$(*top*) and carrier density N (*bottom*) of a single peaked two-dimensional moving cavity soliton at different times. Parameters are $C = 0.45$, $\theta = -2$, $\alpha = 5$, $\gamma = 0.05$, $d = 0.052$, $\mu = 2$, $E_i = 0.8$, $\tau = 200$, $\eta = 0.07$, $\varphi = 3.5$. Results obtained using (1) and (2). Redrawn from [98]

absence of delay feedback, it has been shown that the VCSEL with saturable absorber without optical injection may exhibit LSs that drift and oscillate simultaneously, and a chaotic behavior [102, 103].

7 Conclusions and Perspectives

In this chapter we have investigated the formation of localized structures in a Vertical-Cavity Surface-Emitting Laser subject to optical injection. This device consists of a medium size bottom-emitting InGaAs multiple quantum well VCSEL to remove, as stated later. In this regime, we have described experimentally the formation of stationary localized structures of light in the transverse section of this device. The experimental part has been performed in an injection locked regime and in the absence of delay feedback control. We have characterized LSs by drawing their bifurcation diagram and performed a numerical simulation for the full model and the generalized Swift-Hohenberg equation.

Then we have described the space-time dynamics of a VCSEL by adding the delay feedback control in the modelling by adopting a mean-field approach. The time-delayed feedback is modelled following a Rosanov-Lang-Kobayashi approach [70, 71]. We have then analysed theoretically the effect of time delayed feedback from an external mirror on the stability of transverse localized structures in a broad area

VCSEL. We have derived a real order parameter equation of the Swift-Hohenberg type with delay feedback. This analysis is only valid close the nascent optical bistability and close to large wavelength pattern forming regime. In this double limit, we have estimated the threshold associated with the drift-instability leading to the spontaneous motion of LS. Explicitly, the threshold is given by a simple formula $\eta\tau = 1$. We conclude that the condition under which transition from motionless LS to a moving one, depends only on the delay feedback η and the delay time τ and not on the other dynamical parameters of the VCSEL system. This conclusion is valid for the variational and nonvariational Swift-Hohenberg equations, and in reaction-diffusion systems. However, in optics, the role of the phase is important because the intensity and the phase of the light operate on the same time scale. We have investigated in the last part of this chapter the role of the phase of the feedback on the mobility of LS. We have shown that, depending on the phase of the feedback, it can have either stabilizing or destabilizing effect on the LSs. In particular, when the interference between the LS field and the feedback field is destructive, the LS can be destabilized via a pitchfork bifurcation, where a branch of uniformly moving LS bifurcates from the stationary one. We have calculated analytically the threshold value of the feedback rate corresponding to this bifurcation and demonstrated that the faster the carrier relaxation rate in the semiconductor medium, the lower the threshold of the spontaneous drift instability induced by the feedback. This is a generic and robust destabilization mechanism in one and two spatial dimensions settings and could be applied to a large class of optical systems under time-delay control.

We have described spatially localized structures, and recent investigations have shown that temporal localized structures have been found in fibre resonators [90, 104–108] and in VCSELS with a saturable absorber [109]. On the other hand, it has been shown that the combinated influence of diffraction and chromatic dispersion leads to the formation of three dimensional localized structures often called light bullet [110–113]. We plan in the future to investigate the effect of delayed feedback on the spontaneous motion of three dimensional light bullets.

In order to check our theoretical predictions, we also plan to investigate experimentally the formation of moving LS in VCSELs. In addition, we will analyse the role of local polarization dynamics in the formation of LSs in the transverse plane of the VCSEL. This would allow us to study the spontaneous motion of vector LSs with different polarizations under the effect of delayed feedback.

A.G.V. and A.P. acknowledge the support from SFB 787 of the DFG. A.G.V. acknowledges the support of the EU FP7 ITN PROPHET and E.T.S. Walton Visitors Award of the Science Foundation Ireland. M.T. received support from the Fonds National de la Recherche Scientifique (Belgium). This research was supported in part by the Interuniversity Attraction Poles program of the Belgian Science Policy Office under Grant No. IAP P7-35.

References

1. Lugiato, L.A., Lefever, R.: Phys. Rev. Lett. **58**, 2209 (1987). doi:10.1103/PhysRevLett.58.2209
2. Tlidi, M., Mandel, P., Lefever, R.: Phys. Rev. Lett. **73**, 640 (1994). doi:10.1103/PhysRevLett.73.640
3. Scroggie, A.J., Firth, W.J., McDonald, G.S., Tlidi, M., Lefever, R., Lugiato, L.A.: Chaos Solitons Fractals **4**(8), 1323 (1994). doi:10.1016/0960-0779(94)90084-1
4. Vladimirov, A., McSloy, J., Skryabin, D., Firth, W.: Phys. Rev. E **65**, 046606 (2002). doi:10.1103/PhysRevE.65.046606
5. Tlidi, M., Vladimirov, A.G., Mandel, P.: IEEE J. Quantum Electron. **39**(2), 216 (2003). doi:10.1109/JQE.2002.807193
6. Tlidi, M., Lefever, R., Vladimirov, A.: Lect. Notes Phys. **751**, 381 (2008)
7. Turaev, D., Vladimirov, A.G., Zelik, S.: Phys. Rev. Lett. **108**, 263906 (2012). doi:10.1103/PhysRevLett.108.263906
8. Fauve, S., Thual, O.: Phys. Rev. Lett. **64**, 282 (1990). doi:10.1103/PhysRevLett.64.282
9. Rosanov, N.N.: In: Wolf, E. (ed.) Progress in Optics, Progress in Optics, vol. 35, pp. 1–60. Elsevier (1996). doi:10.1016/S0079-6638(08)70527-4
10. Slekys, G., Staliunas, K., Weiss, C.: Opt. Commun. **149**(1–3), 113 (1998). doi:10.1016/S0030-4018(97)00667-6
11. Vladimirov, A.G., Skryabin, D.V., Kozyreff, G., Mandel, P., Tlidi, M.: Opt. Express **14**(1), 1 (2006). doi:10.1364/OPEX.14.000001. http://www.opticsexpress.org/abstract.cfm?URI=oe-14-1-1
12. Staliunas, K., Sánchez-Morcillo, V.J.: Opt. Commun. **139**(4–6), 306 (1997). doi:10.1016/S0030-4018(97)00109-0
13. Longhi, S., Opt. Lett. **23**(5), 346 (1998). doi:10.1364/OL.23.000346. http://ol.osa.org/abstract.cfm?URI=ol-23-5-346
14. Kockaert, P., Tassin, P., Van der Sande, G., Veretennicoff, I., Tlidi, M.: Phys. Rev. A **74**, 033822 (2006). doi:10.1103/PhysRevA.74.033822
15. Gelens, L., Van der Sande, G., Tassin, P., Tlidi, M., Kockaert, P., Gomila, D., Veretennicoff, I., Danckaert, J.: Phys. Rev. A **75**, 063812 (2007). doi:10.1103/PhysRevA.75.063812
16. Kozyrev, A.B., Shadrivov, I.V., Kivshar, Y.S.: Appl. Phys. Lett. **104**(8), 084105 (2014). doi:10.1063/1.4866856
17. Tlidi, M., Kockaert, P., Gelens, L.: Phys. Rev. A **84**, 013807 (2011). doi:10.1103/PhysRevA.84.013807
18. Werner, A., Egorov, O.A., Lederer, F.: Phys. Rev. B **90**, 165308 (2014). doi:10.1103/PhysRevB.90.165308
19. Werner, A., Egorov, O.A., Lederer, F.: Phys. Rev. B **89**, 245307 (2014). doi:10.1103/PhysRevB.89.245307
20. Brand, H., Deissler, R.: Phys. Rev. Lett. **63**, 2801 (1989). doi:10.1103/PhysRevLett.63.2801
21. Malomed, B.: Phys. Rev. A **44**, 6954 (1991). doi:10.1103/PhysRevA.44.6954
22. Malomed, B.: Phys. Rev. E **58**, 7928 (1998). doi:10.1103/PhysRevE.58.7928
23. Besse, V., Leblond, H., Mihalache, D., Malomed, B.: Phys. Rev. E **87**, 012916 (2013). doi:10.1103/PhysRevE.87.012916
24. Skarka, V., Aleksić, N.B., Lekić, M., Aleksić, B.N., Malomed, B.A., Mihalache, D., Leblond, H.: Phys. Rev. A **90**, 023845 (2014). doi:10.1103/PhysRevA.90.023845
25. Staliunas, K., Sánchez-Morcillo, V.J.: Phys. Lett. A **241**(1–2), 28 (1998). doi:10.1016/S0375-9601(98)00084-X. http://www.sciencedirect.com/science/article/pii/S037596019800084X
26. Tlidi, M., Mandel, P., Lefever, R.: Phys. Rev. Lett. **81**, 979 (1998)
27. Tlidi, M., Mandel, P., Berre, M.L., Ressayre, E., Tallet, A., Menza, L.D.: Opt. Lett. **25**(7), 487 (2000). doi:10.1364/OL.25.000487. http://ol.osa.org/abstract.cfm?URI=ol-25-7-487
28. Izús, G., San Miguel, M., Santagiustina, M.: Phys. Rev. E **64**, 056231 (2001). doi:10.1103/PhysRevE.64.056231

29. Fernandez-Oto, C., de Valcárcel, G.J., Tlidi, M., Panajotov, K., Staliunas, K.: Phys. Rev. A **89**, 055802 (2014). doi:10.1103/PhysRevA.89.055802
30. Fernandez-Oto, C., Clerc, M., Escaff, D., Tlidi, M.: Phys. Rev. Lett. **110**, 174101 (2013). doi:10.1103/PhysRevLett.110.174101
31. Lugiato, L.A.: Chaos, Solitons Fractals 4, 1251 (1994). doi:10.1016/0960-0779(94)90080-9. http://www.sciencedirect.com/science/article/pii/0960077994900809. Special Issue: Nonlinear Optical Structures, Patterns, Chaos¡/ce:title¿
32. Mandel, P.: Theoretical Problems in Cavity Nonlinear Optics, Cambridge University Press (1997). doi:10.1017/CBO9780511529337. Cambridge Books Online
33. Arecchi, F., Boccaletti, S., Ramazza, P.: Phys. Rep. **318**(1–2), 1 (1999). doi:10.1016/S0370-1573(99)00007-1. http://www.sciencedirect.com/science/article/pii/S0370157399000071
34. Pismen, L.M.: Vortices in nonlinear fields: from liquid crystals to superfluids, from non-equilibrium patterns to cosmic strings. In: International Series of Monographs on Physics, vol. 100, Clarendon press edn. Oxford University Press (1999)
35. Rosanov, N.N.: Spatial Hysteresis and Optical Patterns. Springer Series in Synergetics. Springer, Berlin, Heidelberg (2002). doi:10.1007/978-3-662-04792-7
36. Staliunas, K., Sánchez-Morcillo, V.: Transverse Patterns in Nonlinear Optical Resonators. Springer tracts in modern physics. Springer, Berlin, Heidelberg (2003). doi:10.1007/3-540-36416-1
37. Kivshar, Y.S., Agrawal, G.P.: Optical Solitons: From Fibers to Photonic Crystals. Elsevier (2003). http://www.sciencedirect.com/science/book/9780124105904
38. Denz, C., Schwab, M., Weilnau, C.: Transverse-Pattern Formation in Photorefractive Optics, Springer Tracts in Modern Physics, vol. 188. Springer, Berlin, Heidelberg (2003). doi:10.1007/b13583
39. Mandel, P., Tlidi, M.: J. Opt. B: Quantum Semiclassical Opt. **6**(9), R60 (2004). http://stacks.iop.org/1464-4266/6/i=9/a=R02
40. Malomed, B.A., Mihalache, D., Wise, F., Torner, L.: J. Opt. B: Quantum Semiclassical Opt. **7**(5), R53 (2005). http://stacks.iop.org/1464-4266/7/i=5/a=R02
41. Tlidi, M., Taki, M., Kolokolnikov, T.: Chaos: an interdisciplinary. J. Nonlinear Sci. **17**(3), 037101 (2007)
42. Akhmediev, N., Ankiewicz, A. (eds.): Dissipative solitons: from optics to biology and medicine, Lect. Notes Phys. vol. 751 (Springer, 2008)
43. Ackemann, T., Firth, W.J., Oppo, G.L.: In: Arimondo, P.R.B.E., Lin, C.C. (eds.) Advances in Atomic, Molecular, and Optical Physics, Advances in Atomic, Molecular, and Optical Physics. vol. 57, chapter 6, p. 323. Academic Press (2009). doi:10.1016/S1049-250X(09)57006-1. http://www.sciencedirect.com/science/article/pii/S1049250X09570061
44. Kuszelewicz, R., Barbay, S., Tissoni, G., Almuneau, G.: Eur. Phys. J. D **59**(1), 1 (2010). doi:10.1140/epjd/e2010-00167-7
45. Purwins, H.G., Bödeker, H.U., Amiranashvili, S.: Adv. Phys. **59**(5), 485 (2010). doi:10.1080/00018732.2010.498228
46. Descalzi, O., Clerc, M., Residori, S.: Localized States in Physics: Solitons and Patterns Springer (2011). http://books.google.be/books?id=PWJLOKeeAQIC
47. Leblond, H., Mihalache, D.: Phys. Rep. **523**(2), 61 (2013). doi:10.1016/j.physrep.2012.10.006. http://www.sciencedirect.com/science/article/pii/S0370157312003511
48. Tlidi, M., Staliunas, K., Panajotov, K., Vladimirov, A.G., Clerc, M.G.: Philos. Trans. R. Soc. Lond. A Math. Phys. Eng. Sci. **372**, 20140101 (2014)
49. Taranenko, V.B., Ganne, I., Kuszelewicz, R.J., Weiss, C.O.: Phys. Rev. A **61**, 063818 (2000). doi:10.1103/PhysRevA.61.063818
50. Pedaci, F., Tissoni, G., Barland, S., Giudici, M., Tredicce, J.: Appl. Phys. Lett. **93**(11), 111104 (2008). doi:10.1063/1.2977603. http://link.aip.org/link/?APL/93/111104/1
51. Barland, S., Tredicce, J.R., Brambilla, M., Lugiato, L.A., Balle, S., Giudici, M., Maggipinto, T., Spinelli, L., Tissoni, G., Knödl, T., et al.: Nature **419**(6908), 699 (2002)
52. Hachair, X., Pedaci, F., Caboche, E., Barland, S., Giudici, M., Tredicce, J.R., Prati, F., Tissoni, G., Kheradmand, R., Lugiato, L.A., Protsenko, I., Brambilla, M.: IEEE J. Sel. Top. Quantum Electron. **12**(3), 339 (2006). doi:10.1109/JSTQE.2006.872711

53. Hachair, X., Tissoni, G., Thienpont, H., Panajotov, K.: Phys. Rev. A **79**, 011801 (2009). doi:10.1103/PhysRevA.79.011801
54. Tanguy, Y., Ackemann, T., Firth, W.J., Jäger, R.: Phys. Rev. Lett. **100**, 013907 (2008). doi:10.1103/PhysRevLett.100.013907
55. Paulau, P.V., Gomila, D., Ackemann, T., Loiko, N.A., Firth, W.J.: Phys. Rev. E **78**, 016212 (2008). doi:10.1103/PhysRevE.78.016212
56. Genevet, P., Barland, S., Giudici, M., Tredicce, J.R.: Phys. Rev. Lett. **101**, 123905 (2008). doi:10.1103/PhysRevLett.101.123905
57. Columbo, L., Prati, F., Brambilla, M., Maggipinto, T.: Eur. Phy. J. D **59**(1), 115 (2010). doi:10.1140/epjd/e2010-00110-0
58. Rosanov, N.N., Khodova, G.V.: Opt. Spectrosc. **65**, 449 (1988)
59. Vladimirov, A.G., Fedorov, S.V., Kaliteevskii, N.A., Khodova, G.V., Rosanov, N.N.: J. Opt. B: Quantum Semiclassical Opt. **1**(1), 101 (1999). http://stacks.iop.org/1464-4266/1/i=1/a=019
60. Fedorov, S.V., Vladimirov, A.G., Khodova, G.V., Rosanov, N.N.: Phys. Rev. E **61**, 5814 (2000). doi:10.1103/PhysRevE.61.5814
61. Elsass, T., Gauthron, K., Beaudoin, G., Sagnes, I., Kuszelewicz, R., Barbay, S.: Eur. Phys. J. D **59**(1), 91 (2010). doi:10.1140/epjd/e2010-00079-6
62. Elsass, T., Gauthron, K., Beaudoin, G., Sagnes, I., Kuszelewicz, R., Barbay, S.: Appl. Phys. B **98**(2–3), 327 (2010). doi:10.1007/s00340-009-3748-9
63. Pedaci, F., Genevet, P., Barland, S., Giudici, M., Tredicce, J.R.: Appl. Phys. Lett. **89**(22), 221111 (2006). doi:10.1063/1.2388867
64. Pedaci, F., Barland, S., Caboche, E., Genevet, P., Giudici, M., Tredicce, J.R., Ackemann, T., Scroggie, A.J., Firth, W.J., Oppo, G.L., Tissoni, G., Jäger, R.: Appl. Phys. Lett. **92**(1), 011101 (2008). doi:10.1063/1.2828458. http://link.aip.org/link/?APL/92/011101/1
65. Soda, H., Iga, K., Kitahara, C., Suematsu, Y.: Jpn. J. Appl. Phys. **18**(12), 2329 (1979). http://stacks.iop.org/1347-4065/18/i=12/a=2329
66. Li, H.E., Iga, K. (eds.): Vertical-Cavity Surface-Emitting Laser Devices, Springer Series in Photonics, vol. 6. Springer, Berlin, Heidelberg (2003)
67. Michalzik, R. (ed.): VCSELs: Fundamentals, Technology and Applications of Vertical-Cavity Surface-Emitting Lasers, Springer Series in Optical Sciences, vol. 166. Springer, Berlin, Heidelberg (2013)
68. Panajotov, K., Sciamanna, M., Arteaga, M., Thienpont, H.: IEEE J. Sel. Top. Quantum Electron. **19**(4), 1700312 (2013). doi:10.1109/JSTQE.2012.2235060
69. Panajotov, K., Gatare, I., Valle, A., Thienpont, H., Sciamanna, M.: IEEE J. Quantum Electron. **45**(11), 1473 (2009). doi:10.1109/JQE.2009.2024958
70. Rosanov, N.: Sov. J. Quantum Electron. **10**, 1191 (1975)
71. Lang, K.K.R.: IEEE J. Quantum Electron. **16**, 347 (1980)
72. Iga, K.: Jpn. J. Appl. Phys. **47**(1R), 1 (2008). http://stacks.iop.org/1347-4065/47/i=1R/a=1
73. Iga, K.: IEEE J. Sel. Top. Quantum Electron. **6**(6), 1201 (2000). doi:10.1109/2944.902168
74. Michalzik, R.: In: Michalzik, R. (ed.) VCSELs, Springer Series in Optical Sciences, vol. 166, pp. 3–18. Springer, Berlin, Heidelberg (2013). doi:10.1007/978-3-642-24986-0_1
75. Grabherr, M., Miller, M., Jager, R., Michalzik, R., Martin, U., Unold, H.J., Ebeling, K.J.: IEEE J. Sel. Top. Quantum Electron. **5**(3), 495 (1999). doi:10.1109/2944.788411
76. Averlant, E., Tlidi, M., Thienpont, H., Ackemann, T., Panajotov, K.: Opt. Express **22**(1), 762 (2014). doi:10.1364/OE.22.000762. http://www.opticsexpress.org/abstract.cfm?URI=oe-22-1-762
77. Tlidi, M., Vladimirov, A.G., Pieroux, D., Turaev, D.: Phys. Rev. Lett. **103**, 103904 (2009). doi:10.1103/PhysRevLett.103.103904
78. Panajotov, K., Tlidi, M.: Eur. Phys. J. D **59**(1), 67 (2010). doi:10.1140/epjd/e2010-00111-y
79. van Tartwijk, G.H.M., Lenstra, D.: J. Eur. Opt. Soc. Part B Quantum Semiclassical Opt. **7**(2), 87 (1995). http://stacks.iop.org/1355-5111/7/i=2/a=003
80. Tlidi, M., Averlant, E., Vladimirov, A., Panajotov, K.: Phys. Rev. A **86**, 033822 (2012). doi:10.1103/PhysRevA.86.033822

81. Kozyreff, G., Chapman, S., Tlidi, M.: Phys. Rev. E **68**, 015201 (2003). doi:10.1103/PhysRevE.68.015201
82. Kozyreff, G., Tlidi, M.: Chaos Interdisc. J. Nonlinear Sci. **17**(3), 037103 (2007). doi:10.1063/1.2759436
83. Clerc, M.G., Escaff, D., Kenkre, V.M.: Phys. Rev. E **72**, 056217 (2005). doi:10.1103/PhysRevE.72.056217
84. Pomeau, Y.: Physica D **23**(1–3), 3 (1986). doi:10.1016/0167-2789(86)90104-1. http://www.sciencedirect.com/science/article/pii/0167278986901041
85. Champneys, A.: Physica D **112**(1–2), 158 (1998). doi:10.1016/S0167-2789(97)00209-1. http://www.sciencedirect.com/science/article/pii/S0167278997002091 Proceedings of the Workshop on Time-Reversal Symmetry in Dynamical Systems
86. Coullet, P., Riera, C., Tresser, C.: Phys. Rev. Lett. **84**, 3069 (2000). doi:10.1103/PhysRevLett.84.3069
87. Clerc, M.G., Falcon, C., Tirapegui, E.: Phys. Rev. Lett. **94**, 148302 (2005). doi:10.1103/PhysRevLett.94.148302
88. Burke, J., Knobloch, E.: Phys. Rev. E **73**, 056211 (2006). doi:10.1103/PhysRevE.73.056211
89. Burke, J., Knobloch, E.: Chaos: Interdisc. J. Nonlinear Sci. **17**(3), 037102 (2007). doi:10.1063/1.2746816
90. Tlidi, M., Gelens, L.: Opt. Lett. **35**(3), 306 (2010). doi:10.1364/OL.35.000306. http://ol.osa.org/abstract.cfm?URI=ol-35-3-306
91. Vladimirov, A.G., Lefever, R., Tlidi, M.: Phys. Rev. A **84**, 043848 (2011). doi:10.1103/PhysRevA.84.043848
92. Haudin, F., Rojas, R., Bortolozzo, U., Residori, S., Clerc, M.: Phys. Rev. Lett. **107**, 264101 (2011). doi:10.1103/PhysRevLett.107.264101
93. Barbay, S., Hachair, X., Elsass, T., Sagnes, I., Kuszelewicz, R.: Phys. Rev. Lett. **101**, 253902 (2008). doi:10.1103/PhysRevLett.101.253902
94. Tlidi, M., Vladimirov, A.G., Turaev, D., Kozyreff, G., Pieroux, D., Erneux, T.: Eur. Phys. J. D **59**(1), 59 (2010). doi:10.1140/epjd/e2010-00144-2
95. Tlidi, M., Sonnino, A., Sonnino, G.: Phys. Rev. E **87**, 042918 (2013). doi:10.1103/PhysRevE.87.042918
96. Gurevich, S.V.: Phys. Rev. E **87**, 052922 (2013). doi:10.1103/PhysRevE.87.052922
97. Gurevich, S.: Philos. Trans. R. Soc. Lond. A (2014)
98. Pimenov, A., Vladimirov, A.G., Gurevich, S.V., Panajotov, K., Huyet, G., Tlidi, M.: Phys. Rev. A **88**, 053830 (2013). doi:10.1103/PhysRevA.88.053830
99. Vladimirov, A.G., Pimenov, A., Gurevich, S.V., Panajotov, K., Averlant, E., Tlidi, M.: Philos. Trans. R. Soc. Lond. A Math. Phys. Eng. Sci. **372**(2027) (2014). doi:10.1098/rsta.2014.0013
100. Averlant, E., Tlidi, M., Vladimirov, A.G., Thienpont, H., Panajotov, K.: In: Semiconductor Lasers and Laser Dynamics V, vol. 8432, p. 84321D (2012). doi:10.1117/12.921867
101. Panajotov, K., Tlidi, M.: Opt. Lett. **39**(16), 4739 (2014). doi:10.1364/OL.39.004739. http://ol.osa.org/abstract.cfm?URI=ol-39-16-4739
102. Prati, F., Tissoni, G., Lugiato, L.A., Aghdami, K.M., Brambilla, M.: Eur. Phys. J. D **59**(1), 73 (2010). doi:10.1140/epjd/e2010-00123-7
103. Vahed, H., Prati, F., Turconi, M., Barland, S., Tissoni, G.: Philos. Trans. R. Soc. Lond. A Math. Phys. Eng. Sci. **372**(2027) (2014). doi:10.1098/rsta.2014.0016
104. Leo, F., Coen, S., Kockaert, P., Gorza, S.P., Emplit, P., Haelterman, M.: Nat. Photonics **4**, 471 (2010). doi:10.1038/nphoton.2010.120
105. Tlidi, M., Bahloul, L., Cherbi, L., Hariz, A., Coulibaly, S.: Phys. Rev. A **88**, 035802 (2013). doi:10.1103/PhysRevA.88.035802
106. Schmidberger, M.J., Novoa, D., Biancalana, F., Russell, P.S., Joly, N.Y.: Opt. Express **22**(3), 3045 (2014). doi:10.1364/OE.22.003045. http://www.opticsexpress.org/abstract.cfm?URI=oe-22-3-3045
107. Milián, C., Skryabin, D.: Opt. Express **22**(3), 3732 (2014). doi:10.1364/OE.22.003732. http://www.opticsexpress.org/abstract.cfm?URI=oe-22-3-3732

108. Bahloul, L., Cherbi, L., Hariz, A., Tlidi, M.: Philos. Trans. R. Soc. Lond. A Math. Phys. Eng. Sci. **372**(2027) (2014). doi:10.1098/rsta.2014.0020
109. Marconi, M., Javaloyes, J., Balle, S., Giudici, M.: Phys. Rev. Lett. **112**, 223901 (2014). doi:10.1103/PhysRevLett.112.223901
110. Tlidi, M.: J. Opt. B Quantum Semiclassical Opt. **2**(3), 438 (2000). http://stacks.iop.org/1464-4266/2/i=3/a=335
111. Tlidi, M., Haelterman, M., Mandel, P.: Quantum Semiclassical Opt. J. Eur. Opt. Soc. Part B **10**(6), 869 (1998). http://stacks.iop.org/1355-5111/10/i=6/a=018
112. Veretenov, N., Tlidi, M.: Phys. Rev. A **80**, 023822 (2009). doi:10.1103/PhysRevA.80.023822
113. Dai, C.Q., Wang, X.G., Zhou, G.Q.: Phys. Rev. A **89**, 013834 (2014). doi:10.1103/PhysRevA.89.013834

Mathematical Study of Two-Patches of Predator-Prey System with Unidirectional Migration of Prey

Radouane Yafia and M.A. Aziz Alaoui

Abstract In this chapter we consider a model describing the dynamics of predator-prey populations living in two patches. The two patches follow the Lotka-Volterra type and are coupled through prey migration. Our purpose is to study the effect of migration rate on the behavior of the coupled systems. We prove the positivity of solutions and find the upper and lower bounds with respect to the migration rate of prey. Also, we show the stability/instability of the possible steady states and we establish the global stability of the positive steady state by giving a candidate lyapunov function. Some numerical simulations are provided to graphically demonstrate the population dynamics of the system.

1 Introduction

One of the oldest and well known mathematical model which describes the interaction between two species predator and prey was introduced by Lotka [1] and Volterra [2], known as Lotka-Volterra mathematical model. The model was given by a system of two differential equations as follows:

R. Yafia (✉)
Polydisciplinary Faculty of Ouarzazate, Ibn Zohr University,
B.P: 638, Ouarzazate, Morocco
e-mail: yafia1@yahoo.fr

M.A. Aziz Alaoui
Normandie Univ, Caen, France

M.A. Aziz Alaoui
ULH, LMAH, 76600 Le Havre, France

M.A. Aziz Alaoui
FR CNRS 3335, ISCN, 25 rue Philippe Lebon,
76600 Le Havre, France
e-mail: aziz.alaoui@univ-lehavre.fr

M. Belhaq (ed.), *Structural Nonlinear Dynamics and Diagnosis*,
Springer Proceedings in Physics 168, DOI 10.1007/978-3-319-19851-4_21

$$\begin{cases} \frac{dx}{dt} = ax - byx \\ \\ \frac{dy}{dt} = -cy + dxy \end{cases} \tag{1}$$

where $x(t)$ and $y(t)$ are the total numbers of prey and predator at time t, respectively, the constants a, b, c and d are nonnegative and the rate $\frac{c}{d}$ is related to the conversion of prey biomass into predator biomass. One weakness of the above model is the exponential growth of the prey in the absence of predator. This is not the case as while the prey continues to grow, space and resources will run out eventually, thereby limiting the growth of the prey population. To handle this case, the predator-prey system (1) can be modified to:

$$\begin{cases} \frac{dx}{dt} = ax - fx^2 - byx \\ \\ \frac{dy}{dt} = -cy + dxy \end{cases} \tag{2}$$

In the last years, this model have been studied in various forms by many authors (see, [3–5]) by changing the functional response, by taking into account the effect of diffusion terms or including the time delay in order to better understanding the dynamics of population interaction or studying the model with different form of functional response (see, [6–10]. Other authors consider some models which describe the interaction between two patches or more by taking into account the effect of the migration of one or two species from one patch to another (see, [11–16] and references therein). The analysis of these models focuses on the existence of possible steady states and their qualitative behavior: local and global stability/instability, bifurcation and when the dynamics of the two interacting patches are synchronous and asynchronous.

In [17], Kuang et al. introduce a model in which a single specie disperses between two patches of a heterogenous environment with barriers between patches and a predator for which the dispersal between patches involve a barrier. The model is given by a system of three ordinary differential equations, and the authors studied the existence of steady states with local and global stability. Also, the uniform persistence is proved and an example of Lotka-Volterra is given in order to prove that the dispersion stabilizes the system when the dispersal rate is small and destabilizes the system when this rate is increased.

In [18], the author introduced a two diffusively coupled predator prey populations. The coupled system is composed of four differential equations that is modelling the interaction of two identical patches in which dynamics are coupled through the migration of individuals of predator population only. This interaction between the predator and prey populations takes the form given by Rosenzweig and MacArthur [19] in which the prey population grows logistically and the predator has a Holling type II functional response. It was shown by numerical simulations that oscillations synchronize for very small migration rate and instability of synchronous oscillations for intermediate migration rate and periodicity, quasi-periodicity, and chaotic attractors with asynchronous dynamics. The existence of attractors in the form of equilibria or

limit cycles in which one of the patches contains no prey for large predator migration rates was also proved. The qualitative behavior (stability/instability, numerical simulations) of the possible steady state of this model are studied by Feng et al. [20]. In [21], Feng et al. consider the same model by taking into account the migration of both prey and predator population and studied the stability/instability of the possible steady states.

Recently, Quaglia et al. [22] considered a model of two patches coupled by the migration of both species. The model given by two identical patch with the same reproduction rate and different carrying capacities in each patch. The authors studied the existence and stability of the possible equilibrium points.

At now all the presented coupled patches of predator prey models take into account the migration of one species in one direction (from one patch to another patch only) or in the two directions (mutual migration) and the migration of both species in one direction or in two directions without considering the effect of the migrated (refuged) population on the refuge patch.

In the current chapter we consider two symmetric (identical) patch given by Lotka-Volterra system as follows (before migration):

$$\begin{cases} \frac{dx_i}{dt} = ax_i(1 - x_i) - bx_i y_i \\ \frac{dy_i}{dt} = cx_i y_i - dy_i \\ \qquad i \in \{1, 2\} \end{cases} \tag{3}$$

In the next, we take into account the migration of the prey population from the first patch to the second patch only (in one direction only) with a migration rate k and we consider the contribution of the migrated (refuged) prey population in the growth of the predator population of the refuge patch (second patch). The model is given by a system of four ordinary differential equations as follows:

$$\begin{cases} \frac{dx_1}{dt} = ax_1(1 - x_1) - bx_1 y_1 - kx_1 \\ \frac{dy_1}{dt} = cx_1 y_1 - dy_1 \\ \frac{dx_2}{dt} = ax_2(1 - x_2) - bx_2 y_2 + kx_1 \\ \frac{dy_2}{dt} = c(x_2 + kx_1)y_2 - dy_2 \end{cases} \tag{4}$$

The chapter is organized as follows. In Sects. 2 and 3 we prove the positivity and boundedness of solutions. In Sects. 4 and 5 we show the existence of possible steady states and their local and global stability, while in Sect. 6, we present some numerical simulations to illustrate the theoretical results.

2 Positivity

Consider now the uncoupled systems (3) which correspond to the case when $k = 0$. By integrating from 0 to t, from the $(3)_1$ and for any initial data $x_{i0} > 0, i = 1, 2$ and $y_{i0} > 0, i = 1, 2$, we have

$$x_i(t) = x_{i0} e^{\int_0^t (a(1-x_i(s))-by_i(s))ds} > 0, i = 1, 2 \tag{5}$$

From the $(3)_2$, we have

$$y_i(t) = y_{i0} e^{\int_0^t (cx_i(s)-d)ds} > 0, i = 1, 2 \tag{6}$$

Then we deduce that for $k = 0$ the uncoupled systems has a positive solution for any positive initial data.

Let us now consider the case when the migration rate is positive ($k > 0$) which corresponds to the coupled system (4). From $(4)_1$ and $(4)_2$, we have

$$x_1(t) = x_{10} e^{\int_0^t (a(1-x_1(s))-by_1(s)-k)ds} > 0 \tag{7}$$

and

$$y_1(t) = y_{10} e^{\int_0^t (cx_1(s)-d)ds} > 0$$

From $(4)_3$,

$$x_2(t) = x_{20} e^{\int_0^t (a(1-x_2(s))-by_2(s))ds} + k \int_0^t e^{\int_s^t (a(1-x_2(u))-by_2(u))du} x_1(s)ds \tag{8}$$

and from (7), we have $x_1(t) > 0, \forall t > 0$. Then, we deduce that $x_2(t) > 0, \forall t > 0$.

3 Boundedness

In this section we focus on the finding of the upper and lower bounds of the predator and prey populations, These bounds will give us information about the extinction, co-existence and exponential behavior of both species. The following comparison argument will be employed in the proofs associated to the upper and lower bounds of species.

Consider the following differential equations

$$\begin{cases} \frac{dx_i}{dt}(t) = f_i(t, x_i(t)), i = 1, 2 \\ x_i(0) = x_{i0}, i = 1, 2 \end{cases} \tag{9}$$

where $f_i, i = 1, 2$ are continuous functions on $[0, T] \times \mathbb{R}$.

Proposition 1 *Let x_1 and x_2 the solution of equations (9) with initial conditions $x_1(0) = x_{10}$ and $x_2(0) = x_{20}$, respectively. Assume that $\frac{\partial f_1}{dx}$ and $\frac{\partial f_2}{dx}$ are continuous on $[0, T] \times \mathbb{R}$.*

If $f_1(t, x) \leq f_2(t, x)$ on $[0, T] \times \mathbb{R}$ and the initial conditions verify $x_{10} \leq x_{20}$, then the solutions x_1 and x_2 satisfy $x_1(t) \leq x_2(t)$ on $[0, T]$.

Theorem 1 *Let $X(t) = x_1(t) + x_2(t)$ the total number of the prey population of the two patches and $X_0 = x_{10} + x_{20}$, $X(t)$ satisfies the following inequality*

$$0 \leq X(t) \leq \left(\left(\frac{1}{X_0} - \frac{1}{2}\right)e^{-at} + \frac{1}{2}\right)^{-1}$$

and

$$\limsup_{t \longrightarrow +\infty} X(t) \leq 2, \forall t \in]0, +\infty[$$

for $X_0 < 2$.

Proof Let $X(t) = x_1(t) + x_2(t)$ the total number of the prey population of the two patches. From $(4)_1$ and $(4)_3$ we have,

$$\begin{aligned} \frac{dX}{dt} &\leq a(x_1 + x_2) - a(x_1^2 + x_2^2) \\ &\leq a(x_1 + x_2) - \frac{a}{2}(x_1 + x_2)^2 \\ &\leq aX(1 - \frac{X}{2}) \end{aligned}$$

As the following logistic equation

$$\begin{cases} \frac{du}{dt} = au(1 - \frac{u}{2}) \\ u(0) = u_0 \end{cases} \tag{10}$$

with solution

$$u(t) = \left(\left(\frac{1}{u_0} - \frac{1}{2}\right)e^{-at} + \frac{1}{2}\right)^{-1}$$

From Proposition 1 and from the positivity of $x_1(t)$ and $x_2(t)$, we have

$$0 \leq X(t) \leq \left(\left(\frac{1}{X_0} - \frac{1}{2}\right) e^{-at} + \frac{1}{2}\right)^{-1}$$

Then, for any initial conditions x_{10} and x_{20} satisfy $X(0) = X_0 = x_{10} + x_{20} < 2$, we get

$$\limsup_{t \longrightarrow +\infty} X(t) \leq 2, \forall t \in]0, +\infty[$$

The following result gives us the boundedness of the predator population.

Theorem 2 *Let $Y(t) = y_1(t) + y_2(t)$ the total population of the predator specie of the two patches. Then, we have*

$$Y_0 e^{-dt} \leq Y(t) \leq \left(Y_0 - \frac{2ck}{2c-d}\right) e^{-(2c-d)t} + \frac{2ck}{2c-d}$$

and for $2c > d$ and for $Y_0 \geq \frac{2ck}{2c-d}$ we obtain

$$\limsup_{t \longrightarrow +\infty} Y(t) \leq \frac{2ck}{2c-d}$$

where $Y_0 = y_{10} + y_{20}$.

Proof From the $(4)_2$ and $(4)_4$, we have

$$\begin{aligned} \frac{dY}{dt}(t) &= \frac{y_1}{dt}(t) + \frac{y_2}{dt}(t) \\ &= c(x_1 y_1 + x_2 y_2) - d(y_1 + y_2) + ckx_1 \\ &\geq -dY(t) \end{aligned}$$

leading to

$$Y(t) \geq Y_0 e^{-dt}$$

As $x_1 \leq X \leq 2$ and $x_2 \leq X \leq 2$, we have

$$\frac{dY}{dt}(t) \leq (2c-d)\, Y(t) + 2ck$$

Let us consider the following equation

$$\begin{cases} \frac{du}{dt}(t) = (2c-d)\, u(t) + 2ck \\ u(0) = u_0 \end{cases} \tag{11}$$

By applying the variation of constant formula, we obtain

$$u(t) = \left(u_0 - \frac{2ck}{2c-d}\right) e^{-(2c-d)t} + \frac{2ck}{2c-d}$$

From Proposition 1, we have

$$Y(t) \leq \left(Y_0 - \frac{2ck}{2c-d}\right) e^{-(2c-d)t} + \frac{2ck}{2c-d}$$

As $2c > d$ and for $Y_0 \geq \frac{2ck}{2c-d}$, we deduce that

$$\limsup_{t \longrightarrow +\infty} Y(t) \leq \frac{2ck}{2c-d}$$

If $k = 0$, we have

$$\limsup_{t \longrightarrow +\infty} Y(t) = 0$$

4 Steady States and Stability

4.1 Steady States

In this section we will determine the possible equilibrium points and we will study their stability/instability with respect to the migration rate k (Table 1).

The possible steady states are given by resolving the following equations

$$\begin{cases} \frac{dx_1}{dt} = ax_1(1-x_1) - bx_1y_1 - kx_1 = 0 \\ \frac{dy_1}{dt} = cx_1y_1 - dy_1 = 0 \\ \frac{dx_2}{dt} = ax_2(1-x_2) - bx_2y_2 + kx_1 = 0 \\ \frac{dy_2}{dt} = c(x_2 + kx_1)y_2 - dy_2 = 0 \end{cases} \tag{12}$$

Proposition 2 *Under some conditions, system (4) has seven equilibrium points. The following table summarize the existence of the steady states: where* $D = a^2 + am$, $D_1 = a^2 + 4ak\frac{d}{c}$ *and* $m = k(1 - \frac{k}{a})$.

Proof The first steady state is trivial $E_0 = (x_{10}, y_{10}, x_{20}, y_{20}) = (0, 0, 0, 0)$.

Table 1 Existence of possible steady states of system (4)

Equilibrium point	Conditions of existence
$E_0 = (x_{10}, y_{10}, x_{20}, y_{20}) = (0, 0, 0, 0)$	No conditions
$E_1 = (x_{11}, y_{11}, x_{21}, y_{21}) = (0, 0, 1, 0)$	No conditions
$E_2 = (x_{12}, y_{12}, x_{22}, y_{22}) = \left(0, 0, \frac{d}{c}, \frac{a\left(1-\frac{d}{c}\right)}{b}\right)$	$c > d$
$E_3 = (x_{13}, y_{13}, x_{23}, y_{23}) = \left(1-\frac{k}{a}, 0, \frac{a+\sqrt{a^2+am}}{2a}, 0\right)$	$a > k$
$E_4 = (x_{14}, y_{14}, x_{24}, y_{24}) = \left(1-\frac{k}{a}, 0, \frac{d-cm}{c}, \frac{ax_{24}(1-x_{24})+m}{bx_{24}}\right)$	$cm < d < cm + \frac{c}{2a}\left(a + \sqrt{D}\right)$ and $a > k$ where $m = k(1-\frac{k}{a}) > 0$ and $D = a^2 + am > 0$
$E_5 = (x_{15}, y_{15}, x_{25}, y_{25}) = \left(\frac{d}{c}, \frac{a}{b}\left(1-\frac{k}{a}-\frac{d}{c}\right), \frac{a+\sqrt{D_1}}{2a}, 0\right)$	$1 > \frac{k}{a} - \frac{d}{c}$
$E_6 = (x_{16}, y_{16}, x_{26}, y_{26}) = \left(\frac{d}{c}, \frac{a}{b}\left(1-\frac{k}{a}-\frac{d}{c}\right), \frac{d}{c}(1-k), \frac{ax_{26}(1-x_{26})+k\frac{d}{c}}{bx_{26}}\right)$	$k < 1 < \frac{c}{d}\left(a + \frac{\sqrt{D_1}}{2a}\right) + k$ and $1 > \frac{k}{a} - \frac{d}{c}$ where $D_1 = a^2 + 4ak\frac{d}{c} > 0$

If $c > d$, from $(4)_2$ we obtain

$$y_1 = 0 \Longrightarrow \begin{cases} x_1 = 0 \\ \text{or} \\ x_1 = 1 - \frac{k}{a} \end{cases}$$

In the case when $x_1 = 0$, system (4) have two steady states

$$E_1 = (x_{11}, y_{11}, x_{21}, y_{21}) = (0, 0, 1, 0)$$

and

$$E_2 = (x_{12}, y_{12}, x_{22}, y_{22}) = \left(0, 0, \frac{d}{c}, \frac{a\left(1-\frac{d}{c}\right)}{b}\right).$$

In the case when $x_1 = 1 - \frac{k}{a}$ and if $c > d$ and $a > k$, we have

$$\begin{cases} ax_2(1-x_2) - bx_2y_2 + m = 0 \\ c(x_2+m)y_2 - dy_2 = 0 \end{cases} \tag{13}$$

where $m = k(1-\frac{k}{a}) > 0$.

From $(13)_2$, if $y_2 = 0$ the forth component of the equilibrium point is given by resolving the second order equation in x_2

$$ax_2 - ax_2^2 + m = 0$$

If $D = a^2 + am > 0$ then $x_2 = \frac{-a+\sqrt{D}}{-2a} < 0$ or $x_2 = \frac{a+\sqrt{D}}{2a} > 0$.

Therefore, the third equilibrium point is as follows

$$E_3 = (x_{13}, y_{13}, x_{23}, y_{23}) = \left(1 - \frac{k}{a}, 0, \frac{a+\sqrt{D}}{2a}, 0\right).$$

From $(13)_2$, if $x_{24} = \frac{d-cm}{c}$ and $d > cm$, from the $(13)_1$ the forth component of the equilibrium point is given by

$$y_{24} = \frac{ax_{24}(1 - x_{24}) + m}{bx_{24}}$$

To determine the region of nonnegativity of y_{24}, let us consider the following second order polynomial for $x > 0$:

$$-ax^2 + ax + m = 0 \tag{14}$$

which is nonnegative if $0 < x < \frac{a+\sqrt{D}}{2a}$. Then, if $0 < x_{24} < \frac{a+\sqrt{D}}{2a}$ which is satisfied if

$$cm < d < cm + \frac{c}{2a}\left(a + \sqrt{D}\right).$$

Then the steady state is given by

$$E_4 = (x_{14}, y_{14}, x_{24}, y_{24}) = \left(1 - \frac{k}{a}, 0, \frac{d-cm}{c}, \frac{ax_{24}(1 - x_{24}) + m}{bx_{24}}\right)$$

From $(3)_2$, we have $x_{15} = \frac{d}{c}$ and from $(3)_1$ we have $y_{15} = \frac{a}{b}\left(1 - \frac{k}{a} - \frac{d}{c}\right)$ which is positive if $1 > \frac{k}{a} - \frac{d}{c}$.

From $(3)_3$ and $(3)_4$, we get

$$\begin{cases} ax_2(1 - x_2) - bx_2y_2 + k\frac{d}{c} = 0 \\ c(x_2 + k\frac{d}{c})y_2 - dy_2 = 0 \end{cases} \tag{15}$$

from $(15)_2$, we have $y_{25} = 0$ and from $(15)_1$ and solving the following polynomial for $x > 0$

$$-ax^2 + ax + k\frac{d}{c} = 0 \tag{16}$$

we find

$$x_{25} = \frac{a + \sqrt{D_1}}{2A}$$

where $D_1 = a^2 + 4ak\frac{d}{c} > 0$.

Then, the sixth steady state is given as follows

$$E_5 = (x_{15}, y_{15}, x_{25}, y_{25}) = \left(\frac{d}{c}, \frac{a}{b}\left(1 - \frac{k}{a} - \frac{d}{c}\right), \frac{a + \sqrt{D_1}}{2a}, 0\right)$$

From $(15)_2$, we have:

$$x_{26} = \frac{d}{c}(1 - k)$$

which is positive if $1 > k$ and from $(15)_1$ we have

$$y_{26} = \frac{ax_{26}(1 - x_{26}) + k\frac{d}{c}}{bx_{26}}$$

As the last equilibrium point y_{26} is nonnegative if $0 < x_{26} < x_{25}$ which is equivalent to

$$k < 1 < \frac{c}{d}\left(a + \frac{\sqrt{D_1}}{2a}\right) + k$$

then the sixth steady state is:

$$E_6 = (x_{16}, y_{16}, x_{26}, y_{26}) = \left(\frac{d}{c}, \frac{a}{b}\left(1 - \frac{k}{a} - \frac{d}{c}\right), \frac{d}{c}(1 - k), \frac{ax_{26}(1 - x_{26}) + k\frac{d}{c}}{bx_{26}}\right)$$

Remark 1 $\underline{E_0 = (0, 0, 0, 0)}$: Extinction of both the predator and prey in each of the two patches (i.e. if there is no prey there is no predator, in this case there is no migration $k = 0$).

$\underline{E_1 = (0, 0, 1, 0)}$: Extinction of both the predator and the prey in the first patch and persistence of the prey and extinction of the predator in the second patch (i.e. if there is no predation there is a persistence in prey and the prey will grow in the absence of the predator population. As there is extinction of the prey in the first patch there is no migration of prey population from the first patch to the second patch $k = 0$).

$\underline{E_2 = \left(0, 0, \frac{d}{c}, \frac{a\left(1 - \frac{d}{c}\right)}{b}\right)}$: Extinction of both the predator and prey in the first patch and there is no migration to the second patch and persistence of both the

predator and prey in the second patch for the value rate of numerical response bigger than the mortality rate of the predator in the second patch.

$E_3 = \left(1 - \frac{k}{a}, 0, \frac{a+\sqrt{a^2+am}}{2a}, 0\right)$: Extinction of the predator and persistence of the prey of both the patches. In this case there is a migration of the prey population from the first patch to the second patch when the migration rate is smaller than the production rate of the prey a.

$E_4 = \left(1 - \frac{k}{a}, 0, \frac{d-cm}{c}, \frac{ax_{24}(1-x_{24})+m}{bx_{24}}\right)$: Persistence of the prey and extinction of the predator in the first patch and persistence of both the predator and prey in the second patch and there is a migration of the prey population from the first patch to the second patch.

$E_5 = \left(\frac{d}{c}, \frac{a}{b}\left(1 - \frac{k}{a} - \frac{d}{c}\right), \frac{a+\sqrt{D_1}}{2a}, 0\right)$: Persistence of both the predator and prey in the first patch and persistence of the prey and extinction of the predator in the second patch and there is a migration of the prey population from the first patch to the second patch.

$E_6 = \left(\frac{d}{c}, \frac{a}{b}\left(1 - \frac{k}{a} - \frac{d}{c}\right), \frac{d}{c}(1-k), \frac{ax_{26}(1-x_{26})+k\frac{d}{c}}{bx_{26}}\right)$: Persistence of both the predator and prey in each of the two patches and there is a migration of the prey population from the first patch to the second patch.

4.2 Local Stability

Definition 1 Let $Pr_1(x_1, y_1, x_2, y_2) = (x_1, y_1)$ the projection of the point (x_1, y_1, x_2, y_2) on the $(4)_1$-$(4)_2$ describing the first patch (x_1, y_1) and $Pr_2(x_1, y_1, x_2, y_2) = (x_2, y_2)$ the projection of the point (x_1, y_1, x_2, y_2) on the $(4)_3$-$(4)_4$ describing the second patch (x_2, y_2).

To study the local stability of the possible equilibrium points, one needs to linearize system (3) around the concerned steady state.

Theorem 3 *Consider that* $E_* = \left(x_1^*, y_1^*, x_2^*, y_2^*\right)$ *is a steady state of system (4). The stability of* E_* *is deduced from the stability of* $Pr_1E_* = \left(x_1^*, y_1^*\right)$ *and* $Pr_2E_* = \left(x_2^*, y_2^*\right)$.

(1) If Pr_1E_* *and* Pr_2E_* *are asymptotically stable, then* E_* *is also asymptotically stable.*

(2) If Pr_1E_* *or* Pr_2E_* *is unstable, then* E_* *is also unstable*

Proof By linearizing around the steady state $E_* = \left(x_1^*, y_1^*, x_2^*, y_2^*\right)$ we obtain the following linearized system:

$$\begin{cases} \frac{dx_1}{dt} = \left(a(1-x_1^*) - by_1^* - ax_1^* - k\right)x_1 - bx_1^* y_1 \\ \frac{dy_1}{dt} = cy_1^* x_1 + \left(cx_1^* - d\right)y_1 \\ \frac{dx_2}{dt} = \left(a(1-x_2^*) - by_2^* - ax_2^*\right)x_2 - bx_2^* y_2 + kx_1 \\ \frac{dy_2}{dt} = cky_2^* x_1 + cky_2^* x_2 + \left(c(kx_1^* + x_2^*) - d\right)y_2 \end{cases} \tag{17}$$

and the jacobian matrix is given by

$$J(E_*) = \begin{pmatrix} A_1 - k & -bx_1^* & 0 & 0 \\ cy_1^* & cx_1^* - d & 0 & 0 \\ k & 0 & A_2 & -bx_2^* \\ cky_2^* & 0 & cy_2^* & c(kx_1^* + x_2^*) - d \end{pmatrix}$$

where

$$A_i = a(1-x_i^*) - by_i^* - ax_i^* = a(1-2x_i^*) - by_i^*,\ i = 1, 2$$

Then

$$\det(\lambda I_4 - J(E_*)) = \det \begin{pmatrix} \lambda I_2 - M_1 & 0_2 \\ M & \lambda I_2 - M_2 \end{pmatrix}$$

where

$$M_1 = \begin{pmatrix} A_1 - k & -bx_1^* \\ cy_1^* & cx_1^* - d \end{pmatrix}, M_2 = \begin{pmatrix} A_2 & -bx_2^* \\ cy_2^* & c(kx_1^* + x_2^*) - d \end{pmatrix}, M = \begin{pmatrix} k & 0 \\ cky_2^* & 0 \end{pmatrix}$$

and I_2 is the 2×2 unit matrix and 0_2 is the 2×2 vanishing matrix.

From the determinant property, we have

$$\det(\lambda I_4 - J(E_*)) = \det(\lambda I_2 - M_1) \times (\lambda I_2 - M_2) \tag{18}$$

Then, $\det(\lambda I_2 - M_1) = 0$ is the characteristic equation associated to $Pr_1 E_*$ and $\det(\lambda I_2 - M_2) = 0$ is the characteristic equation associated to $Pr_2 E_*$.

Therefore, we deduce the result.

Theorem 4 (Stability of E_0)

The equilibrium point $E_0 = (0, 0, 0, 0)$ is unstable.

Proof The value of A_2 at E_0 is $A_2 = 0$ and $Pr_2(E_0) = (0, 0)$. From Theorem 3, the stability of $Pr_2(E_0)$ is determined from the following associated characteristic

equations

$$\begin{aligned}\det(\lambda I_2 - M_2) &= \begin{vmatrix} \lambda - a & 0 \\ 0 & \lambda + d \end{vmatrix} \\ &= (\lambda - a)(\lambda + d) \\ &= 0\end{aligned}$$

As $\lambda_1 = a > 0$ and $\lambda_2 = -d < 0$, then $Pr_1(E_0)$ is unstable. Therefore, from Theorem 3 E_0 is unstable.

Remark 2 If we consider system (4) with vanishing migration (i.e. there is no migration of the prey population from the first patch to the second patch: $k = 0$), we obtain system (3). Then $Pr_1(E_0) = Pr_2(E_0) = (0, 0)$ is a equilibrium point of system (3) and the stability of E_0 can be deduced from the stability of the trivial equilibrium solution $(0, 0)$ of (3). Therefore, the migration rate does not have any effect on the stability of the equilibrium solution E_0.

Theorem 5 (Stability of E_1)

The equilibrium point $E_1 = (0, 0, 1, 0)$ is asymptotically stable if $a < k$ and unstable if $a > k$.

Proof From the expression of A_1 and A_2 at E_1, we have $A_1 = 0$ and $A_2 = -a$.

As $\det(\lambda I_2 - M_1) = (\lambda - a + k)(\lambda + d) = 0$. Therefore, $\lambda_1 = a - k$ and $\lambda_2 = -d < 0$ and we deduce that $Pr_1(E_1) = (0, 0)$ is asymptotically stable if $a < k$ and unstable if $a > k$.

From $\det(\lambda I_2 - M_2) = (\lambda + a)(\lambda + d) = 0$, we get that $Pr_2(E_1) = (1, 0)$ is asymptotically stable.

From Theorem 3, we deduce that E_1 is asymptotically stable if $a < k$ and unstable if $a > k$.

Remark 3 $Pr_1(E_1) = (0, 0)$ is a trivial equilibrium solution of the first patch when $k = 0$ and $Pr_2(E_1) = (1, 0)$ is an equilibrium solution of the second patch and the stability of E_1 depends on the migration rate k

Theorem 6 (Stability of E_2)

Suppose $c > d$, the equilibrium point $E_2 = \left(0, 0, \frac{d}{c}, \frac{a\left(1-\frac{d}{c}\right)}{b}\right)$ is asymptotically stable if $a < k$ and unstable if $a > k$.

Proof As $Pr_1(E_2) = Pr_1(E_1) = (0, 0)$, $A_1 = 0$ and from the proof of Theorem 5, we have $Pr_1(E_1) = (0, 0)$ is asymptotically stable if $a < k$ and unstable if $a > k$.

From the expression of A_2 at E_2, we have $A_2 = -\frac{ad}{c} < 0$ and the characteristic equation associated to $Pr_1(E_2) = \left(\frac{d}{c}, \frac{a\left(1-\frac{d}{c}\right)}{b}\right)$ is given by

$$\det(\lambda I_2 - M_1) = \lambda^2 + \lambda\frac{ad}{c} + ad\left(1 - \frac{d}{c}\right) = 0$$

As $\Delta = \left(\frac{ad}{c}\right)^2 - 4ad\left(1 - \frac{d}{c}\right)$, if $\Delta > 0$ we get:

$$\lambda_1 = \frac{-\frac{ad}{c} + \sqrt{\Delta}}{2} \text{ and } \lambda_2 = \frac{-\frac{ad}{c} - \sqrt{\Delta}}{2} < 0$$

From the expression of λ_1 and as $c > d$ (condition of the existence of E_2), we have $\lambda_1 < 0$. Then, $Pr_2(E_2)$ is stable asymptotically.

If $\Delta \leq 0$ we get:

$$\lambda_1 = \frac{-\frac{ad}{c} + i\sqrt{-\Delta}}{2} \text{ and } \lambda_2 = \frac{-\frac{ad}{c} - i\sqrt{-\Delta}}{2} < 0$$

and $Re(\lambda_1) = Re(\lambda_2) = -\frac{ad}{c} < 0$. Then, $Pr_2(E_2)$ is stable asymptotically.

From Theorem 3, we deduce that $E_2 = \left(0, 0, \frac{d}{c}, \frac{a\left(1-\frac{d}{c}\right)}{b}\right)$ is asymptotically stable if $a < k$ and unstable if $a > k$.

Remark 4 $Pr_1(E_2) = (0, 0)$ is a trivial equilibrium solution of the first patch when $k = 0$ and $Pr_2(E_2) = \left(\frac{d}{c}, \frac{a\left(1-\frac{d}{c}\right)}{b}\right)$ is not an equilibrium solution of system (3). Then, the stability of E_2 depends on the migration rate k and can be deduced from the stability of $Pr_1(E_2)$.

Let

(H_1): $a(\frac{d}{c} - 1) < k$

(H_2): $c(m + x_{23}) < d$, where $m = k\left(1 - \frac{k}{a}\right) > 0$

Theorem 7 (Stability of E_3)

Suppose $a > k$.

If (H_1) and (H_2) are satisfied, then the equilibrium solution $E_3 = \left(1 - \frac{k}{a}, 0, \frac{a+\sqrt{a^2+am}}{2a}, 0\right)$ is asymptotically stable.

If (H_1) or (H_2) are not satisfied, then the equilibrium solution $E_3 = \left(1 - \frac{k}{a}, 0, \frac{a+\sqrt{a^2+am}}{2a}, 0\right)$ is unstable.

Proof From the expression of A_1 at E_3, the characteristic equation associated to $Pr_1E_3 = \left(1 - \frac{k}{a}, 0\right)$ is as follows:

$$\det(\lambda I_2 - M_1) = (\lambda - k + a)\left(\lambda - c\left(1 - \frac{k}{a}\right) + d\right) = 0$$

and the corresponding eigenvalues are given by $\lambda_1 = k - a$ and $\lambda_2 = c\left(1 - \frac{k}{a}\right) - d$. As $a > k$, we have $\lambda_1 < 0$ and if (H_1) is satisfied, then Pr_1E_3 is asymptotically stable and if not satisfied, Pr_1E_3 is unstable.

From the expression of x_{23} and by computation at E_3, we have

$$A_2 = -\frac{k}{x23}\left(1 - \frac{k}{a}\right) - ax_{23} < 0$$

and the associated characteristic equation to $Pr_2E_3 = \left(\frac{a+\sqrt{a^2+am}}{2a}, 0\right)$ is:

$$\det(\lambda I_2 - M_2) = (\lambda - A_2)(\lambda - c(m + x_{23}) + d) = 0$$

The corresponding eigenvalues are

$$\lambda_1 = A_2 < 0 \text{ and } \lambda_2 = c(m + x_{23}) - d$$

If (H_2) is satisfied, we obtain that $\lambda_2 < 0$. Then, Pr_2E_3 is asymptotically stable and if (H_2) is not satisfied, Pr_2E_3 is unstable.

From Theorem 3, we deduce that, the equilibrium solution E_3 is asymptotically stable if (H_1) and (H_2) are satisfied and unstable if (H_1) or (H_2) is not satisfied.

Theorem 8 (Stability of E_4)

Suppose $a > k$ and $cm < d < cm + \frac{c}{2a}\left(a + \sqrt{D}\right)$, where $D = a^2 + am > 0$.

If (H_1) is satisfied, then the equilibrium solution $E_4 = \left(1 - \frac{k}{a}, 0, \frac{d-cm}{c}, \frac{ax_{24}(1-x_{24})+m}{bx_{24}}\right)$ is asymptotically stable.

If (H_1) is not satisfied, then the equilibrium solution $E_4 = \left(1 - \frac{k}{a}, 0, \frac{d-cm}{c}, \frac{ax_{24}(1-x_{24})+m}{bx_{24}}\right)$ is unstable.

Proof As $Pr_1(E_4) = Pr_1(E_3) = \left(1 - \frac{k}{a}, 0\right)$ and from the proof of Theorem 7, we have, if (H_1) is satisfied. Then Pr_1E_4 is asymptotically stable and if not satisfied, Pr_1E_4 is unstable.

As $Pr_2(E_4) = \left(\frac{d-cm}{c}, \frac{ax_{24}(1-x_{24})+m}{bx_{24}}\right)$, then the associated characteristic equation is given by:

$$\det(\lambda I_2 - M_2) = \lambda^2 - \lambda A_2 + cbx_{24}y_{24} = 0$$

By calculations, we obtain the value of A_2 at E_4, that is

$$A_2 = \frac{-m - ax_{24}^2}{x_{24}} < 0$$

If $\Delta_1 = A_2^2 - 4cbx_{24}y_{24} > 0$, the corresponding eigenvalues are

$$\lambda_1 = \frac{A_2 + \sqrt{\Delta_1}}{2} < 0 \text{ and } \lambda_2 = \frac{A_2 - \sqrt{\Delta_1}}{2} < 0.$$

Then, $Pr_2(E_4)$ is asymptotically stable.

If $\Delta \leq 0$, the corresponding eigenvalues are

$$\lambda_1 = \frac{A_2 + i\sqrt{-\Delta_1}}{2} < 0 \text{ and } \lambda_2 = \frac{A_2 - i\sqrt{-\Delta_1}}{2} < 0.$$

and $Re(\lambda_1) = Re(\lambda_2) = \frac{A_2}{2} < 0$.

Then, $Pr_2(E_4)$ is asymptotically stable.

From Theorem 3, we deduce that the equilibrium solution E_4 is asymptotically stable if (H_1) is satisfied and unstable if (H_1) is not satisfied.

Let:

(H_3): $k < \frac{c}{2a}(a + \sqrt{D_1}) + d$, where $D_1 = a^2 + 4ak\frac{d}{c} > 0$.

Theorem 9 (Stability of E_5)

Suppose that $1 > \frac{k}{a} - \frac{d}{c}$.

$E_5 = \left(\frac{d}{c}, \frac{a}{b}\left(1 - \frac{k}{a} - \frac{d}{c}\right), \frac{a+\sqrt{D_1}}{2a}, 0\right)$ *is asymptotically stable if* (H_3) *is satisfied and unstable if* (H_3) *is not satisfied.*

Proof From the expression of E_5, we have $Pr_1(E_5) = \left(\frac{d}{c}, \frac{a}{b}\left(1 - \frac{k}{a} - \frac{d}{c}\right)\right)$ and the value of A_1 at E_5 is $A_1 = k - ax_{15}$ and the associated characteristic equation is given by:

$$\det(\lambda I_2 - M_1) = \lambda^2 + \lambda a x_{15} + cbx_{15}y_{15}$$

By the same method as in the proof of Theorem 8, we find that the real part of the corresponding eigenvalues is negative and $Pr_1(E_5)$ is asymptotically stable.

From the expressions of E_5 and A_2 at E_5, we have $Pr_2(E_5) = \left(\frac{a+\sqrt{D_1}}{2a}, 0\right)$ and $A_2 = -\frac{kd}{cx_{26}} - ax_{26} < 0$.

The associated characteristic equation is

$$\det(\lambda I_2 - M_2) = (\lambda - A_2)\left(\lambda - c\left(\frac{kd}{c} - x_{25}\right) + d\right) = 0$$

and the corresponding eigenvalues are:

$$\lambda_1 = A_2 < 0 \text{ and } \lambda_2 = c\left(\frac{kd}{c} - x_{25}\right) - d.$$

Then, $\lambda_2 < 0$ if (H_3) is satisfied and $Pr_2(E_5)$ is asymptotically stable and unstable if (H_3) is not satisfied.

Therefore, from Theorem 3 we deduce the result.

Theorem 10 (Stability of E_6)

Suppose $k < 1 < \frac{c}{d}\left(a + \frac{\sqrt{D_1}}{2a}\right) + k$ *and* $1 > \frac{k}{a} - \frac{d}{c}$.

Then, the equilibrium solution $E_6 = \left(\frac{d}{c}, \frac{a}{b}\left(1 - \frac{k}{a} - \frac{d}{c}\right), \frac{d}{c}(1-k), \frac{ax_{26}(1-x_{26})+k\frac{d}{c}}{bx_{26}}\right)$ *is asymptotically stable.*

Proof As $Pr_1E_6 = Pr_1E_5 = \left(\frac{d}{c}, \frac{a}{b}\left(1 - \frac{k}{a} - \frac{d}{c}\right)\right)$, from the proof of Theorem 9, we get Pr_1E_6 is asymptotically stable.

From the expression of E_6, we have $Pr_2E_6 = \left(\frac{d}{c}(1-k), \frac{ax_{26}(1-x_{26})+k\frac{d}{c}}{bx_{26}}\right)$ and A_2 at E_6 is

$$A_2 = \frac{kd}{cx_{26}} - ax_{26} < 0$$

$$\det(\lambda I_2 - M_2) = \lambda^2 - \lambda A_2 + cbx_{26}y_{26}$$

By the same method as in the proof of Theorem 8, we find that the real part of the corresponding eigenvalues is negative and $Pr_2(E_6)$ is asymptotically stable.

From Theorem 3, we find that E_6 is asymptotically stable.

5 Global Stability

In this section we try to study the global stability of the a possible steady state $E_* = \left(x_1^*, y_1^*, x_2^*, y_2^*\right)$ of system (4).

Let V_i the Lyapunov function associated to the patch i with $i = 1, 2$ defined by:

$$V_i(x_i, y_i) = \left(x_i - x_i^*\right) - \frac{d}{c}\ln\left(\frac{x_i}{x_i^*}\right) + \frac{b}{c}\left\{\left(y_i - y_i^*\right) - y_i^*\ln\left(\frac{y_i}{y_i^*}\right)\right\}, i = 1, 2$$

This functions are defined and continuous on $Int(\mathbb{R}^2_+)$.

We are interested in constructing Lyapunov function for the coupled system (4).

Theorem 11 *Let*

$$V(x_1, y_1, x_2, y_2) = \sum_{i=1}^{2} V_i(x_i, y_i)$$

For $a > 0$ *and* k *sufficientlly small, the steady state* $E_* = \left(x_1^*, y_1^*, x_2^*, y_2^*\right)$ *is globally asymptotically stable.*

Proof The proof is based on a positive definite Lyapunov function. It can be easily verified that the function is zero at the equilibrium point $E_* = \left(x_1^*, y_1^*, x_2^*, y_2^*\right)$ and is positive for all other positive values x_1, y_1, x_2 and y_2 and thus, $E_* = \left(x_1^*, y_1^*, x_2^*, y_2^*\right)$ is the global minimum of V.

Differentiating V_i, $i = 1, 2$ along (4) gives:

$$\begin{aligned}\dot{V}_1(x_1, y_1) &= \frac{\dot{x}_1}{x_1^*}(x_1 - x_1^*) + \frac{b}{c}\frac{\dot{y}_1}{y_1^*}(y_1 - y_1^*)\\ &= -a(x_1 - x_1^*)^2\end{aligned}$$

and

$$\begin{aligned}\dot{V}_2(x_2, y_2) &= \frac{\dot{x}_2}{x_2^*}(x_2 - x_2^*) + \frac{b}{c}\frac{\dot{y}_2}{y_2^*}(y_2 - y_2^*)\\ &= -a(x_2 - x_2^*)^2 + k\left(\frac{x_1}{x_2} - \frac{x_1^*}{x_2^*}\right)(x_2 - x_2^*) + bk(x_1 - x_1^*)(y_2 - y_2^*)\\ &= -a(x_2 - x_2^*)^2 + kx_1^*\left(\frac{x_1}{x_1^*} - \frac{x_2}{x_2^*} + 1 - \frac{x_1x_2^*}{x_1^*x_2}\right) + bk(x_1 - x_1^*)(y_2 - y_2^*)\end{aligned}$$

Let $G(x_i) = -\frac{x_i}{x_i^*} + \ln\left(\frac{x_i}{x_i^*}\right)$, $i = 1, 2$. By using $1 - x + \ln(x) \leq 0$ for $x > 0$ and equality holding if $x = 1$ we have

$$G(x_2) - G(x_1) + 1 - \frac{x_1x_2^*}{x_1^*x_2} + \ln\left(\frac{x_1x_2^*}{x_1^*x_2}\right) \leq G(x_2) - G(x_1)$$

and

$$\begin{aligned}\dot{V}(x_1, y_1, x_2, y_2) &= -a(x_1 - x_1^*)^2 - a(x_2 - x_2^*)^2 + kx_1^*\left(\frac{x_1}{x_1^*} - \frac{x_2}{x_2^*} + 1 - \frac{x_1x_2^*}{x_1^*x_2}\right)\\ &\quad + bk(x_1 - x_1^*)(y_2 - y_2^*)\\ &= -a(x_1 - x_1^*)^2 - a(x_2 - x_2^*)^2 + kx_1^*\left(G(x_2) - G(x_1) + 1 - \frac{x_1x_2^*}{x_1^*x_2} + \ln\left(\frac{x_1x_2^*}{x_1^*x_2}\right)\right)\\ &\quad + bk(x_1 - x_1^*)(y_2 - y_2^*)\\ &\leq -a(x_1 - x_1^*)^2 - a(x_2 - x_2^*)^2 + kx_1^*\left(G(x_2) - G(x_1)\right) + bk(x_1 - x_1^*)(y_2 - y_2^*)\end{aligned}$$

As the solutions of system (4) are bounded and $a > 0$ and $k > 0$ is sufficiently small, we deduce that $\dot{V} \leq 0$ and $\dot{V} = 0$ if and only if $x_i = x_i^*$ and $y_i = y_i^*$, $i = 1, 2$. By the classical Lyapunov theory, E^* is globally asymptotically stable.

6 Numerical Simulations

In this section, via Matlab software and by using ode45 discretization we give some numerical simulations in order to illustrate the theoretical results presented in the previous sections (Figs. 1, 2, 3, 4, 5, 6, 7, 8).

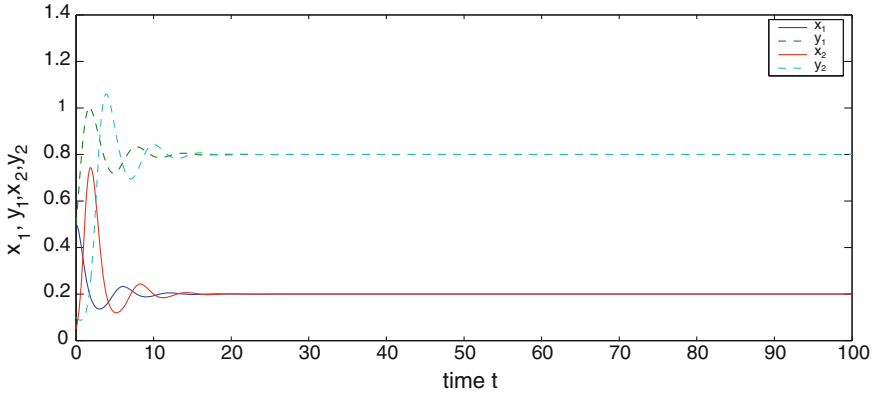

Fig. 1 Identification of solutions of the two patches with a vanishing migration rate $k = 0$

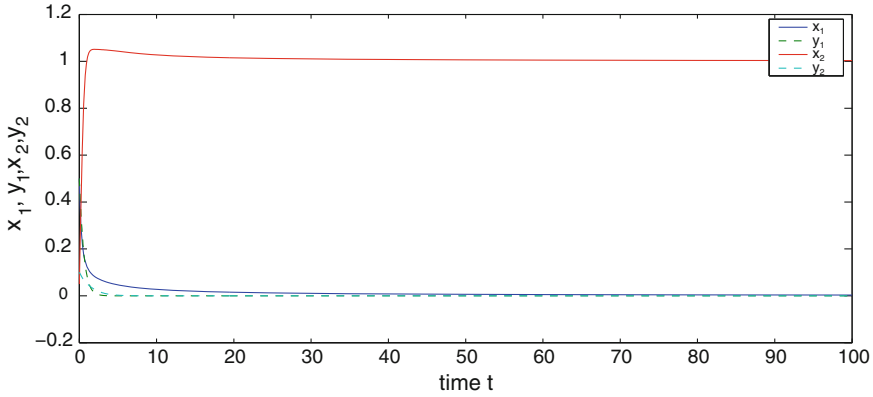

Fig. 2 Stability of E_1 with the following parameters values $a = 2$, $b = 3$, $c = 2$, $d = 0.5$ and $k = 0.5$

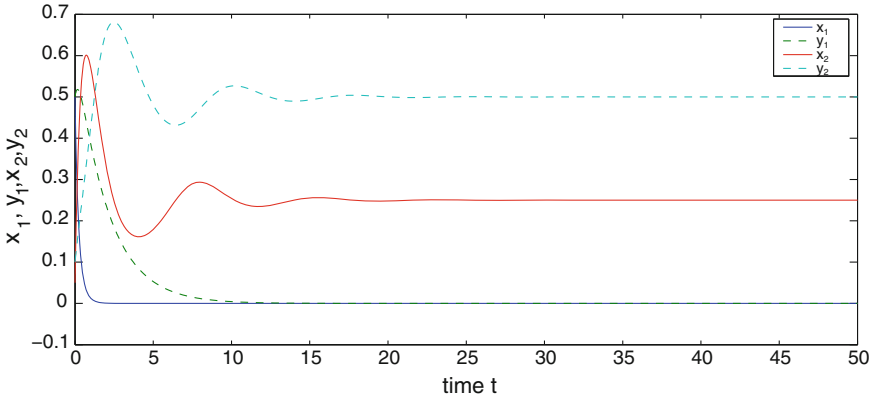

Fig. 3 Stability of E_2 with the following parameters values $a = 2$, $b = 3$, $c = 2$, $d = 0.5$ and $k = 4$

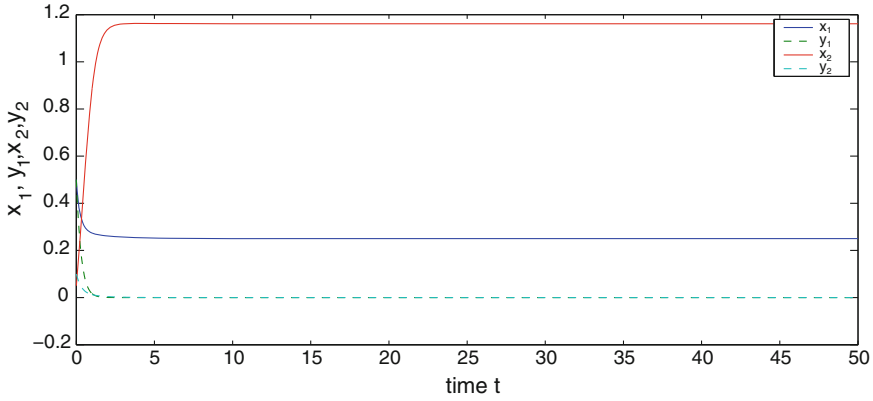

Fig. 4 Stability of E_3 with the following parameters values $a = 2$, $b = 3$, $c = 2$, $d = 4$ and $k = 1.5$

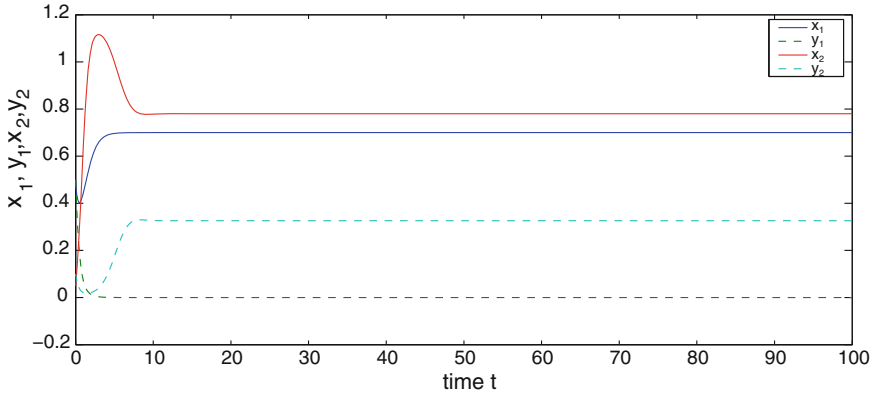

Fig. 5 Stability of E_4 with the following parameters values $a = 2$, $b = 3$, $c = 2$, $d = 4$ and $k = 5$

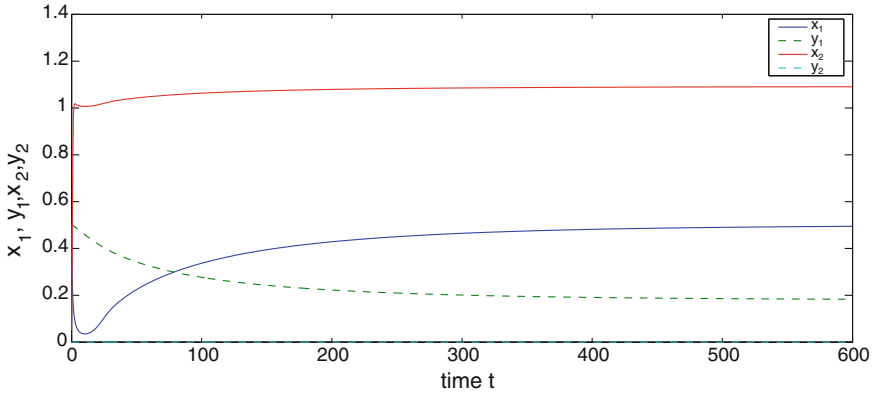

Fig. 6 Stability of E_5 with the following parameters values $a = 3$, $b = 5$, $c = 0.02$, $d = 0.01$ and $k = 0.6$

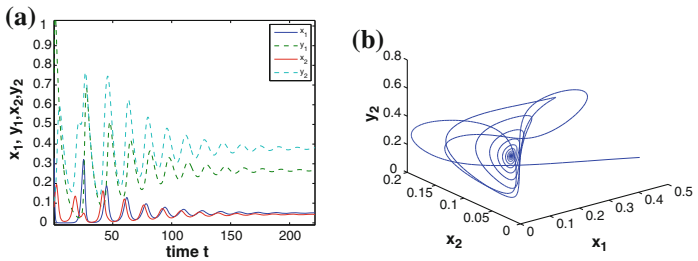

Fig. 7 Stability of E_5 in $(t, x_1y_1x_2y_2)$ plane and in (x_1, x_2, y_2) space with the following parameters values $a = 2$, $b = 3$, $c = 2$, $d = 0.5$ and $k = 0.25$

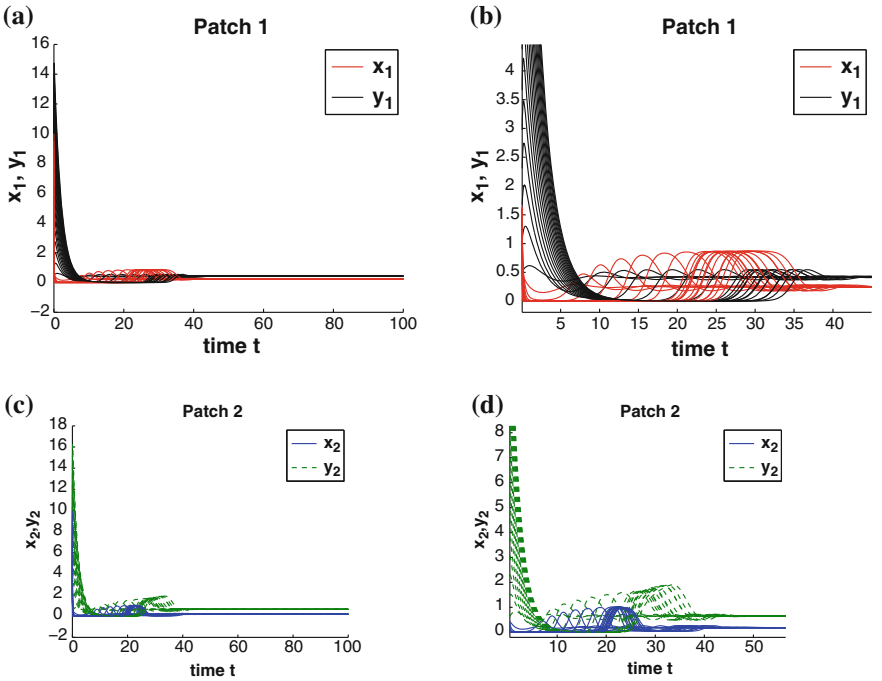

Fig. 8 Global stability of the positive steady state E_6 with different initial conditions values which vary from 0.5 to 20 where $a = 2$, $b = 3$, $c = 2$, $d = 0.5$ and $k = 0.25$; the figure in the right is the zoom of one in the left

References

1. Lotka, A.J.: Elements of Physical Biology. Williams and Wilkins, Baltimore (1925)
2. Volterra V.: Variations and fluctuations in the numbers of coexisting animal species. In: The Golden Age of Theoretical Ecology; (1933–1940). Lecture notes in Biomathematics, vol. 22, issue1, pp. 65–273. Springer, Berlin (1927)
3. Alligood, T., Sauer, T.D., Yorke, J.A.: Chaos: An Introduction to Dynamical Systems. Springer, New York (1996)
4. Cosner, C., DeAngelis, D.L., Ault, J.S., Olson, D.B.: Effects of spatial grouping on the function response of predators. Theor. Popul. Biol. **56**, 65–75 (1999)
5. Edelstein-Keshet, L.: Mathematical Models in Biology. McGraw-Hill Inc., New York (1977)
6. Aziz-Alaoui, M.A., Daher Okiye, M.: Boundedness and global stability for a predatorprey model with modified Leslie-Gower and Holling-type II schemes. Appl. Math. Lett. **16**, 1069–1075 (2003)
7. Nindjin, A.F., Aziz-Alaoui, M.A., Cadivel, M.: Analysis of a predator-prey model with modified Leslie-Gower and Holling-type II schemes with time delay. Nonlinear Anal. Real World Appl. **7**(5), 1104–1118 (2006)
8. Nindjin, A.F., Aziz-Alaoui, M.A.: Persistence and global stability in a delayed Leslie-Gower type three species food chain. J. Math. Anal. Appl. **340**(1), 340–357 (2008)

9. Yafia, R., El Adnani, F.,Talibi, H.A.: Stability of limit cycle in a predator-prey model with modified Leslie-Gower and Holling-type II schemes with time delay. Appl. Math. Sci. **1**(3), 119–131 (2007)
10. Yafia, R., El Adnani, F., Talibi, H.A.: Hopf bifurcation analysis in a predator-prey model with modified Leslie-Gower and Holling-type II schemes with time delay. Nonlinear Anal. Real World Appl **9**(5), 2055–2067 (2008)
11. Jansen, V.A.A.: Theoretical aspects of metapopulation dynamcs. Ph. D. thesis, Leiden University, The Netherlands (1994)
12. Jansen, V.A.A.: Regulation of predator-prey systems through spatial interactions: a possible solution to the paradox of nrichment. Oikos **74**, 384–390 (1995)
13. Jansen, V.A.A., DeRoos, A.M.: The role of space in reducing predator-prey cycles. In: The Geometry of Ecological Interactions Simplifying Spacial Compelxity, pp. 183–201. Cambridge University Press, Cambridge (2000)
14. Jansen, V.A.A., Lloyd, A.L.: Local stability analysis of spatially homogenous solutions of multi-patch systems. J. Math. Biol. **41**, 232–252 (2000)
15. Murray, J.D.: Lectures on Nonlinear Differential Equation Models in Biology. Oxford University Press, Oxford (1977)
16. Murray, J.D.: Mathematical Biology. Springer, Berlin (1993)
17. Kuang, Y., Takeuchi, Y.: Predator-prey dynamics in models of prey dispersal in two-patch environments. Math. Bisci. **120**, 77–98 (1994)
18. Jansen, V.A.A.: The dynamics of two diffiusively coupled predator-prey populations. Theor. Popul. Biol. **59**, 119–131 (2001)
19. Rosenzweig, M.L., MacArthur, R.H.: Graphical representation and stability conditions of predator-prey interactions. Am. Nat. **97**, 209–223 (1963)
20. Feng, W., Rock, B., Hinson, J.: On a new model of two-patch predator prey system with migration of both species. J. Appl. Anal. Comp. **1**(2), 193–203 (2011)
21. Feng, W., Hinson, J.: Stability and pattern in two-patch predator-prey population dynamics. Dis. Cont. Dun. Sys. 268–279 (2005)
22. Quaglia, G., Re, E., Rinaldi, M., Venturino, E.: A two-patch predator-prey metapopulation model. East Asian J. Appl. Math. **2**(3), 238–265 (2012)

Hysteretic Nonlinearity in Inverted Pendulum Problem

Mikhail E. Semenov, Peter A. Meleshenko, Andrey M. Solovyov and Andrey M. Semenov

Abstract This work is dedicated to the problem of inverted pendulum under hysteretic nonlinearity in the form of backlash in the suspension point. We present the results for various motion of the suspension point, namely, the vertical and horizontal motions. We consider the mathematical model of inverted pendulum with vertically oscillating suspension and in the frame of presented model the explicit stability criteria for the linearized equations of motion are found. Dependencies between initial conditions and driven parameters, that provide periodic oscillations of the pendulum, are obtained. In the next step we consider the mathematical model of inverted pendulum under state feedback control (horizontal motion of suspension). Analytic results for the stability criteria as well as for the solution of linearized equation are observed and analyzed. The theorems that determine stabilization of the considered system are formulated and discussed together with the question on the optimal control. We also investigate the elastic inverted pendulum with backlash in the suspension point (horizontal motion). The problem of stabilization together with an optimization problem for such a system is considered. Algorithm (based on the bionic model) which provides the effective procedure for finding of optimal parameters is presented and applied to considered system. Phase portraits and dynamics of the Lyapunov function are also presented and discussed.

M.E. Semenov (✉)
Meteorology Department, Zhukovsky–Gagarin Air Force Academy,
Starykh Bolshevikov St. 54 "A", 394064 Voronezh, Russia
e-mail: mkl150@mail.ru

M.E. Semenov · P.A. Meleshenko · A.M. Solovyov
Digital Technologies Department, Voronezh State University,
Universitetskaya Sq. 1, 394006 Voronezh, Russia

M.E. Semenov
Mathematics Department, Voronezh State University of Architecture
and Civil Engineering, XX-letiya Oktyabrya St. 84, 394006 Voronezh, Russia

P.A. Meleshenko
Communication Department, Zhukovsky–Gagarin Air Force Academy,
Starykh Bolshevikov St. 54 "A", 394064 Voronezh, Russia
e-mail: melechp@yandex.ru

A.M. Semenov
Materials Science and Nanosystems Technologies Department, Voronezh State University,
Universitetskaya Sq. 1, 394006 Voronezh, Russia

M. Belhaq (ed.), *Structural Nonlinear Dynamics and Diagnosis*,
Springer Proceedings in Physics 168, DOI 10.1007/978-3-319-19851-4_22

1 Introduction

The problem of inverted pendulum has a long history [17, 18, 45] and remains relevant even in the present days (see, e.g., [2, 6–8, 15, 24, 28, 30, 34, 38, 40–42, 47, 49, 51] and related references). As is well known the model of inverted pendulum plays a central role in the control theory [1, 5, 6, 11, 16, 19, 27, 36, 47, 49]. It is well established benchmark problem that provides many challenging problems to control design. Because of their nonlinear nature pendulums have maintained their usefulness and they are now used to illustrate many of the ideas emerging in the field of nonlinear control [3]. Typical examples are feedback stabilization, variable structure control, passivity based control, back-stepping and forwarding, nonlinear observers, friction compensation, and nonlinear model reduction. The challenges of control made the inverted pendulum systems a classic tools in control laboratories. Namely, it should be noted that although a lot of control algorithm are researched in the systems control design, Proportional-Integral-Derivative (PID) controller is the most widely used controller structure in the realization of a control system [47]. The advantages of PID controller, which have greatly contributed to its wide acceptance, are its simplicity and sufficient ability to solve many practical control problems.

According to control purposes of the inverted pendulum, the control of inverted pendulum can be divided into three aspects. The first aspect which is widely researched is the swing-up control of inverted pendulum [11, 27, 36].[1] Interesting and important results on the time optimal control of inverted pendulum were obtained in [11, 36]. In particular, in [36] the optimal transients (taking into account the cylindrical character of the states space of the system under control) were built for different values of the parameters and constraints on the control torque. The second aspect is the stabilization of the inverted pendulum [4, 10]. The third aspect is the tracking control of the inverted pendulum [9]. In practice, stabilization and tracking control are more useful for application.

Such a mechanical system can be found in various field of technical sciences, from robotics to cosmic technologies. E.g., the stabilization of inverted pendulum is considered in the problem of missile pointing because the engine of missile is placed lower than the center of mass and such a fact leads to aerodynamical unstability. Similar problem is solved in the self-balancing transport device (the so-called segway). Also the model of the inverted pendulum (especially, under various kinds of control of the motion of the suspension point) is widely used in the various fields of physics [43], applied mathematics [49], engineer sciences [23, 40–42, 44], neuroscience [50], economics [39] and others.

The model of inverted pendulum with oscillating suspension point (see panel *a* in Fig. 1) was studied in detail by Kapitza [17, 18]. Let us recall that the equation of

[1] The one-dimensional swinging inverted pendulum with two degrees of freedom is a popular demonstration of using feedback control to stabilize an open-loop unstable system. Since the system is inherently nonlinear, it has been using extensively by the control engineers to verify a modern control theory. In this system, an inverted pendulum is attached to a cart equipped with a motor that drives it along a horizontal track [14].

motion of pendulum has the form:

$$\ddot{\phi} - \frac{1}{l}[g + \ddot{f}(t)] \sin \phi = 0 \tag{1}$$

where ϕ is the angle of vertical deviation of the pendulum, l is the pendulum's length, g is the gravitational acceleration and $f(t)$ is the law of motion of the suspension point (of course, this equation should be considered together with the corresponding initial conditions). In the following consideration we will use this equation as primal.

As is known, if the motion of suspension point is of harmonic character then the (1) reduces to the Mathieu equation, studied in detail, e.g., in [26].

In order to make an adequately description of the dynamics of real physical and mechanical systems, it is necessary to take into account the effects of hysteretic nature such as "backlash", "stops" etc. [32]. The mathematical models of such nonlinearities according to the classical patterns of Krasnosel'skii and Pokrovskii [21], reduce to operators that are treated as converters in an appropriate function spaces. The dynamics of such converters are described by the relation of "input-state" and "state-output".

Backlash in the suspension point is a kind of a hysteretic nonlinearity. The hysteretic phenomenons (especially in the form of control parameters) play an important role in such a fields as physics, chemistry, biology, economics etc. It should also be pointed out that the hysteretic phenomenons are insufficiently known in our days. This fact leads to an interesting problem on the presence of a backlash in the suspension point of a pendulum.

As is known, most of the real physical and technical systems contain a various kind of parts that can be represented as a cylinder with a piston [32]. Inevitably, the backlashes appear in such systems during its long operation due to "aging" of the materials. As was mentioned above, such backlashes are of hysteretic nature and the analysis of such nonlinearities is quiet important and actual problem. In this work, we investigate various aspects of hysteretic control in the problem of inverted pendulum (for various forms of motion of the suspension point). More specific, we investigate the dynamical features of such a system depending on the control parameters. Let us note also that the system under consideration can be considered as a successful model for a real mechanical system with a hysteretic type of nonlinearity.

This work is organized in the following way. In Sect. 2 we consider the vertical motion of the suspension point of inverted pendulum. Namely, in Sect. 2.1 we construct the mathematical model of the inverted pendulum under hysteretic control. Section 2.2 is dedicated to the problem of stability of the linearized equation of motion. In particular, in this section the monodromy matrix and the stability condition for inverted pendulum under hysteretic control are found in the explicit form. In Sect. 2.3 the stability zones of the presented system are analyzed in detail. Section 2.4 is dedicated to the analysis of the periodic solutions for the system under consideration taking into account that the hysteretic control takes place. In Sect. 3 we consider the horizontal motion of the suspension point of inverted pendulum. In Sect. 3.1 we consider a mathematical model of this system. In Sect. 3.2 we consider

the backlash as a hysteretic nonlinearity using operator technique of Krasnosel'skii and Pokrovskii.[2] In Sect. 3.3 the dynamical characteristics of the system under consideration are presented in the explicit form. Namely, the expression for stability zones of the system under consideration is obtained and analyzed. In this section we also consider the dissipative motion of the inverted pendulum. Corresponding theorem is formulated and proved. Section 3.4 is dedicated to the problem of non-ideal relay in feedback. Here we formulate and prove the theorem on Lyapunov stability of the system with non-ideal relay in feedback. In Sect. 3.5 we consider the question on optimal control for the system under consideration. In this section we discuss the theorem on the optimal control of pendulum. In Sect. 4 we consider the problem of elastic inverted pendulum with hysteretic nonlinearity in the form of a backlash in suspension point. In Sect. 4.1 we consider the general view of elastic inverted pendulum together with the operator technique for hysteretic nonlinearities. Also in this section we obtain the equation of motion of the elastic pendulum with a hysteretic nonlinearity in the suspension point. Section 4.2 is dedicated to numerical solution of the obtained equations (we use the difference scheme). In Sect. 4.3 we analyze the problem of optimization for the system under consideration. The numerical realization of optimization procedure is made using the so-called bionic algorithm. In Sect. 4.4 the results of numerical simulations are discussed and analyzed. In the last section the main results of the presented work are summarized.

2 Inverted Pendulum Under Hysteretic Nonlinearity: Vertical Oscillation of Suspension

In this section we describe the inverted pendulum under hysteretic nonlinearity in the form of backlash in vertically oscillating suspension point [42].

2.1 Mathematical Model

Let us consider a system where the base of the pendulum is a physical system (P, S) formed by a cylinder of length H and the piston P.[3] Both the cylinder and piston can move in the direction of the vertical axis as it is shown in panel b of the Fig. 1.

We determine the piston's position by the coordinate $f(t)$ and the cylinder's position by coordinate $\upsilon(t)$. Let us assume also that the "leading" element in the

[2]Here we would like to note that in three considered cases we introduce the mathematical description of backlash in the ways that are comfortable to use in the concrete case. However all these descriptions are based on the operator technique with small variations that are presented in the corresponding sections.

[3]Here we would like to note that both of the cylinder and piston are ideal, absolutely rigid and can move along the y-axis in the infinite ranges.

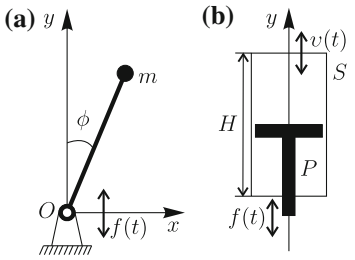

Fig. 1 Geometry of the problem. **Panel a** General view of the inverted pendulum. **Panel b** The suspension point (*cylinder* and *piston*)

system (P, S) is a cylinder P. In this assumption the system (P, S) can be considered as a converter Γ with the input signal $f(t)$ (piston's position) and the output signal $\upsilon(t)$ (cylinder's position). Such a converter is called *backlash*. The set of its possible states is $f(t) \le \upsilon(t) \le f(t) + H$ $(-\infty < f(t) < \infty)$. The cylinder's position $\upsilon(t)$ at $t > t_0$ is defined by $\upsilon(t) = \Gamma[t_0, \upsilon(t_0)]f(t)$, where $\Gamma[t_0, \upsilon(t_0)]$ is the operator defined for each $\upsilon_0 = \upsilon(t_0)$ on the set of continuous inputs $f(t)$ $(t > t_0)$ for which $\upsilon_0 - H < f(t) < \upsilon_0$ [21].

We assume that the piston's acceleration periodically changes from $-a\omega^2$ to $a\omega^2$ with the frequency ω. This assumption consists in the fact that the linearized equation of motion of such a pendulum can be written in the form[4]:

$$\begin{aligned} &\ddot{\phi} - \frac{1}{l}[g + a\omega^2 G(t, H)w(t)]\phi = 0, \\ &w(t) = -\text{sign}[\sin(\omega t)], \\ &\phi(0) = \phi_{10}, \ \dot{\phi}(0) = \phi_{20}, \end{aligned} \tag{2}$$

where $\text{sign}(z)$ is the usual signum function, $a\omega^2 G(t, H)w(t)$ is the acceleration of the suspension point and

$$G(t, H) = \begin{cases} 0, \ t \in (t^*, t^* + \Delta t), \\ 1, \ t \text{ out of } (t^*, t^* + \Delta t), \end{cases}$$

where t^* are the moments after which the acceleration's sign change takes place, $\Delta t = \sqrt{\frac{2H}{a\omega^2}}$ is the time for which the piston passes through the cylinder.

[4]It should be pointed out that such a periodic behavior of the piston's acceleration (i.e., the fact that the acceleration of the piston changes from $-a\omega^2$ to $a\omega^2$) is an assumption of the model presented in this paper. Such a model allows us to obtain some analytical results (the explicit conditions for the stability zones). Also, the numerical simulations are most effectively in the frame of this model. Moreover, such a model of the piston's behavior most effectively and adequately describes the dynamics of the parts of real technical devices.

2.2 Stability of Linearized Equation

Let we pass to dimensionless units in (2) using the following change:

$$x \equiv \phi,\ \tau = \omega t,\ k = \frac{g}{l\omega^2},\ s = \frac{a}{l},\ \Delta\tau = \sqrt{\frac{2H}{sl}}.$$

As a result, we obtain an equation similar to Meissner equation [26], but with the negative coefficients and hysteretic nonlinearity:

$$\begin{gathered}\ddot{x} - [k - sG(\tau, H)\text{sign}(\sin\tau)]x = 0,\\ G(\tau, H) = \begin{cases} 0,\ \tau \in (\tau^*, \tau^* + \Delta\tau), \\ 1,\ \tau \text{ out of } (\tau^*, \tau^* + \Delta\tau), \end{cases}\\ x(0) = x_{10},\ \dot{x}(0) = x_{20},\end{gathered} \tag{3}$$

We can write the (3) in the form of an equivalent system:

$$\begin{gathered}\begin{cases} \dot{x}_1 = x_2, \\ \dot{x}_2 = p(\tau)x_1, \end{cases}\\ x_1(0) = x_{10},\ x_2(0) = x_{20}.\end{gathered} \tag{4}$$

The matrix of this system has the form:

$$\mathbf{P}(\tau) = \begin{pmatrix} 0 & 1 \\ p(\tau) & 0 \end{pmatrix},$$

where $p(\tau) = k - sG(\tau, H)\text{sign}(\sin\tau)$. In the frame of our assumptions the matrix $\mathbf{P}(\tau)$ is a periodic function of time with the period 2π, namely: $\mathbf{P}(\tau + 2\pi) \equiv \mathbf{P}(\tau)$.

Let we say that the (3) is stable (or unstable) according to Lagrange if the system (4) is stable (or unstable, respectively). It means, that all solutions $x(\tau)$ of the stable (3) are bounded in $[\tau_0, \infty)$ together with the derivatives $\dot{x}(\tau)$.

Following the results of Floquet [35], the investigation of the stability of such systems reduces to the problem of finding the fundamental matrix of the solutions at the moment 2π (the so-called *monodromy matrix*) and evaluation of its eigenvalues (the so-called *multipliers*). For the stability of the periodic system it is necessary and sufficient that the following condition takes place $|\rho| < 1$ (all the multipliers are placed inside the unit circle).

Due to the fact that the matrix $\mathbf{P}(\tau)$ is a piecewise-constant, the fundamental system of solutions and the monodromy matrix can be constructed in the closed form. In order to do this, let us consider behavior of a piecewise-constant function $r(\tau) = -G(\tau, H)\text{sign}(\sin\tau)$ with the period 2π, and a function $p(\tau)$, respectively (see Fig. 2).

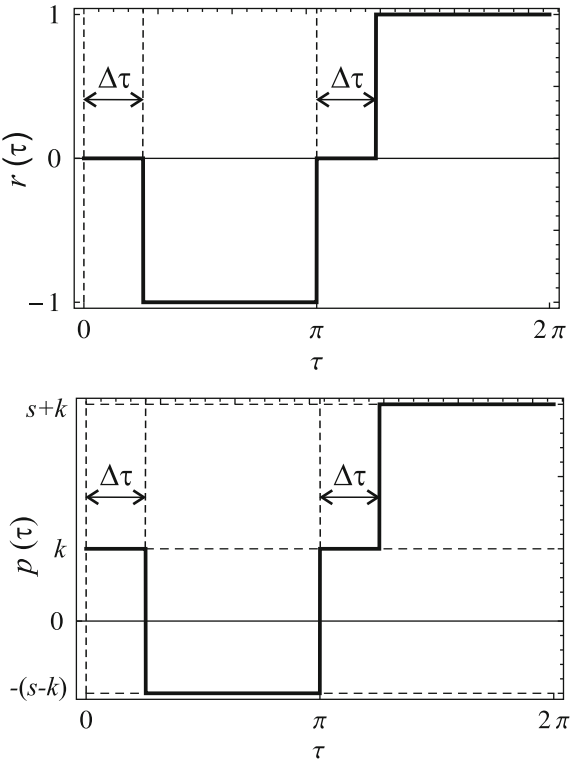

Fig. 2 Functions $r(\tau)$ and $p(\tau)$

As we see from Fig. 2, in the interval $(0, 2\pi)$ the system (4) can be described by the following linear systems with the constant coefficients:

$$\begin{cases} \dot{x}_1^1 = x_2^1, \\ \dot{x}_2^1 = kx_1^1, \end{cases} \quad \tau \in [0, \Delta\tau], \tag{5}$$

$$\begin{cases} \dot{x}_1^2 = x_2^2, \\ \dot{x}_2^2 = -(s-k)x_1^2, \end{cases} \quad \tau \in [\Delta\tau, \pi], \tag{6}$$

$$\begin{cases} \dot{x}_1^3 = x_2^3, \\ \dot{x}_2^3 = kx_1^3, \end{cases} \quad \tau \in [\pi, \pi + \Delta\tau], \tag{7}$$

$$\begin{cases} \dot{x}_1^4 = x_2^4, \\ \dot{x}_2^4 = (k+s)x_1^4, \end{cases} \quad \tau \in [\pi + \Delta\tau, 2\pi]. \tag{8}$$

Since the fundamental matrix should be continuous, the solutions of (5)–(8) should match at the corresponding points, namely:

$$\mathbf{X}^1(0) = \mathbf{E},\ \ \mathbf{X}^j(\tau_j^*) = \mathbf{X}^{j+1}(\tau_j^*),$$

where $i = 1, 2, 3$, τ_i^* are the moments at which the control changes during the period, $\mathbf{E}$ is the unity matrix.

Consistent integration of the systems (5)–(8) leads to the following fundamental matrices:

$$\mathbf{X}^1(\tau) = \begin{pmatrix} \cosh(\sqrt{k}\tau) & \frac{1}{\sqrt{k}}\sinh(\sqrt{k}\tau) \\ \sqrt{k}\sinh(\sqrt{k}\tau) & \cosh(\sqrt{k}\tau) \end{pmatrix},$$

$$\mathbf{X}^2(\tau) = \mathbf{X}^1(\Delta\tau) \times \begin{pmatrix} \cos[k_2(\tau-\Delta\tau)] & \frac{1}{k_2}\sin[k_2(\tau-\Delta\tau)] \\ -k_2\sin[k_2(\tau-\Delta\tau)] & \cos[k_2(\tau-\Delta\tau)] \end{pmatrix},$$

$$\mathbf{X}^3(\tau) = \mathbf{X}^2(\pi) \times \begin{pmatrix} \cosh[\sqrt{k}(\tau-\pi)] & \frac{1}{\sqrt{k}}\sinh[\sqrt{k}(\tau-\pi)] \\ \sqrt{k}\sinh[\sqrt{k}(\tau-\pi)] & \cosh[\sqrt{k}(\tau-\pi)] \end{pmatrix},$$

$$\mathbf{X}^4(\tau) = \mathbf{X}^3(\pi+\Delta\tau) \times \begin{pmatrix} \cosh[k_1(\tau-\pi-\Delta\tau)] & \frac{1}{k_1}\sinh[k_1(\tau-\pi-\Delta\tau)] \\ k_1\sinh[k_1(\tau-\pi-\Delta\tau)] & \cosh[k_1(\tau-\pi-\Delta\tau)] \end{pmatrix}.$$

Putting $\tau = 2\pi$ in $\mathbf{X}^4(\tau)$, we obtain the following form of the monodromy matrix of the system (4):

$$\begin{aligned} \mathbf{A} &= \mathbf{X}(2\pi) \\ &= \begin{pmatrix} \cosh(\sqrt{k}\Delta\tau) & \frac{1}{\sqrt{k}}\sinh(\sqrt{k}\Delta\tau) \\ \sqrt{k}\sinh(\sqrt{k}\Delta\tau) & \cosh(\sqrt{k}\Delta\tau) \end{pmatrix} \times \begin{pmatrix} \cos(k_2\gamma) & \frac{1}{k_2}\sin(k_2\gamma) \\ -k_2\sin(k_2\gamma) & \cos(k_2\gamma) \end{pmatrix} \\ &\times \begin{pmatrix} \cosh(\sqrt{k}\Delta\tau) & \frac{1}{\sqrt{k}}\sinh(\sqrt{k}\Delta\tau) \\ \sqrt{k}\sinh(\sqrt{k}\Delta\tau) & \cosh(\sqrt{k}\Delta\tau) \end{pmatrix} \times \begin{pmatrix} \cosh(k_1\gamma) & \frac{1}{k_1}\sinh(k_1\gamma) \\ k_1\sinh(k_1\gamma) & \cosh(k_1\gamma) \end{pmatrix}, \end{aligned} \tag{9}$$

where $(k_1)^2 = k + s$, $(k_2)^2 = s - k$ $(s > k)$, $\gamma = \pi - \Delta\tau$. Let we write also the characteristic equation for the matrix $\mathbf{A}$:

$$\|\mathbf{A} - \rho\mathbf{E}\| = \begin{vmatrix} a_{11}-\rho & a_{12} \\ a_{21} & a_{22}-\rho \end{vmatrix} = \rho^2 + \alpha\rho + \beta = 0, \tag{10}$$

where $\beta = (-1)^2 \exp\left(\int_0^T \mathrm{Sp}[\mathbf{P}(\tau)]\mathrm{d}\tau\right) = 1$ [29] and $\alpha = -(a_{11} + a_{22})$.

The product of the roots ρ_1 and ρ_2 of (10) is equal to unity, so the motion will be stable at $|\alpha| < 2$ only, i.e., when the modules of multipliers are equal to unity, but these multipliers are different. Thus, we obtain the following condition for the stability of solutions of (3):

$$|a_{11} + a_{22}| < 2. \tag{11}$$

Using (9) the condition (11) can be written in the explicit form:

$$\begin{aligned}&\Big|\cos(k_2\gamma)\left[2\cosh(2\sqrt{k}\Delta\tau)\cosh(k_1\gamma) + \sinh(2\sqrt{k}\Delta\tau)\sinh(k_1\gamma)\left(\tfrac{\sqrt{k}}{k_1} + \tfrac{k_1}{\sqrt{k}}\right)\right]\\ &+\sin(k_2\gamma)\Big[\sinh(2\sqrt{k}\Delta\tau)\cosh(k_1\gamma)\left(\tfrac{\sqrt{k}}{k_2} - \tfrac{k_2}{\sqrt{k}}\right)\\ &+\cosh^2(\sqrt{k}\Delta\tau)\sinh(k_1\gamma)\left(\tfrac{k_1}{k_2} - \tfrac{k_2}{k_1}\right) + \sinh^2(\sqrt{k}\Delta\tau)\sinh(k_1\gamma)\left(\tfrac{k}{k_1k_2} - \tfrac{k_1k_2}{k}\right)\Big]\Big| < 2.\end{aligned} \tag{12}$$

Thus, the *stability zone* of the system (4) in the space of parameters is defined by the inequality (12).

2.3 Stability Zones

Let us consider the (3) at $H = 0$, i.e., in the absence of the hysteretic nonlinearity:

$$\ddot{x} - [k - s \cdot \mathrm{sign}(\sin\tau)]x = 0, \tag{13}$$

then $\Delta\tau = 0$ and the inequality (12) takes the form:

$$\left|\cosh(\pi k_1)\cos(\pi k_2) + \frac{1}{2}\left(\frac{k_1}{k_2} - \frac{k_2}{k_1}\right)\sinh(\pi k_1)\sin(\pi k_2)\right| < 1. \tag{14}$$

Now we construct numerically a solution of (14) with relation to the parameters k and s (see the panel a in Fig. 3). In panel b of the Fig. 3 we show also the stability zone for the Meissner equation obtained by Sato [37].

As we can see, these diagrams are the mirror images of each other because of opposite signs at x in the corresponding equations.

Let us construct the stability zone for the system (9). Such a system has a three-dimensional parameter space because of dependence on the three parameters takes place (the dimensionless variables k, s and the piston's length H). We set the length of the pendulum as $l = 1$ m.

Figure 4 shows that the stability zones do not qualitatively change, but only slightly deformed with growth of H. Note that in the presented problem the parameters k and s can take the positive values only. The change of the stability zone in the positive half-plane is shown in Fig. 5. Also in this figure we see that the growth of the parameter

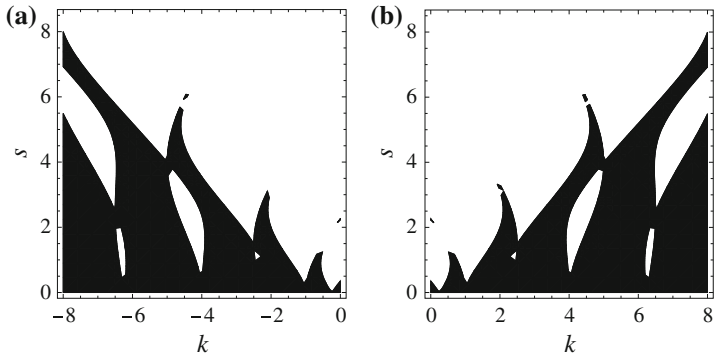

Fig. 3 Stability zones in the absence of the hysteretic control ($H = 0$): **panel a** corresponds to (refeq1.13); **panel b** corresponds to the Meissner equation

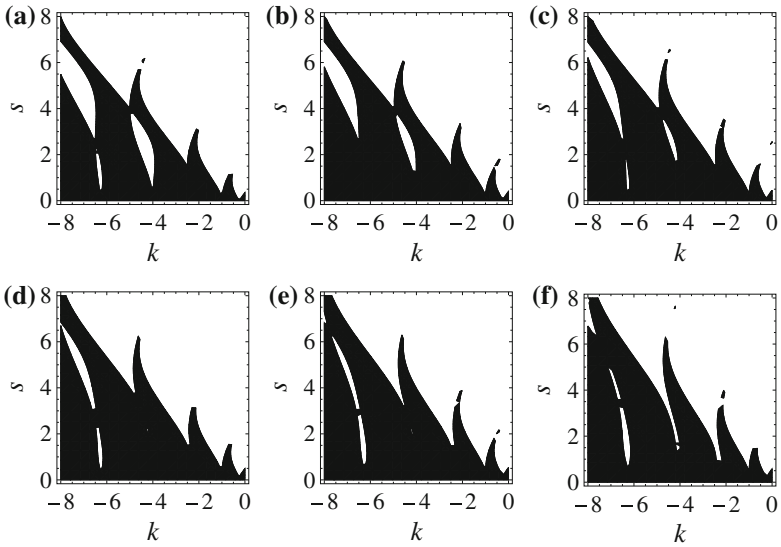

Fig. 4 Stability zones in the presence of the hysteretic control. **Panel a** is $H = 0\,\text{m}$, **panel b** is $H = 0.2\,\text{m}$, **panel c** is $H = 0.4\,\text{m}$, **panel d** is $H = 0.6\,\text{m}$, **panel e** is $H = 0.8\,\text{m}$, **panel f** is $H = 1\,\text{m}$

H leads to the increasing of the lower boundary of the stability zone. Moreover, we see in this figure that with increasing of the hysteretic parameter (see the panel f) the boundaries of the stability zones become multi-valued functions (namely, the function $s(k)$). Such a behavior of the boundaries is connected with the fact that the main equation of the model contains the hysteretic nonlinearity (hysteretic behavior of the control parameter H).

Stability zones in the space of parameters of the system (see (2)) are shown in Fig. 6. This figure shows that the area of stability zone essentially unchanged with

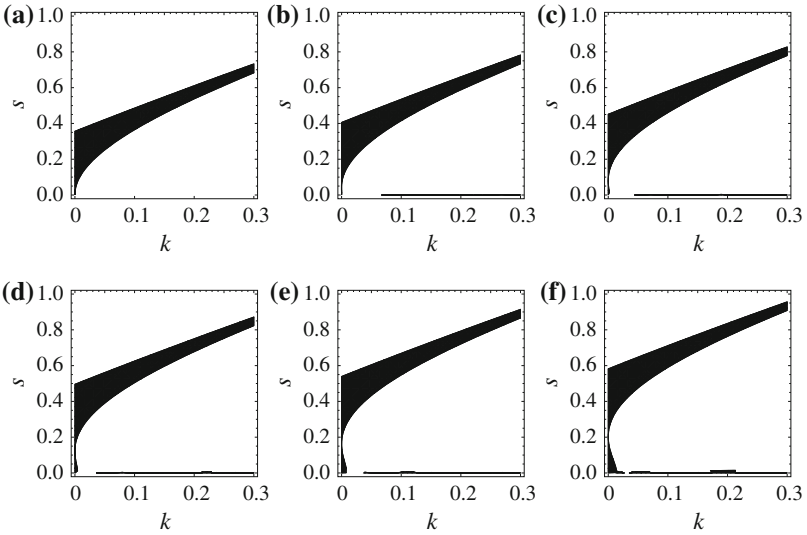

Fig. 5 Stability zones in the positive half-plane ($k > 0$, $s > 0$) in the presence of the hysteretic control. **Panel a** is $H = 0\,\text{m}$, **panel b** is $H = 0.2\,\text{m}$, **panel c** is $H = 0.4\,\text{m}$, **panel d** is $H = 0.6\,\text{m}$, **panel e** is $H = 0.8\,\text{m}$, **panel f** is $H = 1\,\text{m}$

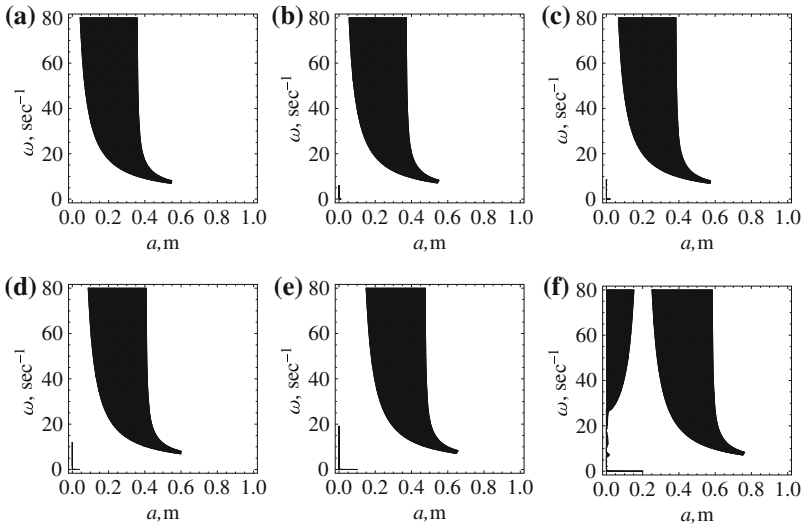

Fig. 6 Stability zones in the coordinates a and ω for different values of the parameter H. **Panel a** is $H = 0\,\text{m}$, **panel b** is $H = 0.05\,\text{m}$, **panel c** is $H = 0.1\,\text{m}$, **panel d** is $H = 0.2\,\text{m}$, **panel e** is $H = 0.5\,\text{m}$, **panel f** is $H = 1\,\text{m}$

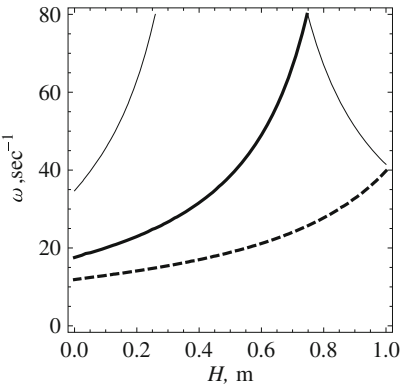

Fig. 7 The dependence of the frequency ω on the hysteretic parameter H (on the border of the stability zone, i.e., the condition $|a_{11} + a_{22}| = 2$ takes place) for various a: *thin curve* is $a = 0.1$ m, *thick curve* is $a = 0.2$ m, *dashed curve* is $a = 0.3$ m

increasing of the length of piston H, just only shifted (for the values of H in the interval $H \in [0, 0.5]$). This means that for any H in the presented interval there exists a pair of values ω and a to ensure the stability of the vertical position of the inverted pendulum with oscillating suspension and the hysteretic nonlinearity. However, as we can see in panel *f*, at $H = 1$, there are two domains of values ω and a that ensure the stability of the vertical position. It should also be pointed out that in full analogy with the Fig. 5 the boundaries of the stability zones become multi-valued functions (in this case, the function $\omega(a)$) when the hysteretic parameter H increases. Such a behavior of the boundaries follows from the fact that in the presence of the hysteretic control the main (2) (together with the corresponding monodromy matrix (9)) becomes essentially nonlinear.

In Fig. 7 we plot the dependencies of the oscillation frequency (the frequency which lies on the border of the stability zone, in other words, the frequency which ensuring the stability of solutions of (2)), on the length of the piston H at different values of a (oscillation amplitude for the piston).

Let us note, that the parameters which satisfy the inequality (12) correspond to the almost periodic oscillations [20] relative to the top of the pendulum. In order to confirm these results we present the plots of characteristics of oscillations (in the linearized model described by (2)) of the inverted pendulum with length $l = 1$ m and hysteretic nonlinearity $H = 0.05$ m (Fig. 8). The amplitude and frequency of oscillation of the piston are $a = 0.15$ m and $\omega = 30\,\mathrm{s}^{-1}$, respectively. The initial conditions are $\phi(0) = 0.2$ and $\dot{\phi}(0) = 1\,\mathrm{s}^{-1}$.

2.4 Periodic Solutions

Now, let us consider behavior of pendulum on the edges of stability zone. In the characteristic equation for the monodromy matrix (10) such a situation corresponds

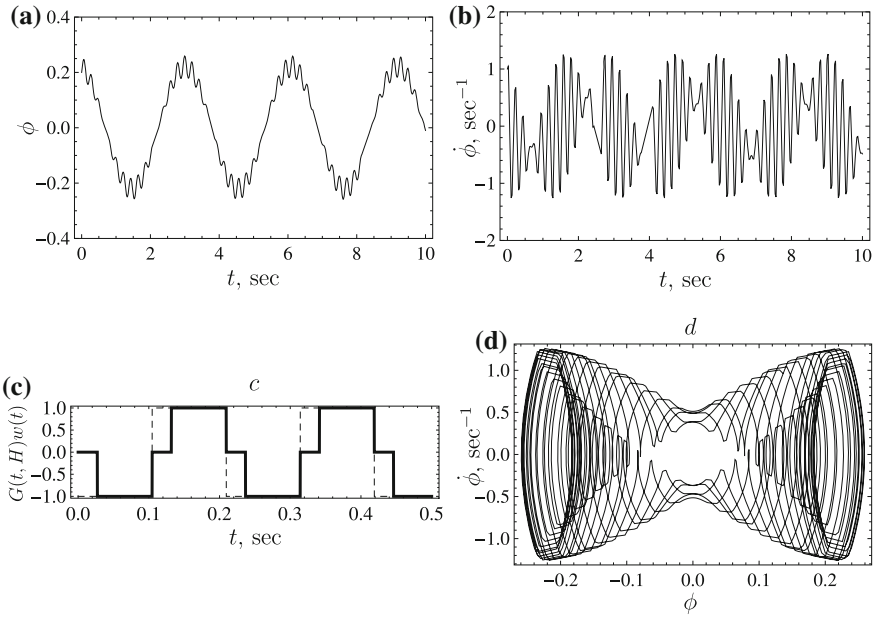

Fig. 8 **Panels a** and **b** characteristics of the inverted pendulum described by (2) (modeling parameters are presented in the main text); **panel c** the control function (*solid line* corresponds to hysteretic control, *dashed line* corresponds to the absence of the hysteretic control); **panel d** phase portrait

to two cases: $\alpha = -2$ (left edge) and $\alpha = 2$ (right edge). The multipliers in this case have took the values $\rho_1 = \rho_2 = 1$ and $\rho_1 = \rho_2 = -1$, respectively.

If $\rho_1 = \rho_2 = 1$ then the corresponding normal solution will satisfy the equality $\mathbf{X}(t + 2\pi) = \mathbf{X}(t)$. Therefore the (2) has a periodic solution and the period of such a solution coincides with the period of the coefficients $T_1 = \frac{2\pi}{\omega}$.

In the second case ($\rho_1 = \rho_2 = -1$) the corresponding normal solution will satisfy the equality $\mathbf{X}(t + 2\pi) = -\mathbf{X}(t)$ (through the one more period $\mathbf{X}(t + 4\pi) = -\mathbf{X}(t + 2\pi) = \mathbf{X}(t)$). This fact means that in the case when the multipliers equal to -1 the (2) has a periodic solution with the period $T_2 = \frac{4\pi}{\omega}$.

The solutions are periodic (and, hence, limited) in both of the presented cases. We will say that they are stable by Lagrange. We assume also that all of the pendulum's parameters (in periodic regime of oscillations) should satisfy the following condition:

$$a_{11} + a_{22} = 2, \text{ for the period } T_1, \tag{15}$$

$$a_{11} + a_{22} = -2, \text{ for the period } T_2. \tag{16}$$

However, these conditions are necessary only, but not sufficient due to the fact that not for all of the non-zero initial values (for a given control with the parameters which

satisfy to one of these equations) the periodic solutions will exist. Note also that for the presented control described by the function $\upsilon(t) = -a\omega^2 G(t, H)\text{sign}[\sin(\omega t)]$ the initial conditions lie in the first and third quadrants.

Put the following initial condition (ϕ_{10}, ϕ_{20}), and consider the case of periodic oscillations with the period T_1. In this case the equality $\mathbf{X}(0+T_1) = \mathbf{A}\mathbf{X}(0) = \mathbf{X}(0)$ takes place and, also:

$$\begin{pmatrix} a_{11} & a_{12} \\ a_{21} & a_{22} \end{pmatrix} \begin{pmatrix} \phi_{10} \\ \phi_{20} \end{pmatrix} = \begin{pmatrix} \phi_{10} \\ \phi_{20} \end{pmatrix}. \tag{17}$$

This implies that the initial conditions satisfy the following expressions:

$$\phi_{10} = \frac{a_{12}}{a_{11} - 1}\phi_{20}, \;\; \phi_{20} = \frac{a_{21}}{a_{22} - 1}\phi_{10}, \tag{18}$$

i.e., lie on a straight line $z_1 : \dot{\phi} = K_1\phi$, where the coefficient K_1 is:

$$K_1 = \frac{a_{11} - 1}{a_{12}} = \frac{a_{21}}{a_{22} - 1}. \tag{19}$$

This equality ensures that the condition (15) is valid. If for the initial conditions (ϕ_{10}, ϕ_{20}) can be found a pair of the parameters a and ω which lies on the border of the stability zone (at fixed H) and satisfies the (18) then this pair is unique. The opposite statement is also true.

In similar manner, we find that the periodic solutions with period T_2 exist for initial conditions that satisfy the equations:

$$\phi_{10} = \frac{a_{12}}{1 + a_{11}}\phi_{20}, \;\; \phi_{20} = \frac{a_{21}}{1 + a_{22}}\phi_{10}. \tag{20}$$

In analogous manner, these initial conditions lie on a straight line $z_2 : \dot{\phi} = K_2\phi$ with the coefficient

$$K_2 = \frac{a_{11} + 1}{a_{12}} = \frac{a_{21}}{a_{22} + 1}. \tag{21}$$

Corresponding parameters a and ω have been obtained from the numerical solution of (19) and (21). For the solutions of (2) with the initial conditions that satisfy (19) the parameters a and ω are $a = 0.2\,\text{m}$ and $\omega = 18.73\,\text{s}^{-1}$ (hysteretic nonlinearity $H = 0.05\,\text{m}$). For the solutions with the initial conditions that satisfy (21) the corresponding parameters are $a = 0.43\,\text{m}$ and $\omega = 15.02\,\text{s}^{-1}$ (at the same value of the hysteretic nonlinearity). However, the obtained periodic solutions (using the corresponding parameters a and ω) are not stable (in the strict sense). Therefore, the numerical simulation of these solution is can not be made without special regularization procedure.

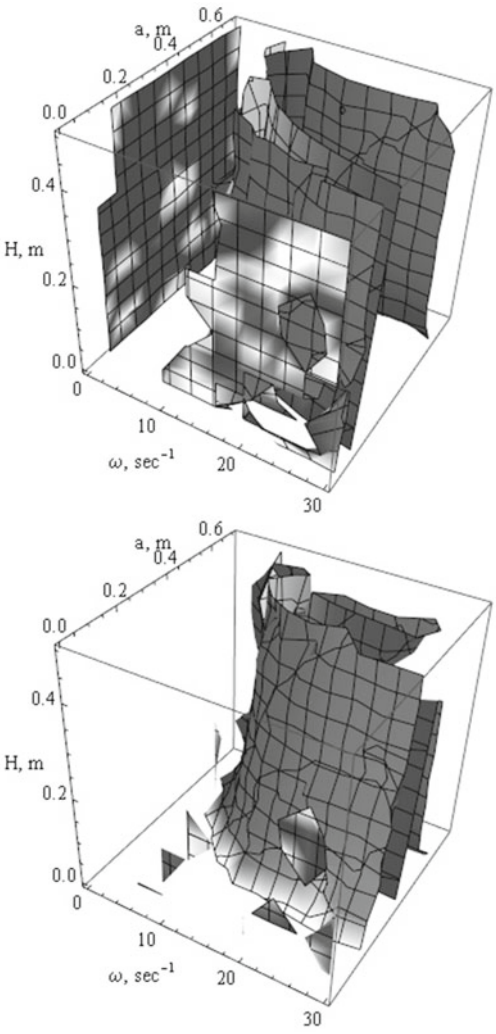

Fig. 9 Surfaces in the space of parameters ω, a and H that satisfy the (19) (*top panel*) and (21) (*bottom panel*)

However, let we plot (see the Fig. 9) the surfaces in the space of parameters ω, a and H that satisfy the existence conditions for the periodic solutions (19) and (21). The complicated shape of the obtained surfaces is connected with the fact that the values of the parameters that determine the periodic solutions are placed on the boundary of the stability zone (see, e.g., the (10) and (11)) where the corresponding solutions are not stable. Moreover, the obtained surfaces (more specific, the dependencies that determine such surfaces) are the solutions of the essentially nonlinear (19) and (21) (the parameters a_{ij} in these equations are the elements of the monodromy matrix (9)).

3 Inverted Pendulum Under Hysteretic Nonlinearity: Horizontal Oscillation of Suspension

In this section we briefly describe the mathematical model of the inverted pendulum with the horizontal moving suspension point [40]. Also, in terms of the *in-out* converter we mathematically describe such a nonlinearity as backlash.

3.1 Mathematical Model

The equations of motion of the inverted pendulum with the horizontal moving suspension point together with the initial conditions (see the Fig. 10) can be written in the following form:

$$\begin{gathered} A\ddot{\varphi} = mgl\sin\varphi - m\ddot{u}l\cos\varphi, \\ \varphi(0) = \varphi_0, \;\; \dot{\varphi}(0) = \omega(0) = \omega_0, \end{gathered} \tag{22}$$

$$u(t) = \Gamma[u_0, h]x(t), \tag{23}$$

where A is a general moment of inertia of the pendulum, $\varphi(t)$ is the angle of vertical deviation of the pendulum, $u(t)$ is a law of motion for the cylinder of the length h, $x(t)$ is a law of motion for the piston which can be interpreted as a control parameter, $\Gamma[u_0, h]$ is defined below. The (22) describes the so-called *in-out* relations of the hysteretic converter in the form of backlash.

In the following we will consider the case, when the acceleration of the piston is constant, namely

$$|\ddot{x}| = k = \text{const}.$$

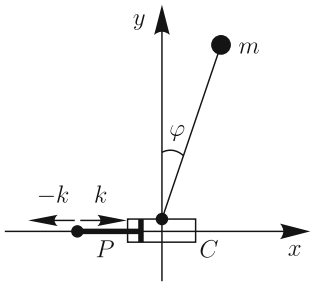

Fig. 10 General view of the inverted pendulum with the suspension point in the form of a cylinder C with a piston P

Let us assume also that the deviations of the pendulum are small so we can rewrite the (22) in the linearized form:

$$\begin{gathered} A\ddot{\varphi} = mgl\varphi - m\ddot{u}l, \\ \varphi(0) = \varphi_0, \ \ \dot{\varphi}(0) = \omega(0) = \omega_0. \end{gathered} \tag{24}$$

3.2 Backlash as Hysteretic Nonlinearity

The mathematical models of hysteretic nonlinearities according to classical patterns of Krasnosel'skii and Pokrovskii [21], reduce to operators that are treated as converters in an appropriate function spaces. The dynamics of such converters are described by the relation of "input-state" and "state-output".

The out state of the converter in the form of backlash (such an out state is considered on the monotonic inputs) can be described by the following relation

$$u(t) = \Gamma[u_0, h]x(t) = \begin{cases} u_0, & \text{for } u_0 \leqslant x(t) \leqslant u_0 + h, \\ x(t), & \text{for } x(t) < u_0, \\ x(t) - h, & \text{for } u_0 + h < x(t). \end{cases} \tag{25}$$

This relation can be illustrated by the Fig. 11.

With a special limit construction and using the semigroup identity in the form

$$\Gamma[u(t_1), h]x(t) = \Gamma\left[\Gamma[u_0, h]x(t_1), h\right]x(t), \tag{26}$$

the Γ-operator can be applied to all continuous inputs. It should also be noted that the presence of hysteretic-type operator in the (24) complicates the stabilization of the pendulum as a whole. In general, the control impact for such a system will be retarded (we should "predict" the future position of the pendulum).

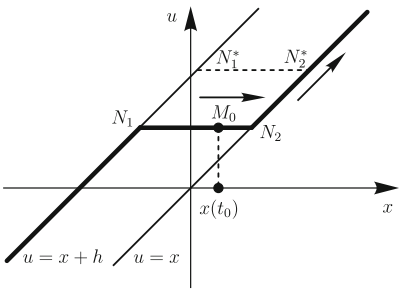

Fig. 11 Schematic view of the backlash (25) action

3.3 Stabilization of Inverted Pendulum with Hysteretic Nonlinearity

In this section we consider the state feedback control of the inverted pendulum with hysteretic nonlinearity in the form of backlash. We obtain the analytic expression for the stability zones of such a system as well as we formulate the theorems that determine the stabilization of the considered system.

3.3.1 Dynamical Characteristics: Analytic Results

Let us consider the state feedback control of the inverted pendulum, i.e., we assume that the input state of the hysteretic converter obeys the following relation:

$$\ddot{x} = k\,\mathrm{sign}(\alpha\varphi + \omega), \tag{27}$$

where $\alpha > 0$ and $\mathrm{sign}(z)$ is the usual signum function.

The linearized (24) can be rewritten in the equivalent matrix form (we determine the general moment of inertia as $A = ml^2$ and use the notation $B = \sqrt{\frac{g}{l}}$) as follows:

$$\begin{pmatrix} \dot{\varphi} \\ \dot{\omega} \end{pmatrix} = V \begin{pmatrix} \varphi \\ \omega \end{pmatrix} + W, \tag{28}$$

where

$$V = \begin{pmatrix} 0 & 1 \\ B^2 & 0 \end{pmatrix}, \quad W = \begin{pmatrix} 0 \\ -\frac{\ddot{u}}{l} \end{pmatrix},$$

$$u(t) = \Gamma[u_0, h]x(t), \quad \ddot{x} = k\mathrm{sign}(\alpha\varphi + \omega),$$

$$\varphi(0) = \varphi_0, \quad \dot{\varphi}(0) = \omega(0) = \omega_0.$$

The eigenvalues of the matrix V are B and $-B$ so that the corresponding eigenvectors are $\begin{pmatrix} 1 \\ B \end{pmatrix}$ and $\begin{pmatrix} -1 \\ B \end{pmatrix}$, respectively. Here, it should be noted that if the phase coordinates of the system under consideration at some time moment will be placed on the line $B\varphi + \omega = 0$, then in the future (in the next time moments), in the absence of control, the phase coordinates will asymptotically tend to zero. Therefore, the control should be arranged (on the conceptual level) in such a manner as to "preserve" the phase coordinates in the vicinity of this line.

On each of the interval where the function $\ddot{u}$ is constant the system (28) can be solved and the result is:

$$\begin{pmatrix} \varphi(t) \\ \omega(t) \end{pmatrix} = \Lambda(t) \begin{pmatrix} \varphi_0 \\ \omega_0 \end{pmatrix} + \ddot{u}_0 \upsilon(t). \tag{29}$$

Here

$$\Lambda(t) = \begin{pmatrix} \cosh Bt & \frac{1}{B}\sinh Bt \\ B\sinh Bt & \cosh Bt \end{pmatrix}$$
$$\upsilon(t) = \begin{pmatrix} -\frac{1}{g}(\cosh Bt - 1) \\ -\frac{B}{g}\sinh Bt \end{pmatrix}, \tag{30}$$

φ_0 and ω_0 are initial deviation and frequency of the pendulum respectively, $\ddot{u}_0$ is an acceleration of the cylinder on the interval where the function $\ddot{u}$ is constant.

The behavior of the system (29) on the whole time interval can be represented by the following recurrent relation:

$$\begin{pmatrix} \varphi_k(t) \\ \omega_k(t) \end{pmatrix} = \Lambda(t - t_{k-1}) \begin{pmatrix} \varphi_{t_{k-1}} \\ \omega_{t_{k-1}} \end{pmatrix} + \ddot{u}_{t_{k-1}} \upsilon(t - t_{k-1}). \tag{31}$$

Here t_k are the moments at which the control changes, $\varphi_{t_{k-1}}$ and $\omega_{t_{k-1}}$ are the values of angle and angle velocity at the moment t_{k-1}, respectively, and $\ddot{u}_{t_{k-1}}$ is an acceleration of the cylinder on the interval $[t_{k-1}, t_k]$.

3.3.2 Dissipative Motion

The (24) is called *dissipative* if there exists a limited domain Ω on the product of the phase space of the system (28) and the state space of the hysteretic converter (25) that for any initial values $(\varphi_0, \omega_0, u) \in \Omega$, the solutions of the (24) remain uniformly limited. In other words, this system is called *dissipative* if there exists a region in the phase space and matching region in the state space of the hysteretic converter that the solution which began in this region do not go to infinity.

Let us formulate the following theorem:

Theorem 1 *The sufficient condition for existence of the dissipative regime of the pendulum's motion in a vicinity of the upper position is:*

$$e^{B\tau}\ |B\varphi_0 + \omega_0| \leqslant \left|\frac{kB}{g}\right|, \tag{32}$$

where $\tau = \sqrt{\frac{2h}{k}}$ *is the time for which the piston passes through the cylinder.*

Proof As is followed from the (31), the movement of the phase parameters on the line $B\varphi + \omega = 0$ (such a line corresponds to stabilization of the system) occurs during the time t:

$$t = \frac{1}{B}\ln\left(\frac{-\frac{Bk}{g}}{B\varphi_0 + \omega_0 - \frac{Bk}{g}}\right). \tag{33}$$

Let the piston passes through the cylinder during the time τ. Then, the phase parameters of a pendulum are:

$$B\varphi_\tau + \omega_\tau = e^{B\tau}(B\varphi_0 + \omega_0). \tag{34}$$

After substitution of (34) into (33) one gets:

$$t = \frac{1}{B}\ln\left(\frac{-\frac{Bk}{g}}{e^{B\tau}(B\varphi_0 + \omega_0) - \frac{Bk}{g}}\right).$$

This equation has a real value if

$$\frac{-\frac{Bk}{g}}{e^{B\tau}(B\varphi_0 + \omega_0) - \frac{Bk}{g}} > 0,$$

or

$$e^{B\tau}|B\varphi_0 + \omega_0| < \left|\frac{Bk}{g}\right|.$$

Let us note that the inequality (32) determines the stability zones of the system under consideration.

3.4 Non-ideal Relay in Feedback

As is known, the measuring devices of any mechanical systems do not always work perfectly. So, let us consider the problem stabilization of the inverted pendulum in the case when the uncertainty in the control takes place. Let us assume that this uncertainty is fixed, then the acceleration of the suspension point (control parameter) corresponds to the output state of the non-ideal relay converter:

$$\begin{aligned} y(t) &= B\varphi(t) + \omega(t), \\ \ddot{u} &= kR\left[-\varepsilon, \varepsilon, \operatorname{sign}(\ddot{u}(t_0)), y_0\right] y(t), \end{aligned} \tag{35}$$

where $\varepsilon > 0$. Detailed description of this converter is given in [21].

The parameter ε can be considered as an uncertainty in the measurement of the value $B\varphi + \omega$. Let us assume also that the following inequality takes place:

$$\varepsilon < \frac{kB}{g}.$$

Otherwise the stabilization of the pendulum can not be observed.

Dynamics of the system with non-ideal relay in the feedback described by the equations:

$$\begin{gathered}\begin{pmatrix}\dot{\varphi}\\ \dot{\omega}\end{pmatrix} = V\begin{pmatrix}\varphi\\ \omega\end{pmatrix} + W,\\ \ddot{u} = kR\left[-\varepsilon, \varepsilon, \operatorname{sign}\left(\ddot{x}(t_0)\right), y_0\right] y(t),\\ \varphi(0) = \varphi_0,\ \ \omega(0) = \omega_0\end{gathered} \tag{36}$$

Let us assume that at initial time $y(t_0) = \varepsilon$. The time for which the phase coordinates of the system (30) under influence of the control will move to the position $y(t_c) = -\varepsilon$ can be found using the following expressions:

$$-\varepsilon = y(t_c);$$

$$-\varepsilon = \begin{pmatrix} B & 1\end{pmatrix} \Lambda(t_c)\begin{pmatrix}\varphi_0\\ \omega_0\end{pmatrix} + \begin{pmatrix} B & 1\end{pmatrix} k\upsilon(t_c); \tag{37}$$

$$-\varepsilon = e^{Bt_c}\varepsilon - \frac{kB}{g}\left(e^{Bt_c} - 1\right);$$

$$t_c = \frac{1}{B}\ln\left(\frac{\frac{kB}{g} + \varepsilon}{\frac{kB}{g} - \varepsilon}\right). \tag{38}$$

A similar result takes place if $y(t_0) = -\varepsilon$. Thus, the total period of the control (35) is $T = 2t_c$ and $y(2t_c) = y(t_0) = \varepsilon$. If $y(t_0) \neq \varepsilon$ and $y(t_0) \neq -\varepsilon$, then for a finite time the phase coordinates of the system (under the control (35)) will move to the position $y(t) = \varepsilon$ or $y(t) = -\varepsilon$.

Using the results presented above we can consider the question on the asymptotical (Lyapunov) stability of solutions of the system (36). We can formulate the following theorem:

Theorem 2 *The system (36) has an asymptotically (Lyapunov) stable solution in the form of closed loop:*

$$\begin{pmatrix}\varphi(\theta)\\ \omega(\theta)\end{pmatrix} = \begin{pmatrix}\cosh B\theta & \frac{1}{B}\sinh B\theta\\ B\sinh B\theta & \cosh B\theta\end{pmatrix}\begin{pmatrix}0\\ \varepsilon\end{pmatrix} + \begin{pmatrix}-\frac{k}{g}(\cosh B\theta - 1)\\ -\frac{Bk}{g}\sinh B\theta\end{pmatrix}, \tag{39}$$

at $0 \leqslant \theta < t_c$,

$$\begin{pmatrix}\varphi(\theta)\\ \omega(\theta)\end{pmatrix} = \begin{pmatrix}\cosh B\theta & \frac{1}{B}\sinh B\theta\\ B\sinh B\theta & \cosh B\theta\end{pmatrix}\begin{pmatrix}0\\ -\varepsilon\end{pmatrix} + \begin{pmatrix}\frac{k}{g}(\cosh B\theta - 1)\\ \frac{Bk}{g}\sinh B\theta\end{pmatrix}, \tag{40}$$

at $t_c \leqslant \theta \leqslant 2t_c$ *with the attraction domain for solution* $|B\varphi_0 + \omega_0| \leqslant \left|\frac{kB}{g}\right|$.

Proof In order to prove this theorem it is needed to validate that for any initial conditions from the attraction region the following relations will take place:

$$\lim_{n\to\infty} |y(nt_c)| = \varepsilon, \tag{41}$$

$$\lim_{n\to\infty} \varphi(nt_c) = 0. \tag{42}$$

It is evident that the condition (41) is executed for any n (this fact can be proved by a direct substitution). The condition (42) for $\varphi(nt_c)$ determines by the following equality (this equality can be obtained by a simple but cumbersome calculations):

$$\varphi(nt_c) = \left(\frac{1}{1+\frac{k}{g}}\right)^n \varphi_0 .$$

Of course,

$$\lim_{n\to\infty} \left(\frac{1}{1+\frac{k}{g}}\right)^n = 0.$$

As an illustration of this result, in the Fig. 12 we present the phase portrait of the system (36). The simulation parameters are: $m = 1\,\text{kg}$, $k = 0.2\,\text{m}\cdot\text{s}^{-2}$, $g = 9.8\,\text{m}\cdot\text{s}^{-2}$, $l = 0.3\,\text{m}$, $\varepsilon = 0.02\,\text{s}^{-1}$, $\varphi_0 = -0.01$, $\omega_0 = 0.0771\,\text{s}^{-1}$.

The case when measuring devices have the random uncertainty in the measurements (desynchronization in the control) is of particular interest. Our numerical experiments show that increasing of the simulation time leads to the fact that the

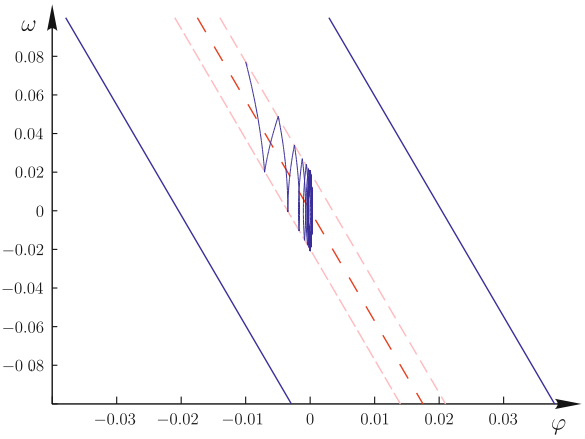

Fig. 12 Phase portrait of the system (36). *Blue straight lines* limit the zone of dissipative motion; *pink lines* are $B\varphi + \omega = \varepsilon$ and $B\varphi + \omega = -\varepsilon$; *red line* is $-B\varphi + \omega = 0$. Simulation parameters are $k = 0.2\,\text{m}\cdot\text{s}^{-2}$, $g = 9.8\,\text{m}\cdot\text{s}^{-2}$, $l = 0.3\,\text{m}$, $\varepsilon = 0.02\,\text{s}^{-1}$, $\varphi_0 = -0.01$, $\omega_0 = 0.0771\,\text{s}^{-1}$

probability of the stabilization of the system decreases and tends to zero. This means that the pendulum can not save upright position under desynchronization.

3.5 Optimal Control

In many technical problems the question on stabilization has a general interest. However, together with the stabilization of the system there is the problem of optimal control (this problem corresponds to asymptotically optimal characteristics of the system). In the considered problem of stabilization of the inverted pendulum the problem of optimal control corresponds to minimizing of the functional which determines the deviation of the pendulum from the vertical position. Let us consider a functional (the so-called objective functional) as follows:

$$\mathfrak{J} = \frac{1}{2T} \int_{t_0}^{T} \left(\varphi^2 + \gamma \omega^2 \right) \mathrm{d}t. \tag{43}$$

When the equations describing the dynamics of the system (23) are executed it is necessary to achieve the minimization of the functional (43). Let us note also that the law of stabilization should be sought only in the set of functions that stabilize the system (28), i.e., when the following phase restrictions take place:

$$|B\varphi(t) + \omega(t)| \leqslant \left| \frac{Bk}{g} \right|. \tag{44}$$

Solution of the posed problem can be expressed in the form of the following *theorem on the optimal control of the pendulum*:

Theorem 3 *Let a system of (28) is given together with the initial conditions that correspond to a dissipative regime of motion of the pendulum. Then, under the control (25), the functional (43) will be minimized, and the trajectory of the pendulum* $\begin{pmatrix} \varphi \\ \omega \end{pmatrix}$ *will lie entirely in the dissipativeness region in a vicinity of the upper position (44).*

The proof of this theorem is based on the Pontryagin's maximum principle as well as on the analysis of a zero-dynamics set [31].

Here we would like to note that the law of optimal control (following the presented theorem), moves the phase coordinates of the system (28) to the position $y(t) = 0$, and then stops. Such a control stabilizes the pendulum in the upper position. But, it is absolutely clear that in real systems it is difficult to get such a position, so it is necessary to consider the problem of finding the optimal control in another way.

One way of finding the optimal control is based on the assumption that the measuring instruments (in most cases) laid "errors" (or, uncertainties) and, thus, the switching of control is based on the principle of non-ideal relay.

4 Elastic Inverted Pendulum Under Hysteretic Nonlinearity: Stabilization and Optimal Control

4.1 Elastic Inverted Pendulum

4.1.1 Problem

Let us consider the model of stabilization of inverted pendulum in the vicinity of vertical position. The pendulum is considered as an elastic rod which is hingedly fixed on the cylinder. Motion of cylinder is excited by the horizontal motion of a piston (see Fig. 13).

Mathematical model of a similar mechanical system was considered in [48]. Investigation of dynamics of an elastic inverted pendulum was carried out in [12, 13, 25, 46].

Here (x, y) is an inertial base of an elastic rod with mass m and density ρ; the Ox axis coincides with a tangent to rod's profile in the suspension point; θ is an angle of slope for the co-ordinates of a rod, I is a centroidal moment of inertia of the rod's section; $(X, \bar{x})$ is a co-ordinates of a considered mechanical system, M is a mass of a cylinder with length L, F is a force joined to a piston with mass m_p (such a force is treated as control).

The purpose of this section is the investigation of the possible stabilization (in a vicinity of vertical position) of elastic inverted pendulum in the presence of backlash in a suspension point together with investigation of various aspect of such a dynamical system.

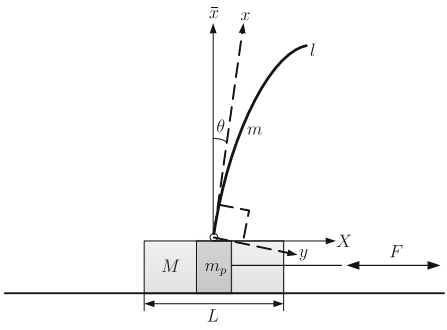

Fig. 13 Model of elastic inverted pendulum: geometry of the problem

4.1.2 Hysteretic Nonlinearity

As previously (see the Sect. 3.2), we consider the hysteretic nonlinearity using operator technique of Krasnosel'skii and Pokrovskii [21]. Namely, output of the backlash-inverter on the monotonic inputs can be described by the following expression:

$$X(t) = \Gamma[X_0, L]Y(t) = \begin{cases} 0, & |Y(t) - X_0| \leqslant \frac{L}{2}; \\ Y(t) - \frac{L}{2}, & Y(t) - X_0 > \frac{L}{2}; \\ Y(t) + \frac{L}{2}, & Y(t) - X_0 < -\frac{L}{2}; \end{cases}$$

As is noted above, using special limit construction and semigroup identity the Γ-operator can be applied to all continuous inputs.

4.1.3 Physical Model

Let us assume that the deviation y and angle θ are small, i.e., $x \approx \bar{x}$ and the boundary conditions that determine the curvature of the pendulum are[5]:

$$\begin{cases} y(0,t) = y_{xx}(0,t) = 0, \\ y_{xx}(l,t) = y_{xxx}(l,t) = 0. \end{cases} \tag{45}$$

The function $X(\bar{x}, t)$ describes behavior of the pendulum's profile in time and shows deviation of the pendulum's points relative to vertical axis, $(X, \bar{x})$ are coordinates of the pendulum's profile, $X(0,t) = s(t)$ is a displacement of the suspension point in horizontal plane.

Coordinate system transformation in the matrix form is given by

$$\begin{pmatrix} X \\ \bar{x} \end{pmatrix} = \begin{pmatrix} \cos\theta & \sin\theta \\ -\sin\theta & \cos\theta \end{pmatrix} \begin{pmatrix} y \\ x \end{pmatrix} + \begin{pmatrix} X(0,t) \\ 0 \end{pmatrix}. \tag{46}$$

Let us construct the physical model of the considered mechanical system taking into account the backlash in the suspension point of an elastic rod. In order to do this we use the Lagrange formalism, i.e., we analyze relation between the kinetic and potential energies in this system.

Taking into account that y and θ are small the Lagrange function can be written as:

[5]Here we use the following notations: $a_x = \frac{\partial a}{\partial x}, a_t = \frac{\partial a}{\partial t}$.

$$L(t) = \frac{Ms_t^2}{2} + \frac{1}{2}\int_0^l \left[\rho s_t^2 + \rho y_t^2 + \rho(x\theta_t)^2 + \rho(2s_t x\theta_t + 2x\theta_t y_t + 2s_t y_t) + 2\rho g y\theta - EIy_{xx}^2\right] \mathrm{d}x. \tag{47}$$

We can integrate the (47) in the interval (t_0, t_f) and obtain the action function:

$$W = \frac{1}{2}\int_{t_0}^{t_f} Ms_t^2 \mathrm{d}t + \frac{1}{2}\int_{t_0}^{t_f}\int_0^l \left[\rho\left(s_t^2 + y_t^2 + x^2\theta_t^2 + 2s_t x\theta_t + 2x\theta_t y_t + 2s_t y_t + 2gy\theta\right) - \frac{EI}{\rho}y_{xx}^2\right] \mathrm{d}x\mathrm{d}t. \tag{48}$$

Using the variational principle and using Taylor's expansion we obtain the following equation:

$$y_{tt} + \frac{EI}{\rho}y_{xxxx} = -s_{tt} - x\theta_{tt} + g\theta. \tag{49}$$

Taking θ as the generalized coordinate in the Lagrange function we obtain:

$$\frac{\mathrm{d}}{\mathrm{d}t}\frac{\partial L}{\partial \theta_t} - \frac{\partial L}{\partial \theta} = 0. \tag{50}$$

Substitution of (47) in (50) gives:

$$\int_0^l x\left(x\theta_{tt} + y_{tt} + s_{tt}\right) \mathrm{d}x = g\int_0^l y \mathrm{d}x. \tag{51}$$

Taking into account (49) we have

$$\int_0^l x\left(g\theta - \frac{EI}{\rho}y_{xxxx}\right) \mathrm{d}x = g\int_0^l y \mathrm{d}x. \tag{52}$$

or

$$\frac{gl^2\theta}{2} - \frac{EI}{\rho}\int_0^l x y_{xxxx} \mathrm{d}x = g\int_0^l y \mathrm{d}x. \tag{53}$$

Using the initial conditions (45) we can show that the integral in the left part of (53) is equal to zero. Then, multiplying both parts of this equality by $\frac{\rho}{g}$ we obtain

$$\frac{ml\theta}{2} = \rho \int_0^l y \mathrm{d}x. \tag{54}$$

Integrating (49) and multiplying by ρ we have

$$\begin{gathered} \rho \int_0^l \left(y_{tt} + \frac{EI}{\rho} y_{xxxx} \right) \mathrm{d}x = \rho \int_0^l \left(-s_{tt} - x\theta_{tt} + g\theta \right) \mathrm{d}x, \\ EI \left[y_{xxx}(l,t) - y_{xxx}(0,t) \right] + \rho \int_0^l y_{tt} \mathrm{d}x = -s_{tt}\rho l - \frac{\rho l^2 \theta_{tt}}{2} + \rho g l \theta. \end{gathered} \tag{55}$$

Taking into account the relations $\rho l = m$, $y_{xxx}(l,t) = 0$ (from initial conditions), and using

$$\rho \int_0^l y_{tt} \mathrm{d}x = \frac{ml\theta_{tt}}{2},$$

which follows from (54), we have the following equation:

$$ml\theta_{tt} + ms_{tt} = mg\theta + EIy_{xxx}(0,t). \tag{56}$$

In the next step, taking s as the generalized coordinate in the Lagrange function we obtain:

$$\frac{\mathrm{d}}{\mathrm{d}t} \frac{\partial L}{\partial s_t} - \frac{\partial L}{\partial s} = f(t). \tag{57}$$

Here $f(t)$ is a force joined to the suspension point of a rod.

General peculiarity of the system under consideration is the presence of backlash in the suspension point. Due to the fact that the backlash can be considered as a hysteretic nonlinearity we can use the technique of hysteretic converters. As was mentioned above, according to classical patterns of Krasnosel'skii and Pokrovskii [21], the hysteretic operators are treated as converters in an appropriate function spaces. The dynamics of such converters are described by the relation of "input-state" and "state-output".

Thus, the force joined to suspension point can be found from the relation:

$$f(t) = \Gamma \left[X(0,t), Y(t), L, F_0 \right] F = \begin{cases} 0, & |X(0,t) - Y(t)| \leqslant L; \\ F, & |X(0,t) - Y(t)| > L, \end{cases} \tag{58}$$

where L is the length of a cylinder, F is a force (this force affects the piston) which can be treated as a control.

The equation of motion of piston is:

$$m_p Y_{tt}(t) = F. \tag{59}$$

Here Y is a displacement of the piston in a horizontal plane.

Substitution of (47) in (57) gives the following:

$$Ms_{tt} + \rho \int_0^l (s_{tt} + x\theta_{tt} + y_{tt})\,\mathrm{d}x = f(t). \tag{60}$$

Using (49) we obtain

$$Ms_{tt} + \rho \int_0^l \left(g\theta - \frac{EI}{\rho} y_{xxxx}\right)\mathrm{d}x = f(t). \tag{61}$$

Making the same transformations as in (55), we obtain the following equality:

$$Ms_{tt} = f(t) - mg\theta - EIy_{xxx}(0,t). \tag{62}$$

Thus, we have the following system of equations:

$$\begin{cases} ml\theta_{tt} + ms_{tt} = mg\theta + EIy_{xxx}(0,t), \\ Ms_{tt} = f(t) - mg\theta - EIy_{xxx}(0,t). \end{cases} \tag{63}$$

Passing to coordinate system $(X, \bar{x})$, the system of equation which describes the physical model of the considered mechanical system will have the following form:

$$\begin{cases} X_{tt} + \dfrac{EI}{\rho} X_{xxxx} = gX_x(0,t), \\ MX_{tt}(0,t) = f(t) - mgX_x(0,t) - EIX_{xxx}(0,t), \\ ml(X_{tt})_x(0,t) + mX_{tt}(0,t) = mgX_x(0,t) + EIX_{xxx}(0,t), \\ f(t) = \Gamma\left[X(0,t), Y(t), L, F_0\right]F, \\ m_p Y_{tt}(t) = F, \end{cases} \tag{64}$$

where $X = X(x,t)$, due to $\bar{x} \approx x$.

Let us express $X_{tt}(0,t)$ from the first equation of the system and substitute it into the second equation:

$$g(M+m)X_x(0,t) - \frac{MEI}{\rho}X_{xxxx} + EIX_{xxx} = f(t). \tag{65}$$

Let us integrate the (65) over x, the result is

$$g(M+m)X(0,t) - \frac{MEI}{\rho}X_{xxx} + EIX_{xx} = \int_0^l f(t)\mathrm{d}x = lf(t). \tag{66}$$

Taking into account (45) we have:

$$g(M+m)X(0,t) - \frac{MEI}{\rho}X_{xxx} = lf(t). \tag{67}$$

Finally, the system of equations that describes the dynamics of the system under consideration has the following form:

$$\begin{cases} X_{tt} + \dfrac{EI}{\rho}X_{xxxx} = gX_x(0,t), \\ MX_{tt}(0,t) + mgX_x(0,t) + EIX_{xxx}(0,t) = f(t), \\ (M+m)X_{tt}(0,t) + ml(X_{tt})_x(0,t) = f(t), \\ g(M+m)X(0,t) - \dfrac{MEI}{\rho}X_{xxx} = lf(t), \\ f(t) = \Gamma\left[X(0,t), Y(t), L, F_0\right]F, \\ m_p Y_{tt}(t) = F. \end{cases} \tag{68}$$

4.1.4 Stabilization

Let us consider the problem of control of the pendulum using the feedback principles, i.e., the force which affects the piston can be presented by the following equality:

$$F = k\,\mathrm{sign}(\alpha e_1 + e_2), \tag{69}$$

where $\alpha > 0,\ k > 0$ and

$$e_1 = \int_0^l X_x \mathrm{d}l, \tag{70}$$

$$e_2 = \int_0^l (X_t)_x \mathrm{d}l. \tag{71}$$

Here e_1 is an average angle of rod's deviation, e_2 is an average angular velocity of the rod.

Thus, in order to solve the stabilization problem for the elastic inverted pendulum we should use the system of (68) together with the equalities (69)–(71):

$$\begin{cases} X_{tt} + \dfrac{EI}{\rho} X_{xxxx} = g X_x(0,t), \\ M X_{tt}(0,t) + mg X_x(0,t) + EI X_{xxx}(0,t) = f(t), \\ (M+m) X_{tt}(0,t) + ml (X_{tt})_x(0,t) = f(t), \\ g(M+m) X(0,t) - \dfrac{MEI}{\rho} X_{xxx} = lf(t), \\ f(t) = \Gamma\,[X(0,t), Y(t), L, F_0]\, F, \\ m_p Y_{tt}(t) = F, \\ F = k\,\mathrm{sign}(\alpha e_1 + e_2), \\ e_1 = \displaystyle\int_0^l X_x \mathrm{d}l, \\ e_2 = \displaystyle\int_0^l (X_t)_x \mathrm{d}l. \end{cases} \tag{72}$$

The solution of the posed problem on stabilization of elastic inverted pendulum in the vicinity of the upper position is consisted in search of the optimal values for coefficients α and k.

4.2 Numerical Realization

4.2.1 Difference Scheme

Let us introduce the rectangular lattice. To do so, let we cross the domain of function $X = X(x, t)$ by the net of straight lines that are parallel to coordinate axis (see Fig. 14).

It is evident that the value of $X(x, t)$ in the knots of presented lattice is:

$$X_{i,j} = X(ih_{\mathrm{x}}, jh_{\mathrm{t}}), \tag{73}$$

where h_x is the step of a lattice by the x axis, h_t is the step of a lattice by the t axis, $i = \overline{0, n}$, $j = \overline{0, m}$, $h_x = \frac{L}{n}$, $h_t = \frac{T}{m}$, T is the time interval for calculation of the single iteration by time.

For the calculation of derivatives we can use the right finite difference:

$$X_x(x, t) \approx \frac{X_{i+1,j} - X_{i,j}}{h_{\mathrm{x}}}, \tag{74}$$

$$X_t(x, t) \approx \frac{X_{i,j+1} - X_{i,j}}{h_{\mathrm{t}}}. \tag{75}$$

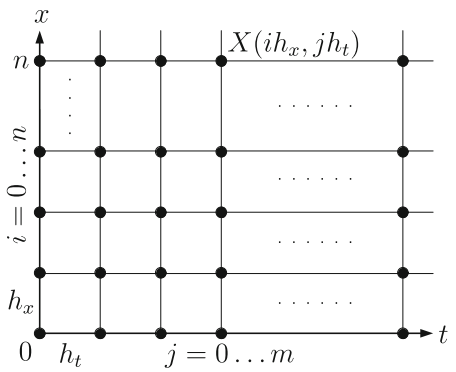

Fig. 14 Rectangular lattice which corresponds to domain of function $X(x, t)$

Then the system (72) in the finite differences will have the following form:

$$
\begin{cases}
\dfrac{X_{i,j+2} - 2X_{i,j+1} + X_{i,j}}{h_{\mathrm{t}}^2} \\
+\dfrac{EI}{\rho}\dfrac{6X_{i+2,j} - 4X_{i+1,j} - 4X_{i+3,j} + X_{i+4,j} + X_{i,j}}{h_{\mathrm{x}}^4} = g\dfrac{X_{1,j} - X_{0,j}}{h_{\mathrm{x}}}, \\
M\dfrac{X_{0,j+2} - 2X_{0,j+1} + X_{0,j}}{h_{\mathrm{t}}^2} + mg\dfrac{X_{1,j} - X_{0,j}}{h_{\mathrm{x}}} \\
+EI\dfrac{3X_{1,j} - 3X_{2,j} + X_{3,j} - X_{0,j}}{h_{\mathrm{x}}^3} = f_j, \\
(M+m)\dfrac{X_{0,j+2} - 2X_{0,j+1} + X_{0,j}}{h_{\mathrm{t}}^2} \\
+ml\dfrac{2X_{0,j+1} - X_{0,j+2} - 2X_{1,j+1} + X_{1,j+2} - X_{0,j} + X_{1,j}}{h_{\mathrm{t}}^2 h_{\mathrm{x}}} = f_j, \\
g(M+m)X_{0,j} - \dfrac{MEI}{\rho}\dfrac{3X_{1,j} - 3X_{2,j} + X_{3,j} - X_{0,j}}{h_{\mathrm{x}}^3} = f_j h_{\mathrm{x}}, \\
f_j = \Gamma\left[X_{0,j}, Y_j, L, F_0\right] F_j, \\
m_p\dfrac{Y_{j+2} - 2Y_{j+1} + Y_j}{h_{\mathrm{t}}^2} = F_j, \\
F_j = k\,\mathrm{sign}(\alpha e_{1j} + e_{2j}), \\
e_{1j} = \sum\limits_{i=0}^{n}\left(X_{i+1,j} - X_{i,j}\right), \\
e_{2j} = \sum\limits_{i=0}^{n}\dfrac{X_{i,j} - X_{i,j+1} - X_{i+1,j} + X_{i+1,j+1}}{h_{\mathrm{t}}},
\end{cases}
\tag{76}
$$

together with the initial conditions, i.e., the angle, linear and angular velocities:

Fig. 15 Calculation scheme

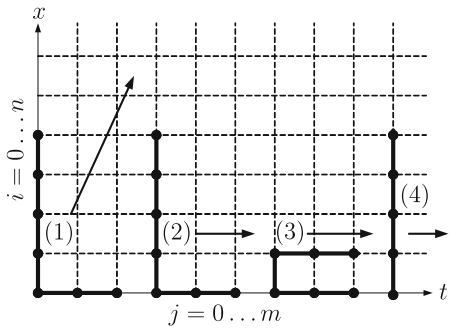

$$\begin{cases} \dfrac{X_{1,0} - X_{0,0}}{h_{\mathrm{x}}} = \varphi, \\ \dfrac{X_{0,1} - X_{0,0}}{h_{\mathrm{t}}} = V, \\ \dfrac{X_{0,0} - X_{0,1} - X_{1,0} + X_{1,1}}{h_{\mathrm{t}} h_{\mathrm{x}}} = V_{\varphi}, \\ \dfrac{X_{2,j} - 2X_{1,j} + X_{0,j}}{h_{\mathrm{x}}^2} = 0. \end{cases} \tag{77}$$

On the basis of (76) and (77) we can obtain the explicit difference scheme. In Fig. 15 we show all the knots of a net that are took part in the solution of system (72) on the each consequent iteration together with the direction of calculation. In brackets we show the number of equation in the system (76).

In the next step we would like to construct the algorithm for solution of (72) taking into account the explicit difference scheme (76) together with the initial conditions (77).

4.2.2 Algorithm

The algorithm contains two stage of calculations: the forward and inverse stages. In the forward stage we compute the lower four layers by i, i.e., the values of $X_{i,j}$, where $i = \overline{0,3}$, $j = \overline{0,m}$. In the inverse stage we compute the residuary layers, i.e., $X_{i,j}$, where $i = \overline{4,n}$, $j = \overline{0,m}$. At the same time, in order to find the position of the rod's profile at the present time moment it is enough to find the values of $X_{i,j}$ in the region bordered by a triangle (see Fig. 16). In other words, we need to organize the net with $n = 2m$ for the comfortable simulations.

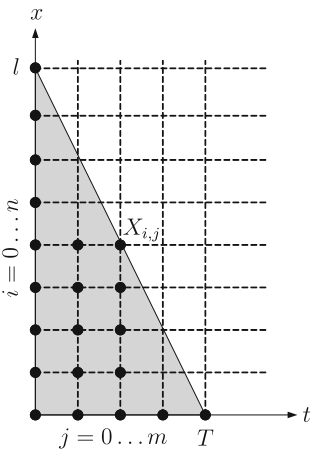

Fig. 16 Domain of calculations

The algorithm:

1. Let us assign the parameters of system $m,\ M,\ l,\ I,\ E,\ \rho$;
2. Let us assign the initial conditions $X_{0,0},\ Y_0,\ \varphi,\ V,\ V_\varphi$;
3. Let us assign the parameters of difference schema $n,\ m,\ h_\mathrm{x},\ h_\mathrm{t}$;
4. Let us assign the parameters of control $F_0,\ \alpha,\ k$.
5. ***Forward stage:*** From the initial conditions (77) and fourth equation of the system (76) we find:

$$f_j = \Gamma\left[X_{0,j}, Y_j, L, F_0\right] F;$$

$$\begin{aligned}
&j = 0,\\
&X_{1,0} = \varphi h_\mathrm{x} + X_{0,0},\\
&X_{2,j} = 2X_{1,j} - X_{0,j},\\
&X_{3,j} = \left[(M+m)gX_{0,j} - f_j h_\mathrm{x}\right]\frac{\rho h_\mathrm{x}^3}{MEI} + 3X_{2,j} + X_{0,j} - 3X_{1,j};
\end{aligned}$$

$$\begin{aligned}
&j = 1,\\
&X_{0,1} = V h_\mathrm{t} + X_{0,0},\\
&X_{1,1} = V_\varphi h_\mathrm{t} h_\mathrm{x} - X_{0,0} + X_{0,1} + X_{1,0},\\
&X_{2,j} = 2X_{1,j} - X_{0,j},\\
&X_{3,j} = \left[(M+m)gX_{0,j} - f_j h_\mathrm{x}\right]\frac{\rho h_\mathrm{x}^3}{MEI} + 3X_{2,j} + X_{0,j} - 3X_{1,j};
\end{aligned}$$

6. Let us calculate the residuary points at $i = \overline{0,3},\ j = \overline{0,m}$:

$$
\begin{aligned}
&j = 0 \ldots (m-2),\\
&Y_{j+2} = \frac{F h_{\mathrm{t}}^2}{m_p} + 2Y_{j+1} - Y_j,\\
&f_j = \Gamma\left[X_{0,j}, Y_j, L, F_0\right] F,
\end{aligned}
$$

$$
\begin{aligned}
X_{0,j+2} = {} & \frac{h_{\mathrm{t}}^2}{M}\left(f_j - mg\frac{X_{1,j} - X_{0,j}}{h_{\mathrm{x}}} - EI\frac{3X_{1,j} - 3X_{2,j} + X_{3,j} - X_{0,j}}{h_{\mathrm{x}}^3}\right)\\
& + 2X_{0,j+1} - X_{0,j},
\end{aligned}
$$

$$
\begin{aligned}
X_{1,j+2} = {} & \frac{h_{\mathrm{t}}^2 h_{\mathrm{x}}}{ml}\left[f_j - (M+m)\frac{X_{0,j+2} - 2X_{0,j+1} + X_{0,j}}{h_{\mathrm{t}}^2}\right]\\
& + 2X_{0,j+1} + X_{0,j+2} + 2X_{1,j+1} + X_{0,j} - X_{1,j},
\end{aligned}
$$

$$
\begin{aligned}
&X_{2,j+2} = 2X_{1,j+2} - X_{0,j+2},\\
&X_{3,j+2} = \left[(M+m)gX_{0,j+2} - f_j h_{\mathrm{x}}\right]\frac{\rho h_{\mathrm{x}}^3}{MEI} + 3X_{2,j+2} + X_{0,j+2} - 3X_{1,j+2};
\end{aligned}
$$

7. ***Inverse stage:*** Let we find $X_{i,j}$ at $i = \overline{4,n},\ j = \overline{0,m}$:

$$
\begin{aligned}
X_{i+4,j} = {} & \left(g\frac{X_{1,j} - X_{0,j}}{h_{\mathrm{x}}} - \frac{X_{i,j+2} - 2X_{i,j+1} + X_{i,j}}{h_{\mathrm{t}}^2}\right)\frac{\rho h_{\mathrm{x}}^4}{EI}\\
& - 6X_{i+2,j} + 4X_{i+1,j} + 4X_{i+3,j} - X_{i,j};
\end{aligned}
$$

8. Let we redefine the initial parameters $X_{0,0},\ \varphi,\ V,\ V_\varphi$;
9. Let we redefine the control parameters

$$
e_1 = \sum_{i=0}^{n}\left(X_{i+1,0} - X_{i,0}\right),
$$

$$
e_2 = \sum_{i=0}^{n}\frac{X_{i,0} - X_{i,1} - X_{i+1,0} + X_{i+1,1}}{h_{\mathrm{t}}},
$$

$$
F = k\,\mathrm{sign}(\alpha e_1 + e_2);
$$

10. Let we turn to step 5.

As we can see from this algorithm, the numerical value of force F should be recalculated on each new time interval T.

4.3 Optimization

As was mentioned above, the solution of the problem on stabilization of elastic inverted pendulum in the vicinity of the upper position is consisted in search of the optimal values for coefficients α and k from the equality (69). In the system under consideration the problem of optimization corresponds to minimizing of the functional which determines the deviation of the pendulum from the vertical position. Let us consider an objective functional:

$$\Im = \frac{1}{T}\int_0^T \left\{ \int_0^l (X_x)^2 \mathrm{d}l + \int_0^l [(X_t)_x]^2 \mathrm{d}l \right\} \mathrm{d}t. \tag{78}$$

Here T is the time interval in which we find an optimal control.

Solution of the (72) that describe the dynamics of the system under consideration should be obtained under conditions that provides the minimization of functional (78). Physically this means that the problem is equivalent to minimization of mean-square deviation of the pendulum relative to vertical position.

In order to solve the optimization problem in the system under consideration, we use the bionic algorithms of adaptation because the hysteretic peculiarities in the considered pendulum's model lead to some difficulties in use of the classical optimization algorithms due to non-differentiability of the functions in the system of equations.

Such algorithms are a part of the line of investigation which can be called as "adaptive behavior". Main method of this line consists in the investigation of artificial organisms (in the form of computer program or a robot) that are called as animats (these animats can be adapted to environment). The behavior of animats emulates the behavior of animals.

One of the actual line of investigation in the frame of animat-approach is an emulation of searching behavior of animals [22, 33]. Let us consider the bionic model of adaptive searching behavior on the example of caddis flies larvae or *Chaetopteryx villosa*. Main schema of searching behavior can be characterized by two stages:

- Motion in a chosen direction (conservative tactics);
- Random change of the motion direction (stochastic searching tactics).

We consider this model for the simple case of maximum search for the function of two variables. Let we describe main stage of the considered model:

1. We consider an animat which is moved in the two-dimensional space x, y. Main purpose of animat is maximum search for the function $f(x, y)$.
2. Animat is functioned in discrete time $t = 0, 1, 2, \ldots$. Animat estimates the change of current value of $f(x, y)$ in comparison with the previous time $\Delta f(t) = f(t) - f(t-1)$.
3. Every time animat moves so its coordinates x and y change by $\Delta x(t)$ and $\Delta y(t)$ respectively.

4. Animat has two tactics of behavior: (a) conservative tactics; (b) stochastic searching tactics.

Displacement of animat in the next time $\Delta x(t+1)$, $\Delta y(t+1)$ for these tactics determines in a different ways. Switching between the cycles drives by $M(t)$. Time dependence of $M(t)$ can be determined using the equation:

$$M(t) = k_1 M(t-1) + \xi(t) + I(t), \tag{79}$$

where k_1 is a parameter which determines the switching persistence of tactics ($0 < k_1 < 1$), $\xi(t)$ is a normal distributed variate with an average value equal to zero and mean-square deviation equal to σ, $I(t)$ is an intensity of irritant. For the value of $I(t)$ there are two possibilities:

$$I(t) = k_2 \Delta f(t) \tag{80}$$

and

$$I(t) = k_2 \frac{\Delta f(t)}{f(t-1)}, \tag{81}$$

where $k_2 > 0$. As follows from (80) to (81) the intensity is positive when the step leads to increasing of function, otherwise the intensity is negative. It should be noted also that the (81) can be applied in the case $f(t) > 0$.

We assume that at $M(t) > 0$ animat follows the tactics (a) and at $M(t) < 0$ it follows tactics (b). So, the value of $M(t)$ can be considered as a motivation to selection of tactics (a).

Thus, the algorithm of maximum search can be considered as follows:

Tactics (a): Animat moves in the chosen direction. The displacement of animat is determined by R_0

$$\Delta x(t+1) = R_0 \cos\varphi_0, \tag{82}$$

$$\Delta y(t+1) = R_0 \sin\varphi_0, \tag{83}$$

where the angle φ_0 defines the constant direction of motion of animat:

$$\cos\varphi_0 = \frac{\Delta x(t)}{\sqrt{\Delta x^2 + \Delta y^2}}, \tag{84}$$

$$\sin\varphi_0 = \frac{\Delta y(t)}{\sqrt{\Delta x^2 + \Delta y^2}}. \tag{85}$$

Tactics (b): Animat makes an accidental turn. The displacement of animat is determined by r_0 but the direction of motion is accidentally varied

$$\Delta x(t+1) = r_0 \cos\varphi, \tag{86}$$

$$\Delta y(t+1) = r_0 \sin\varphi, \tag{87}$$

where $\varphi = \varphi_0 + w$, φ_0 is an angle which characterizes the direction of motion at current time t, w is a normal distributed variate (average value of w equal to zero and mean-square deviation equal to w_0), φ is an angle which characterizes the direction of motion at time $t + 1$.

In that way we can use the proposed algorithm for searching the optimal control in the problem of stabilization of elastic inverted pendulum. Taking into account the reasoning presented above we can apply the presented algorithm to functional $\mathfrak{J}(\alpha, k)$ where the coefficients α and k determine the character of control of the mechanical system under consideration following the (69). Due to the fact that the presented bionic algorithm is used to maximum search of the function of two variables we will consider minimization of functional (78) as a procedure for finding the coefficients α and k that lead to realization of the condition

$$-\mathfrak{J}(\alpha, k) \to \max. \tag{88}$$

4.4 Numerical Results

4.4.1 Elastic Inverted Pendulum

Now we can make a simulation of the behavior of elastic inverted pendulum using the corresponding difference scheme in the absence of backlash ($L = 0$). Using the bionic algorithm we can find the optimal values of coefficients α and k.

The characteristics and initial conditions for the mechanical system under consideration are:

$$m = 1\,\text{kg},\ M = 10\,\text{kg},\ l = 1\,\text{m},\ \rho = 0.5,\ E = 10,\ I = 4,\ \theta_0 = 0.06^\circ.$$

In the searching process for optimization using the bionic algorithm we have obtained the following values of the coefficients: $\alpha = 22.04$ and $k = 1.15$.

In order to estimate the stability of the system under consideration we use the Lyapunov criterion. Namely, we use the following Lyapunov function:

$$V = e_1^2 + e_2^2.$$

Phase trajectory of such a system together with the dynamics of Lyapunov function in time (in discrete time which corresponds to difference scheme) are presented in the Fig. 17. In this figure the integral angle e_1 and integral angular velocity e_2 correspond to (70) and (71), respectively.

In the Fig. 18 we present the phase trajectory and Lyapunov function for another values of α and k: $\alpha = 50$ and $k = 0.4$.

As we can see from presented figures the Lyapunov function satisfies the following condition (during all the considered time interval):

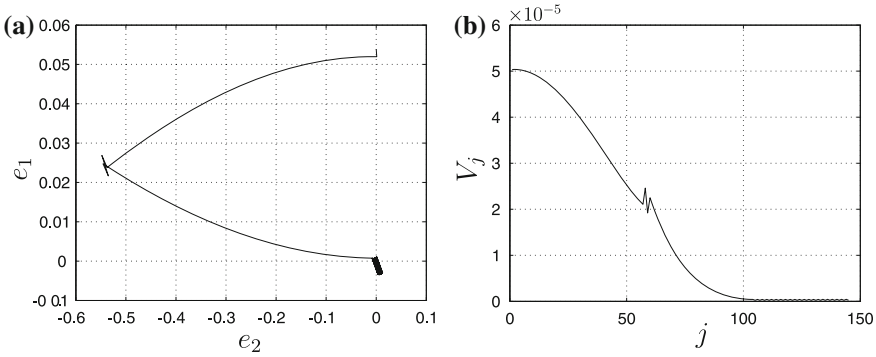

Fig. 17 Phase trajectory (*left panel*) and dynamics of Lyapunov function (*right panel*) in the absence of backlash ($L = 0$). The parameters are $\alpha = 22.04$ and $k = 1.15$

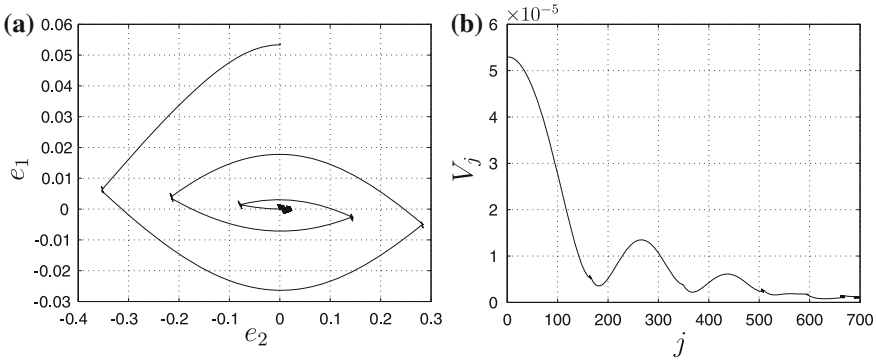

Fig. 18 The same as in Fig. 17 but for another values of parameters α and k, i.e., $\alpha = 50$ and $k = 0.4$

$$V(t) < \text{const.}$$

This means that the considered inverted pendulum eventually tends to stable vertical position.

4.5 Elastic Inverted Pendulum with Backlash in Suspension

Now, let we add the backlash in the suspension point of a considered mechanical system and let we investigate the behavior of such a system with the same parameters as in previous subsection. Using the bionic algorithm we have obtained the following optimal values of coefficients: $\alpha = 9$ and $k = 2$.

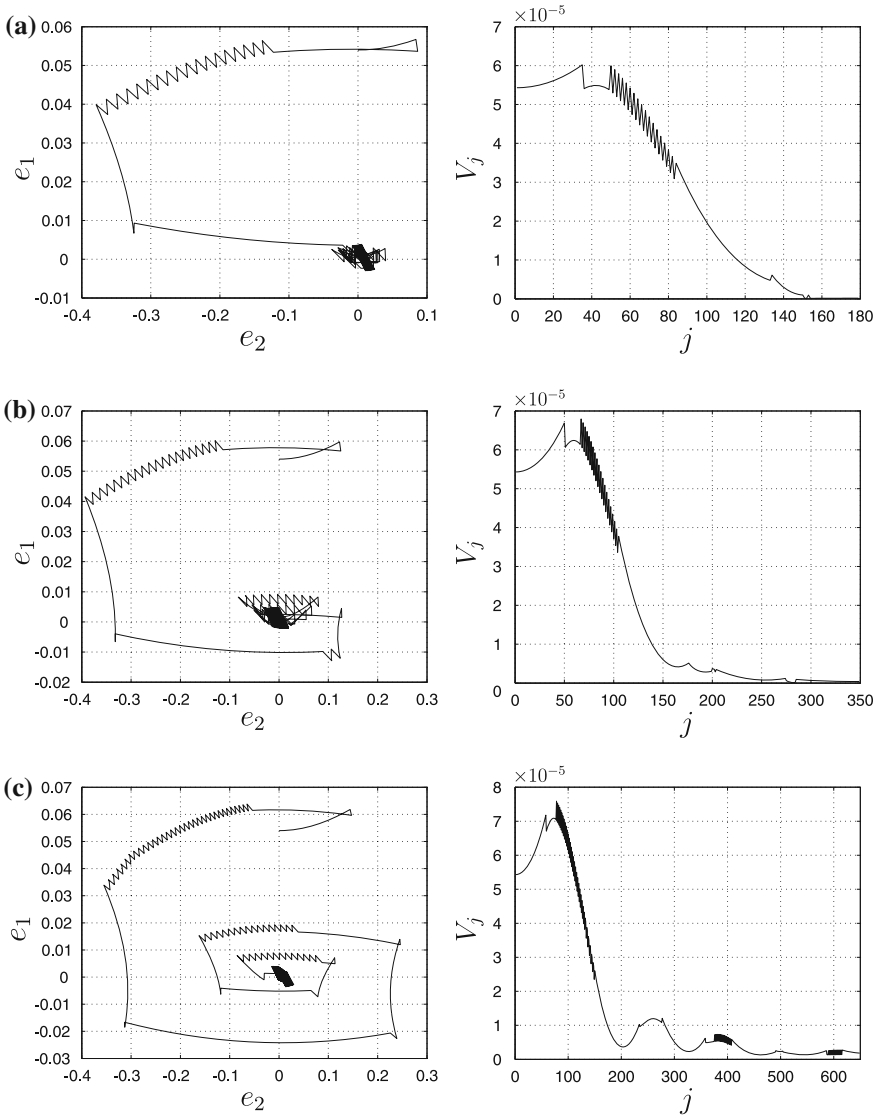

Fig. 19 Phase trajectories (*left panels*) and dynamics of Lyapunov function (*right panels*) in the presence of a backlash in suspension point. Parameters of a backlash and control coefficients are: (*a*) $L = 0.01$ m, $\alpha = 9$, $k = 2$; (*b*) $L = 0.02$ m, $\alpha = 9$, $k = 2$; (*c*) $L = 0.02$ m, $\alpha = 10.5$, $k = 1.5$

The mass of a piston is $m_p = 1$ kg. Main parameters of the system are the same as in previous section. The phase trajectories of such a system (as previously we use (e_1, e_2) coordinates) and dynamics of Lyapunov function for different values of a control coefficients are presented in Fig. 19.

As we can see from the presented figure (both from the phase trajectories and Lyapunov function) the considered system (at the same main parameters and different values of L and control coefficients α and k) also eventually tends to stable state.

5 Conclusions

In this work we have considered the problem of inverted pendulum under hysteretic control in the form of a backlash in suspension. In the first part of this work the explicit condition for the stability of such a system has been obtained using the monodromy matrix technique (for the monodromy matrix is also obtained the explicit expression). The periodic solutions in such a system is also analyzed and the corresponding equations for the parameters a and ω are obtained. Here it should be pointed out that the dynamics of the inverted pendulum with hysteretic control qualitatively differs from the dynamics of the pendulum with conventional control. The presence of the hysteresis element complicates the study of the dynamics of mechanical systems. As a result, the main results were obtained using the numerical simulations only.

In the second part of this work we have considered the mathematical model of the inverted pendulum with hysteretic nonlinearity under state feedback control. The obtained results not only accurately predict the behavior of a pendulum under hysteretic control, but also allow to determine the possibility of the dissipative motion in the vicinity of the top position. The existence of dissipative motion depends on the initial deviation of the pendulum's position as well as on the physical parameters of the system under consideration. Introduction of non-ideal relay in the state feedback control allows us to describe the periodic modes of the system (28). However, it should also be noted that the results obtained for the presence of non-ideal relay in the state feedback control can be used for description of real physical (and, in particular, mechanical) systems because the parameters of such systems can be measured with the inevitable uncertainties only. Also, our numerical experiments show that the presence of the backlash with nonzero step in the feedback control of inverted pendulum leads to dissipative motion only and asymptotic convergence to an upright position is fundamentally unattainable. We have also considered the question on the optimal control of the system under consideration. The theorem on the optimal control of pendulum has been formulated and discussed.

In the last part we investigate the stabilization problem of elastic inverted pendulum with a backlash in suspension point. Also the problem of optimization for the system under consideration is analyzed. Main coefficients that provide the solution of optimization problem for the considered system are obtained using the so-called bionic algorithm. All the numerical results on stabilization of the system under consideration have been obtained using the numerical method based on the difference scheme. The results of numerical simulations shown that the considered system eventually tends to stable state both in the case of the absence of backlash and in the case of its presence. These facts have been presented in the form of corresponding phase portraits for the considered system. Moreover, in order to estimate the stability of

elastic pendulum with hysteretic nonlinearity in the suspension point we have used the Lyapunov criterion and the dynamics of corresponding Lyapunov function has also been presented.

Acknowledgments This work is supported by the RFBR grant 13-08-00532-a.

References

1. Aguilar-Ibáñez, C., Mendoza-Mendoza, J., Dávila, J.: Stabilization of the cart pole system: by sliding mode control. Nonlinear Dyn. **78**, 2769–2777 (2014)
2. Arinstein, A., Gitterman, M.: Inverted spring pendulum driven by a periodic force: linear versus nonlinear analysis. Eur. J. Phys. **29**, 385–392 (2008)
3. Åström, K.J., Furuta, K.: Swinging up a pendulum by energy control. Automatica **36**, 287–295 (2000)
4. Bloch, A.M., Leonard, N.E., Marsden, J.E.: Controlled lagrangians and the stabilization of mechanical systems. I. The first matching theorem. IEEE Trans. Autom. Control **45**, 2253–2270 (2000)
5. Boubaker, O.: The inverted pendulum: a fundamental benchmark in control theory and robotics. In: International Conference on Education and e-Learning Innovations (ICEELI 2012), pp. 1–6 (2012)
6. Butikov, E.I.: Subharmonic resonances of the parametrically driven pendulum. J. Phys. A: Math. Theor. **35**, 6209 (2002)
7. Butikov, E.I.: An improved criterion for Kapitza's pendulum stability. J. Phys. A: Math. Theor. **44**, 295202 (2011)
8. Butikov, E.I.: Oscillations of a simple pendulum with extremely large amplitudes. Eur. J. Phys. **33**, 1555–1563 (2012)
9. Chang, L.H., Lee, A.C.: Design of nonlinear controller for bi-axial inverted pendulum system. IET Control Theor. Appl. **1**, 979–986 (2007)
10. Chaturvedi, N.A., McClamroch, N.H., Bernstein, D.S.: Stabilization of a 3d axially symmetric pendulum. Automatica **44**, 2258–2265 (2008)
11. Chernous'ko, F.L., Reshmin, S.A.: Time-optimal swing-up feedback control of a pendulum. Nonlinear Dyn. **47**, 65–73 (2007)
12. Dadfarnia, M., Jalili, N., Xian, B., Dawson, D.M.: A lyapunov-based piezoelectric controller for flexible cartesian robot manipulators. J. Dyn. Syst. Meas. Control **126**, 347–358 (2004)
13. Dadios, E.P., Fernandez, P.S., Williams, D.J.: Genetic algorithm on line controller for the flexible inverted pendulum problem. J. Adv. Comput. Intell. Intell. Inform. **10**, 155–160 (2006)
14. Hasan, M., Saha, C., Rahman, M.M., Sarker, M.R.I., Aditya, S.K.: Balancing of an inverted pendulum using pd controller. Dhaka Univ. J. Sci. **60**, 115–120 (2012)
15. Henders, M., Soudack, A.: Dynamics and stability state-space of a controlled inverted pendulum. Int. J. Nonlinear Mech. **31**, 215–227 (1996)
16. Huang, J., Ding, F., Fukuda, T., Matsuno, T.: Modeling and velocity control for a novel narrow vehicle based on mobile wheeled inverted pendulum. IEEE Trans. Control Syst. Technol. **21**, 1607–1617 (2013)
17. Kapitza, P.L.: Dynamic stability of a pendulum when its point of suspension vibrates. Soviet Phys. JETP **21**, 588–592 (1951)
18. Kapitza, P.L.: Pendulum with a vibrating suspension. Usp. Fiz. Nauk (in Russian) **44**, 7–15 (1951)
19. Kim, K.D., Kumar, P.: Real-time middleware for networked control systems and application to an unstable system. IEEE Trans. Control Syst. Technol. **21**, 1898–1906 (2013)
20. Krasnosel'skii, M.A., Burd, V.S., Kolesov, J.S.: Nonlinear Almost Periodic Oscillations. Wiley, New York (1973)

21. Krasnosel'skii, M.A., Pokrovskii, A.V.: Systems with Hysteresis. Springer, Berlin-Heidelberg-New York-Paris-Tokyo (1989)
22. Kuwana, Y., Shimoyama, I., Sayama, Y., Miura, H.: Synthesis of pheromone-oriented emergent behavior of a silkworm moth. In: Intelligent Robots and Systems '96, IROS 96, Proceedings of the 1996 IEEE/RSJ International Conference on, vol. 3, pp. 1722–1729 (1996)
23. Li, G., Liu, X.: Dynamic characteristic prediction of inverted pendulum under the reduced-gravity space environments. Acta Astronaut. **67**, 596–604 (2010)
24. Lozano, R., Fantoni, I., Block, D.J.: Stabilization of the inverted pendulum around its homoclinic orbit. Syst. Control Lett. **40**, 197–204 (2000)
25. Luo, Z.H., Guo, B.Z.: Shear force feedback control of a single-link flexible robot with a revolute joint. IEEE Trans. Autom. Control **42**, 53–65 (1997)
26. Magnus, K., Popp, K.A.: Schwingungen: eine Einfuehrung in die physikalische Grundlagen und die theoretische Behandlung von Schwingungsproblemen. Teubner B.G, GmbH (1997)
27. Mason, P., Broucke, M., Piccoli, B.: Time optimal swing-up of the planar pendulum. IEEE Trans. Autom. Control **53**, 1876–1886 (2008)
28. Mata, G.J., Pestana, E.: Effective hamiltonian and dynamic stability of the inverted pendulum. Eur. J. Phys. **25**, 717 (2004)
29. Merkin, D.R.: Introduction to the Theory of Stability. Springer, New York (1997)
30. Mikheev, Y.V., Sobolev, V.A., Fridman, E.M.: Asymptotic analysis of digital control systems. Autom. Remote Control **49**, 1175–1180 (1988)
31. Miroshnik, I.V.: Automatic Control Theory. Piter, St.Peterburg (2006). (in Russian)
32. Nelepin, R.A. (ed.): Methods of Investigation of Automatic Control Nonlinear Systems. Nauka, Moscow (1975). (in Russian)
33. Pierce-Shimomura, J.T., Morse, T.M., Lockery, S.R.: The fundamental role of pirouettes in caenorhabditis elegans chemotaxis. J. Neurosci. **19**, 9557–9569 (1999)
34. Pippard, A.B.: The inverted pendulum. Eur. J. Phys. **8**, 203 (1987)
35. Pliss, V.A.: Nonlocal Problems of the Theory of Oscillations. Academic Press (1966)
36. Reshmin, S.A., Chernous'ko, F.L.: A time-optimal control synthesis for a nonlinear pendulum. J. Comput. Syst. Sci. Int. **46**, 9–18 (2007)
37. Sato, C.: Correction of stability curves in Hill-Meissner's equation. Math. Comput. **20**, 98–106 (1966)
38. Sazhin, S., Shakked, T., Katoshevski, D., Sobolev, V.: Particle grouping in oscillating flows. Eur. J. Mech. B-Fluid. **27**, 131–149 (2008)
39. Semenov, M.E., Grachikov, D.V., Mishin, M.Y., Shevlyakova, D.V.: Stabilization and control models of systems with hysteresis nonlinearities. Eur. Res. **20**, 523–528 (2012)
40. Semenov, M.E., Grachikov, D.V., Rukavitsyn, A.G., Meleshenko, P.A.: On the state feedback control of inverted pendulum with hysteretic nonlinearity. In: MATEC Web of Conferences 16, 05009 (2014)
41. Semenov, M.E., Meleshenko, P.A., Nguyen, H.T.T., Klinskikh, A.F., Rukavitcyn, A.G.: Radiation of inverted pendulum with hysteretic nonlinearity. In: PIERS Proceedings, Guangzhou, China, August 25–28, pp. 1442–1445 (2014)
42. Semenov, M.E., Shevlyakova, D.V., Meleshenko, P.A.: Inverted pendulum under hysteretic control: stability zones and periodic solutions. Nonlinear Dyn. **75**, 247–256 (2014)
43. Sieber, J., Krauskopf, B.: Complex balancing motions of an inverted pendulum subject to delayed feedback control. Physica D **197**, 332–345 (2004)
44. Siuka, A., Schöberl, M.: Applications of energy based control methods for the inverted pendulum on a cart. Robot. Auton. Syst. **57**, 1012–1017 (2009)
45. Stephenson, A.: On an induced stability. Philos. Mag. **15**, 233 (1908)
46. Tang, J., Ren, G.: Modeling and simulation of a flexible inverted pendulum system. Tsinghua Sci. Technol. **14**(Suppl. 2), 22–26 (2009)
47. Wang, J.J.: Simulation studies of inverted pendulum based on pid controllers. Simul. Model. Pract. Theor. **19**, 440–449 (2011)
48. Xu, C., Yu, X.: Mathematical model of elastic inverted pendulum control system. Control Theor. Technol. **2**, 281–282 (2004)

49. Yavin, Y.: Control of a rotary inverted pendulum. Appl. Math. Lett. **12**, 131–134 (1999)
50. Yue, J., Zhou, Z., Jiang, J., Liu, Y., Hu, D.: Balancing a simulated inverted pendulum through motor imagery: an eeg-based real-time control paradigm. Neurosci. Lett. **524**, 95–100 (2012)
51. Zhang, Y.X., Han, Z.J., Xu, G.Q.: Expansion of solution of an inverted pendulum system with time delay. Appl. Math. Comput. **217**, 6476–6489 (2011)

Index

M. Belhaq (ed.), *Structural Nonlinear Dynamics and Diagnosis*,
Springer Proceedings in Physics 168, DOI 10.1007/978-3-319-19851-4